Journal of Applied Mathematics

Mathematical and Numerical Modeling in Geotechnical Engineering

Guest Editors: Ga Zhang, Pengcheng Fu, and Fayun Liang

Mathematical and Numerical Modeling in Geotechnical Engineering

Journal of Applied Mathematics

Mathematical and Numerical Modeling in Geotechnical Engineering

Guest Editors: Ga Zhang, Pengcheng Fu, and Fayun Liang

Editorial Board

Contents

Hindawi Publishing Corporation
Journal of Applied Mathematics
Volume 2013, Article ID 123485, 1 page
http://dx.doi.org/10.1155/2013/123485

Editorial

Mathematical and Numerical Modeling in Geotechnical Engineering

Ga Zhang,[1] Pengcheng Fu,[2] and Fayun Liang[3]

[1] *School of Civil Engineering, Tsinghua University, Beijing 100084, China*
[2] *Atmospheric, Earth, and Energy Division, Lawrence Livermore National Laboratory, Livermore, CA 94550, USA*
[3] *Department of Geotechnical Engineering, College of Civil Engineering, Tongji University, Shanghai 200092, China*

Correspondence should be addressed to Ga Zhang; zhangga@tsinghua.edu.cn

Received 2 October 2013; Accepted 2 October 2013

Mathematical and numerical modeling is a mature yet vibrant research area in geotechnical engineering. Its advancement has been accelerated in recent years by many emerging computational techniques as well as the increasing availability of computational power. A wide spectrum of approaches, on the basis of continuously advancing understanding of soil behavior, has been developed and applied to solve various problems in geotechnical engineering. These methods are increasingly playing important roles not only in achieving better understanding of fundamental behavior of geomaterials and geostructures but also in ensuring the safety and sustainability of large-scale complex geoengineering projects.

The aim of this special issue is to present original research articles on mathematical and numerical modeling in geotechnical engineering. A total of 26 high-quality peer-reviewed papers were selected to be published in this special issue. The topics cover various aspects as follows.

(1) Development and discussion of constitutive models of geomaterials including unsaturated soil, granular, rockfill, joint rock mass, and soil-structure interface.

(2) Proposal of analytical solutions to soil-structure interaction systems.

(3) Development of numerical methods to evaluate response of retaining wall, pile foundation.

(4) Novel applications of mathematical and numerical modeling to practical geotechnical projects such as pile foundations, soil nails, mining, joint rock mass, rock grouting, rockfill dams, and arc dams.

These papers are expected to be helpful references for all those in the field of mathematical and numerical modeling in geotechnical engineering.

Acknowledgments

The guest editors of this special issue would express their sincere gratitude to all the authors and anonymous reviewers who have generously contributed to this special issue.

Ga Zhang
Pengcheng Fu
Fayun Liang

Hindawi Publishing Corporation
Journal of Applied Mathematics
Volume 2013, Article ID 258721, 11 pages
http://dx.doi.org/10.1155/2013/258721

Research Article

Application of Taguchi Method and Genetic Algorithm for Calibration of Soil Constitutive Models

M. Yazdani,[1] A. Daryabari,[1] A. Farshi,[1,2] and S. Talatahari[3]

[1] *Civil and Environmental Engineering Faculty, Tarbiat Modares University, Tehran 1411713116, Iran*
[2] *Civil Engineering Faculty, Islamic Azad University of Tehran, Central Tehran Branch, Tehran, Iran*
[3] *Department of Civil Engineering, University of Tabriz, Tabriz 51666-14766, Iran*

Correspondence should be addressed to S. Talatahari; siamak.talat@gmail.com

Received 30 April 2013; Revised 27 August 2013; Accepted 18 September 2013

Academic Editor: Pengcheng Fu

A special inverse analysis method is established in order to calibrate soil constitutive models. Taguchi method as a systematic sensitivity analysis is conducted to determine the real values of mechanical parameters. This technique was applied on the hardening soil (as an elastoplastic constitutive model) which is calibrated using the results from pressuremeter test performed on "Le Rheu" clayey sand. Meanwhile, a genetic algorithm (GA) as a well-known optimization technique is used to fit the computed numerical results and observed data of the soil model. This study indicates that the Taguchi method can reasonably calibrate the soil parameters with minimum number of numerical analyses in comparison with GA which needs plenty of analyses. In addition, the contribution of each parameter on mechanical behavior of soil during the test can be determined through the Taguchi method.

1. Introduction

One of the most important aspects of geotechnical problems is to adopt a suitable constitutive model for each material. Then, one or more appropriate experimental and/or field tests should be conducted to find the mechanical parameters of each constitutive model. When a set of parameters used in a model is selected so that it creates the most precise coincidence with the soil behavior, then the constitutive model is said to be calibrated. Generally, there are different methods ranging from simple to advanced for calibration of soil constitutive models. Simple conventional calibration techniques typically use stress and strain levels at certain states in which a material undergoes during specific types of laboratory tests. Sometimes, this method of calibration fails to capture the overall behavior of a material, that is, behavior at every point in stress-strain path [1]. For example, in a direct shear test, sets of normal and shear stresses in failure condition are used to find the peak values of internal friction angle and cohesion. However, often the other features of soil behavior such as the variation of shear stress versus shear displacement are not considered. Therefore, there is a vital need to fill this gap and find a much more comprehensive way to calibrate the constitutive models for soils. The best-proposed method to satisfy this requirement is the inverse analysis technique, which is based on mathematical solutions to find the best match between stress-strain curves.

Many researchers adopted inverse analysis method with different modifications. Cekerevac et al. [2] proposed an inverse calibration approach in which quasi-Newton and stochastic methods were used as optimization tools. They employed this method to calibrate Hujeux constitutive model for the results of isotropically consolidated drained triaxial compression tests. Quasi-Newton and stochastic methods were used to search for local and global minimums, respectively [2]. Calvelloet applied the inverse analysis techniques to calibrate hardening soil (HS) constitutive model for Chicago glacial clays. They used the results of triaxial compression tests along with the displacement profile recorded from inclinometer readings in a supported excavation in glacial clays [3]. In these researches, classical optimization tools were used. These methods are based on the derivatives of the objective function. However, such optimization techniques may lead to computational difficulties during the calculation of error function derivatives [4–6].

In this research, a new systematic search technique is proposed on the basis of genetic algorithm (GA) [7–12] and Taguchi method [13–16]. GA as a well-known metaheuristic algorithm can be utilized to calibrate any soil constitutive model by means of the results obtained from any laboratory test and/or in situ experiment [2]. GA needs only an objective function rather than its derivatives. In this way, the shortcomings of classical methods will be eliminated as a result. However, in order to decrease the computational time, sensitivity analyses are required to select only the dominant parameters when the input parameters affecting the mechanical behavior are numerous. In this study, sensitivity analyses are carried out systematically using the well-known Taguchi method. This method which is conventionally used for the design of laboratory experiments can be treated as a modern technique in geotechnical application.

Genichi Taguchi, who first introduced this method during the late 1940s, utilized the conventional statistical tools in a simplified form by identifying a set of stringent guidelines for experiment layout and the analysis of results [13]. He made an applicable method for design and analysis of factorial experiments which is mainly used in quality engineering. This method, well known for its industrial applications to identify sensitive parameters for a given target, has fewer applications in geotechnics, particularly on material property identification [13].

In this paper, the results of pressuremeter tests [17, 18] which are performed on clayey sand in "Le Rheu" site located in France have been adopted for calibration of soil constitutive model [19]. The proposed method for inverse calibration is expressed using a special example which entails the $P-\Delta V/V_0$ curve obtained by pressuremeter test in a particular depth [20]. The constitutive law of this soil is assumed to be HS model due to the behavior that is exhibited during laboratory results. Thereafter, the inverse calibration is repeated with the reduced number of input parameters, obtained from the Taguchi method.

2. Specifications of the Soil in "Le Rheu" Site

The site is located in the west part of France, in a region called "Le Rheu." The soil of this site contains reddish sand for tens of meters. Several in situ and laboratory tests have been performed on this soil to identify its mechanical and engineering characteristics. The main reason for selection of this site in current research is the uniformity of the soil type in different depths and the existence of water table at very low levels. These conditions reduce the complexity of modeling process and let all efforts be concentrated on the mathematical solution for inverse calibration.

The results of pressuremeter tests are available at three points of B4, P1, and P2 (Figure 1) in various depths of 2 m, 3 m, 4 m, and 5 m [19]. However, in this study, only the curve related to point B4 at the depth of 2 m was selected. Figure 1 illustrates the results of tests at point B4 in the form of $P-\Delta V/V_0$ curve.

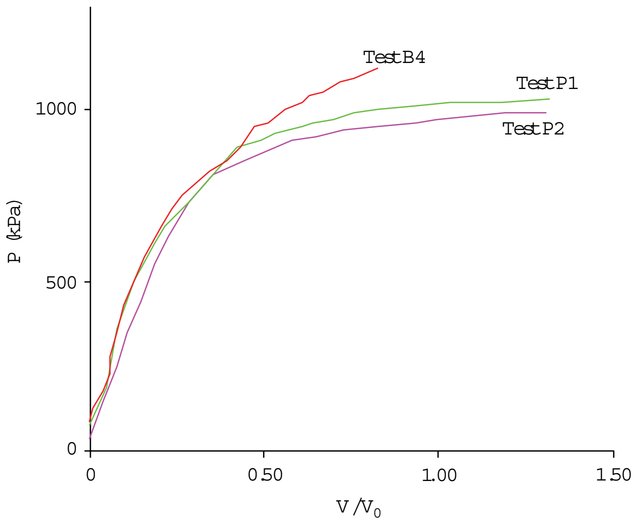

Figure 1: Pressuremeter curves at a depth of 2 m after being modified by lift-off method.

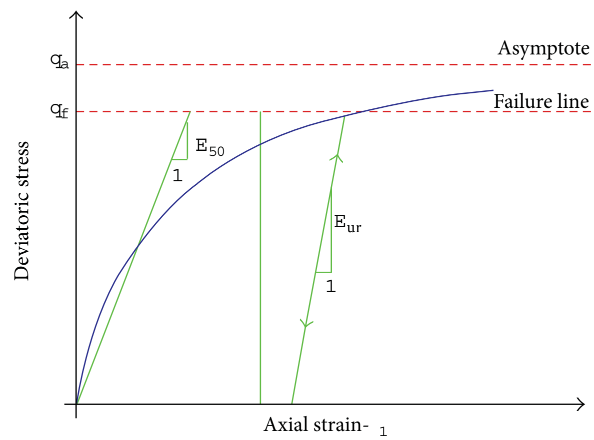

Figure 2: Hyperbolic stress-strain relation in primary loading for a standard drained triaxial test.

3. Hardening Soil Model

The hardening soil model is an advanced model for simulating the behavior of both soft and stiff soils. When subjected to primary deviatoric loading, the soil shows a decreasing stiffness and simultaneously irreversible plastic strains developing. In the special case of a drained triaxial test, the observed relationship between the axial strain and the deviatoric stress can be well approximated by a hyperbola function, as (Figure 2):

$$-\varepsilon_1 = \frac{1}{2E_{50}} \frac{q}{1-q/q_a} \quad \text{for } q < q_f. \tag{1}$$

In contrast to an elastic-perfectly plastic model, the yield surface of a hardening plasticity model is not fixed in principal stress space, but it can expand due to plastic straining. Distinction can be made between two main types of hardening, namely, shear hardening and compression hardening. Shear hardening is used to model irreversible strains

Table 1: HS input parameters [3].

Basic parameters	Explanation	Initial estimates
c	Cohesion	y-axis intercept in $\sigma_n - \tau$ stress space
φ	Friction angle	Slope of failure line in $\sigma_n - \tau$ stress space
ψ	Dilatancy angle	Function of φ_{peak} and φ_{failure}
E_{50}^{ref}	Secant stiffness in standard drained triaxial test	y-axis intercept in $\log_{(\sigma_3/P^{\text{ref}})} - \log_{(E_{50})}$ space
$E_{\text{oed}}^{\text{ref}}$	Tangent stiffness for primary oedometer loading	y-axis intercept in $\log_{(\sigma_v/P^{\text{ref}})} - \log_{(E_{50})}$ space
m	Power for stress-level dependency of stiffness	Slope of trend line in $\log_{(\sigma_3/P^{\text{ref}})} - \log_{(E_{50})}$ space

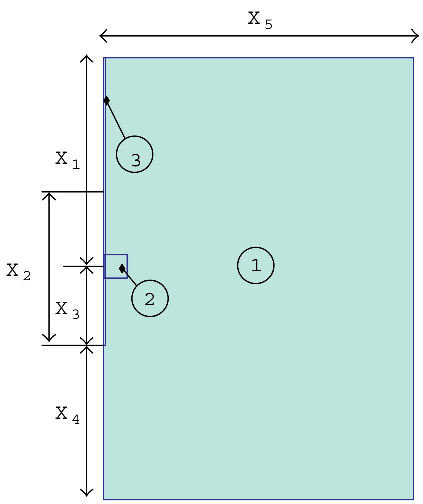

Figure 3: Geometry of Menard pressuremeter test model.

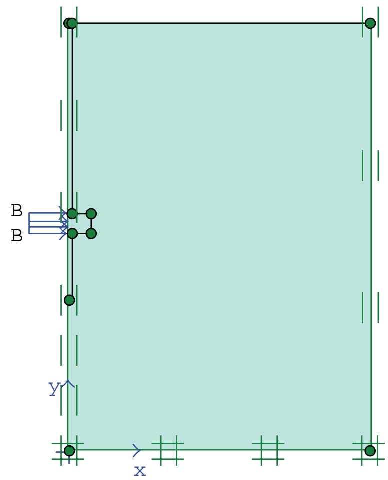

Figure 4: Boundary conditions and loading position.

due to primary deviatoric loading. Compression hardening is used to model irreversible plastic strains due to primary compression in oedometer loading and isotropic loading. Both types of hardening are contained in the present model. Table 1 presents input parameters of the HS model.

4. Numerical Modeling of Menard Pressuremeter Test

The first step of numerical modeling is generating the geometry. A mass of soil should be considered in which a borehole is dug to model the pressuremeter test. Then the pressure is induced to the boundary of the soil element adjacent to the middle cell of the probe. Because of the symmetric geometry and loading, only a half of the geometry is modeled (Figure 3). Three regions are identified in Figure 3, as follows:

Region *1* shows soil mass around the borehole in which the stress-field induced by loading can be assumed negligible.

Region *2* is the area exposed to direct impact of induced pressure, so it needs a finer mesh. This area consists of a 20 cm × 20 cm square, where the height implies the height of pressuremeter probe middle cell. Loading occurs on the inner boundary of this square (left side of the square in Figure 3).

Region *3* stands for the borehole which will be eliminated at the first phase of analysis. Illustrated dimensions in Figure 3 are as follows:

X_1: distance between probe center and ground surface (i.e., depth of experiment) = 2 m;

X_2: probe height = 1.5 m;

X_3: probe center distance to the bottom of the borehole (i.e., half height of the probe) = 75 cm;

X_4: depth of the probe = 1.5 m;

X_5: 50 times of the borehole diameter (50 × 0.06 m = 3 m).

The boundary conditions and loading position are defined in Figure 4. The pressure, which is made by expansion of the middle cell of the probe, will be induced in analysis phase.

Mesh is generated in the next step as shown in Figure 5. Since the displacements and stresses produced in region 2 are very important, a finer mesh is considered for this part. According to high value of height-width ratio of region 3, a refined mesh is needed in this region. To increase the precision of calculations, 15-node triangular elements have been used.

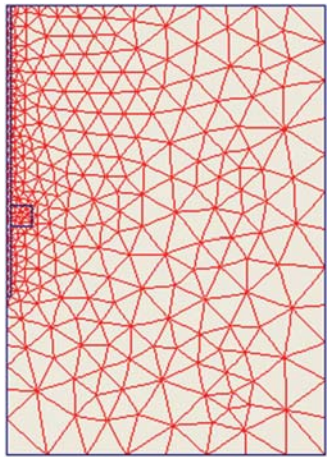

Figure 5: Mesh generation for pressuremeter model.

For the current pressuremeter test modeling, analysis phases have been defined as follows:

Phase 1. Borehole is excavated and the stresses due to the excavation are calculated. Calculations in this phase are in the plastic zone of the soil.

Phase 2. Pressuremeter apparatus is planted in the desired depth of the borehole (2 meters in this case) and the experiment starts by inducing a 100 kPa pressure. In this phase, displacements of the previous phase, due to the borehole excavation, are set to zero.

Phases 3 to 46. In subsequent phases, pressure increases gradually. In this experiment a 100 kPa incensement is considered for each step. Therefore, in phase 3, we have $p = 200$ kPa and in phase 4, $p = 300$ kPa, and so forth until phase 46 which it is $p = 4500$ kPa. It should be mentioned that from phase 2 on, calculations are updated according to the mesh type and produced large displacements and they may not necessarily continue to phase 46. The final step depends on the time of failure.

5. Inverse Analysis for Calibration of Soil Constitutive Models

In inverse analysis, a given model is calibrated by iteratively changing input values until the simulated output values match the observed data [3]. The basic form of inverse analysis technique can be categorized as a trial and error approach (Figure 6). When the number of input parameters is too large, this method may be inefficient or impractical. Therefore, to avoid this troublesome effort, providing a systematic approach seems to be necessary. In the following section, an optimization tool is introduced in order to systematically minimize the difference between numerical and experimental results.

5.1. Systematic Inverse Analysis Method. The given constitutive model is calibrated by a repetitive procedure in systematic inverse analysis. In this cycle, input parameters of the constitutive model are changed until the results of numerical simulation match the experimental responses. In this research, the results of Menard pressuremeter tests have been considered as the soil response used for calibration of HS model. A set of input parameters for soil constitutive model which leads to the coincidence of in situ pressuremeter curve and model pressuremeter simulation curve is desired. There is an extreme need for a quantity, which shows the degree of coincidence between the two mentioned curves in order to solve the problem. This quantity which is error function is generally defined as “area between the two curves,” as

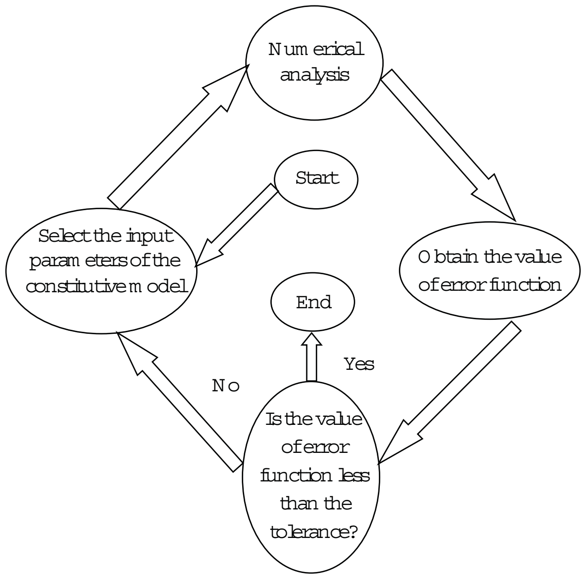

Figure 6: General inverse analysis diagram for calibration of soil constitutive models.

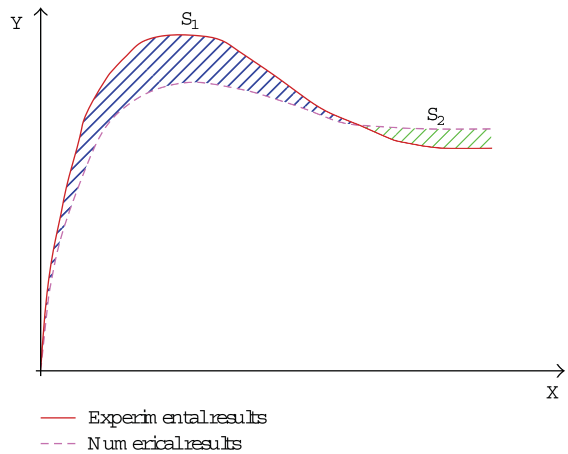

Figure 7: Concept of error function.

$$\text{Error Function} = S_1 + S_2 = \int \left| Y^{\text{Experimental}} - Y^{\text{Numerical}} \right| dx. \quad (2)$$

This concept is illustrated in Figure 7.

Table 2: The best set of parameters obtained by systematic inverse analysis via GA optimization tool.

Err. fun (kPa)	m	ψ (deg)	φ (deg)	C (kPa)	E (kPa)
21.8	0.76	0.23	35.11	20.14	72913

In this paper, an error function with the following form is used, as

$$\text{Objective Function} = \sum_{i=1}^{n} \frac{\left|P^{\text{Experimental}} - P^{\text{Numerical}}\right|}{n}, \quad (3)$$

where Σ represents the summation of its subsequent term (n discrete values) and n is the number of used experimentally obtained data in the process.

Therefore, the calibration is changed into a familiar optimization problem in which finding a feasible set of soil's model parameters leads to the least value for error function. Soil constitutive model parameters are those 6 parameters previously introduced in Table 1. Since there is a need to change the level of each parameter without any limitations, the parameter $E_{\text{oed}}^{\text{ref}}$ is eliminated from the inverse analysis procedure. As there is not the possibility for $E_{\text{oed}}^{\text{ref}}$ to be changed freely, this parameter should be removed from the cycle and the default value for this parameter will be accepted ($E_{\text{oed}}^{\text{ref}} = E_{50}^{\text{ref}}$). Thus, the number of input parameters reduces to 5.

Now, this idealized problem is ready to be solved. The optimization tool used in this research is GA. There are many computer programs written for GA, but none is able to communicate with PLAXIS. To solve this problem, instead of using available programs for GA, a code is written for GA by Visual Basic (VB), which has the ability to interface with the PLAXIS, a useful finite element program which can perform the analysis according to predefined stages. Therefore, this code can change the value of each parameter in that optimization process and obtain the objective function. Figure 8 presents the algorithm with more details.

The best set of parameters obtained by this method is gained after 496 cycles as shown in Table 2. Figure 9 illustrates a very good coincidence between the in situ and simulation curves. Inverse analysis algorithms allow simultaneous calibration of multiple input parameters [3]. On the other hand, the required time for inverse analysis intensively increases by increasing the number of parameters. However, the computational time can be reduced to a large extent by removing some unimportant parameters. A sensitivity analysis attains the degree of importance of each parameter [21, 22]. In this paper, "Taguchi method" is used to fulfill this aim.

5.2. Sensitivity Analysis by Taguchi Method. Taguchi method is conventionally an approach for sensitivity analysis method, by changing a selected factor in different levels, while the other factors are kept constant. Then, the same process repeats exactly for each of the remaining factors. In Taguchi method, all factors are changed simultaneously according to predefined tables called "orthogonal arrays." Choosing the appropriate orthogonal array for a given problem is called "experiment design." The first step to perform a systematic sensitivity analysis is to define experiment design. In order to generate design experiments (i.e., finding the suitable orthogonal array), "degrees of freedom" is needed, which is obtained as follows:

$$(\text{df})_{\text{EXP}} = \sum (\text{df})_{\text{factor}} + \sum (\text{df})_{\text{interaction}}. \quad (4)$$

In this study, for each of the 5 factors, 4 levels are considered. Therefore, the degree of freedom for each factor equals 3 ($(\text{df})_A = k_A - 1$, k_A = number of levels for factor A). Interactions' degree of freedom will be zero since no interaction is considered. By substituting the mentioned values into (4), $(\text{df})_{\text{EXP}}$ will be 15.

The smallest orthogonal array with the degree of freedom greater than (or equal to) the experiment degree of freedom should be found in this step. Degree of freedom for L16 array is 15: ($(\text{df})_{\text{O.A}}$ = No. Trial $- 1 \rightarrow 16 - 1 = 15$), so L16 array can be obtained (Table 3). But L16 contains only 2-level factors, while an orthogonal array with 4-level factors is needed. Therefore, using the rule of converting 2-level columns into 4-level columns, M16 orthogonal array is achieved (Table 4). Variation interval of each factor is divided into 4 equal divisions as mentioned before, thus factor levels will be as Table 5. Factors can be assigned to columns of orthogonal array M16, now. Here, as interaction between factors has not been taken into account, the factors will arbitrarily be assigned to any desired column of M16.

Final plan of experiments is shown in Table 6. In this table, each row stands for an experiment, so the pressuremeter finite element model should be run 16 times, according to the conditions of the orthogonal array M16. The results obtained after running these experiments are shown in the last column of Table 6.

Obtained data of Table 6 are analyzed according to Taguchi ANOVA table (Analysis of variance). Results are shown in Table 7. The last column of Table 7 shows the contribution percent of each parameter. Contribution percent shows the sensitivity degree of numerical model response with respect to each parameter variations. As it can be seen in this table, parameter c has the most, and parameter ψ has the least degree of importance (sensitivity degree).

The parameter with the degree of importance less than 10% of the most significant factor will be assigned a constant value and removed from the inverse analysis process. As a result, parameter ψ has a very small degree of importance (4.8%). This value is less than 10% of the importance degree of the most significant parameter (here c with contribution percent of 53.2%). Therefore, a constant value is assigned to ψ (here, $\psi = 2^\circ$). Now, inverse analysis can be performed with the 4 remaining parameters. The result of this analysis is shown in Table 8. Figure 9 illustrates the simulated pressuremeter curve obtained from numerical analysis based on Table 8 parameters in comparison with the in situ pressuremeter curve.

5.3. Comparing to Results of Direct Calibration. The HS constitutive model for "Le Rheu" soil has been calibrated directly [5]. In situ and laboratory tests were utilized to

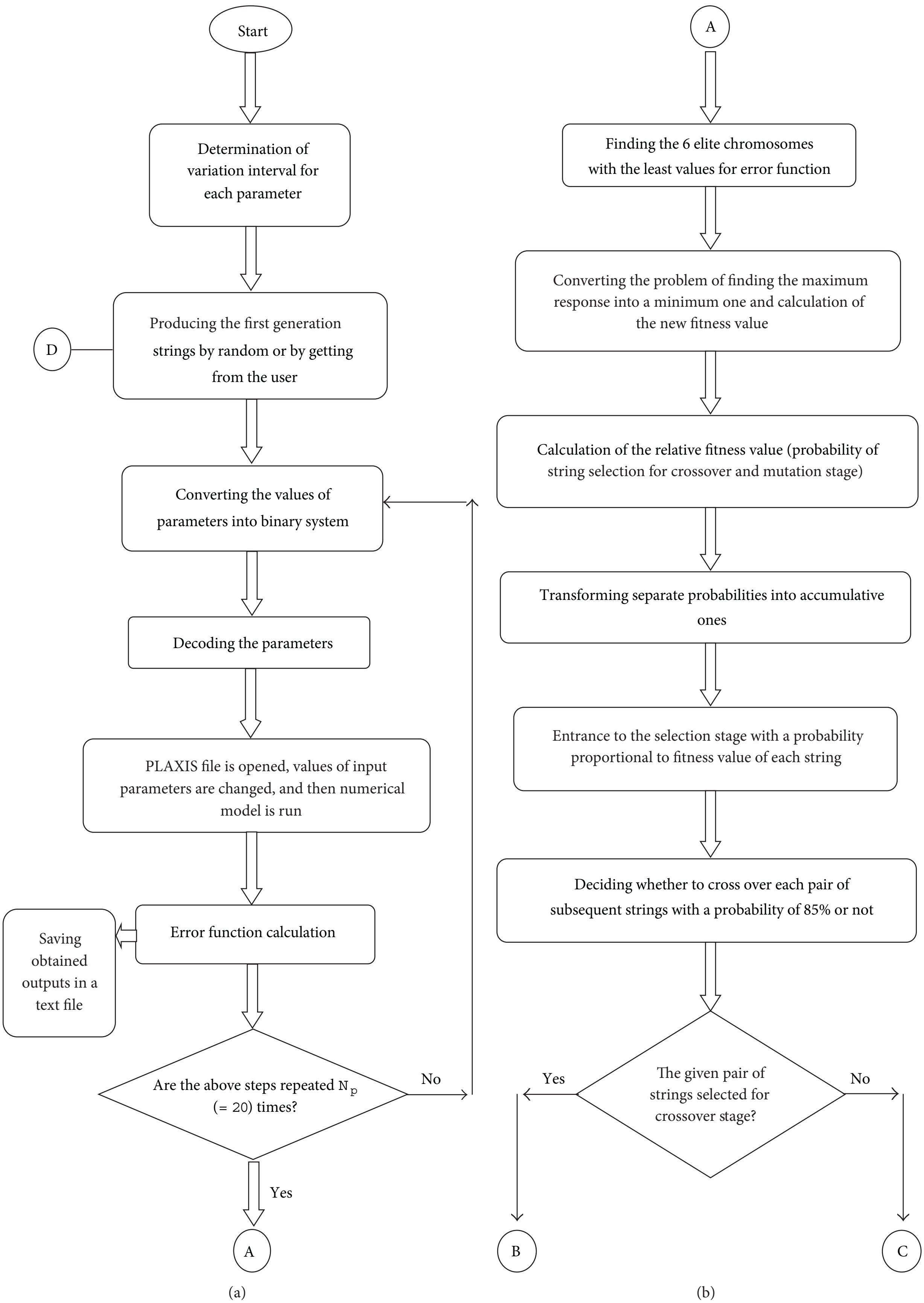

Figure 8: Continued.

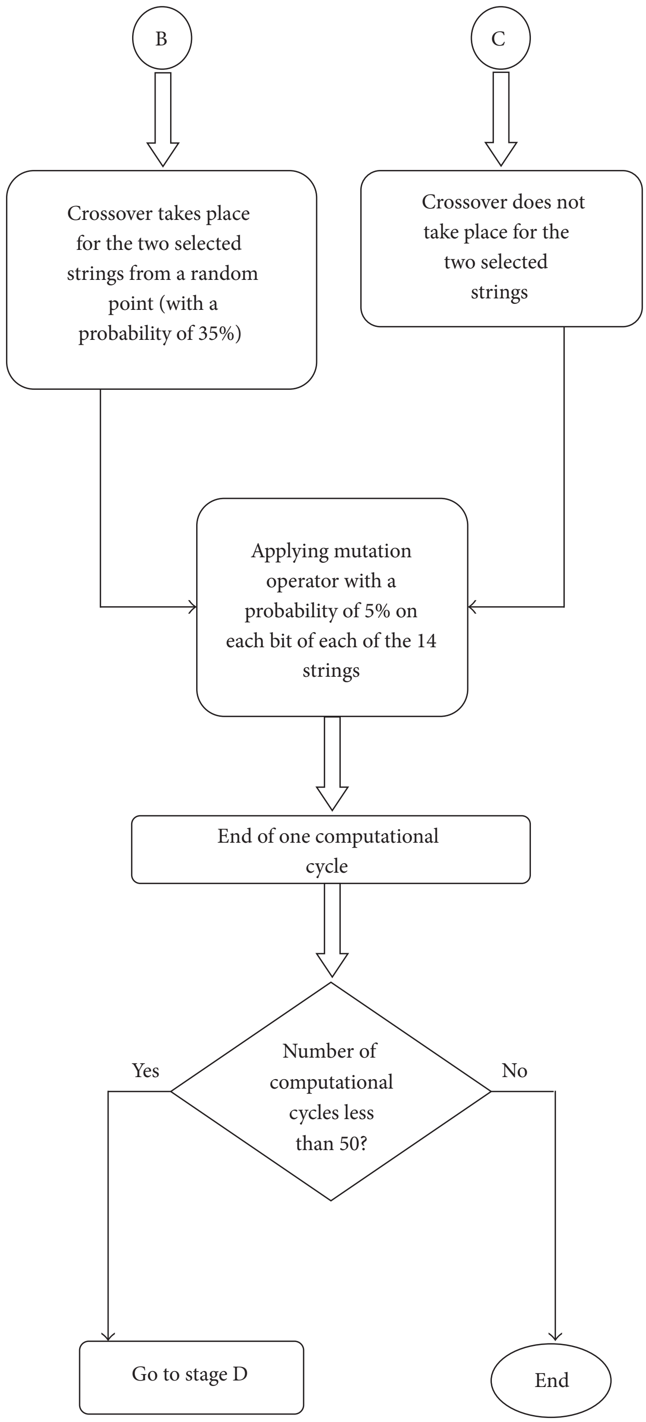

(c)

Figure 8: The algorithm of the written code for systematic inverse analysis.

assess the value of HS soil model parameters as shown in Table 9. For example, vane shear test is used to estimate the values of c and φ. After substituting obtained parameters into the simulated pressuremeter test model and running the numerical model, stress-volumetric strain curve is attained. This curve is shown in company with in situ pressuremeter curve in Figure 9. As it can be seen, the two curves have a similar trend and they are nearly parallel but there is no close coincidence.

6. Discussion

The main purpose of the paper is to introduce a systematic approach to derive mechanical parameters of a typical soil

Table 3: L16 orthogonal array.

	1	2	3	4	5	6	7	8	9	10	11	12	13	14	15
1	1	1	1	1	1	1	1	1	1	1	1	1	1	1	1
2	1	1	1	1	1	1	1	2	2	2	2	2	2	2	2
3	1	1	1	2	2	2	2	1	1	1	1	2	2	2	2
4	1	1	1	2	2	2	2	2	2	2	2	1	1	1	1
5	1	2	2	1	1	2	2	1	1	2	2	1	1	2	2
6	1	2	2	1	1	2	2	2	2	1	1	2	2	1	1
7	1	2	2	2	2	1	1	1	1	2	2	2	2	1	1
8	1	2	2	2	2	1	1	2	2	1	1	1	1	2	2
9	2	1	2	1	2	1	2	1	2	1	2	1	2	1	2
10	2	1	2	1	2	1	2	2	1	2	1	2	1	2	1
11	2	1	2	2	1	2	1	1	2	1	2	2	1	2	1
12	2	1	2	2	1	2	1	2	1	2	1	1	2	1	2
13	2	2	1	1	2	2	1	1	2	2	1	1	2	2	1
14	2	2	1	1	2	2	1	2	1	1	2	2	1	1	2
15	2	2	1	2	1	1	2	1	2	2	1	2	1	1	2
16	2	2	1	2	1	1	2	2	1	1	2	1	2	2	1

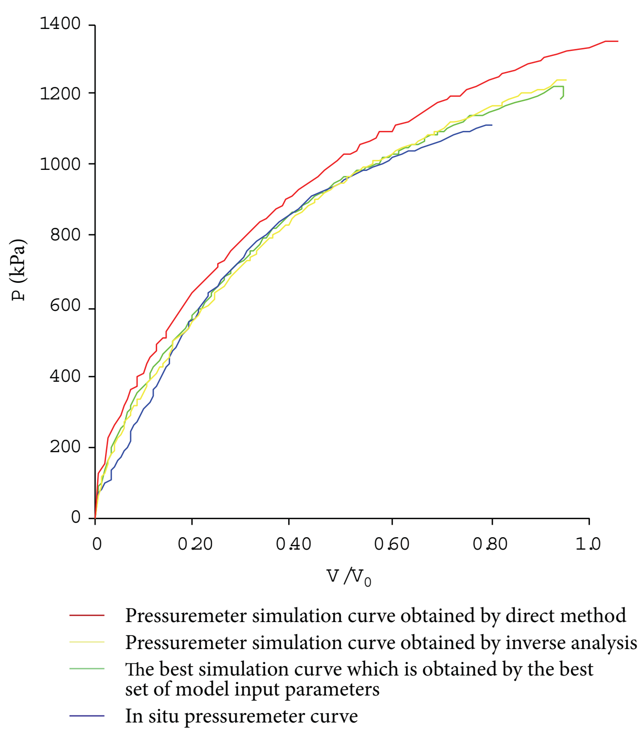

Figure 9: In situ pressuremeter curve in comparison with the best simulation curve, pressuremeter simulation curve obtained by inverse analysis (performed after sensitivity analysis), and pressuremeter simulation curve obtained by substituting field attained-parameters (direct method).

Table 4: Modified L16 orthogonal array (M16).

	1	2	3	4	5
1	1	1	1	1	1
2	1	2	2	2	2
3	1	3	3	3	3
4	1	4	4	4	4
5	2	1	2	3	4
6	2	2	1	4	3
7	2	3	4	1	2
8	2	4	3	2	1
9	3	1	3	4	2
10	3	2	4	3	1
11	3	3	1	2	4
12	3	4	2	1	3
13	4	1	4	2	3
14	4	2	3	1	4
15	4	3	2	4	1
16	4	4	1	3	2

Table 5: Considered levels for each factor.

Columns	Factors	Level (1)	Level (2)	Level (3)	Level (4)
1	E (kPa)	20000	40000	60000	80000
2	m	0.5	0.666	0.832	1
3	C (kPa)	1	15.66	30.32	45
4	φ	30	33.33	36.66	40
5	ψ	0	3.33	6.66	10

constitutive model based on an available test data. For adopted example of "Le Rheu" clayey sand, three different test data related to three points of B4, P1, and P2 were available at depth of 2 m. The proposed approach can be applied to the curve of each point independently, and then the corresponding mechanical parameters may be averaged to represent the mean values of the soil mechanical parameters of "Le Rheu" clayey sand at depth of 2 m. According to Figure 1, the parameters obtained from the points P1 and P2 should

Table 6: Final plan of experiments for this project.

Test number	E (kPa)	m	C (kPa)	φ (deg)	ψ (deg)	Result
1	20000	0.5	1	30	0	648
2	20000	0.666	15.66	33.33	3.33	410
3	20000	0.832	30.32	36.66	6.66	281
4	20000	1	45	40	10	191
5	40000	0.5	15.66	36.66	10	44
6	40000	0.666	1	40	6.66	660
7	40000	0.832	45	30	3.33	93
8	40000	1	30.32	33.33	0	159
9	60000	0.5	30.32	40	3.33	315
10	60000	0.666	45	36.66	0	256
11	60000	0.832	1	33.33	10	910
12	60000	1	15.66	30	6.66	203
13	80000	0.5	45	33.33	6.66	549
14	80000	0.666	30.33	30	10	272
15	80000	0.832	15.66	40	0	550
16	80000	1	1	36.66	3.33	750

Table 7: Results of ANOVA table.

Col. number	Factor	DOF (f)	Sum of Sqrs. (S)	Variance (V)	F-ratio (F)	Pure sum (S')	Percent contribution P (%)
1	E	3	308775.687	102925.229	—	308775.687	14.418
2	m	3	203893.687	67964.562	—	203893.687	9.52
3	C	3	1138383.187	379461.062	—	1138383.187	53.156
4	φ	3	386871.687	128957.229	—	386871.687	18.064
5	ψ	3	103635.187	34545.062	—	103635.187	4.839
Other/error		0					
Total:		15	2141559.437				100.00%

Table 8: The best set of soil constitutive model parameters obtained by systematic inverse analysis after performing sensitivity analysis and removing the unimportant parameter.

E (kPa)	C (kPa)	φ	ψ	m	Err. fun.
60629	28	34.8	2	0.98	28

Table 9: The set of parameters obtained by direct method (experimental method).

E (kPa)	C (kPa)	φ	ψ	m	Err. fun.
55000	35	32	2	0.5	75.30

be similar but they might be different from the point of B4. Therefore, there was no specific reason for selection of point B4, since the target was a presentation of the method.

Taguchi method was originally proposed to design experiments. However, in this paper it was adopted to derive the mechanical parameters of a soil through systematic inverse analyses. On the other hand, GA is an optimization technique which was utilized here to obtain the optimum parameters fitting to an available soil test data. Though, the above two methods are different tools in engineering and scientific practice, in this paper they were utilized for a single specific application, that is, the calibration of a soil constitutive model. Accordingly, the comparison achieved in the paper between Taguchi and GA methods is only attributed to the precision of the results and the number of analyses needed in each method. In addition, giving the relative significance of each mechanical parameter in soil constitutive model is another ability of the method based on Taguchi approach.

The results of obtained parameters (Table 8) and its corresponding Figure 9 have been obtained only through the Taguchi method without any need to GA. In the first cycle of Taguchi method, 5 soil parameters were selected (5 factors). However, since one of those parameters (ψ) observed to have little significance respect to the others, it was decided to assign it a constant value ($\psi = 2^{\circ}$) and run the second cycle of Taguchi with only 4 parameters. For this study, in each cycle of Taguchi method 16 analyses have been carried out based on orthogonal arrays of L16 (or M16). Table 4 presents the level of every factor (parameter) for each of 16 analyses. The values of factors in each of the 16 tests (analyses) were presented in Table 6. Thus, there is no need for GA in this approach.

Taguchi method is a systematic approach for designing experiments which investigates how different parameters affect the mean and variance of a process performance characteristic. However, it is very important to determine the most important parameters (factors) governing the process since the total number of parameters involving the process

Table 10: Comparison of used methods.

	Direct method	GA	Taguchi
Error function (kPa)	75	21.8	28
Number of analyses	1	496	16
Importance of parameters	NA	NA	√

might be high. In addition, the variation range of each parameter should be introduced as much as limited in order to define minimum number of levels. These considerations may need some experiences and, without such information, the method may not be effective and useful. Having a large number of parameters (factors) with a wide range of variation for each parameter tends to select the orthogonal arrays with numerous tests. This will be time consuming and expensive from computational costs point of view.

Regarding the ability of the method to be applied on other tests or constitutive behaviors, it can be useful to say that we have already utilized the method in order to extract the Mohr-Coulomb perfect plastic parameters of soil from the results of pile load tests [23]. In another research, the HS constitutive parameters of rock masses in site of "*Siah-bisheh*" were estimated from the monitoring results of powerhouse cavern [24].

7. Conclusions

In this research, a systematic inverse analysis approach is introduced for calibration of soil constitutive models. The capability of this method has been shown in the case of calibrating HS constitutive model for "Le Rheu" soil in pressuremeter stress path. The benefits of using this method are being able to be used for many laboratory or field tests, and also constitutive models, giving the whole parameters simultaneously, automatic procedure of calibration with least interpretation, and considering overall soil behavior (i.e., behavior at every point in stress-strain path).

The Taguchi method is a useful tool for parametric analysis which can be beneficial in geotechnical engineering due to its relatively high precision and low time consumption. Furthermore, the significance of the parameters can be evaluated quantitatively using the Taguchi method. In the current research, it was exhibited that the parameters of soil cohesion and internal friction angle have the most influence on the hardening soil elastoplastic constitutive model and the dilatancy angle has the least influence. This conclusion is probably valid only for clayey sand located in Le Rheu site. For granular soils with large size grains such as gravels in which the dilatancy angle is large, it is possibly expected to observe more contribution of dilatancy.

As illustrated in Tables 2, 8, and 9, based on the error function values and the calculation time, it is obvious that the Taguchi method is faster than both direct method and the single GA and more precise than the direct method. The results obtained from the Taguchi method are close to the GA, but with less computational time. As shown in Table 10, an error function of 21.8 was achieved with 496 analyses of the GA method. The direct method gave an error function of 75.3 with a very low precision. However, an error function of 28 was concluded with mere 16 analyses, using the Taguchi method. Hence, it is obvious that the Taguchi method is a cheap and fast method to gain acceptable results.

References

[1] S. Pal, G. W. Wathugala, and S. Kundu, "Calibration of a constitutive model using genetic algorithms," *Computers and Geotechnics*, vol. 19, no. 4, pp. 325–348, 1996.

[2] C. Cekerevac, S. Girardin, G. Klubertanz, and L. Laloui, "Calibration of an elasto-plastic constitutive model by a constrained optimisation procedure," *Computers and Geotechnics*, vol. 33, no. 8, pp. 432–443, 2006.

[3] M. Calvello and R. J. Finno, "Selecting parameters to optimize in model calibration by inverse analysis," *Computers and Geotechnics*, vol. 31, no. 5, pp. 411–425, 2004.

[4] A. Kaveh and S. Talatahari, "Particle swarm optimizer, ant colony strategy and harmony search scheme hybridized for optimization of truss structures," *Computers and Structures*, vol. 87, no. 5-6, pp. 267–283, 2009.

[5] A. Kaveh and S. Talatahari, "A novel heuristic optimization method: charged system search," *Acta Mechanica*, vol. 213, no. 3-4, pp. 267–289, 2010.

[6] A. Kaveh and S. Talatahari, "Optimal design of skeletal structures via the charged system search algorithm," *Structural and Multidisciplinary Optimization*, vol. 41, no. 6, pp. 893–911, 2010.

[7] D. Goldberg, *Genetic Algorithms in Search, Optimization and Machine Learning*, Addison-Wesley, Boston, Mass, USA, 1989.

[8] M. D. Vose, *The Simple Genetic Algorithm: Foundations and Theory*, MIT, Cambridge, Mass, USA, 1999.

[9] M. Gen and R. Cheng, *Genetic Algorithms and Engineering Design*, John Wiley & Sons, New York, NY, USA, 1997.

[10] H. Demuth and M. Beale, *Genetic Algorithm and Direct Search Toolbox User's Guide for Use with MATLAB*, version 1, MathWorks, 1st edition, 2004.

[11] W. M. Spear, *Adapting Crossover in a Genetic Algorithm*, Naval Research Laboratory, Washington, DC, USA, 2003.

[12] S. Levasseur, Y. Malécot, M. Boulon, and E. Flavigny, "Soil parameter identification using a genetic algorithm," *International Journal for Numerical and Analytical Methods in Geomechanics*, vol. 32, no. 2, pp. 189–213, 2008.

[13] R. K. Roy, *A Primer on the Taguchi Method*, Van Nostrand Rein hold, New York, NY, USA, 1990.

[14] P. J. Ross, *Taguchi Techniques for Quality Engineering: Loss Function, Orthogonal Experiments, Parameter and Tolerance Design*, McGraw-Hill, New York, NY, USA edition, 1996.

[15] K. Balaraman, S. Mukherjee, A. Chawla, and R. Malhotra, *Inverse Finite Element Characterization of Soft Tissues Using Impact Experiments and Taguchi Method*, SAE International, 2005.

[16] R. K. . Roy, *Design of Experiments Using the Taguchi Approach: 16 Steps to Product and Process Improvement*, Wiley, New York, NY, USA, 2001.

[17] B. G. Clarke, *Pressuremeters in Geotechnical Design*, Blackie Academic and Professional, an Imprint of Chapman and Hall, 1st edition, 1995.

[18] F. Baguelin, J. F. Jezequel, and D. H. Shields, *The Pressuremeter and Foundation Engineering*, Trans Tech, Clausthal, Germany, 1978.

[19] *Simulation of the Menard Pressuremeter Test Using the F.E.M Method*, Ecole Centrale, Paris, France, 1997.

[20] "Standard test method for pressuremeter testing in soils," ASTM Standard D4719-87, 1988.

[21] Z. Yang and A. Elgamal, "Application of unconstrained optimization and sensitivity analysis to calibration of a soil constitutive model," *International Journal for Numerical and Analytical Methods in Geomechanics*, vol. 27, no. 15, pp. 1277–1297, 2003.

[22] N. Dien, F. Jean-Marie, and M. Arezou, "Identification of parameters and validation of Hujeux model for a coarse soil," Laboratory of Soil, Structure and Material Mechanics CNRS UMR 8579, Ecole Centrale, Paris, France.

[23] M. Yazdani and P. Ghahremani, "Determination of bearing capacity for piles using systematic numerical analyses of pile load testing based on Taguchi method," *Civil Engineering Sharif Journal*, vol. 28-2, no. 4, pp. 39–51, 2013.

[24] A. Majnouni, *Estimation of rock mass parameters in Siah-Bisheh powerhouse cavern using Taguchi method [M.S. thesis]*, Tarbiat Modares University, Tehran, Iran, 2012.

Hindawi Publishing Corporation
Journal of Applied Mathematics
Volume 2013, Article ID 269594, 9 pages
http://dx.doi.org/10.1155/2013/269594

Research Article

Steering Parameters for Rock Grouting

Gunnar Gustafson, Johan Claesson, and Åsa Fransson

School of Civil Engineering, Chalmers University of Technology, 41296 Gothenburg, Sweden

Correspondence should be addressed to Åsa Fransson; asa.fransson@chalmers.se

Received 31 May 2013; Accepted 3 September 2013

Academic Editor: Ga Zhang

In Swedish tunnel grouting practice normally a fan of boreholes is drilled ahead of the tunnel front where cement grout is injected in order to create a low permeability zone around the tunnel. Demands on tunnel tightness have increased substantially in Sweden, and this has led to a drastic increase of grouting costs. Based on the flow equations for a Bingham fluid, the penetration of grout as a function of grouting time is calculated. This shows that the time scale of grouting in a borehole is only determined by grouting overpressure and the rheological properties of the grout, thus parameters that the grouter can choose. Pressure, grout properties, and the fracture aperture determine the maximum penetration of the grout. The smallest fracture aperture that requires to be sealed thus also governs the effective borehole distance. Based on the identified parameters that define the grouting time-scale and grout penetration, an effective design of grouting operations can be set up. The solution for time as a function of penetration depth is obtained in a closed form for parallel and pipe flow. The new, more intricate, solution for the radial case is presented.

1. Introduction

In Swedish tunnelling pregrouting is normally used when considered necessary for the reduction of groundwater inflows. Cement grout, occasionally with plasticisers added, is preferred for economical and environmental reasons. Recently, the increased demands on tunnel tightness have led to an approach to pregrouting where the whole tunnel is systematically pregrouted according to a few predetermined standard strategies. This has led to a massive increase of performed grouting, and subsequently there is a strong need for effective design methods and steering parameters for the grouting activities.

In pregrouting a fan of boreholes is drilled around the tunnel periphery ahead of the tunnel front, grout is injected through the boreholes in order to create a low permeability zone around the tunnel, and finally the tunnel is excavated by the drill and blast method within the zone until the next cycle starts with drilling of the grouting fan. Normally grouting boreholes, 15–18 m long, are used which give 3-4 blasting rounds per cycle.

Figure 1 shows the grouting fan and some fractures as a background for the design problem. Through the borehole grout is injected, which spreads through the fractures. At any time the grout has penetrated a distance, I, from the borehole, which is individual for each fracture. For a successful grouting the penetration between the boreholes should bridge the distance between the boreholes, L, for water-bearing fractures having a transmissivity, T, above a critical value determined by their frequency and the demands on tunnel tightness. Recent investigations of the transmissivity distributions of fractures in Swedish Precambrian crystalline rocks [1–3] have shown that only a small portion of the fractures and joints, 5–15% at a threshold level of $T = 10^{-9}$ m^2/s, are pervious and that the statistical distribution of the transmissivities of the conductive fractures is approximately lognormal.

The transmissivity is coupled to the hydraulic aperture of the fracture by the cubic law [4, 5]:

$$T = \frac{\rho_w g b^3}{12\mu_w}, \tag{1}$$

where μ_w is the viscosity, ρ_w is the density of water, and b is the so-called hydraulic aperture of the fracture. The hydraulic aperture determined by the cubic law has shown to be a good estimate for the grouting aperture [6, 7].

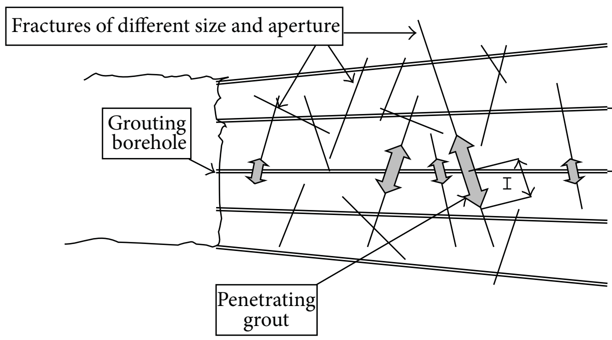

FIGURE 1: Grouting fan and grout penetration. Borehole distance L, grout penetration I.

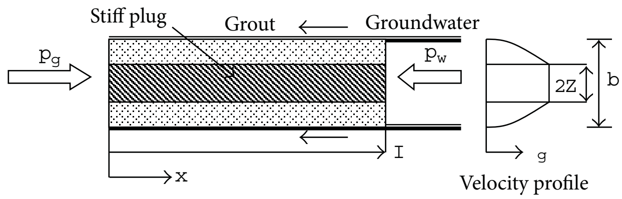

FIGURE 2: Grout penetrating a fracture.

From this it follows that in a borehole to be grouted, only a few fractures are pervious and only a small number of these contribute significantly to the groundwater flow through the rock because of the large skewness of the transmissivity distribution.

The normally used cement grouts can reasonably well be characterised as Bingham fluids [8–10]. They are thus characterised by a yield strength, τ_0, and a plastic viscosity μ_g. From the Bingham model it follows that flow can only take place in the parts of the fluid where the internal shear stresses exceed the yield strength. This means that a stiff plug is formed in the centre of the flow channel surrounded by plastic flow zones; see Figure 2. The advance of the grout front ceases when the shear stresses at the walls of the fracture equal the yield strength of the grout. A simple force balance of the difference between the grouting and the resisting water pressures, $\Delta p = p_g - p_w$, and the shear stress gives the maximum grout penetration, $I_{\max}$, for a fracture of aperture b (e.g. [9, 11]):

$$I_{\max} = \frac{\Delta p \cdot b}{2\tau_0}. \tag{2}$$

The relevant design question is thus how to make sure that the penetration length is long enough to bridge the distance between the grouting boreholes for the critical fractures and the length of time it takes to reach the maximum penetration or a significant portion of it.

In order to obtain an analytical solution, the problem has to be simplified. In particular, it is assumed that the aperture is constant, not varying along the fracture. The grout properties are assumed to be constant in time. These limitations should be kept in mind when these analytical solutions are used.

2. Derivation of Equations, Results, and Discussion

2.1. Grout Penetration. Let $I(t)$ be the position of the grout front at time t, Figure 2. The velocity of grout, dI/dt, moving in a horizontal facture of aperture b can according to Hässler [9] be calculated as

$$\frac{dI}{dt} = -\frac{dp}{dx} \cdot \frac{b^2}{12\mu_g}\left[1 - 3 \cdot \frac{Z}{b} + 4 \cdot \left(\frac{Z}{b}\right)^3\right], \tag{3}$$

where

$$Z = \tau_0 \cdot \left|\frac{dp}{dx}\right|^{-1}, \quad Z < \frac{b}{2}. \tag{4}$$

Assuming parallel flow and a viscosity of the grout much higher than for water, the pressure gradient can be simplified to be

$$\frac{dp}{dx} = -\frac{\Delta p}{I}. \tag{5}$$

Equations (4), (5) and (2), give $2Z/b = I/I_{\max}$. The equation for the relative penetration depth $I_D = I/I_{\max}$ becomes from (3) after simplifications

$$\frac{dI_D}{dt} = \frac{(\tau_0)^2}{6\mu_g \Delta p} \cdot \frac{2 - 3I_D + (I_D)^3}{I_D}, \qquad I_D = \frac{I}{I_{\max}} = \frac{2Z}{b}. \tag{6}$$

We define the characteristic time t_0 and the dimensionless time t_D:

$$t_0 = \frac{6\mu_g \Delta p}{(\tau_0)^2}, \qquad t_D = \frac{t}{t_0}. \tag{7}$$

Equation (6) gives the derivative dI_D/dt_D. The derivative of t_D as a function of I_D is

$$\frac{dt_D}{dI_D} = \frac{I_D}{2 - 3I_D + (I_D)^3} = \frac{I_D}{(2 + I_D)(1 - I_D)^2}. \tag{8}$$

The right-hand function of I_D is the ratio between two polynomials, which may be expanded in partial fractions. These are readily integrated. We obtain the following explicit equation for the t_D as a function of I_D:

$$t_D = F_1(I_D), \qquad F_1(s) = \frac{s}{3(1-s)} + \frac{2}{9} \cdot \ln\left[\frac{2(1-s)}{2+s}\right]. \tag{9}$$

It is straightforward to verify that derivative of (9) is given by (8) and that $I_D = 0$ for $t_D = 0$.

A plot of $I_D = I/I_{\max}$ as a function of $t_D = t/(6\mu_g \Delta p/\tau_0^2)$ is shown in Figure 3.

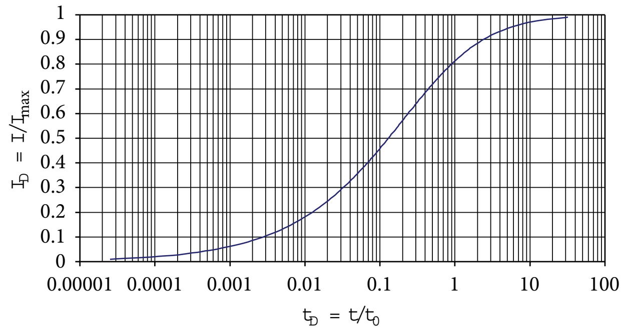

FIGURE 3: Relative penetration length as a function of dimensionless time in horizontal fracture.

From (8) and Figure 3 some interesting observations can be drawn.

(i) The relative penetration is not a function of the fracture aperture, b. This means that the penetration process has the same time scale for all fractures with different apertures penetrated by a borehole.

(ii) The time scale is only a function of the grouting pressure, Δp, and the grout properties, μ_g and τ_0. Thus the parameters are decided by choice of the grouter.

(iii) The time scale is determined by $t_0 = 6\mu_g \Delta p/\tau_0^2$ so that at this grouting time about 80% of the possible penetration length is reached in all fractures and after $5t_0$ about 95% is reached. After that the growth is very slow and the economy of continued injection could be put in doubt.

2.2. Experimental Verification. A series of grouting experiments were published by Håkansson [10]. He used thin plastic pipes instead of a parallel slot for his experiments, and several constitutive grout flow models were tested against experimental data. As could be expected more complex models could give better fit to data, but the Bingham model gave adequate results especially in the light of its simplicity.

The velocity of grout moving in a pipe of radius r_0 can be calculated to be [10]

$$\frac{dI}{dt} = -\frac{dp}{dx} \cdot \frac{(r_0)^2}{8\mu_g} \left[1 - \frac{4}{3} \cdot \frac{Z_p}{r_0} + \frac{1}{3} \cdot \left(\frac{Z_p}{r_0} \right)^4 \right],$$
$$Z_p = 2\tau_0 \cdot \left| \frac{dp}{dx} \right|^{-1}, \quad Z_p < r_0. \tag{10}$$

Here, Z_p is the radius of the plug flow in the pipe.

A force balance between the driving pressure, Δp, and the resisting shear forces inside the pipe gives the maximum grout penetration $I_{\max,p}$:

$$I_{\max,p} = \frac{\Delta p \cdot r_0}{2\tau_0}. \tag{11}$$

TABLE 1: Experimental data for grout penetration, from Håkansson [10].

Experiment	r_0 (m)	Δp (kPa)	τ_0 (Pa)	μ_g (Pa s)	$I_{\max,p}$ (m)	t_0 (s)
3 mm	0.0015	50	6.75	0.292	5.55	1922
4 mm	0.002	50	6.75	0.292	7.40	1922

Inserting (5) and (10), observing that $dx/dt = dI/dt$, and using the relative penetration depth $I_{D,p} = I/I_{\max,p}$ give after simplifications:

$$\frac{dI_{D,p}}{dt} = \frac{(\tau_0)^2}{6\mu_g \Delta p} \cdot \frac{3 - 4I_{D,p} + (I_{D,p})^4}{I_{D,p}},$$
$$I_{D,p} = \frac{I}{I_{\max,p}}. \tag{12}$$

Inserting $t_D = t/(6\mu_g \Delta p/\tau_0^2)$, the previous equation gives the derivative $dI_{D,r}/dt_D$. The derivative of t_D as a function of $I_{D,p}$ is

$$\frac{dt_D}{dI_{D,p}} = \frac{I_{D,p}}{3 - 4I_{D,p} + (I_{D,p})^4}$$
$$= \frac{I_{D,p}}{[1 - I_{D,p}]^2 \left[3 + 2I_{D,p} + (I_{D,p})^2\right]}. \tag{12'}$$

This equation may with some difficulty be integrated. We obtain the following explicit equation for the t_D as a function of $I_{D,p}$:

$$t_D = F_p(I_{D,p}),$$
$$F_p(s) = \frac{s}{6(1-s)} + \frac{1}{36} \cdot \ln\left[\frac{3(1-s)^2}{3 + 2s + s^2}\right]$$
$$- \frac{5\sqrt{2}}{36} \cdot \arctan\left(\frac{s\sqrt{2}}{s+3}\right). \tag{13}$$

A long, but straightforward calculation shows that the derivative satisfies (12). It is easy to see that $t_D = 0$ for $I_{D,p} = s = 0$.

In Håkansson [10] two grouting experiments in 3 and 4 mm pipes are reported. In Table 1, the relevant parameters for the experiments are shown based on the reported data. In Figure 4, a direct comparison between the function $I_{D,p}(t_D)$ and experimental data is shown.

The experimental data follow the theoretical function extremely well up to a value of $t_D \approx 2$. It shall also be borne in mind that the grout properties were taken directly from laboratory tests and no curve fitting was made. Håkansson [10], who assumed them to be a result from differences between laboratory values and experiment conditions, also identified the differences at the end of the curves. As predicted the $I_{D,r} - t_D$-curves are almost identical for the two experiments. Another striking fact is that more than 90% of the predicted penetration is reached for $t_D \approx 2$.

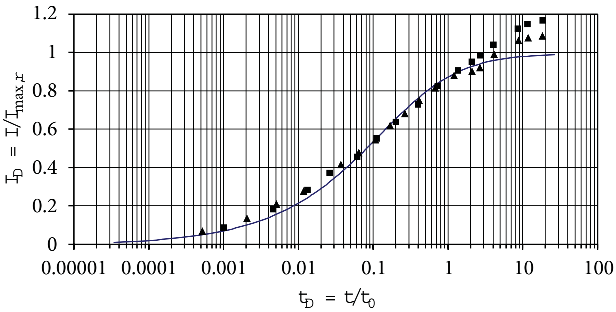

Figure 4: Comparison of grout penetration function in a pipe with experimental data from Håkansson [10].

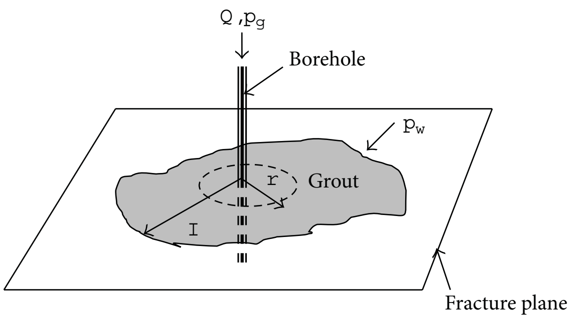

Figure 5: Radial penetration of grout in a fracture.

2.3. Penetration in a Two-Dimensional Fracture. A more realistic model of a fracture to grout is perhaps a pseudo-plane with a system of conductive areas and flow channels [5]. If the transmissivity of the fracture is reasonably constant, a parallel plate model with constant aperture b can approximate it. If it is grouted through a borehole, there will be a radial, two-dimensional, flow of grout out from the borehole; see Figure 5. In reality, however, the flow will as for flow of water from a borehole be something in between a system of one-dimensional channels and radial flow [12].

Equations (3) and (4) give the grout flow in the plane case. The grout flow velocity is constant (in x) and equal to the front velocity dI/dt. In the radial case we replace x by r. The grout flow velocity v_g (m/s) decreases as $1/r$, [16]. Let r_b be the radius of the injection borehole, and let r_b+I be the radius of the grout injection front at any particular time t. We have

$$v_g = -\frac{dp}{dr} \cdot \frac{b^2}{12\mu_g} \left[1 - 3 \cdot \frac{Z}{b} + 4 \cdot \left(\frac{Z}{b}\right)^3\right], \quad r_b \le r \le r_b + I, \tag{14}$$

where

$$Z = \tau_0 \cdot \left|\frac{dp}{dr}\right|^{-1}, \quad Z < \frac{b}{2}. \tag{15}$$

Let the grout injection rate be $Q(\mathrm{m}^3/\mathrm{s})$. The total grout flow is the same for all r:

$$Q = 2\pi rb \cdot v_g, \qquad r_b \le r \le r_b + I. \tag{16}$$

Combing (14) and (16), we get after some calculation the following implicit differential equation for the pressure as a function of the radius:

$$\frac{6\mu_g Q}{\pi b^2 \tau_0} \cdot \frac{1}{r} = s \cdot \left[2 - 3 \cdot s^{-1} + s^{-3}\right], \qquad s = \frac{b}{2Z} = \frac{b}{2\tau_0} \cdot \left|\frac{dp}{dr}\right| \tag{17}$$

or

$$r = \frac{2\mu_g Q}{\pi b^2 \tau_0} \cdot \frac{3s^2}{2s^3 - 3s^2 + 1}, \qquad s = -\frac{b}{2\tau_0} \cdot \frac{dp}{dr}, \qquad r_b \le r \le r_b + I. \tag{18}$$

The injection excess pressure is Δp. We have the boundary condition

$$p(r_b) - p(r_b + I) = \Delta p. \tag{19}$$

Here, we neglect a pressure fall in the ground water, since the viscosity of grout is much larger than that of water.

The solution $p(r)$ of (18)-(19) has the front position I as parameter. The value of Q has to be adjusted so that the pressure difference Δp is obtained in accordance with (19). The front position $I = I(t)$ increases with time. The flow velocity at the grout front $r = r_b + I(t)$ is equal to the time derivative of $I(t)$. We have from (16)

$$Q(I) = 2\pi b \cdot [r_b + I(t)] \cdot \frac{dI}{dt}, \qquad I(0) = 0. \tag{20}$$

This equation determines the motion of the grout front. It depends on the required grout injection rate $Q(I)$, which is obtained from the solution of (18)-(19) for each front position I.

The solution for radial grout flow is much more complicated than for the plain case and the pipe case. We must first solve the implicit differential equation for $p(r)$. This involves the solution of a cubic equation in order to get the derivative dp/dr and an intricate integration in order to get $p(r)$. From the solution, we get the required grout flux for any front position I.

With known function $Q(I)$, we may determine the motion of the grout front from (20) by integration.

The front position I increases from zero at $t = 0$ to a maximum value for infinite time. Then the flux Q must be zero. Equation (18) gives $Q = 0$ for $s = 1$. Then we have a linear pressure variation:

$$Q = 0, \qquad s = 1 \Longrightarrow -\frac{dp}{dr} = \frac{2\tau_0}{b} \Longrightarrow p = K - \frac{2\tau_0}{b} \cdot r. \tag{21}$$

Here, K is a constant. The boundary condition (19) determines the maximum value of I:

$$p(r_b) - p(r_b + I_{\max}) = \frac{2\tau_0}{b} \cdot (-r_b + r_b + I_{\max}) = \Delta p \Longrightarrow I_{\max} = \frac{b\Delta p}{2\tau_0}. \tag{22}$$

We get the same value (2) as in the plain case.

The complete solution in the radial case involves the following constants:

$$I_{\max} = \frac{b\Delta p}{2\tau_0}, \qquad \gamma = \frac{I_{\max}}{r_b} = \frac{b\Delta p}{2r_b\tau_0},$$
$$t_0 = \frac{6\mu_g\Delta p}{(\tau_0)^2}, \qquad Q_0 = \frac{6\pi b(I_{\max})^2}{t_0} = \frac{\pi b^3\Delta p}{4\mu_g}. \tag{23}$$

2.4. Solution for the Pressure. In the dimensionless solution for the pressure, we use the borehole radius as scaling length:

$$r' = \frac{r}{r_b}, \quad I' = \frac{I}{r_b}, \quad r_b \le r \le r_b + I \Longleftrightarrow 1 \le r' \le 1 + I'. \tag{24}$$

The pressure is scaled by $\Delta p/\gamma$. The variable s for the derivative of the pressure in (18) becomes

$$p' = \frac{\gamma \cdot (p - p_w)}{\Delta p} \Longrightarrow s = \frac{b}{2\tau_0} \cdot \left(-\frac{dp}{dr}\right) = -\frac{b\Delta p/\gamma}{2\tau_0 r_b} \cdot \frac{dp'}{dr'} = -\frac{dp'}{dr'}. \tag{25}$$

The dimensionless form of (18)-(19) becomes after some recalculations

$$r' = Q' \cdot g\left(-\frac{dp'}{dr'}\right), \qquad g(s) = \frac{3s^2}{2s^3 - 3s^2 + 1},$$
$$Q' = \frac{2\mu_g Q}{\pi b^2 \tau_0 r_b}, \qquad p'(1) - p'(1 + I') = \gamma,$$
$$1 \le r' \le 1 + I'. \tag{26}$$

This is the basic equation to solve for the pressure distribution. It is to be solved for $0 < I' < \gamma$ for positive values of the parameter γ.

The solution is derived in detail in [14]. A brief derivation is presented in the appendix. The dimensionless pressure is given by

$$p'(r') = \gamma - Q' \cdot \left[\widetilde{G}(Q') - \widetilde{G}\left(\frac{Q'}{r'}\right)\right], \quad 1 \le r' \le 1 + I'. \tag{27}$$

The composite function $\widetilde{G}(q)$, which is used for $q = Q'$ and $q = Q'/r'$, is defined by

$$\widetilde{G}(q) = G(\widetilde{s}(q)),$$
$$\widetilde{s}(q) = \frac{1}{2\sqrt{1+q} \cdot \sin\left\{(1/3) \cdot \arcsin\left[(1+q)^{-1.5}\right]\right\}},$$
$$G(s) = \frac{4}{3} \cdot \ln(s-1) + \frac{1}{6} \cdot \ln(2s+1) - \frac{1}{s-1} - \frac{3s^3}{(2s+1)(s-1)^2}. \tag{28}$$

The function $\widetilde{s}(q)$ is the root to the cubic equation $q \cdot g(s) = 1$ for $s > 1$. The function $G(s)$ is an integral of $s \cdot dg/ds$.

The value of the factor Q' has to be chosen so that the total pressure difference corresponds to the injection pressure, (26). This gives

$$\gamma = Q' \cdot \left[\widetilde{G}(Q') - \widetilde{G}\left(\frac{Q'}{1+I'}\right)\right]. \tag{29}$$

This equation determines Q' as a function of I' and γ:

$$Q' = f'(I', \gamma), \quad 0 \le I' \le \gamma, \ \gamma > 0. \tag{30}$$

The value of Q' for $I' = \gamma$ is zero in accordance with (21)-(22): $f'(\gamma, \gamma) = 0$.

2.5. Motion of Grout Front. In the dimensionless formulation of the equation for the motion of the grout front, we use $I_{\max}$ as scaling length. We also use Q_0 and t_0 from (23)

$$I_D = \frac{I}{I_{\max}}, \qquad I' = \gamma I_D,$$
$$Q_D = \frac{Q}{Q_0}, \qquad t_D = \frac{t}{t_0}. \tag{31}$$

The grout flux becomes from (23) and (26)

$$\frac{Q_0}{\gamma} = \frac{\pi b^2 \tau_0 r_b}{2\mu_g} \Longrightarrow Q = \frac{Q_0}{\gamma} \cdot f'(I', \gamma) = Q_0 \cdot Q_D(I_D, \gamma). \tag{32}$$

The dimensionless grout flux is then

$$Q_D(I_D, \gamma) = \frac{f'(\gamma I_D, \gamma)}{\gamma}, \quad 0 \le I_D \le 1. \tag{33}$$

The dimensionless equation for the front motion is now from (32), (20), (31), and (23)

$$\frac{Q_0}{\gamma} \cdot f'(\gamma I_D, \gamma) = 2\pi b \cdot \frac{(I_{\max})^2}{t_0} \cdot \left(\frac{1}{\gamma} + I_D\right) \cdot \frac{dI_D}{dt_D}$$
$$\text{or} \quad \frac{dt_D}{dI_D} = \frac{\gamma}{3} \cdot \frac{1/\gamma + I_D}{f(\gamma I_D, \gamma)}. \tag{34}$$

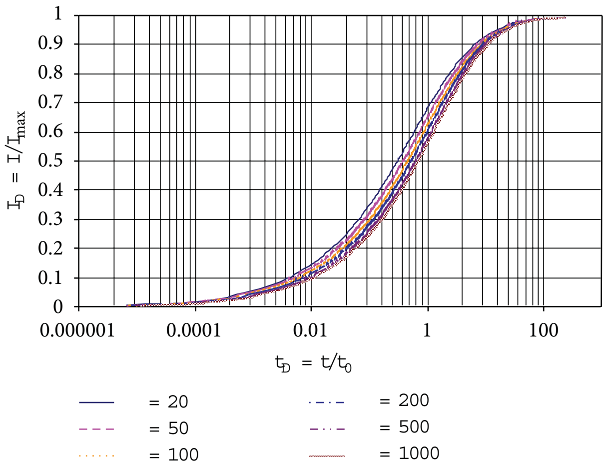

FIGURE 6: Grout penetration function $I_D = I_D(t_D, \gamma)$ for radial flow.

By integration we get the time $t_D = t/t_0$ as an integral in I_D:

$$t_D = \frac{1}{3} \cdot \int_0^{I_D} \frac{1 + \gamma I'_D}{f(\gamma I'_D, \gamma)} dI'_D, \quad 0 \le I_D < 1. \tag{35}$$

We get t_D as a function of the grout front position I_D. Also in this case the inverse function describes the relative penetration as a function of the dimensionless grouting time. Figure 6 shows this relation for a few γ-values.

A comparison of Figures 3, 4, and 6 shows that the curves for $I_D(t_D)$ are similar for the three flow cases. The main difference to parallel flow is that penetration is somewhat slower for the radial case. Around 80% of maximum penetration is reached after $3t_0$ and to reach 90% takes about $7t_0$. The principle is, however, the same and the curves could be used in the same way.

2.6. Injected Volume of Grout. The injected volume of grout as a function of time is of interest. The volume is

$$\begin{aligned} V_g(t) &= \pi b\left[(r_b + I(t))^2 - (r_b)^2\right] \\ &= \pi b I(t)^2 \cdot \left[1 + \frac{2r_b}{I(t)}\right]. \end{aligned} \tag{36}$$

Let $V_{g,\max}$ be maximum injection volume and V_D the dimensionless volume of injected grout:

$$V_D = \frac{V_g}{V_{g,\max}}, \qquad V_{g,\max} = \pi b (I_{\max})^2 \cdot \left[1 + \frac{2}{\gamma}\right]. \tag{36$'$}$$

Then we get, using (31), (24), (23), and the relation (35) between I_D and t_D,

$$V_D(t_D, \gamma) = (I_D)^2 \cdot \frac{1 + 2/(\gamma I_D)}{1 + 2/\gamma}, \quad I_D = I_D(t_D, \gamma). \tag{37}$$

Equations presented in this paper have been used in Gustafson and Stille [15] when considering stop criteria for grouting. Grouting projects where estimates of penetration length have been made are, for example, [13, 15, 16]. Penetration length has also been a key to presenting a concept for estimation of deformation and stiffness of fractures based on grouting data [13]. In addition to grouting of tunnels, theories have also been applied for grouting of dams [18].

3. Conclusions

The theoretical investigation of grout spread in one-dimensional conduits and radial spread in plane parallel fractures have shown very similar behavior for all the investigated cases. The penetration, I, can be described as a product of the maximum penetration, $I_{\max} = \Delta p \cdot \tau_0/2b$, and a time-dependent scaling factor, $I_D(t_D)$, the relative penetration length. Here Δp is the driving pressure, τ_0 is the yield strength of the grout, and b is the aperture of the penetrated fracture. The time factor or dimensionless grouting time, $t_D = t/t_0$, is the ratio between the actual grouting time, t, and a time scaling factor, $t_0 = 6\mu_g \Delta p/{\tau_0}^2$, the characteristic grouting time. Here μ_g is the Bingham viscosity of the grout. The relative penetration depth has a value of 70–90% for $t = t_0$ and reaches a value of more than 90% for $t > 7t_0$ for all fractures.

From this a number of important conclusions can be drawn.

(i) The relative penetration is the same in all fractures that a grouted borehole cuts. This means that given the same grout and pressure the grouting time should be the same in high and low yielding boreholes in order to get the same degree of tightening of all fractures. This means that the tendency in practice to grout for a shorter time in tight boreholes will give poor results for sealing of fine fractures.

(ii) The maximum penetration is governed by the fracture aperture and pressure and yield strength of the grout. The latter are at the choice of the grouter.

(iii) The relative penetration, which governs much of the final result, is determined by the grouting time.

(iv) The pressure and the grout properties determine the desired grouting time. These are the choice of the grouter alone.

(v) It is poor economy to grout for a longer time than about $5t_0$ since the growth of the penetration is very slow for a time longer than that. On the other hand, if the borehole takes significant amounts of grout after $5t_0$, there is reason to stop since it indicates an unrestricted outflow of grout somewhere in the system.

The significance of this for grouting design is as follows.

(i) The conventional stop criteria based on volume or grout flow can be replaced by a minimum time criterion based only on the parameters that the grouter can chose, that is, grouting pressure and yield strength of the grout.

(ii) Based on an assessment of how fine fractures it is necessary to seal, a maximum effective borehole distance can be predicted given the pressure and the properties of the grout.

(iii) The time needed for effective grouting operations can be estimated with better accuracy.

(iv) In order to avoid unrestricted grout pumping also a maximum grouting time can be given, where further injection of grout will be unnecessary.

Appendix

Derivation of the Solution for the Pressure

We seek the solution $p'(r')$ to (26):

$$r' = Q' \cdot g\left(-\frac{dp'}{dr'}\right), \quad 1 \leq r' \leq 1 + I',$$
$$g(s) = \frac{3s^2}{2s^3 - 3s^2 + 1}, \quad 0 \leq I' \leq \gamma. \tag{A.1}$$

Here, $1 + I'$ is the position of the grout front. The parameter γ is positive. Taking zero pressure at the grout front, the boundary conditions for the dimensionless pressure become

$$p'(1) = \gamma, \qquad p'\left(1 + I'\right) = 0. \tag{A.2}$$

The dimensionless grout flux Q' is to be chosen so that the previous boundary conditions are fulfilled. The value of Q' will depend on the front position I'.

Solution in Parameter Form. In order to see more directly the character of the equation, we make the following change of notation:

$$x \longleftrightarrow r', \qquad y \longleftrightarrow -p', \qquad f(s) = Q' \cdot g(s). \tag{A.3}$$

The equation is then of the following type:

$$x = f\left(\frac{dy}{dx}\right). \tag{A.4}$$

There is a general solution in a certain parameter form to this type of implicit ordinary differential equation [19]. The solution is

$$x(s) = f(s), \qquad y(s) = s \cdot f(s) - \int^{s} f\left(s'\right) ds'. \tag{A.5}$$

We have to show that this is indeed the solution. We have

$$\frac{dx}{ds} = \frac{df}{ds}, \qquad \frac{dy}{ds} = 1 \cdot f(s) + s \cdot \frac{df}{ds} - f(s) = s \cdot \frac{df}{ds}. \tag{A.6}$$

The ratio between these equations gives that s is equal to the derivative dy/dx. We have

$$\frac{dy}{dx} = \frac{dy/ds}{dx/ds} = s \Longrightarrow f\left(\frac{dy}{dx}\right) = f(s) = x. \tag{A.7}$$

The right-hand equation shows that (A.5) is the solution to (A.4).

Explicit Solution. Applying this technique to (A.1), we get the solution

$$r' = Q' \cdot g(s),$$
$$-p'(s) = s \cdot Q' \cdot g(s) - Q' \cdot \int^{s} g\left(s'\right) ds'. \tag{A.8}$$

We introduce the inverse to $g(s)$ in the following way:

$$1 = q \cdot g(s) \Longleftrightarrow s = g^{-1}\left(\frac{1}{q}\right) = \tilde{s}(q) \Longleftrightarrow 1 = q \cdot g(\tilde{s}(q)). \tag{A.9}$$

The pressure with a free constant K for the pressure level may now be written as

$$p'(s) = Q' \cdot G(s) + K, \qquad G(s) = \int^{s} g\left(s'\right) ds' - s \cdot g(s). \tag{A.10}$$

The solution is then from (A.8)–(A.10) (with $q = Q'/r'$)

$$p'(s) = Q' \cdot G(s) + K, \quad s = \tilde{s}\left(\frac{Q'}{r'}\right) \tag{A.11}$$

or, introducing the composite function $\widetilde{G}(q)$,

$$\widetilde{G}(q) = G(\tilde{s}(q)), \qquad p'\left(r'\right) = Q' \cdot \widetilde{G}\left(\frac{Q'}{r'}\right) + K. \tag{A.12}$$

The boundary condition (A.2) at $r' = 1$ is fulfilled for a certain choice of K. The explicit solution is

$$p'\left(r'\right) = \gamma - Q' \cdot \left[\widetilde{G}\left(Q'\right) - \widetilde{G}\left(\frac{Q'}{r'}\right)\right], \quad 1 \leq r' \leq 1 + I'. \tag{A.13}$$

The other boundary condition (A.2) at $r' = 1 + I'$ is fulfilled when Q' satisfies the equation

$$\gamma = Q' \cdot \left[\widetilde{G}\left(Q'\right) - \widetilde{G}\left(\frac{Q'}{1 + I'}\right)\right]. \tag{A.14}$$

We note that the derivative $-dp'/dr'$ is given by s:

$$s = -\frac{dp'}{dr'}. \tag{A.15}$$

The pressure derivative is equal to -1 for zero flux, (21) and (25), in the final stagnant position $I' = \gamma$. The magnitude of this derivative is larger than 1 for all preceding positions $I' < \gamma$. This means that s is larger than (or equal to) 1 in the solution.

The Function $G(s)$. The solution (A.13) and the composite function (A.12) involve the function $G(s)$ defined in (A.10) and (A.1). The integral of $g(s)$ is obtained from an expansion in partial fractions. We have

$$\begin{aligned} g(s) &= \frac{3s^2}{2s^3-3s^2+1} = \frac{3s^2}{(2s+1)(s-1)^2} \\ &= \frac{1}{3}\cdot\frac{1}{2s+1} + \frac{4}{3}\cdot\frac{1}{s-1} + \frac{1}{(s-1)^2}. \end{aligned} \tag{A.16}$$

The integral of $g(s)$ is readily determined. The function $G(s)$ becomes from (A.10) and (A.16)

$$\begin{aligned} G(s) = {} & \frac{1}{6}\cdot\ln(2s+1) + \frac{4}{3}\cdot\ln(s-1) - \frac{1}{s-1} \\ & - \frac{3s^3}{2s^3-3s^2+1}, \quad s > 1. \end{aligned} \tag{A.17}$$

We will use the function for $1 < s < \infty$.

The Inverse $\tilde{s}(q)$. The inverse (A.9) is, for any $q \geq 0$, the solution of the cubic equation

$$2s^3 - 3s^2 + 1 = 3qs^2. \tag{A.18}$$

The solution is reported in detail in [14]. The cubic equation has three real-valued solutions for positive q-values, one of which is larger than 1 (for $q = 0$ there is a double root $s = 1$ and a third root $s = -0.5$, (A.16)). We need the solution $s > 1$. It is given by

$$\tilde{s}(q) = \frac{1}{2\sqrt{1+q}\cdot\sin\left\{(1/3)\cdot\arcsin\left[(1+q)^{-1.5}\right]\right\}}, \quad q \geq 0. \tag{A.19}$$

A plot shows that $\tilde{s}(q)$ is an increasing function from $\tilde{s}(0) = 1$ for $q \geq 0$. It has the asymptote $1.5\cdot(1+q)$ for large q.

We will show that (A.19) is the inverse. We use the notations

$$\begin{aligned} \tilde{s}(q) = s &= \frac{1}{2\sqrt{1+q}\cdot\sin(\phi/3)}, \\ \phi &= \arcsin\left[(1+q)^{-1.5}\right]. \end{aligned} \tag{A.20}$$

In (A.18), we put $3qs^2$ on the left-hand side, divide by s^3, and insert $s = \tilde{s}(q)$ from (A.20). Then we have

$$\begin{aligned} & \left(\frac{1}{s}\right)^3 - 3(1+q)\cdot\frac{1}{s} + 2 \\ & = \left(2\sqrt{1+q}\cdot\sin\left(\frac{\phi}{3}\right)\right)^3 - 3(1+q)\cdot 2\sqrt{1+q}\cdot\sin\left(\frac{\phi}{3}\right) + 2 \\ & = 2 - 2\cdot(1+q)^{1.5}\cdot\left[3\cdot\sin\left(\frac{\phi}{3}\right) - 4\cdot\sin^3\left(\frac{\phi}{3}\right)\right] \\ & = 2 - 2\cdot(1+q)^{1.5}\cdot\sin(\phi) \\ & = 2 - 2\cdot(1+q)^{1.5}\cdot(1+q)^{-1.5} \\ & = 0. \end{aligned} \tag{A.21}$$

On the third line we use a well-known trigonometric formula relating $\sin(\phi/3)$ to $\sin(\phi)$. We have shown that (A.19) is the inverse.

Symbols and Units

b (m):	Fracture aperture
I (m):	Penetration length of injected grout
$I_{\max}$ (m):	Maximum penetration length of grout
$I_{\max,p}$ (m):	Maximum penetration length of grout in a pipe
I' (—):	Ratio between penetration and borehole radius
I_D (—):	Relative penetration length
$I_{D,p}$ (—):	Relative penetration length in a pipe
L (m):	Distance between grouting boreholes
p (Pa):	Pressure
p_D (—):	Dimensionless pressure
p_g (Pa):	Grout pressure
p_w (Pa):	Water pressure
Q (m^3/s):	Grout injection flow rate
r (m):	Pipe radius, radial distance from borehole centre
r_b (m):	Borehole radius
r_D (—):	Dimensionless radius
r_p (m):	Grout plug radius
r_0 (m):	Pipe radius
r' (—):	Ratio between distance from borehole centre and borehole radius
T (m^2/s):	Transmissivity
t (s):	Grouting time
t_0 (s):	Characteristic grouting time
t_D (—):	Dimensionless grouting time
V_g (m^3):	Injected volume of grout
$V_{\max}$ (m^3):	Maximum grout volume in a fracture
V_D (—):	Dimensionless grout volume
x (m):	Length coordinate
Z (—):	Bingham half-plug thickness
γ (—):	Ratio between maximum penetration and borehole radius
Δp (Pa):	Driving pressure for grout
μ_g (Pas):	Plastic viscosity of grout
μ_w (Pas):	Viscosity of water
ρ_w (kg/m^3):	Density of water
τ_0 (Pa):	Yield strength of grout.

Acknowledgments

The authors would like to acknowledge the effort of Gunnar Gustafson who deceased during the study.

References

[1] J. D. Osnes, A. Winberg, and J. E. Andersson, "Analysis of well test data—application of probabilistic models to infer hydraulic properties of fractures," Topical Report RSI-0338, RE/SPEC, Rapid City, Dakota, 1988.

[2] C. L. Axelsson, E. K. Jonsson, J. Geier, and W. Dershowitz, “Discrete facture modelling,” SKB Progress Report 25-89-21, SKB, Stockholm, Sweden, 1990.

[3] Å. Fransson, “Nonparametric method for transmissivity distributions along boreholes,” *Ground Water*, vol. 40, no. 2, pp. 201–204, 2002.

[4] D. T. Snow, “The frequency and apertures of fractures in rock,” *International Journal of Rock Mechanics and Mining Sciences and Geomechanics Abstracts*, vol. 7, no. 1, pp. 23–40, 1970.

[5] R. W. Zimmerman and G. S. Bodvarsson, “Hydraulic conductivity of rock fractures,” *Transport in Porous Media*, vol. 23, no. 1, pp. 1–30, 1996.

[6] Å. Fransson, “Characterisation of a fractured rock mass for a grouting field test,” *Tunnelling and Underground Space Technology*, vol. 16, no. 4, pp. 331–339, 2001.

[7] M. Eriksson, “Grouting field experiment at the Äspö Hard Rock Laboratory,” *Tunnelling and Underground Space Technology*, vol. 17, no. 3, pp. 287–293, 2002.

[8] M. Wallner, *Propagation of Sedimentation Stable Cement Pastes in Jointed Rock*, University of Aachen, Rock Mechanics and Waterways Construction, BRD, 1976.

[9] L. Hässler, *Grouting of rock—simulation and classification [thesis]*, Department of Soil and Rock Mechanics, KTH, Stockholm, Sweden, 1991.

[10] U. Håkansson, *Rheology of fresh cement-based grouts [thesis]*, Department of Soil and Rock Mechanics, KTH, Stockholm, Sweden, 1993.

[11] G. Gustafson and H. Stille, “Prediction of groutability from grout properties and hydrogeological data,” *Tunnelling and Underground Space Technology*, vol. 11, no. 3, pp. 325–332, 1996.

[12] J. A. Barker, “A generalized radial flow model for hydraulic tests in fractured rock,” *Water Resources Research*, vol. 24, no. 10, pp. 1796–1804, 1988.

[13] Å. Fransson, C.-F. Tsang, J. Rutqvist, and G. Gustafson, “Estimation of deformation and stiffness of fractures close to tunnels using data from single-hole hydraulic testing and grouting,” *International Journal of Rock Mechanics and Mining Sciences*, vol. 47, no. 6, pp. 887–893, 2010.

[14] J. Claesson, “Radial bingham flow. background report of a detailed solution,” Tech. Rep., Department of Building Technology, Chalmers University of Technology, Göteborg, Sweden, 2003.

[15] G. Gustafson and H. Stille, “Stop criteria for cement grouting,” *Felsbau*, vol. 23, no. 3, pp. 62–68, 2005.

[16] L. Hernqvist, Å. Fransson, G. Gustafson, A. Emmelin, M. Eriksson, and H. Stille, “Analyses of the grouting results for a section of the APSE tunnel at Äspö Hard Rock Laboratory,” *International Journal of Rock Mechanics and Mining Sciences*, vol. 46, no. 3, pp. 439–449, 2009.

[17] C. Butrón, G. Gustafson, Å. Fransson, and J. Funehag, “Drip sealing of tunnels in hard rock: a new concept for the design and evaluation of permeation grouting,” *Tunnelling and Underground Space Technology*, vol. 25, no. 2, pp. 114–121, 2010.

[18] H. Stille, G. Gustafson, and L. Hässler, “Application of new theories and technology for grouting of dams and foundations on rock,” *Geotechnical and Geological Engineering*, vol. 30, no. 3, pp. 603–624, 2012.

[19] E. Kamke, *Differentialgleichungen. Lösungsmetoden und Lösungen*, Becker & Erler, Leipzig, Germany, 1943.

Hindawi Publishing Corporation
Journal of Applied Mathematics
Volume 2013, Article ID 756854, 10 pages
http://dx.doi.org/10.1155/2013/756854

Research Article

Strength Theory Model of Unsaturated Soils with Suction Stress Concept

Pan Chen, Changfu Wei, Jie Liu, and Tiantian Ma

State Key Laboratory of Geomechanics and Geotechnical Engineering, Institute of Rock and Soil Mechanics, Chinese Academy of Sciences, Xiaohongshan, Wuchang, Wuhan, Hubei 430071, China

Correspondence should be addressed to Changfu Wei; cfwei@whrsm.ac.cn

Received 24 June 2013; Revised 12 September 2013; Accepted 18 September 2013

Academic Editor: Pengcheng Fu

A theoretical model is developed for describing the strength property of unsaturated soils. The model is able to predict conveniently the strength changes of unsaturated soils undergoing repeated changes of water content. Suction stress is adopted in the new model in order to get the sound form of effective stress for unsaturated soils. The shear strength of unsaturated soils is dependent on its soil-moisture state based on the results of shear experiments. Hence, the parameters of this model are related tightly to hydraulic properties of unsaturated soils and the strength parameters of saturated soils. The predictive curves by the new model are coincident with experimental data that underwent single drying and drying/wetting cycle paths. Hence, hysteretic effect in the strength analysis is necessary to be considered to predict the change of shear strength of unsaturated soils that underwent drying/wetting cycles. Once the new model is used to predict the change of shear strength, lots of time could be saved due to avoiding heavy and complicated strength tests of unsaturated soils. Especially, the model can be suitable to evaluate the shear strength change of unsaturated soils and the stability of slopes experienced the drying/wetting cycles.

1. Introduction

The change of soil strength is very important to evaluate the stability of slopes and road embankment. In this case, the strength model of unsaturated soils is always concerned in geotechnical engineering. Until now, many researchers have shown that the shear strength of unsaturated soils was tightly related to soil-moisture state [1–3]. The strength of unsaturated soils will increase or decrease during the intermittent precipitation and fluctuant water tables [4, 5]. Hence, a new model should be necessarily developed, in which the change of soil strength can be reasonably predicted under the repeated change of water content. The model will be critical to analyze these problems that soil slopes become destabilized during the intermittent rainfall process.

The theoretical model for shear strength of unsaturated soils is generally developed based on the concept of effective stress, which is similar to the equation of shear strength of saturated soils. There are two types of description for effective stress of unsaturated soils that are prevalent in the literature. One type bases on the single stress variable [6] and the other on the double stress variable [7]. The equations of shear strength are given in Formulas (1) and (2), respectively, as follows:

$$\tau = c' + \left[\sigma - p^N + \chi\left(p^N - p^W\right)\right]\tan\varphi', \tag{1}$$

$$\tau = c' + \left(\sigma - p^N\right)\tan\varphi' + \left(p^N - p^W\right)\tan\phi^b, \tag{2}$$

where τ is the shear strength; c' is the cohesion at the saturated state; σ is the normal total stress; φ' is the effective internal friction angle; and p^N and p^W are the pore air pressure and pore water pressure, respectively. There are two parameters χ and ϕ^b in Formulas (1) and (2) which cause the difference of strength equations in form between saturated soils and unsaturated soils. $\chi(p^N - p^W)\tan\varphi'$ and $(p^N - p^W)\tan\phi^b$ are the change of shear strength arising by the change of matric suction (water content) in unsaturated soils. On the one hand, χ in single stress variable framework will change with the degree of saturation S_r. But the results of some experiments show that the relationship is not unique between χ and S_r [1, 8]. χ is strongly depended on the soil structure and soil-moisture state. On the other hand, the definition of the two-state variable exists some confusion in the scales from the view of continuum mechanics [9]. Normal stress loads on the skeleton of soils, but matric suction stresses on the air-water interface. Unfortunately, the two stress state variables are treated as stress variables acting on the representative elementary volume for the soils (REV). In Formula (2), the relationship of ϕ^b and matric suction s_c ($s_c = p^N - p^W$) is nonlinear for the same soil [10]. And the functional relation is different for each type of soil between ϕ^b and s_c. Vanapalli et al. [10] proposed an empirical relation for calculating ϕ^b based on experiments of unsaturated soils. Khalili and Khabbaz [11] and Kayadelen et al. [12] gave different strength models based on the analysis of effective stress, respectively. Other forms of strength model are also found in the literature [13–15].

Although the existing models of shear strength have been used to analyze the geotechnical problems by many researchers, some problems may come out in practical application. Firstly, the parameters χ and ϕ^b in these formulas are not easy to be directly determined through the experiments of unsaturated soils. Secondly, the physical basis of these formulas is not definite. Hence, it could be suitable for some soils, but it is difficult to be adapted for other soils under different soil-moisture conditions. Thirdly, matric suction is one of the main variables in the expression of soil strength. There are some difficulty questions in the measurement of matric suction, which limit the development of experimental technology in laboratory and field conditions, such as cavitation phenomenon [16]. The application of these models is perhaps not reasonable to evaluate some problems in the field. Last but not least, most of the equations were limited to be used under only the drying process of unsaturated soils. But the strength characteristics of unsaturated soils are different which underwent the drying and wetting processes due to the existent of hysteretic effect at varying water content conditions [17].

Focusing on these problems of the existing shear strength models, a new model will be developed to describe the strength property of unsaturated soils. A conception of suction stress is introduced in order to modify the formula of effective stress of unsaturated soils. Based on the modified formula of effective stress, the formula of shear strength can be obtained using Mohr-Coulomb's theory. Shear strength envelope of unsaturated soils is unique on the plane with modified effective stress and shear strength at different matric suction or water content states. Then the soil-water retention curve is used to replace empirical parameters χ and ϕ^b. Therefore, the strength of unsaturated soils can be predicted by the measurement of water content, which is easy to be determined both in the laboratory and field. In order to explore the strength property of unsaturated soils that underwent drying/wetting cycles, the hysteretic model (ISVH) [18] is introduced. The new model is able to simulate the strength evolution of unsaturated soils under repeated hydraulic paths. Lastly the predictive results from the model are compared with experimental data.

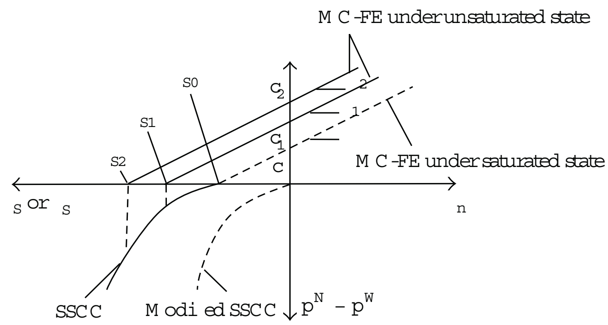

FIGURE 1: Suction stress characteristic curve from Mohr-Coulomb failure envelopes.

2. The Concept of Suction Stress and Suction Strength

2.1. The Concept of Suction Stress. Based on the analysis of the composites of microscopic forces in details, Lu and Likos [19] defined suction stress which is the macroscopic expression of different interactions in microscale (such as physical-chemical force, van der Waals force, electrical double-layer repulsion, and surface tension). The theoretical basis of the suction stress has been discussed by Lu and Likos [19]. Here, the method for obtaining suction stress is given from direct shear test and triaxial shear test of unsaturated soils. Traditionally, the data of shear strength under different normal stresses are plotted on the plane of normal effective stress σ_n' and shear strength τ or net mean effective stress p' and deviatoric stress q, seen in Figure 1. c', c_1', and c_2' are the intercept that Mohr-Coulomb failure envelops (MC-FE) and cut τ-axis. c', c_1', and c_2' are called effective cohesion under saturated state and unsaturated state, respectively. φ', φ_1', and φ_2' are effective internal friction angle at different saturated state. The cohesion is the bond force or attractive effect among soil particles. The intercept on the τ-axis gives the frictional action among soil particles. It is puzzled that the intercept can be called cohesion. Further, the intercept on the τ-axis cannot fully represent the bond strength among the soil skeletons. Actually, the intersection is the attractive effect that MC-FE is prolonged and cuts the σ_n'-axis, which can be expressed by σ_S, called suction stress by Lu and Likos [19]. The formula of suction stress can be given from direct shear test as follows:

$$\sigma_S = \frac{-c'}{\tan\varphi'}. \tag{3}$$

The suction stress can be obtained by Formula (3) at different water content state. The relationship of suction stress and matric suction is called suction stress characteristic curve (SSCC). It is to be noted that suction stress is not zero for fine grain soils under saturated state, called σ_{S0}. The original SSCC needs to be modified by the suction stress σ_{S0} to go through the origin, which is consistent with soil-water retention curve (SWRC), seen in Figure 1.

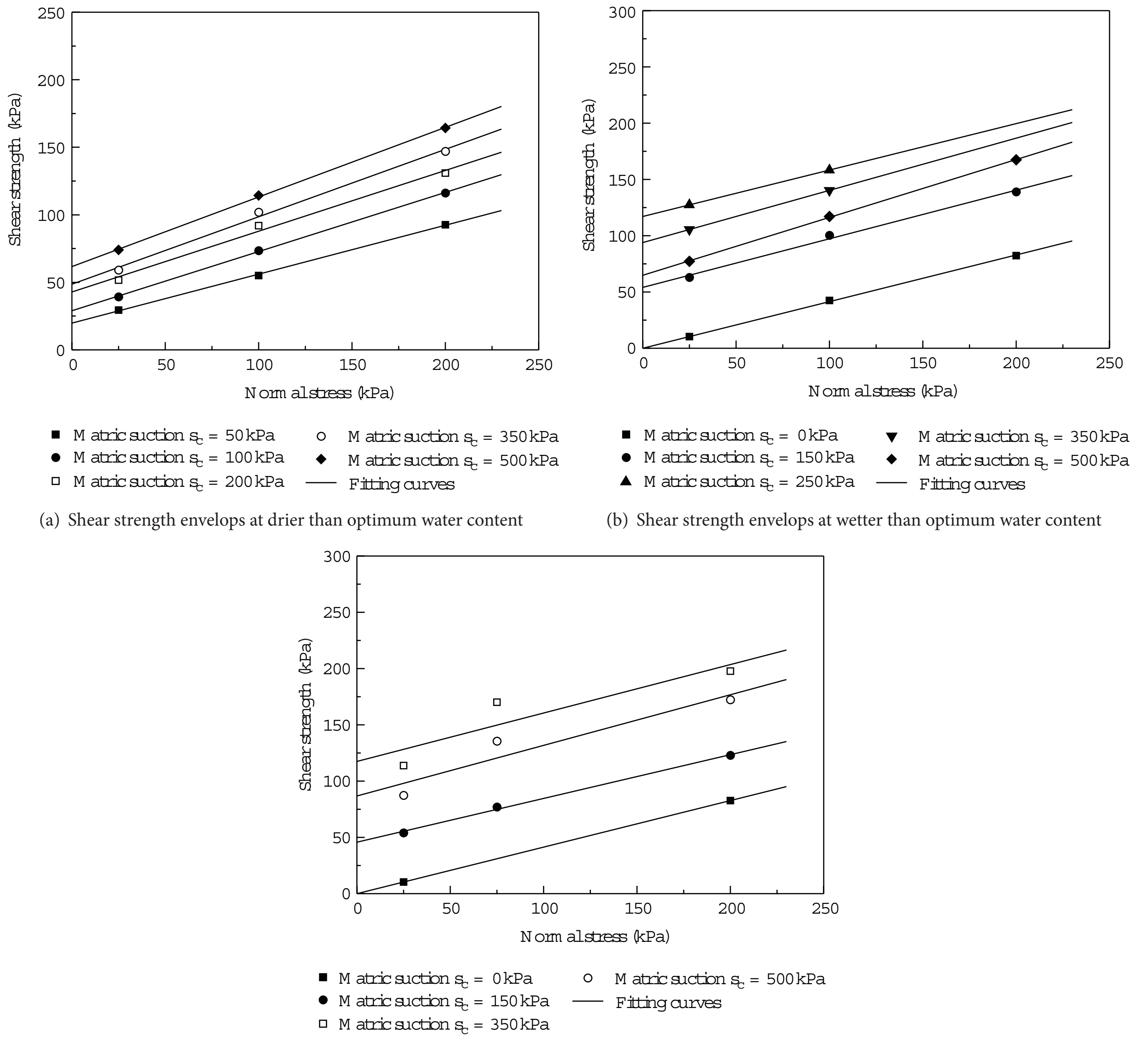

(a) Shear strength envelops at drier than optimum water content

(b) Shear strength envelops at wetter than optimum water content

(c) Shear strength envelops at optimum water content

Figure 2: The curves of normal stress and shear strength at different initial water content state of soil (experimental data from Vanapalli et al. [10]).

The suction stress can also be obtained from triaxial shear tests according to Mohr-Coulomb criterion. The formula is given as follows:

$$\sigma_S = -\frac{\sigma_1' - p^N}{2\tan(\pi/4 + \varphi'/2)\tan\varphi'} + \frac{\left(\sigma_3' - p^N\right)\tan\left(\pi/4 + \varphi'/2\right)}{2\tan\varphi'} + \frac{c'}{\tan\varphi'}, \tag{4}$$

where σ_1' and σ_3' are the major and minor principle stress, respectively.

The new effective stress can be defined based on suction stress as follows:

$$\sigma' = \left(\sigma - p^N\right) - \sigma_S, \tag{5}$$

where σ' is the effective stress and σ is the total stress. In order to verify the expression of effective stress is reasonable, the experimental data of shear strength or deformation tests of unsaturated soils could be used.

Sandy-clay till was used to do shear strength test at three types of water content state by Vanapalli et al. [10]. Shear failure envelops go upward drift with matric suction increasing, which is shown in Figure 2(a). Simultaneously, Figures 2(a), 2(b), and 2(c) show that the shear strengths are

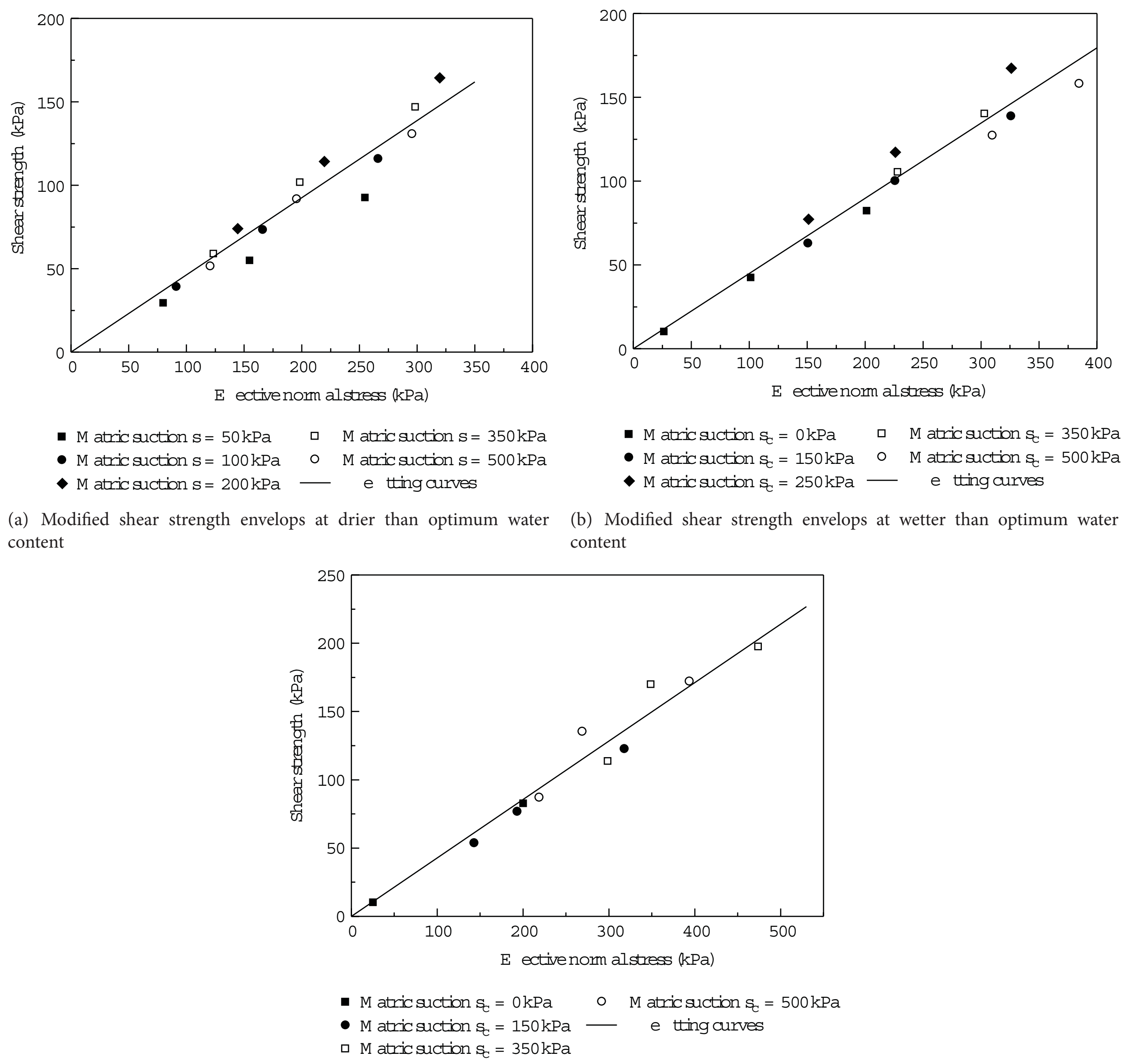

(a) Modified shear strength envelops at drier than optimum water content

(b) Modified shear strength envelops at wetter than optimum water content

(c) Modified shear strength envelops at optimum water content

Figure 3: The curves of effective normal stress and shear strength at different initial water content state of soil (experimental data from Vanapalli et al. [10]).

not the same, although the matric suction and normal stress are completely identical. The unique difference is the initial state of the soils. The shear strength is largest at wetter than optimum water content state, and it is smallest at drier than optimum water content state. Obviously, the shear strength of unsaturated soils τ is strongly depended on the state of water content. We can obtain suction stresses from Formula (3) or (4) using the tested data from Figures 2(a), 2(b), and 2(c). Then the new effective stress is achieved. The strength failure envelops are redrawn in the plane $\sigma' - \tau$ in Figure 3.

It is interesting that these data points at failure state tend to a line. The phenomenon is not coincidental. There are many measured data from literatures that are not given due to the limited space of this paper, which can be seen detailedly in the literature [21, 22]. That is to say, the critical state failure envelop is unique under the new effective stress framework of unsaturated soils. And the effective stress can be also used for saturated soils, which is coincident with Terzaghi's effective theory. The new effective stress is the reasonable one with suction stress. The problem of nonunique failure envelops of unsaturated soils in traditional framework is solved by the new effective stress framework. The meaning of effective stress with suction stress is clear in the framework of continuum mechanics. And it is deduced that the properties in deformation and strength of unsaturated soils could be described in the unified way by the mathematics Formula (5).

2.2. Suction Strength of Unsaturated Soils. The shear strength equation of unsaturated soils is obtained based on the effective stress Formula (5):

$$\tau_f = c' + \left(\sigma - p^N - \sigma_S\right)\tan\varphi', \tag{6}$$

where c' and φ' are the effective cohesion and the effective internal friction angle at saturated state, respectively.

Suction stress is macrorepresentation of interaction of soil particles in microscale, which increases the attraction of soil skeleton and shear strength. Compared with saturated soil, there is a difference that the shear strength is related to water content. The change of strength due to the fluctuate of water content is defined as suction strength c_S':

$$c_S = -\sigma_S \tan\varphi'. \tag{7}$$

Based on these literatures [11–13], the suction strength can be obtained from the shear strength tests. The apparent cohesion c is defined as

$$c = c' + c_S. \tag{8}$$

The shear strength equation can be modified as follows:

$$\tau_f = c + \left(\sigma - p^N\right)\tan\varphi'. \tag{9}$$

The equation is coincident with the one of saturated soils in form. Therefore, the shear strength of unsaturated and saturated soils can be both expressed by Formula (9). The formula of shear strength is obtained in the unified framework of soils, in which new empirical parameters are not introduced.

3. Shear Strength Model of Unsaturated Soils Depending on Hydraulic State

The suction stress is related to water content of unsaturated soils from the above analyses. The relationship is derived by Lu et al. [21] based on the principles of thermodynamics:

$$\sigma_S = -S_e\left(p^{N'} - p^W\right), \tag{10}$$

where p^W is the water pressure and matric suction s_c is defined as follows:

$$s_c = p^{N'} - p^W. \tag{11}$$

S_e is the effective degree of saturation:

$$S_e = \frac{\left(S_r - S_r^{\mathrm{irr}}\right)}{\left(1 - S_r^{\mathrm{irr}}\right)}, \tag{12}$$

where S_r is the degree of saturation and S_r^{irr} is the residual degree of saturation.

Introducing Formulas (10), (11), and (12) to Formulas (7) and (9), the suction strength and shear strength equations can be given as follows:

$$c_S = S_e s_c \tan\varphi', \tag{13}$$

$$\tau_f = c' + S_e s_c + \left(\sigma - p^N\right)\tan\varphi'. \tag{14}$$

As seen from Formula (14), the shear strength of unsaturated soils is only related to the degree of saturation but also related to matric suction. The relationship of the shear strength and matric suction (the degree of saturation) can be obtained by introducing the soil-water retention curve (SWRC). The change of soil-water state is generally not monotonic under intermittent precipitation and fluctuating water tables. The capillary hysteresis (hydraulic hysteresis) often exits during the increment and decrement of water content in the seepage process of unsaturated soils. Capillary hysteresis refers to the nonunique relationship between the degree of saturation and matric suction and describes the irreversible changes in the degree of saturation occurring during the preceding sequence of drying and wetting of a porous medium. The importance of hysteretic effect (hydraulic hysteresis) in the unsaturated flow has been found in the literatures [23]. Furthermore, hysteretic effect can also significantly influence the shear strength and the shear behaviour, as seen in works such as those performed by Kwong [24] and Khoury and Miller [25]. Kwong [24] found that the strengths of unsaturated soils getting wetter are lower than those getting drier. Khoury and Miller [25] found that shear strength following a drying/wetting process was higher than that for the drying process alone at the similar matric suction and net normal stress. These results give an important conclusion that the water content and matric suction are of equal importance to obtain the shear strength of unsaturated soils. The two soil-water state parameters are affected by the hydraulic hysteresis. The effect of hysteresis should be considered in the analysis of the strength problems related to unsaturated soils.

In order to conclude the hysteretic effect in the shear strength problems, the hysteretic soil-water relationship should be developed for constructing the shear strength model of unsaturated soils. There are some methods which may be used to consider hysteretic effect during the process of the water content change history [26–28]. The main object of this paper is to develop a new strength model to reproduce the change of shear strength that underwent the effect of capillary hysteresis in unsaturated soils. Recently, a capillary hysteretic model with internal state variables (ISVH-model) was developed by Wei and Dewoolkar [18]. The boundary surface plasticity theory is used to model the hysteretic behavior of the soil water retention curves. In this model, the arbitrary water content variable path can be traced between the main boundary curves. The equations of the model are presented here for the integrality of this paper. Feng and Fredlund [29] offered an equation which was used to well fit the boundary curves of the soil water retention curves. The main drying curve is

$$S_{rD} = \frac{1 + S_{rD}^{\mathrm{irr}}\left(s_c/b_D\right)^{a_D}}{1 + \left(s_c/b_D\right)^{a_D}}, \tag{15a}$$

and the main wetting curve is

$$S_{rW} = \frac{1 + S_{rW}^{\mathrm{irr}}\left(s_c/b_W\right)^{a_W}}{1 + \left(s_c/b_W\right)^{a_W}}, \tag{15b}$$

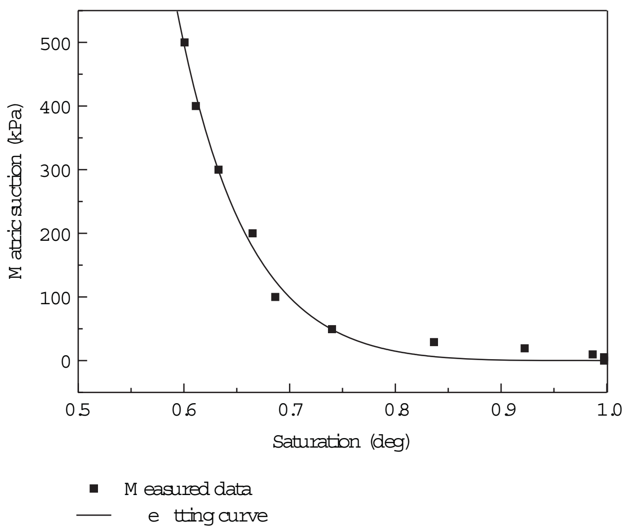

Figure 4: The fitting tested curve of SWRC for the completely decomposed granite soil (measured data from Hossain and Yin [20]).

where S_{rD} and S_{rW} are the degrees of saturation of the drying and wetting boundaries, respectively; S_{rD}^{irr} and S_{rW}^{irr} are the residual degrees of saturation at the drying and wetting conditions, respectively; b_D, a_D, b_W, and a_W are the four material parameters.

The evolution equation of the degree of saturation that underwent the drying and wetting cycles is described as follows:

$$\dot{S}_r = -\frac{\dot{s}_c}{K_p\left(S_r, s_c, \widehat{n}\right)}, \tag{16}$$

where $\widehat{n}$ is the direction of the hydraulic path and its value is −1 or 1. For the wetting path, $\widehat{n} = -1$, and for the drying path, $\widehat{n} = 1$; $K_p(S_r, s_c, \widehat{n})$ is given as follow:

$$K_p\left(S_r, s_c, \widehat{n}\right) = \overline{K}_p\left(S_r, \widehat{n}\right) + \frac{d\left|s_c - \overline{s}_c\left(S_r, \widehat{n}\right)\right|}{r\left(S_r^W\right) - \left|s_c - \overline{s}_c\left(S_r, \widehat{n}\right)\right|}, \tag{17}$$

where d is a fit parameter, which is an additional parameter to describe all of the scanning curves in the hysteretic cycle; matric suction in the main drying and wetting boundary curves is expressed by $\overline{s}_c = \kappa_D(S_r)$ and $\overline{s}_c = \kappa_W(S_r)$, respectively; $r(S_r)$ is the difference of the matric suction between the main boundary curves when the soil water state is at the degree of saturation S_r, $r(S_r) = \kappa_D(S_r) - \kappa_W(S_r)$; $\overline{K}_p$ and $\overline{s}_c(S_r, \widehat{n})$ are respectively the slope and matric suction of the main drying and wetting boundary curves as follows.

(1) Drying path ($\widehat{n} = 1$):

$$\overline{s}_c\left(S_r, 1\right) = \kappa_D\left(S_r\right), \qquad \overline{K}_p\left(S_r, 1\right) = \frac{d\kappa_D\left(S_r\right)}{dS_r}. \tag{18a}$$

(2) Wetting path ($\widehat{n} = -1$):

$$\overline{s}_c\left(S_r, -1\right) = \kappa_W\left(S_r\right), \qquad \overline{K}_p\left(S_r, -1\right) = \frac{d\kappa_W\left(S_r\right)}{dS_r^W}. \tag{18b}$$

Introducing the hysteretic model (ISVH), suction strength and shear strength are expressed as follows:

$$c_S = s_c \tan\varphi', \quad s_c \le 0, \tag{19a}$$

$$c_S = S_e\left(\dot{S}_r\right) s_c \tan\varphi', \quad s_c > 0, \tag{19b}$$

$$\tau_f = c' + \left(\sigma - p^N\right)\tan\varphi' + s_c \tan\varphi', \quad s_c \le 0, \tag{20a}$$

$$\tau_f = c' + \left(\sigma - p^N\right)\tan\varphi' + S_e\left(\dot{S}_r\right) s_c \tan\varphi', \quad s_c > 0. \tag{20b}$$

If the current soil-water state (s_c, S_r) and the increment of the degree of saturation $\dot{S}_r$ are given, the change of shear strength of unsaturated soils can be predicted by Formulas (20a) and (20b) during any drying/wetting cycle, combined with the shear strength of saturated soils (c' and φ').

4. Model Verification

The suction strength and shear strength of unsaturated soils are predicted based on Formulas (18a), (18b), (20a), and (20b). And the predictive curves are compared with experimental strength data. The parameters of soil-water retention curves from fitting the measured soil-water data are used to predict the change of shear strength.

4.1. Strength Property under Single Drying Hydraulic Path. The soil-water retention curve and direct shear strength tests of unsaturated completely decomposed granite soil are performed in the laboratory by Hossain and Yin [20]. The measured soil-water retention curve is given in Figure 4. And the shear strength parameters at saturated state are $c' = 0.0$ kPa and $\varphi' = 29.9°$. Formula (15a) is adopted to fit the measured soil-water data for the drying process alone. The fitting curve is also shown in Figure 4. And the parameters of the soil-water retention curve are listed in Table 1. Formulas (19b) and (20b) are adopted to predict the suction strength and shear strength of the soils, combining with the shear strength parameters at saturated state. The predictive curves are shown in Figure 5. The coincidence of suction strength is well under low suction conditions. And a little deviation comes out in high suction conditions (Figure 5(a)). The prediction of shear strength of the soils is acceptable at low effective stresses. However, the deviation between measured data and the predictive curve is large at higher effective stresses. The similar results are shown by Hossain and Yin [20]. The distinct dilative behavior of unsaturated compacted completely decomposed granite soil was observed in the measurement by Hossain and Yin [20]. The apparent cohesion intercept and angle of internal friction increase with matric suction due to the effect of dilative behavior. It is to be note that the effective stress is obtained based on Formula (5) (Figure 5(b)).

The same method is also adopted to predict shear strength of Diyarbakir residual clays. The shear strength and soil-water

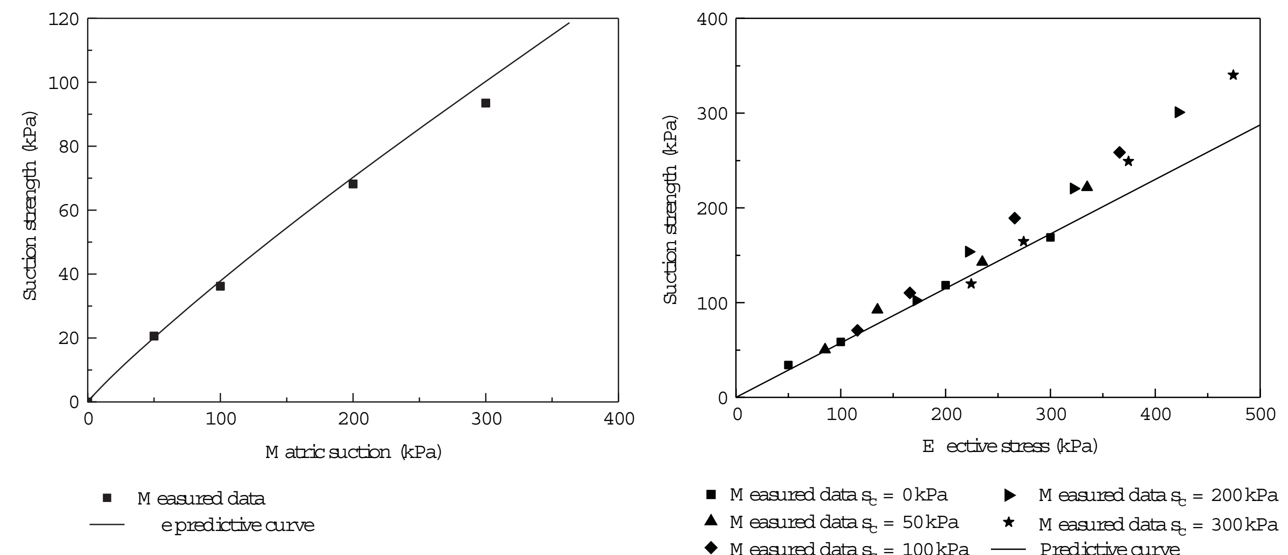

(a) Suction strength

(b) Shear strength

Figure 5: Comparison of tested data with the predictive curve of suction strength and shear strength (measured data from Hossain and Yin [20]).

Table 1: Parameters of SWRC of unsaturated soil and shear strength of saturated soil for predicting suction strength of unsaturated soils that underwent single drying hydraulic path.

Soil types	Parameters of SWRC				Strength parameters	
	n	S_r^{irr}	a	b (kPa)	c' (kPa)	φ'
Completely decomposed granite soil	0.36	0.120	0.2961	917.35	0	29.9
Diyarbakir residual clays	0.581	0.442	0.4679	488.74	14.82	21.9

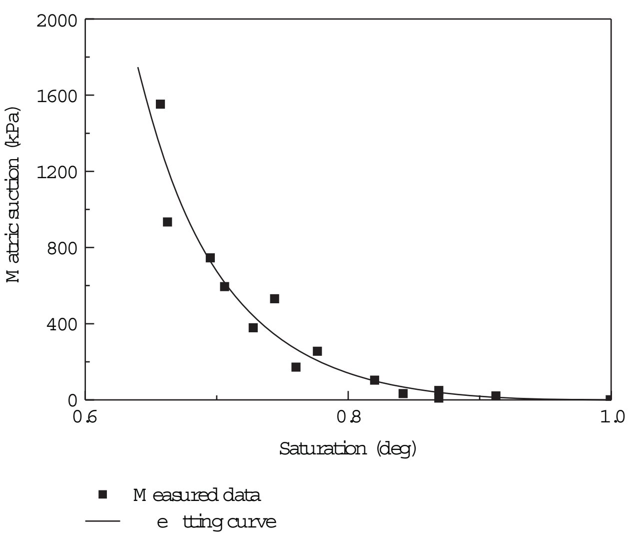

Figure 6: The fitting tested curve of SWRC for Diyarbakir residual clays (measured data from Kayadelen et al. [12]).

retention tests are performed by Kayadelen et al. [12]. The fitting soil-water retention curve is shown in Figure 6. And the parameters of the soil-water retention curve are listed in Table 1. The shear strength parameters of Diyarbakir residual clays at saturated state are $c' = 14.82$ kPa and $\varphi' = 21.9°$. The predictive curves of suction strength and shear strength of the residual clays are shown in Figure 7. As seen from Figures 7(a) and 7(b), the suction strength and shear strength both well match up to experimental data. The distribution of the shear strength data at different matric suctions is approximately linear again in Figure 7(b). The critical state failure is unique under the new effective stress state based on suction stress. It does not exist that the failure envelops are nonunique, based on the new shear strength model.

4.2. Strength Property under Drying/Wetting Paths. The shear strength is very important for predicting the slope stability under the intermittent precipitation conditions, for example, Gvirtzman et al. [30]. The variation in strength of unsaturated soils will be studied in the section under the repeating change of water content conditions. However, the measured data of shear strength that underwent drying/wetting process are little seen in the literature. The main reasons are that the test instruments are not well established and these experiments are time-consuming in the laboratory.

Goh et al. [5] performed a series of unsaturated consolidation drained triaxial tests under drying and wetting, in which compacted sand-kaolin specimens were adopted. The soil-water retention curves are also measured by tempecell and pressure plate in Goh et al. [5]. The c' and φ' of

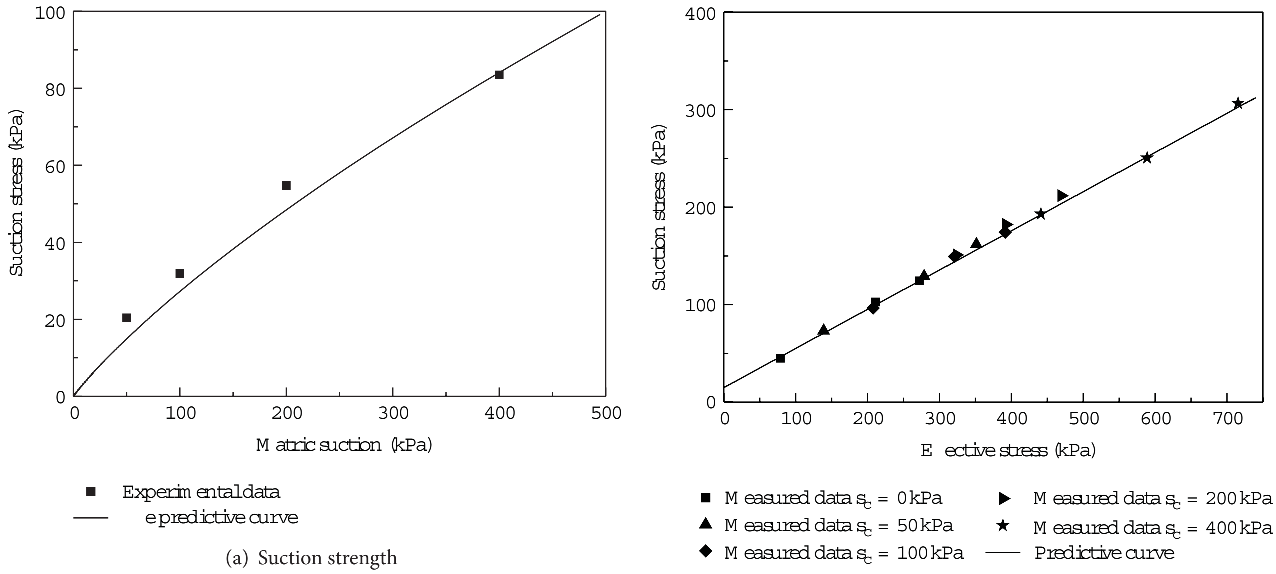

(a) Suction strength

(b) Shear strength

Figure 7: Comparison of tested data with the predictive curve of suction strength and shear strength (measured data from Kayadelen et al. [12]).

Table 2: Parameters of SWRC of unsaturated soil and shear strength of saturated soil for predicting suction strength of unsaturated soils that underwent drying/wetting paths.

Soil types	Parameters of SWRC								Strength parameters	
	n	S_{rD}^{irr}	a_D	b_D (kPa)	S_{rW}^{irr}	a_W	b_W (kPa)	d	c' (kPa)	φ'
Sand-kaolin mixture	0.470	0.055	0.566	1520.30	0.055	0.481	874.81	19620.0	8.5	26.9

the compacted saturated sand-kaolin mixture are 8.5 kPa and 26.9°, respectively. The soil-water retention data and the fitting curves are given in the Figure 8. The main drying and main wetting curve are fitted by Formulas (15a) and (15b), respectively. The wetting scanning data are used to correct the parameter d in Formula (17). Then the parameter d is adopted to predict the drying scanning curve. The parameters for fitting SWRC are listed in Table 2.

The parameters of the main drying and wetting curves and the parameter d are used to predict the change of suction strength of the unsaturated sand-kaolin mixture that underwent the drying/wetting cycle. The predictive results are presented in Figure 9. The suction strength obtained from the drying process was predicted by these parameters of the main drying and drying scanning curves, respectively. The coincidence is well compared with the measured data. At the low suction state, the predictive curve is much nearer the measured results using the parameters from the drying scanning curve than those from the main drying curve. However, the tendency of the predictive curves is the same at the high suction state. That is, due to that the drying scanning curve and the main drying curve are coincident at the high suction condition, seen in Figure 8. The similar comparisons were done between the measured suction strength from the wetting process with the predictive curves. The predictive tendency from the wetting process is different from the one from the drying state. At the high suction state, the predictive curve is much nearer the measured results using the parameters from the wetting scanning curve than those from the main wetting curve. However, the tendency of the predictive curves is also the same at the low suction state. That is, due to that the wetting scanning curve and the main wetting curve are coincident at the high suction condition, which can be also seen in Figure 8. The soil-water state is not always along the main boundary curves due to hysteretic effect. The soil-water state is perhaps along the scanning drying or wetting curve at the shear strength tests. Hence, the predictive results by the scanning curves are nearer to the measured strength data than the ones by the main boundary curves.

It noted to say that the correlation of suction strength and soil-water state is evident, seen in Figure 9. Furthermore, the difference of suction strength is increasing with the increment of matric suction for the drying or wetting path. And the suction strength along the drying path is larger than the ones along the wetting path. That is to say, the shear strength is closely related to the water content and matric suction. Due to the existence of hysteretic effect, the water content may be different at the same matric suction through different drying/wetting paths. The shear strength will be different, though the matric suction is the same. Hence, it is indispensable that the research work should be carried out on the change of shear strength of unsaturated soils that underwent the repeating changes of water content.

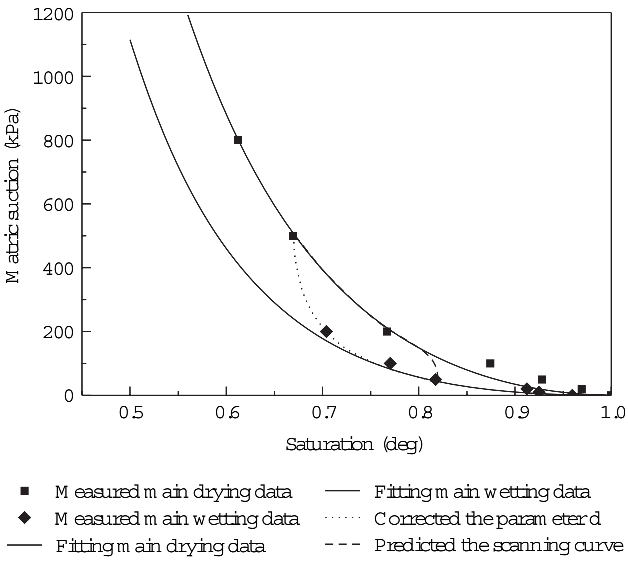

Figure 8: The fitting tested curve of SWRC for sand-kaolin mixture (measured data from Goh et al. [5]).

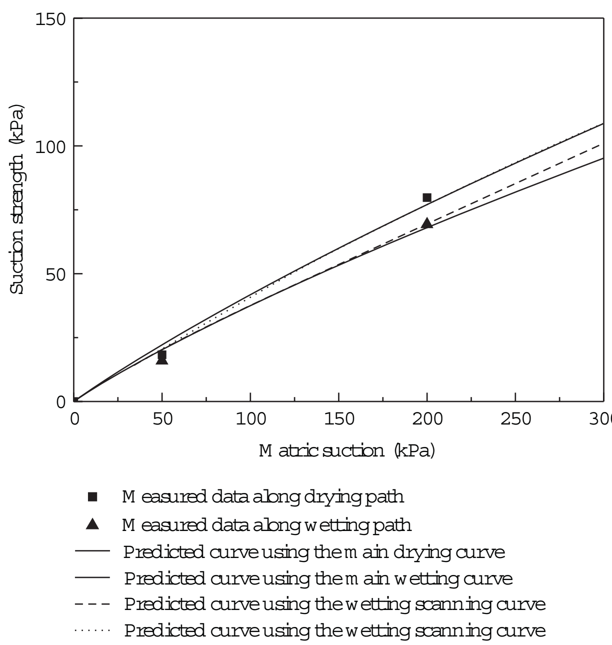

Figure 9: Comparison of tested data with the predictive curve of suction strength under drying-wetting paths (measured data from Goh et al. [5]).

5. Conclusions

The theoretical strength model is developed based on the concept of suction stress. The predictive curves of the model are compared with experimental data. And its validity of the strength model is verified. There are some conclusions as follows.

(1) Suction stress is the macroscopic effect of many different microscopic forces in unsaturated soils. Redundant parameters need not to be introduced to describe these microscopic forces, respectively. The effective stress framework of unsaturated soils is improved. The failure envelop of unsaturated soils is unique at different matric suction and net normal stresses, based on the new effective stress framework. The cohesion arisen by tension among soil particles expresses its real concept. The relation of matric suction and suction stress can be uniquely expressed by the suction stress characteristic curve (SSCC), which is very important for describing the stress state, similar with SWRC for describing the soil-water state. The uncertainty of the parameters of shear strength of soils can be avoided in the effective stress frame.

(2) In the new strength model, the SWRC and SSCC are combined to predict the change of shear strength of unsaturated soils under repeated water content (matric suction) change. The SWRC is used to predict the change of suction strength and shear strength of unsaturated soils. The SWRC is widely adopted in geotechnical engineering and soil physics. The parameters of SWRC are much easier to obtain in laboratory or field, compared with the shear strength tests of unsaturated soils. Furthermore, the time can be saved largely once the SWRC is used to predict the strength of unsaturated soils, especially for fine gained soils.

(3) The predictive curves of suction strength and shear strength of the soils both well match up to experimental data for the completely decomposed granite soil and Diyarbakir residual clays that underwent single drying paths. Furthermore, the coincidence is well compared with the measured suction strength for the sand-kaolin mixture under the repeated change of water content. Hence, the new strength theory model with suction effective concept is validated for predicting the change of shear strength of unsaturated soils that underwent the fluctuation of water content. In the new strength model, only the parameters of SWRC of unsaturated soils and shear strength of saturated soil were used to predict the change of shear strength of unsaturated soils under the arbitrary change of water content.

(4) Based on the measured strength data and predictive curves, the shear strength is closely related to the water content and matric suction. The shear strength can be different at the same matric suction due to the existence of hysteretic effect. Hence, hysteretic effect in the seepage process should be considered to predict the change of shear strength of unsaturated soils that underwent drying/wetting cycles.

Acknowledgments

The research is supported by the National Natural Science Foundation of China (11302243, 11072255), the Natural Science Foundation of GuangXi (no. 2011 GXNSFE018004), and the planed major science and technology projects of Zhejiang (no. 2009C13010).

References

[1] J. E. B. Jennings and J. B. Burland, “Limitations to the use of effective stresses in partly saturated soils,” *Geotechnique*, vol. 12, no. 2, pp. 125–144, 1962.

[2] D. G. Fredlund, N. R. Morgenstern, and R. A. Widger, "Shear strength of unsaturated soils," *Canadian Geotechnical Journal*, vol. 15, no. 3, pp. 313–321, 1978.

[3] S. K. Vanapalli, D. E. Pufahl, and D. G. Fredlund, "The effect of stress state on the soil-water characteristic behavior of a compacted sandy-clay till," in *Proceedings of the 51st Canadian Geotechnical Conference*, pp. 81–86, 1998.

[4] L. Cao and X.-Q. Luo, "Experimental study of dry-wet circulation of Qianjiangping Landslide's unsaturated soil," *Rock and Soil Mechanics*, vol. 28, pp. 93–97, 2007 (Chinese).

[5] S. G. Goh, H. Rahardjo, and E. C. Leong, "Shear strength equations for unsaturated soil under drying and wetting," *Journal of Geotechnical and Geoenvironmental Engineering*, vol. 136, no. 4, pp. 594–606, 2010.

[6] A. W. Bishop, "The principle of effective stress," *Teknisk Ukeblad*, vol. 106, no. 39, pp. 859–863, 1959.

[7] D. G. Fredlund and N. R. Morgenstern, "Stress state variables for unsaturated soils," *Journal of the Geotechnical Engineering Division*, vol. 103, no. 5, pp. 447–466, 1977.

[8] N. Khalili, F. Geiser, and G. E. Blight, "Effective stress in unsaturated soils: review with new evidence," *International Journal of Geomechanics*, vol. 4, no. 2, pp. 115–126, 2004.

[9] N. Lu, "Is matric suction a stress variable?" *Journal of Geotechnical and Geoenvironmental Engineering*, vol. 134, no. 7, pp. 899–905, 2008.

[10] S. K. Vanapalli, D. G. Fredlund, D. E. Pufahl, and A. W. Clifton, "Model for the prediction of shear strength with respect to soil suction," *Canadian Geotechnical Journal*, vol. 33, no. 3, pp. 379–392, 1996.

[11] N. Khalili and M. H. Khabbaz, "A unique relationship for χ for the determination of the shear strength of unsaturated soils," *Geotechnique*, vol. 48, no. 5, pp. 681–687, 1998.

[12] C. Kayadelen, M. A. Tekinsoy, and T. TaşkIran, "Influence of matric suction on shear strength behavior of a residual clayey soil," *Environmental Geology*, vol. 53, no. 4, pp. 891–901, 2007.

[13] A. L. Oberg and G. Sallfors, "Determination of shear strength parameters of unsaturated silts and sands based on the water retention curve," *Geotechnical Testing Journal*, vol. 20, no. 1, pp. 40–48, 1997.

[14] L. Miao, S. Liu, and Y. Lai, "Research of soil-water characteristics and shear strength features of Nanyang expansive soil," *Engineering Geology*, vol. 65, no. 4, pp. 261–267, 2002.

[15] Y. F. Xu, "Fractal approach to unsaturated shear strength," *Journal of Geotechnical and Geoenvironmental Engineering*, vol. 130, no. 3, pp. 264–273, 2004.

[16] N. Lu and W. J. Likos, *Unsaturated Soil Mechanics*, John Wiley, New York, NY, USA, 2004.

[17] D. Tami, H. Rahardjo, and E.-C. Leong, "Effect of hysteresis on steady-state infiltration in unsaturated slopes," *Journal of Geotechnical and Geoenvironmental Engineering*, vol. 130, no. 9, pp. 956–967, 2004.

[18] C. F. Wei and M. M. Dewoolkar, "Formulation of capillary hysteresis with internal state variables," *Water Resources Research*, vol. 42, Article ID W07405, 2006.

[19] N. Lu and W. J. Likos, "Suction stress characteristic curve for unsaturated soil," *Journal of Geotechnical and Geoenvironmental Engineering*, vol. 132, no. 2, pp. 131–142, 2006.

[20] M. A. Hossain and J.-H. Yin, "Shear strength and dilative characteristics of an unsaturated compacted completely decomposed granite soil," *Canadian Geotechnical Journal*, vol. 47, no. 10, pp. 1112–1126, 2010.

[21] N. Lu, J. W. Godt, and D. T. Wu, "A closed-form equation for effective stress in unsaturated soil," *Water Resources Research*, vol. 46, Article ID W05515, 2010.

[22] P. Chen, *A Study on Seepage and Slope Stability of Unsaturated Soils Subjected to Drying/Wetting Cycles*, Institute of Rock and Soil Mechanics; Chinese Academy of Sciences, Wuhan, China, 2011.

[23] C. Yang, D. Sheng, and J. P. Carter, "Effect of hydraulic hysteresis on seepage analysis for unsaturated soils," *Computers and Geotechnics*, vol. 41, pp. 36–56, 2012.

[24] H. K. Kwong, *Effect of hysteresis, infiltration and tensile stress on the strength of an unsaturated soil [Ph.D. thesis]*, Nanyang Technological University, Singapore, 1997.

[25] C. N. Khoury and G. A. Miller, "Influence of hydraulic hysteresis on the shear strength of unsaturated soils and interfaces," *Geotechnical Testing Journal*, vol. 35, no. 1, 2012.

[26] H. Q. Pham, D. G. Fredlund, and S. L. Barbour, "A study of hysteresis models for soil-water characteristic curves," *Canadian Geotechnical Journal*, vol. 42, no. 6, pp. 1548–1568, 2005.

[27] H.-C. Huang, Y.-C. Tan, C.-W. Liu, and C.-H. Chen, "A novel hysteresis model in unsaturated soil," *Hydrological Processes*, vol. 19, no. 8, pp. 1653–1665, 2005.

[28] A. Maqsoud, B. Bussiere, M. Aubertin, and M. Mbonimpa, "Predicting hysteresis of the water retention curve from basic properties of granular soils," *Geotechnical and Geological Engineering*, vol. 30, pp. 1147–1159, 2012.

[29] M. Feng and D. G. Fredlund, "Hysteretic influence associated with thermal conductivity sensor measurements," in *Proceeding from Theory to the Practice of Unsaturated Soil Mechanics, 52nd Canadian Geotechnical Conference and Unsaturated Soil Group, Regina, 1999*.

[30] H. Gvirtzman, E. Shalev, O. Dahan, and Y. H. Hatzor, "Large-scale infiltration experiments into unsaturated stratified loess sediments: monitoring and modeling," *Journal of Hydrology*, vol. 349, no. 1-2, pp. 214–229, 2008.

Hindawi Publishing Corporation
Journal of Applied Mathematics
Volume 2013, Article ID 673057, 12 pages
http://dx.doi.org/10.1155/2013/673057

Research Article

Elastoplastical Analysis of the Interface between Clay and Concrete Incorporating the Effect of the Normal Stress History

Zhao Cheng, Zhao Chunfeng, and Gong Hui

Key Laboratory of Geotechnical and Underground Engineering of Ministry of Education, Department of Geotechnical Engineering, Tongji University, Shanghai 200092, China

Correspondence should be addressed to Zhao Chunfeng; structure.zhao@gmail.com

Received 8 June 2013; Revised 23 August 2013; Accepted 10 September 2013

Academic Editor: Ga Zhang

The behaviour of the soil-structure interface is crucial to the design of a pile foundation. Radial unloading occurs during the process of hole boring and concrete curing, which will affect the load transfer rule of the pile-soil interface. Through large shear tests on the interface between clay and concrete, it can be concluded that the normal stress history significantly influences the shear behaviour of the interface. The numerical simulation of the bored shaft-soil interaction problem requires proper modelling of the interface. By taking the energy accumulated on the interface as a hardening parameter and viewing the shearing process of the interface as the process of the energy dissipated to do work, considering the influence of the normal stress history on the shearing rigidity, a mechanical model of the interface between clay and concrete is proposed. The methods to define the model parameters are also introduced. The model is based on a legible mathematical theory, and all its parameters have definite physical meaning. The model was validated using data from a direct shear test; the validation results indicated that the model can reproduce and predict the mechanical behaviour of the interface between clay and concrete under an arbitrary stress history.

1. Introduction

The bearing behaviour of geotechnical structures embedded in soil, such as deep foundations, tunnels, and retaining structures, is influenced by the contact behaviour at the interface between the surface of the structure and the surrounding soil. A systematic understanding of the shearing behaviour will enable a more accurate analysis and improve the ability to design these structures more accurately. The mechanism that transfers the load through the interface to the surrounding soil has received significant attention in the literature. Over recent decades, many constitutive models have been developed for the soil-structure interface, such as the hyperbolic model and the extended hyperbolic model [1, 2], the Ramberg-Osgood nonlinear elastic model [3], the directionally dependent constitutive model [4], the rate-type model [5], the elastoplastic model [6], and the damage model [7].

A series of shear tests on soil-concrete interfaces were performed using the independent developed visual large scale direct shear apparatus by G. A. Zhang and J. M. Zhang [8, 9], by using that, the interface behaviour is visible with matching image measurement [10]. Evgin and Fakharian also developed the interface apparatus with the name of C3DSSI to carry out the two-way cyclic tangential-displacement-controlled tests and cyclic rotational tests [11]. In geotechnical engineering, the pre- and postconstruction stress paths followed by the interface may be complex, as well as the unloading and reloading. Gómez et al. evaluated the effect of the unloading-reloading paths on the shear behaviour at the sand-concrete interface [12]. By analysing the test data of the groups of staged shear, unload-reload and multidirectional stress path tests, a four-parameter extended hyperbolic model was developed to account for the complex stress paths. However, there are no tests or models for the clay-concrete interface found in the literature that can consider the effect of the stress path; thus, there is a need for more investigation, although it may be more sensitive to stress history. Therefore, it is urgent to develop a model that can incorporate the influence of normal stress history.

In this study, a large direct test apparatus was used to study the clay-concrete interface. The model of the interface

Table 1: Main properties of clay.

Water content	Plastic limit	Liquid limit	Cohesion	Internal friction angle
ω	ω_p	ω_l	c (kPa)	φ (°)
30%	22.4%	45.6%	11.5	22.3

between clay and concrete is proposed, followed by the definition of the parameters in the model. Finally, the model was validated by a comparison with the results from the direct tests.

2. Large Direct Test

2.1. Test Apparatus. Despite some inherent problems, the direct shear apparatus is a commonly used device for interface testing because of its simplicity in sample preparation procedures and its suitability for interface testing. Therefore, a large displacement direct shear test machine in Tongji University was used to conduct the shear strength test on the soil-concrete interface. Compared to conventional direct shear box devices, the large displacement direct shear test results in more accurate interface shear measurements because the proportion of the overall interface affected by the boundaries is smaller for large devices than for smaller ones [13].

2.2. Soil Specimen. The soil specimen was remoulded clay. The main properties of the soil are listed in Table 1. The clay ash was acquired thorough the procedure of airing, crushing, and screening through a sieve (pore size of 0.05 mm). To achieve the desired water content of 30%, appropriately selected amounts of clay ash were thoroughly mixed with calculated amounts of water. Prior to being placed in the shear box, the mixture was left to cure for a period of 12 hours to ensure even water content in the specimen.

2.3. Concrete Plate Specimen. Ruled surface patterns were used to model the concrete surface in this study. The asperity height was changed to quantify the surface roughness, while the asperity angle was altered with the asperity height; the span of the sawtooth was zero in the tests. The asperity heights of the concrete samples were 0, 10, and 20 mm, with asperity angles of 0, 21.8 and 38.66 degrees, respectively. In the analysis, samples number 0, #1, and #2 represent the concrete plates with a sawtooth height of 0, 10, and 20 mm, respectively.

The concrete specimen for testing was 600 mm long by 400 mm wide by 50 mm thick, as illustrated in Figure 1. The specimen was poured against plywood to produce the ruled surface. A wooden frame was attached along the plywood. After the specimen was poured, it was left to cure for 28 days to attain a standard strength. Subsequently, the wooden frame and plywood were removed.

2.4. Test Procedures. The prepared specimens were installed in the shear box in such a way that the bottom half contained the concrete plate, while the top half contained the soil. The interface between the soil and concrete was located exactly between the two halves of the shear box, as shown in Figure 2, to investigate the effect of the normal stress history and the degree of unloading on the shear behaviour and strength at the soil-concrete interface. The specimens were consolidated under an initial normal stress σ_{ni} of 400, 300, and 200 kPa for 1 hour, then unloaded to a specified normal stress (50 kPa to 350 kPa). Both of the loading and unloading rates are 1 KPa/min. After 1 hour of being under a constant applied normal stress, the interface was sheared at a constant rate while the results were monitored. The normal load acting on the interface remained constant during the shear process. Each test was conducted with a rate of shear deformation of 0.3 mm/min to a total of 30 mm. This rate is sufficiently slow to ensure that the excess pore water pressures of the specimens are dissipated during the shearing. The 30 mm displacement criterion was selected because it was observed that under operational conditions, the accumulation of 30 mm of lateral displacement could result in excessive leakage of soil. All data regarding the test (horizontal shear force, shear, and normal displacement) were collected by a computerised data logging system. The results were monitored and saved using the computer software TEST.

Figure 1: The topography of the concrete plate in the test.

2.5. Test Results

2.5.1. Effect of the Applied Normal Stress. Figure 3 shows typical test results for the interaction between clay and concrete plate #0 with an identical initial normal stress of σ_{ni} = 400 kPa. The data from the direct shear tests performed on the interface between clay and concrete plates #1 and #2 are presented in Figures 4 and 5 for comparison. At the beginning of shearing, the shear stress increases sharply with the horizontal displacement. For the applied normal stresses of 50 kPa and 100 kPa, as shear progresses, the stress-strain curves gradually trend to be flatter as the shear stress remains approximately constant for any further increment in the horizontal displacement. However, for other higher normal stresses, the shear stress increases relatively slowly with horizontal displacement in the later-shearing phase, and no strain-softening phenomenon is observed in the tests, which agrees with the results observed by Nasir and Fall [14]. From Figures 3, 4, and 5, it is also observed that the higher applied normal stress during shearing offers a shear

Figure 2: Setup of the specimen box.

stiffness increase for all the values of horizontal displacement. In the meantime, a dilative phenomenon was observed during the tests. Figures 3, 4, and 5 also exhibit this dilative behaviour for the interface between the clay and concrete plates. Before the dilation, the dilative force must offset the applied normal stress acting on the soil specimen, so the more significant dilative displacement was observed in the tests in which a lower normal stress was applied. For the highest applied normal stress of 350 kPa, the clay-concrete interface first exhibits a short contracting behaviour followed by dilatation. The contracting behaviour can be attributed to the lack of complete settlement due to the high normal stress and inadequate consolidation time for clay. For the applied normal stress of 350 kPa and interface #0, no significant dilative behaviour was observed during the shearing process, which may be due to the higher applied normal stress and the low roughness.

2.5.2. Effect of the Initial Normal Stress. Figure 6 shows the test results for interface #0 with different initial normal stresses of shearing under a normal stress of 100 kPa. The shear-stress—displacement and vertical-displacement—shear-displacement relationships for the interface between clay and concrete plates #1 and #2 are presented in Figures 7 and 8, respectively. From these plots, it is observed that higher initial normal stresses produce higher shear stresses during shearing, apart form the curve of initial normal stress 300 kPa on plate #1 and plate #2. This result may be attributed to shear test uncertainties and experimental variations from sample to sample. The shear stiffness was not found to be significantly influenced by the initial normal stress. Figures 6, 7, and 8 exhibit the influence of the initial normal stress on the dilation phenomenon of the interface under the normal stress of 100 kPa. For interfaces not experiencing the progress of normal unloading, the soil near the interface is contracted before dilating. Note that the dilation from the start of shear for the interfaces of initial normal stress over 100 kPa experiences normal unloading. Moreover, a greater vertical displacement occurred for a higher initial normal stress. Therefore, the results validate the effect of the normal stress history on the deformational behaviour of the interface.

2.5.3. Effect of Interface Roughness. For an interface not experiencing normal unloading, the conclusions that a rougher interface exhibits higher shear strength and higher shear stiffness have been stated by many researchers. The roughness of the interface was found to have an effect on the shear zone thickness and shear failure model and to even control the movement style of the soil particles along the interface [7, 15]. However, the strength of the interface does not increase indefinitely with the roughness, according to Zeghal et al. [15]. They identified a bilinear relationship between the surface roughness and the interface friction. Below a certain "critical" roughness, the interface shear resistance increased with roughness, up to the point where the interface shear efficiency parameter reached 1.0. Dove and Jarret took the ruled topography interface to validate the existence of a "critical" roughness; asperity angles greater than approximately 50 degrees caused shear within the soil above the interface, resulting in the lack of the observation of increasing strength [13]. In this experiment, the original planed heights of asperity were 0, 1, 2, and 3 cm. The stress from #3 interface was found to be below the corresponding value of #2 and, sometimes, even below that of the #1 interface. This phenomenon can be explained by the conclusion given by Dove and Jarret [13]. Through a comparison of the shear stresses of #0, #1, and #2 interfaces in Figure 9, the same conclusion can be made: higher asperity offers a higher shear stress. The shear-contractive phase was found at the beginning of the shear for the interfaces not experiencing normal unloading, with a longer shear-contractive phase for a smoother interface. Interface #0 traversed from the shear-contractive phase to the shear-dilative phase at a shear displacement of 11 mm, while the traversal occurred at a shear displacement of 8 mm for interface #1 and of 2 mm for interface #2. The higher contractive value was found to correspond to the smoother interface. The higher asperity results in a higher asperity angle if the width of the asperity remains constant, and the soil near the interface was found to receive more of the vertical component of the force for a higher asperity angle. Therefore, more shear-dilative displacement occurs for a rougher interface.

For the interfaces experiencing normal unloading, the effect from the roughness can be analysed through the maximum shear stress during shear. Similar to the interface

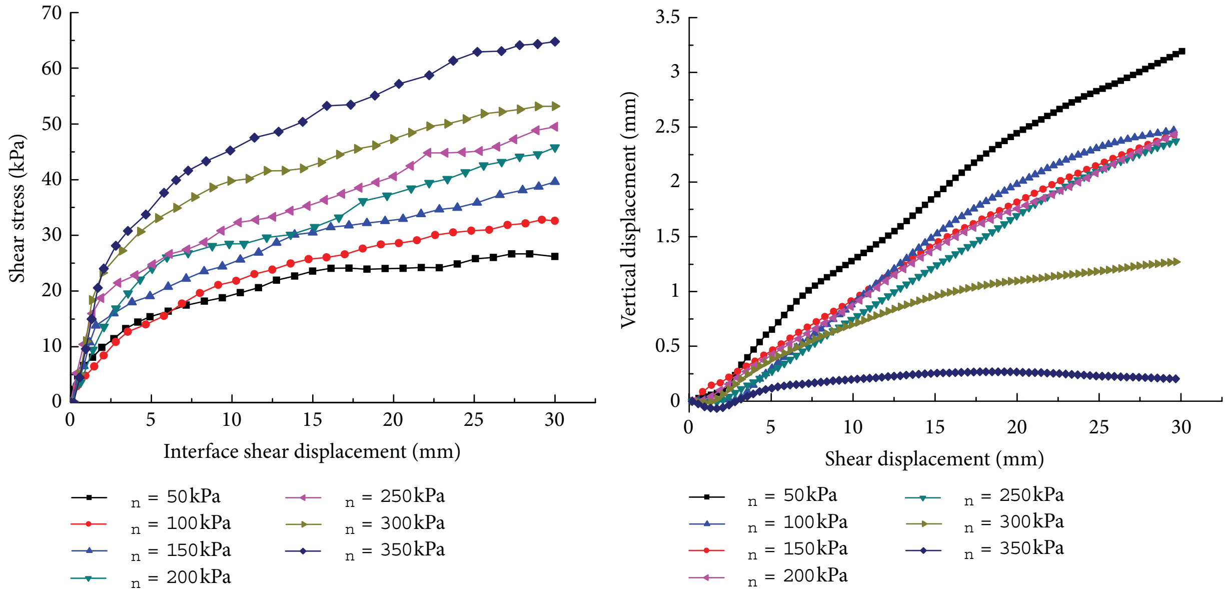

Figure 3: Test results for the interface between clay and #0 plate (initial normal stress of 400 kPa).

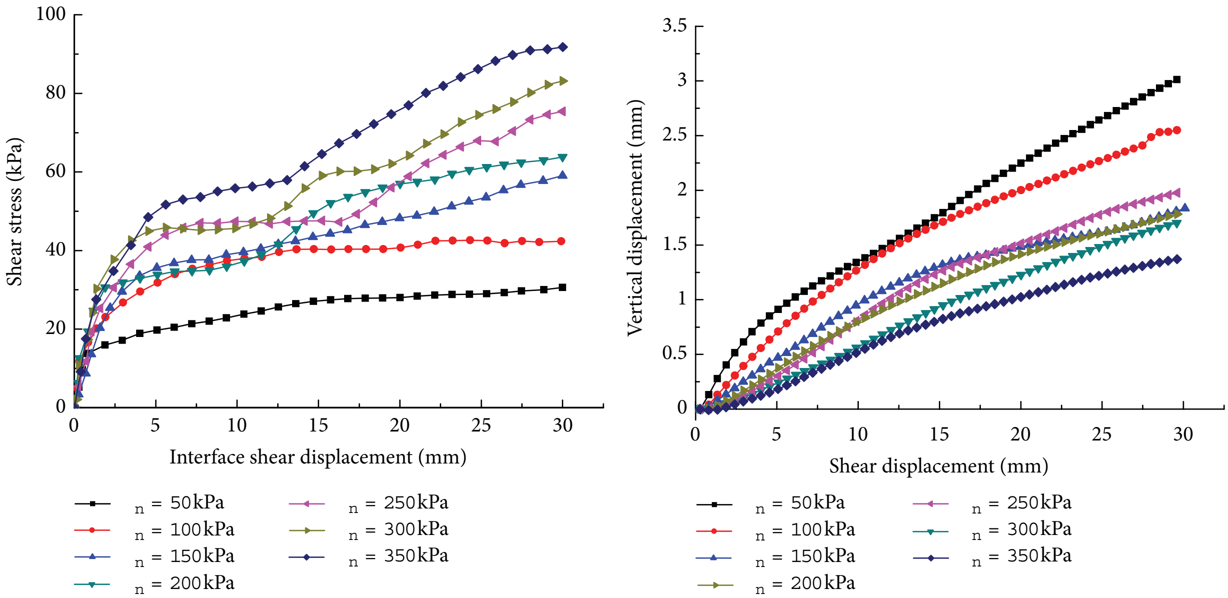

Figure 4: Test results for the interface between clay and #1 plate (initial normal stress of 400 kPa).

not experiencing normal unloading, the rougher interface exhibits a higher maximum shear stress, as depicted in Figure 10; #2 interface exhibited the highest maximum shear stress under the same stress history, the second highest was for #1 interface, and #0 interface had the lowest value. As the initial normal stress increased, the effect from the roughness on the maximum shear stress became increasingly obvious. To analyse the effect of roughness on the dilative phenomenon, we take the data from the interfaces experiencing normal stress unloading in the range from 200 kPa to 100 kPa as an example (the other interfaces had the same shear-dilative trend). Figure 11 shows the higher dilative displacement observed for a rougher interface; the maximum vertical displacement was 2.87 mm for #2 interface, 2.49 mm for #1 interface, and only 1.81 mm for #0 interface.

3. Model Description

Due to the analogy between the behaviours of soil and the interface between soils and structures, the proposed model frame is based on the model of internal shear in soils [16]. According to Liu et al. [16], the incremental stress tensor can be expressed as

$$\{d\sigma\} = \begin{Bmatrix} d\sigma_n \\ d\tau \end{Bmatrix} = [K] \begin{Bmatrix} du_n \\ du_s \end{Bmatrix}, \qquad (1)$$

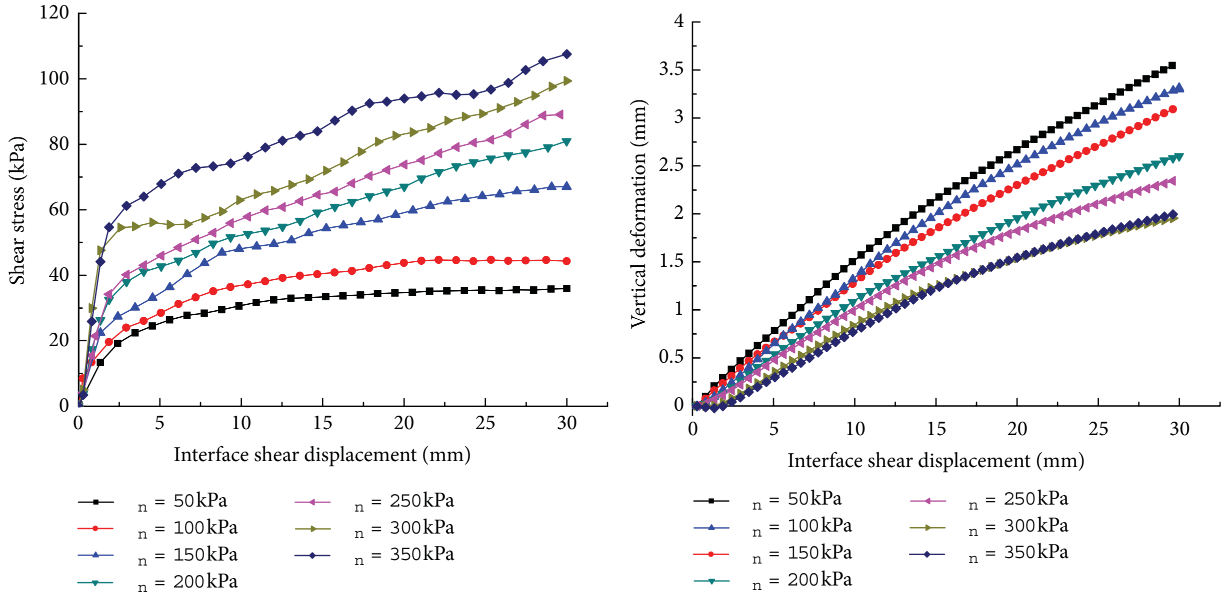

FIGURE 5: Test results for the interface between clay and #2 plate (initial normal stress of 400 kPa).

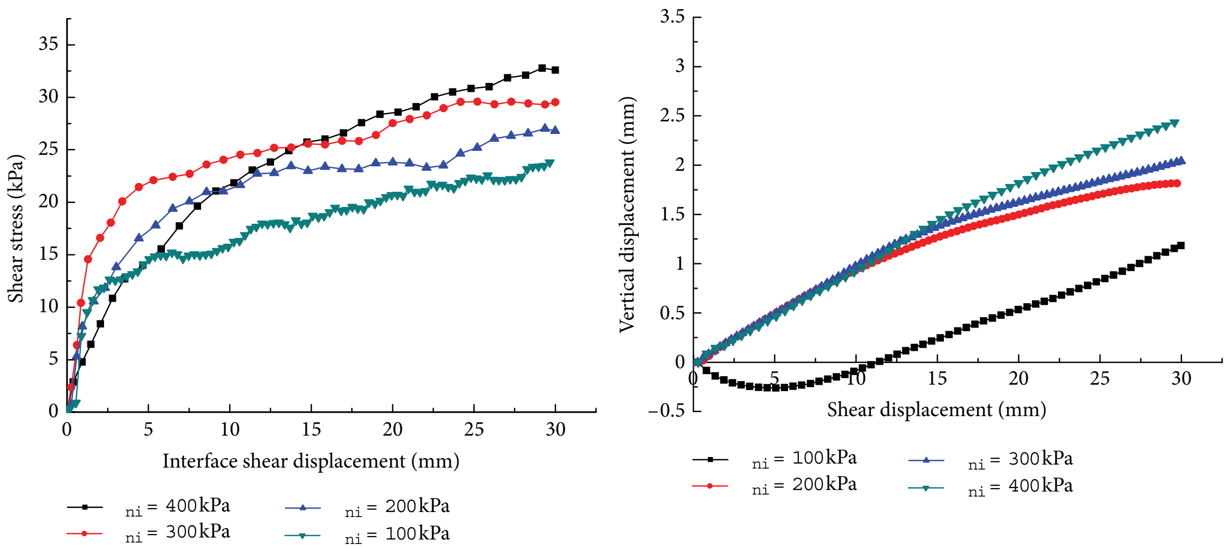

FIGURE 6: Test results for the interface between plate #0 and clay (applied normal stress of 100 kPa).

in which $d\sigma_n$ and $d\tau$ are the incremental normal and shear stresses, respectively, and du_n and du_s are the incremental normal and tangential displacements, respectively. All the parameters can be obtained directly from the test. While the interface is not purely smooth, the researchers [7, 12, 17, 18] found that a shear band exists near the interface during shear. The thickness t was observed to equal five times the diameters of the sand at the interface between the sand and the structure. For the interface with clay, determining the value of t has not been studied. In the direct shear test, the thickness of the shear band cannot be determined because the shear is limited along the plane. As a result, the value of t is set to a constant value in the sections below. An internal strain was assumed, even in the shear band. Consider

$$d\varepsilon_n = \frac{du_n}{t},$$
$$d\varepsilon_s = \frac{du_s}{t}, \tag{2}$$

where $d\varepsilon_n$ and $d\varepsilon_s$ are the incremental normal and shear strain, respectively. Thus, the matrix can be expressed as

$$[K] = t\left[D^{ep}\right]. \tag{3}$$

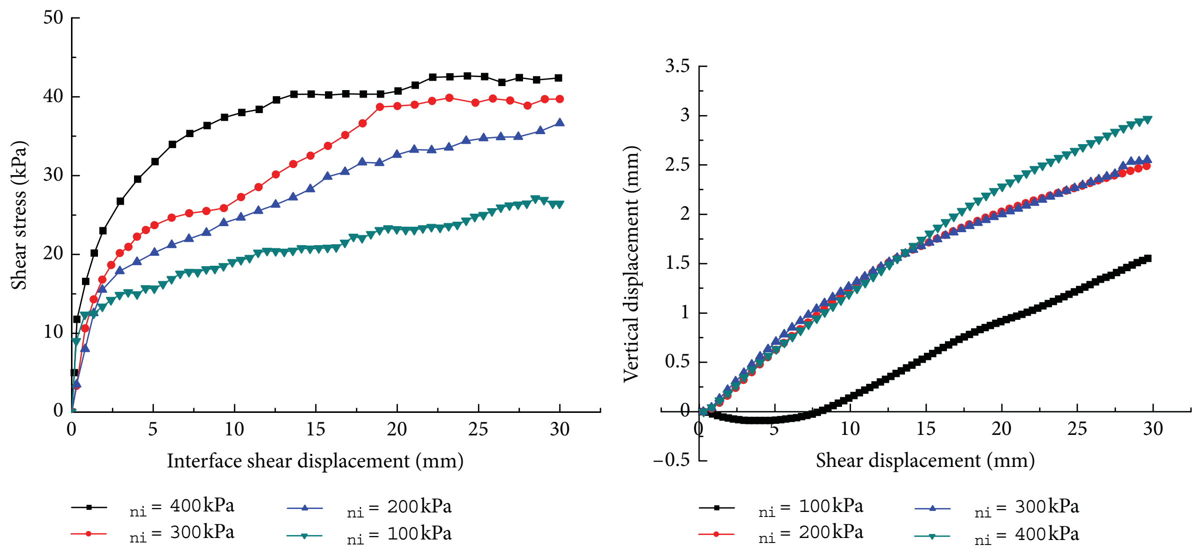

FIGURE 7: Test results for the interface between plate #1 and clay (applied normal stress of 100 kPa).

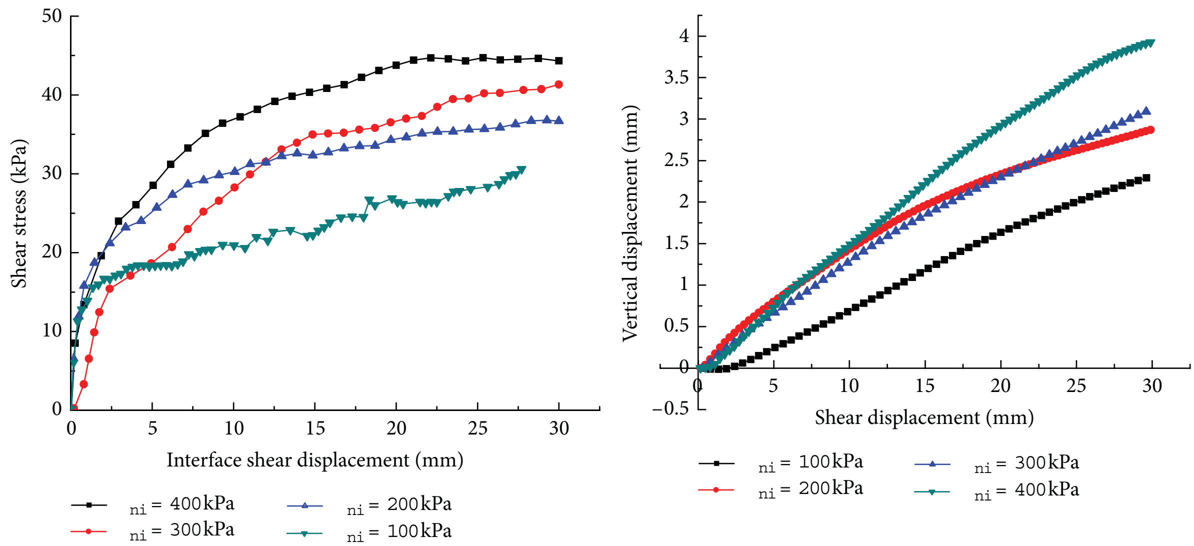

FIGURE 8: Test results for the interface between plate #2 and clay (applied normal stress of 100 kPa).

Here, $[D^{ep}]$ is the elastoplastic constitutive matrix; Morched Zeghal et al. and Zhou Guo-qing et al. proposed the expression of $[D^{ep}]$. To simplify the model, the associated flow rule is applied in the proposed model as follows:

$$[D^{ep}] = [D^{e}] - \frac{[D^{e}]\{n\}^{T}\{n\}[D^{e}]}{H + M + \{n\}[D^{e}]\{n\}^{T}}, \tag{4}$$

where H is the hardening parameter, while M describes the influence of the change in the interfacial frictional coefficient with the stress state. In this proposed model, the interfacial frictional coefficient is assumed to be constant during shear ($M = 0$) to perform the research on the effect of normal stress history. The energy accumulated at the interface, W_p, is taken as the hardening parameter:

$$H = W_p = \int_{\text{loading}} d\sigma\, d\mu_n + \int_{\text{loading}} \sigma_{ni}\, d\mu_n - \int_{\text{unloading}} d\sigma\, d\mu_n - \int_{\text{sheering}} d\sigma\, d\mu_n - \int_{\text{sheering}} d\tau\, d\mu_s. \tag{5}$$

During the loading, the initial energies accumulated at the interface are $\int_{\text{loading}} d\sigma\, d\mu_n$ and $\int_{\text{loading}} \sigma_{ni}\, d\mu_n$, and the energy released during the normal unloading is $\int_{\text{unloading}} d\sigma\, d\mu_n$. During shearing, the energy consumed to

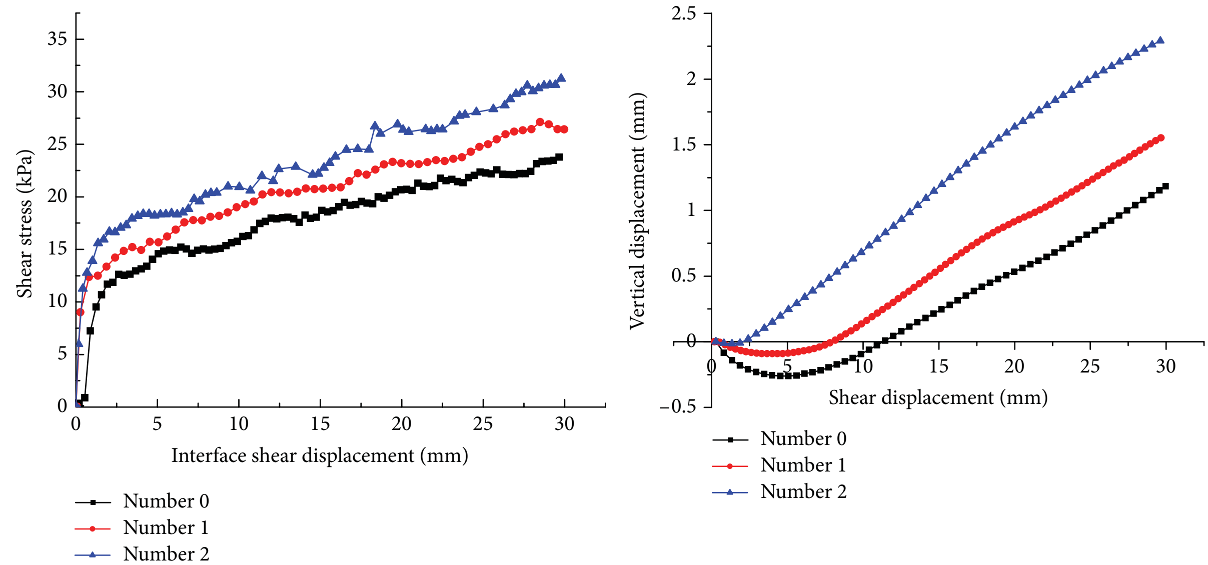

FIGURE 9: Test results for an interface not experiencing normal unloading (normal stress of 100 kPa).

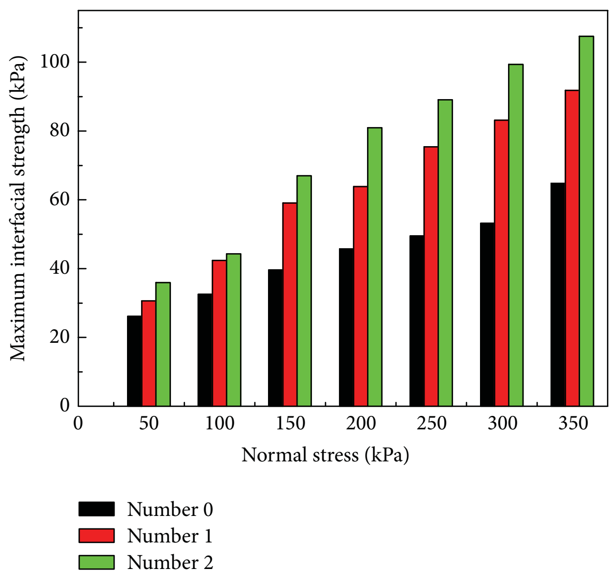

FIGURE 10: The maximum shear stress versus the normal stress for interfaces of different roughness.

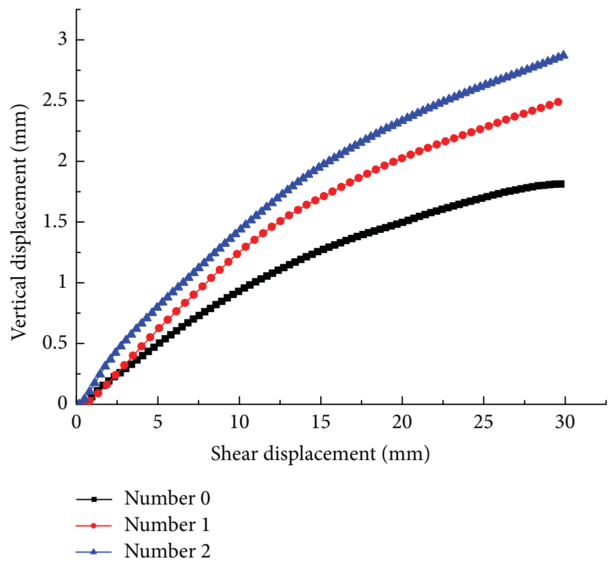

FIGURE 11: The vertical dilative displacement for interfaces of different roughness.

do work is $\int_{\text{sheering}} d\tau\, d\mu_s$. Meanwhile, energy continues to be accumulated in the amount of $\int_{\text{sheering}} d\sigma\, d\mu_n$ for the shear-contractive interface but is consumed for the shear-dilatant interface.

$[D^e]$ is the elastic constitutive matrix, in which nonlinear elasticity is used. For simplicity, the elastic moduli in the normal and tangential directions are assumed to be uncoupled:

$$[D^e] = \begin{bmatrix} D_n & 0 \\ 0 & D_s \end{bmatrix}, \tag{6}$$

where D_n and D_s are the normal and tangential moduli, respectively, which are both influenced by the stress history and stress state, according to Desai C. S.

Liu et al. [16] identified the loading direction vector $\{n\}$ as

$$\{n\} = \left(\frac{d_f}{\sqrt{1 + d_f^2}} \quad \frac{1}{\sqrt{1 + d_f^2}} \right). \tag{7}$$

The parameter d_f is related to the stress state and the initial state of the interface; however, it cannot capture the loading direction of the sawtooth interface in our large test. Morched Zeghal and coworkers modelled the interface as

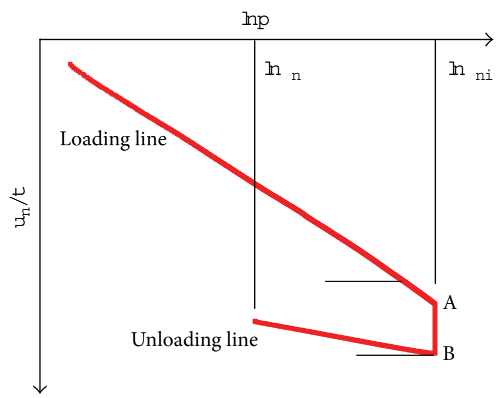

Figure 12: u_n-ln$p$ plots of the loading and unloading process in the tests.

a ruled sawtooth. According to their approach, the loading direction of the sawtooth should be

$$\{n\} = \left\{ \frac{\partial F}{\partial \sigma_n} \quad \frac{\partial F}{\partial \tau} \right\} = \{\sin \alpha_k + u \cos \alpha_k \quad \cos \alpha_k - u \sin \alpha_k\}. \tag{8}$$

Here, u is the frictional coefficient of the interface when the sawtooth height is equal to zero. α_k is the topography parameter.

4. Identification of the Model Parameters

4.1. Elastic Moduli: D_n and D_s. The normal elastic moduli D_n can be determined from the loading-unloading curve of u_n-ln$p$, as shown in Figure 12; the displacement of the AB section is deduced from the primary consolidation of the clay under the initial normal stress, and the resilience occurring as the initial normal stress σ_{ni} is unloaded to the normal stress σ_n. The slope coefficient of the resilience line was signified by κ. Thus, the normal moduli can be determined as.

$$D_n = \frac{\sigma_n}{\kappa}. \tag{9}$$

The hyperbolic model was validated by many test results, which measured the shear moduli changes with shear displacement. Consider

$$D_s = \frac{a}{(a + b\varepsilon_s)^2}, \tag{10}$$

where $a = 1/D_{si}$, $b = \sigma_n/\tau_{\mathrm{ult}}$, and τ_{ult} is the ultimate shear strength of the critical state in the test; thus, $b = 1/\eta_c$. From Figures 3–8, the peak shear strength is not yet reached, even when the shear displacement is accumulated to 30 mm, which is the limit displacement of this test because, under operational conditions, the accumulation of 30 mm of lateral displacement was observed to possibly result in excessive leakage of soil. Thus, the destructional ratio R_f is introduced:

$$R_f = \frac{\tau_f}{\tau_{\mathrm{ult}}}, \tag{11}$$

$$D_s = D_{si}\left(1 - R_f \frac{\tau}{\tau_f}\right)^2, \tag{12}$$

where τ_f is the shear stress as the shear displacement reaches 30 mm and τ_{ult} is determined through curve fitting. D_{si} are the initial tangent shear moduli, which are described by Anubhav P.K. and coworkers; where an increase in the normal stress will result in steeper shear-relative displacement curves and a higher strength, and the values of D_{si} and τ_{ult} therefore will increase with the increase in normal stress. This stress dependence is taken into account by using empirical equations to represent the variation of D_{si} with normal stress:

$$D_{si} = KP_a\left(\frac{\sigma_n}{P_a}\right)^n, \tag{13}$$

where K is the modulus number and n is the modulus exponent (both are dimensionless numbers), and P_a is the atmospheric pressure. However, the modulus number and the modulus exponent must be determined through curve fitting, which limits the application of the proposed model. At the beginning of shear, the deformation can be assumed to be elastic, so the initial shear modulus can be expressed as follows. According to the relationship between the normal elastic modulus and the shear elastic modulus and by analogy between the behaviours of soil and the interface between soil and structures,

$$D_{si} = \frac{D_n}{2(1+\nu)} = \frac{\sigma_n}{2\kappa(1+\nu)}, \tag{14}$$

where ν is Poisson's ratio of the soil. However, the above equation cannot incorporate the influence of normal stress history on the initial shear modulus. G.T. Houlsby and C.P. Wroth performed a research on the stress history of soil; the initial shear modulus that can account for the effect of stress history was expressed as

$$G_{oc} = G_{nc}\left(\frac{\sigma_{ni}}{\sigma_n}\right)^{0.7}, \tag{15}$$

where G_{oc} is the initial shear modulus during overconsolidation of soil and G_{nc} is the initial shear modulus during normal consolidation of soil. Note that the exponent has the value of 0.7 only for the situation of an overconsolidation ratio below 10. Therefore, the initial shear modulus of the proposed model can be given by

$$D_{si} = \frac{\sigma_n}{2\kappa(1+\nu)}\left(\frac{\sigma_{ni}}{\sigma_n}\right)^{0.7}. \tag{16}$$

Finally, the shear modulus that accounts for the effect of normal stress history is

$$D_s = \frac{\sigma_n}{2\kappa(1+\nu)}\left(\frac{\sigma_{ni}}{\sigma_n}\right)^{0.7}\left(1 - R_f\frac{\tau}{\tau_f}\right)^2. \tag{17}$$

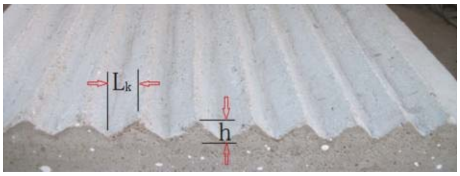

Figure 13: The topography parameters of the concrete plate used in the test.

4.2. The Topography Parameter α_k. The ruled topography concrete plates were used in the large shear test. For such a sawtooth interface, Morched Zeghal defined α_k as

$$\alpha_k = \frac{\pi h}{2L_k} \sin \frac{\pi}{2} \left(1 + \frac{u_s}{L_k}\right) \tag{18}$$

in which h and L_k are the height and width, respectively, of the sawtooth, as illustrated in Figure 13.

4.3. Hardening Parameter H. $\int_{\text{loading}} d\sigma\, d\mu_n$ and $\int_{\text{unloading}} d\sigma\, d\mu_n$ could by computed from the normal loading-unloading curve, as shown in Figure 12. Consider

$$\int_{\text{loading}} d\sigma\, d\mu_n = \int_1^{\sigma_{ni}} \left(u_{n0} + \lambda \ln p\right) dp, \tag{19}$$

$$\int_{\text{unloading}} d\sigma\, d\mu_n = \int_{\sigma_{\text{ni}}}^{\sigma_n} \left(u_{ni} - \kappa \ln p\right) dp, \tag{20}$$

where u_{n0} is the normal displacement at the normal stress of 1 kPa and u_{ni} is the normal displacement at the beginning of unloading (the B point in Figure 12), while λ and κ are the slope coefficients of the loading and unloading lines, respectively.

$\int_{\text{loading}} \sigma_{ni}\, d\mu_n$ is the power accumulated during the progress of consolidation under the initial normal stress, and the stress remains constant in this period. Thus, the power is

$$\int_{\text{loading}} \sigma_{ni}\, d\mu_n = \sigma_{ni} \left(u_{nB} - u_{nA}\right). \tag{21}$$

As illustrated in Figure 11, u_{nA} and u_{nB} are the displacement at the end of the loading period and the beginning of the unloading, respectively.

Both $\int_{\text{sheering}} d\tau\, d\mu_s$ and $\int_{\text{sheering}} d\sigma\, d\mu_n$ should be determined through iteration. First, assuming the relationship τ-μ_s follows a hyperbolic model, the initial value of τ can be computed by substituting the shear displacement (0–30 mm) into the hyperbolic model. Next, the initial value of τ can be substituted into (1) to determine the new displacement value, which enables the initial hardening parameter to be computed. The new value of τ is then recomputed based on the initial hardening parameter, and then, the new shear displacement and new shear stress are calculated. The final shear stress and displacement are computed when the error tolerance is satisfied.

5. Model Validation

The predicted results of the model are shown in Figures 14(a), 14(b), and 14(c) together with the experimental results for the #0, #1, and #2 interfaces first under the initial normal stress of 400 kPa then being unloaded to the normal stress of 50–350 kPa. The model is able to reproduce the behaviour of the clay-concrete interface with different normal stresses, different initial normal stresses, and roughness. Note that the model simulated the shear-stress-displacement relationship to a satisfactory degree, which is very important for pile-soil interface and retaining wall problems. From Figure 14, the shear stress is found to increase quickly with displacement, and as shear progressed, the dissipative power $\int_{\text{sheering}} d\tau\, d\mu_s$ increased; meanwhile, the power accumulated at the interface H was consumed slowly. During the last half of the shear progress, the shear stress increases gradually with displacement and finally approaches a constant value.

Figures 15(a), 15(b), and 15(c) show the shear stress versus horizontal displacement along the interface between concrete plates #0, #1, and #2, respectively, and clay with different initial normal stresses and shearing under a normal stress of 100 kPa. The higher initial normal stress results in higher power $\int_{\text{loading}} d\sigma\, d\mu_n$ and $\int_{\text{loading}} \sigma_{ni}\, d\mu_n$ accumulated at the interface and results in higher shear stiffness. From the microcosmic viewpoint, the higher initial normal stress causes the soil near the interface to reach a higher compressive strength. Another reasonable explanation is that the clay is more closely embedded into the sawtooth topography for the higher initial normal stress. The cohesive section of the shear strength of the interface is formed by the absorption of water molecules in the clay and the surface of the concrete plate; under the pressure of the initial normal stress, the water molecules in the clay will penetrate into the concrete plate and keep inside.

6. Conclusions

First, using sawtooth-surfaced concrete plates to quantify the roughness of the interface, a series of shear tests were conducted to analyse the effects of roughness and unloading on the shear behaviour of the interface between clay and concrete. Based on the results of direct shear tests on the clay-concrete interface, the following conclusions can be proposed.

Through the process of loading to an initial normal stress, unloading to normal stress and shearing under this normal stress, the shear behaviour of the interface between clay and concrete was found to be influenced by the initial normal stress and the roughness of the interface. A higher initial normal stress results in a higher shear stress during the shearing. Under the same initial normal stress, a lower value of shear stiffness was observed for a higher unloading ratio (a lower normal stress during shearing). The effect of roughness on the shear behaviour is revealed through the shear stress-displacement relation and the normal dilative phenomenon. Regardless of whether normal unlading occurred or not the

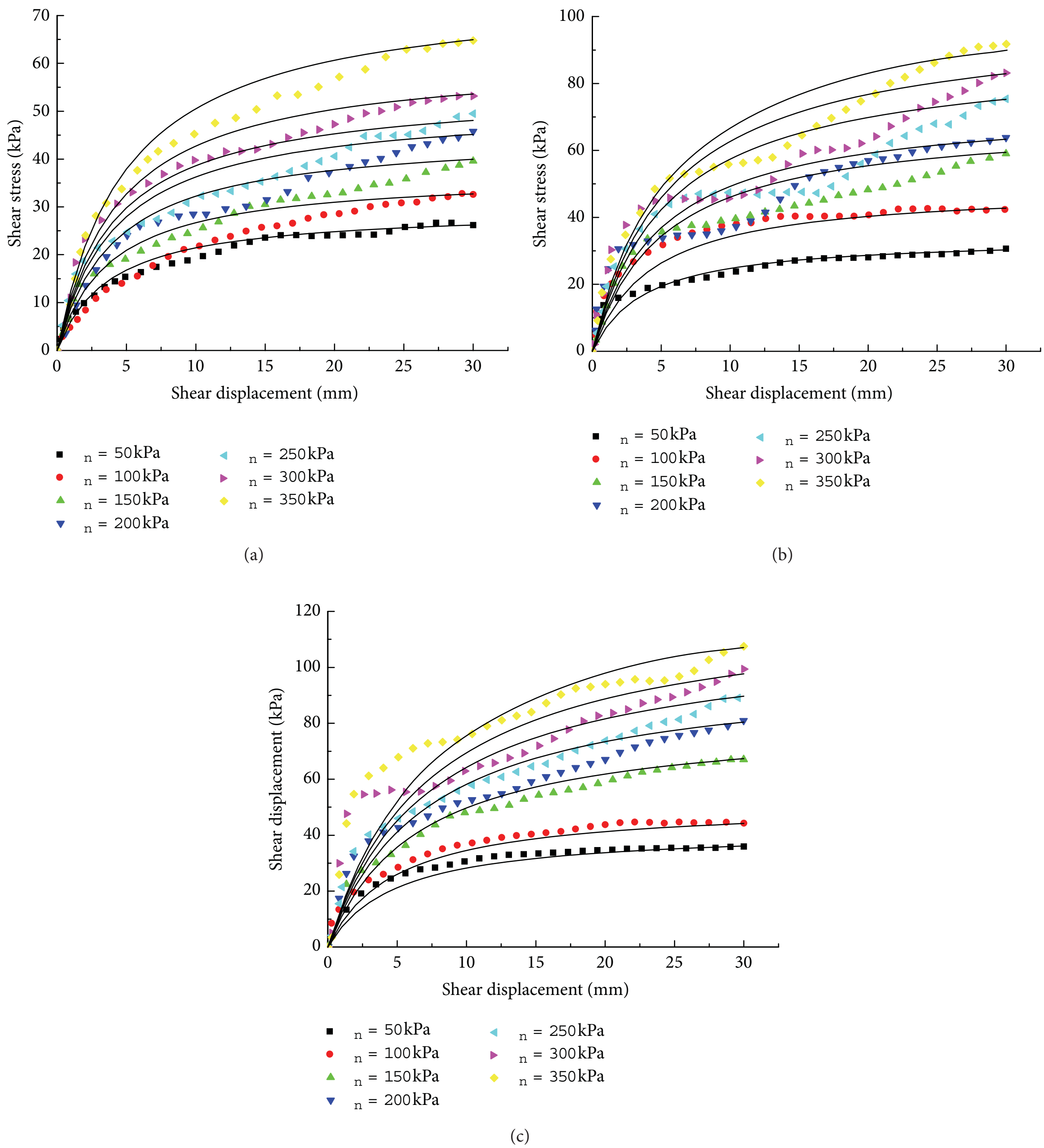

FIGURE 14: Shear-stress-displacement curves of the interface between clay and concrete (σ_{ni} = 400 kPa).

rougher interface offers a higher shear stress and vertical displacement.

The shear-dilative behaviour is significantly influenced by the stress history. The shear-contractive phase occurs at the beginning of shear for the interfaces that do not experience normal unloading, while no such contractive displacement was found for interfaces experiencing unloading of the initial normal stress σ_{ni} to the applied normal stress σ_n before shear.

Finally, a model that can account for the effect of normal stress history was proposed. The parameters of the model all have definite physical meanings. The calibration and validation of the model were performed by simulating laboratory test results conducted in a newly developed large direct shear apparatus. The results demonstrated that the model is capable of predicting the behaviour of clay-concrete interfaces and of capturing the effects of different normal stress history and roughness.

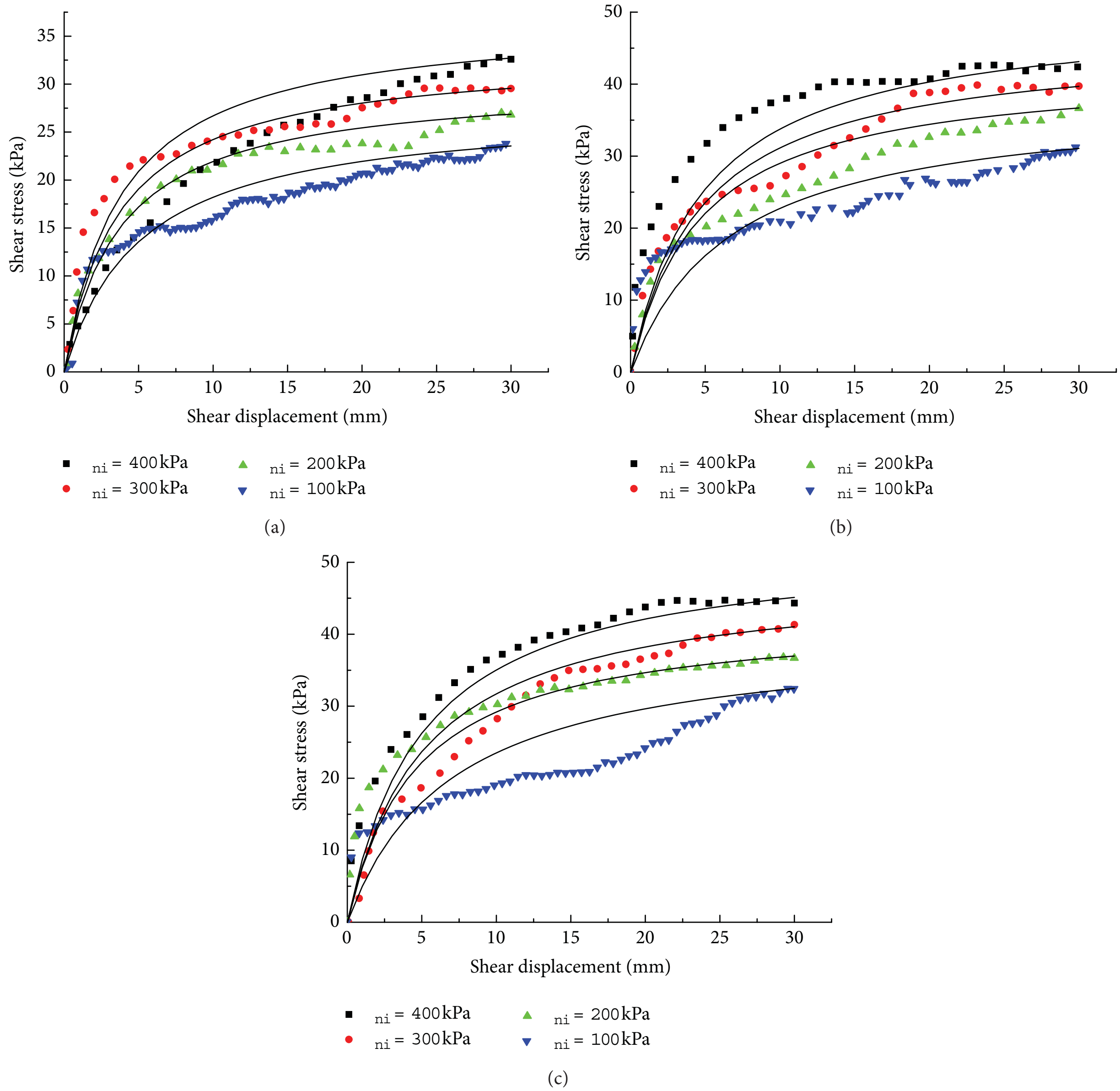

FIGURE 15: Shear-stress-displacement curves of the interface between clay and concrete (σ_n = 100 kPa).

Acknowledgments

The present study was supported by the National Natural Science Foundation Project (41202193), the Shanghai Pujiang Program (11PJ1410100), and the Kwang-Hua Fund for the College of Civil Engineering, Tongji University.

References

[1] G. W. Clough and J. M. Dunan, "Finite element analyses of retaining wall behavior," *Journal of the Soil Mechanics and Foundations Division*, vol. 97, no. 12, pp. 1657–1673, 1971.

[2] J. E. Ǵomez, G. M. Filz, and R. M. Ebeling, "Extended hyperbolic model for sand-to-concrete interfaces," *Journal of Geotechnical and Geoenvironmental Engineering*, vol. 129, no. 11, pp. 993–1000, 2003.

[3] C. S. Desai, E. C. Drumm, and M. M. Zaman, "Cyclic testing and modeling of interfaces," *Journal of Geotechnical Engineering*, vol. 111, no. 6, pp. 793–815, 1985.

[4] M. Boulon and C. Plytas, "Soil-structure directionally dependent interface constitutive equation—application to the prediction of shaft friction along piles," in *Proceedings of the 2nd International Symposium on Numerical Models in Geomechanics*, pp. 43–54, Ghent, Belgium.

[5] M. Boulon and R. Nova, "Modelling of soil-structure interface behaviour a comparison between elastoplastic and rate type laws," *Computers and Geotechnics*, vol. 9, no. 1-2, pp. 21–46, 1990.

[6] V. N. Ghionna and G. Mortara, “An elastoplastic model for sand-structure interface behaviour,” *Geotechnique*, vol. 52, no. 1, pp. 41–50, 2002.

[7] L. Hu and J. Pu, “Testing and modeling of soil-structure interface,” *Journal of Geotechnical and Geoenvironmental Engineering*, vol. 130, no. 8, pp. 851–860, 2004.

[8] G. A. Zhang and J. M. Zhang, “Large-scale apparatus for monotonic and cyclic soil-structure interface test,” *Geotechnical Testing Journal*, vol. 29, no. 5, pp. 401–408, 2006.

[9] G. A. Zhang and J. M. Zhang, “Monotonic and cyclic tests of interface between structure and gravelly soil,” *Soils and Foundations*, vol. 46, no. 4, pp. 505–518, 2006.

[10] G. Zhang, D. Liang, and J. M. Zhang, “Image analysis measurement of soil particle movement during a soil-structure interface test,” *Computers and Geotechnics*, vol. 33, no. 4-5, pp. 248–259, 2006.

[11] E. Evgin and K. Fakharian, “Cyclic rotational simple-shear behaviour of sand-steel interfaces,” *Soils and Foundations*, vol. 38, no. 2, pp. 191–199, 1998.

[12] J. E. Gómez, G. M. Filz, R. M. Ebeling, and J. E. Dove, “Sand-to-concrete interface response to complex load paths in a large displacement shear box,” *Geotechnical Testing Journal*, vol. 31, no. 4, pp. 358–369, 2008.

[13] J. E. Dove and J. B. Jarrett, “Behavior of dilative sand interfaces in a geotribology framework,” *Journal of Geotechnical and Geoenvironmental Engineering*, vol. 128, no. 1, pp. 25–37, 2002.

[14] O. Nasir and M. Fall, “Shear behaviour of cemented pastefill-rock interfaces,” *Engineering Geology*, vol. 101, no. 3-4, pp. 146–153, 2008.

[15] M. Zeghal, T. B. Edil, and M. E. Plesha, “Discrete element method for sand-structure interaction,” in *Proceedings of the 3rd International Conference on Discrete Element Methods*, pp. 317–322, Santa Fe, NM, USA, September 2002.

[16] H. Liu, E. Song, and H. I. Ling, “Constitutive modeling of soil-structure interface through the concept of critical state soil mechanics,” *Mechanics Research Communications*, vol. 33, no. 4, pp. 515–531, 2006.

[17] C. S. Desai and D. B. Rigby, “Cyclic interface and joint shear device including pore pressure effects,” *Journal of Geotechnical and Geoenvironmental Engineering*, vol. 123, no. 6, pp. 568–579, 1997.

[18] M. T. Luan and Y. J. Wu, “Nonlinear elasto-perfectly plastic model of interface element for soil-structure interaction and its applications,” *Rock and Soil Mechanics*, vol. 25, no. 4, pp. 507–513, 2004 (Chinese).

Hindawi Publishing Corporation
Journal of Applied Mathematics
Volume 2013, Article ID 795962, 14 pages
http://dx.doi.org/10.1155/2013/795962

Research Article

Analytical Analysis and Field Test Investigation of Consolidation for CCSG Pile Composite Foundation in Soft Clay

Jin Yu,[1] Yanyan Cai,[1] Zhibo Qi,[1] Yunfei Guan,[2] Shiyu Liu,[1] and Bingxiong Tu[1]

[1] *Geotechnical Engineering Institute, Huaqiao University, Xiamen 361021, China*
[2] *Geotechnical Engineering Department, Nanjing Hydraulic Research Institute, Nanjing, Jiangsu 210024, China*

Correspondence should be addressed to Jin Yu; bugyu0717@163.com

Received 6 June 2013; Revised 25 August 2013; Accepted 6 September 2013

Academic Editor: Fayun Liang

Low-grade concrete-cored sand-gravel (CCSG) pile composite foundation is a new kind of composite foundation for thick and soft clay ground treatment. An analytical solution was derived for calculating the consolidation process of this composite foundation by considering coefficients of horizontal permeability in smear zone, the radial flow within the sand-gravel shell, and the impervious property of concrete-cored pile. The results show that Terzaghi's one-dimensional consolidation solution and the consolidation analytical solution of ordinary composite foundation were special cases of this solution. Curves of the average consolidation degree of the composite foundation under various nondimensional parameters were observed using the program based on the theoretical formula. Meanwhile, a series of in situ measurements including the settlement of pile and soil, the pore water pressure, and the total stress under embankment load were obtained on the CCSG pile composite foundation on a section of Zhenjiang-Liyang highway. The analyzed results show that the new style composite foundation patent technology has many advantages such as small differential postconstruction settlement (differential is not good, small is), reliable quality, high bearing capacity, and stability. And the consolidation of composite foundation is largely affected by the nondimensional parameters. The analytical solution is finally verified with the actual measurement data.

1. Introduction

Composite foundation technology has been widely used in the foundation treatment of soft soil. Concrete-cored sand-gravel pile composite foundation (CCSG pile composite foundation), which is composed by prefabricated low-grade concrete-cored pile and sand-gravel shell, consisting of soil between piles, cushion, and the composite pile, is a new type of multivariate composite foundation that has been put forward in the recent years. Based on the idea of controlling and differentiating post-construction settlement, this foundation uses low-grade concrete-cored pile as the vertical reinforcement, sand-gravel shell as the vertical drainage body, and cushion as the horizontal drainage body, as shown in Figure 1. The outstanding advantages of this new style technology lie in using the concrete-cored sand-gravel shell as the vertical drainage body to speed up the consolidation of soil between piles during construction and preloading periods, to control post-construction settlement and differential post-construction settlement within allowed extent in applied periods, and to make full use of the bearing capacity of soil between piles. A surcharge load larger than the structure load was adopted for preloading to accelerate the process of compression. In deep soft foundation treatment, the hierarchical heap load and the drainage reinforcement advantages of sand shell in preloading period help to speed up pore water pressure dissipation and degree of consolidation in soft soil. And the deep foundation compression consolidation effect is remarkable.

On the other hand, the consolidation theories for composite foundations reinforced by columns are developed on the basis of those well-drained foundations. The only difference between these theories is that the former one considers the stress concentration between soil and column but the latter does not. The most well-known theoretical study on the radial consolidation of vertical drains was carried out by Barron [1] firstly. A large number of studies have been conducted after. Recently, the consolidation of composite

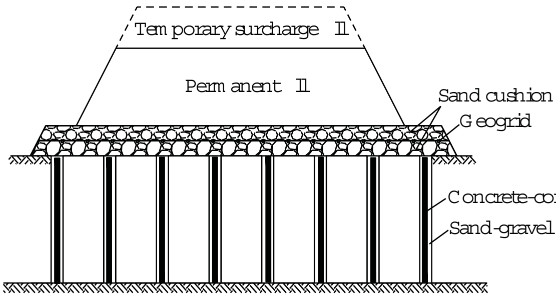

FIGURE 1: Schematic diagram of section.

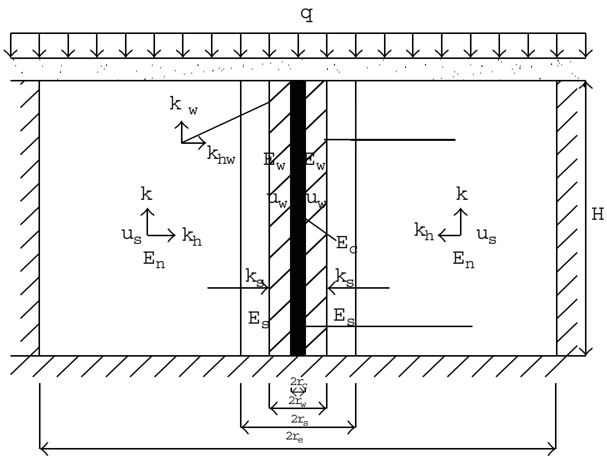

FIGURE 2: Computing model of single CCSG pile.

foundation theory based on the sand drain consolidation theory has made great progress, with the consideration of the stress concentration phenomenon, well resistance, and smear effect. Goughnour and Bayuk [2] thought that composite foundation consolidation problem could be analyzed by the sand drain consolidation theory; Tang and Onitsuka [3] and Xie [4, 5] have established the consolidation equation for discrete material-pile composite foundation based on the equal strain assumption of Barron [1] and have also put forward the radial average degree of consolidation calculation formulae and the analytical solution of shaft drainage considering well resistance and the smudge effect. By incorporating the radial and vertical drainage in a coupling fashion, Leo [6] presented a series of closed-form solutions for equal strain consolidation of vertical drains subjected to instantaneous and ramp loading. The smear effect and well resistance were studied. Furthermore, this solution was extended by Lei et al. [7] to consider a time and depth-dependent loading. Zhu and Yin [8, 9] presented an analytical solution for the consolidation analysis of soil with a vertical drain under ramp loading considering the smear effect. Wang and Jiao [10] introduced the double porosity model into the analysis of vertical drain consolidation. With this approach, the variation of horizontal soil permeability can be depicted by an arbitrary function, which presents a relatively simple way to consider the gradual variation of soil permeability within the smear zone. Walker and Indraratna [11] have shown that the overlapping smear zone due to the reduction of drain spacing could also influence the drain performance. By incorporating the relationship of e-logσ' and e-logk_h, Indraratna et al. [12] found a new solution for the radial consolidation of vertical drains. Basu and Prezzi [13], Castro and Sagaseta [14] and Xie et al. [15, 16] utilized a stress increment independent of time and depth for the simplicity and effectiveness in solving engineering problems, in which the external load was assumed to be applied instantly and the corresponding stress increment resulted within the foundation was considered to be uniformly distributed along the column depth. A large number of laboratory studies [15–21] have shown that the coefficient of permeability within the smear zone was highly variable. To reflect the variability, some researchers included the gradual decay of horizontal permeability of soil toward the drain, such as linear decay in their analyses of vertical drain consolidation [22]. Recently, researchers have done lots of work on composite foundation [15, 16, 23–29]. A general theoretical solution has been put forward for the consolidation of a composite foundation, and the consolidation theory has been presented for the composite foundation considering radial and vertical flows within the column, the variation of soil permeability within the disturbed soil zone, the depth-varying stress induced by multistage loading, and time- and depth-dependent stress increment along with different distribution patterns of soil permeability.

The above results have important reference value to study the reinforcement mechanism of composite foundation. But the studies of consolidation characteristic of CCSG pile composite foundation, which is new, under complicated conditions and multivariate, have not been reported yet. The authors have tried to study the consolidation calculation method of CCSG pile composite foundation in simple cases, but the influence factors of CCSG pile composite foundation consolidation characteristic are not considered, such as the change of horizontal penetration parameter in influence area, radial flow in sand shell, and the impervious character of low grade concrete core pile.

This paper introduces a series of field tests on CCSG pile composite foundation and the consolidation analysis model of CCSG pile composite foundation is established, which is based on equal strain hypothesis and considering the change of horizontal penetration parameters in influence zone and radial flow within sand-gravel shell. The consolidation general solution was obtained by the theoretical derivation. The analytical solution was finally validated with the data obtained from field tests and has verified the correctness of the theoretical solution.

2. General Solution for Consolidation of CCSG Pile Composite Foundation

2.1. Calculation Diagram. The idealized CCSG composite foundation is shown in Figure 2. In this figure, H is the thickness of the soil; r_c, r_w, r_s, and r_e are radius of the concrete-cored pile, the sand-gravel shell, the smear zone, and the influence zone (consisting of strong smear zone and weak smear zone), respectively; E_c, E_w, E_s, and E_n are modulus of compressibility of the concrete-cored pile, the sand-gravel shell, the strong smear zone, and the weak smear zone respectively; k_s and k_h are the horizontal permeability coefficient of the strong smear zone and the weak smear zone, respectively; k_v is the vertical permeability coefficient of soil; k_{hw} and k_{vw} are the horizontal and vertical permeability coefficient of sand-gravel shell, respectively; u_w and u_s are excess pore water pressures within the sand-gravel shell and in the soil; q is external load.

2.2. Basic Assumptions. In order to obtain a simplified analytical solution, the following assumptions were made for the calculation.

(1) The relative displacement between CCSG pile and soil was ignored. The column and the surrounding soil were assumed to deform only vertically and had equal strain at same depth. Concrete-cored pile was simplified as an impervious cylindrical pile with the corresponding radius, and the interaction between the concrete-cored pile and the sand-gravel shell was also ignored.

(2) Darcy's law was obeyed.

(3) The soil within the scope of drainage influence zone was divided into strong smear zone and weak smear zone, in which the horizontal permeability coefficient changed along radial direction, as $k_r(r)$.

(4) The radial flow was taken into account in sand shell.

(5) The load was applied instantly. The additional stress of composite foundation distributed uniformly along the depth.

2.3. Consolidation Equations and Solving Conditions

2.3.1. Equilibrium Condition and Stress-Strain Relationship. In order to investigate the consolidation properties of CCSG pile composite foundation, the stress concentration effect should be considered, which concludes the stress of the concrete-cored pile and the sand-gravel shell, the excess pore water pressures of the sand-gravel shell, and the composite modulus of compression of the soil. At any time, both the column and the surrounding soil share the total stress in a composite foundation; that is,

$$\pi r_c^2 \overline{\sigma}_c + \pi\left(r_e^2 - r_w^2\right)\overline{\sigma}_s + \pi\left(r_w^2 - r_c^2\right)\overline{\sigma}_w = \pi r_e^2 \sigma_0,$$
$$\frac{\overline{\sigma}_c}{E_c} = \frac{\left(\overline{\sigma}_s - \overline{u}_s\right)}{E} = \frac{\left(\overline{\sigma}_w - \overline{u}_w\right)}{E_w} = \varepsilon_v, \tag{1}$$

where $\overline{\sigma}_w$, $\overline{\sigma}_c$, and $\overline{\sigma}_s$ are the average total stresses within the sand-gravel shell, the concrete-cored pile, and the soil, respectively, and σ_0 is the additional stress of composite foundation in any depth caused by the uniform load; ε_v is the vertical strain of the column and the surrounding soil; $E = ((n^2-s^2)/(n^2-1))E_n + ((s^2-1)/(n^2-1))E_s$ is the composite modulus of compression of the soil; $\overline{u}_s$ and $\overline{u}_w$ are the excess pore water pressure within the soil and within the sand-gravel shell, respectively, which can be defined as

$$\overline{u}_s = \frac{\int_{r_w}^{r_e} 2\pi r u_s dr}{\pi\left(r_e^2 - r_w^2\right)}, \tag{2}$$

$$\overline{u}_w = \frac{\int_{r_c}^{r_w} 2\pi r u_w dr}{\pi\left(r_w^2 - r_c^2\right)}, \tag{3}$$

where r is the radial distance away from the centre of concrete-cored pile.

From (1), ε_v can be derived as

$$\begin{aligned}\varepsilon_v &= \frac{n^2\sigma_0 - \left(n^2-1\right)\overline{u}_s - \left(1-a^2\right)\overline{u}_w}{E\left[\alpha + \left(n^2 - 1 + Y\right)\right]} \\ &= \frac{n^2\sigma_0 - \left(n^2 - a^2\right)\overline{u}}{E\left[\alpha + \left(n^2 - 1 + Y\right)\right]}.\end{aligned} \tag{4}$$

Derivation (4) about time is as follow

$$\frac{\partial \varepsilon_v}{\partial t} = -\frac{n^2 - a^2}{E\left[\alpha + \left(n^2 - 1 + Y\right)\right]}\frac{\partial \overline{u}}{\partial t}, \tag{5}$$

where $\overline{u}$ is the total average excess pore water pressure in the soil at any depth, which can be defined as

$$\begin{aligned}\overline{u} &= \frac{1}{\pi\left(r_e^2 - r_c^2\right)}\left(\int_{r_c}^{r_w} 2\pi r u_w d_r + \int_{r_w}^{r_e} 2\pi r u_s d_r\right) \\ &= \frac{\left[\left(1-a^2\right)\overline{u_w} + \left(n^2-1\right)\overline{u_s}\right]}{\left(n^2 - a^2\right)};\end{aligned} \tag{6}$$

$s = r_s/r_w$ is the radius ratio of the drainage influence zone to the column; $n = r_e/r_w$ and $a = r_c/r_w$ are the radius ratio, respectively; $Y = E_w/E$ is the compression modulus ratio of the sand-gravel shell to the surrounding soil, $X = E_c/E$ is the compression modulus ratio of the concrete-cored pile to the surrounding soil; $\alpha = a^2(X - Y)$ is an expression.

2.3.2. Continuity Conditions of Seepage. The expression of the horizontal permeability coefficient of the soils in drainage influence zone that varies linearly with respect to the radial distance away from the column can be assumed to be

$$k_r(r) = k_h f(r), \tag{7}$$

where k_h is the horizontal permeability coefficients of the weak smear zone and $f(r)$ is the function depending on radial distance away from column. The equation describes the variation pattern of the soil permeability along horizontal direction.

The concrete-cored pile of CCSG pile is set to be impervious pile and the sand-gravel shell is made of discrete material pile. The consolidation equations of the soil of composite foundation and the sand-gravel shell are used, which can be defined as

$$\frac{\partial}{\partial r}\left[\frac{r\cdot k_r(r)}{\gamma_w}\frac{\partial u_s}{\partial r}\right]=-r\left(\frac{\partial\varepsilon_v}{\partial t}+\frac{k_v}{\gamma_w}\frac{\partial^2\overline{u}_s}{\partial z^2}\right),\quad r_w\le r\le r_e \tag{8}$$

$$\frac{\partial}{\partial r}\left(\frac{r\cdot k_{hw}}{\gamma_w}\frac{\partial u_w}{\partial r}\right)=-r\left(\frac{\partial\varepsilon_v}{\partial t}+\frac{k_{vw}}{\gamma_w}\frac{\partial^2\overline{u}_w}{\partial z^2}\right),\quad r_c\le r\le r_w, \tag{9}$$

where γ_w is the unit weight of water.

2.3.3. Solving Conditions. Consider the following

① $r=r_e$, $\partial u_s/\partial r=0$;

② $r=r_w$, $u_s=u_w$;

③ $r=r_c$, $\partial u_w/\partial r=0$; (considering the concrete-cored pile as an impervious pile)

④ $r=r_w$, $k_r(r_w)(\partial u_s/\partial r)=k_{hw}(\partial u_w/\partial r)$; (the radial velocity of pile- soil interface is equal).

The vertical boundary conditions can be written as

⑤ $z=0$, $u_w=0$, $\overline{u}=0$;

⑥ $z=H$, $\partial u_w/\partial z=0$, $\partial\overline{u}/\partial z=0$; (in single-drainage condition)

⑦ $z=H$, $u=0$, $\overline{u}=0$; (in double-drainage condition).

Assuming that there is no deformation of the pile and the soil at initial time and the external load is bore all by pore water, so the initial condition can be written as $t=0$, $\overline{u}(z,0)=\sigma_0$.

2.4. The Establishment of the Governing Equations. Equation (10) can be obtained by integrating both sides of (8) about r and using solving condition ①:

$$\frac{\partial u_s}{\partial r}=\frac{\gamma_w}{2k_h}\left(\frac{\partial\varepsilon_v}{\partial t}+\frac{k_v}{\gamma_w}\frac{\partial^2\overline{u}_s}{\partial z^2}\right)\left[\frac{r_e^2}{rf(r)}-\frac{r}{f(r)}\right]. \tag{10}$$

Integrating both sides of (10) about r again and using solving condition ②, the following can be obtained:

$$u_s(r)=u_w|_{r=r_w}+\frac{\gamma_w}{2k_h}\left(\frac{\partial\varepsilon_v}{\partial t}+\frac{k_v}{\gamma_w}\frac{\partial^2\overline{u}_s}{\partial z^2}\right)\times\left[r_e^2A_0(r)-B_0(r)\right], \tag{11}$$

$$A_0(r)=\int_{r_w}^{r}\frac{d\xi}{\xi f(\xi)},\qquad B_0(r)=\int_{r_w}^{r}\frac{\xi d\xi}{f(\xi)}. \tag{12}$$

Equation (11) is substituted into (2):

$$\overline{u}_s=u_w|_{r=r_w}+\frac{r_e^2\gamma_wF_c}{2k_h}\left(\frac{\partial\varepsilon_v}{\partial t}+\frac{k_v}{\gamma_w}\frac{\partial^2\overline{u}_s}{\partial z^2}\right), \tag{13}$$

where $F_c=2(A_1r_e^2-B_1)/r_e^2r_w^2(n^2-1)$, $A_1=\int_{r_w}^{r_e}rA_0(r)\,dr$, and $B_1=\int_{r_w}^{r_e}rB_0(r)dr$.

By integrating both sides of (9) about r and using solving condition ③, the following is obtained:

$$\frac{\partial u_w}{\partial r}=\frac{\gamma_w}{2k_{hw}}\left(\frac{\partial\varepsilon_v}{\partial t}+\frac{k_{vw}}{\gamma_w}\frac{\partial^2\overline{u}_w}{\partial z^2}\right)\left(\frac{r_c^2}{r}-r\right). \tag{14}$$

Equation (14) is integrated about r both sides to get

$$u_w(r)=u_w|_{r=r_w}+\frac{\gamma_w}{2k_{hw}}\left(\frac{\partial\varepsilon_v}{\partial t}+\frac{k_{vw}}{\gamma_w}\frac{\partial^2\overline{u}_w}{\partial z^2}\right)\cdot\left[r_w^2\left(\frac{1}{2}+a^2\ln\frac{r}{r_w}\right)-\frac{1}{2}r^2\right]. \tag{15}$$

Equation (15) is substituted into (3):

$$\overline{u_w}=u_w|_{r=r_w}+\frac{\gamma_wR}{8k_{hw}}\left(\frac{\partial\varepsilon_v}{\partial t}+\frac{k_{vw}}{\gamma_w}\frac{\partial^2\overline{u}_w}{\partial z^2}\right), \tag{16}$$

where $R=r_w^2[(4a^2/(1-a^2))(\ln r_w-a^2\ln ar_w)-2a^2-4a^2\ln r_w-(1-a^4)/(1-a^2)+2]$.

Equation (13) minus (16) meanwhile combining the expression of $\overline{u}$ in (4) and (5) deduces

$$\begin{aligned}\overline{u}-\overline{u}_w=&-\frac{(n^2-1)}{E(\alpha+n^2-1+Y)}\left(\frac{r_e^2F_c\gamma_w}{2k_h}-\frac{\gamma_wR}{8k_{hw}}\right)\frac{\partial\overline{u}}{\partial t}\\&+\frac{r_e^2F_ck_v}{2k_h}\frac{\partial^2\overline{u}}{\partial z^2}\\&-\left[\frac{(1-a^2)}{(n^2-a^2)}\frac{r_e^2F_ck_v}{2k_h}+\frac{(n^2-1)}{(n^2-a^2)}\frac{Rk_{vw}}{8k_{hw}}\right]\frac{\partial^2\overline{u}_w}{\partial z^2}.\end{aligned} \tag{17}$$

Substituting (10) and (14) into solving condition ④, meanwhile combining (5), the equation can be deduced as

$$\frac{-(n^2-a^2)^2}{E(\alpha+n^2-1+Y)}\frac{\partial\overline{u}}{\partial t}=(a^2-1)\frac{k_{vw}}{\gamma_w}\frac{\partial^2\overline{u}_w}{\partial z^2}-(n^2-1)\frac{k_v}{\gamma_w}\frac{\partial^2\overline{u}_s}{\partial z^2}. \tag{18}$$

Substituting the expression of $\overline{u}$ in (4) into (18) we get equation

$$\frac{\partial^2\overline{u}_w}{\partial z^2}=A\frac{\partial\overline{u}}{\partial t}-B\frac{\partial^2\overline{u}}{\partial z^2}, \tag{19}$$

where $A=(n^2-a^2)\gamma_w/(1-a^2)(k_{vw}-k_v)E(\alpha+n^2-1+Y)$, $B=(n^2-a^2)k_v/(1-a^2)(k_{vw}-k_v)$.

Equation (19) is substituted into (17) and we get

$$\overline{u}_w=\overline{u}+C\frac{\partial\overline{u}}{\partial t}-D\frac{\partial^2\overline{u}}{\partial z^2}, \tag{20}$$

where $C=(\gamma_w[(n^2-1)k_{vw}+k_v]/E(\alpha+n^2-1+Y)(k_{vw}-k_v))[r_e^2F_c/2k_h+R(n^2-1)/8k_{hw}]$ $D=(k_{vw}k_v/(k_{vw}-k_v))[r_e^2F_c/2k_h+(n^2-1)R/(1-a^2)8k_{hw}]$.

Deduce from (20) as

$$\frac{\partial \overline{u}_w}{\partial z^2} = \frac{\partial^2 \overline{u}}{\partial z^2} + C\frac{\partial^3 \overline{u}}{\partial t \partial z^2} - D\frac{\partial^4 \overline{u}}{\partial z^4}. \tag{21}$$

Substituting (19) into (21) is deduced as

$$D\frac{\partial^4 \overline{u}}{\partial z^4} - C\frac{\partial^3 \overline{u}}{\partial t \partial z^2} - (B+1)\frac{\partial^2 \overline{u}}{\partial z^2} + A\frac{\partial \overline{u}}{\partial t} = 0. \tag{22}$$

So far, the governing equations as (20) and (22) are obtained.

The solution can be obtained by using the method of separation of variables for (22), which can be expressed as

$$\overline{u}(z,t) = \sigma_0 \sum_{m=1}^{\infty} \frac{2}{M} \sin\left(\frac{M}{H}z\right) e^{-\beta_m t}, \tag{23}$$

$$\begin{aligned} \overline{u}_w(z,t) = \sigma_0 \sum_{m=1}^{\infty} \frac{2}{M}\left[1 - C\beta_m + D\left(\frac{M}{H}\right)^2\right] \\ \cdot \sin\left(\frac{M}{H}z\right) e^{-\beta_m t}, \end{aligned} \tag{24}$$

$$U = 1 - \sum_{m=1}^{\infty} \frac{2}{M^2} e^{-\beta_m t}, \tag{25}$$

where $M = ((2m+1)/2)\pi$, $(m = 0, 1, 2, \ldots)$,

$$\begin{aligned} \beta_m = E\left(\alpha + n^2 - 1 + Y\right)\Bigg\{k_{vw}k_v\left(\frac{M}{H}\right)^2 \\ \times\left[\frac{r_e^2 F_c}{2k_h} + \frac{\left(n^2-1\right)R}{(1-a^2)\,8k_{hw}}\right] \\ + \left[\left(n^2-1\right)k_v + k_{vw}\right]\Bigg\} \\ \times\Bigg(\gamma_w\Bigg\{\frac{\left(n^2-a^2\right)^2}{1-a^2}\cdot\left(\frac{H}{M}\right)^2 + \left[\left(n^2-1\right)k_{vw} + k_v\right] \\ \times\left[\frac{r_e^2 F_c}{2k_h} + \frac{\left(n^2-1\right)R}{8k_{hw}}\right]\Bigg\}\Bigg)^{-1}. \end{aligned} \tag{26}$$

In order to verify the rationality of the assumptions and the methods of the consolidation in this paper, the consolidation solution can be degraded.

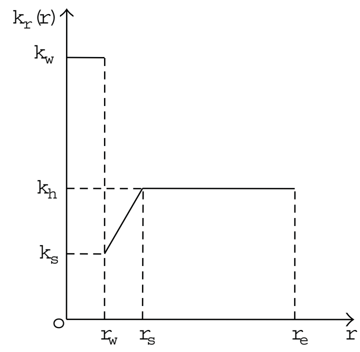

Figure 3: Five variation patterns of horizontal permeability coefficient in smear zone.

When $X = 1$ and $a = 0$, β_m changes into

$$\begin{aligned} \beta_m = E\left(n^2 - 1 + Y\right)\Bigg\{k_{vw}k_v\left(\frac{M}{H}\right)^2 \\ \times\left[\frac{r_e^2 F_c}{2k_h} + \frac{\left(n^2-1\right)r_w^2}{8k_{hw}}\right] \\ + \left[\left(n^2-1\right)k_v + k_{vw}\right]\Bigg\} \\ \times\Bigg(\gamma_w\Bigg\{n^4\left(\frac{H}{M}\right)^2 + \left[\left(n^2-1\right)k_{vw} + k_v\right] \\ \times\left[\frac{r_e^2 F_c}{2k_h} + \frac{\left(n^2-1\right)r_w^2}{8k_{hw}}\right]\Bigg\}\Bigg)^{-1}. \end{aligned} \tag{27}$$

This is the consolidation solution of common composite foundation provided by Lu et al. [30] that considered the radial flow within the pile.

When $Y = 1$, $k_v = k_{vw}$, and $k_h = k_{hw}$, β_m and U change into

$$\begin{aligned} \beta_m = \frac{k_v E}{\gamma_w}\left(\frac{M}{H}\right)^2 = c_v\left(\frac{M}{H}\right)^2, \\ U = 1 - \sum_{m=1}^{\infty}\frac{2}{M^2}e^{-M^2 T_v}, \end{aligned} \tag{28}$$

where $c_v = k_v E/\gamma_w$, $T_v = c_v t/H^2$.

This is the one-dimensional consolidation solution of Terzaghi's theory. The rationality of the consolidation solution in this paper can be reflected through the above answer to degradation.

From (13), (23), and (25), it can be seen that the influence of horizontal permeability coefficient in the influenced zone to the consolidation solution is reflected mainly by the parameter F_c, which is related to the changing pattern of horizontal permeability coefficient. Figure 3 displays a typical changing pattern of horizontal permeability coefficient versus r. The solutions of F_c had been given by Zhang et al. [24] as

$$F_c = \frac{n^2}{n^2-1}\left\{\frac{s-1}{\kappa s-1}\ln(\kappa s) - \frac{(s-1)^2}{n^2(1-\kappa)} + \frac{2}{n^2}\frac{(s-1)(\kappa s-1)}{(1-\kappa)^2}\ln\frac{1}{\kappa} - \frac{2}{n^4}\frac{s-1}{1-\kappa} \times\left(\frac{s^3-1}{3}-\frac{s^2-1}{3}\right) - \frac{1}{n^4}\frac{(s-1)(\kappa s-1)}{(1-\kappa)^2} \times\left[\frac{s^2-1}{2}-\frac{(s-1)(\kappa s-1)}{1-\kappa} + \frac{(\kappa s-1)^2}{(1-\kappa)^2}\ln\frac{1}{\kappa}\right] - \frac{n^2-s^2}{n^4}\frac{(1-s)^2}{1-\kappa} + \ln\frac{n}{s} - \frac{3}{4} + \frac{4n^2s^2-s^4}{4n^4}\right\}. \tag{29}$$

3. Parametric Study and Discussion

In order to study the characters of consolidation of CCSG pile composite foundation, β_m should be converted to dimensionless, which can be expressed as

$$\beta_m t = \tau_m T_h, \tag{30}$$

where T_h is the horizontal time factor of the soil, which can be expressed as

$$T_h = \frac{c_h t}{4r_e^2}, \qquad c_h = \frac{Ek_h}{\gamma_w}. \tag{31}$$

In this case, (25) changes into

$$U = 1 - \sum_{m=1}^{\infty}\frac{2}{M^2}e^{-\tau_m T_h}, \tag{32}$$

where

$$\tau_m = r_e^2\left(\alpha + n^2 - 1 + Y\right) \times\left\{\frac{k_{vw}}{k_h}\left(\frac{M}{H}\right)^2\left[\frac{r_e^2F_c}{2} + \frac{(n^2-1)Rk_h}{(1-a^2)8k_{hw}}\right] + (n^2-1) + \frac{k_{vw}}{k_v}\right\} \times\left(\left\{\frac{(n^2-a^2)^2}{1-a^2}\cdot\frac{k_h}{k_v}\left(\frac{H}{M}\right)^2 + \left[(n^2-1)\frac{k_{vw}}{k_v}+1\right]\cdot\left(\frac{r_e^2F_c}{2} + \frac{R(n^2-1)k_h}{8k_{hw}}\right)\right\}\right)^{-1}. \tag{33}$$

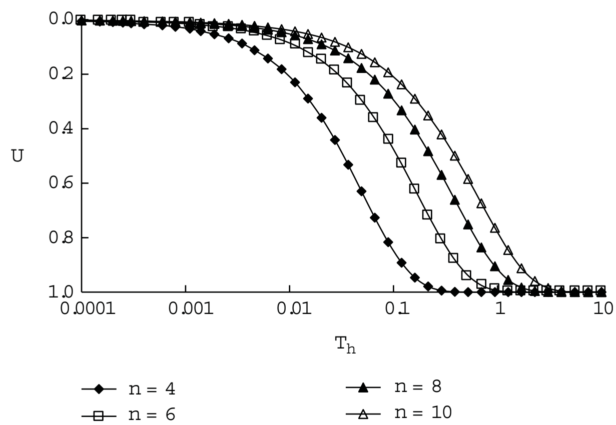

Figure 4: Influence of n on consolidation process.

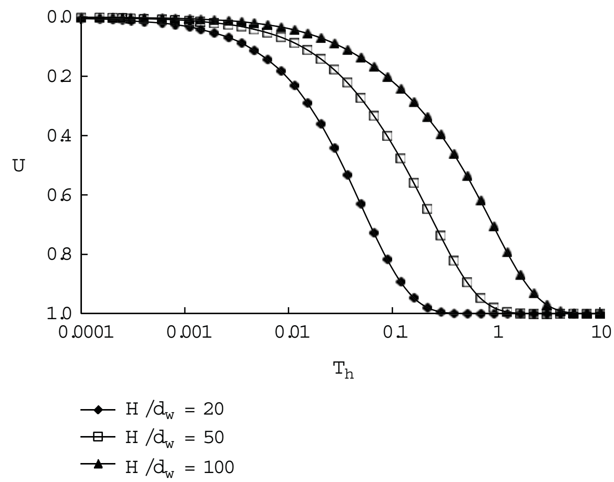

Figure 5: Influence of H/d_w on consolidation process.

From the expression of τ_m, the dimensionless parameters influencing the consolidation character of CCSG pile composite foundation include n, a, s, X, Y, H/d_w ($d_w = 2r_w$), k_h/k_v, k_s/k_h, k_h/k_{vw}, k_h/k_{hw}, and k_{hw}/k_{vw}. The influences of several dimensionless parameters on the consolidation behaviour of CCSG pile composite foundation were investigated and some numerical results from different solutions were compared according to the above formula. The specific calculation results are shown in Figures 4–11. The calculating parameters are shown in Table 1.

Table 1: Parameters used for calculation (I).

Figure no.	n	a	s	H/d_w	X	Y	k_s/k_h	k_h/k_v	k_h/k_{vw}	k_{hw}/k_{vw}
4	—	0.2	1.5	20	1000	10	0.6	2	0.001	1
5	4	0.2	1.5	—	1000	10	0.6	2	0.001	1
6	4	0.2	1.5	20	1000	10	0.2	2	0.001	1
7	4	—	1.5	20	—	—	0.6	2	0.001	1
8	4	0.2	1.5	20	—	—	0.2	2	0.001	1
9	4	0.2	1.5	20	1000	10	0.2	2	—	1
10	4	0.2	1.5	20	1000	10	—	2	0.001	1
11	4	0.2	1.5	20	1000	10	—	2	0.001	1

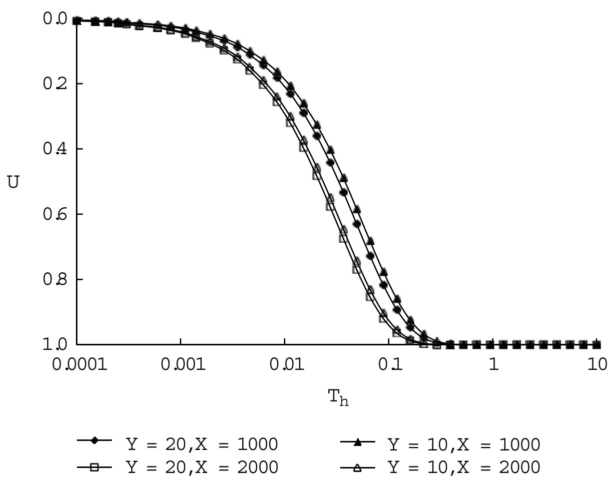

Figure 6: Influence of X and Y on consolidation process.

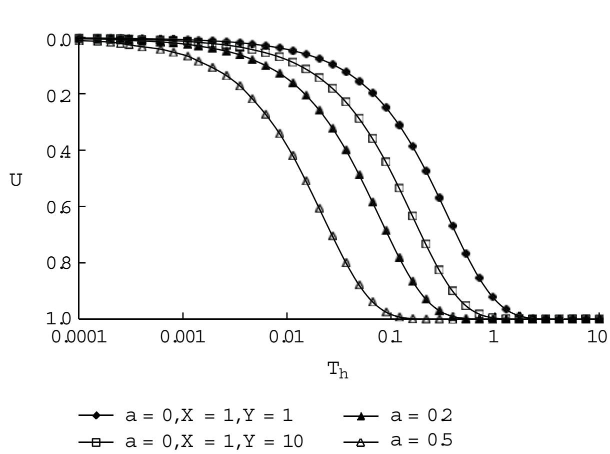

Figure 7: Influence of a on consolidation process.

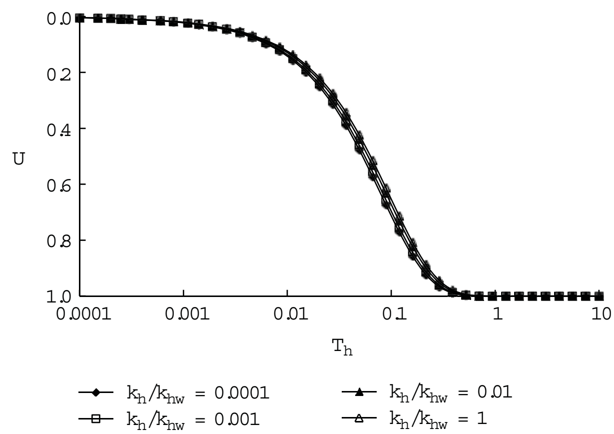

Figure 8: Influence of k_h/k_{hw} on consolidation process.

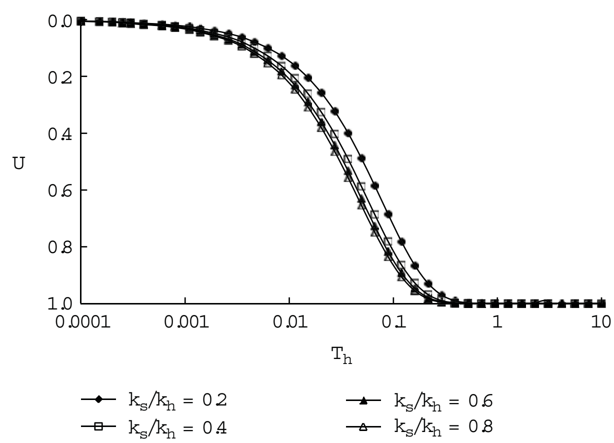

Figure 9: Influence of k_s/k_h on consolidation process.

Figures 4 and 5 show the influence of n and H/d_w on consolidation behaviour of CCSG pile composite foundation. It can be seen that consolidation velocity is reduced with the increase of n and H/d_w. In other words, the bigger the scope of influenced zone, the slower the consolidation rate is. Figure 4 also shows that the reducing rate of consolidation velocity decreases with the increase of n.

Figure 6 shows the influence of X and Y on the consolidation behaviour of CCSG pile composite foundation. As shown in the figure, when the value of Y is constant, the consolidation rate increases with the value of X. Similarly, with X constant, the larger the value of Y, the faster the consolidation rate is. So, the consolidation rate should be accelerated with the increasing of X and Y.

Figure 7 shows the comparison between several solutions, including the solution for ordinary granular material pile composite foundation proposed by Lu et al. [26] and Terzaghi's solution for natural foundation. When $a = 0$, $X = 1$, $Y = 1$, $k_v = k_{vw}$, and $k_h = k_{hw}$, the curve presents the changing of consolidation degree with time for natural foundation. When

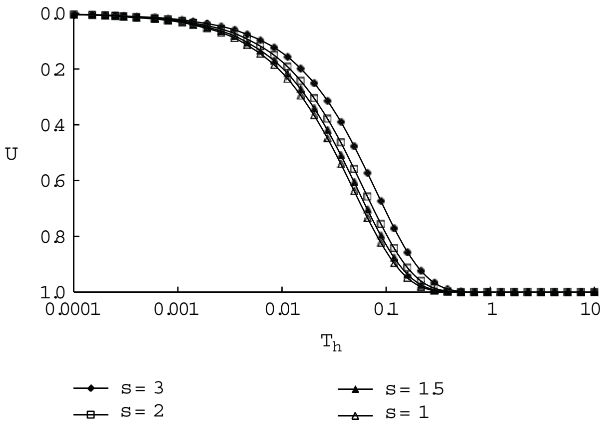

Figure 10: Influence of s on consolidation process.

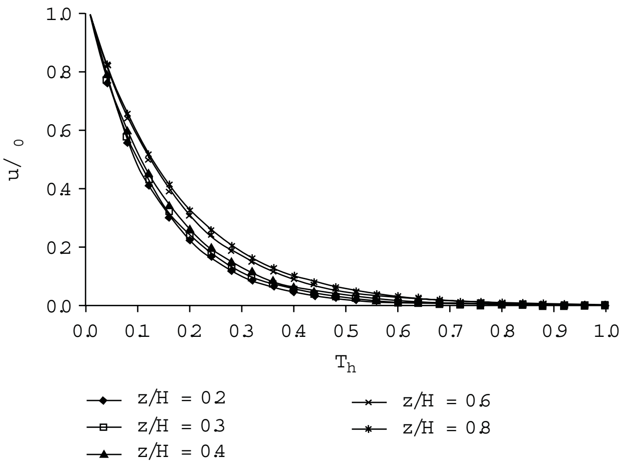

Figure 11: Dissipation curves of average pore-pressure at different depth in foundation.

$a = 0$, $X = 1$, and $Y = 10$, the curve shows the changing of consolidation degree with time for ordinary granular material pile composite foundation. The curves of $a = 0.2$ and $a = 0.5$ are the consolidation degree curves changing with time of CCSG pile composite foundation. Among these solutions, only the solution presented in this study takes the characters of CCSG pile composite foundation into account. As shown in Figure 7, the consolidation rates given by the present solution are greater than those given by the other solutions. It also can be seen that the consolidation rates given by the present solution and the Lu et al. [26] solution are both greater than that given by Terzaghi's solution because the former two solutions both take the stress concentration from soil to column into account. These conclusions indicate that CCSG pile composite foundation performs best in the drainage consolidation. Because CCSG pile composite foundation has large diameter of the drainage channel, and the concrete-core pile as vertical reinforcement, the postloading settlement of the foundation finished quickly. In addition, the larger the value of a, the faster the consolidation rate of CCSG pile composite foundation is. So, the consolidation rate should be accelerated with the increase of a. However, when the value of a reaches 1, CCSG pile composite foundation will convert to pile foundation and has no drainage function.

Figure 8 shows the influence of k_h/k_{hw} on consolidation behaviour of CCSG pile composite foundation under three different patterns of horizontal permeability coefficient. It can be seen that when the horizontal permeability coefficient within soil is smaller than that within the sand-gravel shell, the consolidation rate is accelerated limited with the decrease of k_h/k_{hw}. In addition, the curves of consolidation degree are close to each other, which indicate that the influence of k_h/k_{hw} on consolidation behaviour of CCSG pile composite foundation is weak. As the concrete-cored pile is considered as an impervious pile, both the solutions of the soil and sand-gravel shell are obtained using the consolidation equations, so taking the radial flow within sand-gravel shell into account is necessary.

Figure 9 shows the influence of k_s/k_h on consolidation behaviour of CCSG pile composite foundation under the change of horizontal permeability coefficient of the soil. The value of k_s/k_h can reflect the intensity of disturbance to the surrounding soil during column construction: the bigger the value is, the more the disturbance intensity is. It can be seen from Figure 9 that the consolidation rate of a composite foundation reduces with the decrease of k_s/k_h. In other words, the consolidation rate of a composite foundation is enhanced by reducing the disturbance intensity.

Figure 10 shows the influence of s on consolidation behaviour of CCSG pile composite foundation, which represents the size of the disturbed zone. It can be seen from the graph that the consolidation rate of a composite foundation reduces with the increase of s. In another word, the larger the disturbance area, the slower the consolidation rate is.

Figure 11 represents the average pore-pressure dissipation. It can be seen from the graph that the deeper the depth of foundation, the slower the pore-pressure dissipation speed is, which means slow consolidation rate of deep foundation and is consistent with the actual situation.

4. Case Application

4.1. Survey of Experimental Sections. The construction section, Liyang Second Bid of Zhenjiang, Liyang Highway, is located in the Yangtze River valley. The area of treated embankment of thick and soft ground in section K63 + 046 ~ K63 + 087 was 41 m × 63 m, which was 2583 m^2. The CCSG pile composite foundation treatment was adopted, with a diameter of 50 cm (the prefabricated low-grade concrete-cored pile was 20 cm × 20 cm, and the outside diameter of the sand-gravel shell was 50 cm) and a length of 22 m. The piles were prefabricated in 3 parts and arranged in equilateral triangle, with 2.1 m spacing between section K63 + 046 and K63 + 066 and 1.9 m between section K63 + 066 and K63 + 087. One layer of hardcore bed with 50 cm thickness was placed as cushion together with one layer of geogrid after the construction of concrete-cored sand-gravel pile. The ground altitude was 3.1 m, the designed altitude at the centre of roadbed superface was 8.5 m, and the surcharge

Table 2: Physical and mechanical parameters of soils.

Soil layer	Name of soil layer	Soil layer thickness/m	ω/%	γ/(kN/m^3)	e_0	I_P	I_L	$\alpha_{(1\text{-}2)}$/MPa^{-1}	$E_{s(1\text{-}2)}$/MPa	Direct shear (Quick shear) c/kPa	φ/(°)	f_{ak}/kPa
①	Miscellaneous fill	2.0~3.7										
②	Silty clay	1.6~2.6	32.3	18.4	0.91	10.7	1.01	0.30	7.28	2.0	17.1	125
③	Muddy silty clay	6.6~10.9	38.8	17.9	1.07	11.7	1.35	0.49	4.47	7.0	24.5	65
④-1	Silty clay-silt	0.6~2.5	35.2	18.3	0.96	11.6	1.27	0.45	5.37	18.0	16.5	105
④-2	Silt-silty clay	0.7~2.9	33.9	18.5	0.93	10.9	1.35	0.41	5.68	10.0	25.5	150
④-3	Silty clay-silt	0~4.4	26.6	19.3	0.75	11.7	0.76	0.45	3.94	25.0	13.7	165
⑤	Silty clay	9.6~10.1	35.0	18.7	0.93	13.0	1.16	0.43	5.29	13.0	12.2	105
⑥	Angular pebbles											250

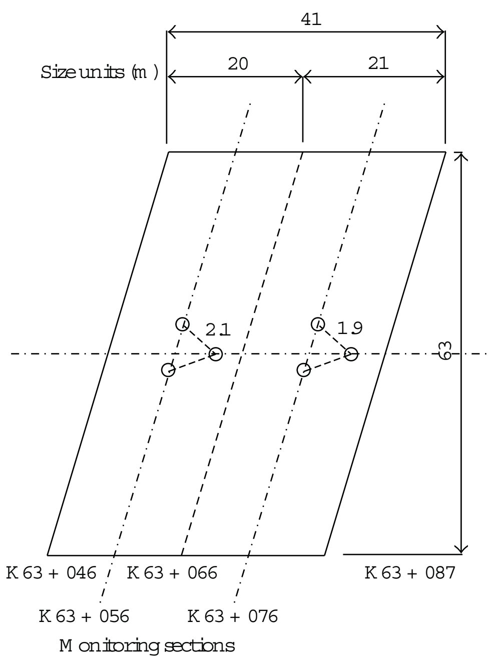

Figure 12: Test section layout drawing.

preloading altitude was 11.1 m. The maximum dry density of embankment filler was 1.84 g/m^3, and the slope of the embankment was 1 : 2. The subgrade was 35 m wide, and the groundwater level was 1 ~ 2 m below surface. Vibrating sunk-tube method was used for construction. According to exploratory boring, CPT, vane shear test and geotechnical parameter test, the physical and mechanical parameters of soils in experimental sections are shown in Table 2. The layout of tested section is shown in Figure 12.

The profile map of instruments at site monitored section is shown in Figure 13. The layout of instruments at each section was as follows.

(1) Three ground settlement poles were placed in the left, middle, and right position along the width of the subgrade, respectively.

(2) One 30-meter long layered settlement pile was embedded at subgrade centre. Twelve settlement rings were layered on the pile every two meters along the depth. Meanwhile, nine pore-pressure detectors were embedded every two meters along the depth.

(3) One inclinometer pile was embedded at subgrade slope.

(4) Ten soil pressure boxes were embedded in the pile top, the sand top, and the soil, respectively, at the triangular area consisting of three piles at the subgrade centre.

(5) Six steel bar stress detectors including one at pile top, one at pile bottom, and four at pile body were embedded in each pile of the two chosen piles.

4.2. Comparative Analysis of the Engineering Example

4.2.1. Settlement of Pile Top and Soil. Three settlement meters were embedded in the right and left shoulders and the centre of section K63 + 056 and K63 + 076, respectively, to measure the settlement of soils. Meanwhile another two meters were embedded in the concrete-cored pile top in the centre of section K63 + 056 and K63 + 076, respectively, to measure the settlement of concrete-cored pile top. Settlement meters with a size of 70 cm × 70 cm were used in the soil. To prevent from interfering with the settlement of the concrete-cored pile and to avoid the deflection of the settlement meter on the top of the pile, meters with a size the same as the concrete-cored pile section, which was 20 cm × 20 cm, were used on the top of the pile and were welded to the top directly. Settlement observation points were set up on tops of the sand-gravel shell and concrete-cored pile. Stable control point was established to measure the elevation changes with high precision water level. The measurement reading was obtained daily in the early stage of construction and then in every two or three days after the reading was stable for the settlement-time curve. The settlement observation process lasted for 285 days. The variation of settlement in soil in the centre of section K63 + 056 and K63 + 076 is shown in Figure 14.

From Figure 14, by comparing the settlement of section K63 + 056 and K63 + 076, it can be seen that until the end, the settlement in the centre of the section K63 + 056, which was farther away from the abutment, was 64.9 cm, and the other one was 47.9 cm. The result indicates that the bigger the

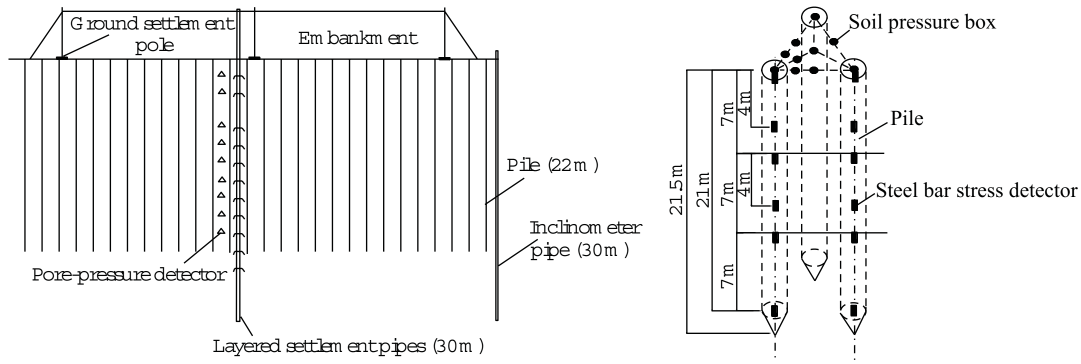

(a) The layout section of monitoring section instruments

(b) The layout drawing of earth pressure boxes and steel bar stress detectors

Figure 13: Profile drawing of instruments.

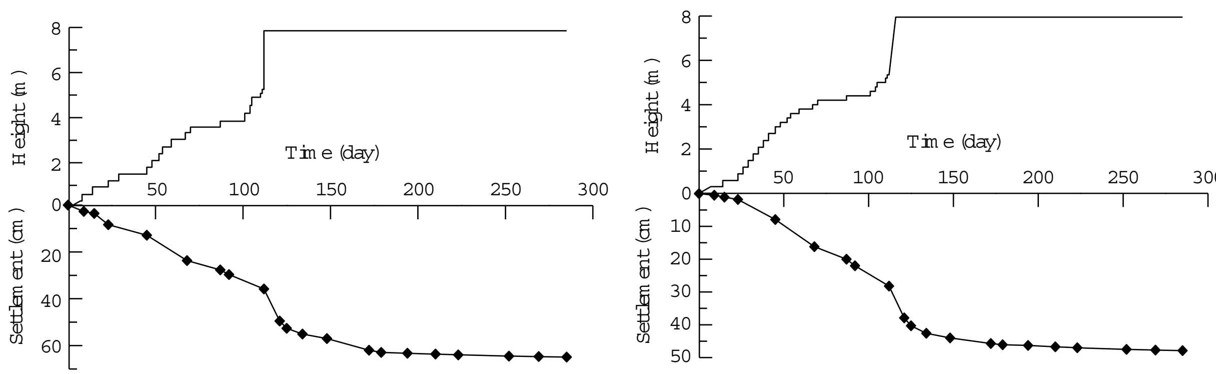

(a) K63 + 056 Section centre

(b) K63 + 076 Section centre

Figure 14: Settlement of soil surface.

pile spacing is, the bigger the settlement ratio and settlement are, which also reflects the influence of the pile spacing on the composite foundation settlement. During the construction of embankment (the first 110 days), the maximum settlement rates at section K63 + 056 and K63 + 076 were 0.6 cm and 0.4 cm per day, respectively. During the period of preloading (the next 10 days), the maximum settlement rate at section K63 + 056 was 1.5 cm per day and was 1.1 cm per day at section K63 + 076. As shown in Figure 14, the settlement curves became horizontal straight, while the maximum lateral displacement was only 1 mm per day by now, indicating that the immediate settlement of soil was larger. After the applying of dead load, the settlement rate tended to reduce steadily. The first-measured settlement rate was 5 mm per month after dead load had been applied for four months indicating that the surface settlement had become steady.

In order to validate the theoretical formula derived in this paper, the construction data of the testing section and the field measured data at section K63 + 076 were used for calculating validation and contrastive analysis.

Asaoka method was used to predict the final settlement of composite foundation according to the settlement data measured from section K63 + 076. Then, the field test curve of overall average consolidation degree of CCSG pile composite foundation changing with time was obtained. Finally, the formula in this paper was amended using the improved Terzaghi method to satisfy the conditions of step loading in practical engineering.

As shown in Figure 15, the manner of the theoretical curve of average consolidation degree changing with time is similar to that of the curve obtained from field test. The hysteresis phenomenon is due to the existing settlement hysteresis after completion of loading. From the figure, it can be seen that the consolidation rate given by the solution in this paper is greater than that deduced from field test data. Considering the error between the observation and test, a good agreement can be affirmed, which validates the theoretical solution in this paper.

4.2.2. Pore Water Pressure. The steel-string type pore-pressure detector was used to monitor the pore-pressure, with a measuring range up to 200 kPa or 400 kPa. Frequency meter was used to sense the frequency. In order to determine the instrument sensitivity coefficient, temperature coefficient, and sealing performance, the instruments were checked-out and calibrated before being embedded. The embedded way was stated in Section 4.1. Nine pore-pressure detectors were embedded at different depth at section K63 + 056 and K63 + 076, respectively. No test results were obtained from section K63 + 076 as the one detector was damaged during

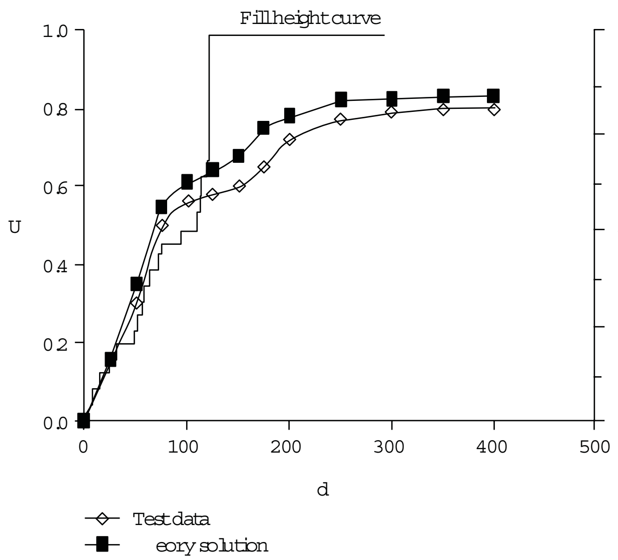

Figure 15: Variation of consolidation degree of the composite foundation.

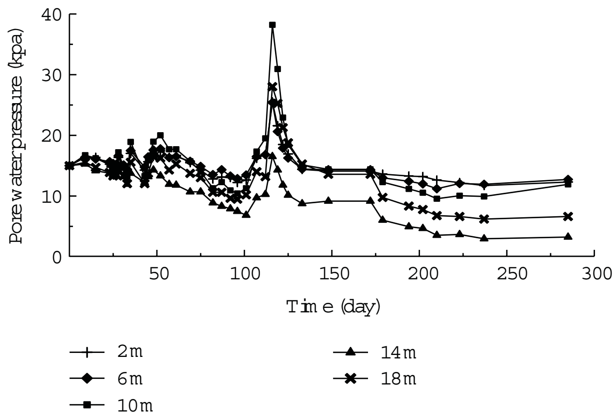

Figure 16: Excess pore water pressure with depth.

the abutment excavation. The observation of pore-pressure went on in parallel with the observation of soil pressure. The observation results of pore water pressure at primary depth at section K63+056 were shown in Figure 16.

As shown in Figure 16, at the first three months, with a filling height of 4.2 m, the variation curves of pore-pressure were smooth. From day 100 to day 120, the filling height rose from 4.2 m to 7.9 m, and the pore-pressure at different depth went up by 9~28 kPa; meanwhile, the steep and sharp variation occurred on the curves. After dead load on day 120, the pore-pressure dissipated rapidly. From the entire depth range, the pore-pressure did not decrease with the increase of depth, and the measured maximum pore-pressure was at the depth of 10 m below surface. The drainage effect of concrete-cored sand gravel pile is very excellent, which could be obtained by the phenomenon that pore-pressure rose and dissipated rapidly.

Figure 17 shows the excess pore water pressure obtained by the amended theoretical equation. The figure is similar

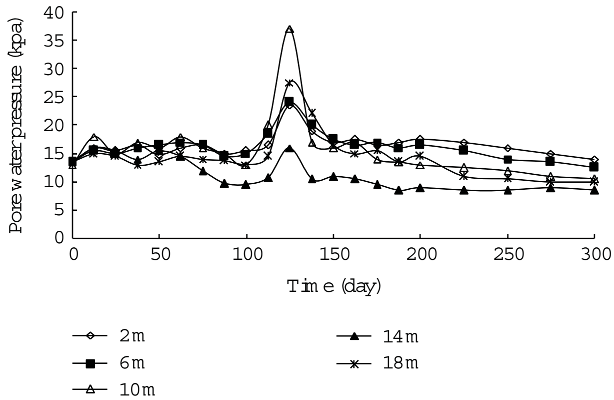

Figure 17: Excess pore water pressure with depth obtained by the theoretical equation.

to Figure 16, which indicates the validity of the theoretical equation in this paper.

4.2.3. Soil Pressure under Embankment Load. Ten soil pressure boxes were embedded in the triangular area consisting of three piles in the centre of section K63 + 056 and K63 + 076, respectively, including three on the top of the pile, three on the top of sand-gravel, and four in the soil between piles. The pressure surface of the soil pressure boxes must face to the measured soil. Meanwhile, the following issues require attention, including that the soil surface under soil pressure boxes must be strictly levelled, the material of backfill soil should be the same with the surrounding soil (stone removed), and artificial compaction in layers must be used carefully. The frequency was sensed by a frequency meter. No test result was obtained from section K63 + 076 because of the damage of soil pressure boxes due to abutment excavation.

Variations of the pile-soil stress ratio n_s and shared load ratio N are shown in Figure 18. During embankment construction and preloading period, n_s and N increased at first and then decreased. In the early filling period (the first 24 days), when the cumulative filling height was 1.2 m, the pile-soil pressure ratio n_s rose from 1.6 to 2.9 and the shared load ratio N rose from 0.09 to 0.16, slowly. From day 25 to day 100, the filling height grew from 1.2 m to 4.2 m, the pile-soil pressure ratio rose from 2.9 to 16.8, and the shared load ratio rose from 0.16 to 0.92. On day 100, after the cumulative filling height reaching 4.2 m, the pile-soil pressure ratio and the shared load ratio reached the maximum values 16.8 and 0.92, respectively. From day 100 to day 120, the filling height rose from 4.2 m to 7.9 m, the pile-soil ratio reduced from 16.8 to 13.2, and the shared load ratio reduced from 0.92 to 0.72. From finishing preloading (day 100) to observation being over (day 150), the pile-soil pressure ratio rose from 13.2 to 15, and the shared load ratio rose from 0.72 to 0.82, indicating that the pile-soil pressure ratio and the shared load ratio still rose gradually after dead load, the load carried by the pile soil transferred to the pile top, and the effect of reinforcement on the composite foundation strengthened continually.

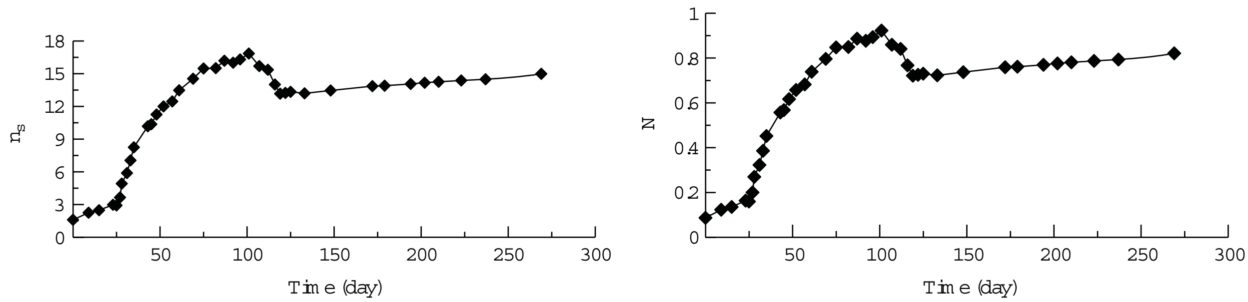

(a) (b)

FIGURE 18: Variation of pile-soil stress ratio n_s and shared load ratio N.

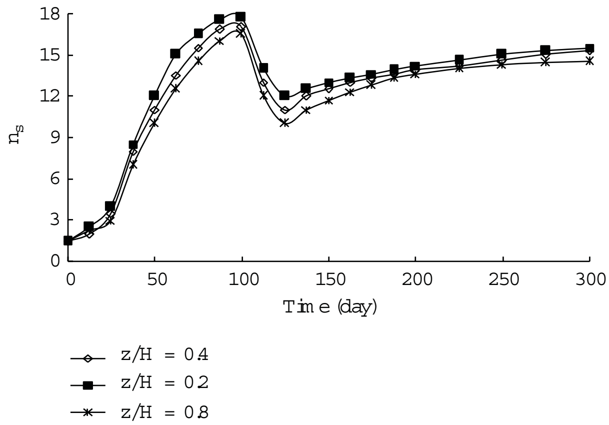

FIGURE 19: Variation of pile-soil stress ratio n_s obtained by theoretical equation.

Figure 19 shows the variation of pile-soil stress ratio n_s obtained by the amended equation, which is similar to Figure 18. It can be seen that the value of n_s varied in different depth and increased when approaching to the surface. It means that the pile shared greater stress and the soil undertakes smaller load at the smaller depth place.

5. Conclusions

The general solution for consolidation of CCSG pile composite foundation under equal strain hypothesis was obtained by considering the variation of horizontal penetration parameter in influence zone, radial flow within the sand-gravel shell, and the impervious characteristic of concrete-cored pile in this paper. Meanwhile, this paper also introduced a series of field tests on CCSG pile composite foundation to prove the correctness of the general solution, including the settlement of pile and soil, the pore water pressure, and the soil pressure under embankment load. It is concluded that the new style composite foundation patent technology has many advantages such as small post-construction and differential post-construction settlement, reliable quality, high bearing capacity, high speed of settlement, and stability. The following main conclusions are obtained.

(1) The solution given by Terzaghi is a limited case of the present solution when $a = 0$, $X = 1$, $Y = 1$, $k_v = k_{vw}$, and $k_h = k_{hw}$; the solution for ordinary granular material pile composite foundation is also a limited case of the present solution when $a = 0$ and $X = 1$. The consolidation rate of CCSG pile composite foundation is greater than that of natural foundation, sand drained ground, and ordinary granular material pile composite foundation.

(2) A parametric study shows that an increase in the values of a, X, and Y and a decrease in the values of n, s, and H/d_w will accelerate the consolidation rate of CCSG pile composite foundation.

(3) The analytical solution in this paper was finally validated with the actual filed measurement data.

(4) The essence of the composite foundation soil is that the reinforcement and subgrade soil mass undertake the load from the upper structure. To improve the bearing capacity of the foundation soil in thick and soft ground area, the area replacement ratio of piles can be appropriately improved with the project cost, and the pile length or the bearing capacity of soft soil can be increased. Meanwhile, the existence of the granular columns and the critical pile length in rigid-flexible piles made the increased pile length difficult to play a full role. Compared with the rigid pile, the concrete-cored sand-gravel pile makes full use of the concrete-cored sand gravel shell capacity of drainage and consolidation to increase the bearing capacity of the soft soil.

(5) The total settlement of subgrade of CCSG pile composite foundation during embankment construction and preloading periods is bigger than that of churning pile and other composite foundations. The reason is that the concrete-cored sand gravel shell provides large diameter vertical drainage channel and reduces the drainage distance of the soil mass greatly, so the subsoil can produce larger consolidation settlement in a short time. Excess pore-pressure can dissipate in a short time, so the subgrade settlement is faster and becomes stable quickly. Four months after the pre-compression at the experimental section, the settlement rate was 5 mm per month, which indicated that

the settlement becames stable, the precompression time fits in with that of the common sand drain.

Experimental results illustrate that adopting the concrete-cored sand-gravel pile composite foundation for thick and soft ground treatment at bridge head and the controlling of post-construction settlement is feasible. The test results also verify the advance, rationality, and validity of CCSG pile composite foundation. Because of the effect of soft soil consolidation and composite foundation that take place at the same time, the soil and the composite foundation interact and the relative displacement and interaction relationship among concrete-cored pile, soil, and sand-gravel shell are very complicated. So the deformation and load characteristics, especially the reinforcement mechanism under soft load, remain to be further studied.

Acknowledgments

This research was supported by the National Nature Foundation of China (Grant nos. 51374112, 51308234 and 51208321) and Natural Science Foundation of Fujian Province (no. 2013J05079); all support is gratefully acknowledged.

References

[1] R. A. Barron, “Consolidation of fine-grained soils by drain wells,” *Transactions of the American Society of Civil Engineers*, vol. 113, no. 2346, pp. 718–742, 1948.

[2] R. R. Goughnour and A. A. Bayuk, “Analysis of stone column soil matrix interaction under vertical load,” in *Proceedings of International Conference on Soil Reinforcement*, pp. 279–285, Paris, France, 1979.

[3] X. W. Tang and K. Onitsuka, “Consolidation of ground with partially penetrated vertical drains,” *Geotechnical Engineering*, vol. 29, no. 2, pp. 209–227, 1998.

[4] K. H. Xie, “Present situation and development of consolidation theory of composite ground,” *Ground Improvement*, vol. 4, no. 3, pp. 1–14, 1993.

[5] K. H. Xie, *Sand drained ground: analytical & numerical solutions of consolidation and optimum design [Ph.D. dissertation]*, Zhejiang University, Hangzhou, China, 1987.

[6] C. J. Leo, “Equal strain consolidation by vertical drains,” *Journal of Geotechnical and Geoenvironmental Engineering*, vol. 130, no. 3, pp. 316–327, 2004.

[7] G. H. Lei, C. X. Jiang, and C. J. leo, “Discussion of “Equal strain consolidation by vertical drains” by Chin Jian Leo,” *Journal of Geotechnical and Geoenvironmental Engineering*, vol. 131, no. 10, pp. 1315–1317, 2005.

[8] G. Zhu and J. H. Yin, “Consolidation of soil with vertical and horizontal drainage under ramp load,” *Geotechnique*, vol. 51, no. 4, pp. 361–367, 2001.

[9] G. Zhu and J. H. Yin, “Consolidation analysis of soil with vertical and horizontal drainage under ramp loading considering smear effects,” *Geotextiles and Geomembranes*, vol. 22, no. 1-2, pp. 63–74, 2004.

[10] X. S. Wang and J. J. Jiao, “Analysis of soil consolidation by vertical drains with double porosity model,” *International Journal for Numerical and Analytical Methods in Geomechanics*, vol. 28, no. 14, pp. 1385–1400, 2004.

[11] R. Walker and B. Indraratna, “Vertical drain consolidation with parabolic distribution of permeability in smear zone,” *Journal of Geotechnical and Geoenvironmental Engineering*, vol. 132, no. 7, pp. 937–941, 2006.

[12] B. Indraratna, C. Rujikiatkamjorn, and L. Sathananthan, “Radial consolidation of clay using compressibility indices and varying horizontal permeability,” *Canadian Geotechnical Journal*, vol. 42, no. 5, pp. 1330–1341, 2005.

[13] D. Basu and M. Prezzi, “Effect of the smear and transition zones around prefabricated vertical drains installed in a triangular pattern on the rate of soil consolidation,” *International Journal of Geomechanics*, vol. 7, no. 1, pp. 34–43, 2007.

[14] J. Castro and C. Sagaseta, “Consolidation around stone columns. Influence of column deformation,” *International Journal for Numerical and Analytical Methods in Geomechanics*, vol. 33, no. 7, pp. 851–877, 2009.

[15] K. H. Xie, M. M. Lu, A. F. Hu, and G. H. Chen, “A general theoretical solution for the consolidation of a composite foundation,” *Computers and Geotechnics*, vol. 36, no. 1-2, pp. 24–30, 2009.

[16] K. H. Xiel, M. M. Lu, and G. B. Liu, “Equal strain consolidation for stone columns reinforced foundation,” *International Journal for Numerical and Analytical Methods in Geomechanics*, vol. 33, no. 15, pp. 1721–1735, 2009.

[17] J. C. Chai and N. Miura, “Investigation of factors affecting vertical drain behaviour,” *Journal of Geotechnical and Geoenvironmental Engineering*, vol. 125, no. 3, pp. 216–226, 1999.

[18] J. S. Sharma and D. Xiao, “Characterization of a smear zone around vertical drains by large-scale laboratory tests,” *Canadian Geotechnical Journal*, vol. 37, no. 6, pp. 1265–1271, 2000.

[19] B. C. Hawlader, G. Imai, and B. Muhunthan, “Numerical study of the factors affecting the consolidation of clay with vertical drains,” *Geotextiles and Geomembranes*, vol. 20, no. 4, pp. 213–239, 2002.

[20] B. Indraratna and I. W. Redana, “Laboratory determination of smear zone due to vertical drain installation,” *Journal of Geotechnical and Geoenvironmental Engineering*, vol. 124, no. 2, pp. 180–184, 1998.

[21] A. Onoue, N. H. Ting, J. T. Germaine, and R. V. Whitman, “Permeability of disturbed zone around vertical drains,” in *Proceedings of the Geotechnical Engineering Congress*, pp. 879–890, Boulder, Colo, USA, 1991.

[22] R. Walker and B. Indraratna, “Vertical drain consolidation with overlapping smear zones,” *Geotechnique*, vol. 57, no. 5, pp. 463–467, 2007.

[23] X. W. Tang and K. Onitsuka, “Consolidation by vertical drains under time-dependent loading,” *International Journal for Numerical and Analytical Methods in Geomechanics*, vol. 24, no. 9, pp. 739–751, 2000.

[24] Y. G. Zhang, K. H. Xie, and Z. Wang, “Consolidation analysis of composite ground improved by granular columns considering variation of permeability coefficient of soil,” in *Ground Modification and Seismic Mitigation*, GSP 152, 2006.

[25] M. M. Lu, K. H. Xie, and B. Guo, “Consolidation theory for a composite foundation considering radial and vertical flows within the column and the variation of soil permeability within the disturbed soil zone,” *Canadian Geotechnical Journal*, vol. 47, no. 2, pp. 207–217, 2010.

[26] M. M. Lu, K. H. Xie, A. F. Hu, and G. H. Chen, “Reply to Comments on “ A general theoretical solution for the consolidation of a composite foundation” [Computers and Geotechnics 36

(2009) 24–30],” *Computers and Geotechnics*, vol. 37, no. 4, pp. 582–583, 2010.

[27] M. M. Lu, K. H. Xie, C. X. Li, and K. Wang, “Consolidation solution for composite foundation considering a time- and depth-dependent stress increment along with three distribution patterns of soil permeability,” *Journal of Zhejiang University: Science A*, vol. 12, no. 4, pp. 268–277, 2011.

[28] M. M. Lu, K. H. Xie, and S. Y. Wang, “Consolidation of vertical drain with depth-varying stress induced by multi-stage loading,” *Computers and Geotechnics*, vol. 38, no. 8, pp. 1096–1101, 2011.

[29] R. C. Wang, K. H. Xie, and S. H. Guan, “Analytical solutions for consolidation of composite ground with granular columns under timedependent loading,” *Journal of Zhejiang University*, vol. 36, no. 1, pp. 12–16, 2002.

[30] M. M. Lu, K. H. Xie, S. Y. Wang, and C. X. Li, “Analytical solution for the consolidation of a composite foundation reinforced by impervious column with an arbitrary stress increment,” *ASCE International Journal of Geomechanics*, vol. 13, no. 1, pp. 33–40, 2013.

Hindawi Publishing Corporation
Journal of Applied Mathematics
Volume 2013, Article ID 658160, 12 pages
http://dx.doi.org/10.1155/2013/658160

Research Article

Fracture Analysis of Brittle Materials Based on Nonlinear FEM and Application in Arch Dam with Fractures

Yuanwei Pan,[1] Yaoru Liu,[1] Zhixiong Cui,[1,2] Xin Chen,[3] and Qiang Yang[1]

[1] *State Key Laboratory of Hydroscience and Hydraulic Engineering, Tsinghua University, Beijing 100084, China*
[2] *State Grid Xin Yuan Construction Co., Ltd., Beijing 100761, China*
[3] *China University of Mining & Technology, Beijing 100083, China*

Correspondence should be addressed to Yaoru Liu; liuyaoru@tsinghua.edu.cn

Received 7 June 2013; Revised 2 September 2013; Accepted 4 September 2013

Academic Editor: Pengcheng Fu

Current fracture analysis models based on fracture mechanics or continuum damage mechanics are still limited in the application to three-dimensional structure. Based on deformation reinforcement theory coming from elastoperfect plastic theory, unbalanced force is proposed to predict initiation and propagation of cracks. Unbalanced force is the driving force of time-dependent deformation according to Perzyna's viscoplasticity theory. It is also related to the damage driving force in viscoplastic damage model. The distribution of unbalanced force indicates cracks initiation area, while its direction predicts possible cracks propagation path. Uniaxial compression test of precrack specimen is performed as verification to this method. The trend and distribution of cracks are in good agreement with numerical results, proving that unbalanced force is feasible and effective for fracture analysis. The method is applied in fracture analysis of Xiaowan high arch dam, which is subjected to some cracks in dam due to the temperature control program. The results show that the deformation and stress of cracks and the stress characteristics of dam are insensitive to grouting of cracks. The existing cracks are stable and dam heel is still the most possible cracking position.

1. Introduction

Rock and concrete are heterogeneous anisotropic materials, containing numerous microcosmic voids and flaws. Fracture is a common and significant failure mode of geotechnical structure. Fracture evaluation for structure under certain loads, including crack initiation, propagation, and penetration, is still an unsolved problem. Thus fracture analysis method for rock and concrete structure is of significant importance in the sense of cracking prevention and global stability evaluation.

There is a key problem remaining in fracture analysis for brittle materials and structures, that is, a feasible fracture criterion. Common fracture criterions include stress criterions and energetic criterions [1–8]. The former state that failure occurs when the maximum principal stress in some local point exceeds the tensile strength. The latter are provided by linear elastic fracture mechanics, which covers some precise measurement, such as the stress intensity factor (SIF), energy release rate, and strain energy density. The stress criterions are acceptable for bodies without cracks, while the energetic criterions only work when a certain large crack already exists.

Current numerical methods on fracture analysis include fracture mechanics [9] and continuum damage mechanics [10]. Some researchers combine both methods for numerical failure analysis [11, 12]. Crack propagation simulation could be concluded as smeared fracture model [1] and discrete fracture model [13]. Besides, numerical tools have developed rapidly, including Finite Element Method (FEM) [14], Extended FEM [15], Element Free Method [16], Boundary Element Method [17], Discrete Element Method [18], Numerical Manifold Method [19], Discontinuous Deformation Analysis [20], and Fast Lagrangian Method [21].

The theories and methods mentioned above work well in planar analysis. There is still severe limitation on the applicability when extended to three-dimensional and complex structure. Besides, behavior of rock and concrete involves complex nonlinear overall deformation, which is beyond the capacity of common numerical methods.

This paper presents a new approach based on deformation reinforcement theory [22] to evaluate cracks growth in three-dimensional structure. Unbalanced force is proposed as a set of equivalent nodal forces of overstress beyond the yield surface. Unbalanced force drives time-dependent deformation, as well as damage evolution. The distribution of unbalanced force indicates crack initiation area, while its direction predicts potential crack propagation path. Uniaxial compression test of precrack specimen is performed, which is in a good agreement with the numerical results. The method is also applied in fracture analysis of Xiaowan high arch dam.

2. Fracture Analysis Method Based on Unbalanced Force

2.1. Deformation Reinforcement Theory. Most geotechnical structures are under complicated configurations and working conditions. Stability analysis of these engineering structure could be summarized as a boundary value problem with some basic equations, including kinematic admissibility, equilibrium condition, and constitutive equations. The classical elastoplastic theory aims at solving the displacement and stress fields that simultaneously satisfy all the aforementioned equations. However, the existence of such solution requires that the structure is stable. Structural instability occurs when action is greater than resistance. The difference between action and resistance is overstress, which is the key concept of the Deformation Reinforcement Theory (DRT) and defined as the unbalanced force.

For perfect elasto-plastic materials with associative flow rule, the constitutive equations can be stated as

$$\begin{gathered}\dot{\boldsymbol{\varepsilon}} = \dot{\boldsymbol{\varepsilon}}^e + \dot{\boldsymbol{\varepsilon}}^p, \quad \dot{\boldsymbol{\varepsilon}}^e = \mathbf{C} : \dot{\boldsymbol{\sigma}}; \\ D^p\left(\boldsymbol{\sigma}, \dot{\boldsymbol{\varepsilon}}^p\right) \geq D^p\left(\boldsymbol{\sigma}^{\mathrm{yc}}, \dot{\boldsymbol{\varepsilon}}^p\right), \quad \forall f\left(\boldsymbol{\sigma}^{\mathrm{yc}}\right) \leq 0,\end{gathered} \tag{1}$$

where D^p is defined as the plastic dissipation, $D^p(\boldsymbol{\sigma}^{\mathrm{yc}}, \dot{\boldsymbol{\varepsilon}}^p) := \boldsymbol{\sigma}^{\mathrm{yc}} : \dot{\boldsymbol{\varepsilon}}^p$. $\dot{\boldsymbol{\varepsilon}}^e$ and $\dot{\boldsymbol{\varepsilon}}^p$ are elastic and plastic strain rates, respectively. $\mathbf{C}$ is the flexibility tensor. f is the yield function and $\boldsymbol{\sigma}^{\mathrm{yc}}$ is an arbitrary stress state satisfying the yield criterion. Inequality (1) is known as principle of maximum plastic dissipation [23], which covers associative flow rule and the Kuhn-Tucker condition.

Assuming that t is a pseudotime, the stress and plastic strain of material are $\boldsymbol{\sigma}_0$ and $\boldsymbol{\varepsilon}_0^p$ at time t_0. With a strain increment in time interval Δt, a new state $\boldsymbol{\sigma}$ and $\boldsymbol{\varepsilon}^p$ is achieved. Thus the linearized plastic strain rate is

$$\dot{\boldsymbol{\varepsilon}}^p = \frac{\Delta\boldsymbol{\varepsilon}^p}{\Delta t} = \frac{\Delta\boldsymbol{\varepsilon} - \mathbf{C} : \left(\boldsymbol{\sigma} - \boldsymbol{\sigma}_0\right)}{\Delta t} = \frac{\mathbf{C} : \left(\boldsymbol{\sigma}^{\mathrm{eq}} - \boldsymbol{\sigma}\right)}{\Delta t}, \tag{2}$$

where $\boldsymbol{\sigma}^{\mathrm{eq}}$ is termed the trial elastic stress while $\dot{\boldsymbol{\varepsilon}}^p = 0$. $\boldsymbol{\sigma}^{\mathrm{eq}}$ is also an equilibrium stress field under given loads;

$$\boldsymbol{\sigma}^{\mathrm{eq}} = \boldsymbol{\sigma}_0 + \mathbf{C}^{-1} : \Delta\boldsymbol{\varepsilon}. \tag{3}$$

Applying (2) into Inequality (1), the process of solving real stress field is turned into the following minimization problem:

$$\begin{gathered}\min E\left(\boldsymbol{\sigma}^{\mathrm{yc}}\right), \quad \forall f\left(\boldsymbol{\sigma}^{\mathrm{yc}}\right) \leq 0, \\ E\left(\boldsymbol{\sigma}^{\mathrm{yc}}\right) = \frac{1}{2}\left(\boldsymbol{\sigma}^{\mathrm{eq}} - \boldsymbol{\sigma}^{\mathrm{yc}}\right) : \mathbf{C} : \left(\boldsymbol{\sigma}^{\mathrm{eq}} - \boldsymbol{\sigma}^{\mathrm{yc}}\right).\end{gathered} \tag{4}$$

Equation (4) is known as the closest-point projection method (CPPM) [24], as shown in Figure 1. $\boldsymbol{\sigma}^{\mathrm{yc}}$ is an arbitrary stress field on the yielding surface, which represents the material resistance after previous minimization process. $\boldsymbol{\sigma}^{\mathrm{eq}}$ is an equilibrium stress field, which could be regarded as certain stress under external actions.

The minimization objective E represents the difference between the plastic dissipations of the external action and the material resistance. It is defined as the volume density of the plastic complementary energy (PCE);

$$E = D^p\left(\boldsymbol{\sigma}^{\mathrm{eq}}, \Delta\boldsymbol{\varepsilon}^p\right) - D^p\left(\boldsymbol{\sigma}^{\mathrm{yc}}, \Delta\boldsymbol{\varepsilon}^p\right). \tag{5}$$

Thus, instability of a material point is equal to the statement that the external action is greater than the material resistance: $E > 0$, for all $f(\boldsymbol{\sigma}^{\mathrm{yc}}) \leq 0$. As indicated by the minimization problem, if $\boldsymbol{\sigma}^{\mathrm{eq}} > \boldsymbol{\sigma}^{\mathrm{yc}}$, the real stress state minimizes the resistance deficiency in the sense of PCE. In other words, material resistance capacity is fully developed.

Drucker-Prager yield criterion is adopted in the following nonlinear calculation:

$$f(\boldsymbol{\sigma}) = \alpha I_1 + \sqrt{J_2} - H, \tag{6}$$

where $I_1 = \operatorname{tr}\boldsymbol{\sigma}$, $J_2 = \boldsymbol{\sigma} : \boldsymbol{\sigma}/2 + I_1/6$, and α and H are material parameters. With the real stress field $\boldsymbol{\sigma}$ solved by (4), the following characteristic can be proved [22]:

$$\left.\frac{\partial f}{\partial\boldsymbol{\sigma}}\right|_{\boldsymbol{\sigma}=\boldsymbol{\sigma}} = \left.\frac{\partial f}{\partial\boldsymbol{\sigma}}\right|_{\boldsymbol{\sigma}=\boldsymbol{\sigma}^{\mathrm{eq}}}. \tag{7}$$

Eventually the following analytical solution of $\boldsymbol{\sigma}$ can be derived:

$$\begin{gathered}\boldsymbol{\sigma} = (1-n)\,\boldsymbol{\sigma}^{\mathrm{eq}} + p\mathbf{I}, \\ n = \frac{wG}{\sqrt{J_2}}, \quad p = -mw + 3nI_1, \\ m = \alpha\left(3\lambda + 2G\right), \quad w = \frac{f}{\left(3\alpha m + G\right)},\end{gathered} \tag{8}$$

where I_1 and J_2 are invariants of $\boldsymbol{\sigma}^{\mathrm{eq}}$ and λ and G are the Lamé constants.

2.2. Demonstration in FEM. PCE and unbalanced force are implemented in FEM analysis. Since the process is restricted to displacement method, the kinematic admissibility is naturally satisfied.

In order to evaluate the global stability of structure under certain actions, two stress field sets, S^{eq} and S^{yc}, are defined for elastoperfect plastic problem. The two stress sets, respectively, satisfy the equilibrium condition and the yield criterion as

$$\begin{gathered}S^{\mathrm{eq}} = \left\{\boldsymbol{\sigma}^{\mathrm{eq}} \mid \mathbf{F} = \int_V \mathbf{B}^T\boldsymbol{\sigma}^{\mathrm{eq}} dV\right\}, \\ S^{\mathrm{yc}} = \left\{\boldsymbol{\sigma}^{\mathrm{yc}} \mid f\left(\boldsymbol{\sigma}^{\mathrm{yc}}\right) \leq 0\right\},\end{gathered} \tag{9}$$

where $\mathbf{B}$ is the displacement gradient matrix, $\mathbf{F}$ is equivalent nodal force vector of external loads, and V is structure

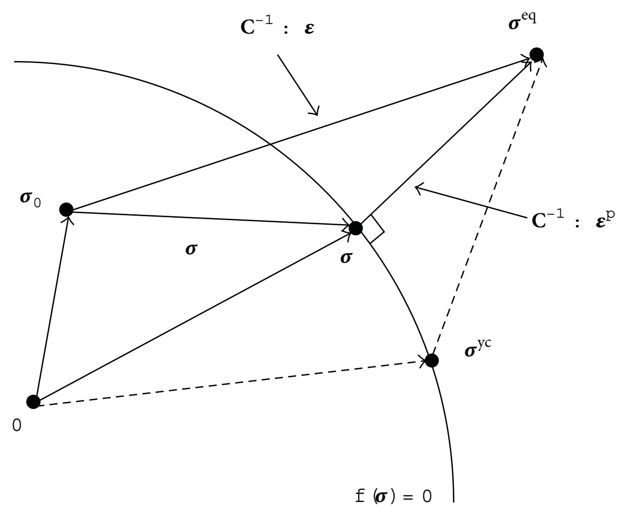

Figure 1: The closest-point projection method.

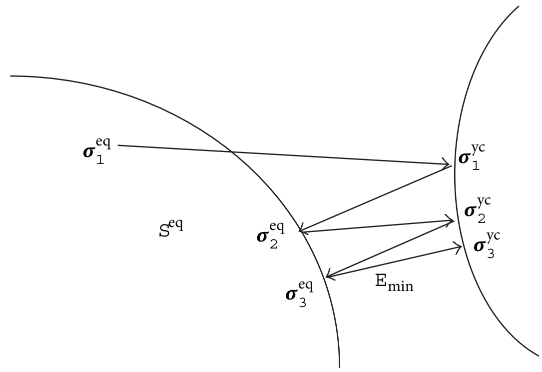

Figure 2: Demonstration of the elastoplastic iteration in FEM analysis.

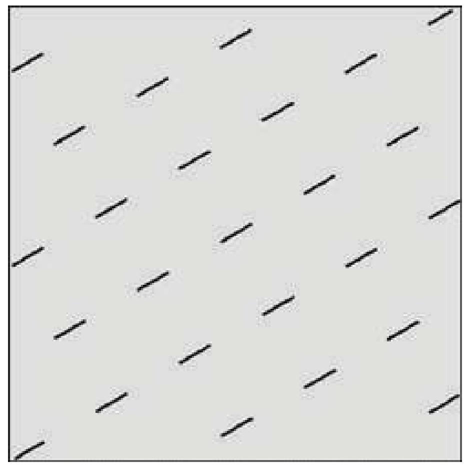

Figure 3: Sketch map of the precrack specimen.

volume. S^{eq} and S^{yc}, respectively, represent external actions and structural resistance. The real stress field must satisfy the yield criterion; $\boldsymbol{\sigma} = \boldsymbol{\sigma}^{\mathrm{yc}}$. Equivalent nodal forces of the difference between the two stress fields, which is the driving force of structure deformation, can be defined as unbalanced force as

$$\Delta \mathbf{U} = \int_V \mathbf{B}^T \left(\boldsymbol{\sigma}^{\mathrm{eq}} - \boldsymbol{\sigma}^{\mathrm{yc}}\right) dV = \mathbf{F} - \int_V \mathbf{B}^T \boldsymbol{\sigma} dV. \quad (10)$$

For a given load step, the unbalanced force is the driving force of deformation in the FE iterations. The principle of minimum PCE implies that elasto-plastic structures deform tending to the state where PCE is minimized under certain actions as

$$\begin{gathered} \min E\left(\boldsymbol{\sigma}^{\mathrm{eq}}, \boldsymbol{\sigma}^{\mathrm{yc}}\right), \quad \forall \boldsymbol{\sigma}^{\mathrm{eq}} \in S^{\mathrm{eq}}, \ \boldsymbol{\sigma}^{\mathrm{yc}} \in S^{\mathrm{yc}}, \\ E\left(\boldsymbol{\sigma}^{\mathrm{eq}}, \boldsymbol{\sigma}^{\mathrm{yc}}\right) = \int_V \frac{1}{2} \left(\boldsymbol{\sigma}^{\mathrm{eq}} - \boldsymbol{\sigma}^{\mathrm{yc}}\right) : \mathbf{C} : \left(\boldsymbol{\sigma}^{\mathrm{eq}} - \boldsymbol{\sigma}^{\mathrm{yc}}\right) dV. \end{gathered} \quad (11)$$

Unbalanced force is the measurement between external actions and structural resistance. The plastic complementary energy E is a norm of unbalanced force. Once E reaches its minimum value E_{min}, the unbalanced force stays constant and the structure suffers steady plastic flow until failure occurs. Only if $E_{\mathrm{min}} = 0$, the structure is stable.

In elastoplastic FEM iteration, PCE and unbalanced force can be calculated by the following steps. First, the nearest stable stress field $\boldsymbol{\sigma}_1^{\mathrm{yc}}$ can be achieved from an arbitrary equilibrium stress field $\boldsymbol{\sigma}_1^{\mathrm{eq}}$. Then, the nearest equilibrium stress field $\boldsymbol{\sigma}_2^{\mathrm{eq}}$ is also obtained from $\boldsymbol{\sigma}_1^{\mathrm{yc}}$. Finally, structure stress state tends to the two closest stress fields $\boldsymbol{\sigma}$ and $\boldsymbol{\sigma}^{\mathrm{eq}}$, as shown in Figure 2. The iteration converges if the plastic complementary energy is reaching a steady value ΔE_0. For ideal model, ΔE_0 is equal to its minimum value ΔE_{min}. If $\Delta E_{\mathrm{min}} = 0$, the structure remains stable and the stress field $\boldsymbol{\sigma}$ is the real stress response. Otherwise, the structure is unstable and PCE is a magnitude estimation of its global instability. Unbalanced force reflects the structural failure behavior, including failure position and pattern.

2.3. Explanation of Unbalanced Force in Viscoplastic Damage Model. Stress state beyond the yielding surface is unacceptable for perfect elastoplasticity. It exists only in the iteration process of FEM calculation. However, in viscoplasticity models, it is of explicit physical significance as the driving force of visco-plasticity deformation. The Perzyna associative visco-plasticity strain rate could be stated as [25, 26]

$$\dot{\varepsilon}_{ij}^{\mathrm{vp}} = \begin{cases} 0, & f \leq 0, \\ \Gamma^{\mathrm{vp}} \Phi(f) \dfrac{\partial Q}{\partial \boldsymbol{\sigma}}, & f > 0, \end{cases} \quad (12)$$

where $\dot{\varepsilon}_{ij}^{\mathrm{vp}}$ is the visco-plasticity strain rate. Γ^{vp} is the viscosity parameter. $f = f(\boldsymbol{\sigma}, \kappa) = 0$ is the yield function. Q is plastic potential function, and for associative flow rule, $Q = f(\boldsymbol{\sigma})$. $\Phi(f)$ is overstress function characterized by the yield function, commonly expressed as $\Phi(f) = (f/f_0)^n$. f_0 is a reference constant of the same dimension with yield function f.

According to Perzyna's visco-plasticity theory, visco-plasticity strain rate is in proportion to overstress function. $\partial f/\partial \sigma$ represents the direction of $\dot{\varepsilon}_{ij}^{\mathrm{vp}}$, while $\Phi(f)$ reflects the magnitude of $\dot{\varepsilon}_{ij}^{\mathrm{vp}}$. If the overstress function is restricted to yield function, plastic flow occurs only on the condition

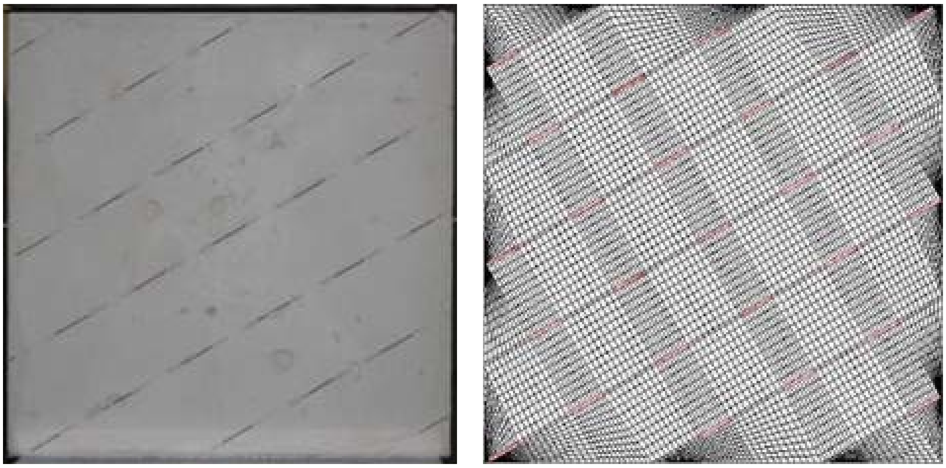

(a) (b)

Figure 4: The precrack specimen and numerical model.

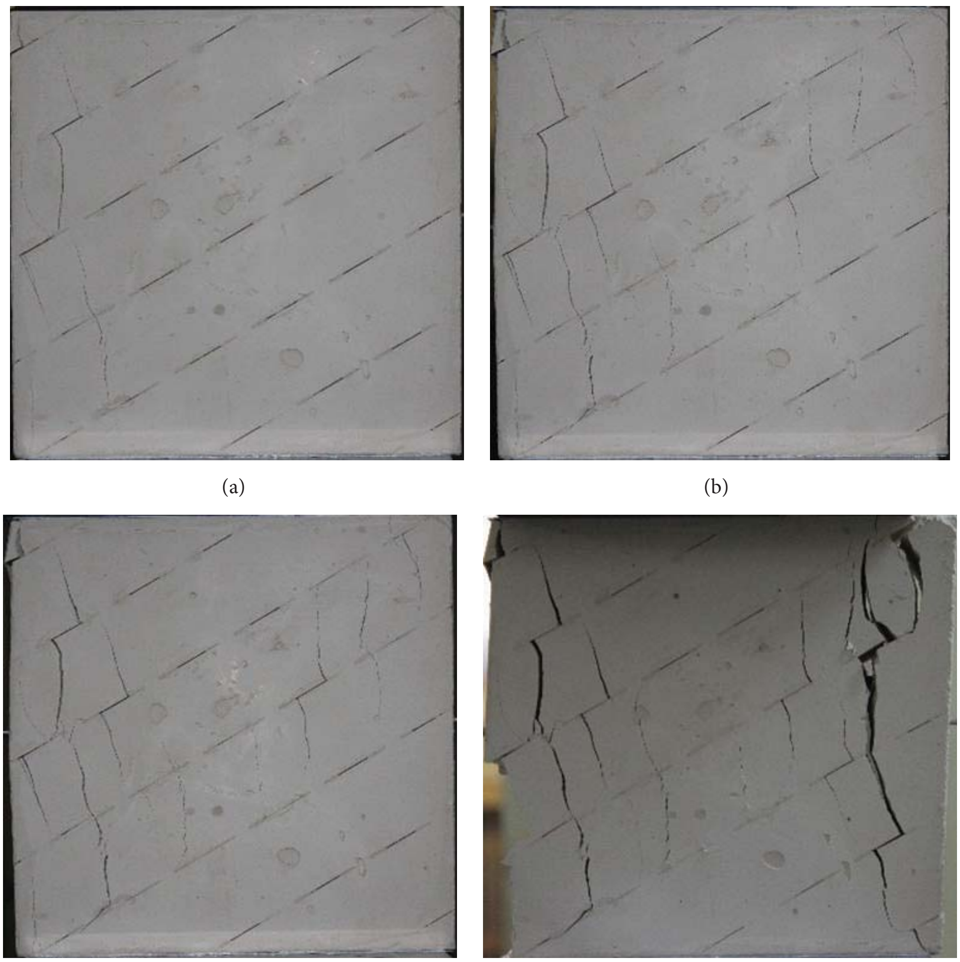

(a) (b)

(c) (d)

Figure 5: Cracks growth and failure mode of specimen test.

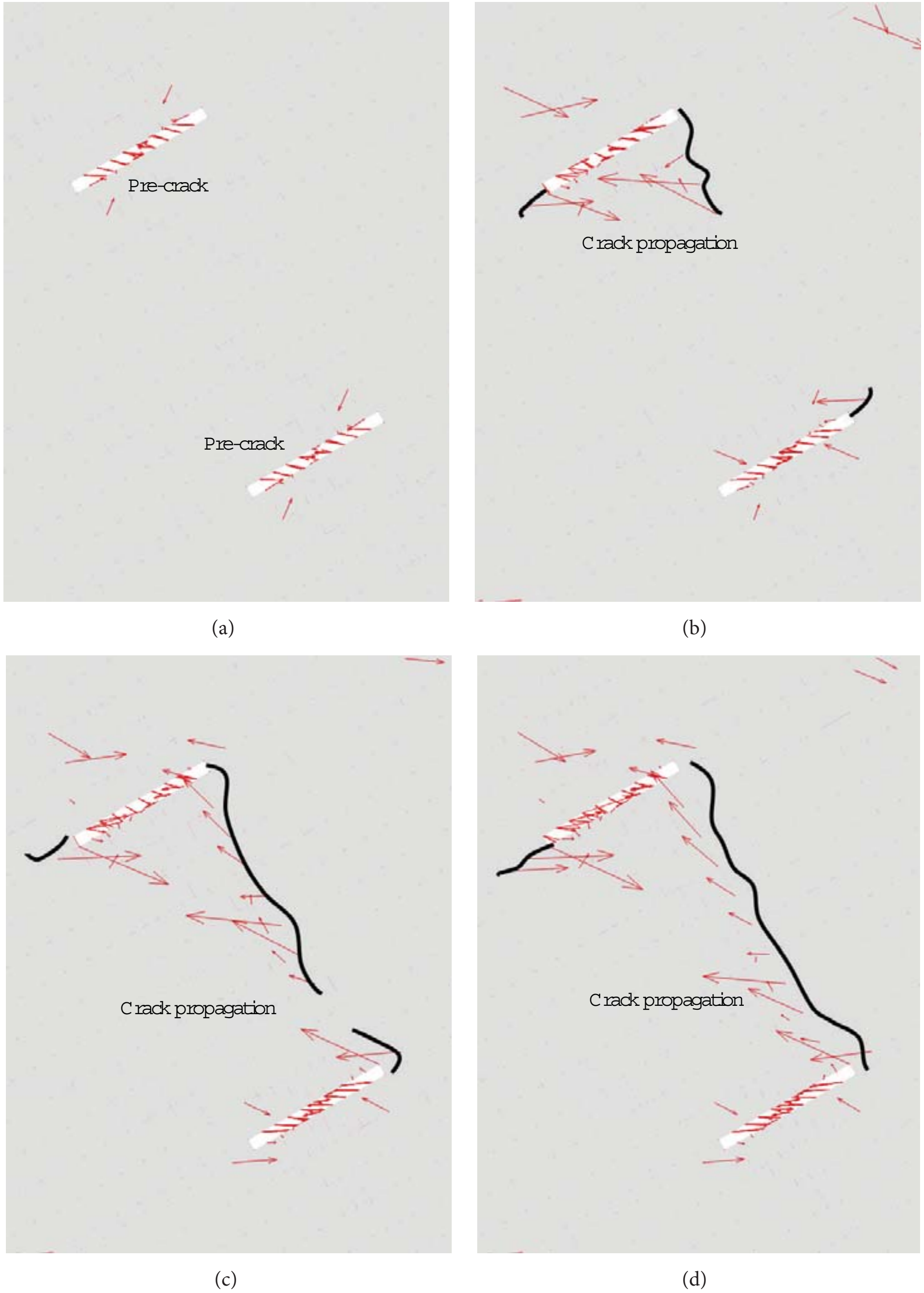

Figure 6: Unbalanced force evolution process at crack tips.

that the yield function value is positive. As the DRT states, unbalanced force is a set of the equivalent nodal forces of stress exceeding the yield function, which can be termed as the driving force of time-dependent deformation.

Unbalanced force is also involved in structural crack growth analysis based on damage mechanics methods. In the concept of continuum damage mechanics, the damage variable is usually related to equivalent plastic strain, that is, the accumulation of time-dependent deformation. A classical definition of damage variable is $\phi = 1 - \overline{A}/A$, where A is total area and $\overline{A}$ is intact area [27, 28]. Effective stress tensor in the undamaged configuration is determined by the damage variable and the nominal Cauchy stress tensor [29, 30] as

$$\overline{\sigma}_{ij} = \frac{\sigma_{ij}}{(1-\phi)^2}, \quad (13)$$

where $\overline{\sigma}_{ij}$ is the effective stress tensor and σ_{ij} is the nominal Cauchy stress tensor.

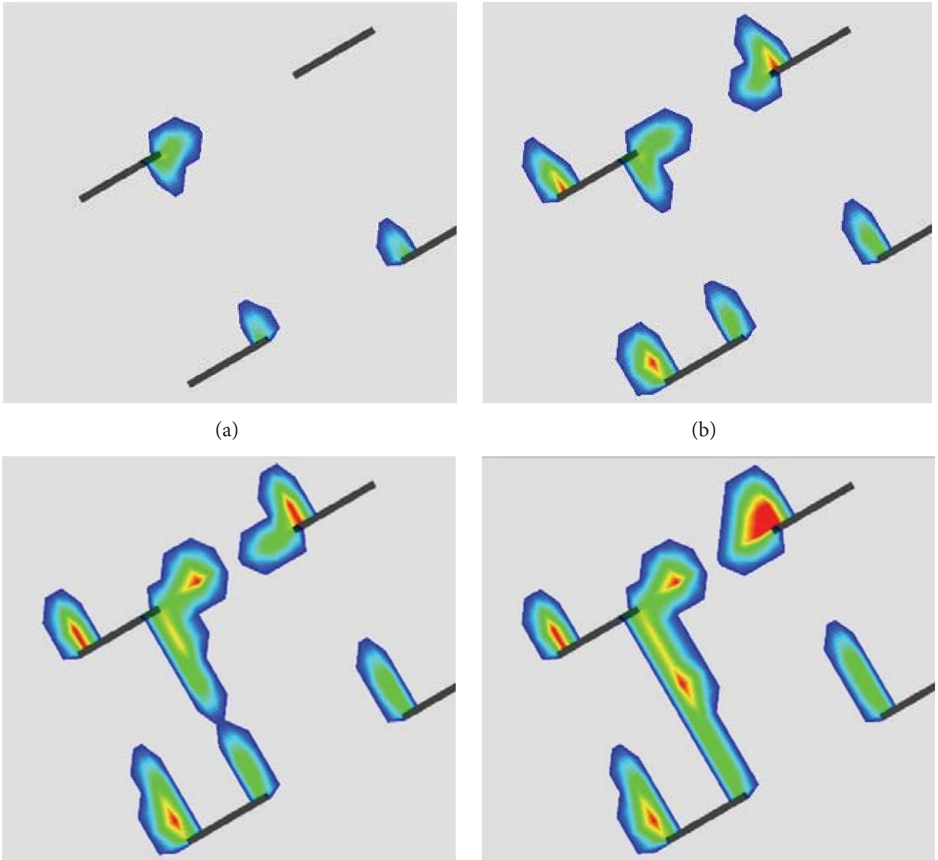

(a) (b)

(c) (d)

Figure 7: Damaged area expansion process at crack tips.

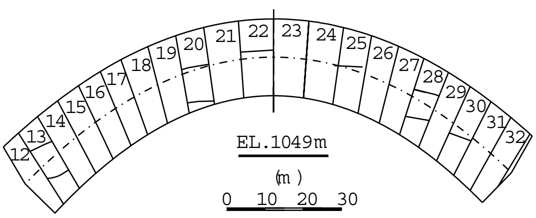

Figure 8: Distribution of cracks on typical elevation.

Darabi et al. [31] presented a thermoviscodamage model to describe the damage evolution law, which could be stated as

$$\dot{\phi} = \Gamma_0^{\varphi}\left(\frac{\overline{Y}(1-\phi)^2}{Y_0}\right)^q \exp\left(k\bar{\varepsilon}_{\text{eff}}^{\text{Tot}}\right) G(T), \tag{14}$$

where $\bar{\varepsilon}_{\text{eff}}^{\text{Tot}} = \sqrt{\bar{\varepsilon}_{ij}\,\bar{\varepsilon}_{ij}}$ is the effective total strain in the effective configuration. $\bar{\varepsilon}_{ij}$ includes both viscoelastic and viscoplastic components. q is the stress dependency parameter and k is a material parameter. Γ_0^{φ} and Y_0 are the reference damage viscosity parameter and the reference damage force, respectively. $G(T)$ is a damage temperature function. $\overline{Y}$ is the damage driving force in the effective configuration, which can be assumed to have a modified Drucker-Prager-type form as

$$\overline{Y} = \alpha\overline{I}_1 + \bar{\tau},$$
$$\bar{\tau} = \frac{\sqrt{\overline{J}_2}}{2}\left[1 + \frac{1}{d} + \left(1 - \frac{1}{d}\right)\frac{\overline{J}_3}{\sqrt{\overline{J}_2^3}}\right], \tag{15}$$

where $\overline{I}_1$ and $\overline{J}_2$ are the invariants of the effective stress tensor. d gives the distinction of material behavior in compression and extension loading conditions, where $d = 1$ implies that $\bar{\tau} = \sqrt{\overline{J}_2}$. Thus the damage driving force is expressed as

$$\overline{Y} = \alpha\overline{I}_1 + \sqrt{\overline{J}_2}. \tag{16}$$

Damage evolution requires that $\overline{Y} > 0$; that is, the equilibrium stress field exceeds the yield function. As stated above, the equivalent nodal force of stress exceeding the yield function is unbalanced force, which is the driving force of damage evolution. Unbalanced force is more explicit than equivalent plastic strain in the sense of physical significance.

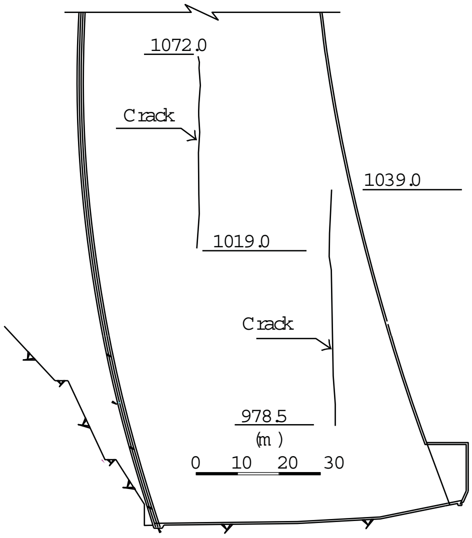

FIGURE 9: Distribution of cracks in typical dam section.

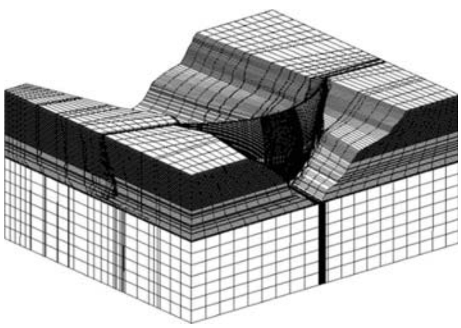

FIGURE 10: Numerical model of Xiaowan arch dam.

2.4. Fracture Analysis Method.

2.4. Fracture Analysis Method. Unbalanced force is a set of equivalent nodal forces of plastic stress in the elements around a node, which reflects the difference between external actions and structural resistance. The process of FEM iteration is to find a set of additional forces to prevent failure from occurring, which is minimized in the sense of PCE. If the additional force, that is, unbalanced force, tends to be zero in the iteration, the cracks will not initiate or stay in a limit state. Otherwise, cracks will initiate and propagate, and the direction and distribution of unbalanced force indicate the potential failure area.

Thus, occurrence of unbalanced force can be the identification of local cracks initiation. Meanwhile, as unbalanced force is related to the damage driving force in the thermo-viscodamage model, the distribution of unbalanced force will expand gradually as material damage accumulates. This process corresponds to the cracks growth and propagation. In general, its direction predicts the possible path of crack's propagation.

Current fracture analysis methods are based on planar problems, which provide good results dealing with a single crack or two cracks. When extended to 3D structures, the fracture criterion and nonlinear calculation efficiency remain to be solved. Unbalanced force is presented in this paper, which is of clear physical concept and could be effectively applied to elato-plastic FEM calculation.

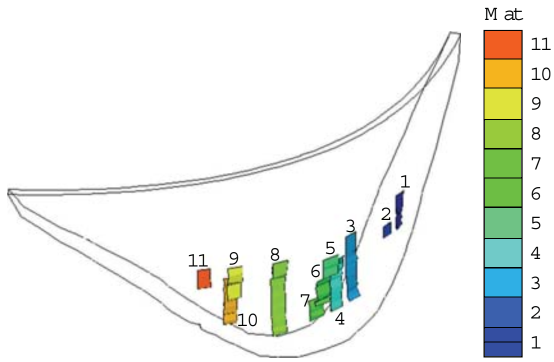

FIGURE 11: Distribution of cracks in the dam.

3. Fracture Test and Numerical Analysis of Precrack Specimen

The strong correlation is found between the distribution of unbalanced force and the initial point of structural cracking, which is verified by the following model test and numerical results.

3.1. Specimen and Numerical Model. The precrack cubic specimen is made with gypsum, which is 15 cm wide, 15 cm high, and 5 cm thick, as shown in Figure 3. Steel slices are inserted during the specimen modeling process and pulled out once the initial set begins. By this means the precracks are manufactured. The angle between precrack and horizontal direction is 30°, and precrack length is 12 mm.

Numerical model is exactly established according to the physical test. Precracks are simulated where the corresponding elements are set null. The precrack specimen and numerical model are illustrated in Figure 4.

3.2. Test and Calculation Results. Uniaxial compression test of the precrack specimen is performed with its bottom restrained. The pressure on the top is gradually increased from 0 MPa to 2.0 MPa by the increment of 0.1 MPa.

The precracks in the left part of specimen initiate first during the uniaxial compression test, when the pressure achieves 1.6 MPa. The cracks initiation direction is almost perpendicular to the precracks trend. With the pressure being gradually increased, cracks propagation path tends to be vertical, and precracks at the top right corner begin to initiate as well. Cracks propagate and eventually penetrate both sides of the specimen, where failure occurs with a compressive strength 2.0 MPa. The cracks growth process and final failure mode are shown in Figure 5.

Nonlinear numerical calculation is applied with the same constraint conditions and loading procedure. As clearly shown in (14), the damage evolution law is influenced by various factors, including stress, strain, strain rate, temperature, and damage history. The loading process duration of this test is relatively short, so the temperature effect is ignored.

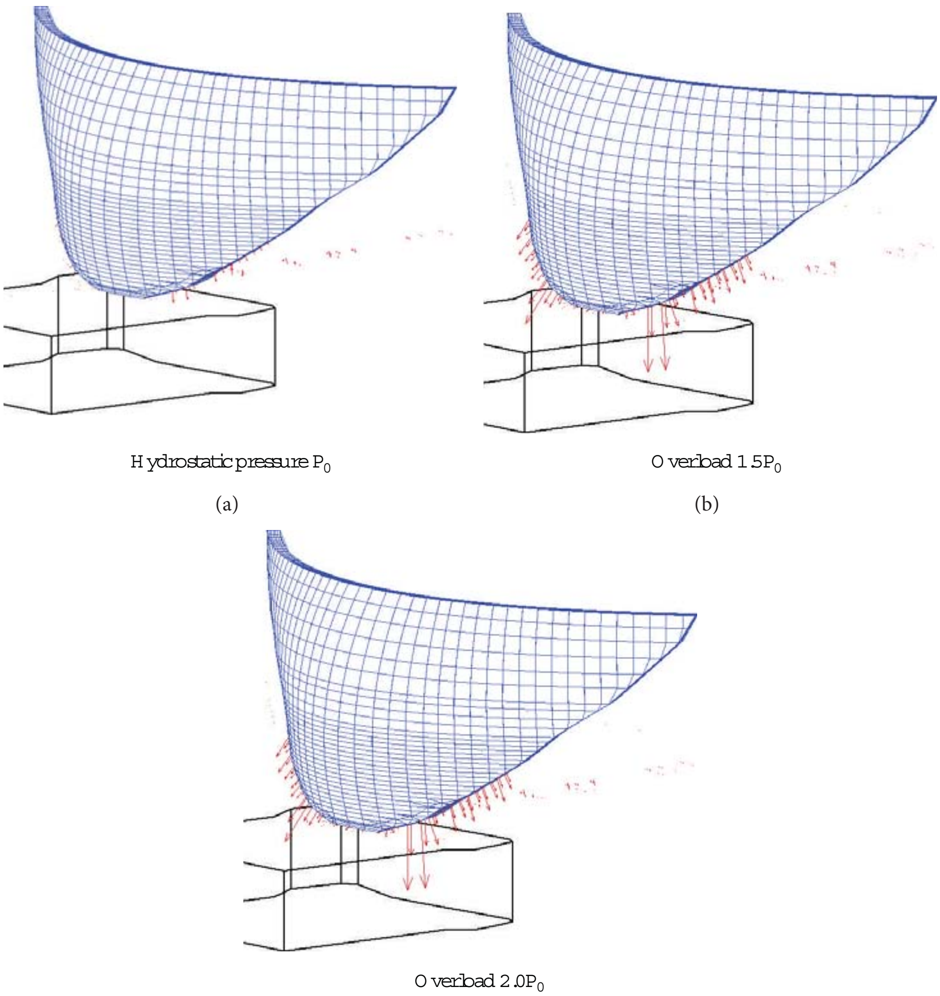

(a) (b) (c)

Figure 12: Distribution of dam heel unbalanced force of scheme 1.

Table 1: Materials parameters.

	E/GPa	μ	r/ kN·m^{-3}	f	c/MPa
Gypsum	5	0.35	2	0.1	0.2
Damaged gypsum	2.5	0.35	2	0.05	0.1

Since gypsum is quasi-brittle material, the time-dependent deformation of damage evolution process is simplified in the numerical calculation. For the region where the damage driving force $\overline{Y}$ is greater than the reference damage force Y_0, gypsum is regarded as damaged and elastic modulus E, and shear strengths f and c are reduced by 50%. In this case, $Y_0 = 10\,\text{MPa}$. Table 1 shows the materials parameters.

Unbalanced force distribution and evolution process at crack tips are shown in Figure 6. When the specimen stays in a stress state of elasticity, there is no unbalanced force. With the pressure being increased, unbalanced force occurs at the precrack tips around the middle left part of the specimen. As the distribution area expands, the direction of unbalanced force growth tends to be perpendicular to the precracks. The unbalanced force eventually goes through the nearest crack tips, which indicates the most possible propagation path of specimen fracture.

Damaged area expanding process is shown in Figure 7. Damaged area appears around the tip of crack and gradually extends to neighbor elements in the perpendicular direction to the precracks. At last, the damaged area unites between the tips of the two parallel precracks.

The existence of unbalanced force indicates that the model is unable to balance the loads and fracture occurs, which agrees with the test results. As cracks propagate, a new structure is achieved and the stress field is redistributed. Since the crack propagation is a local and quasi-static failure process, the new structure retains its bearing capacity. Thus the model is able to sustain the loads and reaches a new equilibrium state. This process continues until the load reaches the compressive strength and structural failure occurs. The distribution of unbalanced force indicates cracks initiation area, while its direction predicts the possible cracks propagation path.

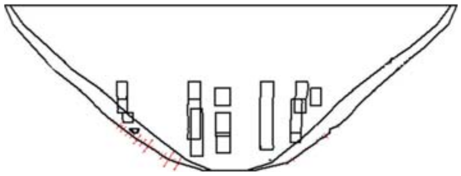

Hydrostatic pressure P_0

(a)

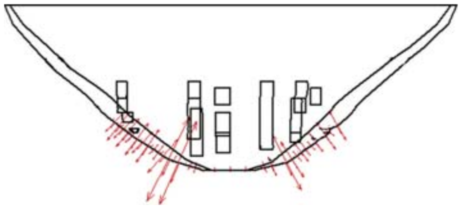

Overload 1.5P_0

(b)

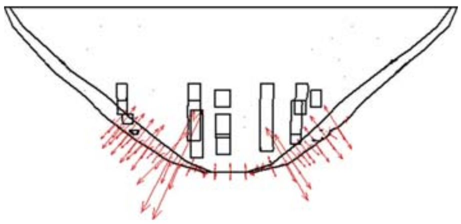

Overload 2.0P_0

(c)

FIGURE 13: Distribution of unbalanced force in dam of scheme 1.

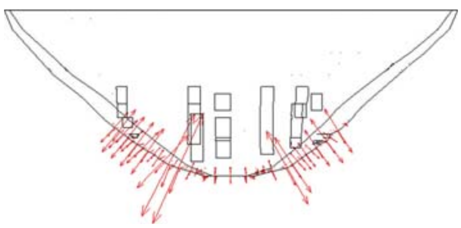

FIGURE 14: Distribution of dam body unbalanced force under overload 2.0P_0 in scheme 2.

4. Fracture Analysis of Arch Dam with Cracks

4.1. Numerical Model. Xiaowan arch dam, with a height of 292 m, is subjected to some cracks in dam due to the temperature control program. Most of the cracks distribute on the middle and bottom elevations of the dam and tend tangentially to the arch. The average width of these cracks is 1 mm. Distribution of cracks on typical elevation and on typical dam section is shown in Figures 8 and 9, respectively.

The size of numerical model is as follows: upstream 300 m, downstream 900 m, and left and right banks 700 m each. Elevations of dam crest and model bottom are ∇1245 m and ∇595 m, and thus the model height is 650 m. The model includes 58989 nodes and 53850 elements, as shown in Figure 10. There are 11 major cracks that are numbered and simulated, as shown in Figure 11 and Table 2.

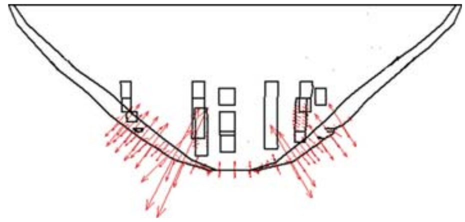

FIGURE 15: Distribution of dam body unbalanced force under overload 2.0P_0 in scheme 3.

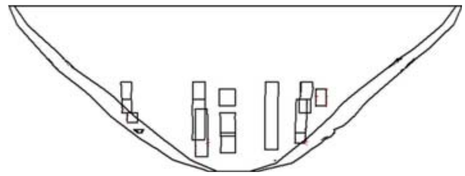

FIGURE 16: Distribution of cracks unbalanced force under overload 2.0P_0 in scheme 1.

TABLE 2: Numbers of cracks in the dam.

Number	Crack
1	13-1
2	13-2
3	20-1
4	20-2
5	22-1
6	22-3
7	22-4
8	25-1
9	28-1
10	28-2
11	30-1

Crack 13-1 in the table means the 1st crack in dam section number 13, and so on.

TABLE 3: Material parameters.

	E/GPa	μ	r/kN·m^{-3}	f	c/MPa
Foundation	18	0.28	28	1.52	1.33
Dam	23.1	0.2	24	1.4	1.6
Crack	5	0.3	27.5	1.12	0.9

The dam cracks are induced by the improper temperature control program during construction. Since concrete grouting in the cracks is operated, the dam cracks are simulated with thin layer elements. The material parameters are shown in Table 3.

4.2. Fracture Analysis. Structural fracture and parameters sensitivity analysis are presented. Three schemes are performed, including normal parameters (scheme 1), crack's shear strengths f and c reduced by 50% (scheme 2), and crack's shear strengths f and c reduced by 75% (scheme 3).

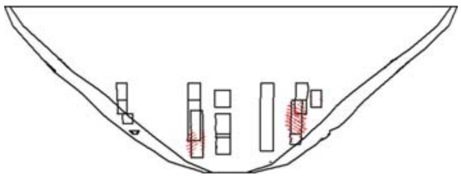

Figure 17: Distribution of cracks unbalanced force under overload $2.0P_0$ in scheme 2.

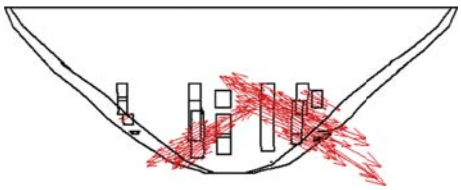

Figure 18: Distribution of cracks unbalanced force under overload $2.0P_0$ in scheme 3.

Table 4: Unbalanced forces of dam heel (10^4 N).

Scheme	P_0	$1.5P_0$	$2.0P_0$
1	40249.56	257289.9	415601.5
2	40216.39	257269.2	415560.7
3	40126.59	256869.2	414973.0

Table 5: Unbalanced force of cracks under overload $2P_0$ (10^4 N).

Number	Crack	Scheme 1	Scheme 2	Scheme 3
1	13-1	0.00	0.00	12.54
2	13-2	0.02	0.87	221.69
3	20-1	0.00	0.00	2.83
4	20-2	0.03	0.70	**7614.90***
5	22-1	0.00	0.00	0.00
6	22-3	0.00	0.00	0.00
7	22-4	0.00	0.00	0.00
8	25-1	0.00	0.00	8.00
9	28-1	0.00	0.94	65.95
10	28-2	1.77	345.54	**15810.91***
11	30-1	0.02	6.04	687.85
	Dam heel	415601.5	415560.7	414973

*Dominating cracks in the propagation process.

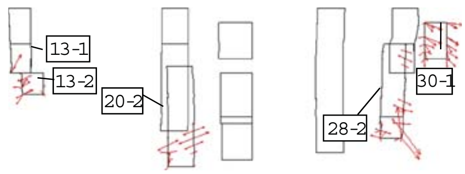

Figure 19: Local distribution of cracks unbalanced force (scheme 1, under overload $2.0P_0$).

Both the hydrostatic pressure P_0 and overload conditions are included in each scheme.

4.2.1. Dam Heel Cracking Analysis. The distribution of unbalanced force at dam heel under different loads in scheme 1 is shown in Figure 12. The other two schemes are of similar distribution. Under the hydrostatic pressure P_0, unbalanced force rarely occurs and dam heel stays as a global steady state. As the hydrostatic pressure is overloaded, unbalanced force area expands and its magnitude increases rapidly, which is concentrated in the dam heel.

Unbalanced forces of dam heel in three schemes are summarized in Table 4. In the overload conditions, unbalanced force increases rapidly in dam heel, which is the most possible location of cracks initiation. As the variation of unbalanced forces between the three schemes is relatively small, the dam heel cracking behavior is insensitive to the change of crack parameters.

4.2.2. Dam Body Cracking Analysis. The distribution of unbalanced force in dam under different loads in scheme 1 is shown in Figure 13. Under the hydrostatic pressure P_0, there is a little unbalanced force existing in the right abutment of the arch dam. As the pressure is overloaded, unbalanced force occurs in both the dam abutments. Distribution of unbalanced force in dam is close to the foundation, where cracks initiate and failure may occur.

Distribution of dam body unbalanced force under overload $2.0P_0$ in schemes 2 and 3 is shown in Figures 14 and 15, respectively. Dam unbalanced force is insensitive to the change of crack parameters. Crack number 10, that is, the second crack in dam section number 28, suffers from some unbalanced force in scheme 3, which indicates the most sensitive and dangerous crack in the dam. Meanwhile, the unbalanced force of cracks is much less than that of dam body, and the latter is still the emphasis of dam cracking prevention.

4.2.3. Analysis for Existing Cracks. The length of unbalanced force vectors in the cracks is enlarged 20 times since it is relatively less than that of dam body. Distribution of cracks unbalanced force under overload $2.0P_0$ in the three schemes is shown in Figures 16, 17, and 18, respectively. Cracks initiation and propagation are very sensitive to the crack parameters. In other words, the stability of the existing cracks relies on the quality of concrete grouting in the cracks.

Unbalanced force of cracks under overload $2.0P_0$ in all three schemes is summarized in Table 5. Unbalanced force in dam heel is also listed in Table 5 as comparison. Unbalanced forces in dam heel increase earlier than the cracks in the dam. Dam heel contributes most of the unbalanced forces in all conditions. Namely, dam heel cracking occurs before any existing crack propagates. Among all existing cracks, 20-2 and 28-2 are the dominating cracks in the process of fracture propagation, while 30-1 and 13-2 are also possible initiation area, as shown in Figure 19. The cracks near the crown cantilever are stable.

4.3. Comparison with Geomechanical Model Test. Results and conclusions of geomechanical model test are presented as comparison with numerical method. The final distribution of

Figure 20: The final distribution of upstream cracks.

upstream cracks is shown in Figure 20. Dam heel cracking occurs as the overload increases to $1.7 \sim 3.0P_0$. There is no sign of existing cracks growth in the dam during the test. Instead, cracks that occur on the dam surface begin to extend after the overload reaches $4.0P_0$. Experimental results indicate that dam heel cracking, compared with existing cracks in dam, is the dominating problem of Xiaowan arch dam, which is corresponding to numerical results.

5. Conclusion

Unbalanced force is proposed based on deformation reinforcement theory to analyze fracture behavior, including initiation and propagation of cracks in 3D structures. Unbalanced force is a set of the equivalent nodal forces of stress exceeding the yield function, which can be termed the driving force of time-dependent deformation, as well as damage evolution.

The unbalanced force and damaged area are in good agreement with precrack specimen test results. The distribution of unbalanced force indicates cracks initiation area, while its direction predicts the possible cracks propagation path.

The method is applied in fracture analysis of Xiaowan high arch dam. Dam heel cracking occurs before any existing crack propagates, which is the most possible failure mode. Among all existing cracks, 20-2 and 28-2 are the dominating cracks in the process of fracture propagation.

Acknowledgments

The work reported here was supported by the State Key Laboratory of Hydroscience and Engineering of Hydroscience with Grant no. 2013-KY-2 and China National Funds for Distinguished Young Scientists with Grant no. 50925931.

References

[1] A. Hillerborg, M. Modéer, and P. E. Petersson, "Analysis of crack formation and crack growth in concrete by means of fracture mechanics and finite elements," *Cement and Concrete Research*, vol. 6, no. 6, pp. 773–781, 1976.

[2] Z. P. Bazant and B. H. Oh, "Crack band theory for fracture of concrete," *Meterials and Structures*, vol. 16, no. 3, pp. 155–177, 1983.

[3] K. J. Willam and E. P. Warnke, "Constitutive models for the triaxial behavior of concrete," in *Proceedings of the International Association for Bridge and Structural Engineering*, vol. 19, p. 174, ISMES, Bergamo, Italy, 1975.

[4] J. Kemeny and N. G. W. Cook, "Effective moduli, non-linear deformation and strength of a cracked elastic solid," *International Journal of Rock Mechanics and Mining Sciences and*, vol. 23, no. 2, pp. 107–118, 1986.

[5] G. R. Irwin, "Fracture dynamics," in *Fracturing of Metals*, pp. 147–166, 1948.

[6] E. Orowan, "Fracture and strength of solids," *Reports on Progress in Physics*, vol. 12, no. 1, pp. 185–232, 1948.

[7] J. R. Rice, "A path independent integral and the approximate analysis of strain concentration by notches and cracks," *Journal of Applied Mechanics*, vol. 35, pp. 379–386, 1968.

[8] G. C. Sih and B. Macdonald, "Fracture mechanics applied to engineering problems-strain energy density fracture criterion," *Engineering Fracture Mechanics*, vol. 6, no. 2, pp. 361–386, 1974.

[9] W. Yang, *Macro-Micro Fracture Mechanics*, National Industry Press, Beijing, China, 1995 (Chinese).

[10] M. G. D. Geers, R. De Borst, and R. H. J. Peerlings, "Damage and crack modeling in single-edge and double-edge notched concrete beams," *Engineering Fracture Mechanics*, vol. 65, no. 2-3, pp. 247–261, 2000.

[11] W. S. Blackburn, "Remeshing algorithm for three-dimensional crack growth and intersection with surfaces or cracks in non-coplanar planes," *Engineering Analysis with Boundary Elements*, vol. 24, no. 4, pp. 343–350, 2000.

[12] J. C. W. van Vroonhoven and R. de Borst, "Combination of fracture and damage mechanics for numerical failure analysis," *International Journal of Solids and Structures*, vol. 36, no. 8, pp. 1169–1191, 1998.

[13] Z. P. Bazant, "Crack band model for fracture of geomaterials," in *Proceedings of the 4th International Conference on Numerical Methods in Geomechanics*, vol. 3, pp. 1137–1152, Alberta, Canada, 1982.

[14] P. O. Bouchard, F. Bay, Y. Chastel, and I. Tovena, "Crack propagation modelling using an advanced remeshing technique," *Computer Methods in Applied Mechanics and Engineering*, vol. 189, no. 3, pp. 723–742, 2000.

[15] N. Moës and E. Béchet, "Modeling stationary and evolving discontinuities with finite elements," in *Proceedings of the 7th International Conference on Computational Plasticity (COMPLAS '03)*, CIMNE, Barcelona, Spain, 2003.

[16] T. Belytschko, Y. Y. Lu, and L. Gu, "Element-free Galerkin methods," *International Journal for Numerical Methods in Engineering*, vol. 37, no. 2, pp. 229–256, 1994.

[17] M. F. Marji, H. Hosseini-Nasab, and A. H. Kohsary, "On the uses of special crack tip elements in numerical rock fracture mechanics," *International Journal of Solids and Structures*, vol. 43, no. 6, pp. 1669–1692, 2006.

[18] A. Baghbanan and L. Jing, "Stress effects on permeability in a fractured rock mass with correlated fracture length and aperture," *International Journal of Rock Mechanics and Mining Sciences*, vol. 45, no. 8, pp. 1320–1334, 2008.

[19] G. H. Shi, "Manifold method," in *Proceedings of the 1st International Forum on DDA and Simulations of Discontinuous Media*, Bekerley, Calif, USA, 1996.

[20] Y. H. Hatzor, A. A. Arzi, Y. Zaslavsky, and A. Shapira, "Dynamic stability analysis of jointed rock slopes using the DDA method: king Herod's Palace, Masada, Israel," *International Journal of Rock Mechanics and Mining Sciences*, vol. 41, no. 5, pp. 813–832, 2004.

[21] H. Hakami, "Rock characterisation facility (RCF) shaft sinking—numerical computations using FLAC," *International Journal of Rock Mechanics and Mining Sciences*, vol. 38, no. 1, pp. 59–65, 2001.

[22] Q. Yang, Y. Liu, Y. Chen, and W. Zhou, "Deformation reinforcement theory and its application to high arch dams," *Science in China E*, vol. 51, no. 2, pp. 32–47, 2008.

[23] R. Hill, *The Mathematical Theory of Plasticity*, Clarendon Press, Oxford, UK, 1950.

[24] J. C. Simo, J. G. Kennedy, and S. Govindjee, "Nonsmooth multisurface plasticity and viscoplasticity. Loading/unloading conditions and numerical algorithms," *International Journal for Numerical Methods in Engineering*, vol. 26, no. 10, pp. 2161–2185, 1988.

[25] O. C. Zienkiewicz and I. C. Cormeau, "Viscoplasticity-plasticity and creep in elastic solids-a unified numerical solution approach," *International Journal for Numerical Methods in Engineering*, vol. 8, no. 4, pp. 821–845, 1974.

[26] P. Perzyna, "Fundamental problems in viscoplasticity," *Advances in Applied Mechanics*, vol. 9, no. 2, pp. 243–377, 1966.

[27] L. M. Kachanov, "Time of the rupture process under creep conditions," *Izvestiya Akademii Nauk SSR Otdelenie Tekhnicheskikh Nauk*, vol. 8, pp. 26–31, 1958.

[28] I. N. Rabotnov, *Creep Problems in Structural Members*, vol. 7, North-Holland, Amsterdam, the Netherlands, 1969.

[29] U. Cicekli, G. Z. Voyiadjis, and R. K. Abu Al-Rub, "A plasticity and anisotropic damage model for plain concrete," *International Journal of Plasticity*, vol. 23, no. 10-11, pp. 1874–1900, 2007.

[30] R. K. Abu Al-Rub and G. Z. Voyiadjis, "Gradient-enhanced coupled plasticity-anisotropic damage model for concrete fracture: computational aspects and applications," *International Journal of Damage Mechanics*, vol. 18, no. 2, pp. 115–154, 2009.

[31] M. K. Darabi, R. K. Abu Al-Rub, E. A. Masad, C. W. Huang, and D. N. Little, "A thermo-viscoelastic-viscoplastic-viscodamage constitutive model for asphaltic materials," *International Journal of Solids and Structures*, vol. 48, no. 1, pp. 191–207, 2011.

Hindawi Publishing Corporation
Journal of Applied Mathematics
Volume 2013, Article ID 709430, 12 pages
http://dx.doi.org/10.1155/2013/709430

Research Article

Comparison between Duncan and Chang's EB Model and the Generalized Plasticity Model in the Analysis of a High Earth-Rockfill Dam

Weixin Dong, Liming Hu, Yu Zhen Yu, and He Lv

State Key Laboratory of Hydro-Science and Engineering, Department of Hydraulic Engineering, Tsinghua University, Beijing 100084, China

Correspondence should be addressed to Yu Zhen Yu; yuyuzhen@tsinghua.edu.cn

Received 4 June 2013; Revised 19 August 2013; Accepted 20 August 2013

Academic Editor: Fayun Liang

Nonlinear elastic model and elastoplastic model are two main kinds of constitutive models of soil, which are widely used in the numerical analyses of soil structure. In this study, Duncan and Chang's EB model and the generalized plasticity model proposed by Pastor, Zienkiewicz, and Chan was discussed and applied to describe the stress-strain relationship of rockfill materials. The two models were validated using the results of triaxial shear tests under different confining pressures. The comparisons between the fittings of models and test data showed that the modified generalized plasticity model is capable of simulating the mechanical behaviours of rockfill materials. The modified generalized plasticity model was implemented into a finite element code to carry out static analyses of a high earth-rockfill dam in China. Nonlinear elastic analyses were also performed with Duncan and Chang's EB model in the same program framework. The comparisons of FEM results and *in situ* monitoring data showed that the modified PZ-III model can give a better description of deformation of the earth-rockfill dam than Duncan and Chang's EB model.

1. Introduction

The constitutive model of soil is the keystone in the finite element analyses of geotechnical structures. A suitable constitutive model can simulate the stress-strain relationships of soils under static or dynamic conditions. Numerical analysis, especially for finite element method incorporated with soil constitutive models, has played a very important role in geotechnical analyses which always include complex boundary conditions, nonlinearity of material, and geometry [1].

Biot presented the famous three-dimensional consolidation theory based on the effective stress theory, equilibrium equation, and continuity condition [2]. However, it is quite difficult to give the theoretical solution of Biot's consolidation theory except for few simple problems. Up to the 1960s, with the rapid development of electronic computer and constitutive models of soils, Biot's consolidation theory was successfully implemented in finite element codes to study the behavior of geotechnical structures [3, 4]. So far, thousands of constitutive models have been proposed, which can be mainly grouped in two categories: nonlinear elastic models and elastoplastic models.

For nonlinear elastic model, the nonlinear characteristic of soil stress-strain relationship is considered by sectionalized linearization. A typical nonlinear elastic model is Duncan and Chang's Model [5, 6], which has been widely used in the numerical analyses of earth-rockfill dams, as the model parameters are quite easy to be determined from conventional triaxial tests. And, a lot of experience of application has been accumulated for this model. However, nonlinear elastic models also have some inherent limitations to represent the stress-strain characteristics of soils, such as shear-induced dilatancy and stress path dependency.

Elastoplastic models would be very adequate in describing many key features of soils. Classical elastoplastic models are based on the plastic incremental theory composed of yield condition, flow rule, and hardening law. In the 1950s, Drucker et al. (1957) [7] suggested a cap yield surface controlled by volumetric strain. Roscoe et al. [8, 9] proposed the concepts of critical state line and state boundary surface, and then they built the Original Cam Clay Model based on triaxial tests. Burland [10] suggested a different energy equation and then established the Modified Cam Clay Model. Since the establishment of Cam Clay Model, some other types of elastoplastic constitutive models have also achieved great development [11–18]. Among these models, the generalized plasticity model [16, 19, 20] can simulate the static and dynamic mechanical behaviors of clays and sands. This model is very flexible and convenient to extend, as the complicated yield or plastic potential surfaces need not to be specified explicitly. And the model has been used successfully in the static or dynamic analyses of some geotechnical structures [21–24]. Furthermore, based on the framework of generalized plasticity theory [16], some limitations of the original model have been solved [25–28], such as pressure dependency, densification under cyclic loading. The details of the generalized plasticity theory and the original and proposed modified Pastor-Zienkiewicz-Chan's models will be introduced in the sections below.

However, little experience has as yet been accumulated in applying the generalized plasticity model to the simulation of rockfill materials. And we know that rockfill material is quite different from sands in mechanical properties [29–31]. The rockfill material has large particle size and sharp edges and corners, which can result in remarkable particle breakage and change the shear-induced dilation [32, 33]. On the other hand, though the generalized plasticity model has gained great success in the modeling of soils, the application of this model in the large-scale finite element analyses of earth dams was less reported.

In this study, the original generalized plasticity model was modified to consider the stress-strain relationships of rockfill materials, as most of previous studies focused on sands and clays. Then, based on conventional triaxial test data, the model parameters for dam materials of the Nuozhadu high earth-rockfill dam in Southwest China are determined. Finally, the static simulation of this dam is carried out by using a finite element code incorporating with Duncan and Chang's EB model and the modified generalize plasticity model. The comparison of numerical results and *in situ* monitoring data illustrates the advantages of modified generalized plasticity model in the simulation of earth-rockfill dams.

2. Constitutive Model Descriptions

Two constitutive models of soils were used in the finite element analyses. One is the Duncan and Chang's EB model belonging to nonlinear elastic model, the other one is the generalized plasticity model.

2.1. Duncan and Chang's Model. Duncan and Chang's model [5] is a nonlinear elastic model, which has been widely used in the geotechnical engineering, especially in the numerical analyses of earth dams. It is attributed to Kondner [34] who proposed the hyperbolic stress-strain function below to describe the deviatoric stress-axial strain curve obtained from triaxial tests.

Consider

$$\sigma_1 - \sigma_3 = \frac{\varepsilon_1}{a + b\varepsilon_1}, \tag{1}$$

in which a and b are model constants.

In this constitutive model, the tangential Young's modulus E_t and tangential bulk modulus B_t are used to simulate the nonlinear elastic response of soils, which are assumed to be

$$\begin{gathered} E_t = KP_a\left(\frac{\sigma_3}{P_a}\right)^n \left(1 - R_f S_l\right)^2, \\ B_t = K_b P_a\left(\frac{\sigma_3}{P_a}\right)^m, \end{gathered} \tag{2}$$

where P_a is the atmospheric pressure, K and K_b are modulus numbers, n and m are exponents determining the rate of variation of moduli with confining pressure, and R_f is the failure ratio with a invariable value less than 1.

The Mohr-Coulomb failure criterion is adopted in the model, and S_l is a factor defined as shear stress level given by

$$S_l = \frac{(1 - \sin\phi)(\sigma_1 - \sigma_3)}{2c \cdot \cos\phi + 2\sigma_3 \cdot \sin\phi}. \tag{3}$$

In the unloading and reloading stage, the tangential Young's modulus is defined as

$$E_{ur} = K_{ur} P_a \left(\frac{\sigma_3}{P_a}\right)^n. \tag{4}$$

So far, the model has 8 parameters, c, φ, K, K_{ur}, n, R_f, K_b, m. These parameters can be determined with a set of conventional triaxial tests.

In general, a curved Mohr-Coulomb failure envelop is adopted by setting $c = 0$ and letting φ vary with confining pressure according to

$$\varphi = \varphi_0 - \Delta\varphi \log\left(\frac{\sigma_3}{P_a}\right). \tag{5}$$

Then parameters c and φ are replaced by φ_0 and $\Delta\varphi$.

Although Duncan and Chang's EB constitutive model is quite simple, it has gained significant success in geotechnical engineering. On one hand, it is easy to obtain the model parameters; on the other hand, much experience has been accumulated. Nevertheless, it cannot incorporate dilatancy which has an important influence in the mechanical behavior of soils. And furthermore, it can only consider unloading process in a crude way.

2.2. Generalized Plasticity Theory and Its Original Constitutive Model

2.2.1. Basic Theory. The generalized plasticity theory was proposed by Zienkiewicz and Mroz (1984) [16] to model the behaviors of sand under monotonic and cyclic loading. The key futures of this theory are that neither yield surface nor plastic potential surface needs to be defined explicitly, and consistency law is not required to determine plastic modulus. In the theory, the total strain increment is divided into elastic and plastic components.

Consider

$$d\varepsilon = d\varepsilon^{e} + d\varepsilon^{p}, \tag{6}$$

where $d\varepsilon^{e}$ and $d\varepsilon^{p}$ = elastic and plastic strain increments, respectively.

The relationship between strain and stress increments is expressed as

$$d\sigma = \mathbf{D}^{ep} : d\varepsilon, \tag{7}$$

where $\mathbf{D}^{ep}$ is the elastoplastic stiffness tensor given as

$$\mathbf{D}^{ep} = \mathbf{D}^{e} - \frac{\mathbf{D}^{e} : \mathbf{n}_{gL/U} : \mathbf{n}^{T} : \mathbf{D}^{e}}{H_{L/U} + \mathbf{n}^{T} : \mathbf{D}^{e} : \mathbf{n}_{gL/U}}, \tag{8}$$

where $\mathbf{D}^{e}$, $\mathbf{n}_{gL/U}$, $\mathbf{n}$, and $H_{L/U}$ are elastic stiffness tensor, plastic flow direction vector, loading direction vector, and plastic modulus under loading or unloading conditions, respectively.

The loading direction vector $\mathbf{n}$ is used to judge the loading and unloading conditions:

$$\begin{gathered} d\sigma_{e}^{T} \cdot \mathbf{n} > 0 \quad \text{loading}, \\ d\sigma_{e}^{T} \cdot \mathbf{n} = 0 \quad \text{neutral loading}, \\ d\sigma_{e}^{T} \cdot \mathbf{n} < 0 \quad \text{unloading}. \end{gathered} \tag{9}$$

Then, the elastoplastic stiffness tensor $\mathbf{D}^{ep}$ can be obtained corresponding to the loading and unloading conditions.

In the framework of generalized plasticity theory, all the components of the elastoplastic constitutive matrix are determined by the current state of stress and loading/unloading condition.

2.2.2. Pastor-Zienkiewicz-Chan Model. This model was presented by Pastor et al. [19]. The relationships between elastic volumetric and shear strain increments and stress increments are defined as

$$dp' = K_{ev} d\varepsilon_{v}^{e}, \qquad dq = 3G_{es} d\varepsilon_{s}^{e}, \tag{10}$$

where K_{ev}, G_{es} are tangential bulk and shear moduli, respectively, and they are assumed to be

$$K_{ev} = K_{eso}\frac{p'}{p_o}, \qquad G_{es} = G_{eso}\frac{p'}{p_o}, \tag{11}$$

where K_{eso}, G_{eso}, and p_o are model parameters.

In order to determine the plastic stiffness tensor, variables $\mathbf{n}_{gL/U}$, $\mathbf{n}$, and $H_{L/U}$ need to be defined. $\mathbf{n}_{gL/U}$ and $\mathbf{n}$ are expressed as follows:

$$\begin{gathered} \mathbf{n}_{gL} = \left(\frac{d_g}{\sqrt{1+d_g^2}}, \frac{1}{\sqrt{1+d_g^2}} \right)^{T}, \\ \mathbf{n} = \left(\frac{d_f}{\sqrt{1+d_f^2}}, \frac{1}{\sqrt{1+d_f^2}} \right)^{T}. \end{gathered} \tag{12}$$

The dilatancy d_g and stress ratio $\eta = q/p$ are related as follows:

$$d_g = \frac{d\varepsilon_v^p}{d\varepsilon_s^p} = \left(1+\alpha_g\right)\left(M_g - \eta\right). \tag{13}$$

And d_f has a similar expression as

$$d_f = \left(1+\alpha_f\right)\left(M_f - \eta\right), \tag{14}$$

where α_f, α_g are model parameters and M_g/M_f is equal to relative density. If $d_f = d_g$, associated flow rule is used, otherwise nonassociated flow rule is used.

In the case of unloading, the unloading plastic flow direction vector $\mathbf{n}_{gU}$ is defined as

$$\mathbf{n}_{gU} = \left(-\left| \frac{d_g}{\sqrt{1+d_g^2}} \right|, \frac{1}{\sqrt{1+d_g^2}} \right)^{T}. \tag{15}$$

The loading plastic modulus H_L is proposed as

$$H_L = H_0 p' H_f \left(H_v + H_s\right) H_{DM}, \tag{16}$$

where $H_f = (1-\eta/\eta_f)^4$ limits the possible state and $\eta_f = (1+1/\alpha_f)M_f$, $H_v = 1-\eta/M_g$ accounts for phase transformation; $H_s = \beta_0\beta_1 \exp(-\beta_0\xi)$ considers soil degradation and ξ is the accumulated plastic shear strain; $H_{DM} = (\varsigma_{\mathrm{MAX}}/\varsigma)^{\gamma}$ accounts for past history and $\varsigma = p[1-\alpha_f\eta/(1+\alpha_f)/M_f]_f^{(-1/\alpha)}$ which is the mobilized stress function; and H_0, β_0, β_1, γ are model parameters.

Under unloading condition, the plastic modulus is defined as

$$\begin{gathered} H_U = H_{u0}\left(\frac{M_g}{\eta_u}\right)^{\gamma_u}, \quad \frac{M_g}{\eta} > 1, \\ H_U = H_{u0}, \quad \frac{M_g}{\eta} \leq 1, \end{gathered} \tag{17}$$

respectively, where H_{u0}, γ_u are model parameters and η_u is the stress ratio from which unloading takes place.

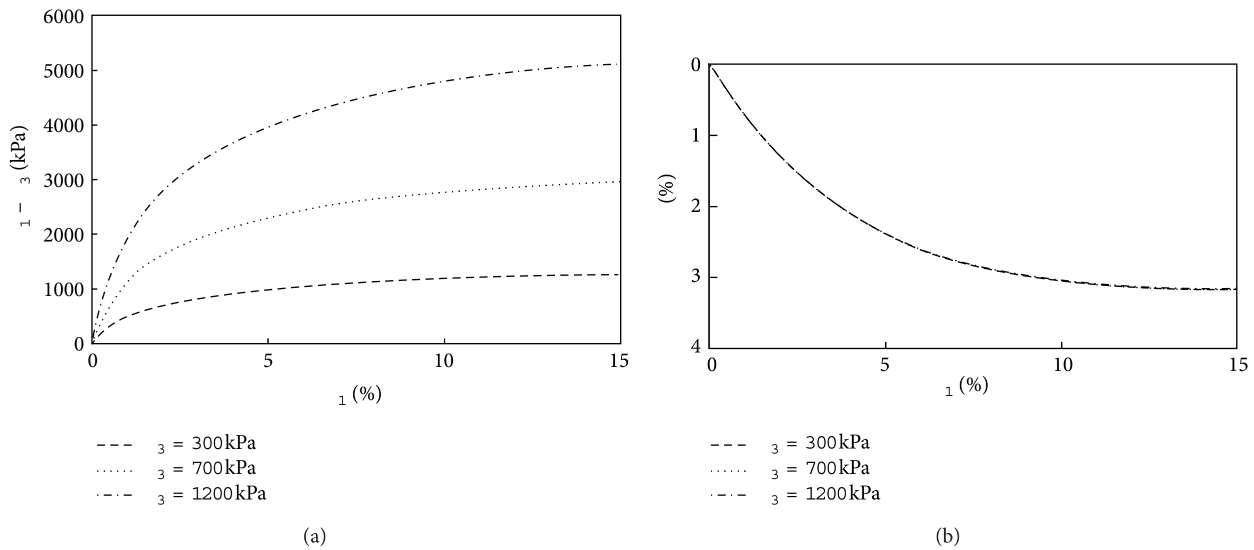

Figure 1: Simulation of stress-strain relationships for Original PZ-III model.

2.2.3. Modified Model. The Pastor-Zienkiewicz-Chan model (PZ-III for short) has gained considerable success in describing the behavior of sands and clays under monotonic and cyclic loadings. But it still has some shortcomings to predict the static or dynamic responds of sands, especially for rockfill materials which are widely used in earth-rockfill dams. The Original PZ-III model has serious limitation in reflecting pressure dependency of soils.

Figure 1 shows the stress-strain relationships of a rockfill material under drained conventional triaxial tests using a set of parameters under different confining pressures, but PZ-III model gives the same ε_1-ε_v curve, where ε_1, ε_v are axial strain and volumetric strain, respectively. As confining pressure ranges from 0 kPa to several MPa for a rockfill dam with height of 200–300 m, the original PZ-III model cannot be used to describe the mechanical behavior of rockfill dams.

Some relations of the original model are modified to take into account the influence of confining pressure as

$$K_{ev} = K_{e0} p_a \left(\frac{p'}{p_a}\right)^m, \qquad G_{es} = G_{e0} p_a \left(\frac{p'}{p_a}\right)^n,$$
$$H_L = H_0 p_a \left(\frac{p'}{p_a}\right)^m H_f \left(H_v + H_s\right) H_{DM}, \tag{18}$$

where K_{e0} and G_{e0} are elastic constants, m and n are model parameters to consider the effect of pressure dependency.

As sand behavior is dependent on densities or void ratio, a state pressure index, I_p, proposed by Wang et al. [35] was introduced in the PZ-III model and (13) was modified as

$$d_g = \frac{d\varepsilon_v^p}{d\varepsilon_s^p} = \left(1 + \alpha_g\right)\left(M_g {I_p}^{m_p} - \eta\right), \tag{19}$$

where m_p is a model parameter and $I_p = p/p_c$ in which p_c is the mean pressure at critical state. The critical state line is given by

$$e_c = \Gamma - \lambda \log\left(p_c\right). \tag{20}$$

3. Nuozhadu Hydropower Project

Nuozhadu hydropower project is located in the Lancang River which is also named Mekong River in the downstream in Yunnan Province, Southwest China, as shown in Figure 2(a). The installed capacity of the powerstation is 5850 MW. The most important part of Nuozhadu hydropower project is the high earth-rockfill dam with a maximum height of 261.5 m, which is the highest one with the same type in China and the fourth highest in the world. The reservoir has a storage capacity of $237.0 \times 10^8\ \mathrm{m}^3$, with the normal storage water level of 812.5 m and dead water level of 765 m.

Figure 3 shows the material zoning and construction stages of the maximum cross-section. The elevation of the earth core bottom and the crest of the dam are 562.6 m and 824.1 m, respectively. The dam crest has a longitudinal length of 630 m with a width of 18 m. The upstream and downstream slopes are at 1.9 : 1 and 1.8 : 1, respectively. The dam body is composed of several different types of materials. The shells of upstream and downstream are composed of decomposed rock materials. Anti-seepage material in the earth core is clay mixed with gravel. Adding gravel to the clay can improve the strength of clay and reduce the arching effect between shells and earth core. The gravel material consists of fresh crushed stone of breccia and granite with a maximum diameter of 150 mm. In addition to these, the fine rockfill and filter materials are filled against the earth core to prevent the fine particle from being washed away.

The dam construction was started in 2008 and was completed at the end of 2012. Figure 2(c) shows the dam

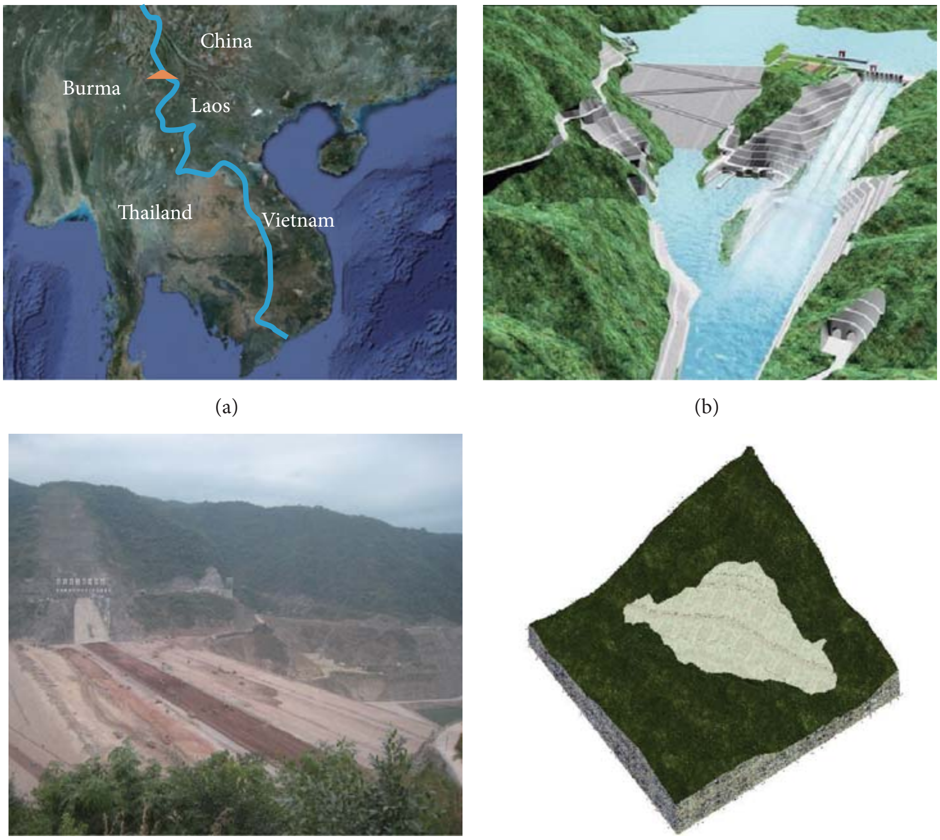

(a) (b) (c) (d)

Figure 2: Nuozhadu dam. (a) Nuozhadu dam location, (b) project blueprint, (c) Nuozhadu dam under construction, and (d) dam site geomorphology.

under construction. Figure 3(b) demonstrates the practical construction process.

4. Experimental Validation of Model Parameters

The modified PZ-III model was implemented in a finite element code which has been successfully used to analyze earth dams with Duncan and Chang's EB model and some other constitutive models. A set of triaxial test data was used to make sure that the model has been incorporated into the FEM code accurately.

The proposed generalized plasticity model totally needs 17 parameters. The model parameters used in the computation of the earth-rockfill dam were obtained by fitting the triaxial test results. Drained triaxial tests under different confining pressures were conducted to test the rockfill materials and mixed gravel clay, which are the main parts of the dam body.

Duncan and Chang's EB model parameters are shown in Table 1 and the modified PZ-III model parameters in Table 2. As shown in Figures 4, 5, 6, 7, 8, and 9, the modified PZ-III model presents a better ability to simulate the mechanics behavior of rockfill materials and mixed gravel clay, especially for dilatancy. With the reduction of confining pressure, the rockfill materials tend to dilate as the experimental volumetric strain curve shows. Especially for the rockfill materials under low confining pressure, negative volumetric strain rapidly develops after a short stage of volumetric contraction. Due to the intrinsic limitation, Duncan and Chang's EB model cannot simulate the dilatancy which is a crucial feature of rockfill materials.

Table 1: Material parameters of Duncan and Chang's EB model.

Material	Rockfill I	Rockfill II	Mixed gravel clay
$\varphi/^{\circ}$	55.82	54.33	39.30
$\Delta\varphi/^{\circ}$	12.29	12.07	9.80
R_f	0.73	0.74	0.77
K	1450	1360	520
K_b	550	600	250
K_{ur}	2800	2500	900
n	0.30	0.43	0.42
m	0.13	0.08	0.25

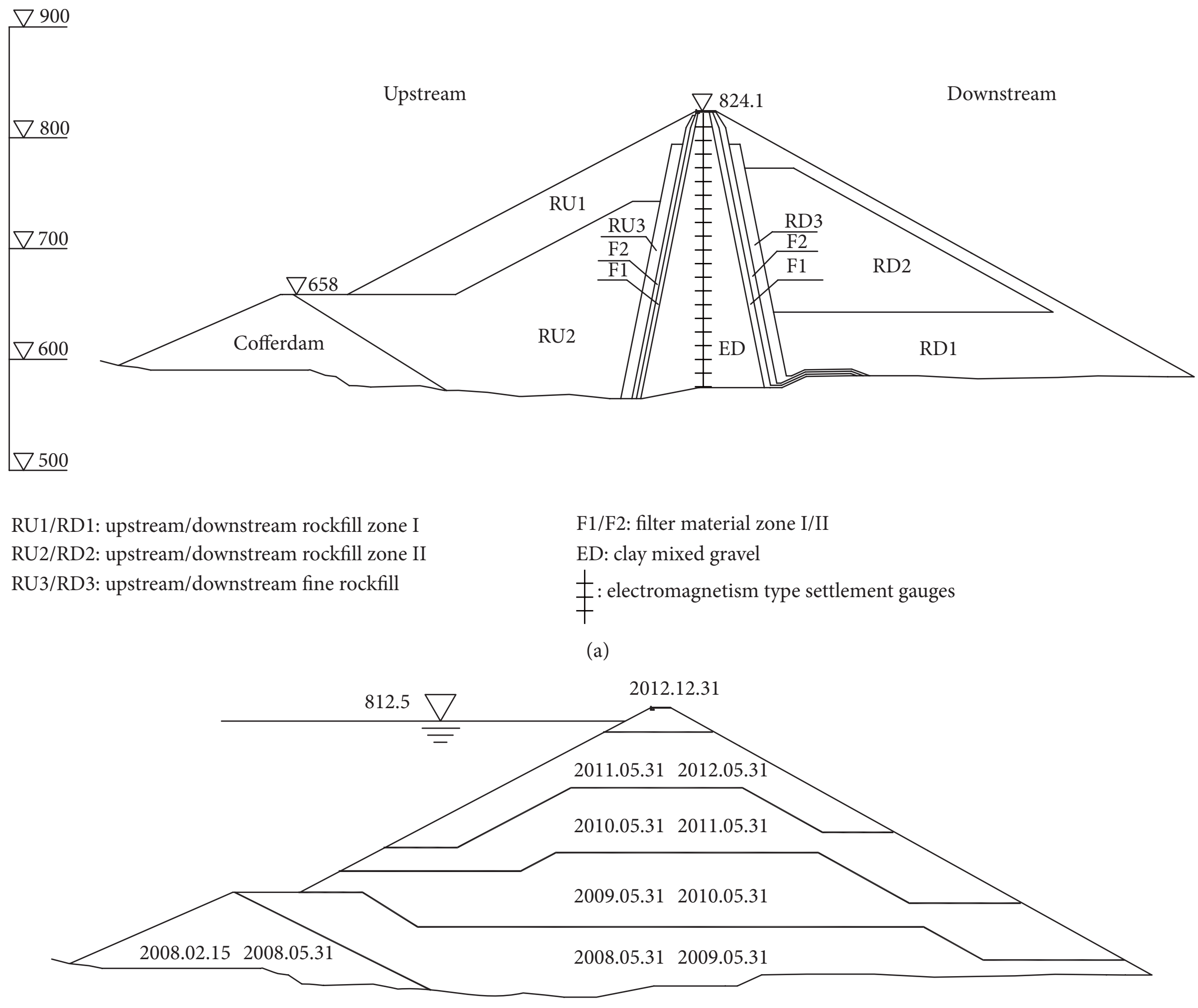

Figure 3: The maximum cross-section. (a) Material zoning and (b) construction stage.

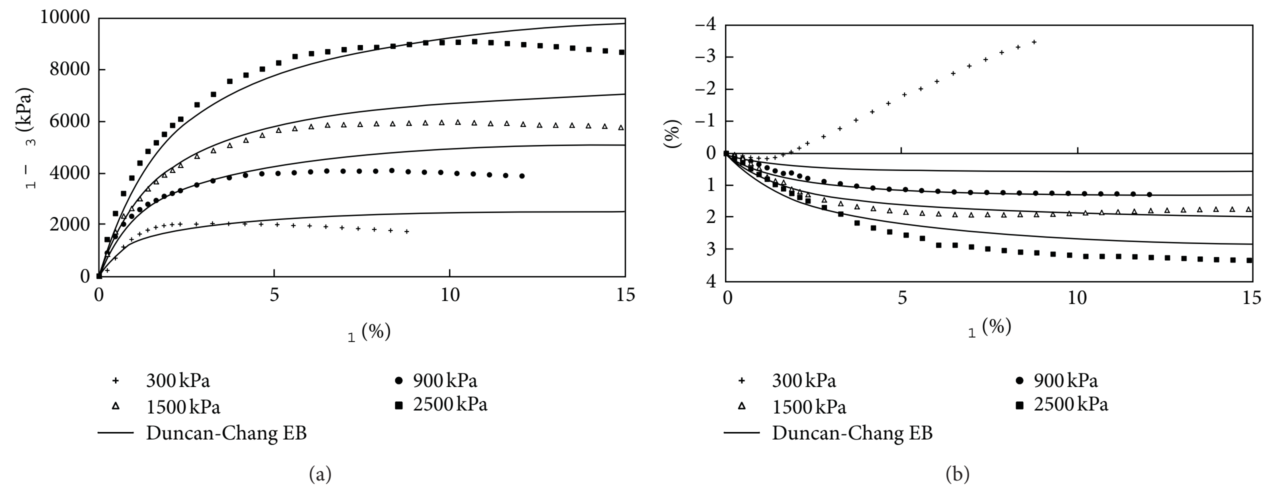

Figure 4: Comparison between fittings of Duncan and Chang's EB model and experimental triaxial tests results for rockfill material I.

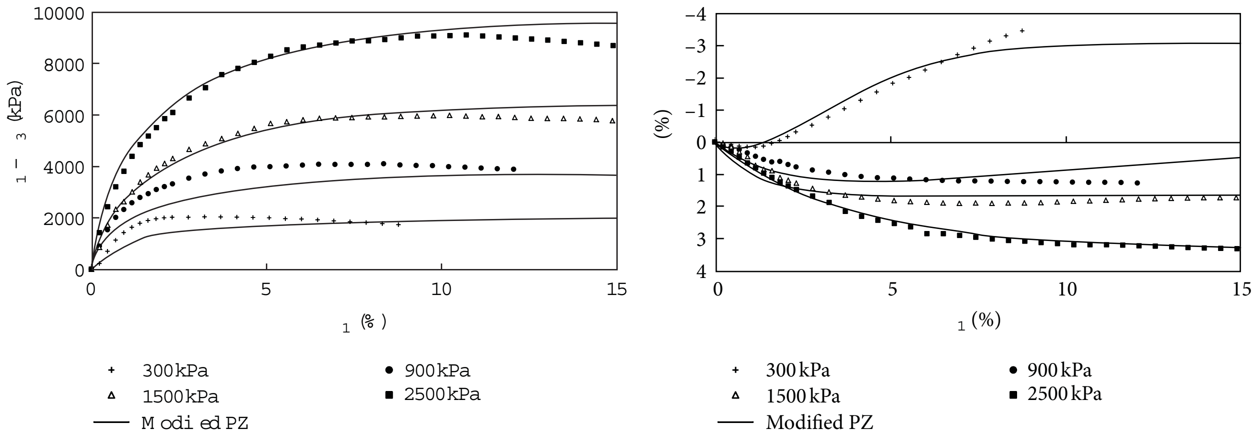

(a) (b)

Figure 5: Comparison between fittings of the modified PZ-III model and experimental triaxial tests results for rockfill material I.

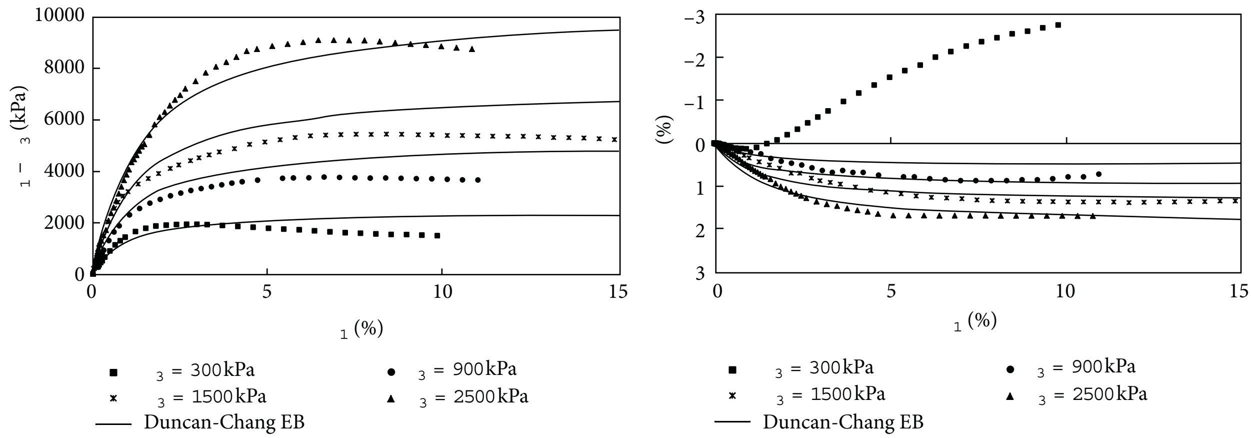

(a) (b)

Figure 6: Comparison between fittings of Duncan and Chang's EB model and experimental triaxial tests results for rockfill material II.

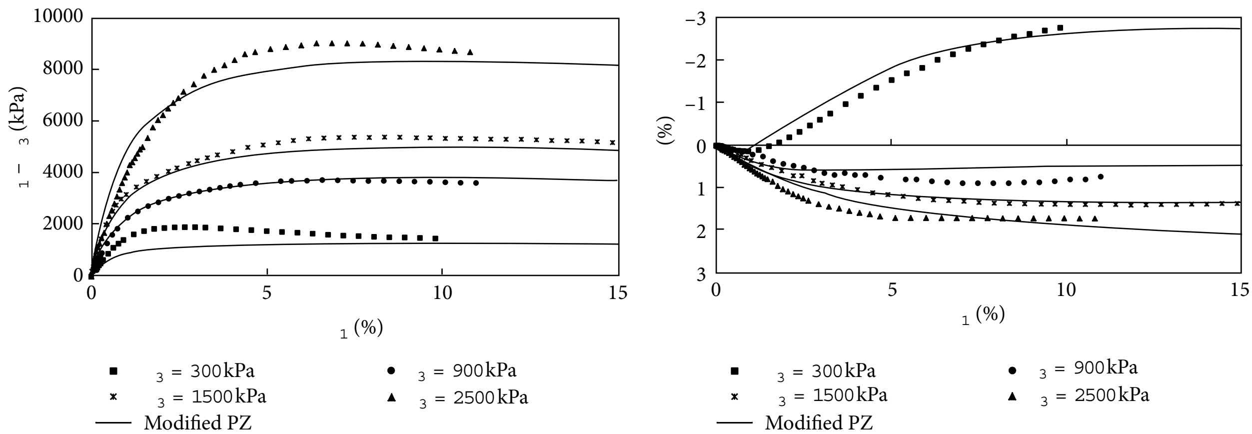

(a) (b)

Figure 7: Comparison between fittings of the modified PZ-III model and experimental triaxial tests results for rockfill material II.

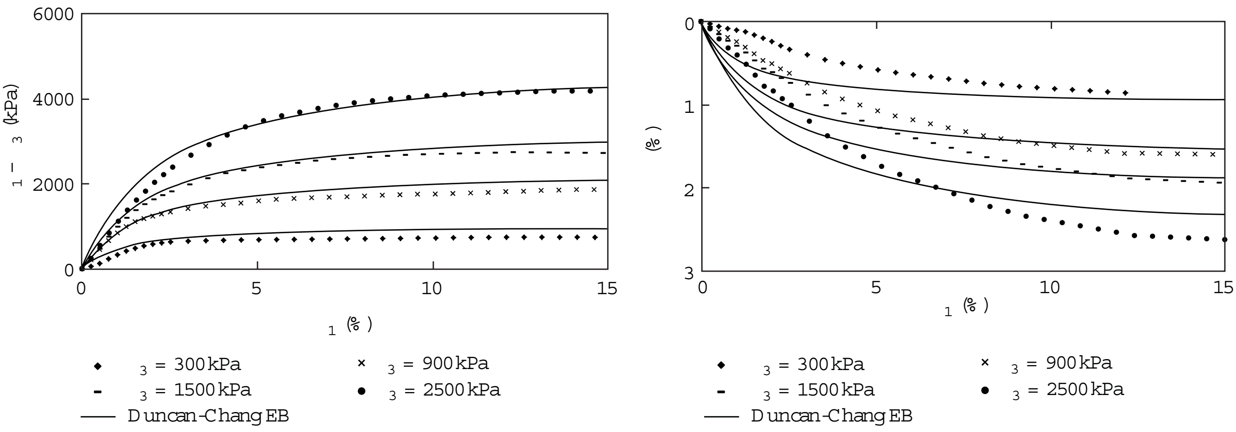

(a) (b)

Figure 8: Comparison between fittings of Duncan and Chang's EB model and experimental triaxial tests results for clay.

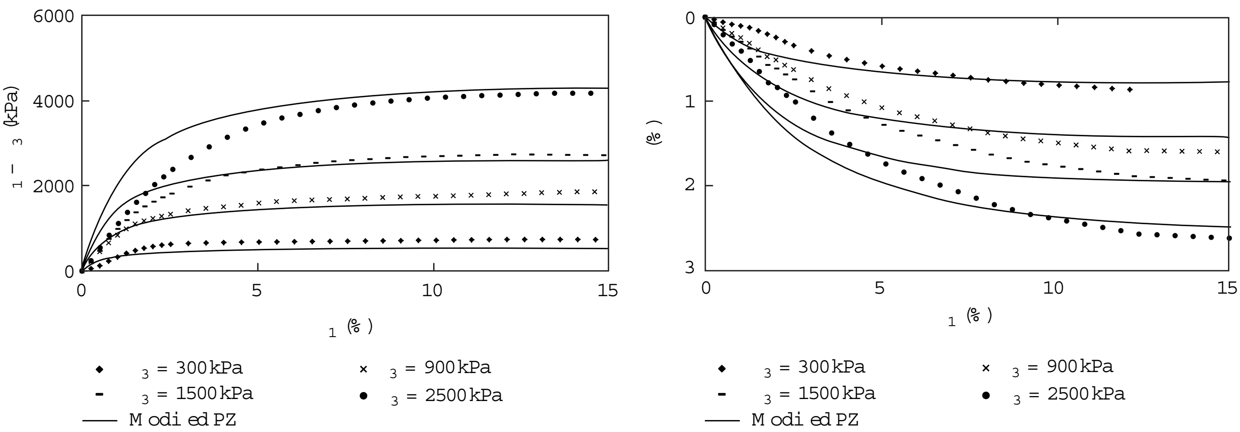

(a) (b)

Figure 9: Comparison between fittings of the modified PZ-III model and experimental triaxial tests results for clay.

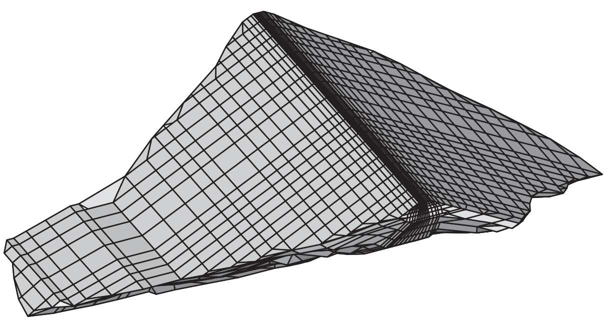

Figure 10: 3D FEM mesh of Nuozhadu dam.

5. Three-Dimensional Finite Element Analyses

5.1. Computation Model. The numerical analyses were performed to simulate the performance of the dam during construction and impounding periods with effective stress finite element analysis.

First, the 2D finite element mesh of the maximum cross-section of the dam was discretized according to the material zoning and construction design (see Figure 3). Then, the 2D mesh was extended to 3D mesh in accordance with contour line of the river valley. Figure 10 shows the 3D mesh of the Nuozhadu dam with 8095 brick and degenerated brick elements and 8340 nodes.

The numerical simulations contain two stages, filling and impounding. During the filling stage, the dam body mainly subjects to body weight. Then, at the end of construction, upstream water level goes up to the normal storage water level. The interaction between pore water and soil skeleton was considered through the whole numerical computation.

5.2. Results and Analyses

5.2.1. Numerical Results Analyses. Figures 11 and 12 show the numerical results of finite element analyses with Duncan and Chang's EB model and the modified PZ-III model, respectively.

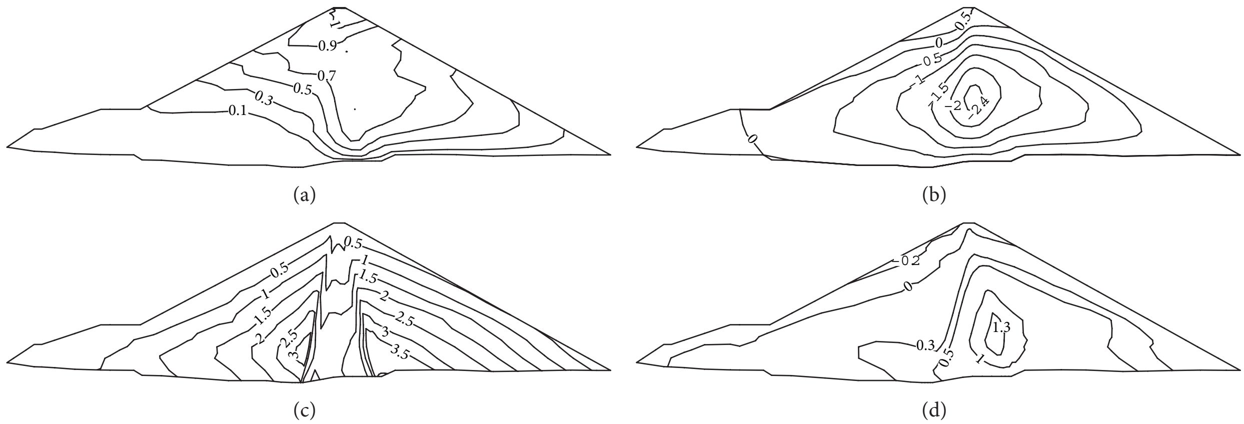

Figure 11: Displacement and stress contour of the maximum section for Duncan and Chang's EB model: (a) displacement along river (m), (b) vertical displacement (m), (c) major principle stress (MPa), and (d) minor principle stress (MPa).

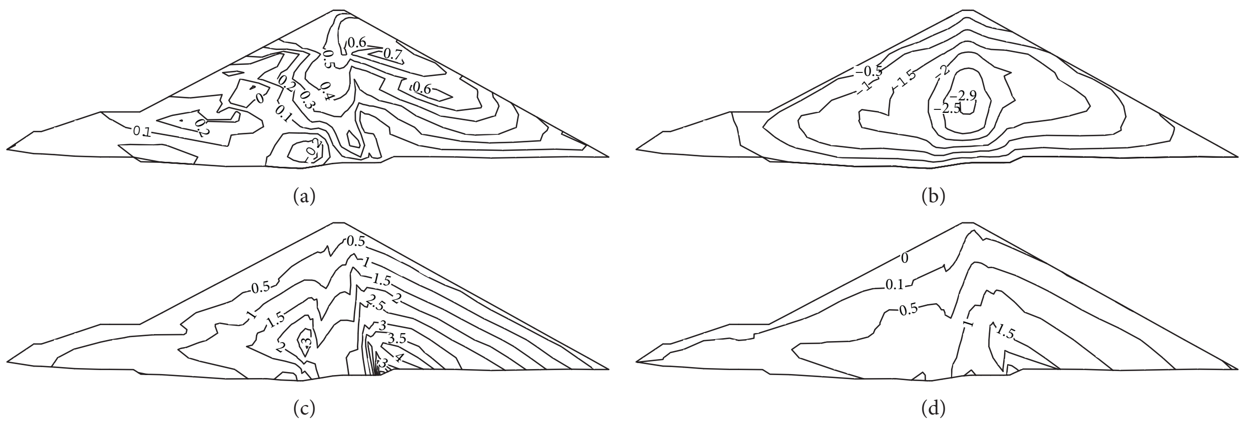

Figure 12: Displacement and stress contour of the maximum section for the modified PZ-III model: (a) displacement along river (m), (b) vertical displacement (m), (c) major principle stress (MPa), and (d) minor principle stress (MPa).

Through the comparison and analysis of the numerical results (Figures 11 and 12), we can find some similarities and differences for these two models.

On one hand, we can see many similar places in the distributions of displacements and stresses.

(1) After the reservoir impounding, due to the huge water pressure on upstream dam, horizontal displacement develops toward the downstream, and the largest displacement is about 1.05 m for EB model and 0.74 m for modified PZ-III model.

(2) The maximum settlement occurs in the middle of core wall due to lower modulus of clayey soil.

(3) Because of the tremendous differences of modulus between rockfill material and clayey soil, there exists obvious arching effect in the core wall.

(4) Effective stress in upstream shell is less than the downstream shell due to the water pressure in the upstream shell.

On the other hand, some differences also exist, which illustrate the advantages of modified PZ-III model.

(1) After the reservoir is impounded, upward displacement as large as 0.7 m (see Figure 11(b)) develops on the upstream shell near dam crest for EB model and nearly 0 m for modified PZ-III model (see Figure 12(b)). In fact, monitoring data of practical engineering projects shows that no large upward displacement happened after impounding. This is due to its weakness of EB model to distinguish the loading and unloading condition during the water impounding.

(2) In the distribution of minor principle stress (Figures 11(d) and 12(d)), negative stress (i.e., tensile stress) occurs in the upstream shell for EB model, whereas very little tensile stress exists for modified PZ-III model. As we know, rockfill material is a typical kind of cohesionless coarse-grained soil, which means that it has no tensile strength. Therefore, the existence of large area of tensile stress in the upstream shell is unreasonable.

5.2.2. Comparison between Numerical and In Situ Monitoring Data. Settlement is a key indicator to assess the safety of an

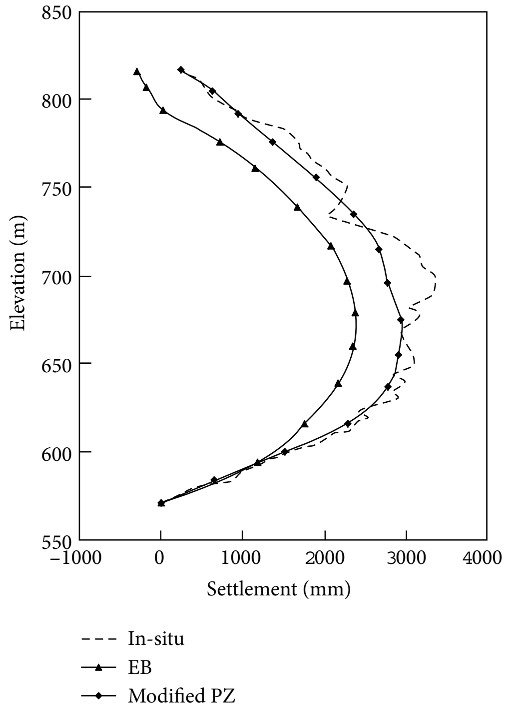

Figure 13: Comparison between *in situ* monitoring settlement and FEM results.

Table 2: Material parameters of the modified PZ-III model.

Material	Rockfill I	Rockfill II	Mixed gravel clay
K_0	500	1000	300
G_0	1500	3000	900
m	0.50	0.50	0.50
n	0.50	0.50	0.50
α_f	0.45	0.45	0.45
α_g	0.45	0.45	0.45
M_{fc}	1.05	0.90	0.60
M_{gc}	1.60	1.35	1.10
β_0	0.00	0.00	0.00
β_1	0.00	0.00	0.00
Γ	0.34	0.31	0.34
λ	0.10	0.09	0.03
m_p	0.35	0.40	0.0
H_0	800	1200	900
γ	5	5	5
γ_u	5	5	5
H_{u0}/MPa	9	9	10

earth dam. Figures 13 and 14 show the *in situ* monitoring data and FEM results of settlement in the maximum cross-section. The *in situ* data were obtained from electromagnetism type settlement gauges which were embedded during construction in the dam (as shown in Figure 3(a)). Through the comparisons of *in situ* monitoring and numerical results, we can see that the modified PZ-III model gave a better prediction than the EB model. However, as deformation induced by wetting

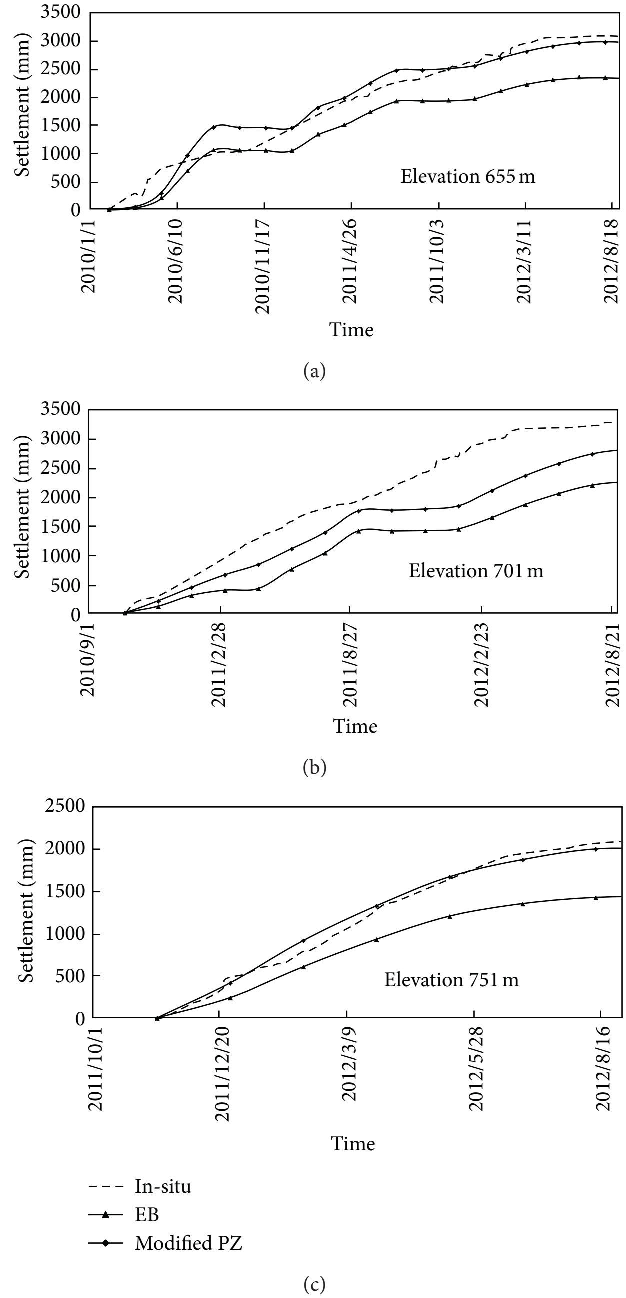

Figure 14: Comparison between *in situ* monitoring settlement and FEM results.

of rockfill materials was not considered, the FEM result of settlement was below than the *in situ* monitoring data.

As an elastoplastic model, the PZ-III model is capable of representing the mechanical behavior of soils better than nonlinear elastic model such as Duncan and Chang's EB model. And the above finite element analyses also proved it.

6. Conclusions

This paper presents a modified PZ-III model based on the generalized theory and original Pastor-Zienkiewicz-Chan model to simulate the stress-strain relationship of rockfill materials.

Triaxial test results of the filling materials of Nuozhadu dam were used to validate the proposed model and determine the model parameters of Duncan and Chang's EB model and the modified PZ-III model, respectively. The simulations of triaxial stress-strain response show that the modified PZ-III model is capable of representing the key features of cohesionless soil, such as nonlinearity, dilatancy, and pressure dependency.

The proposed model has been incorporated into a finite element code to simulate the static response of a high earth-rockfill dam in China. The results were compared with those of Duncan and Chang's EB model. The two set of results have both similarities and differences and the differences illustrate the advantages of the modified PZ-III model. The comparisons of FEM results, and *in situ* monitoring data showed that the modified PZ-III model can give a better description of deformation of the earth-rockfill dam than Duncan and Chang's EB model.

Acknowledgments

This work was supported by the National Nature Science Foundation of China (51179092) and the State Key Laboratory of Hydroscience and Engineering Project (2012-KY-02 and 2013-KY-4).

References

[1] J. M. Duncan, "State of the art: limit equilibrium and finite-element analysis of slopes," *Journal of Geotechnical and Geoenvironmental Engineering*, vol. 122, no. 7, pp. 577–596, 1996.

[2] M. A. Biot, "General theory of three-dimensional consolidation," *Journal of Applied Physics*, vol. 12, no. 2, pp. 155–164, 1941.

[3] R. S. Sandhu and E. L. Wilson, "Finite element analysis of seepage in elastic media," *Journal of the Engineering Mechanics Division*, vol. 95, no. 3, pp. 641–652, 1969.

[4] J. T. Christian and J. W. Boehmer, "Plane strain consolidation by finite elements," *Journal of Soil Mechanics & Foundations Division*, vol. 96, no. 4, pp. 1435–1457, 1970.

[5] J. M. Duncan and C.-Y. Chang, "Nonlinear analysis of stress and strain in soils," *Journal of the Soil Mechanics and Foundations Division*, vol. 96, no. 5, pp. 1629–1653, 1970.

[6] J. M. Duncan, P. M. Byrne, K. S. Wong, and P. Mabry, "Strength, stress-strain and bulk modulus parameters for finite element analyses of stresses and movements in soil masses," Tech. Rep. UCB/GT/80-01, University of California, Berkeley, Calif, USA, 1980.

[7] D. C. Drucker, R. E. Gibson, and D. J. Henkel, "Soil mechanics and work-hardening theories of plasticity," *Transactions of the American Society of Civil Engineers*, vol. 122, pp. 338–346, 1957.

[8] K. Roscoe, A. Schofield, and C. Wroth, "On the yielding of soils," *Geotechnique*, vol. 8, no. 1, pp. 22–53, 1958.

[9] K. Roscoe, A. Schofield, and A. Thurairajah, "Yielding of clays in states wetter than critical," *Geotechnique*, vol. 13, no. 3, pp. 211–240, 1963.

[10] J. Burland, "Correspondence on 'The yielding and dilation of clay'," *Geotechnique*, vol. 15, pp. 211–214, 1965.

[11] P. V. Lade and J. M. Duncan, "Elastoplastic stress-strain theory for cohesionless soil," *Journal of the Geotechnical Engineering Division*, vol. 101, no. 10, pp. 1037–1053, 1975.

[12] I. S. Sandler, F. L. DiMaggio, and G. Y. Baladi, "Generalized cap model for geological materials," *Journal of the Geotechnical Engineering Division*, vol. 102, no. 7, pp. 683–699, 1976.

[13] X.-S. Li, Y. F. Dafalias, and Z.-L. Wang, "State-dependent dilatancy in critical-state constitutive modelling of sand," *Canadian Geotechnical Journal*, vol. 36, no. 4, pp. 599–611, 1999.

[14] Y.-P. Yao and D. Sun, "Application of Lade's criterion to Cam-clay model," *Journal of Engineering Mechanics*, vol. 126, no. 1, pp. 112–119, 2000.

[15] G. Y. Baladi and B. Rohani, "Elastic-plastic model for saturated sand," *Journal of the Geotechnical Engineering Division*, vol. 105, no. 4, pp. 465–480, 1979.

[16] O. Zienkiewicz and Z. Mroz, "Generalized plasticity formulation and applications to geomechanics," in *Mechanics of Engineering Materials*, C. S. Desai and R. H. Gallagher, Eds., pp. 655–679, John Wiley & Sons, New York, NY, USA, 1984.

[17] C. S. Desai and M. O. Faruque, "Constitutive model for geological materials," *Journal of Engineering Mechanics*, vol. 110, no. 9, pp. 1391–1408, 1984.

[18] S. B. R. Murthy, A. Vatsala, and T. S. Nagaraj, "Revised Cam-clay model," *Journal of Geotechnical Engineering*, vol. 117, no. 6, pp. 851–871, 1991.

[19] M. Pastor, O. C. Zienkiewicz, and A. H. C. Chan, "Generalized plasticity and the modelling of soil behaviour," *International Journal for Numerical & Analytical Methods in Geomechanics*, vol. 14, no. 3, pp. 151–190, 1990.

[20] Z. Mroz and O. Zienkiewicz, "Uniform formulation of constitutive equations for clays and sands," in *Mechanics of Engineering Materials*, C. S. Desai and R. H. Gallangher, Eds., pp. 415–449, John Wiley & Sons, New York, NY, USA, 1984.

[21] G. Wang and J.-M. Zhang, "Dynamic consolidation finite element analysis of a sediment-protecting dyke under ocean wave loading," *Rock and Soil Mechanics*, vol. 27, no. 4, pp. 555–560, 2006.

[22] M. Alyami, M. Rouainia, and S. M. Wilkinson, "Numerical analysis of deformation behaviour of quay walls under earthquake loading," *Soil Dynamics and Earthquake Engineering*, vol. 29, no. 3, pp. 525–536, 2009.

[23] H. Li, P. Manuel, and T. Li, "Application of an generalized plasticity model to ultra-high rockfill dam," in *Proceedings of the 12th International Conference on Engineering, Science, Construction, and Operations in Challenging Environments—Earth and Space*, pp. 385–398, Honolulu, Hawaii, USA, March 2010.

[24] T. Li and H. Zhang, "Dynamic parameter verification of P-Z model and its application of dynamic analysis on rockfill dam," in *Proceedings of the 12th International Conference on Engineering, Science, Construction, and Operations in Challenging Environments—Earth and Space*, pp. 2706–2713, Honolulu, Hawaii, USA, March 2010.

[25] M. Pastor, "A generalized plasticity model for anisotropic behaviour of sand," *Computer Methods and Advances in Geomechanics*, vol. 1, pp. 661–668, 1991.

[26] G. Bolzon, B. A. Schrefler, and O. C. Zienkiewicz, "Elastoplastic soil constitutive laws generalized to partially saturated states," *Geotechnique*, vol. 46, no. 2, pp. 279–289, 1996.

[27] H. I. Ling and H. Liu, "Pressure-level dependency and densification behavior of sand through generalized plasticity model,"

Journal of Engineering Mechanics, vol. 129, no. 8, pp. 851–860, 2003.

[28] H. I. Ling and S. Yang, "Unified sand model based on the critical state and generalized plasticity," *Journal of Engineering Mechanics*, vol. 132, no. 12, pp. 1380–1391, 2006.

[29] N. D. Marschi, C. K. Chan, and H. B. Seed, "Evaluation of properties of rockfill materials," *Journal of the Soil Mechanics and Foundations Division*, vol. 98, no. 1, pp. 95–114, 1972.

[30] R. J. Marsal, "Large scale testing of rockfill materials," *Journal of the Soil Mechanics and Foundations Division*, vol. 93, no. 2, pp. 27–43, 1967.

[31] R. J. Marsal, "Mechanical properties of rockfill," in *Embankment Dam Engineering*, pp. 109–200, John Wiley & Sons, New York, NY, USA, 1973.

[32] P. V. Lade, J. A. Yamamuro, and P. A. Bopp, "Significance of particle crushing in granular materials," *Journal of Geotechnical and Geoenvironmental Engineering*, vol. 122, no. 4, pp. 309–316, 1996.

[33] B. O. Hardin, "Crushing of soil particles," *Journal of Geotechnical Engineering*, vol. 111, no. 10, pp. 1177–1192, 1985.

[34] R. L. Kondner, "Hyperbolic stress-strain response: cohesive soils," *Journal of the Soil Mechanics and Foundations Division*, vol. 89, no. 1, pp. 115–143, 1963.

[35] Z.-L. Wang, Y. F. Dafalias, X.-S. Li, and F. I. Makdisi, "State pressure index for modeling sand behavior," *Journal of Geotechnical and Geoenvironmental Engineering*, vol. 128, no. 6, pp. 511–519, 2002.

Hindawi Publishing Corporation
Journal of Applied Mathematics
Volume 2013, Article ID 136132, 10 pages
http://dx.doi.org/10.1155/2013/136132

Research Article

Extended "Mononobe-Okabe" Method for Seismic Design of Retaining Walls

Mahmoud Yazdani,[1] Ali Azad,[1] Abol hasan Farshi,[1,2] and Siamak Talatahari[3]

[1] *Department of Civil and Environmental Engineering, Tarbiat Modares University, Tehran 1411713116, Iran*
[2] *Civil Engineering Faculty, Islamic Azad University, Central Tehran Branch, Tehran, Iran*
[3] *Department of Civil Engineering, University of Tabriz, Tabriz, Iran*

Correspondence should be addressed to Siamak Talatahari; siamak.talat@gmail.com

Received 7 May 2013; Revised 11 July 2013; Accepted 21 August 2013

Academic Editor: Ga Zhang

Mononobe-Okabe (M-O) method is still employed as the first option to estimate lateral earth pressures during earthquakes by geotechnical engineers. Considering some simple assumptions and using a closed form method, M-O solves the equations of equilibrium and suggests seismic active and passive lateral earth pressures. Therefore, the results are true in its assumption range only, and in many other practical cases, M-O method is not applicable. Noncontinues backfill slopes, cohesive soils, and rising water behind the wall are some well-known examples in which the M-O theory is irrelevant. Using the fundamental framework of M-O method, this study proposes an iterative method to overcome the limits of the M-O method. Based on trial and error process, the proposed method is able to cover many of the defects which regularly occur in civil engineering when M-O has no direct answer.

1. Introduction

Retaining walls are those structures which are usually constructed to form roads, stabilize trenches and soil slopes, and support unstable structures. Figure 1 shows one of the common configurations of retaining structures, schematically.

Lateral earth pressure model is belonging to the first group of theories in classical soil mechanics. Coulomb [1] and Rankine [2] proposed their theories to estimate active and passive lateral earth pressures. These kinds of theories propose a coefficient which is a ratio between horizontal and vertical stress behind retaining walls. Using the ratio, lateral pressure is simply calculated by the horizontal stress integration.

Mononobe-Okabe method (M-O), a seismic version of coulomb theory, was proposed based on pseudostatic earthquake loading for granular soils. This method applies earthquake force components using two coefficients called seismic horizontal and vertical coefficients. Beside other complex theoretical models and numerical methods, M-O theory is one of the best initial estimates.

Although M-O is the first choice for engineers to design retaining walls, some limitations make it incapable to model most civil engineering projects. This problem rises according to the simplifier assumptions in M-O method to solve the equations in a closed form fashion. The contribution of this paper is primarily to remove these limits and to cover other problems that M-O has no answer for them. On the other hand, reports on retaining wall failures during major or minor earthquakes confirm the necessity of immune design of retaining structures. Since the stability of retaining walls plays an important role during and right after an earthquake, this study strives to provide a reliable tool for quick engineering designs. The methodology given in this paper can also be used as a model to study the effect of earthquake parameters on retaining structures with a specific geometry or can be reshaped for any other unusual retaining structures.

2. Mononobe-Okabe Method

Mononobe and Matsuo [3] and Okabe [4] proposed a method to determine lateral earth pressure of granular cohesionless soils during earthquake [5]. The method was a modified version of Coulomb theory [1] in which earthquake forces are

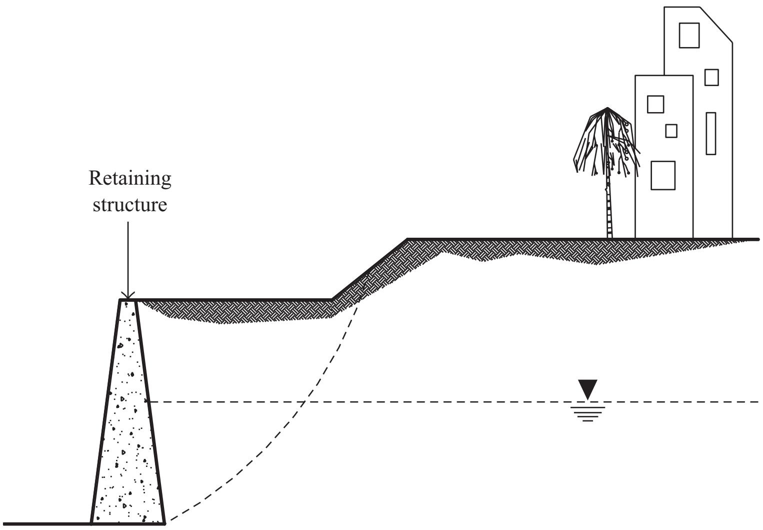

Figure 1: Application of retaining walls in civil engineering.

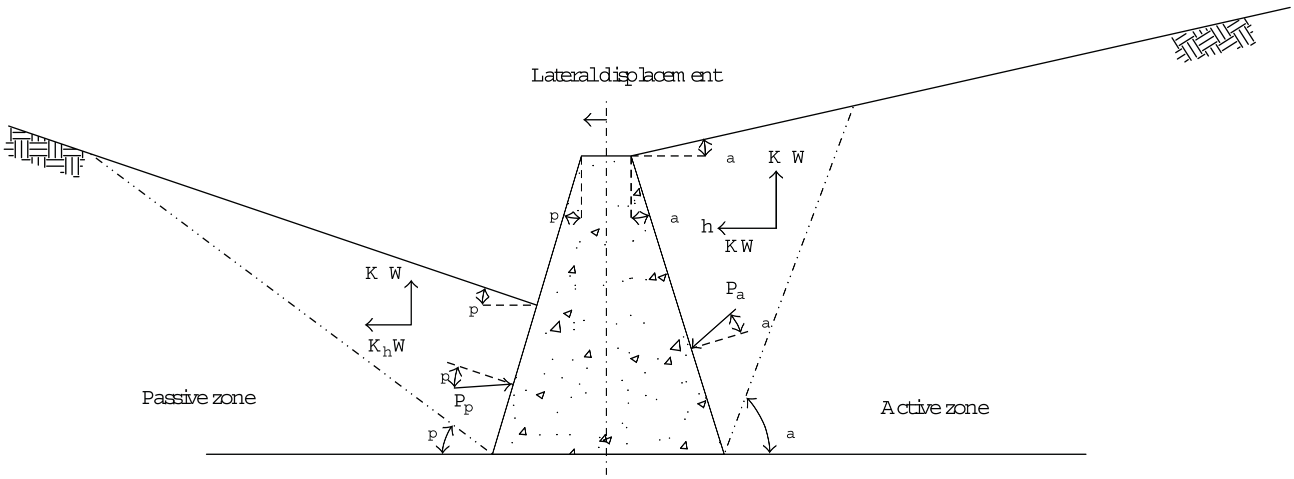

Figure 2: Geometry and parameters of M-O method.

applied to the failure mass by pseudostatic method. To get a final simple formulation like other closed form solutions in geotechnical engineering, M-O uses exact form solution with simple assumption such as simplicity in geometry, material behavior, or dynamic loading to make the equations solvable.

Because of the old age of M-O method, tens of studies have been focused on this area (e.g., [6–8]). An important study on M-O was carried out by Seed and Whitman [9]. They confirmed M-O active pressure after long laboratory runs. However, they recommended more studies on passive theory of M-O. They also proposed a method to find the location of resultant force which acts on 1/3 of height in M-O method. M-O had been studied by others such as Fang and Chen [10] on the direction of seismic force components on the failure mass.

Figure 2 shows the parameters and characteristics of M-O method. In M-O, static force equilibrium is satisfied for a rigid wedge placed on a failure plane with elastic-perfectly plastic behavior based on Mohr-Coulomb failure criteria. Active and passive forces, P_a and P_p, are then calculated using the following equations:

$$\begin{gathered}
\begin{Bmatrix} P_a \\ P_p \end{Bmatrix} = \frac{1}{2}\gamma H^2 \left(1 - K_v\right) \begin{Bmatrix} K_a \\ K_p \end{Bmatrix}, \\
\begin{Bmatrix} K_a \\ K_p \end{Bmatrix} = \left(\cos^2\left(\varphi \mp \alpha - \theta\right)\right) \times \left(\cos\theta \times \cos^2\alpha \times \cos\left(\delta \pm \alpha + \theta\right) \times \left[1 \pm \left(\frac{\sin\left(\varphi + \delta\right) \times \sin\left(\varphi \mp \beta - \theta\right)}{\cos\left(\delta \pm \alpha + \theta\right) \times \cos\left(\beta - \alpha\right)} \right)^{1/2} \right]^2 \right)^{-1}, \\
\theta = \tan^{-1}\left(\frac{K_h}{1 - K_v}\right).
\end{gathered} \tag{1}$$

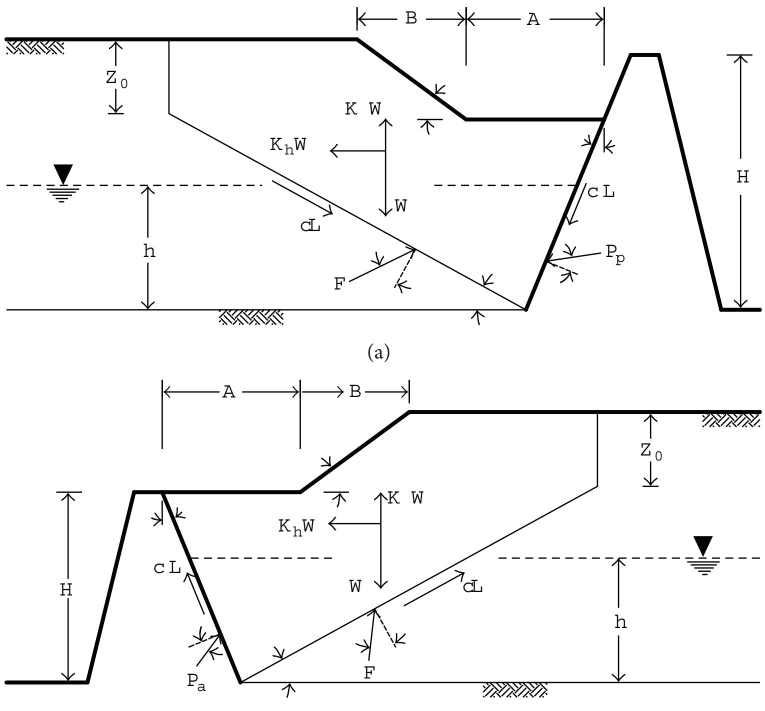

Figure 3: Proposed model for passive (a) and active (b) pressure.

It should be noticed that the above formulations were derived assuming planar failure surfaces. This assumption has significantly simplified the resultant equations that can practically capture the contrast between different design scenarios and parameters. However, in general, planar failure surfaces usually overestimate passive pressures and might underestimate active pressure. Moreover, in reality curved surfaces are more often useable. Therefore, the results of the current study can be used as upper limits while it should be considered with caution for active pressure. The works by Morrison and Ebeling [11], Kumar [12], Subba Rao and Choudhury [13] and Yazdani and Azad [14] explain how the planar models can be extended.

3. Mononobe-Okabe Method Defects and Limitations

Some of the limits of M-O method that cause the method not to cover many of the usual engineering problems are as follows.

(a) M-O method is applicable for cohesionless soils only.

(b) Effect of water table behind the wall has not been considered directly in the formula.

(c) M-O method has no answer when $\varphi - \beta - \theta \leq 0$.

(d) The conventional problems in civil engineering are not always wall with continues backfill. Sometimes, one has to use equivalent forms of M-O method to model a real problem.

4. Overcome Mononobe-Okabe Method Limits

To overcome M-O limits, the fundamental basis of limit equilibrium analysis can be used. The difference is the solution type which is carried out using an iterative process for various values of ρ_a and ρ_b to find the minimum and maximum values of the function instead of using closed form solutions of differential equations.

4.1. Problem Framework. According to Figure 3, wall displacement and also its direction produce effective forces on failure mass in both sides of a retaining wall. Variable parameters have been listed in Table 1. It can be seen that the main differences between current method and M-O method are as follows.

(a) Geometry of backfill soil has been modeled in an engineering configuration. Two real cases with the same geometry have been illustrated in Figures 4 and 5. Both examples are in north side of Tehran, Iran, which are located in a high seismic risk zone. Another similar geometry has been plotted in Figure 6. The figure also shows the failure mechanism of the wall in Chi-Chi Earthquake, Taiwan [15].

(b) In addition to soil cohesion, virtual cohesion between soil and wall material (adhesion) is included in the model.
Seismic active earth pressure considering c–φ backfill has been already evaluated by Prakash and Saran [16] as well as Saran and Prakash [17]. In their methods, adhesion was considered identical to cohesion. Das

Table 1: Parameters of the proposed method.

Parameter	Symbol
Wall height	H
Water depth	h
Wall angle	α
Soil-wall friction angle	δ
Backfill angle	β
Soil special weight	γ
Saturated soil special weight	γ_{sat}
Ref. to Figure 3	A
Ref. to Figure 3	B
Soil internal friction angle	φ
Soil cohesion	c
Soil-wall cohesion	c'
Horizontal earthquake coefficient	K_h
Vertical earthquake coefficient	K_v

and Puri [18] improved the analysis by considering different value of cohesion and adhesion. Shukla et al. [19] presented an idea to extend Mononobe-Okabe concept for $c-\varphi$ backfill in such a way to get single critical wedge surface. Ghosh and Sengupta [20] presented a formulation to evaluate seismic active earth pressure including the influence of both adhesion and cohesion for a nonvertical retaining wall.

(c) Static water table is included in the model to affect the earth pressure, directly.

(d) The effect of tension crack has been considered. This effect is quite important in active earth pressure on retaining wall for cohesive soil backfill [21]. Shukla et al. [19] showed that for soil backfill with tension cracks, the total active earth pressure in static condition will increase up to 20%–40% over the case without tension cracks. Therefore, the effect of tension cracks in cohesive soil backfill should not be neglected in the calculation of active earth pressure. Ghosh and Sharma [22] used the following equation in their analysis to compute the depth of tension cracked zone in seismic condition:

$$Z_0 = \frac{2c}{\gamma\sqrt{K_a}}; \quad K_a\,(\text{Rankine}) = \frac{1-\sin\varphi}{1+\sin\varphi}. \tag{2}$$

This equation is based on the Rankine theory of active earth pressure for cohesive backfill under static condition. The effect of seismic acceleration on the depth of tension crack is neglected in that analysis. Given that the inclination of the stress characteristics depends on acceleration level, a Rankine condition is valid for the vast majority of cantilever wall configurations under strong seismic action [23]. This is applicable even to short heel walls, with an error of about 5% [24, 25].

Shao-jun et al. [21] made an effort to determine the depth of tension cracked zone under seismic loading and used the pseudodynamic approach to compute seismic active force on retaining wall with cohesive backfills.

Figure 4: Geometry of natural slope behind a retaining wall, Tehran, Iran.

Figure 5: Geometry of backfill behind a retaining wall, Tehran, Iran.

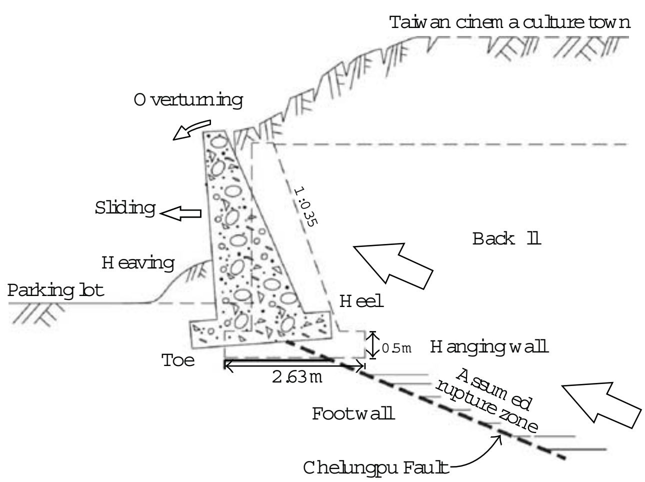

Figure 6: Geometry and failure mechanism of a retaining wall in Chi-Chi Earthquake, Taiwan (after [15]).

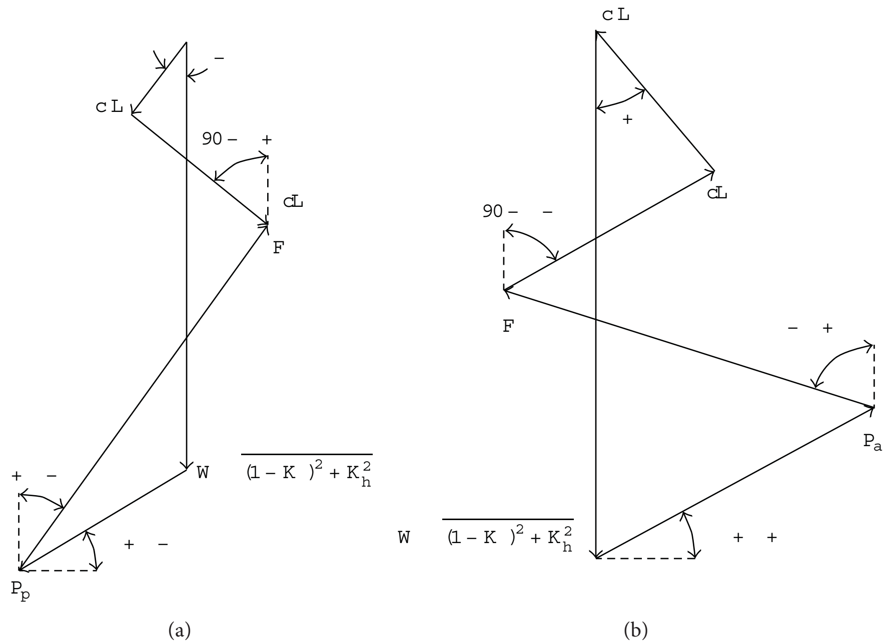

Figure 7: Effective force diagrams on failure mass (wedge).

In the current research, (2) is adopted to take into account the effect of tension crack. By this way, the shape of active wedge in original M-O method is changed from triangular to trapezoidal, and the resultant active earth pressure will be computed more realistically. However, in passive condition, the failure wedge was considered triangular similar to the conventional M-O method, though this assumption causes the passive earth pressure to be overestimated.

4.2. Free Body Diagrams. According to limit analysis on the failure surface which is bilinear in this study, shear stresses are developed based on Mohr-Coulomb theory. A 2D static set of equilibriums can simply connect stresses in a force (or stress) diagram. The diagrams for active and passive conditions have been shown in Figure 7.

4.3. Solution Methodology. As mentioned, using a closed form solution is not applicable herein according to the large number of parameters and nonlinearity of equations. Therefore, semianalytical iterative calculations for searching the favorite conditions (ρ, P_a, and P_p) have been chosen in this study.

The continuity of the equations is plotted in Figure 8, where the active pressure is the maximum while the passive pressure is the minimum points in relevant curves. Since the equations have one unique global maximum or minimum value, no sophisticated search algorithm is needed. A simple scanning search method was coded to pick the critical (extremum) conditions.

5. Parametric Study

Because of the large number of parameters in each analysis, deriving complete series of calculation and results seems useless. Therefore, this section just reflects results of a parametric study on a 10-meter high wall. Backfill soil has specific weight of 2 g/cm^3. Other variables have been explained in the following subsections. Other undefined parameters like parameter "A" have been assumed to be zero.

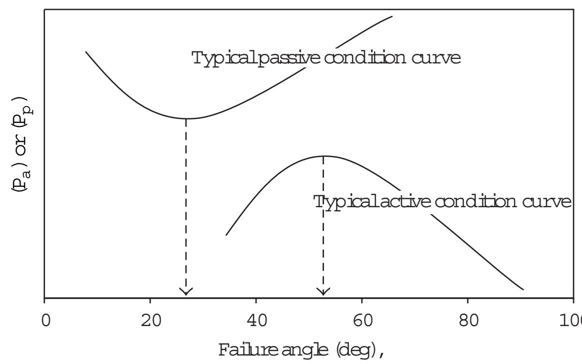

Figure 8: Typical active and passive condition curves.

5.1. Effects of Backfill Soil Geometry. To assess the effects of backfill soil geometry, a backfill soil with various values of β and B/H (the ratio of slope width to wall height as shown in Figure 3) and internal friction of soil equal to 30° was considered. Horizontal component of earthquake was set to $K_h = 0.2$. This problem was solved with the standard M-O and the proposed method. It should be noted that the values of slope angle in M-O were chosen equal to β.

Figure 9 shows the results of this analysis. It is clear that for $\beta \geq 20°$, M-O method has no result. Diagrams explain that when β increases, the difference between the

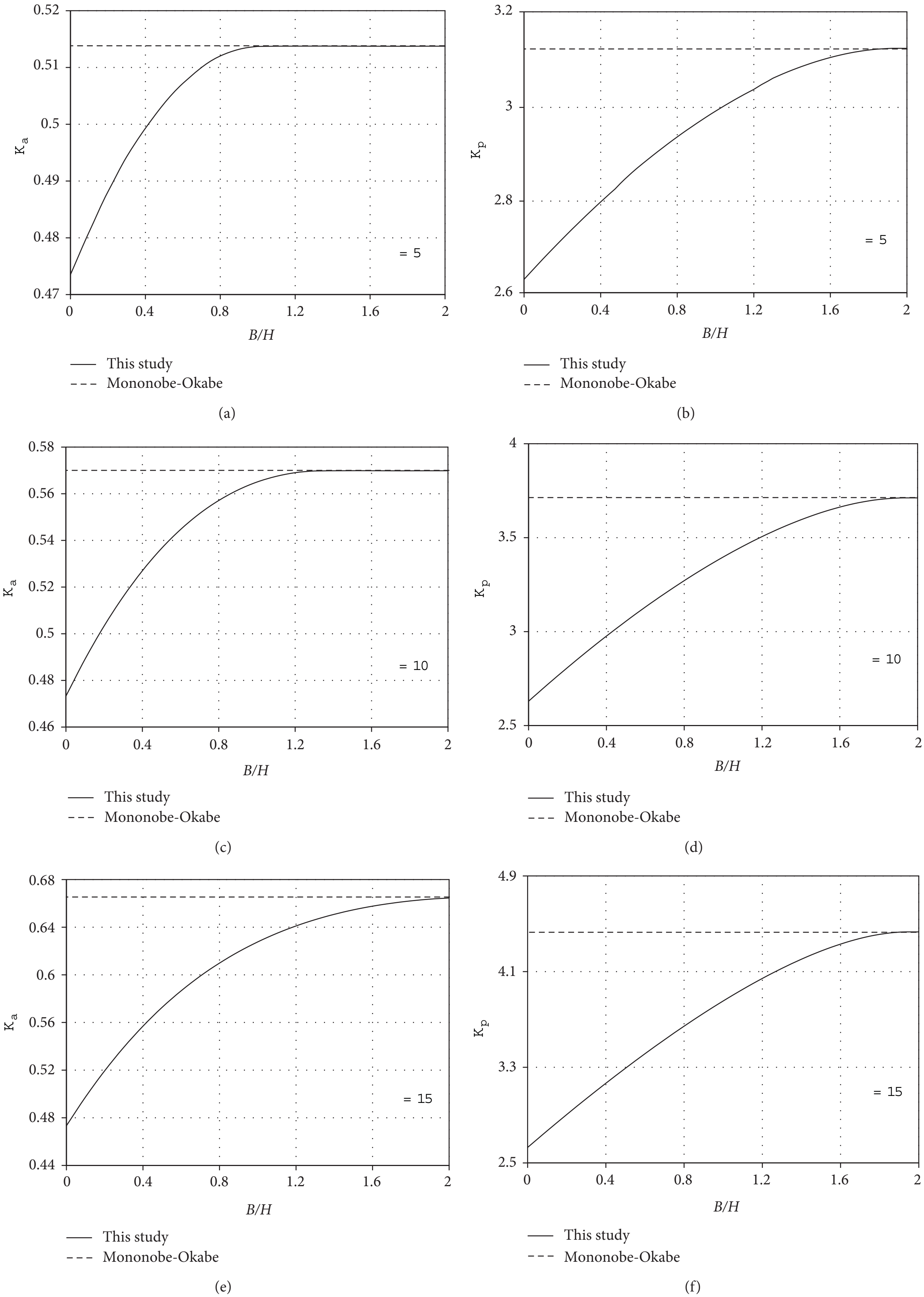

Figure 9: Continued.

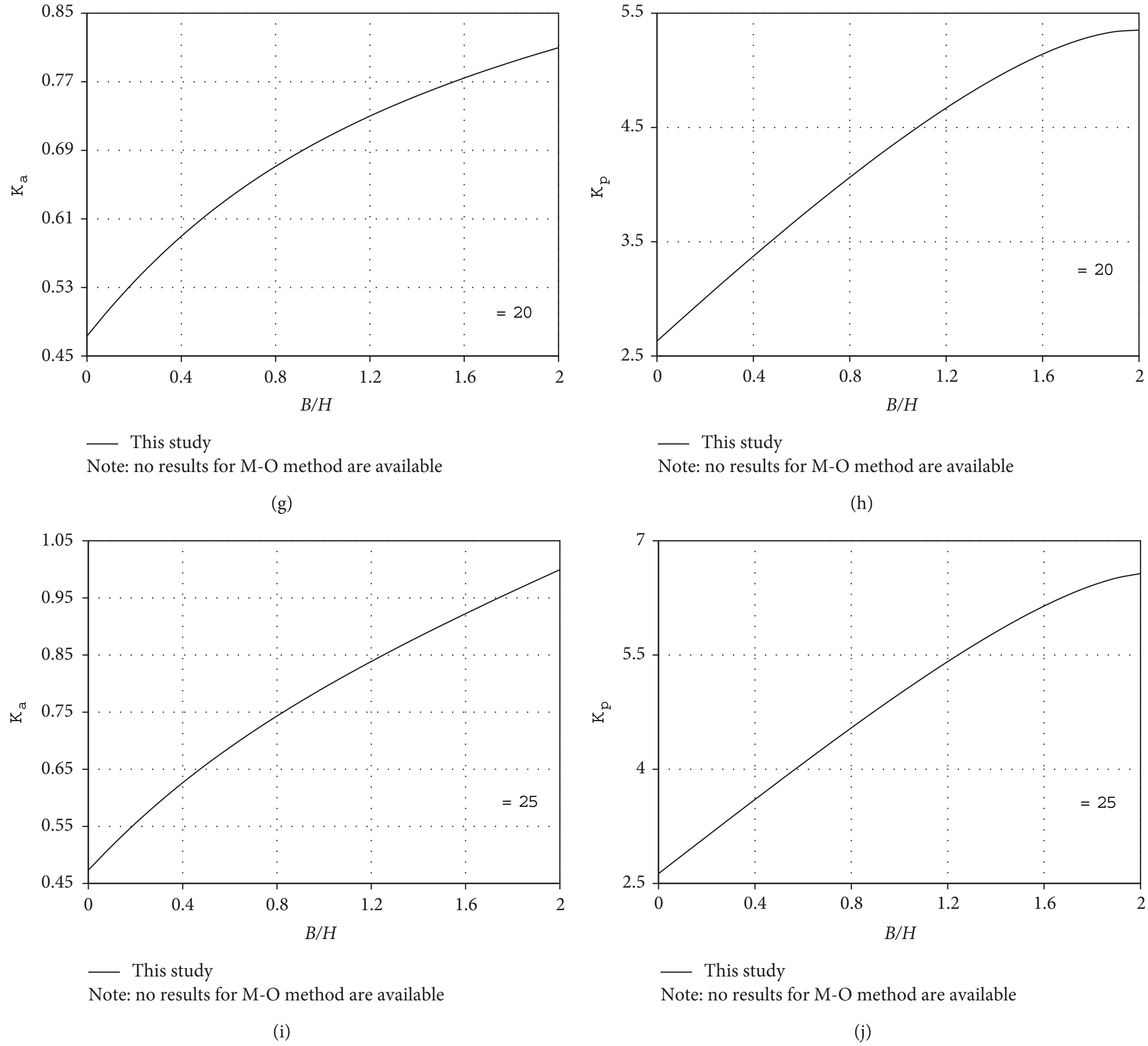

Figure 9: Lateral pressure coefficient for various backfill soil geometry.

proposed method and M-O results is significant. However, this difference decreases when B/H decreases. It means that if variation of β ($0\sim\beta$) occurs near the wall (approximately for $B/H < 1$), between the results of these methods a large difference appears. However, the proposed method is more accurate. As a result, when β is near the wall, M-O method is not economical for active conditions and is not accurate for passive cases.

5.2. Effects of Water Table behind Wall. In the original M-O method, water table is not considered directly in the model, and the earth pressure is given only for the dry condition. To overcome this deficiency, either a correctness factor recommended by some design codes should be utilized or the following relationship must be applied in which the lateral earth pressure ratio in each dry or saturated region is imposed on the relevant unit weight:

$$\text{Total earth pressure (M-O)} = \left\{\frac{1}{2}\gamma(H-h)^2 + \gamma h\,(H-h) + \frac{1}{2}\gamma'\cdot h^2\right\}\times K_a. \tag{3}$$

However, in the proposed method, the total earth pressure can be simply obtained by the following equation:

$$\text{Total earth pressure (this study)} = \frac{1}{2}\gamma\cdot H^2\times K_a. \tag{4}$$

It should be noted that K_a in the above equations has no similar value. The reason is hidden in the philosophy

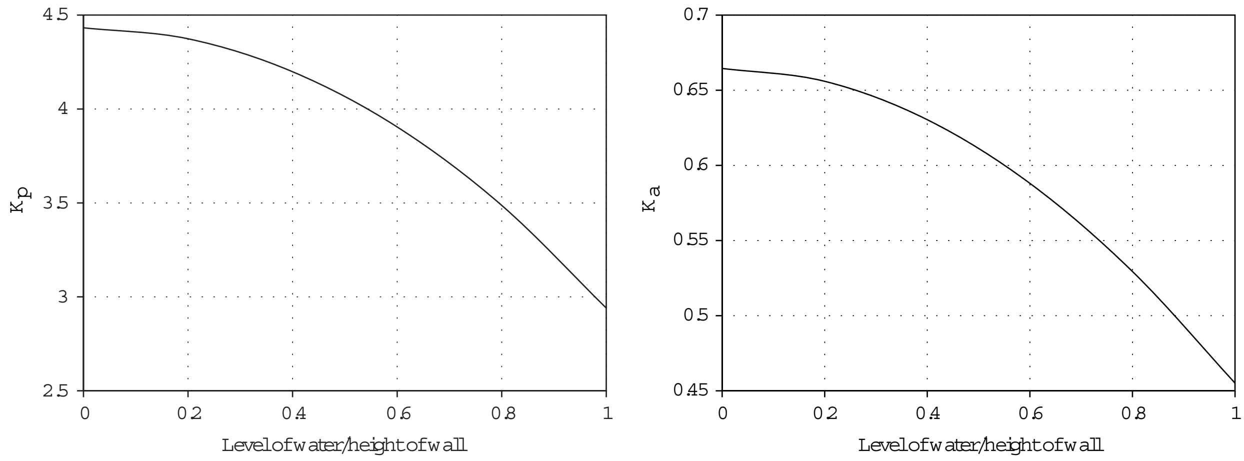

(a) (b)

Figure 10: Effects of water table on lateral earth pressure coefficients.

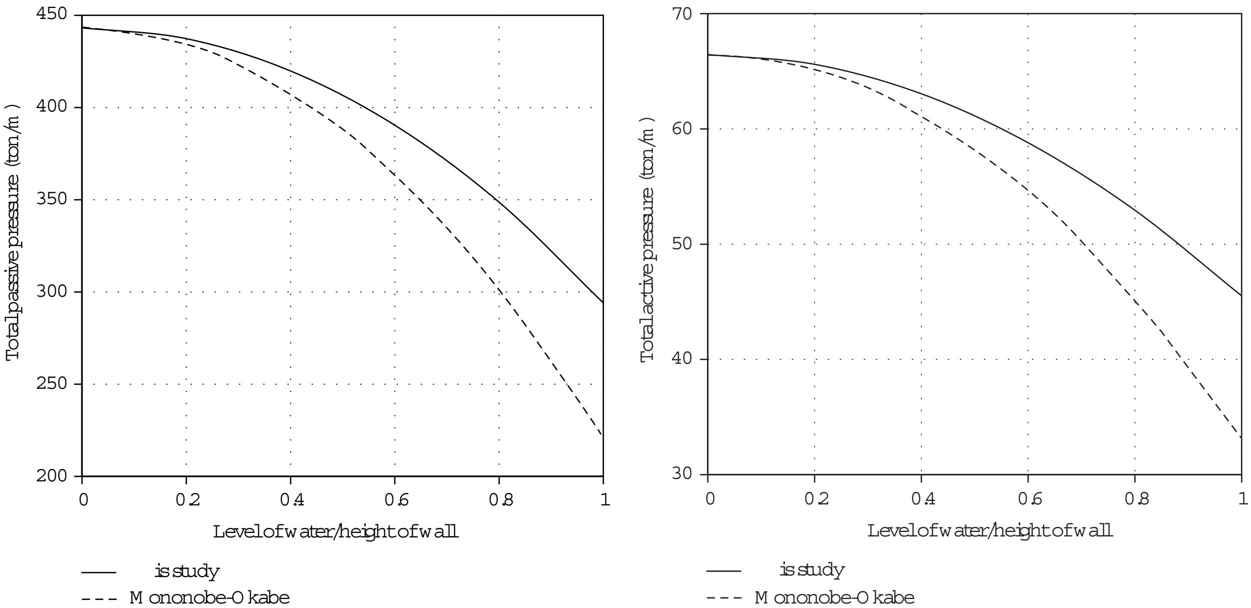

(a) (b)

Figure 11: Effects of water table on total lateral earth pressure compared to M-O.

of calculations. In fact, in (4) the weight of the submerged part of the sliding wedge is considered through the effective unit weight of soil which is reflected in the force equilibrium diagram, and then K_a is calculated. The two equations (3) and (4) can be regenerated in the same way for passive condition as well.

To investigate the ability of the proposed method in accounting for water effect on lateral earth pressures, a simple case has first been solved with the following parameters with no water table: $\beta = 15^{\circ}$, $B/H = 2$, $\phi = 30^{\circ}$, and $K_h = 0.2$. The results are plotted in Figure 9 that shows perfect agreement between M-O and the proposed model for the given geometry. In the second step, the same model was used with water table varying and $\gamma_{\text{sat}} = \gamma = 2\,\text{g/cm}^3$. The sensitivity analysis results are illustrated in Figure 10. This figure shows that increasing water depth will decrease lateral pressure in both active and passive conditions. The comparison between M-O based on (3) and this study based on (4) for passive case is illustrated in Figure 11. These diagrams reveal that the M-O method outputs are not in the safe side of design. Since the proposed model honors the physics of the problem with more details, it offers a better tool for design purposes.

5.3. Effects of Cohesion and Surface Tension Crack. Almost all soils have naturally a very small amount of cohesion. Also, in

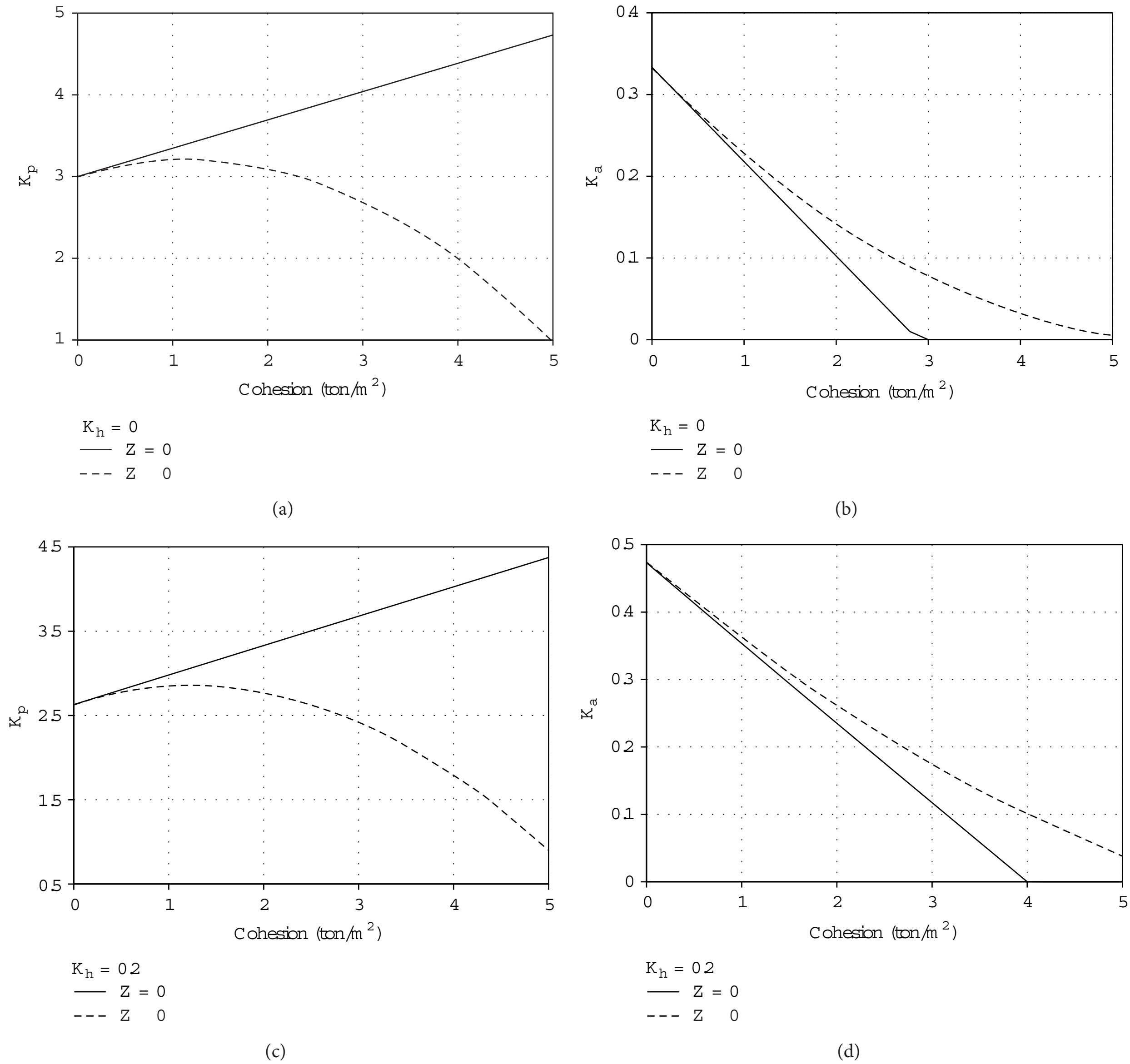

FIGURE 12: Effects of cohesion on lateral earth pressure.

many projects there is no access to a clean granular material or it is not economical to use such soils. Therefore, usage of cohesive soil is inevitable.

To better evaluate the effects of cohesion factor on lateral earth pressure, a wall with horizontal backfill and $\phi = 30^\circ$ was analyzed. Analyses have been repeated in the cases of with and without considering tension cracks for two different categories of $K_h = 0$ and $K_h = 0.2$. Results are reported in Figure 12 which shows the significant difference in active coefficient between cohesionless ($C = 0$) and cohesive ($C > 0$) soils. Where $K_h = 0.2$, for minimum 2 t/m^2 of cohesion, the active pressure changes 50% and the passive pressure changes 27%. These two values for $K_h = 0$ are 70% for the active pressure and 23% for the passive pressure. Also, it seems that tension cracks have small effects on the passive pressure while they are more appropriate for the active conditions.

6. Conclusion

In this paper, the Mononobe-Okabe (M-O) method was revised, and a new approach with more general picture of problems in civil engineering was proposed. Based on the limit equilibrium analysis and a semianalytical procedure, the proposed model can go over the limitations of closed form solutions of M-O method. The modified version is also capable of considering different backfill geometry, cohesion of backfill soil, soil-wall interaction, and water table behind the wall. Using the method explained in this paper, seismic active and passive earth pressure could be calculated in many usual engineering problems without any approximation.

The parametric study on a 10 m wall was also performed in the paper to explain the methodology more clearly. The results reveal this fact that the standard M-O method, in some cases, is incapable of offering an answer. Because of its simple assumptions, M-O sometimes stands in an unsafe side of design or it overestimates and directs the problem into an uneconomical design. However, the proposed methodology relives engineers from some approximations and equivalent methods. This methodology can be easily rederived to any other simple or sophisticated problems.

References

[1] C. A. Coulomb, *Essai sur une application des maximis et minimis a quelques problems de statique relatifs a l'architecture*, vol. 7, Memoires de l'Academie Royal Pres Divers Savants, Paris, France, 1776.

[2] W. Rankine, "On the stability of loose earth," *Philosophical Transactions of the Royal Society of London*, vol. 147, pp. 9–27, 1857.

[3] N. Mononobe and H. Matsuo, "On the determination of earth pressures during earthquakes," in *Proceedings of the World Engineering Congress*, p. 9, Tokyo, Japan, 1929.

[4] S. Okabe, "General theory of earth pressures," *Journal of the Japan Society of Civil Engineering*, vol. 12, no. 1, 1926.

[5] S. L. Kramer, *Geotechnical Earthquake Engineering*, Prentice-Hall, New York, NY, USA, 1996.

[6] R. Richards Jr. and X. Shi, "Seismic lateral pressures in soils with cohesion," *Journal of Geotechnical Engineering*, vol. 120, no. 7, pp. 1230–1251, 1994.

[7] H. Matsuzawa, I. Ishibashi, and M. Kawamura, "Dynamic soil and water pressures of submerged soils," *Journal of Geotechnical Engineering*, vol. 111, no. 10, pp. 1161–1176, 1985.

[8] A. S. Veletsos and A. H. Younan, "Dynamic modeling and response of soil-wall systems," *Journal of Geotechnical Engineering*, vol. 120, no. 12, pp. 2155–2179, 1994.

[9] H. B. Seed and R. V. Whitman, "Design of Earth retaining structures for dynamic loads," in *Proceedings of the ASCE Specialty Conference: Lateral Stresses in the Ground and Design of Earth Retaining Structures*, pp. 103–147, June1970.

[10] Y.-S. Fang and T.-J. Chen, "Modification of Mononobe-Okabe theory," *Geotechnique*, vol. 45, no. 1, pp. 165–167, 1995.

[11] E. E. Morrison and R. M. Ebeling, "Limit equilibrium computation of dynamic passive earth pressure," *Canadian Geotechnical Journal*, vol. 32, pp. 481–487, 1995.

[12] J. Kumar, "Seismic passive earth pressure coefficients for sands," *Canadian Geotechnical Journal*, vol. 38, pp. 876–881, 2001.

[13] K. S. Subba Rao and D. Choudhury, "Seismic passive earth pressures in soils," *Journal of Geotechnical and Geoenvironmental Engineering*, vol. 131, no. 1, pp. 131–135, 2005.

[14] M. Yazdani and A. Azad, "Evaluation of Mononobe-Okabe method and introducing an improved approach to design of retaining walls," *Transportation Journal*, no. 2, pp. 157–171, 2007 (Persian).

[15] Y. S. Fang, Y. C. Yang, and T. J. Chen, "Retaining walls damaged in the Chi-Chi earthquake," *Canadian Geotechnical Journal*, vol. 40, no. 6, pp. 1142–1153, 2003.

[16] S. Prakash and S. Saran, "Static and dynamic earth pressures behind retaining walls," in *Proceedings of the 3rd Symposium on Earthquake Engineering*, vol. 1, pp. 277–288, University of Roorkee, Roorkee, India, November 1966.

[17] S. Saran and S. Prakash, "Dimensionless parameters for static and dynamic Earth pressure behind retaining walls," *Indian Geotechnical Journal*, vol. 7, no. 3, pp. 295–310, 1968.

[18] B. M. Das and V. K. Puri, "Static and dynamic active earth pressure," *Geotechnical and Geological Engineering*, vol. 14, no. 4, pp. 353–366, 1996.

[19] S. K. Shukla, S. K. Gupta, and N. Sivakugan, "Active earth pressure on retaining wall for c-φ soil backfill under seismic loading condition," *Journal of Geotechnical and Geoenvironmental Engineering*, vol. 135, no. 5, pp. 690–696, 2009.

[20] S. Ghosh and S. Sengupta, "Extension of Mononobe-Okabe theory to evaluate seismic active earth pressure supporting c-φ backfill," *Electronic Journal of Geotechnical Engineering*, vol. 17, pp. 495–504, 2012.

[21] M. Shao-jun, W. Kui-hua, and W. Wen-bing, "Pseudo-dynamic active earth pressure behind retaining wall for cohesive soil backfill," *Journal of Central South University of Technology*, vol. 19, pp. 3298–3304, 2012.

[22] S. Ghosh and R. P. Sharma, "Pseudo-dynamic active response of non-vertical retaining wall supporting c-φ backfill," *Geotechnical and Geological Engineering*, vol. 28, no. 5, pp. 633–641, 2010.

[23] D. S. Scotto, A. Penna, A. Evangelista et al., "Experimental investigation of dynamic behaviour of cantilever retaining walls," in *Proceedings of the 15th World Conference on Earthquake Engineering*, Lisbon, Portugal, 2012.

[24] W. Huntington, *Earth Pressures and Retaining Walls*, John Wiley, New York, NY, USA, 1957.

[25] V. R. Greco, "Active earth thrust on cantilever walls with short heel," *Canadian Geotechnical Journal*, vol. 38, no. 2, pp. 401–409, 2001.

Hindawi Publishing Corporation
Journal of Applied Mathematics
Volume 2013, Article ID 394372, 13 pages
http://dx.doi.org/10.1155/2013/394372

Research Article

DEM Simulation of Biaxial Compression Experiments of Inherently Anisotropic Granular Materials and the Boundary Effects

Zhao-Xia Tong,[1] Lian-Wei Zhang,[2] and Min Zhou[1]

[1] *School of Transportation Science and Engineering, Beihang University, Beijing 100191, China*
[2] *Department of Civil Engineering, University of Science and Technology Beijing, Beijing 100083, China*

Correspondence should be addressed to Lian-Wei Zhang; geozhanglw@126.com

Received 6 June 2013; Revised 8 August 2013; Accepted 24 August 2013

Academic Editor: Pengcheng Fu

The reliability of discrete element method (DEM) numerical simulations is significantly dependent on the particle-scale parameters and boundary conditions. To verify the DEM models, two series of biaxial compression tests on ellipse-shaped steel rods are used. The comparisons on the stress-strain relationship, strength, and deformation pattern of experiments and simulations indicate that the DEM models are able to capture the key macro- and micromechanical behavior of inherently anisotropic granular materials with high fidelity. By using the validated DEM models, the boundary effects on the macrodeformation, strain localization, and nonuniformity of stress distribution inside the specimens are investigated using two rigid boundaries and one flexible boundary. The results demonstrate that the boundary condition plays a significant role on the stress-strain relationship and strength of granular materials with inherent fabric anisotropy if the stresses are calculated by the force applied on the wall. However, the responses of the particle assembly measured inside the specimens are almost the same with little influence from the boundary conditions. The peak friction angle obtained from the compression tests with flexible boundary represents the real friction angle of particle assembly. Due to the weak lateral constraints, the degree of stress nonuniformity under flexible boundary is higher than that under rigid boundary.

1. Introduction

The natural granular materials such as sands and gravels universally have the characteristics of anisotropy due to deposition under gravity or compaction. A number of studies in the bearing capacity of shallow foundations [1–3] and slope stability [4, 5] demonstrated that the deformation and strength anisotropy of the granular materials played a significant role on the geotechnical engineering.

The mechanical behavior of granular materials with inherent fabric anisotropy has been investigated using almost all the available laboratory testing methods such as triaxial compression tests [6, 7], direct shear tests [8, 9], plane strain compression tests [6, 10, 11], and hollow cylinder torsion shear tests [10, 12]. All of these experimental results indicate that the deformation and strength of inherently anisotropic granular materials are significantly dependent on the direction of applied stresses with respect to the bedding plane. In order to correlate these macrodeformation behaviors to the evolution of fabric characteristics, various new testing technologies including microstructural observation of thin sections fixed by resin [13], X-ray CT [14, 15], and stereophotogrammetry [16] have been used. However, these methods are too expensive or even impossible to capture the particle-scale quantities during the whole process of deformation.

Instead of making efforts on the particle-scale fabric measurement of real 3D laboratory experiments, the biaxial compression tests were conducted using two-dimensional rod assemblages [19, 20]. In the tests conducted by Konishi et al. [19], the photoelastic rods with oval cross-section were used to investigate the inherent anisotropy and shear strength. Their test results indicated that the deformation behavior of these 2D rods resembled that of real granular materials to a great extent. However, compared to the 3D laboratory experiments, it is much easier to catch the evolution of the fabric characteristics during the deformation process of the specimen.

The discrete element method (DEM) is capable of providing the detailed information about particle movement, rotation, and interaction between particles. A large number of numerical simulations for the biaxial/triaxial compression tests [18, 21–25] and direct/simple shear tests [18, 22, 26–28] have demonstrated that DEM is a powerful tool to study the microdeformation mechanism of granular materials. However, these DEM models differ greatly in the simulation of particle shape and boundary conditions, which have great effects on the macro- and particle-scale responses of granular materials.

The present paper aims at simulating the biaxial compression tests of ellipse-shaped steel rod assembly with high fidelity. The DEM model is validated by comparing the macro- and particle-scale responses of laboratory experiments and numerical simulations for two series of biaxial compression tests. The effects of boundary conditions on the stress-strain relationship, strength, strain localization, and stress nonuniformity are investigated.

2. Validation of Discrete Element Models

2.1. Biaxial Compression Experiments. Two series of biaxial compression tests on ellipse-shaped steel rod assembly are used to validate the DEM models in this paper. The biaxial compression test equipment was developed by the second author [17]. Its structure diagram was shown in Figure 1. A rectangular sample container ①, 240 mm in height and 120 mm in width, was constituted by the top plate ②, bottom plate ④, and two side plates ③. The base ⑤ was supported by the vertical loading platform ⑥ of a conventional triaxial compression apparatus and the component labeled as ⑦ was the reaction frame. During the shearing, the vertical deformation of the sample was controlled by the vertical movement of the loading platform ⑥, while the top plate ② was kept immovable. It should be pointed out that the base ⑤ together with both side plates ③ and bottom plate ④ moved upward at the same speed as the movement of loading platform ⑥ in this equipment, which was not common for the compression tests. The vertical pressure applied on the sample was measured by the force gauge FT_V. The force gauge F_L and F_R was used to measure the confined pressure applied on the left and right side platens, respectively. Each of the left and right side plates ③ together with the base of the frame ⑤ was installed two displacement sensors, and totally six displacement sensors, denoted by *DT1* to *DT6*, were used.

The materials tested were the ellipse-shaped steel rods with a uniform aspect ratio (the ratio of the minor axis length [d] to the major axis length [D]) of 1 : 2 and a length of 40 mm. The aggregate of the specimen was made by mixing three kinds of rods with their major axis length of 4 mm, 2 mm, and 1 mm. And their mass ratio was controlled to be 8 : 2 : 1.

To investigate the loading direction-dependent responses of the rod assembly, the specimens with various tilting angles, denoted by δ, were fabricated as Figure 2 shown. The tilting

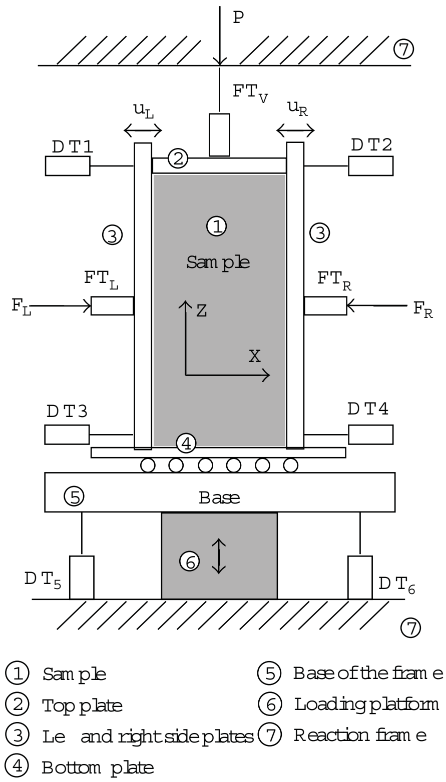

Figure 1: The structure diagram of the biaxial compression test equipment (Zhang [17]).

angle δ is defined as the angle between the bedding plane and the plane of the major principal stress. One black rectangular frame was used to contain the rod assembly, whose inside dimensions were 240 mm high, 120 mm wide, and 50 mm long. To fix the black rectangular frame at a prescribed tilting angle, one transparent organic glass with marked lines and holes was used. The specimen with the tilting angle of δ was fabricated as follows. Firstly, according to the required tilting angle δ, the horizontal black rectangular frame was rotated clockwise by the angle of δ and fixed on the organic glass using bolts. Then the mixed iron rods were placed into the frame layer by layer by hand while keeping the major axis of rods horizontal. When the frame was filled with iron rods, small shaking was applied for 1 minute to uniform the rod assembly. After that, the frame was removed from the organic glass and returned back to the horizontal direction by rotating counterclockwise by δ. Finally the rod assembly was pushed horizontally to the rectangular sample container ① of the biaxial compression equipment using an organic glass plate, which has the same inside width and height as the frame and the rectangular sample container ①. Till now the specimen with the tilting angle of δ was prepared and ready for biaxial compression tests. Two series of biaxial compression tests by changing tilting angles and confining pressures were conducted.

2.2. Discrete Element Model. The DEM simulation package *PPDEM* developed by Fu and Dafalias [18, 22] was used in

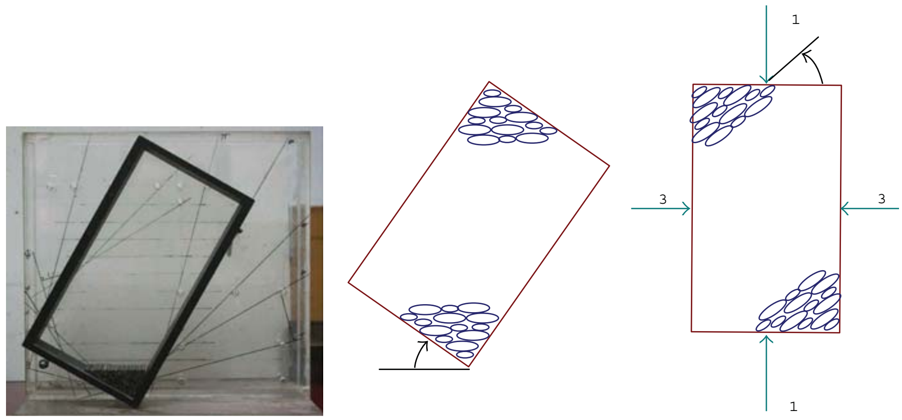

(a) (b)

Figure 2: Specimen fabrication method for the tilting angle of δ: (a) fix the rectangular frame according to the required tilting angle of δ; horizontally place the mixed rods into the frame layer by layer, (b) remove the rectangular frame when it was filled with rods, and rotate back to the horizontal direction.

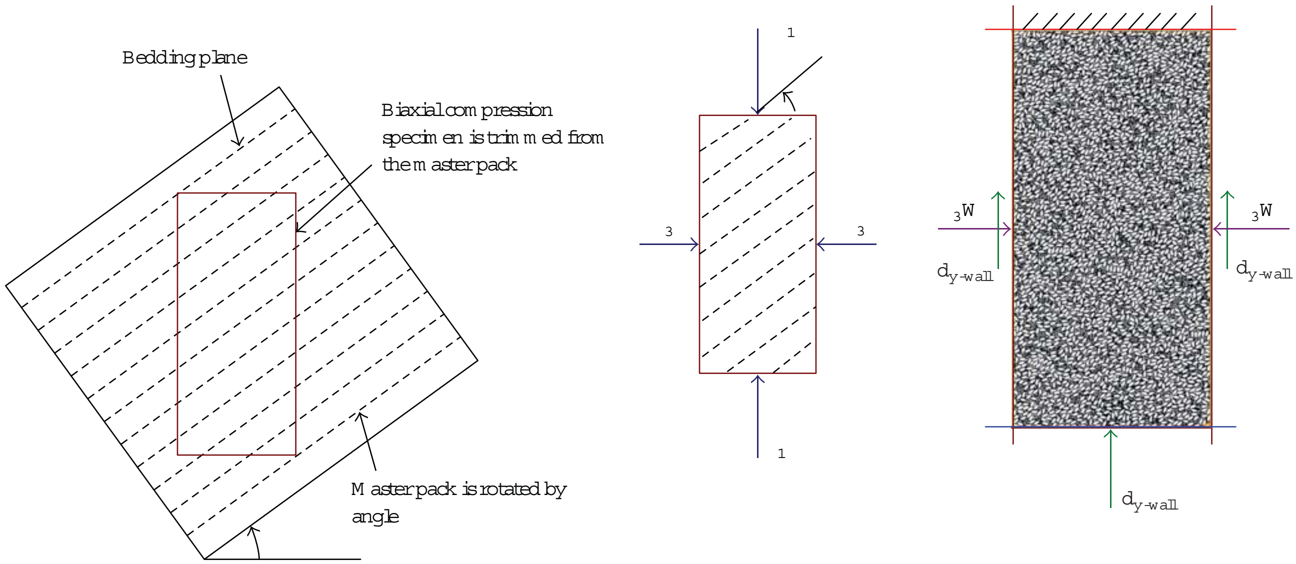

(a) (b)

Figure 3: Specimen preparation and boundary of biaxial compression simulations: (a) fabrication of specimen with a tilting angle of δ (Fu and Dafalias [18]) and (b) the boundary control of the specimen.

this study. As described in the papers of Fu and Dafalias [18, 22], the *PPDEM* is capable of characterizing any noncircular particle shapes by using "polyarc" element. The initial fabric anisotropy of the specimen can be well represented by modeling the deposition process under gravity. In addition, local quantities such as local stress, strain, particle orientation, rotation, and void ratio can be measured conveniently by defining a polygon-shaped "mask", whose vertex is attached to a particle.

To simulate the biaxial compression experiments of the rod assembly described above, three particle sizes with the major axis length of 4 mm, 2 mm, and 1 mm, respectively, were produced with their number ratio of 1 : 1 : 2, which was the same as the tested rod assembly. The biaxial compression specimens with various tilting angles were produced using the same method as described by Fu and Dafalias [18]. As Figure 3(a) shows, a "master pack" of 30000 particles was fabricated firstly by particle pluviation, whose bedding plane is horizontal. Then the "master pack" was rotated counterclockwise by the tilting angle of δ, and the biaxial compression specimens were "trimmed" horizontally out of the master pack. Around 10000 particles were included in the "trimmed" specimen with the initial size of 240 mm in height (H_0) and 120 mm in width (W_0). The initial void ratios of all the specimens with different tilting angles were 0.190 ± 0.01.

When the specimen was fabricated, four rigid walls were applied as the boundary of the specimen. The loading in the numerical simulations was controlled to be the same as that

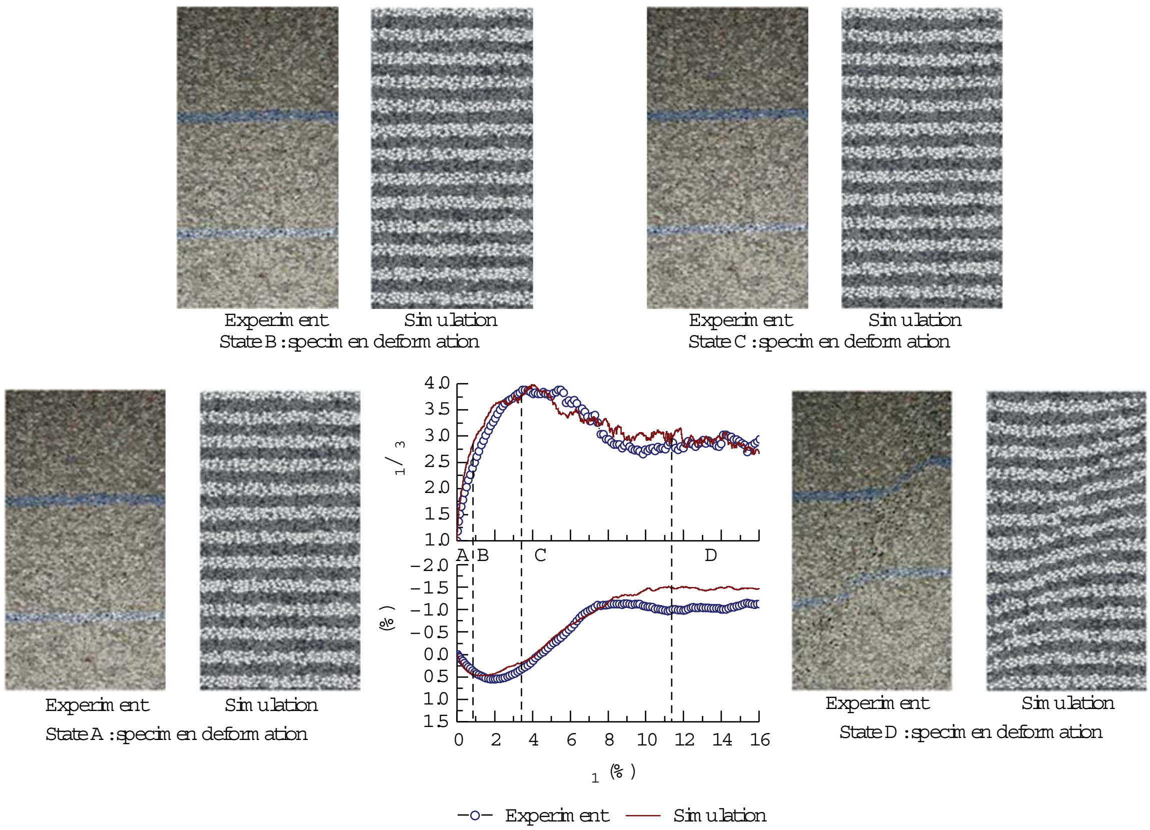

(a) $\delta = 0^{\circ}$; $\sigma_3 = 200$ kpa

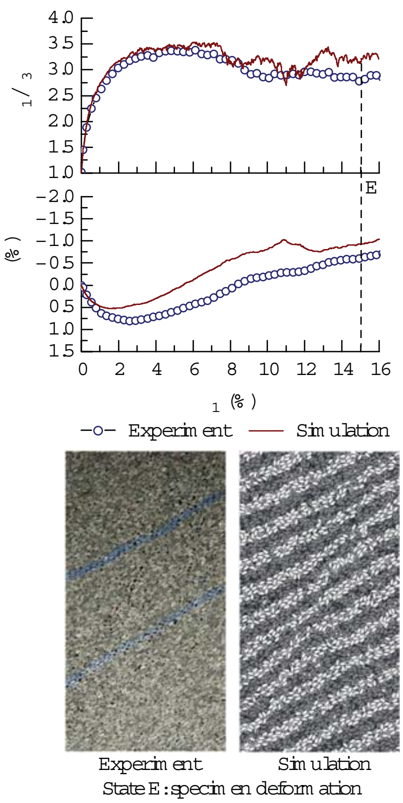

(b) $\delta = 30^{\circ}$; $\sigma_3 = 200$ kpa

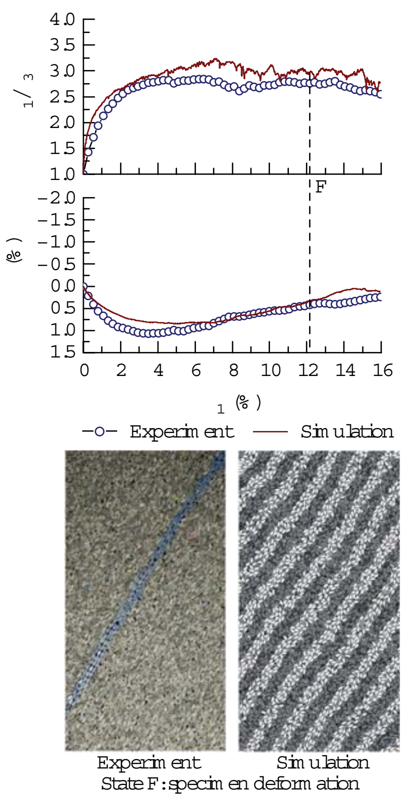

(c) $\delta = 60^{\circ}$; $\sigma_3 = 200$ kpa

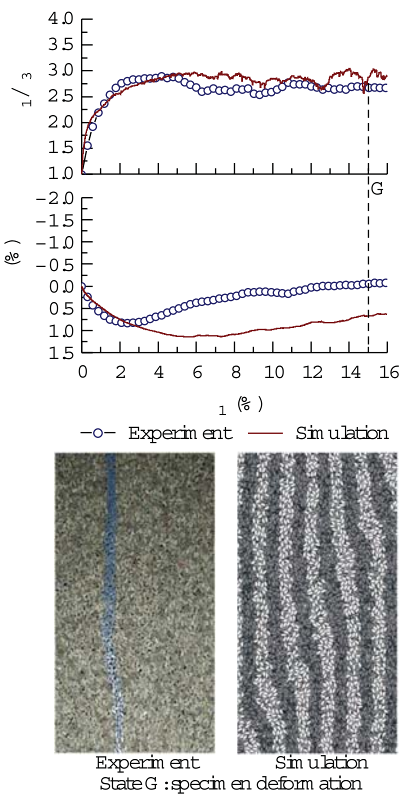

(d) $\delta = 90^{\circ}$; $\sigma_3 = 200$ kpa

FIGURE 4: Stress-strain relationship and deformation comparison between experiments and simulations at different tilting angles: (a) $\delta = 0^{\circ}$, (b) $\delta = 30^{\circ}$, (c) $\delta = 60^{\circ}$, and (d) $\delta = 90^{\circ}$.

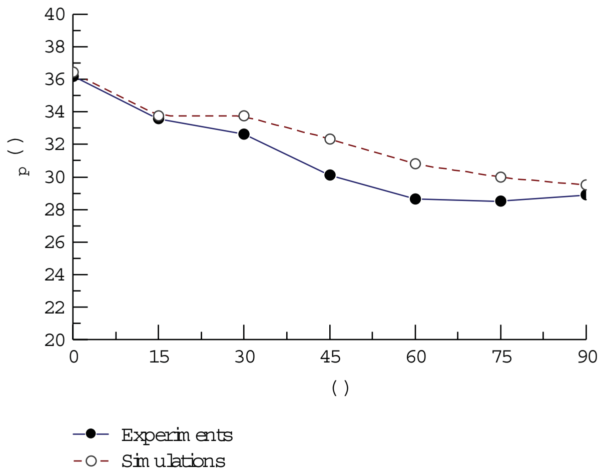

FIGURE 5: Comparison of peak friction angle ϕ_p between experiments and simulations.

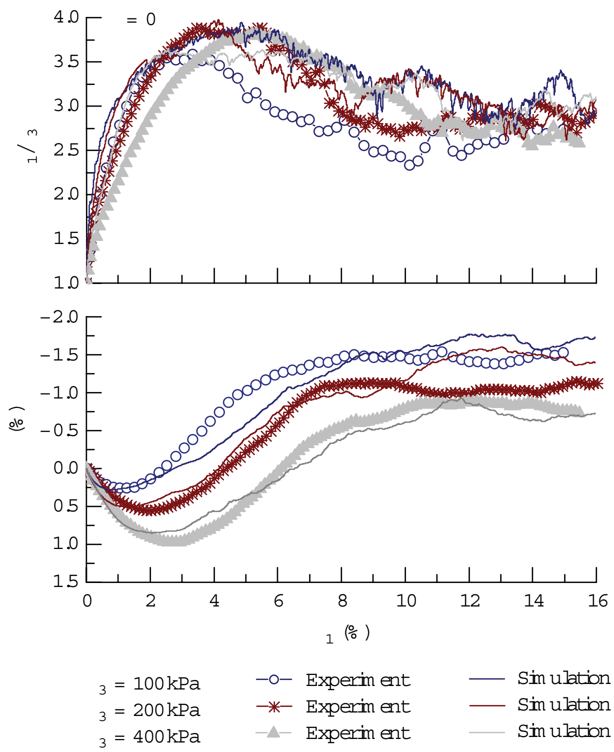

FIGURE 6: Stress-strain relationship comparison between experiments and simulations under different confining pressures.

in laboratory experiments, which was shown in Figure 3(b). After the specimen was consolidated isotropically at the required confining pressure of σ_3, the shearing began. In the vertical direction, the bottom wall moved upward at a specified rate while the top wall was kept immovable. The two end walls were free to move in the horizontal direction. For the left and right lateral walls, the horizontal confining pressure of σ_3 was maintained constant by the wall servocontrol. However, both lateral walls moved vertically at the same speed as the bottom wall.

As described by Fu et al. [29], the overlap-area contact law was adopted for the interparticle behavior in *PPDEM*. The research conducted by Mirghasemi et al. [30] has demonstrated that the format of contact laws has minor effects on the macroscopic behavior of particle assemblage as long as the model parameters are appropriately selected. Thus the contact model for the tested steel rods has not been measured, and the overlap-area contact law is used for the numerical simulations. By conducting parameter sensitivity analysis, it is found that two parameters, the interparticle friction angle and the friction angle between particle and wall, have significant effects on the macromechanical behavior of particle assembly. These two parameters are chosen to be 30° and 10°, respectively, by comparing the stress-strain relationship between experiments and simulations for two series of tests varied in tilting angles and confining pressures.

2.3. Verification of Discrete Element Model. Two series of biaxial compression tests are used to validate the discrete element models. One is the tests with the tilting angle of δ varying from 0° to 90° with interval of 15° while keeping the same confining pressure $\sigma_3 = 200$ kPa; the other is conducted by changing the confining pressures at the same tilting angle $\delta = 0°$. Figures 4(a)–4(d) compare the evolution of the stress ratio σ_1/σ_3, volumetric strain ε_v, and deformation pattern of laboratory experiments and numerical simulations for the first series of tests with $\delta = 0°$, 30°, 60°, and 90°, respectively. The principal stresses of σ_1 and σ_3 are calculated using the same method as the laboratory experiments. The σ_1 is obtained by dividing the average vertical force of two end walls by the specimen width, and the σ_3 is calculated by dividing the horizontal force of two lateral walls by the specimen height.

As Figures 4(a)–4(d) show, the key direction-related mechanical behavior of granular materials with inherent fabric anisotropy can be captured by numerical simulations with high fidelity, although the initial shear modulus of all simulations is a little bit higher than that of experiments. The response of the granular materials is significantly dependent on the loading direction for both simulations and experiments. For $\delta = 0°$ and $\delta = 30°$, the principal stress ratio σ_1/σ_3 reaches a peak followed by strain softening. As the tilting angle δ increases, the strain softening is weakened. For $\delta = 60°$ and $\delta = 90°$, the development of the principal stress ratio σ_1/σ_3 tends to be strain hardening, which progressively approaches plateaus and then remains constant. With the continuation of the deformation, the specimen contracts firstly and then dilates. The dilation is reduced with the increase of the tilting angle δ. It should be pointed out that these results are qualitatively similar to the plane strain test results obtained by Oda et al. [6] and Tatsuoka et al. [10]. In addition, the deformation pattern of specimens at typical states of A to G visually looks similar, which shows that both experiments and simulates should possess the same particle-scale deformation mechanism.

Figure 5 gives the comparison of the peak friction angle ϕ_p with respect to the tilting angle δ. The peak friction angle

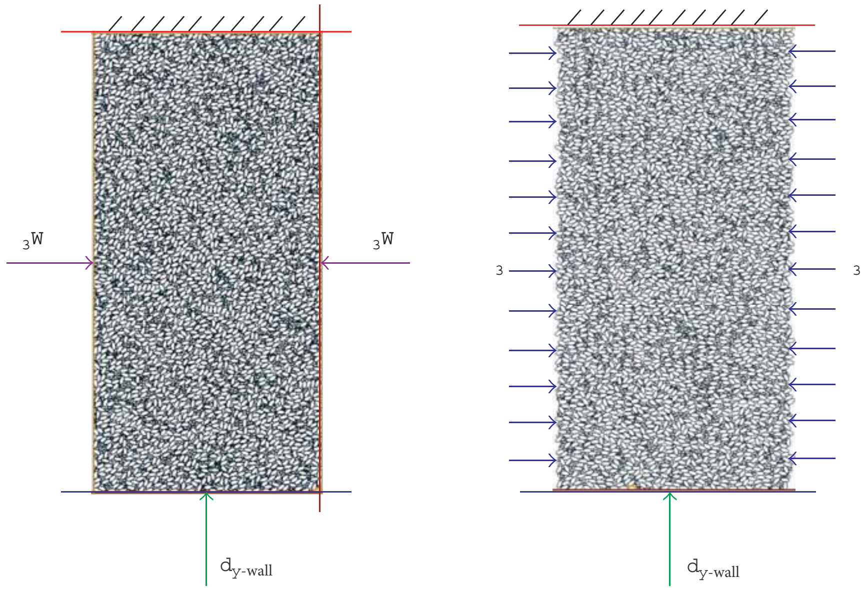

(a) (b)

Figure 7: The other two boundaries used for comparison.

ϕ_p corresponds to the maximum principal stress ratio σ_1/σ_3 in Figures 4(a)–4(d), which is calculated through the curve of the principal stress ratio σ_1/σ_3 versus axial strain ε_1 by assuming zero cohesion. It can be seen that the evolution of the peak friction angle ϕ_p with respect to the tilting angle δ follows the same tendency for both experiments and simulations. As the tilting angle δ increases, the peak friction angle ϕ_p decreases. The biggest difference of ϕ_p between simulations and experiments is about 2°, which happens at $\delta = 60°$.

Figure 6 shows the comparison of experiments and simulations for the second series of tests, in which three different confining pressures are applied for the tilting angle $\delta = 0°$. For $\delta = 0°$, the stress-strain relationship shows the characteristics of strain softening under three different confining pressures. The effects of confining pressure can be modeled. With the increase of confining pressure, the peak strength reduces. The specimen contracts followed by dilation. The maximum volumetric contraction increases as the confining pressure increases.

3. Investigation of Boundary Effects

It should be pointed out that the two lateral platens move vertically at the same speed as the bottom platen in the above biaxial compression tests and simulations, which is not common for compression tests. In the following, this mode of boundary control is denoted by Rigid boundary A. To investigate the effects of boundary condition, two other boundaries are used as Figure 7 shows. One boundary, denoted by Rigid boundary B, is the same as Rigid boundary A except that the two lateral walls are free to move in the vertical direction. The other boundary, denoted by Flexible boundary, resembles the conventional triaxial compression tests. The top and bottom boundaries are simulated by the rigid walls. The two lateral boundaries are flexible like membrane. The confining pressure σ_3 is directly applied on particles as described by Fu and Dafalias [18].

3.1. Boundary Effects on the Stress-Strain Relationship and Strength. Figures 8(a)–8(d) compare the development of the principal stress ratio σ_1/σ_3 and volumetric strain ε_v with axial strain ε_1 under the above three different boundary conditions for the tilting angle $\delta = 0°, 30°, 60°$, and $90°$, respectively. All the principal stresses of σ_1 and σ_3 are calculated by dividing the force applied on the wall by the relevant specimen size, except that the σ_3 is directly applied on particles under Flexible boundary. The averaged specimen width, dividing the specimen volume by the height, is used to calculate σ_1 under Flexible boundary.

It can be seen that the stress-strain relationship and strength are dependent on the boundary condition. Much stronger strain softening happens under Flexible boundary compared to the other two rigid boundaries. For $\delta = 60°$ and $90°$, the development of stress ratio σ_1/σ_3 shows strain hardening characteristics under Rigid boundary A and Rigid boundary B, while the marked drop of σ_1/σ_3 still occurs after the peak under Flexible boundary. The reason for the strong strain softening under Flexible boundary may be due to the lateral bulging of the specimen at large deformation. The maximum peak friction angles ϕ_p and the initial shear modulus are achieved under Rigid boundary A, and the corresponding minimum values are obtained under Flexible boundary for any tilting angle δ. The effects of boundary

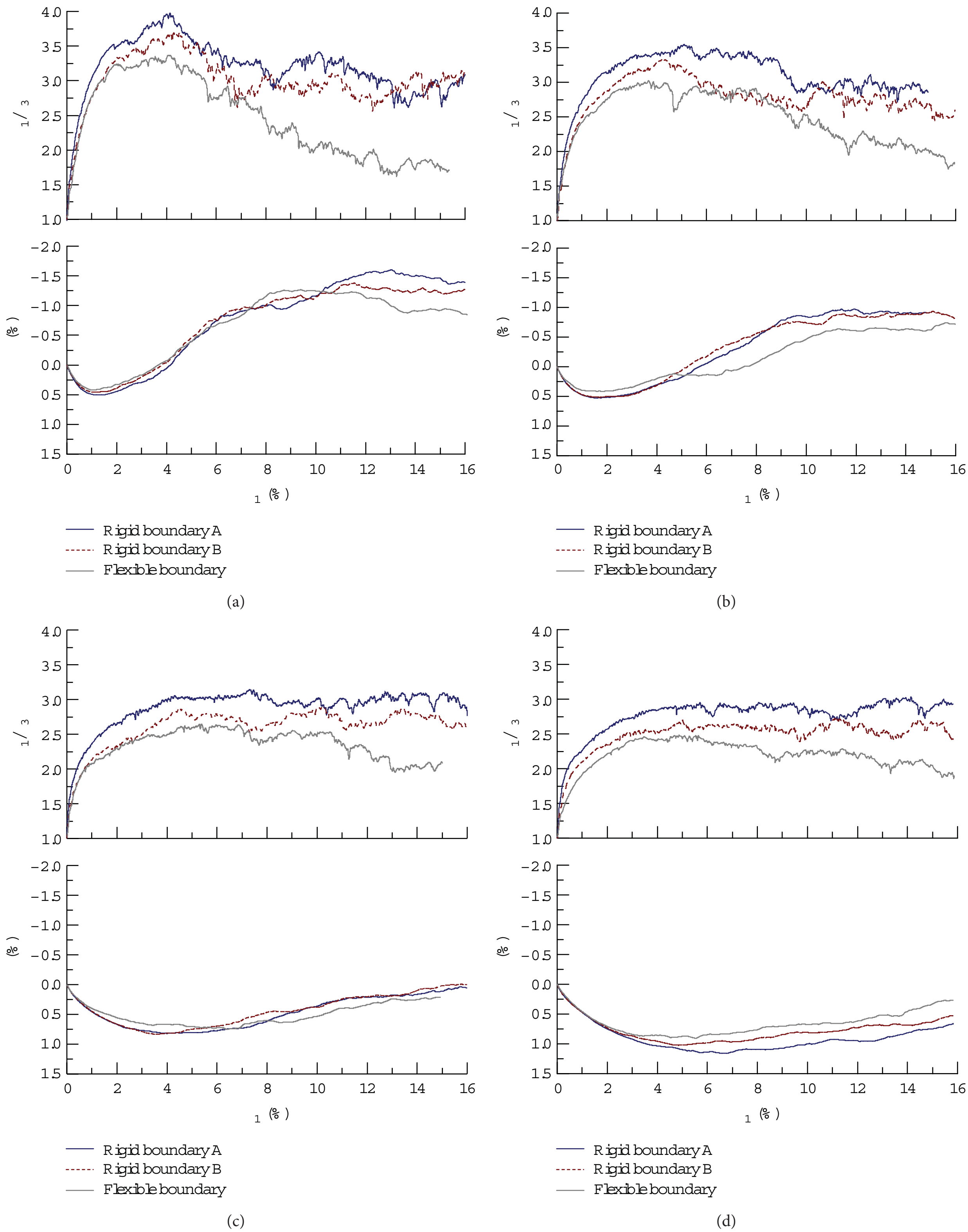

FIGURE 8: The development of stress ratio σ_1/σ_3 and volumetric strain ε_v with axial strain ε_1 for three different boundary conditions: (a) $\delta = 0^{\circ}$, (b) $\delta = 30^{\circ}$, (c) $\delta = 60^{\circ}$, and (d) $\delta = 90^{\circ}$.

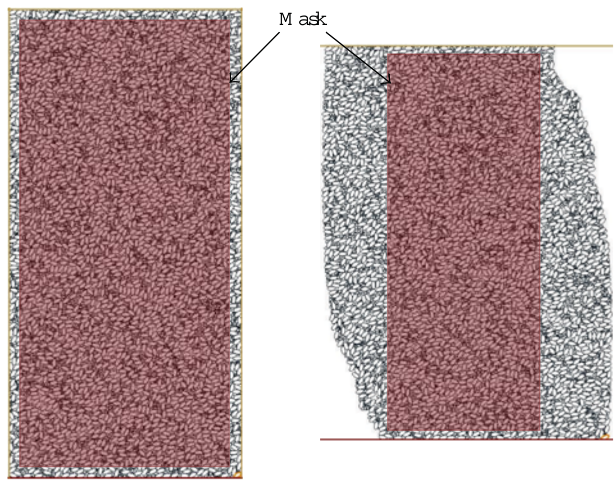

(a) Rigid boundary (b) Flexible boundary

Figure 9: Definition of masks to calculate the stresses inside the specimen.

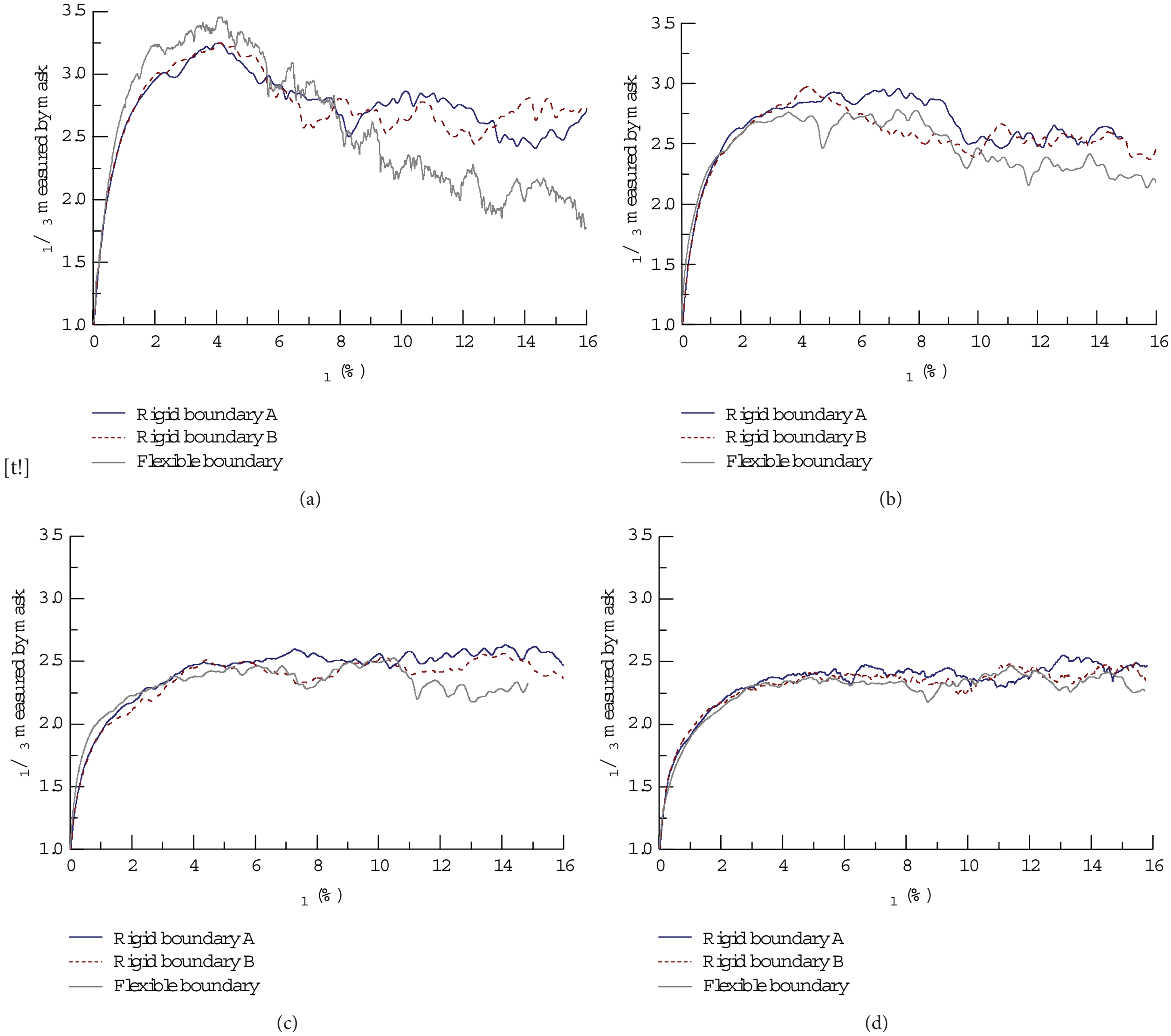

Figure 10: The development of “real” stress ratio σ_1/σ_3 with axial strain ε_1 for three different boundary conditions: (a) $\delta = 0^\circ$, (b) $\delta = 30^\circ$, (c) $\delta = 60^\circ$, and (d) $\delta = 90^\circ$. The σ_1 and σ_3 are measured inside the specimen by defining a mask.

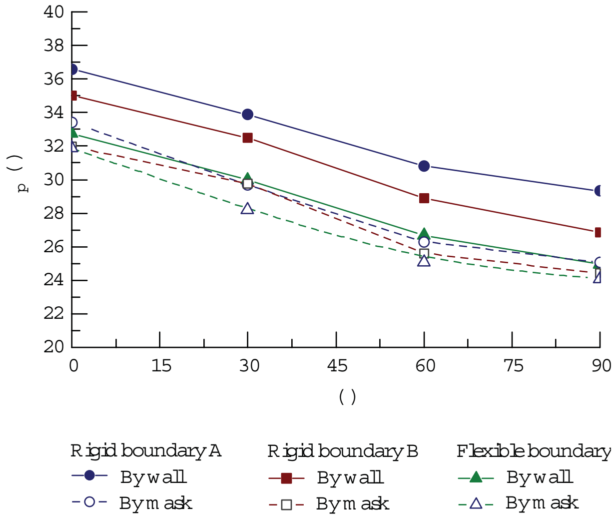

Figure 11: Comparison of peak friction angle ϕ_p under different boundary conditions.

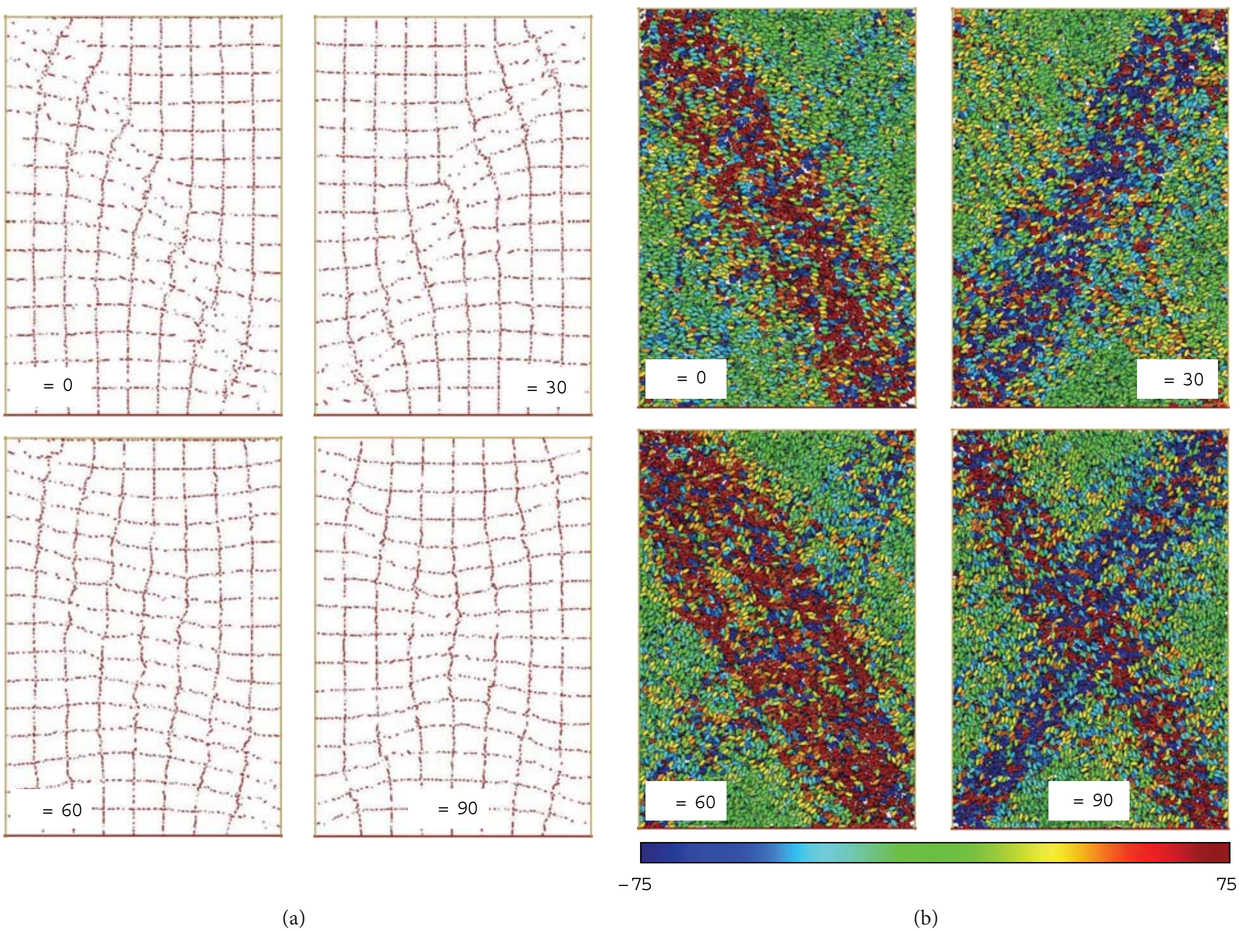

Figure 12: Deformation of biaxial compression tests at axial strain of 15% under Rigid boundary B: (a) overall deformation and (b) contours of individual particle rotation.

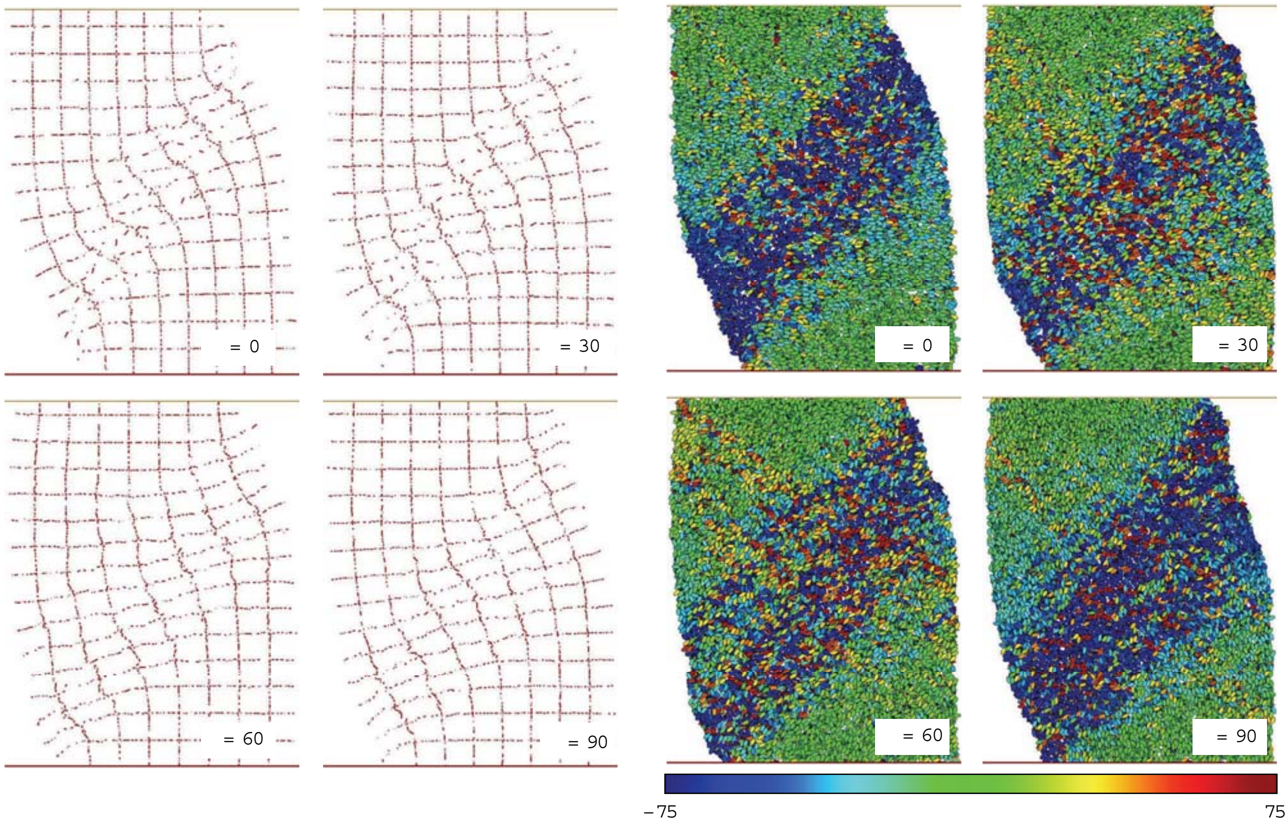

(a) (b)

Figure 13: Deformation of biaxial compression tests at axial strain of 15% under Flexible boundary: (a) overall deformation and (b) contours of individual particle rotation.

condition on the development of volumetric strain ε_v are not as significant as on the stress ratio σ_1/σ_3. At the initial stage of volume contraction, the volumetric strain ε_v is almost the same for three different boundary conditions. As the deformation continues, some minor differences are observed.

The DEM package *PPDEM* used is capable of measuring the average local stresses in any domain inside the specimens by defining a mask as described by Fu and Dafalias [18]. To obtain "real" average stresses inside the specimens, the mask is defined firstly as Figure 9 shows. The mask defined under two rigid boundaries is a little bit smaller than the whole specimen and the same mask is used during the shearing process. However, under Flexible boundary, due to the distortion of the specimen, the particles bulged outside are not included in the mask, and the mask is changed at each 4% axial strain. The average stresses inside the mask are calculated.

The development of the "real" stress ratio σ_1/σ_3 measured by the above masks is shown in Figures 10(a)–10(d) for tilting angle $\delta = 0^\circ$, 30°, 60°, and 90°, respectively. It can be seen that the "real" stress-strain relationship measured inside the specimen is almost the same except that some minor difference happens for $\delta = 0^\circ$. The minor difference of the σ_1/σ_3 among different boundary conditions may be due to the different masks used. However, reviewing the stress-strain relationship presented in Figure 8, in which the stresses are calculated by the force applied on the wall, the stress ratio σ_1/σ_3 is affected significantly by the boundary conditions.

To investigate the boundary effects on the strength, Figure 11 gives the peak friction angle ϕ_p calculated on the basis of Figures 8 and 10, which are indicated with "by wall" and "by mask", respectively, for three different boundary conditions. It can be found that the peak friction angle ϕ_p decreases as the tilting angle δ increases for all cases. The peak friction angle ϕ_p calculated "by wall" under Rigid boundary A is the maximum, which is almost 1.5° higher than that under Rigid boundary B and 3.5° higher than that under Flexible boundary. However, when the "real" stresses inside the specimen are calculated by "mask", the difference of the peak friction angle ϕ_p among three different boundary conditions is less than 1° as far as the same tilting angle is considered. In addition, one interesting phenomenon found in Figure 11 is that, under Flexible boundary, the peak friction angle ϕ_p obtained by "wall" is very close to the real value obtained by mask. The difference between them is less than 1°, which indicates that the peak friction angle ϕ_p obtained usually by triaxial compression tests can represent the true strength of the granular materials.

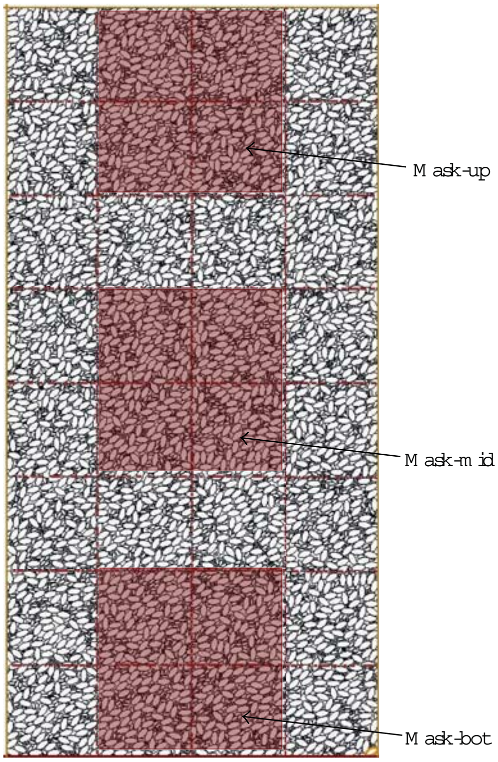

Figure 14: Definition of three different masks.

3.2. Boundary Effects on the Strain Localization. The strain localization happens in almost all kinds of granular materials during the shearing process. The shear localization pattern is very complex and may be affected by many parameters, among which the effect of the boundary condition is significant [10, 16]. To study the effects of boundary conditions on the strain localization, Figures 12 and 13 show the grid deformation and the particle rotation contours at the axial strain of 15% under Rigid boundary B and Flexible boundary for the tilting angle $\delta = 0^\circ, 30^\circ, 60^\circ$, and 90°, respectively. The grid was originally "painted" on the consolidated specimen. Considering that the specimens have almost the same deformation pattern under two rigid boundaries, only the results under Rigid boundary B are presented in Figure 12.

It can be seen that the grid deformation and the particle rotation contour give the same shear localization region. The primary shear plane is dependent on the boundary condition. Under Rigid boundary B, the primary shear plane extends from corner to corner due to the strong constraint of the four rigid walls. However, under Flexible boundary, the constraint of the boundary is much weaker, and large bulging of the particles is found. At any tilting angle δ, the primary shear plane extends upward from left to right, which was denoted as Type-b failure plane in Tatsuoka et al. [10]. And the shear localization mainly focuses in the middle part of the specimen. However, under Rigid boundary B, the primary shear plane produced is significantly dependent on the direction of loading. Different types of shear planes are found when the tilting angle δ changes from 0° to 90° as Figure 12 shows. For $\delta = 0^\circ$ and 60°, the shear plane extending from the left-up corner to the right-down corner is dominant, which was denoted as Type-a failure plane in Tatsuoka et al. [10]. For $\delta = 30^\circ$, the primary shear plane is Type-b mode. The X-type shear plane happens for $\delta = 90^\circ$.

3.3. Boundary Effects on the Stress Nonuniformity Inside the Specimen. To investigate the boundary effects on the stress nonuniformity inside the specimen, three different masks, denoted by mask-up, mask-mid, and mask-bot, respectively, are defined in the upper middle, central middle, and bottom middle part of the specimen as shown in Figure 14. Each mask contains over 1000 particles. The averaged stresses in these masks are calculated. Given typical examples of $\delta = 0^\circ$ and 90°, Figures 15 and 16 show the evolution of stress ratio σ_1/σ_3 measured in different masks with axial strain ε_1 under the conditions of Rigid boundary B and Flexible boundary. The curves of Figure 10 under the same conditions are plotted for comparison, which are indicated with "mask-whole."

It can be found that the boundary conditions affect the stress distribution inside the specimen. The stresses in the central middle part of the specimen are higher than those in the upper and bottom parts. And the stresses denoted by "mask-whole" can represent the average stresses of the upper middle, central middle, and bottom middle masks. In addition, the degree of stress nonuniformity under Flexible boundary is higher than that under Rigid boundary B. The reason for the high stress nonuniformity under Flexible boundary can be explained as follows. Under Flexible boundary, the lateral constraints are weak. More particles in the middle part of the specimen extrude and they cannot transfer the vertical stresses efficiently. Thus high forces concentrate in the central middle particles.

4. Conclusion

The DEM numerical simulations are a very promising tool to investigate the macro- and micromechanical behavior of granular materials. However, its reliability is significantly dependent on the particle-scale parameters and boundary conditions. In this paper, two series of biaxial compression tests varied in bedding plane inclination angles, and confining pressures are conducted on the ellipse-shaped steel rod assembly. The DEM models are validated by comparing the stress-strain relationship, strength, and deformation pattern of experiments and simulations. On this basis, three different boundary conditions are applied to investigate the boundary effects on the macrodeformation, strain localization, and the nonuniformity of stress distribution inside the specimen. The main conclusions can be summarized as follows.

(1) The stress-strain relationship and strength measured by the force on the wall are significantly dependent on the boundary conditions. The peak friction angle obtained under rigid boundary is higher than that under flexible boundary.

(2) The boundary condition has minor effects on the mechanical behavior of particle assembly inside

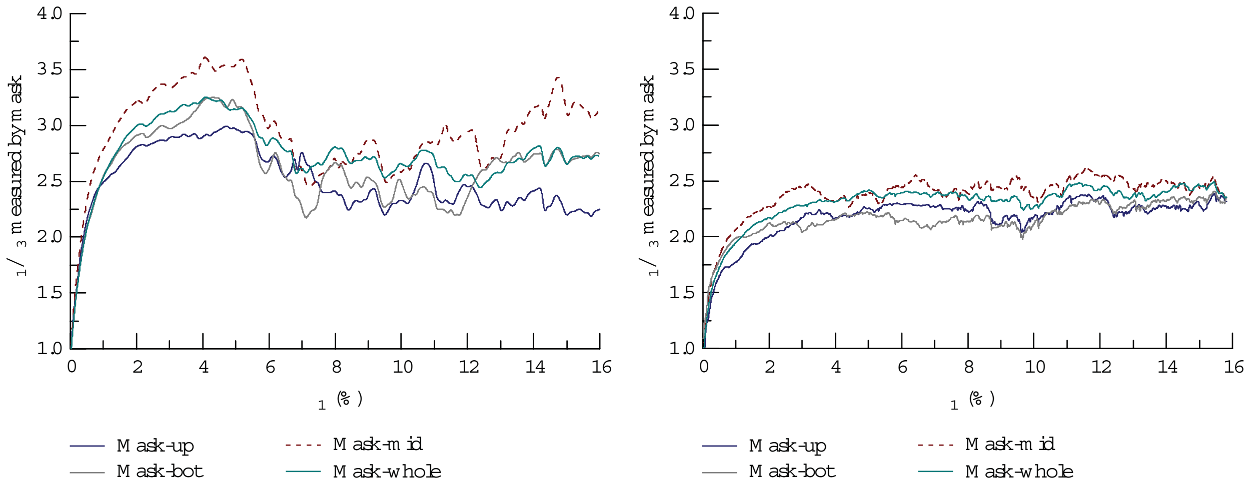

(a) (b)

FIGURE 15: The evolution of stress ratio σ_1/σ_3 measured in different masks with axial strain ε_1 under Rigid boundary B: (a) $\delta = 0^\circ$ and (b) $\delta = 90^\circ$.

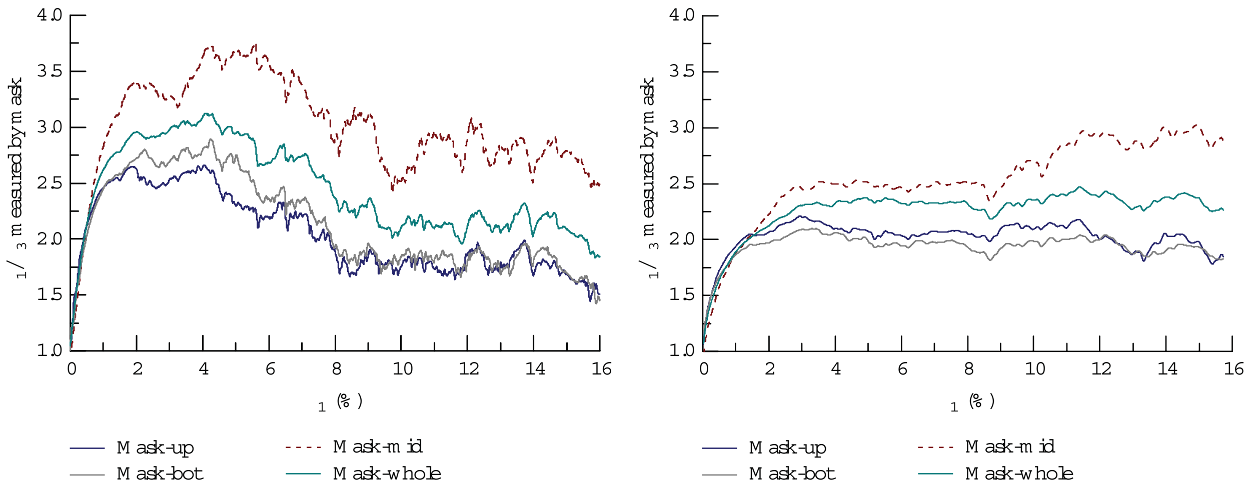

(a) (b)

FIGURE 16: The evolution of stress ratio σ_1/σ_3 measured in different masks with axial strain ε_1 under Flexible boundary: (a) $\delta = 0^\circ$ and (b) $\delta = 90^\circ$.

the specimen. The peak friction angle obtained under flexible boundary is the closest to the real friction angle of granular materials.

(3) The strain localization pattern of granular materials with inherent fabric anisotropy is dictated by the boundary condition and the bedding plane inclination angle. Under the rigid boundary conditions, various types of shear planes are observed for different loading directions.

(4) The boundary condition affects the stress distribution inside the specimen. The degree of stress nonuniformity under flexible boundary is higher than that under rigid boundary due to the weak lateral constrains under flexible boundary.

Acknowledgments

The present work is financially supported by the Beijing Natural Science Foundation (Contract no. 8133053) and the National Natural Science Foundation of China (Contract nos. 51079075 and 51009002).

References

[1] M. Oda and I. Koishikawa, "Effect of strength anisotropy on bearing capacity of shallow footing in a dense sand," *Soils and Foundations*, vol. 19, no. 3, pp. 15–28, 1979.

[2] G. G. Meyerhof, "Bearing capacity of anisotropic cohesionless soils," *Canadian Geotechnical Journal*, vol. 15, no. 4, pp. 592–595, 1978.

[3] A. Azami, S. Pietruszczak, and P. Guo, "Bearing capacity of shallow foundations in transversely isotropic granular media," *International Journal for Numerical and Analytical Methods in Geomechanics*, vol. 34, no. 8, pp. 771–793, 2010.

[4] W. F. Chen, N. Snitbhan, and H. Y. Fang, "Stability of slopes in anisotropic, nonhomogeneous soils," *Canadian Geotechnical Journal*, vol. 12, no. 1, pp. 146–152, 1975.

[5] A. A. Al-Karni and M. A. Al-Shamrani, "Study of the effect of soil anisotropy on slope stability using method of slices," *Computers and Geotechnics*, vol. 26, no. 2, pp. 83–103, 2000.

[6] M. Oda, I. Koishikawa, and T. Higuchi, "Experimental study of anisotropic shear strength of sand by plane strain test," *Soils and Foundations*, vol. 18, no. 1, pp. 25–38, 1978.

[7] W. K. Lam and F. Tatsuoka, "Effects of initial anisotropic fabric and σ_2 on strength and deformation characteristics of sand," *Soils and Foundations*, vol. 28, no. 1, pp. 89–106, 1988.

[8] P. J. Gou, "Modified direct shear test for anisotropic strength of sand," *Journal of Geotechnical and Geoenvironmental Engineering*, vol. 134, no. 9, pp. 1311–1318, 2008.

[9] A. Mahmood and J. K. Mitchell, "Fabric-property relationships in fine granular materials," *Clays and Minerals*, vol. 22, no. 5-6, pp. 397–408, 1974.

[10] F. Tatsuoka, S. Nakamura, C. Huang, and K. Tani, "Strength anisotropy and shear band direction in plane strain tests of sand," *Soils and Foundations*, vol. 30, no. 1, pp. 35–54, 1990.

[11] T. Fumio, M. Sakamoto, T. Kawamura, and S. fukushima, "Strength and deformation characteristics of sand in plane strain compression at extremely low pressures," *Soils and Foundations*, vol. 26, no. 1, pp. 65–84, 1986.

[12] P. V. Lade, J. Nam, and W. P. Hong, "Shear banding and cross-anisotropic behavior observed in laboratory sand tests with stress rotation," *Canadian Geotechnical Journal*, vol. 45, no. 1, pp. 74–84, 2008.

[13] M. Oda and H. Kazama, "Microstructure of shear bands and its relation to the mechanisms of dilatancy and failure of dense granular soils," *Geotechnique*, vol. 48, no. 4, pp. 465–481, 1998.

[14] J. Desrues, R. Chambon, M. Mokni, and F. Mazerolle, "Void ratio evolution inside shear bands in triaxial sand specimens studied by computed tomography," *Geotechnique*, vol. 46, no. 3, pp. 529–546, 1996.

[15] M. Oda, T. Takemura, and M. Takahashi, "Microstructure in shear band observed by microfocus X-ray computed tomography," *Geotechnique*, vol. 54, no. 8, pp. 539–542, 2004.

[16] J. Desrues and G. Viggiani, "Strain localization in sand: an overview of the experimental results obtained in Grenoble using stereophotogrammetry," *International Journal for Numerical and Analytical Methods in Geomechanics*, vol. 28, no. 4, pp. 279–321, 2004.

[17] L. Zhang, *Research on failure mechanism and strength criterion of anisotropic granular materials and its application [Ph.D. thesis]*, Tsinghua Univertisy, Beijing, China, 2007 (Chinese).

[18] P. Fu and Y. F. Dafalias, "Study of anisotropic shear strength of granular materials using DEM simulation," *International Journal for Numerical and Analytical Methods in Geomechanics*, vol. 35, no. 10, pp. 1098–1126, 2011.

[19] J. Konishi, M. Oda, and S. Nemat-Nasser, "Inherent anisotropy and shear strength of assembly of oval cross-sectional rods," in *Proceedings of the Deformation and Failure of Granular Materials, International Union of Theoretical and Applied Mechanics Symposium*, pp. 403–412, A. A. Balkema, Rotterdam, The Netherlands, 1982.

[20] H. Matsuoka and H. Geka, "A stress-strain model for granular materials considering mechanism of fabric change," *Soils and Foundations*, vol. 23, no. 2, pp. 83–97, 1983.

[21] L. Cui, C. O'Sullivan, and S. O'Neill, "An analysis of the triaxial apparatus using a mixed boundary three-dimensional discrete element model," vol. 57, no. 10, pp. 831–844.

[22] P. Fu and Y. F. Dafalias, "Fabric evolution within shear bands of granular materials and its relation to critical state theory," *International Journal for Numerical and Analytical Methods in Geomechanics*, vol. 35, no. 18, pp. 1918–1948, 2011.

[23] T. T. Ng, "Shear strength of assemblies of ellipsoidal particles," *Geotechnique*, vol. 54, no. 10, pp. 659–669, 2004.

[24] C. Thornton, "Numerical simulations of deviatoric shear deformation of granular media," *Geotechnique*, vol. 50, no. 1, pp. 43–53, 2000.

[25] H. Tsunekawa and K. Iwashita, "Numerical simulation of triaxial test using two and three dimensional DEM," in *Powders and Grains*, Y. Kishino, Ed., pp. 177–182, A. A. Balkema, Rotterdam, The Netherlands, 2001.

[26] L. Cui and C. O'Sullivan, "Exploring the macro- and micro-scale response of an idealised granular material in the direct shear apparatus," *Geotechnique*, vol. 56, no. 7, pp. 455–468, 2006.

[27] S. Masson and J. Martinez, "Micromechanical analysis of the shear behavior of a granular material," *Journal of Engineering Mechanics*, vol. 127, no. 10, pp. 1007–1016, 2001.

[28] L. Zhang and C. Thornton, "A numerical examination of the direct shear test," *Geotechnique*, vol. 57, no. 4, pp. 343–354, 2007.

[29] P. Fu, O. R. Walton, and J. T. Harvey, "Polyarc discrete element for efficiently simulating arbitrarily shaped 2D particles," *International Journal for Numerical Methods in Engineering*, vol. 89, no. 5, pp. 599–617, 2012.

[30] A. A. Mirghasemi, L. Rothenburg, and E. L. Matyas, "Numerical simulations of assemblies of two dimensional polygon shaped particles and effects of confining pressure on shear strength," *Soils and Foundations*, vol. 37, no. 3, pp. 43–52, 1997.

Hindawi Publishing Corporation
Journal of Applied Mathematics
Volume 2013, Article ID 320890, 11 pages
http://dx.doi.org/10.1155/2013/320890

Research Article

Comparative Study on Interface Elements, Thin-Layer Elements, and Contact Analysis Methods in the Analysis of High Concrete-Faced Rockfill Dams

Xiao-xiang Qian, Hui-na Yuan, Quan-ming Li, and Bing-yin Zhang

State Key Laboratory of Hydroscience and Engineering, Department of Hydraulic Engineering, Tsinghua University, Beijing 100084, China

Correspondence should be addressed to Bing-yin Zhang; byzhang@tsinghua.edu.cn

Received 3 June 2013; Accepted 15 August 2013

Academic Editor: Pengcheng Fu

This paper presents a study on the numerical performance of three contact simulation methods, namely, the interface element, thin-layer element, and contact analysis methods, through the analysis of the contact behavior between the concrete face slab and the dam body of a high concrete-faced rockfill dam named Tianshengqiao-I in China. To investigate the accuracy and limitations of each method, the simulation results are compared in terms of the dam deformation, contact stress along the interface, stresses in the concrete face slab, and separation of the concrete face slab from the cushion layer. In particular, the predicted dam deformation and slab separation are compared with the in-situ observation data to classify these methods according to their agreement with the in-situ observations. It is revealed that the interface element and thin-layer element methods have their limitations in predicting contact stress, slab separation, and stresses in the concrete face slab if a large slip occurs. The contact analysis method seems to be the best choice whether the separation is finite or not.

1. Introduction

The cracking of the concrete slab is the most important factor affecting the safety of concrete-faced rockfill dams (CFRDs). Accurate computation of stress and deformation in the concrete slab are key issues for slab cracking assessment. Numerical methods can be used to predict the deformation and stress distributions in the concrete face slab, where the behavior of the interface between the concrete face slab and the cushion layer plays a significant role. Because the interface can be treated in different ways, the prediction of displacement and stress distribution around the interface may be different. This study focuses on the comparison of different interface analysis methods through the analysis of stress and displacement distributions near the interface in the Tianshengqiao-I CFRD project. The accuracy and limitations of each method are discussed.

Much attention has been paid to numerical treatment of the interfaces in geotechnical problems such as buried structures, jointed rocks, and rockfill dams [1–5]. Interface behavior often involves large relative movement or even debonding [6]. Over the past three decades, three numerical methods have been proposed for simulating the displacement jump along the interface: the interface element, thin-layer element, and contact analysis methods. The interface element method originated from the Goodman joint element approach [2–6]. The basic idea was to introduce a constitutive model for an interface of zero thickness [6]. This constitutive model may be elastic, rigid-plastic, or elastic-plastic [2, 6, 7]. As an alternative, a thin-layer element method [8] was proposed. The thin-layer element method regards joints or interfaces as conventional continuums described by solid elements. However, the material modulus for this thin layer is much lower than that for the intact solid [8–11]. This thin-layer element method has been successfully applied to jointed rock masses [10], buried pipes [8], and the interaction of foundation and soil masses [9, 11]. Either the interface element or thin-layer element is limited to small deformation. Different from the previous two numerical methods, the contact analysis method was proposed to simulate the contact behaviors between the concrete face slab and the cushion layer in the Tianshengqiao-I concrete-faced rockfill dam [12]. In this contact analysis method, the concrete face slab and dam body were regarded as two independent deformable bodies, and the contact interface was treated using contact mechanics [13]. This method allows large relative displacements between the concrete face slab and cushion layer. The physical and mechanical properties of the interface can also be nonlinear or elastic-plastic. In the contact analysis method, the detection of the contact is the key issue. Zhang et al. [12] proposed a local contact detection method at the element level, where the search is localized between two elements and thus needs less time. However, the accuracy of this contact detection method is not acceptable when the mapping function for element geometry is not identical to that for displacement interpolation and when the deformation is large. In this paper, a global contact search method is proposed based on a radial point interpolation method [14, 15]. The accuracy of this global search method is controllable.

In this study, the numerical performance of three numerical simulation methods, namely, the interface element, thin-layer element, and contact analysis methods is compared through stress-deformation analysis of a high concrete-faced rockfill dam. In Section 2, the fundamentals of the three methods are briefly reviewed. A global search method for contact detection is proposed based on the radial point interpolation method. In Section 3, the constitutive models for the rockfill dam body and the concrete face slab are presented. The Duncan EB model [16] is employed to describe the nonlinearity of rockfill materials, and a linear elastic model is used to describe the mechanical properties of the concrete face slab. In Section 4, the FEM models and material parameters are introduced. Section 5 compares the performance of the three numerical methods using the Tianshengqiao-I CFRD project in China as an example. The separation between the concrete face slab and the cushion layer, stresses in the concrete face slab, contact stress along the interface, displacements along the interface, and deformation of the dam body are compared using the in-situ observations available. Finally, conclusions are drawn in Section 6.

2. Fundamentals of Numerical Methods for the Interfaces

2.1. The Contact Problem. With reference to Figure 1, we consider the contact of two deformable bodies, where the problem domain Ω is divided into two subdomains Ω_1 (bounded by Γ_1) and Ω_2 (bounded by Γ_2). The bodies are fixed at $\Gamma_u = \Gamma_{1u} \cup \Gamma_{2u}$ and subjected to boundary traction t at $\Gamma_t = \Gamma_{1t} \cup \Gamma_{2t}$. Γ_{1c} and Γ_{2c} are the potential contacting boundaries of Ω_1 and Ω_2, respectively, while Γ_c denotes the exact contact part on Γ_{1c} and Γ_{2c}.

2.2. Interface Element Method. For the interface element method (Figure 2), the interface conditions are described by

$$\begin{gathered} \boldsymbol{\sigma} \cdot \mathbf{n}|_{\Gamma_{1c} \cap \Gamma_c} = \boldsymbol{\sigma} \cdot \mathbf{n}|_{\Gamma_{2c} \cap \Gamma_c} \\ [\delta \mathbf{u}] \geq 0, \end{gathered} \tag{1}$$

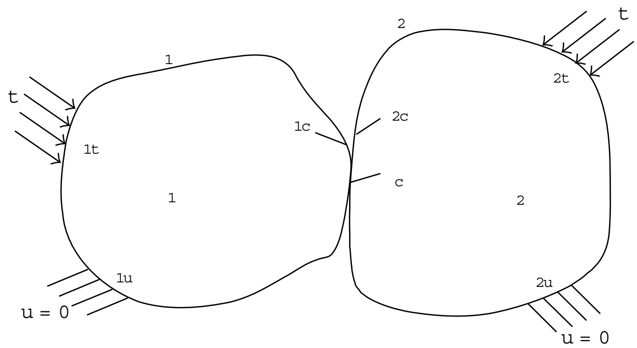

Figure 1: Contact of two deformable bodies.

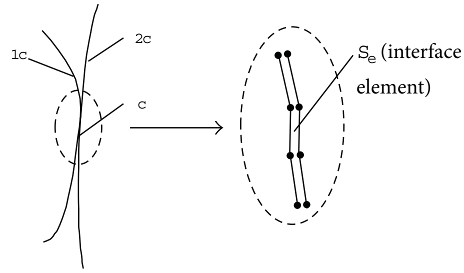

Figure 2: Interface element method.

where $\boldsymbol{\sigma}$ is the stress tensor, $\mathbf{n}$ is the outward normal, and $[\delta\mathbf{u}]$ denotes the increment of a displacement jump [2, 6]. Such a problem has the following weak form:

$$\begin{aligned} &\left\{ \int_{\Omega_1} \{\delta \boldsymbol{\varepsilon}\}^T \{\boldsymbol{\sigma}\} \, d\Omega - \int_{\Omega_1} \{\delta u\}^T \{b\} \, d\Omega - \int_{\Gamma_{1t}} \{\delta u\}^T \{t\} \, d\Gamma \right\} \\ &\quad + \left\{ \int_{\Omega_2} \{\delta \boldsymbol{\varepsilon}\}^T \{\boldsymbol{\sigma}\} \, d\Omega - \int_{\Omega_2} \{\delta u\}^T \{b\} \, d\Omega - \int_{\Gamma_{2t}} \{\delta u\}^T \{t\} \, d\Gamma \right\} \\ &\quad + \int_{\Gamma_c} \{\boldsymbol{\sigma}\} [\delta \mathbf{u}] \, d\Gamma = 0, \end{aligned} \tag{2}$$

where $\boldsymbol{\varepsilon}$ is the strain tensor, u is the displacement, b is the body force, and t is the boundary traction. This weak form is composed of three terms:

$$\pi_1 + \pi_2 + \pi_{\text{interface}} = 0, \tag{3}$$

where π_1 denotes the terms in the first bracket to express the potential in Ω_1, π_2 denotes the terms in the second bracket to express the potential in Ω_2, and $\pi_{\text{interface}}$ denotes the last term to express the potential along the interface Γ_c. On discretizing the interface term $\pi_{\text{interface}}$, the element stiffness is obtained as

$$K_{\text{in}}^e = \int_{S_e} T^T N_u^T \left[\overline{D}\right]_{ep} N_u T \, dS, \tag{4}$$

where T and N_u are the transformation matrix and shape function of the interface element S_e. The material matrix

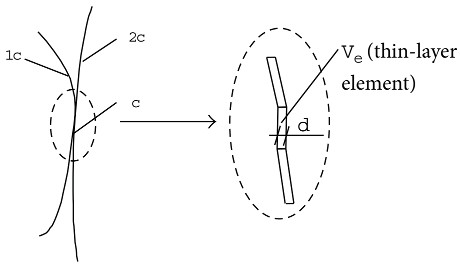

FIGURE 3: Thin-layer element method.

$[\overline{D}]_{ep}$ is defined using the following constitutive law of an interface [6]:

$$\begin{Bmatrix} \Delta\sigma_n \\ \Delta\tau \end{Bmatrix} = \left[\overline{D}\right]_{ep} \begin{Bmatrix} [\Delta u_n] \\ [\Delta u_s] \end{Bmatrix}, \qquad \left[\overline{D}\right]_{ep} = \begin{bmatrix} k_n & k_{ns} \\ k_{sn} & k_s \end{bmatrix}, \tag{5}$$

where σ_n, τ are the normal and shear stresses, u_n, u_s are the normal and shear displacements, k_n, k_s are the normal and shear stiffness, and k_{sn}, k_{ns} are the coupling stiffnesses between normal and shear deformations.

Goodman et al. [2] did not consider the coupling effect between normal and shear deformations. They took the material matrix as

$$\left[\overline{D}\right]_{ep} = \begin{bmatrix} k_n & 0 \\ 0 & k_s \end{bmatrix} \tag{6}$$

and the shear stiffness k_s as

$$k_s = k_1 \gamma_w \left(\frac{\sigma_n}{P_a}\right)^{n_1} \left(1 - \frac{R_{f1}\tau}{\sigma_n tg\phi}\right)^2, \tag{7}$$

where k_1 and n_1 are two parameters, σ_n is the normal stress on the interface, τ is the shear stress along the interface, P_a is the atmospheric pressure, γ_w is the unit weight of water, R_{f1} is the failure ratio, and ϕ is the angle of internal friction. k_1, n_1, R_{f1}, and ϕ are the four parameters to be determined from direct shear tests. The normal stiffness k_n is usually given a large number when the interface element is in compression and a small number when in tension.

2.3. Thin-Layer Element Method. In this method, an interface is treated as a thin-layer solid element (Figure 3). This thin layer is given a relatively low modulus and can experience large deformation [8–11]. The problem shown in Figure 1 with a thin layer has the following weak form:

$$\pi_1 + \pi_2 + \pi_{\text{thin}} = 0, \tag{8}$$

where the term on the thin layer, π_{thin}, is given by

$$\pi_{\text{thin}} = \int_{V_L} \{\delta\boldsymbol{\varepsilon}\}^T \{\boldsymbol{\sigma}\}\, dV, \tag{9}$$

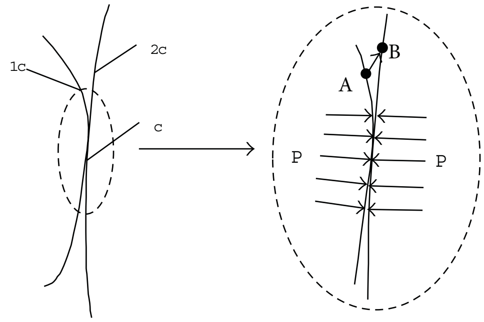

FIGURE 4: Contact analysis method.

with V_L denoting the domain of interface Γ_c. If V_L has a finite thickness of d, the element stiffness of thin layer element V_e is

$$K^e_{\text{th}} = \int_{V_e} B^T DB\, dV \underset{d \ll S_e}{\cong} d \int_{S_e} B^T DB\, dS, \tag{10}$$

where B is the strain matrix, D is the material matrix, and S_e is the element length. Previous studies revealed that the accuracy of element stiffness is sensitive to the aspect ratio d/S_e. When the aspect ratio varies in the range of 0.01–0.1, slippage is modeled quite accurately [8–11].

2.4. Contact Analysis Method

2.4.1. Contact of Two Deformable Bodies. As shown in Figure 4, the potential contact boundaries are Γ_{1c} in Γ_1 and Γ_{2c} in Γ_2, while the exact contact boundary is denoted as interface Γ_c, which is usually unknown beforehand. The weak form of each deformable body is expressed individually as follows.

For deformable body Ω_1

$$\left\{\int_{\Omega_1} \{\delta\boldsymbol{\varepsilon}\}^T \{\boldsymbol{\sigma}\}\, d\Omega - \int_{\Omega_1} \{\delta u\}^T \{b\}\, d\Omega - \int_{\Gamma_{1t}} \{\delta u\}^T \{t\}\, d\Gamma\right\} - \int_{\Gamma_c} \{\delta u\}^T \{P\}\, d\Gamma = 0. \tag{11}$$

For deformable body Ω_2

$$\left\{\int_{\Omega_2} \{\delta\boldsymbol{\varepsilon}\}^T \{\boldsymbol{\sigma}\}\, d\Omega - \int_{\Omega_2} \{\delta u\}^T \{b\}\, d\Omega - \int_{\Gamma_{2t}} \{\delta u\}^T \{t\}\, d\Gamma\right\} - \int_{\Gamma_c} \{\delta u\}^T \{P\}\, d\Gamma = 0, \tag{12}$$

where $\{P\}$ is the interaction force. Upon discretizing the weak forms in (11) and (12), the following discrete system equation is obtained for each deformable body:

$$K_{11}u_1 + K_{12}u_{12} + L_1 P = f_1 \quad \text{for } \Omega_1, \tag{13}$$

$$K_{22}u_2 + K_{21}u_{21} + L_2 P = f_2 \quad \text{for } \Omega_2, \tag{14}$$

where u_1 and u_2 are the displacement increments in Ω_1 and Ω_2 whose boundaries exclude the exact contact boundary, u_{12} is the displacement increment along Γ_{1c}, u_{21} is the displacement increment along Γ_{2c}, and P is the interaction force along the contact interface Γ_c. It can be proved that P is equivalent to the Lagrange multiplier [17, 18].

When the two bodies are not in contact, one body imposes no constraints on the other, and thus (13) and (14) are independent of each other and $P \equiv 0$. The displacement increments u_1 and u_{12} are solved using (13), while u_2 and u_{21} are determined by (14).

When the two bodies are in contact, one deformable body imposes constraints on the other. At this time, u_{12} and u_{21} are no longer independent, and P is introduced as an unknown. The contact boundary should satisfy the kinematic and dynamic constraints. As shown in Figure 4, if point A on Γ_{1c} coincides with point B on Γ_{2c}, the kinematic constraint is expressed as [12]

$$\left(u_{12}^{\mathrm{A}} - u_{21}^{\mathrm{B}}\right)\eta \leq \mathrm{TOL}, \tag{15}$$

where η is the directional cosine at the contact point and TOL is the closure distance or contact tolerance. The dynamic condition is Coulomb's friction law in our computation:

$$P_t \leq -\mu \cdot P_n \cdot \eta_t, \tag{16}$$

where P_t is the tangential friction traction force, P_n is the normal traction force, μ is the friction coefficient, and η_t is the tangential vector in the direction of relative velocity. Therefore, the unknowns u_1, u_{12}, u_2, u_{21}, P, and Γ_c can be completely solved from (13)–(16).

2.4.2. Strategy of Searching Contact Points. The contact interface Γ_c is the key unknown in the contact problem. Zhang et al. [12] used a typical node-edge contact mode to implement contact detection at the element level. The disadvantage of this node-edge contact mode is that the accuracy is low. This study uses curve fitting; that is, the point interpolation method [14, 15], to detect the exact contact interface Γ_c. The numerical procedure is as follows.

Step 1. Assume potential contact interfaces Γ_{1c} on Ω_1 and Γ_{2c} on Ω_2.

Step 2. Locate the nodal points on the interfaces Γ_{1c} and Γ_{2c}. There are M nodes on Γ_{1c}, denoted by $x_{11}, x_{12}, \ldots, x_{1i}, \ldots, x_{1M}$ and N nodes on Γ_{2c}, denoted by $x_{21}, x_{22}, \ldots, x_{2i}, \ldots, x_{2N}$.

Step 3. Interpolate these nodes to form the boundary lines using the radial point interpolation method [14, 15].

One has

$$x = \sum_{i=1}^{M} N_{1i} x_{1i}, \qquad x = \sum_{j=1}^{N} N_{2j} x_{2j}, \tag{17}$$

where the shape functions N_{1i}, N_{2j} are determined using point interpolation methods [14, 15].

Step 4. Establish the distance function δ along either boundary line. The point is not in contact when $\delta > \mathrm{TOL}$. Otherwise, the point is in contact with the other boundary. Identify the exact contact points through (17). Iterate the same procedure to find out the entire contact boundary.

Step 5. Iterate FEM computation to satisfy the equilibrium of two deformable bodies and the contact boundary conditions.

Step 6. Update nodal coordinates on the contact boundary. Carry out the next step computation, and return to Step 3 for the same search procedure for the contact points.

3. Constitutive Models for Dam Materials

3.1. EB Model for Rockfill Materials. Rockfill materials and soil masses behave with strong nonlinearity because of the high stress levels in dams. This nonlinearity is described by the following incremental Hooke's law:

$$\begin{aligned}\begin{Bmatrix} d\sigma_x \\ d\sigma_y \\ d\tau_{xy} \end{Bmatrix} &= [D] \begin{Bmatrix} d\varepsilon_x \\ d\varepsilon_y \\ d\gamma_{xy} \end{Bmatrix} \\ &= \begin{bmatrix} B_t + \frac{4}{3}G_t & B_t - \frac{2}{3}G_t & 0 \\ B_t - \frac{2}{3}G_t & B_t + \frac{4}{3}G_t & 0 \\ 0 & 0 & 2G_t \end{bmatrix} \begin{Bmatrix} d\varepsilon_x \\ d\varepsilon_y \\ d\gamma_{xy} \end{Bmatrix},\end{aligned} \tag{18}$$

where B_t is the bulk modulus, $G_t = 3B_tE_t/(9B_t - E_t)$ is the shear modulus, and E_t is the deformation modulus. The Duncan EB model [16] gives the deformation modulus E_t as follows:

$$E_t = k \cdot P_a \left(\frac{\sigma_3}{P_a}\right)^n \left[1 - R_f \frac{(1 - \sin\phi)(\sigma_1 - \sigma_3)}{2c \cdot \cos\phi + 2\sigma_3 \sin\phi}\right]^2, \tag{19}$$

where $(\sigma_1 - \sigma_3)$ is the deviatoric stress, σ_3 is the confining pressure, c is the cohesion intercept, ϕ is the angle of internal friction, R_f is the failure ratio, P_a is the atmospheric pressure, and k and n are constants.

In the computation, the rockfill material has $c = 0$ and a variable angle of internal friction ϕ

$$\phi = \phi_0 - \Delta\phi \log\left(\frac{\sigma_3}{P_a}\right), \tag{20}$$

where ϕ_0 and $\Delta\phi$ are two constants. Another parameter, bulk modulus B_t, is assumed to be

$$B_t = k_b P_a \left(\frac{\sigma_3}{P_a}\right)^m, \tag{21}$$

where k_b and m are constants.

3.2. Linear Elastic Model for the Concrete Face Slab. A linear elastic model with Young's modulus E and Poisson ratio ν is used to describe the mechanical properties of the concrete face slab. No failure is allowed.

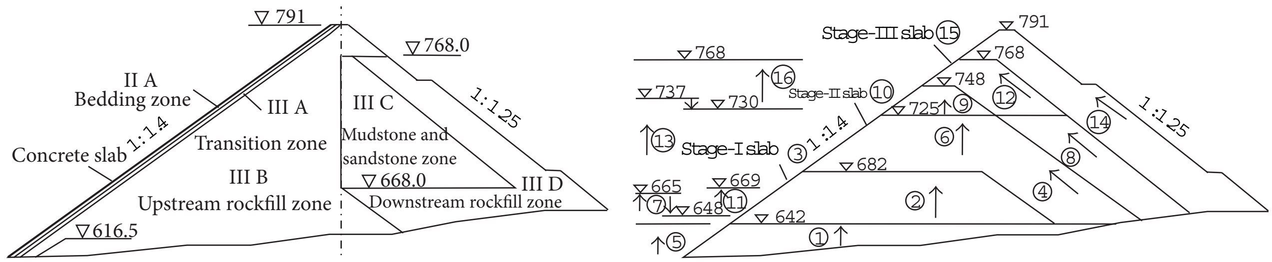

(a) Material zoning (b) Construction stages

Figure 5: Material zones and construction stages of Tianshengqiao-I CFRD.

Table 1: Design parameters of dam materials.

Mat. number	Mat. description	Max. particle size (cm)	Dry unit weight (KN/m^3)	Void ratio (%)
IIA	Processed limestone	8	22.0	19
IIIA	Limestone	30	21.5	21
IIIB	Limestone	80	21.2	22
IIIC	Mudstone and sandstone	80	21.5	22
IIID	Limestone	160	20.5	24

4. Computation Models and Parameters

4.1. Tianshengqiao-I Concrete-Faced Rockfill Dam Project. The Tianshengqiao-I hydropower project is on the Nanpan River in southwestern China [12]. Its water retaining structure is a concrete-faced rockfill dam, 178 m high and 1104 m long. The rockfill volume of the dam body is about 18 million m^3, and the area of the concrete face is 173,000 m^2. A surface chute spillway on the right bank allows a maximum discharge of 19,450 m^3/s. The tunnel in the right abutment is used for emptying the reservoir during operation. The left abutment has four power tunnels and a surface powerhouse with a total capacity of 1,200 MW. Material zoning and construction stages are shown in Figure 5. The design parameters of the dam materials are listed in Table 1, and the details of each construction stage are given in Table 2.

Table 2: Construction stages and time.

Filling step	Time	Remark
①	1996.01–1996.06	Fill dam body
②	1996.07–1997.02	Fill dam body
③	1997.03–1997.05	Cast Phase 1 concrete slab
④ and ⑥	1997.02–1997.10	Fill dam body
⑤	1997.05-1997.05	Water level rises
⑦	1997.06–1997.10	Water level fluctuation
⑧ and ⑨	1997.11–1998.01	Fill dam body
⑩	1997.12–1998.05	Cast Phase 2 concrete slab
⑪	1997.11-1997.12	Water level rises
⑫	1998.02–1998.08	Fill dam body
⑬	1998.06-1998.07	Water level rises
⑭	1998.08–1999.01	Fill dam body
⑮	1999.01–1999.05	Cast Phase 3 concrete slab
⑯	1999.06–1999.09	Store water

4.2. Computation Section, Procedure, and Material Parameters. A two-dimensional finite element analysis was performed [19]. The maximum cross-section (section 0 + 630 m), which is in the middle of the riverbed, was taken for computation. Figure 6(a) shows the finite element mesh for the contact analysis method. It has a total of 402 four-node elements in the dam body and 46 four-node elements in the concrete face slab (the concrete face slab is divided into two layers of elements). The mesh for the interface element method is shown in Figure 6(b), where a row of interface elements is placed along the interface between the concrete face slab and the cushion layer. This mesh model has 23 additional interface elements compared to the mesh for the contact analysis model. If the interface elements in Figure 6(b) are assigned a thickness of 0.3 m, the finite element mesh for the thin-layer element method is obtained. Because the length of each element is 12 m, the thin-layer elements have an aspect ratio of 0.025, in the range of 0.01–0.1 [8–11]. The previous mesh models show that the dam body and concrete face slab can be meshed independently for the contact analysis method. This may produce nonmatching nodes on both sides of the interface [15]. However, the thin-layer element and interface element methods usually require matching nodes on both sides of the interface. This model sets zero displacements along the rock base [12].

The computational procedure follows exactly the construction stages shown in Figure 5(b). First, blocks ① and ② of the dam body were built up to El.682 m. In each block, layer-by-layer elements were activated to simulate the construction process, and the midpoint stiffness [20] was used for the nonlinear constitutive model. Before placement

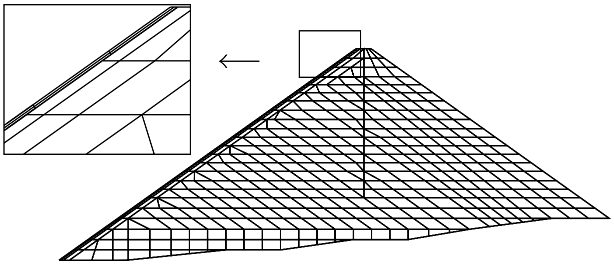

(a) For the contact analysis method

(b) For the interface element method

Figure 6: Two-dimensional finite element mesh.

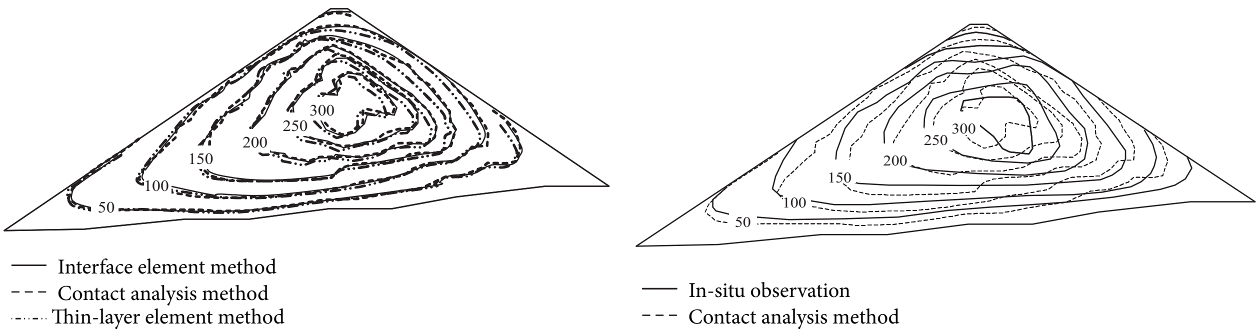

(a) Comparison of the interface element, contact analysis, and thin-layer element methods

(b) Comparison of the contact analysis method and in-situ observation

Figure 7: Contours of settlement in the dam body in August 1999 (unit: cm).

of the freshly cast stage-I slab, the calculated displacements of the dam body were set to zero, and the calculated stresses were retained. The elements of stage-I slab ③ were then activated, and dam construction continued. The impounding process was simulated by increasing the water level by 10 m in each increment. The same procedure was repeated until completion of the whole dam body.

The concrete face slab had an elastic modulus of 3×10^4 MPa and a Poisson's ratio of 0.2. Table 3 gives the computational parameters of the rockfill materials for the EB model. An elastic modulus of 6 MPa and Poisson's ratio of 0.2 were used for the materials in the thin-layer elements. The computational parameters for the Goodman interface model are listed in Table 4.

5. Comparison of the Three Methods

5.1. Deformation of the Dam Body in August 1999. The deformation of the dam body in August 1999 (water level: 768 m) was predicted by the previous three numerical methods. Figure 7 compares the contours of the predicted settlement using these numerical methods with in-situ observations. The in-situ observation data used in this study were provided by the HydroChina Kunming Engineering Corporation [21]. Horizontal displacements were measured using indium steel wire alignment horizontal displacement meters, and settlements were measured using water level settlement gauges. As shown in Figure 7, the three numerical methods provided almost identical results and agreed reasonably with the in-situ observation data.

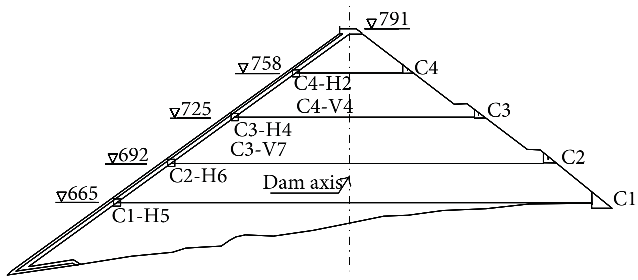

Figure 8: In-situ observation points along the interface at 0 + 630 section.

Figure 8 shows the locations of the observation points along the interface, where C1-H5, C2-H6, C3-H4, and C4-H2 are the horizontal displacement measurement points and C3-V7 and C4-V4 are the settlement measurement points. The settlement-time curves and horizontal displacement-time curves at typical observation points are displayed in Figures 9 and 10, respectively. The in-situ observations are also plotted for comparison. The three numerical methods predicted almost the same settlements and were in reasonable agreement with the in-situ observations. The horizontal displacements predicted by the three numerical methods were also similar and agreed reasonably with the in-situ observations.

5.2. Separation of the Concrete Face Slab from the Cushion Layer. Figures 11 and 12 show the separation of the concrete

Table 3: Computational parameters for the rockfill materials.

Mat. number	Density (kg/m^3)	ϕ' [°]	$\Delta\phi$ [°]	k	n	R_f	k_b	m
IIA	2200	50.6	7.0	1000	0.35	0.71	450	0.24
IIIA	2100	52.5	8.0	900	0.36	0.76	400	0.19
IIIB	2100	51.0	13.0	564	0.35	0.85	204	0.18
IIID	2050	51.0	13.5	432	0.30	0.80	300	−0.18
IIIC	2150	45.0	10.0	250	0.25	0.73	125	0.00

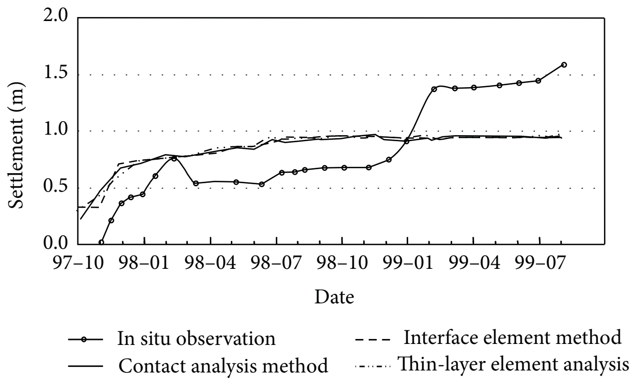

(a) C3-V7 point

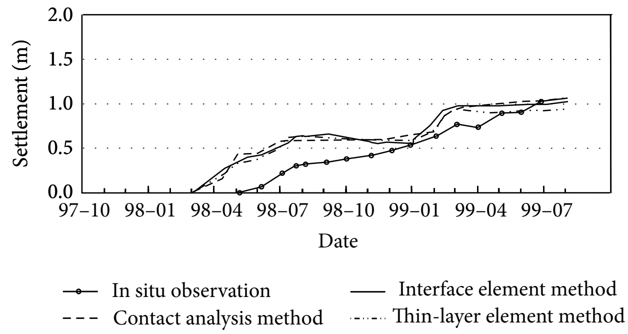

(b) C4-V4 point

Figure 9: Settlement of the dam body along the interface.

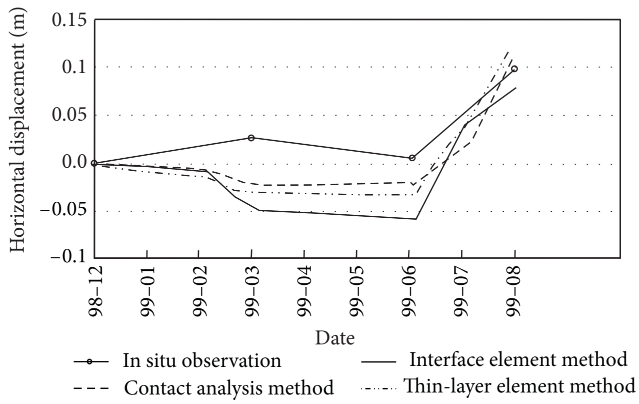

(a) C1-H5 point

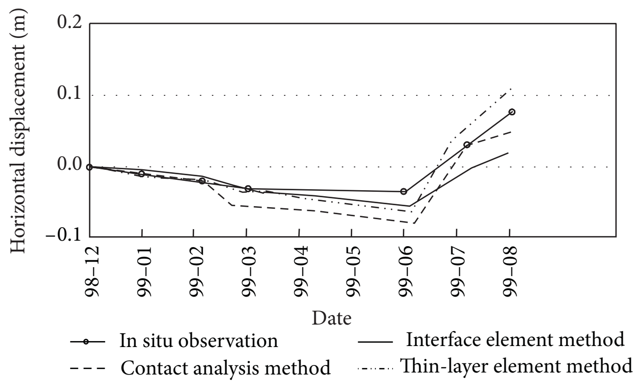

(b) C2-H6 point

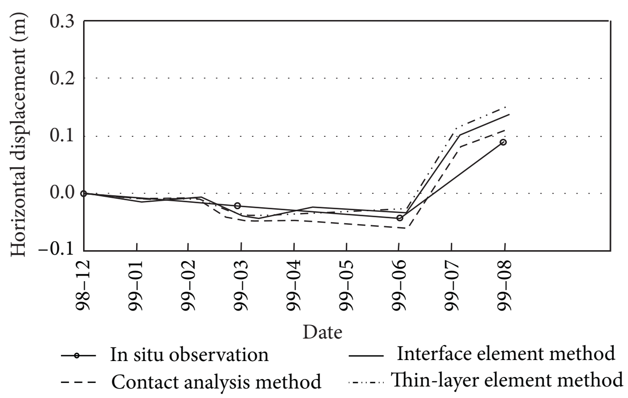

(c) C3-H4 point

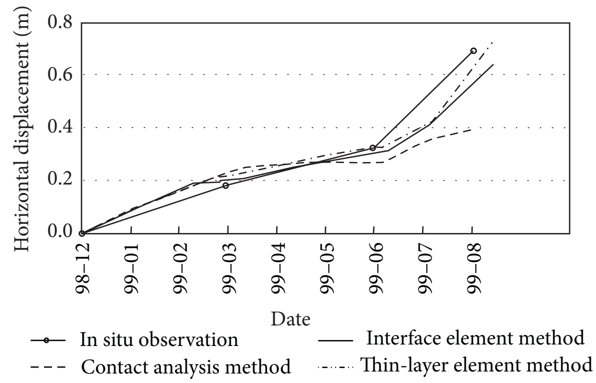

(d) C4-H2 point

Figure 10: Horizontal displacement of the dam body along the interface.

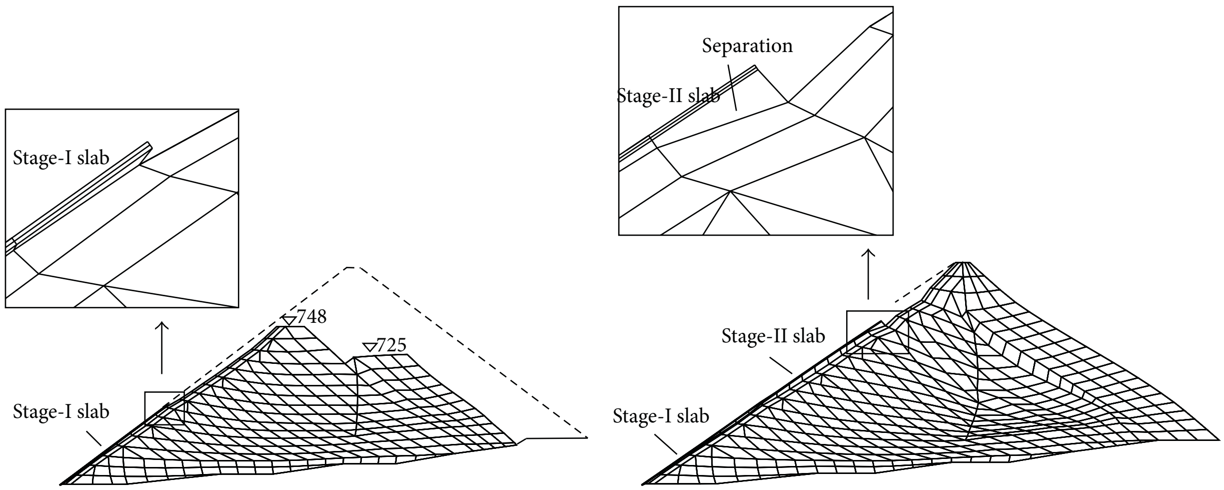

(a) Separation of the stage-I slab

(b) Separation of the stage-II slab

Figure 11: Separation of the slab from the cushion layer at different stages (interface element method).

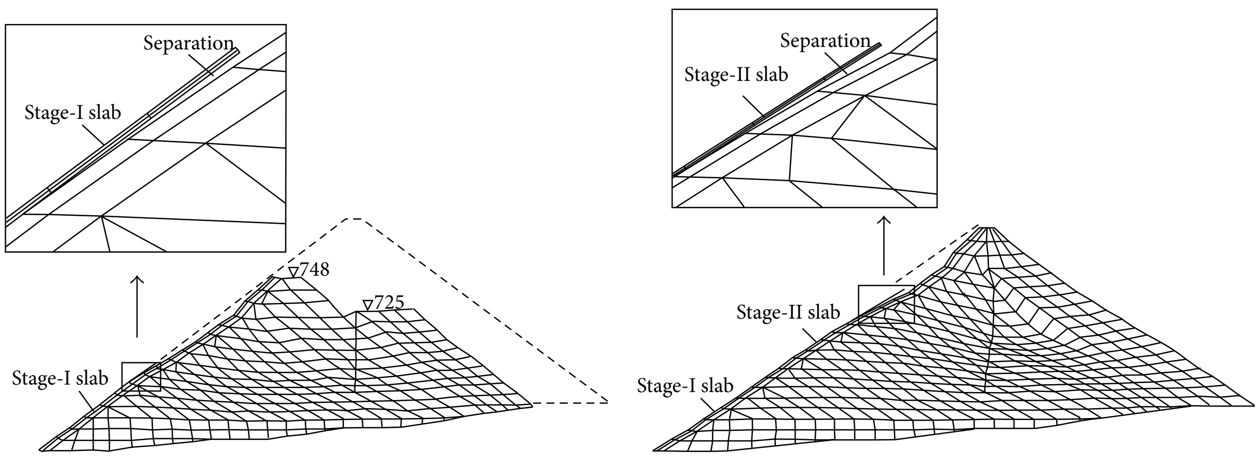

(a) Separation of the stage-I slab

(b) Separation of the stage-II slab

Figure 12: Separation of the slab from the cushion layer at different stages (contact analysis method).

Table 4: Parameters of the Goodman interface model.

ϕ [°]	k_1	n_1	R_{f1}	k_n (MPa) Compression	k_n (MPa) Tension
30	1000	0.3	1	10000	1

face slab from the cushion layer at different construction stages, predicted by the interface element and contact analysis methods, respectively. Table 5 compares the maximum opening width and depth predicted by the three numerical methods with the in-situ observations. The opening width was measured using a TSJ displacement meter, and the depth was measured manually using a ruler.

The contact analysis method predicted a maximum opening width of 0.13 m and a depth of 8.0 m for the stage-I slab, which were in good agreement with the in-situ observations. The thin-layer element and interface element methods predicted no opening for the stage-I slab. At the completion of dam body construction, the contact analysis

Table 5: Comparison of the maximum openings.

	Stage-I slab		Stage-II slab	
	Width (m)	Depth (m)	Width (m)	Depth (m)
In-situ observation	0.15	7.2	0.10	5.0
Contact analysis method	0.13	8.0	0.40	14.0
Thin-layer element method*	0	0	0.05	13.2
Interface element method*	0	0	0.08	26.4

*The depth of the tensile stress zone in the interface/thin-layer element is taken as the opening depth, and the relative displacement is taken as the opening width.

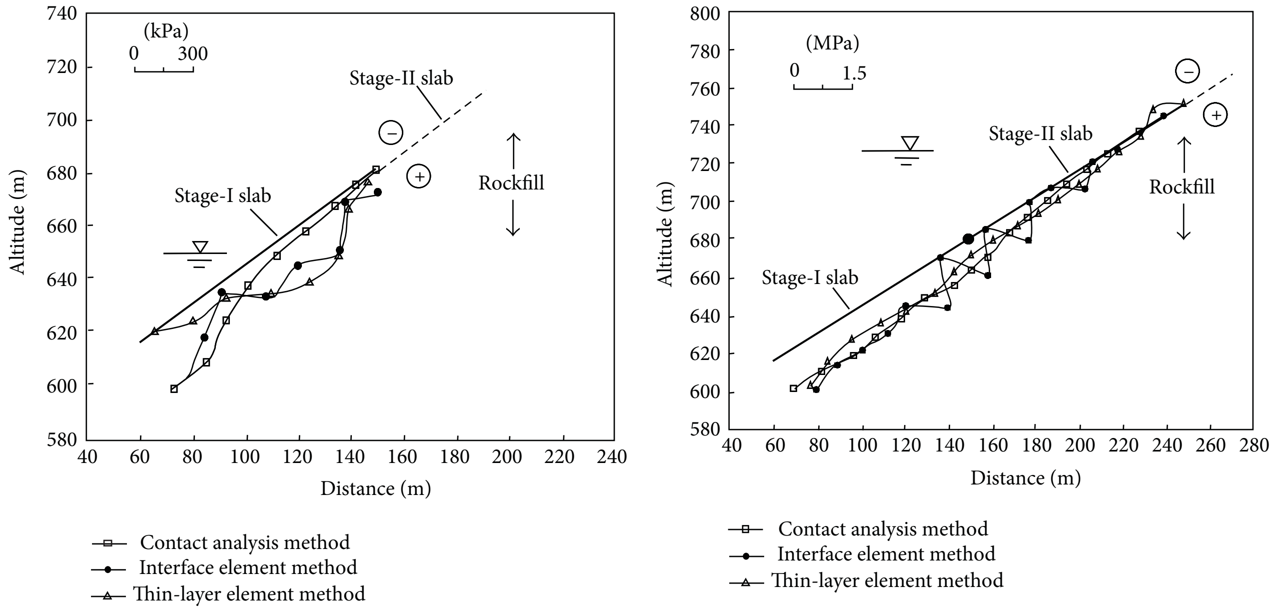

(a) Before casting the stage-II slab

(b) Completion of the dam body construction

FIGURE 13: Comparison of normal contact stress along the interface.

method predicted a maximum opening width of 0.40 m and a depth of 14.0 m for the stage-II slab, while the in-situ observations were much smaller with an opening width of 0.1 m and an opening depth of 5.0 m. The opening widths predicted using the thin-layer element and interface element methods were closer to the in-situ observations. However, the interface element method predicted a much larger opening depth.

As shown in Figure 11, the opening width and depth were mesh-size dependent for both the thin-layer element and interface element methods because they used element information to determine the separation. The opening depth was the depth of the tensile stress zone, and the opening width was the relative displacement. Therefore, the opening width and depth obtained were used only for reference. Conversely, the contact analysis method regarded the concrete face slab and dam body as independent deformable bodies, and thus the separation could be directly calculated and was independent of mesh size as shown in Figure 12. Therefore, it was concluded that the contact analysis method was reliable and accurate in the prediction of the opening width and depth. In summary, the contact analysis method was a better choice for simulating the separation (opening width and depth) of the concrete face slab from the cushion layer.

5.3. Normal Contact Stress along the Interface. The normal contact stress along the interface is compared in Figure 13 for the three numerical methods. Figure 13(a) shows the contact stress immediately before casting the stage-II slab and Figure 13(b) at the completion of dam body construction. As shown in Figure 13(a), the maximum normal stress predicted by the thin-layer element method occurs at the middle of the interface between the stage-I slab and the cushion layer, which is not reasonable because the self-weight of the stage-I slab and water pressure should produce a larger normal stress at the bottom as predicted by the contact analysis method. At this stage, the thin-layer element method failed to predict any separation. Furthermore, thin-layer element method predicted a tensile stress zone at the top of the stage-II slab after completion of the dam body construction (Figure 13(b)). Physically, no tensile stress should exist if separation of the two materials occurs. Because the thin-layer element was basically a solid element, it was unsuitable for separation simulation [9]. The interface element method predicted oscillatory normal contact stress at both stages, and the elimination of such oscillation was difficult [3, 22]. In addition, the interface element method could not predict the separation before casting the stage-II slab, and the opening depth was mesh-size dependent. Therefore, both the thin-layer element and interface element methods could not correctly compute the contact stress or the separation.

5.4. Stresses in the Concrete Face Slab. The stress distribution in the concrete face slab, which was complex because of the deflection of the concrete face slab, was important to the development of cracks. The shear and normal stresses in the concrete face slab at the completion of dam body construction predicted by the three numerical methods, are compared in Figure 14. Both normal and shear stresses predicted by the interface element method were oscillatory and nonzero at the top of the slab. The thin-layer element method predicted less oscillatory stresses; however, its normal and shear stresses were also nonzero at the top of the concrete face slab. The magnitude of the stresses predicted by the contact analysis method was much lower than the other two methods, and the normal and shear stresses were zero at the top of the slab. Moreover, the stress distributions for the concrete face slab looked reasonable.

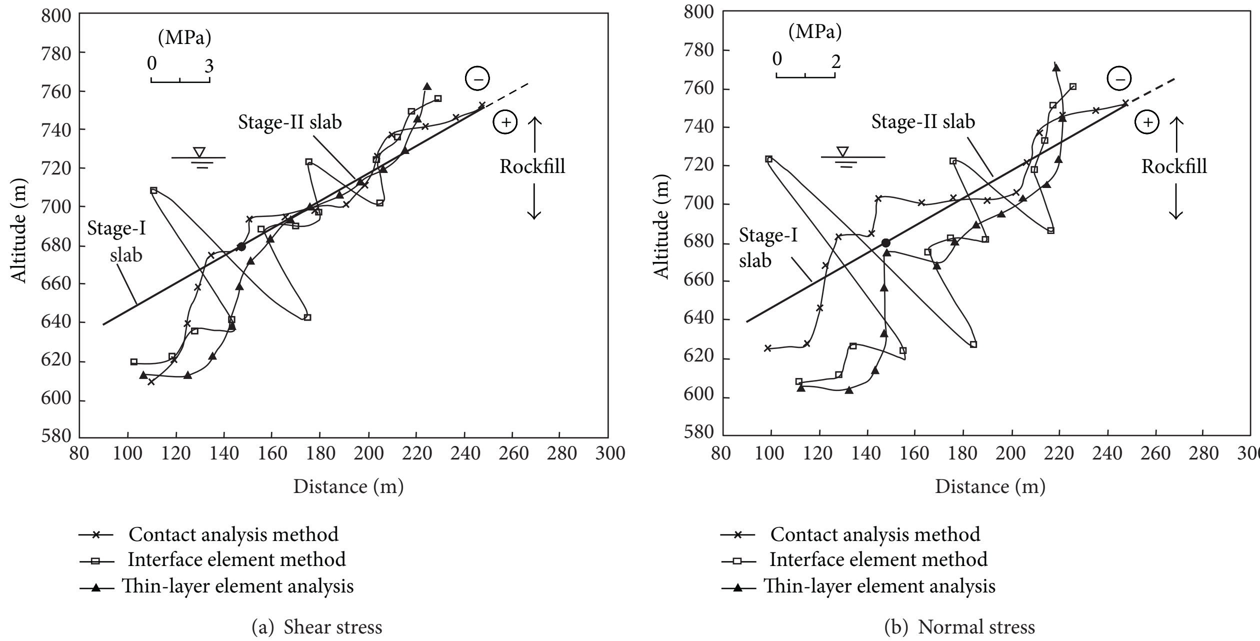

Figure 14: Comparison of stresses in the concrete face slab at completion of the dam body construction.

6. Conclusions

This study compared the interface treatments in the interface element, thin-layer element, and contact analysis methods, and their numerical performance in predicting deformation, slab separation, contact stress along the interface, and stresses in the concrete face slab in the Tianshengqiao-I concrete-faced rockfill dam, through two-dimensional finite element analysis. Numerical results were also compared with the in-situ observations available. Based on these comparisons, the following conclusions and understanding can be drawn.

First, the three numerical methods predicted almost the same settlement and similar horizontal displacement, and the predicted deformation was in good agreement with the in-situ observation data. This indicated that the Duncan EB model used can correctly describe the nonlinearity of this high concrete-faced rockfill dam.

Second, interface element method cannot correctly simulate the slab separation. The predicted normal stress along the interface, and stresses in the concrete face slab were oscillatory and not accurate enough for cracking assessment. The thin-layer element method could reasonably predict the normal stress along the interface in some circumstances. However, because solid elements were used, there were intrinsic difficulties in simulating slab separation, and this often led to inaccurate stress distribution in the concrete slab.

Third, the contact analysis method could physically and quantitatively simulate the slab separation at different construction stages of the Tianshenqiao-I high CFRD dam. The predicted opening width and depth were in reasonable agreement with the in-situ observations. The normal contact stress along the interface and the stresses in the concrete face slab were reasonable. Furthermore, because no elements were used along the interface, the contact analysis method allowed nonmatching nodes on both sides of the interface and could incorporate complex physical and geometrical properties. The stress distributions obtained could be used for the evaluation of potential cracking risk in CFRDs.

The previous discussion indicates that, for contact problems involving large separation or slipping, the contact analysis method (as the most physically realistic approach) is the best numerical method, while the interface element and thin-layer element methods (as simplified contact treatments) are not applicable. Although the performance of these two methods can be largely improved through using more sophisticated constitutive models, applying a tension cut-off criterion, or allowing node-to-node contact, their intrinsic limitations (e.g., contact description based on fixed node pairs) make it difficult for them to obtain satisfactory results for complex contact problems. However, the contact analysis method is a relatively new approach for engineering applications and further studies should be conducted to improve its computational efficiency and stability.

Acknowledgments

The authors are grateful to the HydroChina Kunming Engineering Corporation for providing the in-situ observation data. The authors would like to thank the National Basic Research Program of China no. 2010CB732103, the National Natural Science Foundation of China no. 51209118, and the State Key Laboratory of Hydroscience and Engineering no. 2012-KY-02 for financial support.

References

[1] J. B. Cook and J. L. Sherard, Eds., *Concrete Face Rockfill Dams—Design, Construction and Performance*, ASCE, New York, NY, USA, 1985.

[2] R. E. Goodman, R. L. Taylor, and T. L. Brekke, "A model for the mechanics of jointed rock," *Journal of the Soil Mechanics and Foundations Division*, vol. 94, no. 3, pp. 637–659, 1968.

[3] G. N. Pande and K. G. Sharma, "On joint/interface elements and associated problems of numerical ill-conditioning," *International Journal for Numerical and Analytical Methods in Geomechanics*, vol. 3, no. 3, pp. 293–300, 1979.

[4] G. Beer, "An isoparametric joint/interface element for finite element analysis," *International Journal for Numerical Methods in Engineering*, vol. 21, no. 4, pp. 585–600, 1985.

[5] A. Gens, I. Carol, and E. E. Alonso, "An interface element formulation for the analysis of soil-reinforcement interaction," *Computers and Geotechnics*, vol. 7, no. 1-2, pp. 133–151, 1989.

[6] J. G. Wang, Y. Ichikawa, and C. F. Leung, "A constitutive model for rock interfaces and joints," *International Journal of Rock Mechanics and Mining Sciences*, vol. 40, no. 1, pp. 41–53, 2003.

[7] K. Sekiguchi, R. K. Rowe, and K. Y. Lo, "Time step selection for 6-noded non-linear joint element in elasto-viscoplasticity analyses," *Computers and Geotechnics*, vol. 10, no. 1, pp. 33–58, 1990.

[8] C. S. Desai, M. M. Zaman, J. G. Lightner, and H. J. Siriwardane, "Thin-layer element for interfaces and joints," *International Journal for Numerical and Analytical Methods in Geomechanics*, vol. 8, no. 1, pp. 19–43, 1984.

[9] M. M. Zaman, "Evaluation of thin-layer element and modeling of interface behavior in soil-structure interaction," in *Proceedings of the 5th International Conference on Numerical Methods in Geomechanics*, pp. 1797–1803, Nagoya, Japan, 1985.

[10] O. C. Zienkiewicz, B. Best, C. Dullage, and K. G. Stagg, "Analysis of nonlinear problems in rock mechanics with particular reference to jointed rock systems," in *Proceedings of the 2nd Congress of the International Society for Rock Mechanics*, pp. 8–14, Belgrade, Serbia, 1970.

[11] D. V. Griffiths, "Numerical modeling of interfaces using conventional finite elements," in *Proceedings of the 5th International Conference on Numerical Methods in Geomechanics*, pp. 837–844, Nagoya, Japan, 1985.

[12] B. Zhang, J. G. Wang, and R. Shi, "Time-dependent deformation in high concrete-faced rockfill dam and separation between concrete face slab and cushion layer," *Computers and Geotechnics*, vol. 31, no. 7, pp. 559–573, 2004.

[13] N. Kikuchi and J. T. Oden, *Contact Problems in Elasticity: A Study of Variational Inequalities and Finite Element Methods*, vol. 8 of *SIAM Studies in Applied Mathematics*, SIAM, Philadelphia, Pa, USA, 1988.

[14] J. G. Wang and G. R. Liu, "A point interpolation meshless method based on radial basis functions," *International Journal for Numerical Methods in Engineering*, vol. 54, no. 11, pp. 1623–1648, 2002.

[15] J. G. Wang, T. Nogami, G. R. Dasari, and P. Z. Lin, "A weak coupling algorithm for seabed-wave interaction analysis," *Computer Methods in Applied Mechanics and Engineering*, vol. 193, no. 36–38, pp. 3935–3956, 2004.

[16] J. M. Duncan, P. Byrne, K. Wong, and P. Mabry, "Strength, stress-strain and bulk modulus parameters for finite element analysis of stresses and movements in soil masses," Tech. Rep. UCB/GT/80-01, University of California, Berkeley, Calif, USA, 1980.

[17] K. C. Park, C. A. Felippa, and G. Rebel, "A simple algorithm for localized construction of non-matching structural interfaces," *International Journal for Numerical Methods in Engineering*, vol. 53, no. 9, pp. 2117–2142, 2002.

[18] J.-H. Heegaard and A. Curnier, "An augmented Lagrangian method for discrete large-slip contact problems," *International Journal for Numerical Methods in Engineering*, vol. 36, no. 4, pp. 569–593, 1993.

[19] O. C. Zienkiewicz and R. L. Taylor, *The Finite Element Method: Volume 1: The Basis*, Butterworth-Heinemann, Oxford, UK, 5th edition, 2000.

[20] A. Corigliano and U. Perego, "Generalized midpoint finite element dynamic analysis of elastoplastic systems," *International Journal for Numerical Methods in Engineering*, vol. 36, no. 3, pp. 361–383, 1993.

[21] HydroChina Kunming Engineering Corporation, *Tianshengqiao-I Hydropower Project Engineering Safety Assessment: Analysis of Monitoring Data*, HydroChina Kunming Engineering Corporation, Kunming, China, 2000.

[22] J. C. J. Schellekens and R. de Borst, "On the numerical integrations of interface elements," *International Journal for Numerical Methods in Engineering*, vol. 36, no. 1, pp. 43–66, 1993.

Hindawi Publishing Corporation
Journal of Applied Mathematics
Volume 2013, Article ID 135467, 9 pages
http://dx.doi.org/10.1155/2013/135467

Research Article

Numerical Simulation and Optimization of Hole Spacing for Cement Grouting in Rocks

Ping Fu, Jinjie Zhang, Zhanqing Xing, and Xiaodong Yang

China Institute of Water Resources and Hydropower Research, Beijing 100038, China

Correspondence should be addressed to Ping Fu; fuping@iwhr.com

Received 30 July 2013; Accepted 25 August 2013

Academic Editor: Ga Zhang

The fine fissures of V-diabase were the main stratigraphic that affected the effectiveness of foundation grout curtain in Dagang Mountain Hydropower Station. Thus, specialized in situ grouting tests were conducted to determine reasonable hole spacing and other parameters. Considering time variation of the rheological parameters of grout, variation of grouting pressure gradient, and evolution law of the fracture opening, numerical simulations were performed on the diffusion process of cement grouting in the fissures of the rock mass. The distribution of permeability after grouting was obtained on the basis of analysis results, and the grouting hole spacing was discussed based on the reliability analysis. A probability of optimization along with a finer optimization precision as 0.1 m could be adopted when compared with the accuracy of 0.5 m that is commonly used. The results could provide a useful reference for choosing reasonable grouting hole spacing in similar projects.

1. Introduction

The Dagang Mountain Hydropower Station, located in Shimian county of Ya'an City, is the 14th cascade hydropower station in the main stream of the Dadu River in Sichuan province. grout curtain is more than 450,000 meters in length, and the main rock for grouting is granite. Parts of the grout curtain passed through complex geological conditions, containing V-diabase dikes, slightly fractured and contacted with granite in fault type. This may have a significant influence on the local grout curtain. Therefore, in situ curtain grouting tests were conducted to determine the reasonable hole spacing and other parameters in the curtain grouting.

The grout diffuses from the grouting hole to the rock cracks under grouting pressure in the batholith. The distance between the neighboring grouting holes is determined by the diffusion distance of the grout, which is also the most important reference for selecting the other technical parameters and for evaluating the effect of the grouting. Due to the complex and volatile characteristics of rock mass and the hidden diffusion grouting process, it is difficult to monitor the diffusion process during the construction. Moreover, the previous theoretical and empirical formulas for calculating the diffusion distance of grout were far from mature. Thus, the hole spacing is usually selected on the basis of engineering experiences among several limited numbers with the accuracy of 0.5 m, namely, 1.5 m, 2 m, 2.5 m, and 3 m. With the development of computation techniques, the numerical simulation methods were used to calculate the grouting process with the focus on the grouting technology [1–6]. The flow formula of Bingham slurry in one-dimensional horizontal fissure has been conducted, and the stiff plug in the centre of the flow was considered as one of the grouting stop criteria by Xiaodong in 1987 [7]. The diffusion equation based on the continuity equation and equilibrium equation has been conducted in recent years [8–14]. Serialized studies have been conducted on the grouting using the numerical simulation. However, these researches placed their emphasis on the calculation of the diffusion radius for single grouting fissure. In other words, they failed to consider the time variability of rheological parameters of cement grout, the fracture opening changes, and the precipitation law and the consolidation law of cement grout. There was not quantitative analysis to evaluate the effect of the grouting in the multifractured rock mass. Therefore, it is difficult to establish the macroscopical relationship between the grout diffusion radius (grouting hole spacing) and the effect of the grouting. The analysis results were still far away from the engineering requirements.

In this paper, a fracture network of rock mass was established for dual medium grouting by Monte Carlo random method. The finite element analysis was conducted for the diffusion process in the fissure and the permeability of rock mass after grouting. The grouting hole was accordingly optimized and evaluated on the basis of analysis results. The analysis was performed based on the diffusion motion equation of cement grout in a single fracture, with full consideration of various factors such as the time variability of rheological parameters of cement grout, the opening change and the fissure cracking in the grouting process, and the precipitation of cement particles.

2. Diffusion Equations of Cement Grout in the Single Fracture

2.1. Diffusion Equation. Cement grout in rock mass is essentially a two-phase flow process of the granular liquid in the fissures. According to the flow conservation and balance equation, the diffusion motion equation of grout in the single fissure can be deduced as follows [12–14]:

$$u = -\frac{Jb^2}{2\eta}\left[1-\left(\frac{z}{b}\right)^2 - 2\frac{z_b}{b}\left(1-\frac{z}{b}\right)\right], \tag{1}$$

where u is the velocity of the grout movement at a certain cross-section point; z is the distance of a certain point from the center on the cross-section; z_b is a half of the height of the plug flow; b is a half of the fracture opening on a cross-section; η is the viscosity coefficient of the grout; J is the pressure gradient.

To integrate the above equation along the fractured cross-section, the grout flow in a single fracture at a certain moment can be obtained as follows:

$$q_i = \frac{2Jb^3}{3\eta}\left[1-\frac{3z_b}{2b}+\frac{1}{2}\left(\frac{z_b}{b}\right)^3\right]. \tag{2}$$

Obviously, by adding up all the fracture flow q_i, the injection rate of grouting at a certain moment, U, is obtained, namely,

$$U = \sum_i^t q_i. \tag{3}$$

To make a time integration of the injection rate, grout quantity, Q, can be obtained, namely,

$$Q = \int_0^t \sum_i^t q_i dt. \tag{4}$$

When t is the end time of grouting, Q is the total injection amount of grout.

2.2. Evolution Rules of the Grouting Parameter. From the diffusion equation of a single fissure, it can be seen that the flow q is dependent on the fracture opening, the pressure gradient, and the rheological parameters of grout. All these factors are always changing throughout the grouting process.

2.2.1. Time Variation of the Rheological Parameters of Grout. The rheological parameters of cement grout are time varying and depend significantly on the grouting time, the water-cement ratio, and the water temperature. The pure cement grout within the range of the commonly used water-cement ratio is a typical Bingham rheological material, whose essential features are having structural strength and time-dependent performance [15–18]. To describe the grout rheological model approximately, the following linear equation can be used:

$$\tau = \tau_0(t) + \eta(t)\dot{\gamma}, \tag{5}$$

where τ and $\dot{\gamma}$ are the shear stress and the strain rate of grout, respectively; $\tau_0(t)$ and $\eta(t)$ are the time-dependent yielding strength (dynamic shear force) and the plastic viscosity of grout, respectively.

Different water-cement ratios were used in the grouting tests of Dagang Mountain Hydropower Station. The rheological parameters and time curve were measured by the long homemade capillary rheological parameter meter (Figure 1).

2.2.2. Variation of Pressure Gradient. The rock fracture for grouting is usually filled with groundwater. It was assumed that there was not exchange between the grouting front and the groundwater, and thus there was only hydrostatic pressure. The grouting pressure, in addition to be affected by the local head loss and frictional head loss, will push grout flow in the fracture. Its gradient in the fracture is directly dependent on the attenuation of grouting pressure and the diffusion radius. The variation of pressure gradient could be investigated in the numerical simulation of grout diffusion in the fracture.

2.2.3. Evolution law of the Fracture Opening. The fracture opening is the principal variation in the diffusion equation, which plays a leading role in the diffusion distance [19]. The evolution law of the following five factors in the grouting process directly affects the accuracy of the numerical simulation for the diffusion distance.

(1) *Effect of the Fracture Roughness.* Seepage channels of the grout are mainly the fracture surfaces that are rough and often contain parts of the cementation or filling. This leads to complicated fracture opening with a large influence on the fluid motion. In the fracture hydraulics, the mechanical opening of the fracture, $2b_m$, is replaced by the equivalent hydraulic opening, $2b_h$, which is defined as follows: under the same pressure gradient and flow pattern, the volume flow within the rough fracture is equal to that within the flat and smooth fracture whose opening is $2b_h$. $2b_h$ can be determined comprehensively by the drilling hydraulic document and water pressure test. As a virtual opening, the equivalent hydraulic opening reflects the hydraulic characteristics of

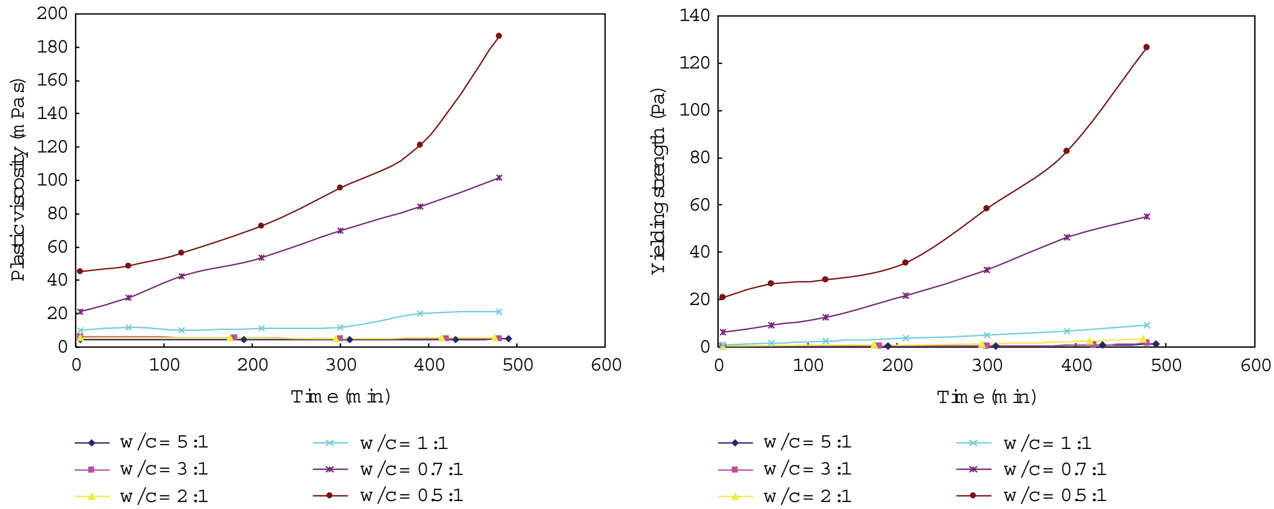

(a) Plastic viscosity of grout

(b) Yielding strength of grout

FIGURE 1: Time variation curves of the rheological parameters for cement grouts at different ratios (w/c is the water-cement ratio of grout).

fractures and shares some internal relations with the mechanical opening $2b_m$. Renshaw (1995) deduced the following equation based on the probability and statistics theory [20]:

$$\frac{b_h}{b_m}=\left[\left(\frac{\sigma_b}{b_m}\right)^2+1\right]^{-1/2}=\left[\frac{\exp\sigma_B^2\cdot\left(\exp\sigma_B^2-1\right)}{\left[\exp\left(\sigma_B^2/2\right)\right]^2}+1\right]^{-1/2}, \tag{6}$$

where σ_b and σ_B are the standard deviation of the opening and the standard deviation of the opening to the values, respectively.

(2) *Change of the Fracture Opening due to the Precipitation of Cement Particles.* The analysis of the instable grout in fractured rock showed that the fracture filled with grout material is mainly caused by the cement particle precipitation. There is a critical velocity value, V_{kp}, in the flow process of cement grout. When the velocity of grout diffusion is less than V_{kp}, the cement particles begin to precipitate, the sediment at the bottom of the fractured wall gradually increases, and the effective opening of the fracture gradually decreases. The reduction of the fracture opening will further slow the grout flow down. The particles will continue to precipitate until the fracture opening becomes less than 0.2 mm, when the cement particles cannot pass through the fractures, and thus the grout seepage channel is regarded to be blocked. The semiempirical formula for the critical velocity value is [21]

$$V_{\mathrm{kp}}=k(g\delta)^{0.5}\left[\frac{V^2\left(\rho_T-\rho_B\right)\sigma^m}{6fgd_{\mathrm{cp}}\rho_B}\right]^{3/7}, \tag{7}$$

where k is the correction coefficient; g is the gravitational acceleration; V is the sinking velocity of cement particles in water; δ is the fracture opening; ρ_T and ρ_B are the density of the cement particles and water, respectively; σ is the content of solid particles in solution; f is the resistance coefficient

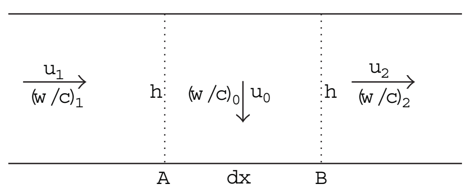

FIGURE 2: Change of the water-cement ratio after the cement particles precipitation.

of water in the fracture; d_{cp} is the feature size of the cement particle; m is the empirical indicators.

The sinking velocity of cement particles in water V can be approximately regarded as obeying the Stokes' law for free settling [14]:

$$V=\frac{d^2\left(\rho_T-\rho_B\right)g}{18\eta}, \tag{8}$$

where d is the mean size of the cement particles and η is the viscosity of the liquid medium or grout.

To understand the cement particles precipitation phenomenon from another angle, it is also a process of the increase of the water-cement ratio caused by free water separating out of grout, leading to the change of rheological parameters of grout. The flow and precipitation process was shown in Figure 2.

According to the conservation of cement mass, the following formula can be obtained:

$$\left(\frac{w}{c}\right)_0=h\cdot\frac{0.316+(w/c)_1}{u_0t+h-1.5W_1}-0.316, \tag{9}$$

where $(w/c)_1$ is the initial water-cement ratio of the grout; $(w/c)_0$ is the water-cement ratio of the grout after precipitation; t is the settling time started from the precipitation; u_0

is the velocity of cement particle precipitation in the grout; h is the fracture opening. The physical meaning of W_1 is the height accumulated from the precipitation of cement particles in the grout and is described as follows:

$$W_1 = \frac{u_0 t}{0.1 + 0.316 \cdot (w/c)_1}, \tag{10}$$

obviously, given that

$$h - 1.5W_1 < 0.2\,\text{mm}. \tag{11}$$

The fracture has been blocked by the cement particles if (11) is satisfied; this demonstrates that the fracture cannot be grouted.

(3) *Change of the Fracture Opening Caused by the Rock Mass Deformation.* In the process of grout diffusion, the grouting pressure always exerts on the upper and lower surfaces of the fissure, tending to make the fissures open. Meanwhile the fissure is constrained by the surrounding rock mass. The displacements of the upper and lower surfaces of the fissure at a particular moment can be calculated through the finite element model that was set up in the entire grout diffusion area by the composite element method containing the fissure network [14].

(4) *Opening Change Led by the Fissure Cracking and Expansion.* In the process of grout diffusion, when the grouting pressure reaches a critical value due to the stress concentration at the crack tip, the cracking will emerge, resulting in the increase of fracture opening. The grouting pressure is always applied to the fractured surfaces in the form of the surface force, and its direction is normal to the surface. The grouting pressure, serving as the inner water pressure, exerts approximate symmetrical distribution of the force on the upper and lower surfaces of the crack, increasing the fracture opening through tension. On the other hand, shear extension happened to the fracture surface due to the grouting pressure. Therefore, for the ordinary characteristics of stratum, the failure of rock mass is always shear failure rather than tension failure under the grouting pressure. The fracture extends along the original fracture direction, which is type I cracking with cracking angle of zero. When the stress intensity factor K_{I} reaches a critical value K_{Ic}, the crack will extend unsteadily [22], which is the cracking criterion at the crack tip in the grouting process. When calculating the fracture unit in the finite element analysis, the stress intensity factor, K_{I}, can be obtained using the following formula:

$$K_{\text{I}} = \lim_{r \to 0} \frac{G(1+\mu)}{(1-\mu)} \sqrt{\frac{2\pi}{r}} u, \tag{12}$$

where G is deformation modulus of rock mass; μ is Poisson's ratio; r is the distance between the fissure and the cracking point; u is the displacements of fissures. The fracture toughness, K_{Ic}, is the inherent characteristics of material and is usually determined by using the experimental methods. Its value is

$$K_{\text{Ic}} = \sqrt{\frac{2EW_r}{1-\mu^2}}, \tag{13}$$

where E is the elastic modulus of rock mass and W_r is the rock-specific surface energy.

(5) *Fracturing Opening of the Same Fissure at Different Locations.* There are some differences in the spatial distribution of the fissures; namely, the fracture openings are different at different locations. The fracture opening changes when the grout diffuses.

3. Simulation Model

Fissures with various geometric characteristics are often contained in the rock mass, and the diffusion distances are also different in different fissures. Therefore, the diffusion and filling of grout in different fractures within a certain distance from the drilling hole should be calculated, and its grouting effect should be analyzed. To analyze the entire grouting effect for the rock mass, the fracture network and computing medium model that can reflect the characteristics of grouting were established in this paper.

3.1. Simulation of the 3D Fracture Network. According to the geometric characteristics of rock mass, the three-dimensional fracture network should be consistent with the facture network of site as much as possible. Monte-Carlo method has been widely used to generate the 3D fracture network [23]. Compared with other engineering applications, grouting works can simply simulate the fracture network near grouting section. The geometric parameters of fracture comply with a certain distribution function whose simulation is to randomly generate a sample. However, concerning the fact that significant differences may exist between the generated network and the practical situation, it is necessary to amend the fracture opening with the greatest impact.

3.1.1. Extreme Value Test. Limiting the simulated fissures of large openings based on the geological survey data or downhole television data is essential so as to prevent the unreasonable ones from generating.

3.1.2. Acoustic Wave Test. The acoustic wave test refers to the calculation of average acoustic velocity according to the distance between two points of rock mass and the time for acoustic wave propagation. The rock mass between two points consists of the rock framework (matrix) and the pore filled with air or liquid. Both the distance between two points and the acoustic wave velocity in rock mass, fresh rock, and water or air are known. Therefore, the sum of the fissure openings can be calculated by using the following formula:

$$\sum l_2 = \frac{(v_1 - v) \cdot v_2}{(v_1 - v_2) \cdot v} \cdot l, \tag{14}$$

where $\sum l_2$ is the sum of the fissure openings; l is the distance between two points of rock mass; v is the acoustic wave velocity in rock mass; v_1 is the acoustic wave velocity in fresh rock; v_2 is the acoustic wave velocity in water or air.

Compared with the sum of fissure openings obtained from the numerical simulation, it can be analyzed whether the sum of fissure openings in fracture network is suitable.

3.1.3. Water Pressure Test. A simple water pressure test is made usually before grouting. The flow equation of water in a single fracture meets the cubic law [24] as follows:

$$q = \frac{2Jb^3}{3\eta}, \tag{15}$$

where q is the water flow in a single fracture; b is half of the fracture opening on a cross-section; η is the viscosity coefficient of water; J is the water test pressure gradient.

To sum up the simulated crack flow, the injection rate at a certain moment can be obtained (3). When $t = 20$ min after the loop calculation, U is the stable flow which meets the law of simple water pressure test, and the permeability rate of the fracture network in simulation can be calculated by the Lugeon calculation formula. Comparing this permeability rate with the results of water pressure test, it can be examined whether the distribution law of fracture opening in the fracture network is consistent with the practical situation.

3.2. Dual Medium Model of Grouting. As for the practice and theory in grouting engineering, it is believed that the pores whose sizes are less than three times D_{85} of material cannot be strictly grouted. In other words, the cracks whose openings are less than 0.2 mm cannot be strictly grouted using the ordinary Portland cement-based materials. The Distribution of fracture opening mostly follows the negative exponential distribution [23], and the microfine fissures less than 0.2 mm account for a higher proportion. In the grouting process, the cement particles are difficult to enter these microfine fissures. Serving as channels for draining excessive water in the grouting process, the microfine fissure are always in a state of compression under the grouting pressure. At the same time, based on the law of Water Cube, the grout diffusion is mainly controlled by the large opening fissures. In order to reduce the amount of calculation, those fissures with the openings greater than 0.2 mm were considered as the structural planes and thus have the strength and the deformation characteristics of structural planes. Those fissures with the openings less than 0.2 mm are believed to distribute uniformly in rock mass. Thus, a dual medium model of grouting reflecting the characteristics of grouting was established if the strength parameters and the deformation parameters of the microfine fissures are distributed to the surrounding rock mass equivalently.

3.3. Evaluation Indicator of the Grouting Effect. The permeability rate after grouting serves as the main indicator of grout curtain evaluation. The rock mass after grouting can still be divided into two parts: the grouted rock and the nongrouted fissure. The grouted rock is regarded as homogeneous continuous medium with a weak water permeability. The nongrouted fissures and the microfine fissures with the opening less than 0.2 mm have strong flow capacity, play the main role of hydraulic conductivity, and serve as important seepage channels. The simulation method for the water pressure test (15) can be used to investigate the water permeability rate at different locations of rock mass after grouting.

4. Simulation of the V-Diabase in Dagang Mountain Hydropower Station

According to the basic model of grouting simulation, combined with the program of the finite element method, the grouting process was simulated with analysis of its effect. The simulation took advantages of the relevant grouting test data of the V-diabase in the Dagang Mountain Hydropower Station.

4.1. Basic Conditions. The 1-1 hole in the downstream of original grouting within the grouting-test area was selected for the simulation of the permeability coefficient of rock mass after grouting. The grouting depth is 55.6 m. However, the simulated grouting depth ranged from 5.5 m to 55.6 m in order to reduce the influence of the abnormal grouting such as the oozing grout and the colluding grout. The integrity of the granite in this area with the depth from 0 m to 60 m, which mainly consisted of a steep fissure group and a gentle sloping fissure group, is poor. The maximum opening of the fissures is 0.5 cm; the acoustic velocity of fresh rock is 6500 m/s; the average velocity of grouting stage, the water permeability before grouting, and other parameters are shown in Table 1. The design grouting hole spacing is 2 m, and the design impermeable standard is less than 1 Lu.

4.2. Computed Results. The simulations of the grouting process for ten grouting stages were conducted. The computed results of the grouting process in Stage 9 are shown in Figure 3. A comparison between the simulation results and the results of practical grouting process during the grouting is shown in Table 2. A comparison of the grouting effect between the simulation results and the measurement results of practical grouting process after grouting is shown in Figure 4.

The results in Table 2 and Figure 4 showed that relative error or absolute error between the numerical simulation and the measurement results was acceptable, including the injection rate, the cumulative amount of grouting, and the accumulated injecting cement content. This indicated that the simulated grouting process basically reflected the practical grouting process. In addition, through comparing the simulated results of the water permeability and the sound wave velocity after grouting with that of the practical grouting, the treatment effect of cement grouting on the V-diabase rock mass could be reflected fundamentally using the numerical simulation.

The single hole calculation results were used to evaluate the effect of the grouting. The permeability rate at a certain distance from the drilling center was analyzed for a quantitative evaluation on the grouting's effect. The corresponding distances of 1 Lu and 3 Lu in different grouting stages were

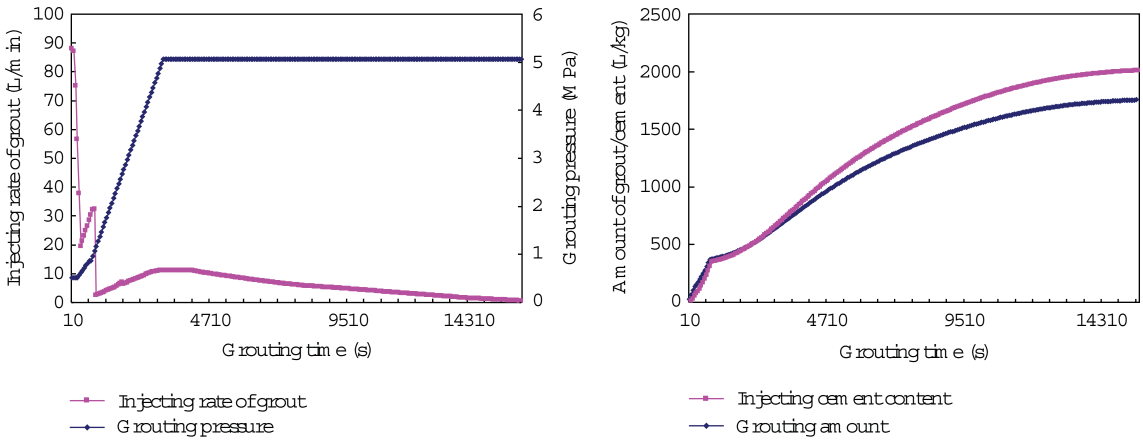

(a) (b)

FIGURE 3: Computed results of grouting in Stage 9 (45.5–50.5 m).

TABLE 1: Acoustic wave velocity and the permeability rate of drilling holes before grouting.

Grout stage	Stage 1	Stage 2	Stage 3	Stage 4	Stage 5	Stage 6	Stage 7	Stage 8	Stage 9	Stage 10
Drilling hole/m	5.5–10.5	–15.5	–20.5	–25.5	–30.5	–35.5	–40.5	–45.5	–50.5	–55.6
Wave velocity/m/s	5140	5119	4629	4565	5077	4994	5061	5053	4816	4756
Permeability rate/Lu	9.94	11.61	10.66	8.33	11.15	8.36	7.17	9.82	9.2	5.56

TABLE 2: Simulation results in each grouting stage.

Grouting stage		Stage 1	Stage 2	Stage 3	Stage 4	Stage 5	Stage 6	Stage 7	Stage 8	Stage 9	Stage 10
Pressure/Pa	Simulation	2.46	2.83	3.08	3.38	3.99	4.67	5.02	5.13	5.07	4.23
	Measurement	2.51	2.88	3.13	3.43	4.04	4.72	5.07	5.18	5.07	5.08
	Difference %	–2.0	–1.7	–1.6	–1.5	–1.2	–1.1	–1.0	–1.0	0.0	–16.7
Grout amount/L	Simulation	1839	2466	3193	3110	1748	1513	1554	2110	1755	735
	Measurement	2674	2982	2493	2509	2674	2515	2451	1121	2732	2513
	Difference %	–31.2	–17.3	28.0	24.0	–34.6	–39.8	–36.6	88.2	–35.8	–70.8
Injection cement content/kg	Simulation	2082	2831	3766	3643	2003	1696	1734	2438	2005	627
	Measurement	2267	2592	2015	2069	2263	2042	1950	393	2320	1787
	Difference %	–8.1	9.2	86.9	76.1	–11.5	–16.9	–11.1	519.7	–13.6	–64.9

shown in Figure 5. When the hole spacing was 2.0 m, that is, the distance from the drilling center was 1.0 m, it can meet the design impermeable standard, which is less than 1 Lu. When the hole spacing was 2.6 m, it can meet the impermeable standards, which is less than 3 Lu.

4.3. Reliability Analysis. The reliability of grouting effect needed to be analyzed due to the randomness of Monte-Carlo method. Under the given grouting pressure, respective simulations on multiple sets of different fracture networks were conducted to obtain different calculation results of corresponding number of times. Making a statistical analysis of the distribution of computed results, the reliability of the results can be examined by obtaining the specific values in different confidence intervals. The Monte-Carlo simulation was conducted with 81 times, and the statistical distribution of the calculated results in Stage 9 is shown in Table 3. Corresponding to different confidence intervals, the grout diffusion distances with the permeability rate less than 1 Lu in each grouting stage are shown in Table 4 and Figure 6.

As for the simulation results with 100% confidence, the grouted stage whose diffusion distance away from the drilling center was the smallest and also satisfied the design standard was Stage 9 (45.5–50.5 m), and the hole spacing in this stage was 1.8 m, less than the design value, 2 m. Among the 81 simulation results, only one result, whose water permeability after grouting at a distance of 1 m from the drilling center was 1.0492 Lu, was slightly more than the design standard. Thus, the analysis of simulation results showed that the hole spacing of 2 m can satisfy the impermeable standard because the confidence was nearly 99%.

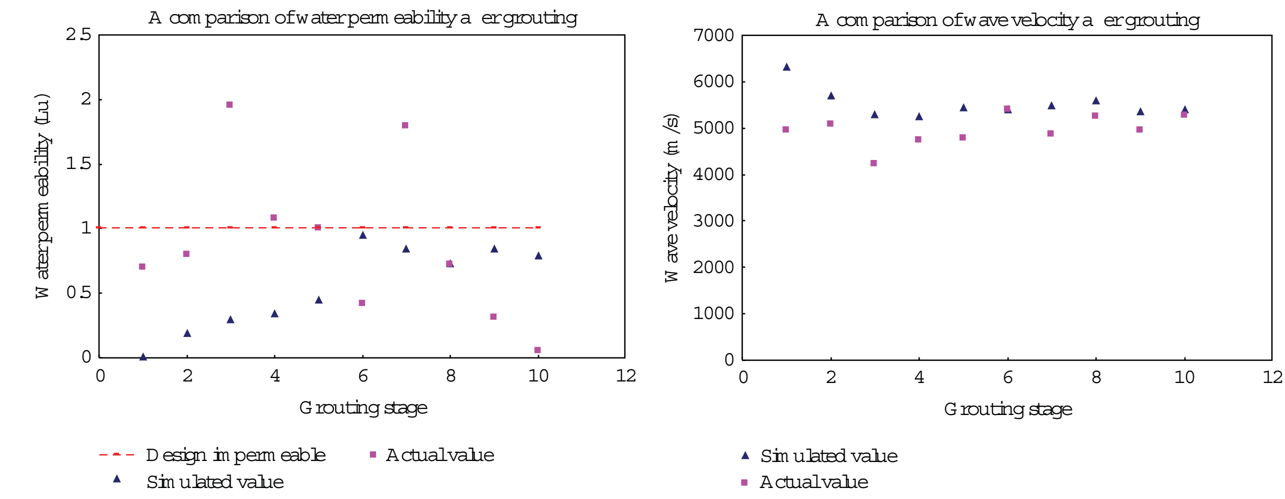

(a) (b)

FIGURE 4: Comparison of the grouting effect after grouting with 1 m as the design diffusion radius.

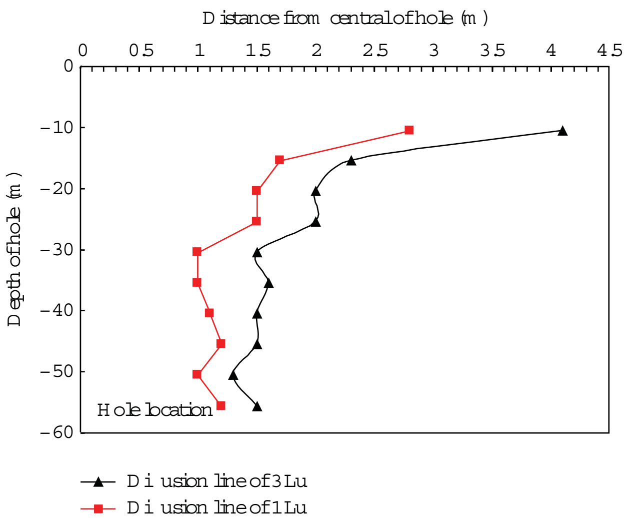

FIGURE 5: Distribution of the water permeability at different distances.

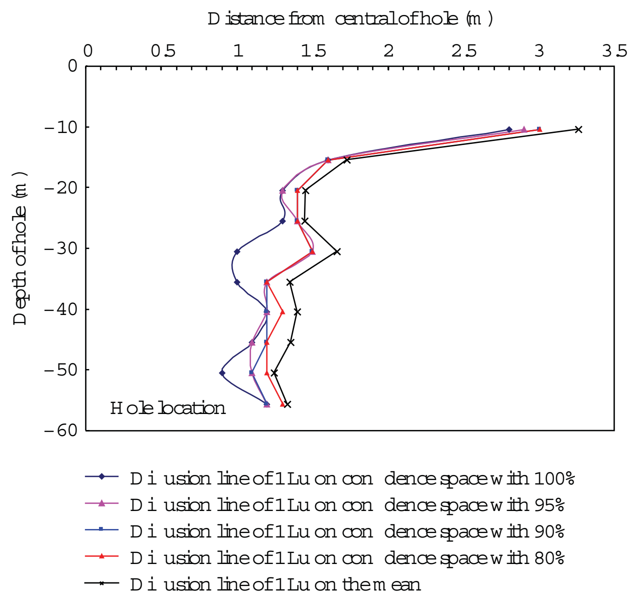

FIGURE 6: Probability of the distance in each grouting stage with permeability rate less than 1 Lu.

As for the simulation results with 95% confidence, the grouted stages whose diffusion distance away from the drilling center was the smallest and also satisfied the design standard were Stage 8 (40.5–45.5 m) and Stage 9. The hole distance in these two stages was 2.2 m, more than the design value, 2 m. Therefore, if the simulation value with that confidence was adopted, the hole spacing could be optimized to 2.2 m, an increase of 0.2 m over the design value, directly saving up to 10% of the project amount.

As for the simulation results with 80% confidence, the grouted stages whose diffusion distance away from the drilling center was the smallest and also satisfied the design standard were Stage 6 (30.5–35.5 m), Stage 8, and Stage 9. The hole spacing in these three stages was 2.4 m. It should not be applied directly due to its 80% confidence.

5. Conclusion

Based on the mutual coupling of the diffusion process of cement grouting in the fissures and the deformation of rock mass under grouting pressure, the diffusion and filling process for cement grouting in V-diabase grouting test in the Dagang Mountain Hydropower Station was simulated using the finite element method, considering the time variability of rheological parameters of cement grout, the changes in the fissure opening, and the precipitation law of the cement particles. Distribution of the permeability rate in grouted rock mass was analyzed, and the reliability and optimization

Table 3: Statistical distribution of permeability rate after grouting in Stage 9 at different distances.

Distance/m	Permeability rate of average/Lu	Variance	Coefficient of variation	Maximum/Lu	Minimum/Lu	Probability less than 1 Lu/%
0.1	0.3044	0.0166	0.0545	0.3428	0.2684	100%
0.2	0.3029	0.0166	0.0548	0.3419	0.2667	100%
0.3	0.301	0.0166	0.0552	0.3405	0.2647	100%
0.4	0.2986	0.0166	0.0556	0.3386	0.2623	100%
0.5	0.3008	0.0215	0.0715	0.3976	0.2596	100%
0.6	0.3121	0.0284	0.0910	0.3967	0.261	100%
0.7	0.3372	0.0409	0.1213	0.4859	0.2703	100%
0.8	0.3856	0.0607	0.1574	0.716	0.2887	100%
0.9	0.4626	0.0895	0.1935	0.9654	0.3131	100%
1.0	0.5848	0.1182	0.2021	1.0492	0.3098	98.77%
1.1	0.7047	0.1459	0.2070	1.2203	0.3818	97.53%
1.2	0.8611	0.1724	0.2002	1.428	0.448	85.19%
1.3	1.1571	0.2501	0.2161	2.1088	0.7335	32.10%
1.4	1.4857	0.315	0.2120	2.9922	0.8091	2.47%
1.5	1.8819	0.4215	0.2241	3.506	0.8186	1.23%
1.6	2.4183	0.5183	0.2143	4.2533	1.4244	0%

Table 4: Probability of distance in each grouting stage with the permeability rate less than 1 Lu.

Different confidence	Distance from the drilling center/m									
	Stage 1	Stage 2	Stage 3	Stage 4	Stage 5	Stage 6	Stage 7	Stage 8	Stage 9	Stage 10
100%	2.8	1.6	1.3	1.3	1.0	1.0	1.2	1.1	0.9	1.2
95%	2.9	1.6	1.3	1.4	1.5	1.2	1.2	1.1	1.1	1.2
90%	3.0	1.6	1.4	1.4	1.5	1.2	1.2	1.2	1.1	1.2
80%	3.0	1.6	1.4	1.4	1.5	1.2	1.3	1.2	1.2	1.3
Mean	3.261	1.728	1.453	1.450	1.660	1.351	1.402	1.357	1.247	1.337

of the hole spacing design were discussed. The following conclusions were derived according to the analysis.

(1) Through numerical simulation of the grout diffusion, the permeability rate of the grouted rock mass was obtained, and the simulation results were compared with the practical grouting results. This showed that the errors in the grouting process, including the injection rate, the accumulated grouting volume, and the accumulated injection cement content, were acceptable. The simulation process basically reflects the grouting process. The simulated grouting results, the water permeability, and the acoustic wave velocity after grouting were comparable with the practical grouting results.

(2) Simulation results of the grouting process with the same parameters for many times showed that various quantities had good repeatability, such as grouting time, the accumulated grouting volume, the accumulated injection cement content, the permeability rate, and the acoustic wave velocity after grouting. Most of the variation coefficients were less than 0.3 and distributed uniformly. The simulating results had better reliability in general.

(3) The numerical simulation results showed that the grouting pressure, the hole spacing, and the materials used in the test area were essentially reasonable and practicable. Diffusion distance of the grout satisfying the design permeability standard could reach 1 m with the confidence of approximately 100%. Thus, the hole spacing of 2 m was reliable.

(4) The analysis results showed that, when the confidence approached 95%, diffusion distance of the grout, which satisfied the design permeability standard, could reach 1.1 m; that is, the hole spacing reached 2.2 m. This demonstrated a probability of optimization along with a finer optimization precision when compared with the accuracy of 0.5 m that is commonly used.

(5) There were differences between the numerical simulating process curve and the measurements. The grouting time, the rising curve of grouting pressure, and the assumptions adopted in the simulation might be the main reason for the differences. It was indicated that the simulation results tended to be more perfect with fewer restrictions.

Conflict of Interests

The authors declare that there is no conflict of interests regarding the publication of this paper.

Acknowledgment

This research is supported by the National Natural Science Fund Project no. 51279217.

References

[1] S. Maghous, Z. Saada, L. Dormieux, J. Canou, and J. C. Dupla, "A model for in situ grouting with account for particle filtration," *Computers and Geotechnics*, vol. 34, no. 3, pp. 164–174, 2007.

[2] A. Contini, A. Cividini, and G. Gioda, "Numerical evaluation of the surface displacements due to soil grouting and to tunnel excavation," *International Journal of Geomechanics*, vol. 7, no. 3, pp. 217–226, 2007.

[3] H. F. Schweiger, C. Kummerer, R. Otterbein, and E. Falk, "Numerical modelling of settlement compensation by means of fracture grouting," *Soils and Foundations*, vol. 44, no. 1, pp. 71–86, 2004.

[4] G. Modoni, P. Croce, and L. Mongiovì, "Theoretical modelling of jet grouting," *Geotechnique*, vol. 56, no. 5, pp. 335–347, 2006.

[5] E. D. Lees and A. Naudts, "New developments in rock and soil grouting design and evaluation," *Dam Engineering*, vol. 6, no. 1, pp. 111–129.

[6] C. Wisser, C. E. Augarde, and H. J. Burd, "Numerical modelling of compensation grouting above shallow tunnels," *International Journal for Numerical and Analytical Methods in Geomechanics*, vol. 29, no. 5, pp. 443–471, 2005.

[7] Y. Xiaodong, *Analysis of Surface Uplift Grouting in Rock Foundation*, China Institute of Water Resources and Hydropower Research, Beijing, China, 1987, Chinese.

[8] L. Hassler et al., "Simulation of grouting in jointed rock," in *Proceedings of the 6th International Conference on Rock Mechanics*, 1987.

[9] L. Hässler, U. Håkansson, and H. Stille, "Computer-simulated flow of grouts in jointed rock," *Tunnelling and Underground Space Technology incorporating Trenchless*, vol. 7, no. 4, pp. 441–446, 1992.

[10] Z. Hao, *A Research on the Rock Grouting Behavior and Its Computer Simulation*, Doctoral Dissertation of Northeastern University, Shenyang, China, 1998, Chinese.

[11] M. Eriksson, H. Stille, and J. Andersson, "Numerical calculations for prediction of grout spread with account for filtration and varying aperture," *Tunnelling and Underground Space Technology*, vol. 15, no. 4, pp. 353–364, 2000.

[12] M. Young, M. X. Chen, and Y. N. HE, "Simulating experiment for grouting seepage in rockmass," *Journal of Experimental Mechanics*, vol. 16, no. 1, pp. 105–112, 2001.

[13] P.-P. Luo, Y.-M. Zhu, Y.-M. Zhao, and S. He, "Numerical simulation of grouting in rock mass," *Chinese Journal of Geotechnical Engineering*, vol. 27, no. 8, pp. 918–921, 2005.

[14] P. Fu and X. D. Yang, "Study on the effect assessment and the numerical simulation of the cement in fractured rockmass," in *Proceedings of the 11th Symposium of the National Water Resources and Hydropower ground and foundation engineering technology*, pp. 9–17, Water Power Press, Beijing, China, 2011.

[15] Shannon & Wilson, *Geotechnical Consultants*, Cement Grout Flow Behavior in Fractured Rock, 1987.

[16] M. Eriksson, M. Friedrich, and C. Vorschulze, "Variations in the rheology and penetrability of cement-based grouts—an experimental study," *Cement and Concrete Research*, vol. 34, no. 7, pp. 1111–1119, 2004.

[17] J. Mirza, M. S. Mirza, V. Roy, and K. Saleh, "Basic rheological and mechanical properties of high-volume fly ash grouts," *Construction and Building Materials*, vol. 16, no. 6, pp. 353–363, 2002.

[18] G. Rudolph, S. luo et al., *Studies of the Setting Behavior of Cement Suspensions*, Institute of Nuclear waste disposal engineering, 1982.

[19] R. Gothäll and H. Stille, "Fracture dilation during grouting," *Tunnelling and Underground Space Technology*, vol. 24, no. 2, pp. 126–135, 2009.

[20] C. E. Renshaw, "On the relationship between mechanical and hydraulic apertures in rough-walled fractures," *Journal of Geophysical Research*, vol. 100, no. 12, pp. 24–636, 1995.

[21] W.-G. Qiao, Y.-X. Zhang, X.-H. Song, and T. Zhao, "Flow deposition mechanism of cement slurry in rock ass fractures," *Rock and Soil Mechanics*, vol. 25, pp. 14–16, 2004 (Chinese).

[22] S. C. Gu, P. L. Su et al., *Numerical Simulation of the Fracture Tip Under the Grouting Pressure*, Ground Treatment, Chinese.

[23] S. G. Du, *The Engineering Properties of the Rockmass on the Structure Surface*, Earthquake Press, Beijing, China, 1999, Chinese.

[24] G. Louis, *A Study of Ground Water Flow in Jointed Rock and its Influence on the Stability of Rock Masses*, Rock Mechanics Research Report, London, UK, 1969.

Hindawi Publishing Corporation
Journal of Applied Mathematics
Volume 2013, Article ID 626287, 13 pages
http://dx.doi.org/10.1155/2013/626287

Research Article

Exact Stiffness for Beams on Kerr-Type Foundation: The Virtual Force Approach

Suchart Limkatanyu,[1] Woraphot Prachasaree,[1] Nattapong Damrongwiriyanupap,[2] Minho Kwon,[3] and Wooyoung Jung[4]

[1] *Department of Civil Engineering, Faculty of Engineering, Prince of Songkla University, Songkhla 90112, Thailand*
[2] *Civil Engineering Program, School of Engineering, University of Phayao, Phayao 5600, Thailand*
[3] *Department of Civil Engineering, ERI, Gyeongsang National University, Jinju 660-701, Republic of Korea*
[4] *Department of Civil Engineering, Gangneung-Wonju National University, Gangneung 210-720, Republic of Korea*

Correspondence should be addressed to Suchart Limkatanyu; suchart.l@psu.ac.th

Received 12 May 2013; Revised 17 July 2013; Accepted 6 August 2013

Academic Editor: Fayun Liang

This paper alternatively derives the exact element stiffness equation for a beam on Kerr-type foundation. The shear coupling between the individual Winkler-spring components and the peripheral discontinuity at the boundaries between the loaded and the unloaded soil surfaces are taken into account in this proposed model. The element flexibility matrix is derived based on the virtual force principle and forms the core of the exact element stiffness matrix. The sixth-order governing differential compatibility of the problem is revealed using the virtual force principle and solved analytically to obtain the exact force interpolation functions. The matrix virtual force equation is employed to obtain the exact element flexibility matrix based on the exact force interpolation functions. The so-called "natural" element stiffness matrix is obtained by inverting the exact element flexibility matrix. One numerical example is utilized to confirm the accuracy and the efficiency of the proposed beam element on Kerr-type foundation and to show a more realistic distribution of interactive foundation force.

1. Introduction

As a numerical counterpart of the continuous medium model, the continuum finite element model has been widely used by geotechnical researchers in studying several complex soil-structure interaction (SSI) problems due to drastic advances in computer technology. The problem of beams on deformable foundation is the most commonly encountered SSI problem and has many applications in engineering and science [1–3]. Even though the continuum finite element model yields the most comprehensive data on the stress and deformation variations within the beam-foundation system, there is still a substantial need in routine engineering practice to use the mechanical subgrade model to analyze and design the beam-foundation system. This lies in the fact that considerable experience and skill of practicing geotechnical engineers are required in constructing a suitable continuum element mesh, interpreting the analysis results, and implementing the numerical model. These could limit the model access by practicing geotechnical engineers. Furthermore, only small beam-foundation systems can be realistically investigated using the continuum finite element model due to high computational costs, and the beam response along the beam-foundation interface, not the stresses or strains inside the foundation medium, is of high interest by the designing engineers. Therefore, most structural-analysis platforms available in the industry still employ the mechanical subgrade model to represent the supporting foundation with a reasonable degree of accuracy.

The Winkler foundation model [4] is the most rudimentary mechanical subgrade model and has been widely adopted in studying the problem of beams on elastic foundation. In the Winkler foundation model, a set of 1D independent springs is attached along the beam to form the beam-foundation system. This type of foundation model is often referred to as the "*one-parameter*" foundation model since it is characterized only by the vertical stiffness of the Winkler-foundation springs. Though simple, the Winkler foundation model can lead to some peculiar responses of many practical beam-foundation systems due to omission of the shear stress inside the foundation medium [5, 6]. This omission results in the uncoupling of the individual Winkler foundation springs and the neglect of the existence of the foundation medium beyond either end of the loaded beam and leads to an unrealistic abrupt change in the foundation surface displacement between the loaded and the unloaded regions. To bridge the gap between the continuum finite element model and the rather crude Winkler foundation model, several researchers [7–9] had improved the Winkler foundation model by introducing the second foundation parameter to account for the existence of shear stress inside the foundation medium, resulting in the so-called "*two-parameter*" foundation model. Even though each researcher group has its own particular way to visualize the second foundation parameter, its proposed expressions for the interactive foundation forces can simply be written in the same mathematical form. For example, Filonenko-Borodich [7] regarded the second foundation parameter as the magnitude of the pretensioned force in the elastic membrane inserted between the beam and Winkler-foundation springs. A detailed discussion of several two-parameter foundation models can be found in Kerr [6].

To further improve the two-parameter foundation model, Hetényi [10] and Kerr [11] had added the third foundation parameter, leading to the so-called "*three-parameter*" foundation model. The major role of the third foundation parameter is to provide more flexibility in controlling the degree of foundation-surface continuity between the loaded and the unloaded regions of the beam-foundation system. This is in compliance with the observation made by Foppl [12] that the foundation-surface displacement outside the loaded region predicted by the continuous medium model decreased too gradually as opposed to what happened in reality, and hence a certain degree of discontinuity at the loaded-unloaded boundary existed. Furthermore, Kerr [6] concluded that for several types of foundation materials (e.g., soil, soft filament, foam, etc.), neither the Winkler-foundation model nor the continuous medium model can realistically represent the interaction mechanisms between the beams and the contacting media. Among several three-parameter foundation models, the Kerr-type foundation model [11] is of particular interest since it stems from the famous Winkler-Pasternak two-parameter foundation model [9] for which several applications and solutions have been available. In the Kerr-type foundation model, the foundation medium is visualized as consisted of lower and upper spring beds sandwiching an incompressible shear layer. Three parameters characterizing the Kerr-type foundation model are the lower and upper spring moduli and the shear-layer section modulus. It is noted that the interactive foundation force of the Kerr-type foundation model can be written in the same mathematical form as obtained with the simplified continuum models of Reissner [13], Horvath [14, 15], and Worku [16]. Synthetic and hierarchical correlations between several mechanical subgrade models and simplified continuum models are comprehensively presented in Horvath [17] and Horvath and Colasanti [18]. The pros and cons of each model are summarized in Horvath and Colasanti [18].

Even though the Kerr-type foundation model was developed since the mid-sixties, there have been only a limited number of researchers studying the problem of beams resting on Kerr-type foundation. Avramidis and Morfidis [19] used the principle of stationary potential energy to derive the governing differential equilibrium equations of the beam-foundation system and its essential boundary conditions. Subsequently, Morfidis [20, 21] derived the exact beam-foundation stiffness matrix based on the exact solution of the governing differential equilibrium equations for static and dynamic analyses, respectively, and calibrated the foundation parameters with the analysis results obtained with high fidelity 2D finite element models. The problem of beams resting on tensionless Kerr-type foundation was also investigated by Zhang [22] and Sapountzakis and Kampitsis [23]. Wang and Zeng [24] used the Kerr-type foundation model to study the interface stress between piezoelectric patches and host structures.

It is worth mentioning that a series of research papers on the so-called "modified Kerr-Reissner hybrid" foundation model have been presented by Horvath and Colasanti [18] and Colasanti and Horvath [25]. This foundation model is also regarded as the three-parameter foundation model and is formulated based on the combination of the modified Kerr-type foundation model with the Reissner simplified continuum subgrade model. In the modified Kerr-type foundation model, a shear layer is replaced by a tensioned membrane for the sake of modeling ease. The modified Kerr-Reissner hybrid foundation model is attractive particularly to practicing geotechnical engineers since it combines the advantages of both mechanical subgrade model and simplified continuum model as comprehensively discussed in Colasanti and Horvath [25]. Horvath and Colasanti [18] discuss the detailed derivation of this foundation model; Colasanti and Horvath [25] illustrate the modeling approach of this foundation model using commercially available structural analysis software. Subsequently, the modified Kerr-Reissner hybrid foundation model is applied to the planar geosynthetics used for tensile earth reinforcement under vertical loads [26].

In this paper, the virtual force principle is employed to reveal the governing differential compatibility equations of the beam-Kerr foundation system, as well as its natural boundary conditions. Thus, this paper can naturally be considered as a companion paper to the earlier work on the beam-Kerr foundation system by Avramidis and Morfidis [19] and Morfidis [20]. Unlike the structural component-based approach used by Horvath and Colasanti [18] and Colasanti and Horvath [25], all system components can be combined effectively into a single element, thus rendering the proposed model more attractive and unique from the theoretical and modeling point of view. The exact beam-Kerr foundation stiffness matrix is alternatively derived based on the exact beam-Kerr foundation flexibility matrix. The exact force interpolation functions of the beam-Kerr foundation system are at the core of the derivation of the exact element flexibility matrix. The governing differential equilibrium equations and constitutive relations of the beam

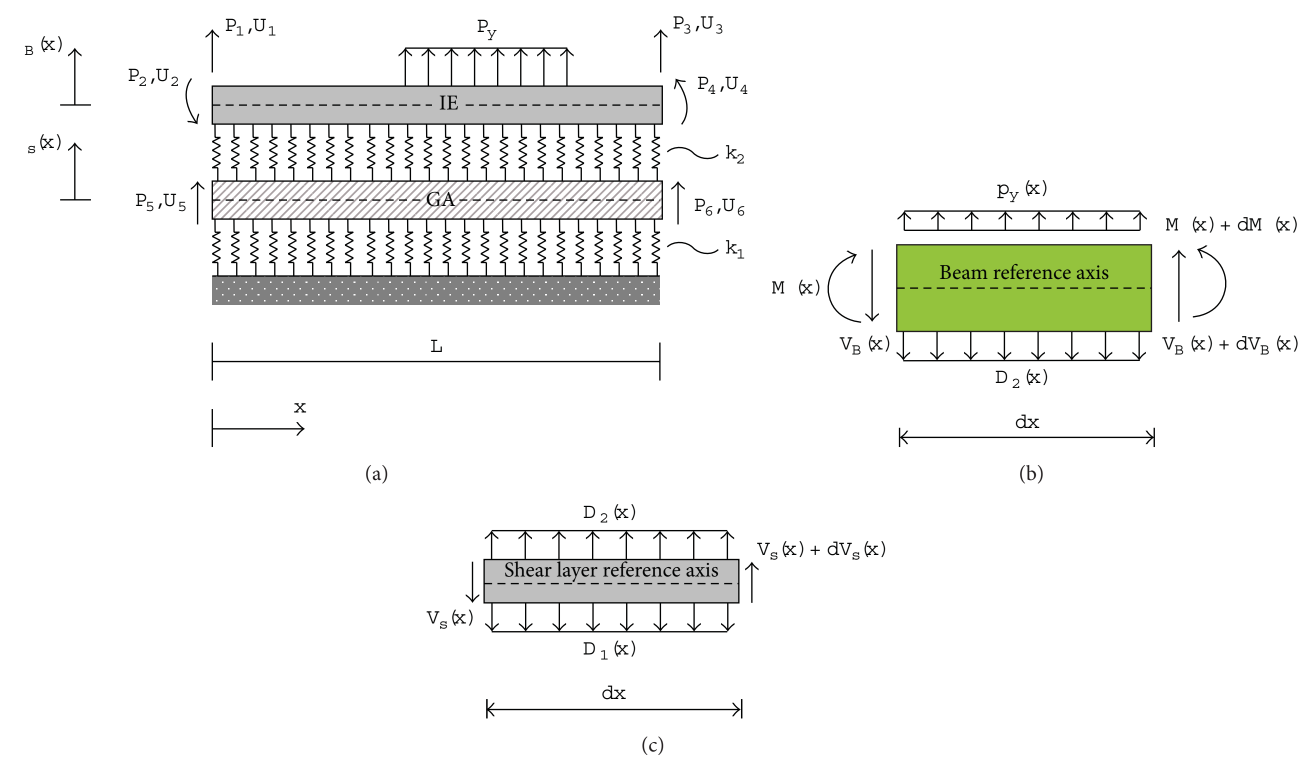

FIGURE 1: (a) A beam on Kerr-type foundation; (b) a differential segment cut from the beam; (c) a differential segment cut from the shear layer.

on Kerr-type foundation are first presented. Next, the sixth-order governing differential compatibility equations, as well as the associated end-boundary compatibility conditions, are derived based on the virtual force principle. The exact force interpolation functions of the beam-foundation system are derived from the analytical solution of the governing differential compatibility equations of the problem. The matrix virtual force equation is employed to obtain the exact element flexibility matrix using the exact force interpolation functions. It is worth mentioning that the element flexibility matrix presented in this paper is different from that presented in Limkatanyu and Spacone [27] in that the foundation force distribution in Limkatanyu and Spacone [27] has to be assumed, thus resulting in the approximate moment interpolation functions and the approximate element flexibility matrix. The exact element stiffness matrix can be obtained directly from the exact element flexibility matrix following the natural approach [28]. It is noted that the natural approach had been used with successes in deriving the exact element stiffness matrices for beams on Winkler foundation [29] as well as beams on Winkler-Pasternak foundation [30]. It is also imperative to emphasize that, in the proposed model, the applied distributed load does not influence the exact force interpolation functions as long as it varies uniformly along the whole length of the beam. This finding renders the proposed flexibility-based model attractive since the analytical solution to the governing differential compatibility equation requires only the homogeneous part. Unfortunately, this beneficial effect is not available in the exact stiffness-based model presented by Avramidis and Morfidis [19] and Morfidis [20] since the analytical solution to the governing differential equilibrium equation requires both homogeneous and particular part with the presence of the applied distributed load. Therefore, the derivation of the exact displacement interpolation functions becomes more involved. A brief discussion on the efficient way to account for the extended-foundation effect is also introduced. All symbolic calculations throughout this paper are performed using the computer software Mathematica [31], and the resulting beam-foundation model is implemented in the general-purpose finite element platform FEAP [32]. A numerical example is used to verify the accuracy and the efficiency of the natural beam element on Kerr-type foundation and to show a more realistic distribution of interactive foundation force. A 2D finite element package VisualFEA [33] is also used to analyze this numerical example for comparison purpose.

2. Governing Equations of Beams on Kerr-Type Foundation

2.1. Differential Equilibrium Equations: Direct Approach. A beam-Kerr foundation system is shown in Figure 1(a) and comprises a beam, the upper and lower springs, and an intermediate shear layer. The governing differential equilibrium equations of the system are derived in a direct manner as follows.

A differential segment dx taken from the beam on Kerr-type foundation is shown in Figure 1(b). The vertical equilibrium of the infinitesimal beam segment dx is written as

$$\frac{dV_B(x)}{dx} + p_y(x) - D_2(x) = 0, \tag{1}$$

where $V_B(x)$ is the beam-section shear force; $p_y(x)$ is the transverse distributed load; and $D_2(x)$ is the interactive force in the upper spring and acts at the bottom face of the beam. Considering the moment equilibrium, this yields

$$\frac{dM(x)}{dx} + V_B(x) = 0, \tag{2}$$

where $M(x)$ is the beam-section bending moment. Following the Euler-Bernoulli beam theory, only flexural contributions are considered in the paper. Enforcing the beam shear equilibrium of (2), (1) and (2) can be combined into a single relation; thus,

$$\frac{d^2M(x)}{dx^2} - p_y(x) + D_2(x) = 0. \tag{3}$$

A differential segment dx taken from the shear layer resting on the lower foundation springs is shown in Figure 1(c). The vertical equilibrium of the infinitesimal shear-layer segment dx can be written as

$$\frac{dV_s(x)}{dx} + D_2(x) - D_1(x) = 0, \tag{4}$$

where $V_s(x)$ is the shear-layer section shear force and $D_1(x)$ is the interactive force in a lower spring. Equations (3) and (4) form a set of governing differential equilibrium equations of the system and are coupled through the upper-spring interactive force $D_2(x)$.

It is noteworthy to remark that this system is internally statically indeterminate and the internal forces cannot be determined simply by equilibrium conditions since there are 4 internal force unknown fields, $M(x)$, $V_s(x)$, $D_1(x)$, and $D_2(x)$, at any system section while only two equilibrium equations are available.

2.2. Deformation-Force Relations. The system sectional deformations can be related to their conjugate-work forces as follows:

$$\begin{aligned} \kappa(x) &= \frac{M(x)}{\mathrm{IE}}, & \gamma_s(x) &= \frac{V_s(x)}{\mathrm{GA}}, \\ \Delta_1(x) &= \frac{D_1(x)}{k_1}, & \Delta_2(x) &= \frac{D_2(x)}{k_2}, \end{aligned} \tag{5}$$

where $\kappa(x)$ is the beam-section curvature; $\gamma_s(x)$ is the shear-layer section shear strain; $\Delta_1(x)$ is the lower-spring deformation; $\Delta_2(x)$ is the upper-spring deformation; IE is the flexural rigidity; GA is the shear-layer section modulus; k_1 is the lower-spring modulus; and k_2 is the upper-spring modulus. Following the comprehensive work by Worku [16], the three foundation parameters (k_1, k_2, and GA) can be related to the elastic modulus, Poisson ratio, and depth of the soil continuum underneath the beam.

2.3. Differential Compatibility Equations and End Compatibility Conditions: The Virtual Force Principle. The virtual force equation is an integral expression of the system compatibility equations and can be expressed in the general form as

$$\delta W^* = \delta W^*_{\mathrm{int}} + \delta W^*_{\mathrm{ext}} = 0, \tag{6}$$

where δW^* is the system total complementary virtual work; $\delta W^*_{\mathrm{int}}$ is the system internal complementary virtual work; and $\delta W^*_{\mathrm{ext}}$ is the system external complementary virtual work.

In the case of the beam-Kerr foundation system, $\delta W^*_{\mathrm{int}}$ and $\delta W^*_{\mathrm{ext}}$ can be expressed as

$$\begin{aligned} \delta W^*_{\mathrm{int}} &= \int_L \delta M(x)\,\kappa(x)\,dx + \int_L \delta V_s(x)\,\gamma_s(x)\,dx \\ &\quad + \int_L \delta D_1(x)\,\Delta_1(x)\,dx + \int_L \delta D_2(x)\,\Delta_2(x)\,dx \\ \delta W^*_{\mathrm{ext}} &= -\int_L \delta p_y(x)\,v_B(x)\,dx - \delta\mathbf{P}^T\mathbf{U}, \end{aligned} \tag{7}$$

where $v_B(x)$ is the beam vertical displacement; the vector $\mathbf{P} = \{P_1\ P_2\ P_3\ P_4\ P_5\ P_6\}^T$ contains shear forces and moments acting at beam ends and shear forces acting at the shear-layer ends; and the vector $\mathbf{U} = \{U_1\ U_2\ U_3\ U_4\ U_5\ U_6\}^T$ contains their conjugate-work displacements and rotations at the beam ends and displacements at the shear-layer ends. At the moment, external force quantity, $\delta p_y(x)$, is arbitrarily chosen to be zero. Thus, (6) becomes

$$\begin{aligned} \delta W^* &= \int_L \delta M(x)\,\kappa(x)\,dx + \int_L \delta V_s(x)\,\gamma_s(x)\,dx \\ &\quad + \int_L \delta D_1(x)\,\Delta_1(x)\,dx + \int_L \delta D_2(x)\,\Delta_2(x)\,dx \\ &\quad - \delta\mathbf{P}^T\mathbf{U} = 0. \end{aligned} \tag{8}$$

Eliminating the internal deformation fields through the deformation-force relations, (8) can be written as

$$\begin{aligned} \delta W^* &= \int_L \delta M(x)\,\frac{M(x)}{\mathrm{IE}}dx + \int_L \delta V_s(x)\,\frac{V_s(x)}{\mathrm{GA}}dx \\ &\quad + \int_L \delta D_1(x)\,\frac{D_1(x)}{k_1}dx + \int_L \delta D_2(x)\,\frac{D_2(x)}{k_2}dx \\ &\quad - \delta\mathbf{P}^T\mathbf{U} = 0. \end{aligned} \tag{9}$$

The lower and upper spring forces ($D_1(x)$ and $D_2(x)$) and their virtual counterparts ($\delta D_1(x)$ and $\delta D_2(x)$) can be eliminated in (9) through the governing differential equilibrium equations of (3) and (4). Therefore, the system virtual force equation can be written as

$$-\delta\mathbf{P}^T\mathbf{U}+\int_L \delta M(x)\frac{M(x)}{\mathrm{IE}}dx+\int_L \delta V_s(x)\frac{V_s(x)}{\mathrm{GA}}dx$$
$$+\int_L \frac{d\delta V_s(x)}{dx}\left(\frac{1}{k_1}\right)\left(-\frac{d^2M(x)}{dx^2}+p_y(x)+\frac{dV_s(x)}{dx}\right)dx$$
$$+\int_L \frac{d^2\delta M(x)}{dx^2}\left(\frac{1}{k_1}\right)\left(\frac{d^2M(x)}{dx^2}-p_y(x)-\frac{dV_s(x)}{dx}\right)dx$$
$$+\int_L \frac{d^2\delta M(x)}{dx^2}\left(\frac{1}{k_2}\right)\left(\frac{d^2M(x)}{dx^2}-p_y(x)\right)dx=0. \tag{10}$$

In order to move all differential operators to the bending moment $M(x)$ and the shear-layer section shear force $V_s(x)$, integration by parts is applied once to the forth term and twice to the fifth and sixth terms of (10), respectively, hence resulting in the following expression:

$$\int_L \delta M(x)\left(\frac{M(x)}{\mathrm{IE}}+\left(\frac{1}{k_1}+\frac{1}{k_2}\right)\left(\frac{d^4M(x)}{dx^4}-\frac{d^2p_y(x)}{dx^2}\right)\right.$$
$$\left.-\frac{1}{k_1}\frac{d^3V_s(x)}{dx^3}\right)dx$$
$$+\int_L \delta V_s(x)\left(\frac{V_s(x)}{\mathrm{GA}}+\frac{1}{k_1}\left(\frac{d^3M(x)}{dx^3}-\frac{dp_y(x)}{dx}\right.\right.$$
$$\left.\left.-\frac{d^2V_s(x)}{dx^2}\right)\right)dx$$
$$+\left[\left(\left(\frac{1}{k_1}+\frac{1}{k_2}\right)\left(\frac{d^2M(x)}{dx^2}-p_y(x)\right)-\frac{1}{k_1}\frac{dV_s(x)}{dx}\right)\right.$$
$$\left.\times\frac{d\delta M(x)}{dx}\right]_0^L$$
$$+\left[\left(\left(\frac{1}{k_1}+\frac{1}{k_2}\right)\left(\frac{dp_y(x)}{dx}-\frac{d^3M(x)}{dx^3}\right)+\frac{1}{k_1}\frac{d^2V_s(x)}{dx^2}\right)\right.$$
$$\left.\times\delta M(x)\right]_0^L$$
$$+\left[\frac{1}{k_1}\left(p_y(x)+\frac{dV_s(x)}{dx}-\frac{d^2M(x)}{dx^2}\right)\delta V_s(x)\right]_0^L$$
$$-\delta\mathbf{P}^T\mathbf{U}=0. \tag{11}$$

Considering the shear-force definition of (2) and following the Cartesian sign convention, (11) can be written as

$$\int_L \delta M(x)\left(\frac{M(x)}{\mathrm{IE}}+\left(\frac{1}{k_1}+\frac{1}{k_2}\right)\left(\frac{d^4M(x)}{dx^4}-\frac{d^2p_y(x)}{dx^2}\right)\right.$$
$$\left.-\frac{1}{k_1}\frac{d^3V_s(x)}{dx^3}\right)dx$$
$$+\int_L \delta V_s(x)\left(\frac{V_s(x)}{\mathrm{GA}}+\frac{1}{k_1}\left(\frac{d^3M(x)}{dx^3}-\frac{dp_y(x)}{dx}\right.\right.$$
$$\left.\left.-\frac{d^2V_s(x)}{dx^2}\right)\right)dx$$
$$-\delta P_1\left(U_1-\left(\left(\frac{1}{k_1}+\frac{1}{k_2}\right)\left(p_y(x)-\frac{d^2M(x)}{dx^2}\right)\right.\right.$$
$$\left.\left.+\frac{1}{k_1}\frac{dV_s(x)}{dx}\right)_{x=0}\right)$$
$$-\delta P_2\left(U_2-\left(\frac{1}{k_1}\frac{d^2V_s(x)}{dx^2}+\left(\frac{1}{k_1}+\frac{1}{k_2}\right)\frac{dp_y(x)}{dx}\right.\right.$$
$$\left.\left.-\left(\frac{1}{k_1}+\frac{1}{k_2}\right)\frac{d^3M(x)}{dx^3}\right)_{x=0}\right)$$
$$-\delta P_3\left(U_3-\left(\left(\frac{1}{k_1}+\frac{1}{k_2}\right)\left(p_y(x)-\frac{d^2M(x)}{dx^2}\right)\right.\right.$$
$$\left.\left.+\frac{1}{k_1}\frac{dV_s(x)}{dx}\right)_{x=L}\right)$$
$$-\delta P_4\left(U_4-\left(\frac{1}{k_1}\frac{d^2V_s(x)}{dx^2}+\left(\frac{1}{k_1}+\frac{1}{k_2}\right)\frac{dp_y(x)}{dx}\right.\right.$$
$$\left.\left.-\left(\frac{1}{k_1}+\frac{1}{k_2}\right)\frac{d^3M(x)}{dx^3}\right)_{x=L}\right)$$
$$-\delta P_5\left(U_5-\frac{1}{k_1}\left(p_y(x)+\frac{dV_s(x)}{dx}-\frac{d^2M(x)}{dx^2}\right)_{x=0}\right)$$
$$-\delta P_6\left(U_6-\frac{1}{k_1}\left(p_y(x)+\frac{dV_s(x)}{dx}-\frac{d^2M(x)}{dx^2}\right)_{x=L}\right)$$
$$=0. \tag{12}$$

Due to the arbitrariness of $\delta M(x)$ and $\delta V_s(x)$, the governing differential compatibility equations of the beam and shear-layer components are obtained; thus

$$\frac{M(x)}{\mathrm{IE}}+\left(\frac{1}{k_1}+\frac{1}{k_2}\right)\left(\frac{d^4M(x)}{dx^4}-\frac{d^2p_y(x)}{dx^2}\right)$$
$$-\frac{1}{k_1}\frac{d^3V_s(x)}{dx^3}=0:\quad \text{for } x\in(0,L), \tag{13}$$

$$\frac{V_s(x)}{\mathrm{GA}} + \frac{1}{k_1}\left(\frac{d^3M(x)}{dx^3} - \frac{dp_y(x)}{dx} - \frac{d^2V_s(x)}{dx^2}\right) = 0: \quad \text{for } x \in (0, L). \tag{14}$$

Equations (13) and (14) form a set of governing differential compatibility equations of the system. It is noted that the compatibility equations of the lower and upper spring deformations are not involved in the virtual force equation since their conjugate-work forces ($D_1(x)$ and $D_2(x)$) are eliminated in (10). However, they can be obtained simply by considering the geometrical deformations of the lower and the upper springs in Figure 1(a) as

$$\begin{gathered}\Delta_1(x) - v_s(x) = 0,\\ \Delta_2(x) - (v_B(x) - v_s(x)) = 0,\end{gathered} \tag{15}$$

where $v_s(x)$ is the shear-layer vertical displacement. Considering the deformation-force relations of (5) and enforcing the equilibrium equations of (3) and (4) and compatibility equations of (15), (13), and (14) are reduced to

$$\kappa(x) - \frac{d^2v_B(x)}{dx^2} = 0, \tag{16}$$

$$\gamma(x) - \frac{dv_s(x)}{dx} = 0. \tag{17}$$

It now becomes clear that (13) and (14) simply state the definitions of the beam section curvature and shear-layer section shear strain, respectively.

To make use of (13) and (14), there is a need to establish the relation between $V_s(x)$ and $M(x)$. This could be accomplished by recalling the governing differential equation of the foundation surface subjected to a continuously distributed load as given by Kerr [11]:

$$\left(1 + \frac{k_1}{k_2}\right)D_2(x) - \frac{\mathrm{GA}}{k_2}\frac{d^2D_2(x)}{dx^2} = k_1v_B(x) - \mathrm{GA}\frac{d^2v_B(x)}{dx^2}. \tag{18}$$

Enforcing the equilibrium equations of (3) and (4) as well as compatibility equations of (15), recalling the curvature definition of (16), and considering the deformation-force relations of (5), (18) relates the first derivative of the shear-layer section shear force to the bending moment and its fourth-order derivative as

$$\frac{dV_s(x)}{dx} = \frac{\mathrm{GA}}{\mathrm{IE}}M(x) + \frac{\mathrm{GA}}{k_2}\frac{d^4M(x)}{dx^4} - \frac{\mathrm{GA}}{k_2}\frac{d^2p_y(x)}{dx^2}. \tag{19}$$

Differentiating (19) twice and substituting into (13) yield the following sixth-order differential equation:

$$\frac{d^6M(x)}{dx^6} + \lambda_1\frac{d^4M(x)}{dx^4} + \lambda_2\frac{d^2M(x)}{dx^2} + \lambda_3M(x) = \frac{d^4p_y(x)}{dx^4} + \lambda_1\frac{d^2p_y(x)}{dx^2}: \quad \text{for } x \in (0, L), \tag{20}$$

where $\lambda_1 = -((k_1 + k_2)/\mathrm{GA})$; $\lambda_2 = k_2/\mathrm{IE}$ and $\lambda_3 = -k_1k_2/\mathrm{IEGA}$.

It is noted that when the upper-spring modulus k_2 approaches infinite, (20) is reduced to a fourth-order governing differential compatibility equation of the beam on Winkler-Pasternak foundation as given by Limkatanyu et al. [30] and when the shear-layer section modulus GA is equal to zero, (20) becomes a fourth-order governing differential compatibility equation of the beam on Winkler foundation as given by Limkatanyu et al. [29]. Furthermore, when compared to the governing differential equation derived by Avramidis and Morfidis [19] using the principle of stationary potential energy (equivalent to the virtual displacement principle), it becomes clear that (20) and the one derived by Avramidis and Morfidis [19] are dual. This illustrates the dualism of the virtual displacement and virtual force principles.

The end-boundary compatibility conditions are obtained by accounting for the arbitrariness of $\delta\mathbf{P}$ in (12) as

$$\begin{aligned}
U_1 &= \frac{1}{k_1}\left(\frac{dV_s(x)}{dx}\right)_{x=0} - \left(\frac{1}{k_1} + \frac{1}{k_2}\right)\left(\frac{d^2M(x)}{dx^2}\right)_{x=0} + \left(\frac{1}{k_1} + \frac{1}{k_2}\right)\left(p_y(x)\right)_{x=0},\\
U_2 &= \frac{1}{k_1}\left(\frac{d^2V_s(x)}{dx^2}\right)_{x=0} - \left(\frac{1}{k_1} + \frac{1}{k_2}\right)\left(\frac{d^3M(x)}{dx^3}\right)_{x=0} + \left(\frac{1}{k_1} + \frac{1}{k_2}\right)\left(\frac{dp_y(x)}{dx}\right)_{x=0},\\
U_3 &= \frac{1}{k_1}\left(\frac{dV_s(x)}{dx}\right)_{x=L} - \left(\frac{1}{k_1} + \frac{1}{k_2}\right)\left(\frac{d^2M(x)}{dx^2}\right)_{x=L} + \left(\frac{1}{k_1} + \frac{1}{k_2}\right)\left(p_y(x)\right)_{x=L},\\
U_4 &= \frac{1}{k_1}\left(\frac{d^2V_s(x)}{dx^2}\right)_{x=L} - \left(\frac{1}{k_1} + \frac{1}{k_2}\right)\left(\frac{d^3M(x)}{dx^3}\right)_{x=L} + \left(\frac{1}{k_1} + \frac{1}{k_2}\right)\left(\frac{dp_y(x)}{dx}\right)_{x=L},\\
U_5 &= \frac{1}{k_1}\left(\frac{dV_s(x)}{dx} - \frac{d^2M(x)}{dx^2}\right)_{x=0} + \frac{1}{k_1}\left(p_y(x)\right)_{x=0},\\
U_6 &= \frac{1}{k_1}\left(\frac{dV_s(x)}{dx} - \frac{d^2M(x)}{dx^2}\right)_{x=L} + \frac{1}{k_1}\left(p_y(x)\right)_{x=L}.
\end{aligned} \tag{21}$$

It is observed that the homogeneous and particular contributions to the end displacements are clearly separated in (21). This observation is unique to the proposed formulation and very useful in determining the equivalent fixed-end force vector due to the element load $p_y(x)$.

3. "Exact" Element Stiffness Matrix: Natural Approach

In this paper, the "*exact*" element stiffness matrix is derived simply by inverting the "*exact*" element flexibility equation. This is feasible since the system does not experience any rigid-body motion (neither rigid-body translation nor rigid-body rotation) due to the presence of supporting foundation. Thus, the exact element flexibility matrix is at the core of the element formulation and requires the "*exact*" moment interpolation functions. The analytical solution to the sixth-order governing differential compatibility equation of (20) is central to obtain the exact moment interpolation functions. For the sake of simplicity, the applied distributed load $p_y(x)$ is assumed to be uniform along the whole length of the beam. Thus, only homogeneous solution is required to derive the exact moment interpolation functions. This merit comes from the fact that the force terms on the right-hand side of (20) disappear as long as $p_y(x)$ varies uniformly along the whole length of the beam, thus rendering the proposed flexibility-based model attractive and unique.

Thanks to the comprehensive investigation performed by Morfidis [34] and Avramidis and Morfidis [19] on all possible solutions to the similar sixth-order differential equation, the general solution of (20) can be written as

$$\begin{aligned} M(x) = {} & \varphi_1(x)c_1 + \varphi_2(x)c_2 + \varphi_3(x)c_3 + \varphi_4(x)c_4 \\ & + \varphi_5(x)c_5 + \varphi_6(x)c_6, \end{aligned} \tag{22}$$

where $\varphi_1(x)$, $\varphi_2(x)$, $\varphi_3(x)$, $\varphi_4(x)$, $\varphi_5(x)$, and $\varphi_6(x)$ are real functions and their forms depend on the values of the system parameters (λ_1, λ_2, and λ_3) as given in Appendix A; and c_1, c_2, c_3, c_4, c_5, and c_6 are constants of integration to be determined by imposing force boundary conditions. These six force boundary conditions are

$$\begin{aligned} -\left[\frac{dM}{dx}\right]_{x=0} &= P_1, \qquad -M(0) = P_2, \\ \left[\frac{dM}{dx}\right]_{x=L} &= P_3, \qquad M(L) = P_4, \\ -[V_s]_{x=0} &= P_5, \qquad [V_s]_{x=L} = P_6. \end{aligned} \tag{23}$$

The first four boundary conditions on the beam ends can be imposed directly while the last two on the shear-layer ends cannot be enforced at the first stage since the beam-section bending moment $M(x)$ is the only variable field in the governing differential compatibility equation of (20). This difficulty can be overcome by establishing the relation between $V_s(x)$ and $M(x)$.

Recalling the shear-layer compatibility condition of (14) and the $V_s(x) - M(x)$ relation of (19), the shear-layer shear force $V_s(x)$ can be expressed in terms of the beam-section bending moment $M(x)$ and its derivatives as

$$\begin{aligned} V_s(x) = {} & \vartheta_1\left(\frac{d^5M(x)}{dx^5} - \frac{d^3p_y(x)}{dx^3}\right) \\ & + \vartheta_2\left(\frac{d^3M(x)}{dx^3} - \frac{dp_y(x)}{dx}\right) + \vartheta_3\frac{dM(x)}{dx}, \end{aligned} \tag{24}$$

where $\vartheta_1 = \mathrm{GA}^2/k_1k_2$, $\vartheta_2 = -\mathrm{GA}/k_1$, and $\vartheta_3 = \mathrm{GA}^2/\mathrm{IE}k_1$.

By imposing force boundary conditions of (23), the moment interpolation relation can be expressed as

$$M(x) = \mathbf{N}_{BB}(x)\,\mathbf{P}, \tag{25}$$

where $\mathbf{N}_{BB}(x) = \lfloor N_{BB1}(x) \quad N_{BB2}(x) \quad N_{BB3}(x) \quad N_{BB4}(x) \quad N_{BB5}(x) \quad N_{BB6}(x)\rfloor$ is an array containing the moment interpolation functions. Imposing the relation of (24) and differential equilibrium equations of (3) and (4), the shear-layer shear force $V_s(x)$, the lower-spring force $D_1(x)$, and the upper-spring force $D_2(x)$ can be expressed in terms of $\mathbf{P}$ as

$$\begin{aligned} V_s(x) &= \mathbf{N}_{V_sB}(x)\,\mathbf{P}, \\ D_1(x) &= \mathbf{N}_{D_1B}(x)\,\mathbf{P}, \\ D_2(x) &= \mathbf{N}_{D_2B}(x)\,\mathbf{P}, \end{aligned} \tag{26}$$

where $\mathbf{N}_{V_sB}(x) = \lfloor N_{V_sB1}(x) \; N_{V_sB2}(x) \; N_{V_sB3}(x) \; N_{V_sB4}(x) \; N_{V_sB5}(x) \; N_{V_sB6}(x)\rfloor$ is an array containing the shear-layer shear-force interpolation functions; $\mathbf{N}_{D_1B}(x) = \lfloor N_{D_1B1}(x) \; N_{D_1B2}(x) \; N_{D_1B3}(x) \; N_{D_1B4}(x) \; N_{D_1B5}(x) \; N_{D_1B6}(x)\rfloor$ is an array containing the lower-spring force interpolation functions; and $\mathbf{N}_{D_2B}(x) = \lfloor N_{D_2B1}(x) \; N_{D_2B2}(x) \; N_{D_2B3}(x) \; N_{D_2B4}(x) \; N_{D_2B5}(x) \; N_{D_2B6}(x)\rfloor$ is an array containing the upper-spring force interpolation functions.

Applying the virtual force expression of (9), substituting (25)-(26), and accounting for the arbitrariness of $\delta\mathbf{P}$ yield the following element flexibility equation:

$$\mathbf{FP} = \mathbf{U} + \mathbf{U}_{p_y}, \tag{27}$$

where $\mathbf{F}$ is the element flexibility matrix, defined as

$$\mathbf{F} = \mathbf{F}_{BB} + \mathbf{F}_{V_sV_s} + \mathbf{F}_{D_1D_1} + \mathbf{F}_{D_2D_2}, \tag{28}$$

where $\mathbf{F}_{BB}$, $\mathbf{F}_{V_sV_s}$, $\mathbf{F}_{D_1D_1}$, and $\mathbf{F}_{D_2D_2}$ are the beam, the shear-layer, the lower-spring, and the upper-spring contributions to the element flexibility matrix, respectively:

$$\begin{aligned} \mathbf{F}_{BB} &= \int_L \mathbf{N}_{BB}{}^T\left(\frac{1}{\mathrm{IE}}\right)\mathbf{N}_{BB}\,dx, \\ \mathbf{F}_{V_sV_s} &= \int_L \mathbf{N}_{V_sB}{}^T\left(\frac{1}{\mathrm{GA}}\right)\mathbf{N}_{V_sB}\,dx, \\ \mathbf{F}_{D_1D_1} &= \int_L \mathbf{N}_{D_1B}{}^T\left(\frac{1}{k_1}\right)\mathbf{N}_{D_1B}\,dx, \\ \mathbf{F}_{D_2D_2} &= \int_L \mathbf{N}_{D_2B}{}^T\left(\frac{1}{k_2}\right)\mathbf{N}_{D_2B}\,dx. \end{aligned} \tag{29}$$

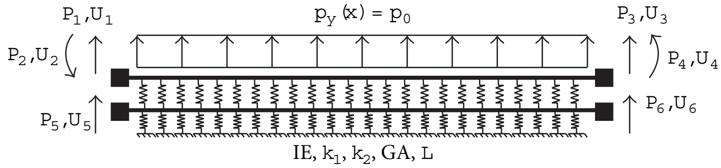

Figure 2: Natural beam element on Kerr-type foundation.

It is noted that element end displacements $\mathbf{U}_{p_y}$ due to the applied load $p_y(x)$ is supplemented into (27). In the case of linear variation of $p_y(x)$, $\mathbf{U}_{p_y}$ can be written in a simple expression as given in Appendix B.

Based on the element flexibility expression of (27), the element stiffness equation can be written as

$$\mathbf{P} = \mathbf{K}_N\mathbf{U} + \mathbf{P}_{p_y}^{FE}, \tag{30}$$

where the complete element stiffness matrix $\mathbf{K}_N$ is $\mathbf{F}^{-1}$ and the fixed-end force vector due to $p_y(x)$ is simply computed as $\mathbf{K}_N\mathbf{U}_{p_y}$. It is worthwhile to note that the subscript N stands for "*natural*." This is due to the fact that the approach employed herein to obtain the element stiffness matrix is known as the natural approach [28]. The configuration of the natural beam element on Kerr-type foundation is shown in Figure 2.

Unlike the stiffness-based formulation, the displacement fields cannot be computed directly since no displacement interpolation function is available in the element formulation. However, the following compatibilities can be used to retrieve the vertical displacement and rotational fields of the beam component and the vertical displacement field of the shear-layer component once the internal force distributions are obtained:

$$\begin{aligned} v_B(x) &= \left(\frac{1}{k_1}+\frac{1}{k_2}\right)\left(p_y(x)-\frac{d^2M(x)}{dx^2}\right)+\frac{1}{k_1}\frac{dV_s(x)}{dx}, \\ \theta_B(x) &= \frac{dv_B(x)}{dx} \\ &= \left(\frac{1}{k_1}+\frac{1}{k_2}\right)\left(\frac{dp_y(x)}{dx}-\frac{d^3M(x)}{dx^3}\right) \\ &\quad +\frac{1}{k_1}\frac{d^2V_s(x)}{dx^2}, \\ v_s(x) &= \frac{1}{k_1}\left(p_y(x)-\frac{d^2M(x)}{dx^2}+\frac{dV_s(x)}{dx}\right). \end{aligned} \tag{31}$$

4. Restrained Effects of Extended Kerr-Type Foundation on the Beam End

When the foundation on either end of the beam is infinitely extended, appropriate modeling of the beam-end condition is deemed essential to account for the foundation continuity [35]. One efficient way to consider this end effect is to place a vertical spring with a stiffness of $\sqrt{k_1\mathrm{GA}}$ at the associated beam end as suggested by Eisenberger and Bielak [36]. A detailed derivation of this stiffness value can be found in Alemdar and Gülkan [35] and Colasanti and Horvath [25]. For the case of finitely extended foundation, a virtual beam-foundation element with a small value of the flexural rigidity and large value of the upper-spring modulus can be assumed beyond its physical end to account for the existence of the extended foundation.

5. Numerical Example

A free-free beam on an infinitely long Kerr-type foundation subjected to various loads along its length is shown in Figure 3. This beam-foundation system was also studied by Morfidis [20] and is used in this study to verify the accuracy and to show the efficiency of the natural beam element on Kerr-type foundation. The flexural stiffness IE and width b of the beam are 248.7×10^3 kN-m^2 and 1 m, respectively. The elastic soil mass underneath the beam is 10 m depth and is assumed to be loose sand with elastic modulus $E_s = 17.5 \times 10^3$ kN/m^2 and Poisson ratio $\nu = 0.3$. Following the modified Kerr-Reissner model [18, 19], the lower-spring k_1 and shear-layer section GA moduli are found to be 2.33×10^3 kN/m^2 and 29.91×10^3 kN, respectively. As suggested by Avramidis and Morfidis [19], the upper-spring modulus k_2 is related to the lower-spring modulus k_1 as

$$n_{k_2k_1} = \frac{k_2}{k_1}, \tag{32}$$

where $n_{k_2k_1}$ is a factor expressing the relative stiffness of the upper and the lower springs. Following comprehensive correlation studies between the three-parameter foundation and the high fidelity 2D finite element models by Avramidis and Morfidis [19], the optimal values of $n_{k_2k_1}$ are suggested depending on the system parameters. In this example, the value of $n_{k_2k_1}$ is equal to 7 which is the optimal value for soft soils [19]. Thus, the value of k_2 is equal to 16.3×10^3 kN/m^2. To account for the effect of infinitely extended foundation beyond both beam ends, a vertical spring with stiffness $k_{\mathrm{end}} = \sqrt{k_1\mathrm{GA}} = 8.35 \times 10^3$ kN/m is placed at each end as shown in Figure 3. Seven natural beam-foundation elements (elements AB, BC, CD, DE, EF, FG, and GH) are used to discretize the system, thus resulting in twenty-four nodal unknowns.

The beam-foundation system of Figure 3 is also analyzed by the 2D finite element model [33]. Figure 4 shows the 2D finite element mesh of the beam-foundation system of Figure 3. The virtual soil mass of the length $2L = 15$ m is

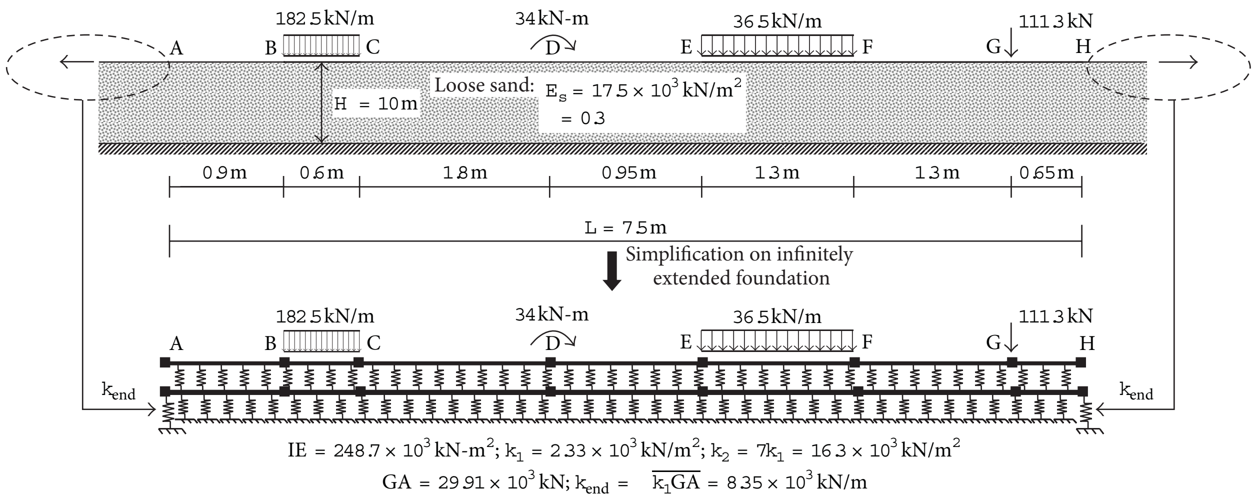

Figure 3: Numerical example: free-free beam on Kerr-type foundation subjected to various loads along its length.

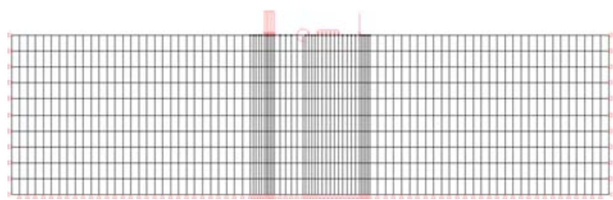

Figure 4: 2D finite element mesh of the beam-foundation system in Figure 3.

assumed beyond each beam end to account for the existence of the infinitely long foundation. The soil mass is discretized into 950 rectangular plane-strain elements while the beam is modeled with 35 conventional beam elements. In order to ensure the sufficiency of the model discretization, a finer finite element mesh was used but yielded the same analysis results.

Figure 5 shows the obtained beam vertical displacement, beam rotation and shear-layer vertical displacement diagrams while Figure 6 shows the obtained beam shear force, beam moment, and shear-layer force diagrams. The exact displacement-based responses given by Avramidis and Morfidis [19] and Morfidis [20] as well as the responses obtained with 2D finite element analysis (2D FEM model) are also superimposed for comparison on the respective diagrams. Clearly, the natural beam-foundation model is capable of representing the exact displacement and force responses using only one element for the beam span. Winkler-foundation responses obtained with the model by Limkatanyu et al. [29] are also presented in the same respective diagrams. The results presented in Figure 5 indicate that the Kerr-type foundation model plays a role in reducing the vertical displacement and rotation of the beam, thanks to the coupling between the Winkler-foundation springs. This coupling effect renders the Kerr-type foundation model with the ability to resemble the displacement and rotation diagrams obtained with the 2D FEM model. When compared to the Winkler-foundation model, Figure 6 shows that the Kerr-type foundation model affects the bending moment response more than the shear-force response along the beam. Furthermore, the bending moment response obtained with the Kerr-type foundation model is closer to that obtained with the 2D FEM model when compared to the Winkler-foundation model. It should be kept in mind that a complete comparison between the proposed model and the more sophisticated finite element model is not to be expected. This is due to the fact that a full compatibility at the beam-soil interface is assumed in the finite element model while only the vertical displacement compatibility is enforced in the proposed model [37]. In this example, introducing the more refined foundation model generally results in reducing the negative moment (concave) but slightly increasing the positive moment (convex).

Figure 7 shows the upper and the lower spring force diagrams. Obviously, the proposed beam-foundation element is capable of representing the exact foundation-spring force distributions along the beam length. Figure 7(a) compares the interactive foundation force acting at the bottom face of the beam obtained with the Winkler and Kerr-type foundation models. Evidently, the distribution characteristics of these two foundation interactive forces are distinctively different. The interactive foundation force distribution obtained with the Kerr-type foundation model corresponds well to the observation made by Foppl [12] that there exists a certain degree of discontinuities in system responses between the loaded and the unloaded regions of the actual beam-foundation system. This feature is unique to the Kerr-type foundation model and clearly indicated by incompatibilities between the upper and the lower foundation spring forces at

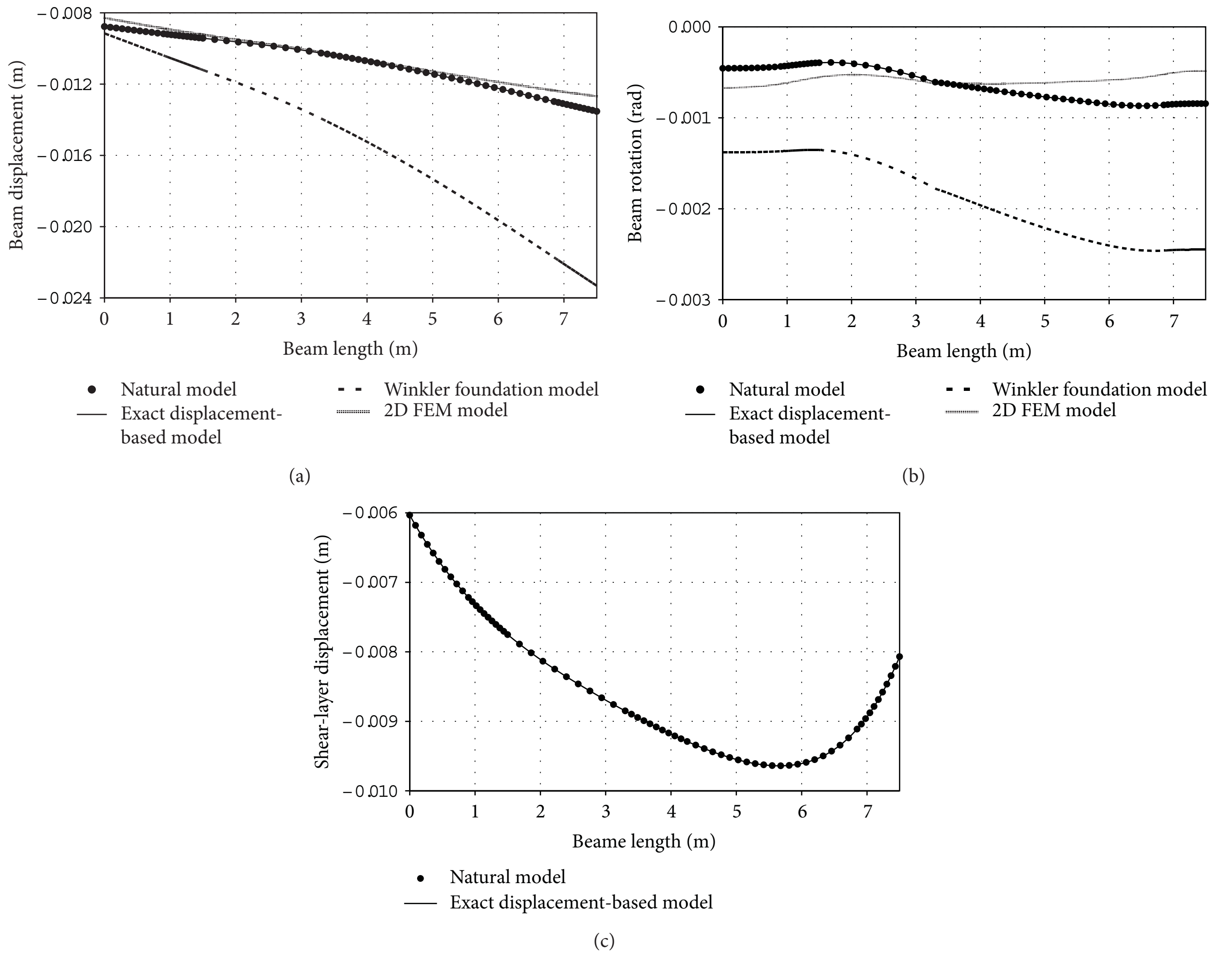

Figure 5: Diagrams for beam displacement, beam rotation, and shear-layer displacement.

both beam ends ($x = 0$ and $x = 7.5$ m), thus resulting in accurately representing the peripheral reactions of the beam ends [6].

6. Summary and Conclusions

The "*natural*" element stiffness matrix and the fixed-end force vector for a beam on elastic foundation subjected to a uniformly distributed load are derived in this paper. The Kerr-type foundation model is employed to model the underlying foundation continua, thus taking into account the shear coupling between the individual Winkler-spring components through the shear-layer component and determining the level of vertical-displacement continuity at the boundaries between the loaded and the unloaded soil surfaces. This feature is unique to the Kerr-type foundation model. The element flexibility matrix forms the core of the natural element stiffness matrix and is derived based on the virtual force principle using the "*exact*" force interpolation functions. The exact force interpolation functions are obtained by solving analytically the sixth-order governing differential compatibility equation. Compared to the stiffness-based models published in the literatures, the effect of the applied element load can readily be included in the proposed formulation. One numerical example is employed to verify the accuracy and efficiency of the natural beam-foundation model. This numerical example shows that the natural beam-foundation element is capable of giving exact system responses. Therefore, the exactness of the proposed element obviates the requirement for discretizing the beam into several elements between loading points. The number of elements needed in the analysis of a beam-foundation system is largely dictated by the convenient way of representing loadings (concentrated or distributed loads). Furthermore, the Kerr-type foundation model results in more realistic interactive foundation forces as compared to the Winkler foundation model. A 2D finite element model is also used to confirm the superiority of the proposed model. The next step forward in this research direction is to account for system nonlinearities and to apply the resulting model to practical soil-structure interaction

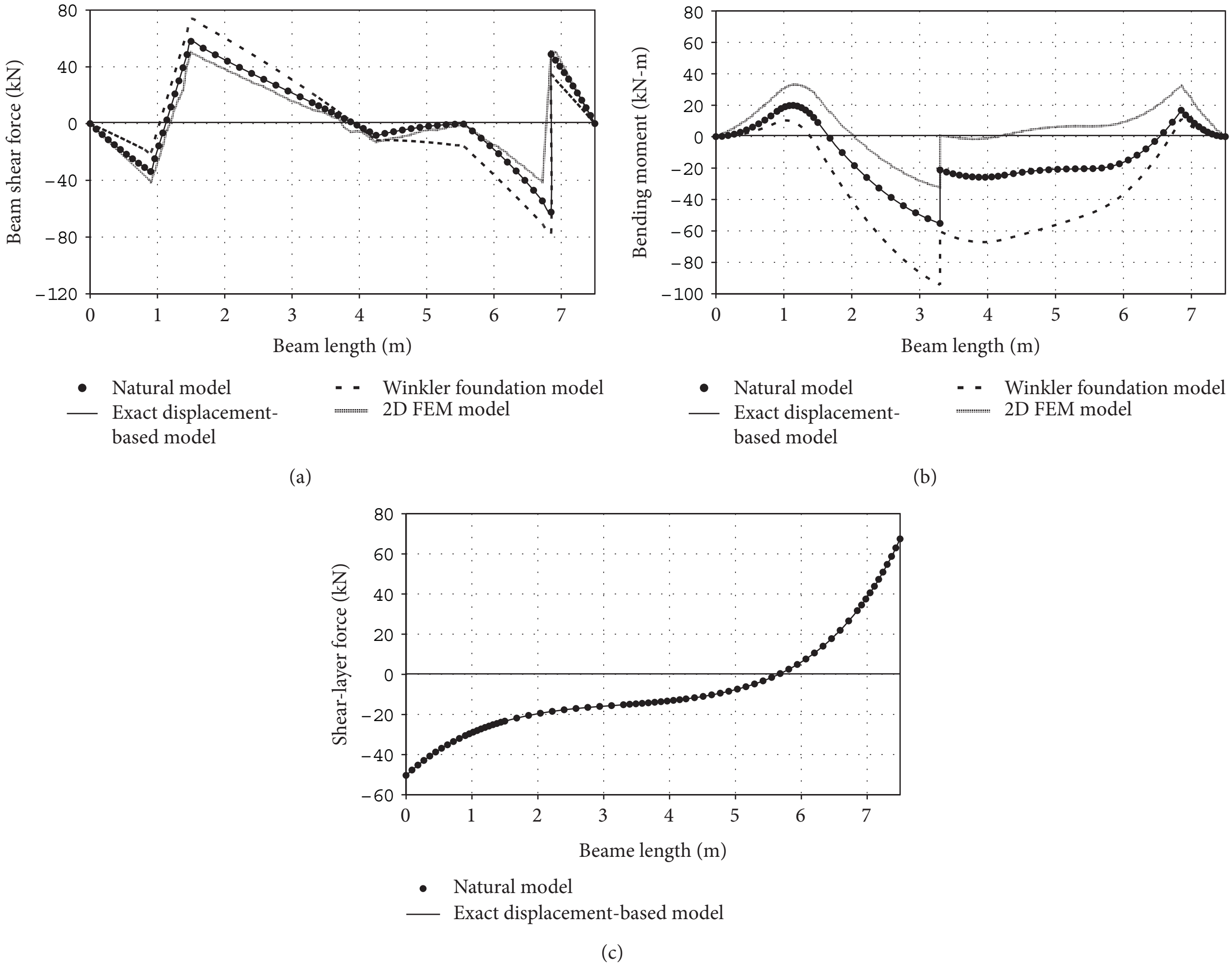

Figure 6: Diagrams for beam shear force, bending moment, and shear-layer force.

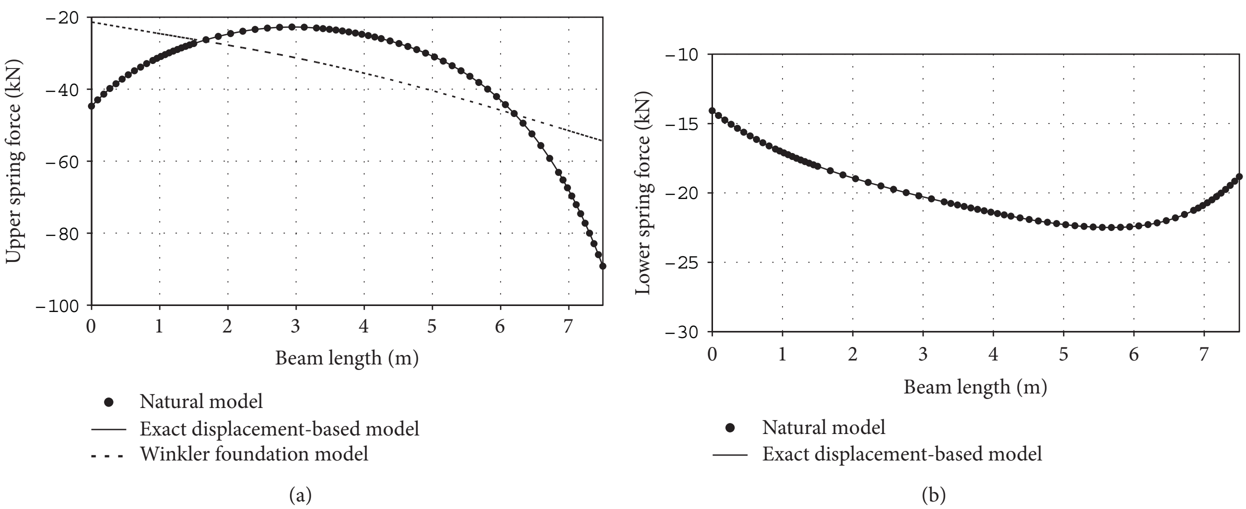

Figure 7: Diagrams for upper and lower spring foundation forces.

problems. This could be accomplished by first following the evolution of beam and foundation mechanical parameters and then updating the force interpolation functions accordingly. Another interesting topic worth investigating in future works is the derivation of consistent mass and geometric stiffness matrices based on the force interpolation functions.

Appendices

A. Homogenous Solution to the Sixth-Order Governing Differential Compatibility Equation (20)

The homogeneous form of (20) can be written as

$$\frac{d^6M(x)}{dx^6}+\lambda_1\frac{d^4M(x)}{dx^4}+\lambda_2\frac{d^2M(x)}{dx^2}+\lambda_3M(x) = 0: \quad \text{for } x\in(0,L). \tag{A.1}$$

For simplicity, the following auxiliary variables are introduced instead of terms of system parameters λ_1, λ_2, and λ_3:

$$\alpha=\frac{\left(-\left(\lambda_1^2/3\right)+\lambda_2\right)}{3},$$
$$\beta=\frac{\left(\left(2\lambda_1^3/27\right)-\left(\lambda_1\lambda_2/3\right)+\lambda_3\right)}{2}, \tag{A.2}$$
$$\Delta=\alpha^3+\beta^2,$$

$$\Phi_1=-\frac{\left(\sqrt[3]{-\beta+\sqrt{\Delta}}+\sqrt[3]{-\beta-\sqrt{\Delta}}+\left(2\lambda_1/3\right)\right)}{2},$$
$$\Phi_2=\frac{\sqrt{3}\left(\sqrt[3]{-\beta+\sqrt{\Delta}}-\sqrt[3]{-\beta-\sqrt{\Delta}}\right)}{2}. \tag{A.3}$$

There are many solution types to (A.1) depending on the sign of the auxiliary parameter Δ. Thanks to the thorough investigations of all possible solution cases, Avramidis and Morfidis [19] and Morfidis [20] suggest the most common solution case corresponding to the positive sign of the auxiliary parameter Δ as follows.

Solution Case (when $\Delta=\alpha^3+\beta^2>0$). The homogeneous solution of (20) can be written as

$$M(x)=\varphi_1(x)c_1+\varphi_2(x)c_2+\varphi_3(x)c_3+\varphi_4(x)c_4+\varphi_5(x)c_5+\varphi_6(x)c_6, \tag{A.4}$$

where

$$\varphi_1(x)=e^{\Gamma_1L},\qquad \varphi_2(x)=e^{-\Gamma_1L},$$
$$\varphi_3(x)=e^{\Gamma_3L}\cos\Gamma_2L,\qquad \varphi_4(x)=e^{\Gamma_3L}\sin\Gamma_2L, \tag{A.5}$$
$$\varphi_5(x)=e^{-\Gamma_3L}\cos\Gamma_2L,\qquad \varphi_6(x)=e^{-\Gamma_3L}\sin\Gamma_2L,$$

$$\Gamma_1=\sqrt{\sqrt[3]{-\beta+\sqrt{\Delta}}+\sqrt[3]{-\beta-\sqrt{\Delta}}-\frac{\lambda_1}{3}},$$
$$\Gamma_2=\sqrt{\frac{\left(\sqrt{\Phi_1^2+\Phi_2^2}-\Phi_1\right)}{2}}, \tag{A.6}$$
$$\Gamma_3=\sqrt{\frac{\left(\sqrt{\Phi_1^2+\Phi_2^2}+\Phi_1\right)}{2}}.$$

B. Nodal Displacements due to $p_y(x)$

The nodal displacements due to the uniformly distributed load $p_y(x)=p_0$ may be written as

$$U_{1p_y}=U_{3p_y}=\left(\frac{1}{k_1}+\frac{1}{k_2}\right)p_0,$$
$$U_{2p_y}=U_{4p_y}=0, \tag{B.1}$$
$$U_{5p_y}=U_{6p_y}=\frac{p_0}{k_1}.$$

Acknowledgments

This study was partially supported by the Thai Ministry of University Affairs (MUA), by the Thailand Research Fund (TRF) under Grant MRG4680109 and Grant RSA5480001, by STREAM Research Group under Grant ENG-51-2-7-11-022-S, Faculty of Engineering, Prince of Songkla University, and by the National Research Foundation of Korea (NRF) Grant funded by the Korean government (MEST) (NRF-2011-0028531). Any opinions expressed in this paper are those of the authors and do not reflect the views of the sponsoring agencies. Special thanks are due to the senior lecturer Mr. Wiwat Sutiwipakorn for reviewing and correcting the English of this paper and Mr. Paitoon Ponbunyanon and Mr. Attpon Sangkeaw for preparing the numerical example. In addition, the authors would also like to thank three anonymous reviewers for their valuable and constructive comments.

References

[1] D. Elata and S. Abu-Salih, "Analysis of electromechanical buckling of a prestressed microbeam that is bonded to an elastic foundation," *Journal of Mechanics of Materials and Structures*, vol. 1, no. 5, pp. 911–923, 2006.

[2] E. Ghavanloo, F. Daneshmand, and M. Rafiei, "Vibration and instability analysis of carbon nanotubes conveying fluid and resting on a linear viscoelastic Winkler foundation," *Physica E*, vol. 42, no. 9, pp. 2218–2224, 2010.

[3] M. M. Shokrieh and M. Heidari-Rarani, "A comparative study for beams on elastic foundation models to analysis of model delamination in DCB specimens," *Structural Engineering and Mechanics*, vol. 37, no. 2, pp. 149–162, 2011.

[4] E. Winkler, *Die Lehre Von Der Und Festigkeit*, Dominicus, Prague, Czech Republic, 1867.

[5] K. Wieghardt, "Ü den balken auf nachgiebiger unterlage," *Zeitschrift für Angewandte Mathematik und Mechanik*, vol. 2, pp. 165–184, 1922.

[6] A. D. Kerr, "Elastic and viscoelastic foundation models," *Journal Applied Mechanics Transaction*, vol. 31, no. 4, pp. 491–498, 1964.

[7] M. M. Filonenko-Borodich, "Some approximate theories of elastic foundation," *Uchenyie Zapiski Moskovskogo Gosudarstvennogo Universiteta Mekhanica*, vol. 46, pp. 3–18, 1940.

[8] S. N. Sokolov, *Circular Plate on a Generalized Foundation*, Inzhinierny Sbornik, Academy of Sciences, Moscow, Russia, 1952.

[9] P. L. Pasternak, *On a New Method of Analysis of an Elastic Foundation by Means of Two Constants*, Gosudarstvennoe Izdatelstvo Literaturi po Stroitelstvu I Arkhitekture, Moscow, Russia, 1954.

[10] M. Hetényi, "A general solution for the bending of beams on an elastic foundation of arbitrary continuity," *Journal of Applied Physics*, vol. 21, no. 1, pp. 55–58, 1950.

[11] A. D. Kerr, "A study of a new foundation model," *Acta Mechanica*, vol. 1, no. 2, pp. 135–147, 1965.

[12] A. Foppl, *Vorlesungen Uber Technische Mechanik*, B. B. Teubner, Leipzig, Germany, 1909.

[13] E. Reissner, "A note on deflection of plates on a viscoelastic foundation," *Journal Applied Mechanics*, vol. 25, pp. 144–155, 1958.

[14] J. S. Horvath, *A study of analytical methods for determining the response of mat foundations to static loads [Ph.D. thesis]*, Polytechnic Institute of New York, Brooklyn, NY, USA, 1979.

[15] J. J. Horvath, "New subgrade model applied to mat foundations," *Journal of Geotechnical Engineering*, vol. 109, no. 12, pp. 1567–1587, 1983.

[16] A. Worku, "Calibrated analytical formulas for foundation model parameters," *International Journal of Geomechanics*, vol. 13, no. 4, pp. 340–347, 2013.

[17] J. S. Horvath, "Discussion of modified Vlasov model for beams on elastic foundations," *Journal of Geotechnical Engineering*, vol. 118, no. 9, pp. 1482–1484, 1992.

[18] J. S. Horvath and R. J. Colasanti, "Practical subgrade model for improved soil-structure interaction analysis: model development," *International Journal of Geomechanics*, vol. 11, no. 1, pp. 59–64, 2010.

[19] I. E. Avramidis and K. Morfidis, "Bending of beams on three-parameter elastic foundation," *International Journal of Solids and Structures*, vol. 43, no. 2, pp. 357–375, 2006.

[20] K. Morfidis, "Exact matrices for beams on three-parameter elastic foundation," *Computers and Structures*, vol. 85, no. 15-16, pp. 1243–1256, 2007.

[21] K. Morfidis, "Vibration of Timoshenko beams on three-parameter elastic foundation," *Computers and Structures*, vol. 88, no. 5-6, pp. 294–308, 2010.

[22] Y. Zhang, "Tensionless contact of a finite beam resting on Reissner foundation," *International Journal of Mechanical Sciences*, vol. 50, no. 6, pp. 1035–1041, 2008.

[23] E. J. Sapountzakis and A. E. Kampitsis, "Nonlinear analysis of shear deformable beam-columns partially supported on tensionless three-parameter foundation," *Archive of Applied Mechanics*, vol. 81, no. 12, pp. 1833–1851, 2011.

[24] J. Wang and S. Zeng, "Dynamics of piezoelectric smart beams using a three-parameter elastic foundation model," *Journal of Intelligent Material Systems and Structures*, vol. 22, no. 1, pp. 3–16, 2011.

[25] R. J. Colasanti and J. S. Horvath, "Practical subgrade model for improved soil-structure interaction analysis: software implementation," *Practice Periodical on Structural Design and Construction*, vol. 15, no. 4, pp. 278–286, 2010.

[26] J. S. Horvath and R. J. Colasanti, "New hybrid subgrade model for soil-structure interaction analysis: foundation and geosynthetics applications," in *Proceedings of the Geo-Frontiers: Advances in Geotechnical Engineering*, pp. 4359–4368, Dallas, Tex, USA, March 2011.

[27] S. Limkatanyu and E. Spacone, "Frame element with lateral deformable supports: formulations and numerical validation," *Computers and Structures*, vol. 84, no. 13-14, pp. 942–954, 2006.

[28] J. H. Argyris, *Energy Theorems and Structural Analysis*, Butterworths & Co., London, UK, 1960.

[29] S. Limkatanyu, K. Kuntiyawichai, E. Spacone, and M. Kwon, "Natural stiffness matrix for beams on Winkler foundation: exact force-based derivation," *Structural Engineering and Mechanics*, vol. 42, no. 1, pp. 39–53, 2012.

[30] S. Limkatanyu, N. Damrongwiriyanupap, M. Kwon, and P. Ponbunyanon, "Force-based derivation of exact stiffness matrix for beams on Winkler-Pasternak Foundation," *Zeitschrift für Angewandte Mathematik und Mechanik*, 2013.

[31] S. Wolfram, *Mathematica Reference Guide*, Addison-Wesley, Redwood City, Calif, USA, 1992.

[32] R. L. Taylor, "FEAP: a finite element analysis program. User manual: version 7.3," Department of Civil and Environmental Engineering, University of California-Berkeley, 2000.

[33] R. D. Cook, *VisualFEA and General User Manual*, John Wiley and Son, New York, NY, USA, 2001.

[34] K. Morfidis, *Research and development of methods for the modeling of foundation structural elements and soil [Ph.D. thesis]*, Department of Civil Engineering, Aristotle University of Thessaloniki, Greece, 2003.

[35] B. N. Alemdar and P. Gülkan, "Beams on generalized foundations: supplementary element matrices," *Engineering Structures*, vol. 19, no. 11, pp. 910–920, 1997.

[36] M. Eisenberger and J. Bielak, "Remarks on two papers dealing with the response of beams on two-parameter elastic foundations," *Earthquake Engineering and Structural Dynamics*, vol. 18, no. 7, pp. 1077–1078, 1989.

[37] C. V. G. Vallabhan and Y. C. Das, "Modified vlasov model for beams on elastic foundations," *Journal of geotechnical engineering*, vol. 117, no. 6, pp. 956–966, 1991.

Hindawi Publishing Corporation
Journal of Applied Mathematics
Volume 2013, Article ID 926097, 12 pages
http://dx.doi.org/10.1155/2013/926097

Research Article

Three-Dimensional Modeling of Spatial Reinforcement of Soil Nails in a Field Slope under Surcharge Loads

Yuan-de Zhou,[1] Kai Xu,[2] Xinwei Tang,[3] and Leslie George Tham[4]

[1] *State Key Laboratory of Hydroscience and Engineering, Department of Hydraulic Engineering, Tsinghua University, Beijing 100084, China*
[2] *Nanjing Hydraulic Research Institute, 223 Guangzhou Road, Nanjing 210029, China*
[3] *School of Civil Engineering and Transportation, South China University of Technology, Guangzhou 510640, China*
[4] *Department of Civil Engineering, The University of Hong Kong, Pokfulam Road, Hong Kong*

Correspondence should be addressed to Xinwei Tang; cttangxw@scut.edu.cn

Received 7 June 2013; Accepted 14 August 2013

Academic Editor: Fayun Liang

Soil nailing has been one of the most popular techniques for improving the stability of slopes, in which rows of nails and a structural grillage system connecting nail heads are commonly applied. In order to examine the spatial-reinforcement effect of soil nails in slopes, a three-dimensional (3D) numerical model has been developed and used to back-analyze a field test slope under surcharge loading. Incremental elastoplastic analyses have been performed to study the internal deformation within the slope and the development of nail forces during the application of top surcharge loads. Different treatments of the grillage constraints at nail heads have been studied. It is shown that the numerical predictions compare favorably with the field test measurements. Both the numerical and the field test results suggest that soil nails are capable of increasing the overall stability of a loose fill slope for the loading conditions considered in this study. The axial force mobilization in the two rows of soil nails presents a strong dependence on the relative distance with the central section. With the surcharge loads increased near the bearing capacity of the slope, a grillage system connecting all the nail heads can affect the stabilizing mechanism to a notable extent.

1. Introduction

Soil nailing is an effective in situ reinforcing technique for retaining excavations and stabilizing slopes. The interaction between a soil nail and the surrounding soil is a key aspect in the design and therefore is of great interest to both engineers and researchers. Soil nails used in slope upgrading works normally consist of an unstressed steel bar grouted in a predrilled hole of soil mass using cement slurry and are usually designed as a passive reinforcement in that resisting axial force is mobilized only when slope instability is triggered by extreme loading. The primary resisting force comes from the tensile resistance of the steel reinforcement. The interaction mechanism is characterized by the mobilization of frictional forces along the entire length of the inclusion, which consequently results in the generation of tensile forces along the reinforcement. Quite several analytical models [1–5] have been developed and used to qualitatively describe the principal mechanism, which are easy to use but may oversimplify the complex stress transfer mechanism.

Numerical simulation is also an important method for investigating the soil nail behavior. Two-dimensional modeling has been commonly applied to simulate the fundamental behavior of soil-nail interactive system as a plane strain problem, such as those by Matsui et al. [6], Cheuk et al. [7], and Fan and Luo [8]. These studies focused on different aspects of soil-nail system, including the force transfer mechanism, soil-nail interaction, and failure mechanism. 3D modeling studies have been also applied by researchers to analyze fundamental behavior of nailed slopes. Zhang et al. [9] and Yang and Drumm [10] analyzed 3D slope behavior to investigate the effects of stage excavation, construction, and the surcharge loading. In addition, Zhou [11] studied the boundary effect on the pullout resistance and the pullout reaction of soil nails in a pullout test box using 3D numerical models. A thorough 3D numerical investigation into the reinforcement effect of multiple soil nails in slopes under varied working conditions is still limited.

Li [12] reported a field slope test to examine the strengthening mechanism of soil nails in a purposely built fill slope under different loading conditions. Typically top surcharge and water infiltration from the slope surface as well as the bottom were considered. The test results demonstrated a global stabilizing effect by the multiple soil nails. Detailed records of the slope movements, the nail force distributions, and the change in water content distributions were provided [12]. This paper describes a 3D numerical model for the investigation of the complex interaction between nails and surrounding soils in this slope test. The response in the surcharge process was focused in this study as significant nail forces were mobilized in this stage. Different to the previous research by the authors [13], the coupled hydromechanical response in the test slope is modeled based on a 3D finite element model in this study, in which the spatial reinforcement by two rows of soil nails is considered. An interface element technique is adopted to simulate the cohesive-frictional behavior along the soil-nail interface. The contribution of the surface grillage beams connecting the nail heads has been also examined through a series of numerical analyses. The numerical results are compared with the field measurements to assess the reinforcement effect of each soil nail in the designed arrangement manner, and the mechanism of nonuniform distribution of nail force mobilization has been also studied.

2. Briefs about the Field Test

2.1. Slope Construction and Geometry. For completeness, a brief introduction to the field test is provided in this section. More details about the field test can be found elsewhere [12]. The test slope is made up of loose completely decomposed granite (CDG) and was constructed on a moderately gentle site with an average gradient of 20°. The basic geometry of the slope is given in Figure 1. It was 4.75 m in height and 9 m in width. The crest of the slope is 4 m long, and the inclination angle is 33°. In order to laterally confine the fill soils, two gravity retaining walls were constructed on both sides, and an apron of 0.8 m in height was built at the toe. A blinding layer was placed underneath the fill slope to isolate it from the ground soil and to provide a drainage path for water infiltration during the wetting stages of the field test. It was constructed by ordinary concrete and reinforced by A252 steel mesh, and a layer of no-fines concrete was arranged above.

Ten cement grouted nails were installed in the test slope for the purpose of stabilization at vertical and horizontal spacings of 1.5 m. All the nails were arranged at an inclination angle of 20° to the horizontal. Similar to common practice, the construction procedures were as follows: firstly a hole of 100 mm in diameter was drilled; then a 25 mm diameter steel ribbed bar was inserted into the hole with centralizers to fix the position; at the last step, the hole was filled with ordinary cement slurry. In the field tests, two types of nail heads were applied, namely, independent head and grillage beams, which allowed an investigation into the influence of different treatments.

2.2. Field Surcharge Test. The field test study was comprised of three stages, namely, (1) surcharge, (2) wetting with surcharge, and (3) wetting without surcharge. For the main attention of this study is placed on the strengthening mechanism of multiple nails, only the surcharge loads during the first stage are described herein. The top surcharge was achieved by layering concrete blocks of $1\,\mathrm{m} \times 1\,\mathrm{m} \times 0.6\,\mathrm{m}$ on the slope crest (Figure 1). A total of 90 blocks were applied sequentially into 5 layers along the vertical direction. The development of resultant pressure from the self-weight of blocks on the central area of the crest can be categorized into 4 main stages (Figure 2), and the final total surcharge pressure was 72 kPa. During the field test, a comprehensive instrumentation system, including inclinometers, strain gauges, moisture probes, and tensiometers, was designed and installed in the fills and nails (Figure 1). The field measurement data formed the basis of the parametric analyses and discussions in this study.

3. Numerical Model

The field test data showed that the slope fills remained unsaturated during the surcharge stage. Even though the contribution of the suction to the overall response of the nailed slope has been demonstrated to be negligibly small by the previous plane strain analyses [13], a coupled hydromechanical numerical approach is adopted in this study for the consideration of consecutive modeling of the complete three stages in the field test. The finite element package ABAQUS [14] is used as a platform for the analyses. The current study adopts exactly the same basic assumptions as described in detail in [13]. Here we will just briefly outline the principles of this numerical model. The loose fill is treated as a porous medium, and a simplified effective stress principle is adopted to describe its mechanical behavior:

$$\overline{\sigma} = \sigma - \chi(s)\, u_w \mathbf{I}, \tag{1}$$

where $\overline{\sigma}$ and σ are the effective and total stresses, respectively; χ is a factor that depends on the saturation degree s; $\mathbf{I}$ is a second-order unit tensor; u_w denotes the pore water pressure. As a common choice, a simple function of $\chi = s$ is adopted in this study.

3.1. Basic Equations. The fundamental equations include stress equilibrium of the soil skeleton and flow continuity of pore water, which are given as follows:

$$\begin{aligned} \int_V (\overline{\sigma} + \chi u_w \mathbf{I}) : \delta\boldsymbol{\varepsilon}\, dV &= \int_s \mathbf{t} \cdot \delta\mathbf{v}\, dS + \int_V \mathbf{f} \cdot \delta\mathbf{v}\, dV \\ &\quad + \int_V sn\rho_w \mathbf{g} \cdot \delta\mathbf{v}\, dV \\ \frac{d}{dt}\left(\int_V \frac{\rho_w}{\rho_w^0} sn\, dV\right) &= -\int_s \frac{\rho_w}{\rho_w^0} sn\mathbf{n} \cdot \mathbf{v}_w\, dS, \end{aligned} \tag{2}$$

where $\delta\boldsymbol{\varepsilon} = \mathrm{sym}(\partial\delta\mathbf{v}/\partial\mathbf{x})$ denotes the virtual rate of deformation; $\delta\mathbf{v}$ is a virtual velocity field; $\mathbf{t}$ and $\mathbf{f}$ denote surface tractions per unit area and body forces per unit volume, respectively; n indicates the soil porosity; $\mathbf{g}$ is the gravitational

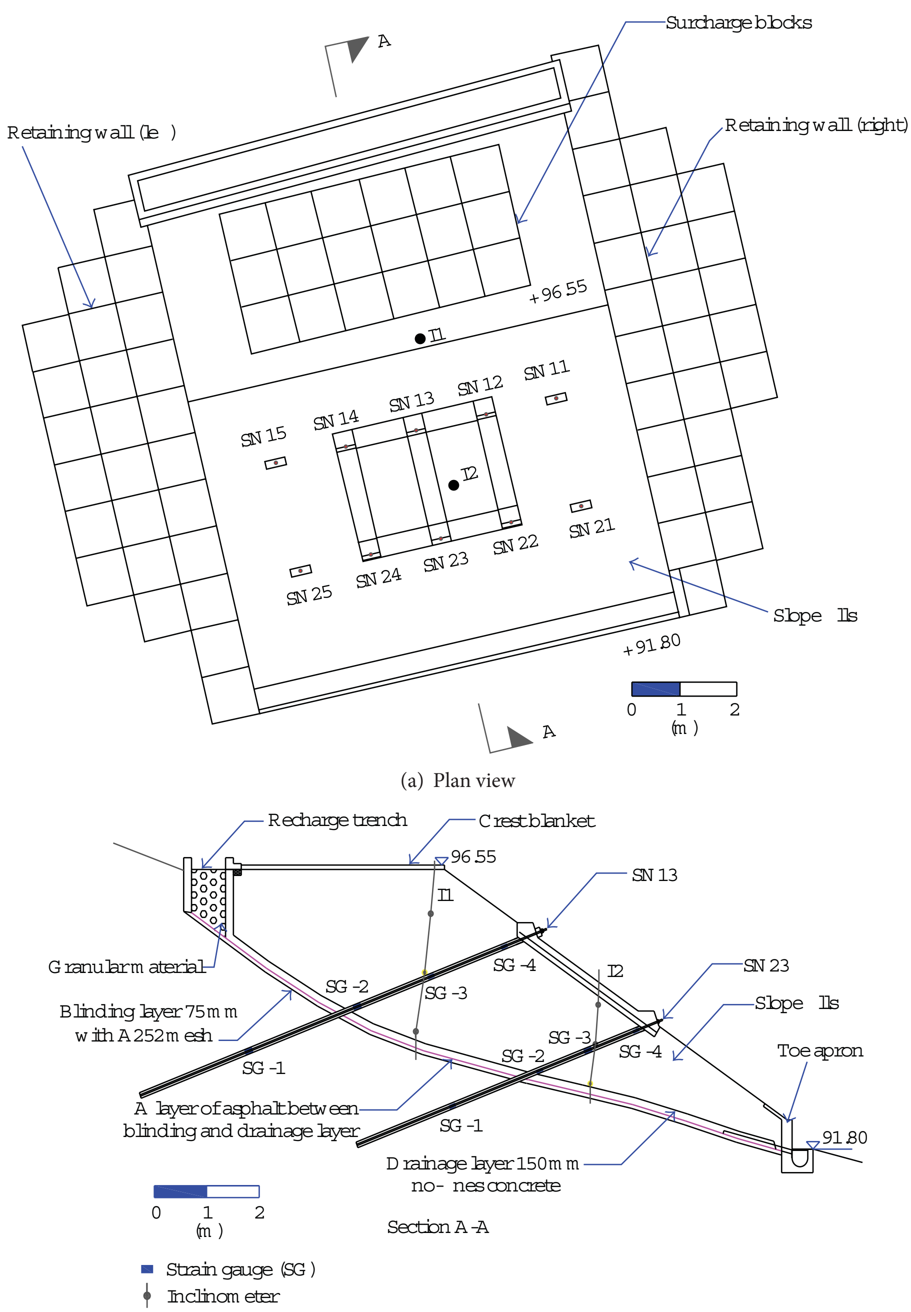

(a) Plan view

(b) Section view

Figure 1: General arrangement of the field test.

acceleration; $\mathbf{v}_w$ is the pore water flow velocity; $\mathbf{n}$ is the outward normal to S; ρ_w and ρ_w^0 denote the water density and a reference density for normalization, respectively.

The coupling stress equilibrium and flow continuity equations are solved simultaneously. A Lagrangian formulation is used in the discretization of the balance equation for the soil skeleton, and displacements are taken as nodal variables. The continuity equation is integrated in time using the backward Euler approximation method, and pore water pressure is taken as a field variable in finite element discretizations. Generally nonlinearity arises from the coupling between seepage and mechanical behavior in the system equations. The Newton-Raphson method is used to calculate the incremental numerical solutions. In addition, Darcy's Law is applied to model the pore fluid flow, which has been shown to be valid for unsaturated soils if the coefficient of permeability, $\mathbf{k}$, is written as a function of the degree of saturation.

3.2. 3D Finite Element Mesh and Boundary Conditions. The symmetry of the nailed slope and load/boundary conditions

Table 1: Summary of material parameters.

	Initial conditions	Elastic properties	Shear strength	Hydraulic properties
CDG fill soil	$\gamma_d = 1.41\,\text{kg/m}^3$, $e_0 = 0.86$, $M_{c0} = 14.9\%$	$\mu = 0.05$ $\kappa = 0.011$	$c' = 2\,\text{kPa}$, $\phi' = 32^\circ$ $\psi = 5^\circ$	k-Figure 4 SWCC-Figure 4
Soil nails	—	$E = 2.5 \times 10^4\,\text{MPa}$, $\mu = 0.2$	—	—
In situ ground	—	$E = 35\,\text{MPa}$, $\mu = 0.25$	—	—
No-fines concrete	—	$E = 1 \times 10^4\,\text{MPa}$, $\mu = 0.2$	—	$k = 1.0 \times 10^{-4}\,\text{m/s}$
Soil-nail interface	—	$E = 10\,\text{MPa}$, $\mu = 0.2$	$c' = 10.6\,\text{kPa}$, $\phi' = 35.8^\circ$	—

E, μ, κ, M_{c0}, γ_d, e_0, k, c', and ϕ' are Young's modulus, Poisson's ratio, the slope of the unloading-reloading line on the $\nu - \ln p'$ diagram, initial moisture content, dry density, initial void ratio, permeability coefficient, cohesion intercept, and internal friction angle, respectively, and the subscript "0" denotes the initial value.

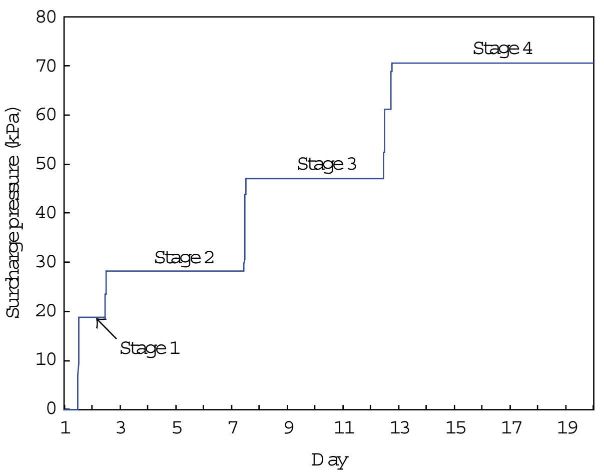

Figure 2: The applied surcharge process during the field test.

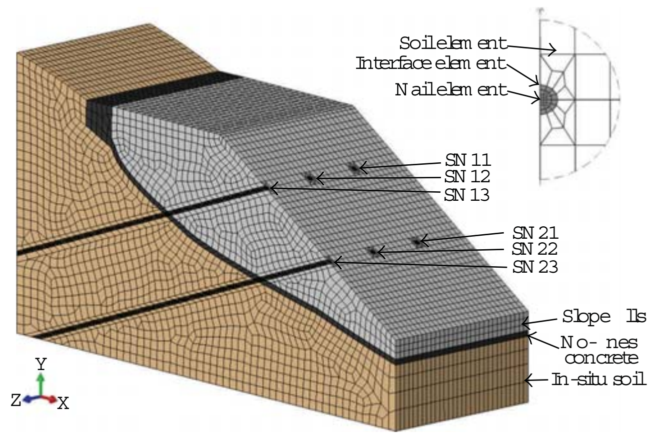

Figure 3: Finite element model of the nailed test slope (the inset figure shows the detailed modeling of soil-nail interaction).

allows only one half of the slope to be modeled. The finite element mesh is set up according to the actual geometry of the slope and the soil nails. As shown in Figure 3, the slope fills and the ground soil are modeled using a finite element mesh consisting of 114815 8-node linear solid elements. Each node has four degrees of freedom, one for pore water pressure and three for displacements. Since a layer of asphalt was applied above the natural ground surface as a watertight measure in the field test, it is assumed in this study that redistribution of water content is negligible within the in situ ground. Hence only displacements are taken as the field variables for the ground soil in the model. The drainage layer (i.e., no-fines concrete layer) is also simulated as a deformable porous medium by solid finite elements with coupled nodal variables. Regarding the soil nails, each steel bar and surrounding grout are idealized as a cylindrical bar of the same diameter and are represented by solid elements with only displacement variables (see the inset of Figure 3).

The displacement boundary conditions of the numerical model are taken as vertical rollers on the left cutting edge and the right side of the test slope and full fixity at the base and the constrained region at the concrete apron near the toe. Since no water could flow out from the unsaturated slope during the surcharge process, no-flow conditions are assumed along the outer boundary of the entire model. Moreover, the interfaces between the no-fines concrete layer and the surrounding soils are assumed to be continuous with no slippage allowed as a deep-seated failure mechanism along the interfaces was not observed in the field test.

The average void ratio and degree of saturation of the soil measured prior to the field test have been adopted as the initial conditions for the analyses (Table 1). The initial distributions of internal stresses and pore water pressures within the slope under the gravity loads are then obtained by initial equilibrium calculations before surcharge loading is imposed on the slope. The surcharge is simplified as a uniformly distributed pressure applied to the crest of the slope, as prescribed by the covering area of the concrete blocks during the field test.

3.3. Soil Models and Parameters. As in previous plane strain study [13], the fill soils are modeled by the Mohr-Coulomb plasticity model with a nonassociated flow rule. To represent the stress-dependent stiffness property of typical residual

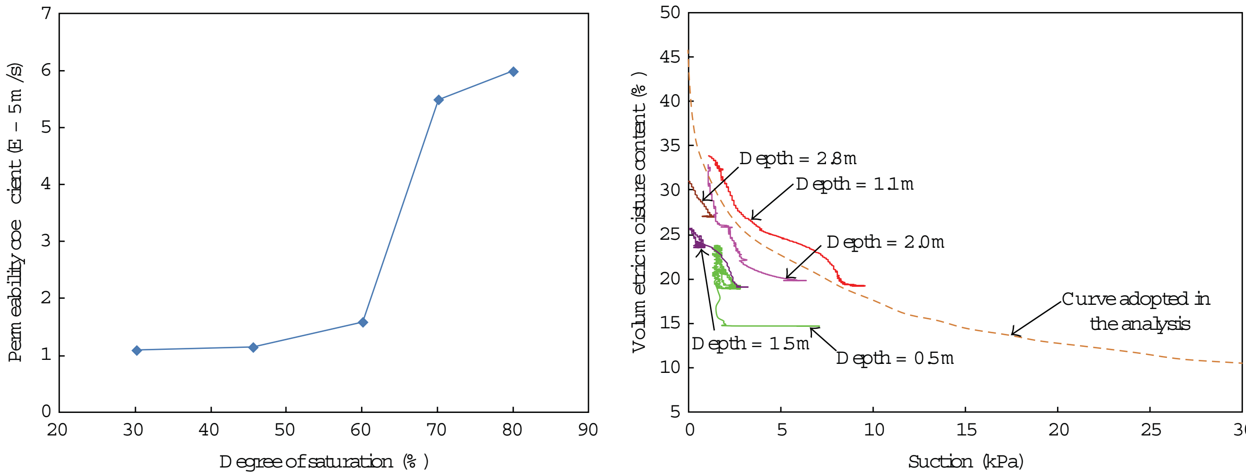

(a) Permeability coefficient versus degree of saturation

(b) Water retention curve (solid lines denote field measurements)

Figure 4: Hydraulic properties of the CDG fill soil.

soils, the bulk modulus, K, of the soil skeleton is defined as a function of the mean effective stress, p', according to

$$K = \frac{\partial p'}{\partial \varepsilon_v^e} = \frac{1+e}{\kappa} p' = \frac{\nu}{\kappa} p', \tag{3}$$

where ε_v^e denotes the elastic volumetric strain, e and ν are the void ratio and the specific volume, respectively, and κ is the slope of the recompression-unloading line on the $\nu - \ln p'$ diagram. The Poisson ratio, μ, is assumed to be a constant, and the shear modulus, G, is calculated by

$$G = \frac{3(1-2\mu)\nu p'}{2(1+\mu)\kappa}. \tag{4}$$

A smooth flow potential function proposed by Menétrey and Willam [15] is adopted in the model. It has a hyperbolic shape in the meridional stress plane and a piecewise elliptic shape in the deviatoric stress plane. Generally plastic flows in the meridional and deviatoric planes are nonassociated, and dilatancy can be controlled by the magnitude of the dilation angle. A perfect plastic hardening law is applied in the following analyses.

Table 1 summarizes the parameters adopted in the analyses. The stiffness and strength parameters are obtained from relevant experiments [12]. A small dilation angle value of $\psi = 5^\circ$ is taken to limit shear-induced volumetric expansion in the loose fill.

Regarding the hydraulic behavior of the unsaturated soil, Figure 4 presents the permeability function and the water retention curve for the loose fill soil, which are obtained based on the observations from laboratory tests and field measurements. The initial compaction degree of the loose fill was ~75% of the maximum dry density measured in a standard Proctor test, and the initial moisture content was 14.9%.

For the in situ ground and the no-fines concrete layer underneath the fill slope, the field test data showed that their deformation is small enough that they are modeled by a linear elastic model with the model parameters given in Table 1. A large coefficient of permeability, $k = 10^{-4}$ m/s, is taken for the no-fines concrete layer to represent its nearly free-draining property.

3.4. Modeling of Soil Nails. As described above, each soil nail is idealized as an elastic homogeneous bar in the finite element model considering the low possibility of steel yielding. By assuming the compatibility of axial deformation between the grout and the steel rod along the nailing direction, the equivalent Young's modulus ($\widetilde{E}$) of the nail elements is determined as follow:

$$\widetilde{E} = \frac{E_r A_r + E_g A_g}{A_r + A_g}, \tag{5}$$

where E_r and E_g denote the elastic modulus of the steel rod and the grout, respectively, and A_r and A_g are their cross-sectional area, respectively.

It has been demonstrated that a modeling approach that is capable of accounting for possible bond and slippage between the soil nail and the surrounding soil is more suitable for the analysis of nail reinforcement effect and the global behavior of the nailed slope [13]. Hence an interface element technique has been adopted in this study. Three-dimensional eight-node interface elements are used to simulate the steel-grout interfacial behavior. As in many previous analyses by other researchers (such as [16]), the elastic stiffness parameters, k_n and k_s, for the grout-soil interface are defined as E_s/t and G/t respectively, where t is the thickness of interface elements; E_s and G are the Young and shear moduli of the surrounding soil material, respectively. Herein t is chosen to be 2 mm, that is about 2 percent of the nail diameter, and it can be considered to be negligibly small with respect to the nail size.

The Mohr-Coulomb shear model is taken as the failure criterion along the nail-soil interface. Tangential slippage will occur when the mobilized shear stress, τ, reaches the shear strength given by

$$\tau = c + \sigma_n' \tan \phi, \quad (6)$$

where c is an equivalent cohesion parameter for the soil-nail interface; ϕ is the friction angle; and σ_n' denotes the effective normal stress exerted on the interface.

The frictional properties of the soil-nail interface are evaluated from pullout tests prior to the field tests. This gives the apparent cohesion intercept and equivalent friction coefficient of 10.6 kPa and 0.72 (35.8°), respectively. The off-diagonal terms in the elastic stiffness matrix are zero, and hence no dilatancy along the interface is considered in the elastic regime. The dilatancy is introduced after the failure criterion has been reached. The flow potential function is of a similar form as (6) with the friction angle replaced by the dilation angle ψ. A summary of the above mechanical parameters for the soil-nail interface is listed in Table 1.

In addition to the interfacial behavior along the soil-nail interface, the boundary conditions at the nail heads also have a direct impact on the nail force mobilization. There are two different constraint options for the nail heads at the slope surface. The first choice is a free end condition, which represents a soil nail without any nail head or facing structure. Alternatively, the nail heads are pinned together using a technique of multiple point constraint, which presumes that the grillage beams made up of reinforced concrete material are strong enough and the displacements of the connecting nail head nodes are enforced to be equal. It should be noted that no interaction between the grid structure and the surface soil in contact has been considered.

3.5. Analysis Programme. A total of four analyses have been conducted in this study, and the analysis conditions are given in Table 2. The surcharge loading process is considered in all the analyses on a real-time scale over a period of ~20 days (Figure 2). Different considerations about the surface constraint have been examined to identify the spatial reinforcement effect of soil nails on the overall response of the field test slope. Besides an assumed case of unreinforced slope, another hypothetical case of the test slope with all the heads of soil nails connected has also been considered to illustrate the possible maximal contribution by the surface structure. All the analysis cases are deemed to form a basis of comparison to examine the stabilizing mechanisms of multiple soil nails in slopes.

Table 2: Summary of the analysis cases.

Cases	Soil nails	Grillage system
1	Yes	No
2	Yes	4 nails heads (SN12, SN13, SN22, SN23) constrained
3	Yes	All 6 nails heads constrained
4	No	—

4. Results and Discussions

4.1. Internal Slope Movement. During the field test, two inclinometers were installed in the slope near the central section, denoted as I1 for the one at 300 mm from the crest corner and I2 for the one installed in the middle (Figure 1). Three sensors were installed on each inclinometer, and the horizontal displacements in the down-slope direction were monitored. Figures 5 and 6 compare the predicted and measured horizontal displacements at the two inclinometer positions at different surcharge stages. The predictions for an assumed case with all nail heads connected by grillage (case 3) and for an unreinforced slope (case 4) are also shown for comparison. The three nailed slope models with different assumptions of the surface grillage effect give very similar deformation patterns, which are also similar to those observed in the field test, except that the magnitude of the predicted movements at I2 location is smaller. The relatively small soil movements at I2 predicted by the numerical model can be mainly attributed to the simplifications made in the modeling of surface grid structure, which only consider the constraint effect of translational displacement at the nail heads, whilst the retaining action by the grillage beam on the adjacent soils has not been included. The expected local strengthening mechanism by the grillage beams is not fully represented by the model. Additionally, as the Mohr-Coulomb shear failure criterion cannot capture any plastic deformation induced by a significant increase in mean confining pressure due to the surcharge, it may also have contributed to the smaller predicted deformations.

Comparing the numerical and test responses at the two inclinometers, larger down-slope soil movements are mobilized at I1. This can be attributed to the fact that it is in the immediate vicinity of the surcharge area. Both the simulation and the field test demonstrate that relatively more considerable horizontal displacements are mobilized at a depth of ~1.0 m below the ground surface at I1 as the surcharge pressure is wholly applied. This implies that a bulge-shaped mechanism similar to a bearing capacity failure is developed in the region beneath the slope crest. This may indicate that the soil nails can help provide stabilizing forces to constrain the formation of a deep-seated sliding mass.

Among the three numerical models with nails considered, it can be observed that the different treatments of nail heads has only negligible influence on the displacement profile at I1, whilst relatively more significant discrepancy is shown by the response at I2, despite that the displacements are relatively smaller in magnitude. It can be attributed to the fact that I2 is mostly located between the two rows of nails, and the local strengthening effect by connecting the nail heads can influence the response at I2 to a more notable extent than that at I1. Reasonably the numerical results demonstrate that with stronger constraint of pinning nail heads together, the horizontal movements of soils surrounded by the rows of nails would be smaller in magnitude.

4.2. Nail Force Distribution. Figures 7, 8, and 9 compare the calculated nail forces with the field measurements. Each figure corresponds to one of the three models with different

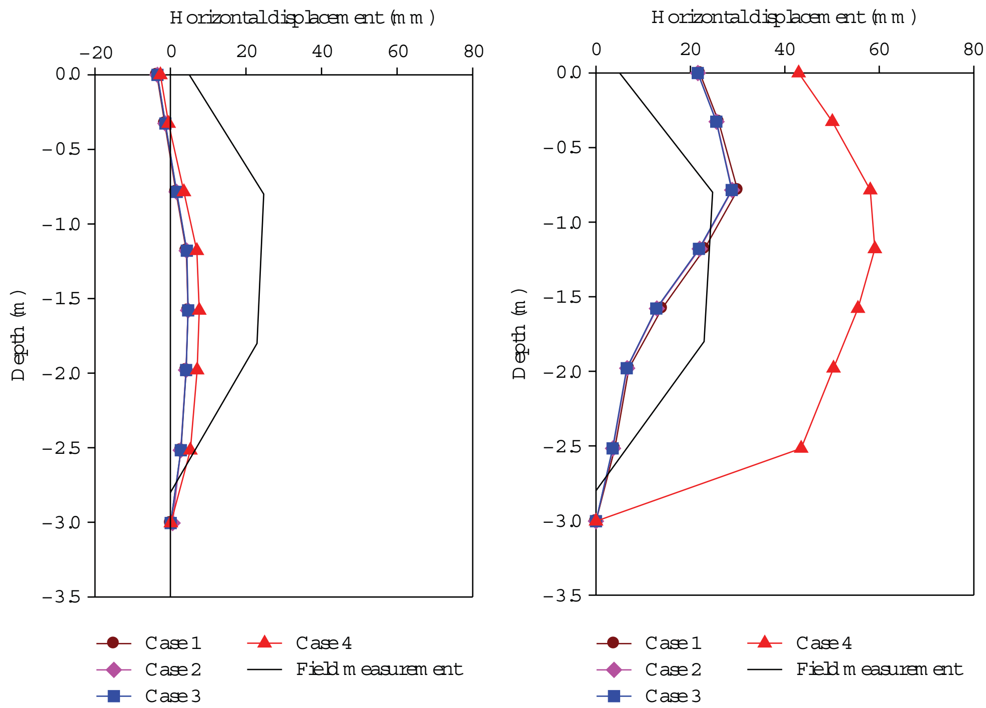

(a) At the end of stage 2 (q_s = 49 kPa)

(b) At the end of stage 4 (q_s = 72 kPa)

FIGURE 5: Distribution of horizontal down-slope displacement at I1 at different surcharge stages (q_s denotes the surcharge pressure).

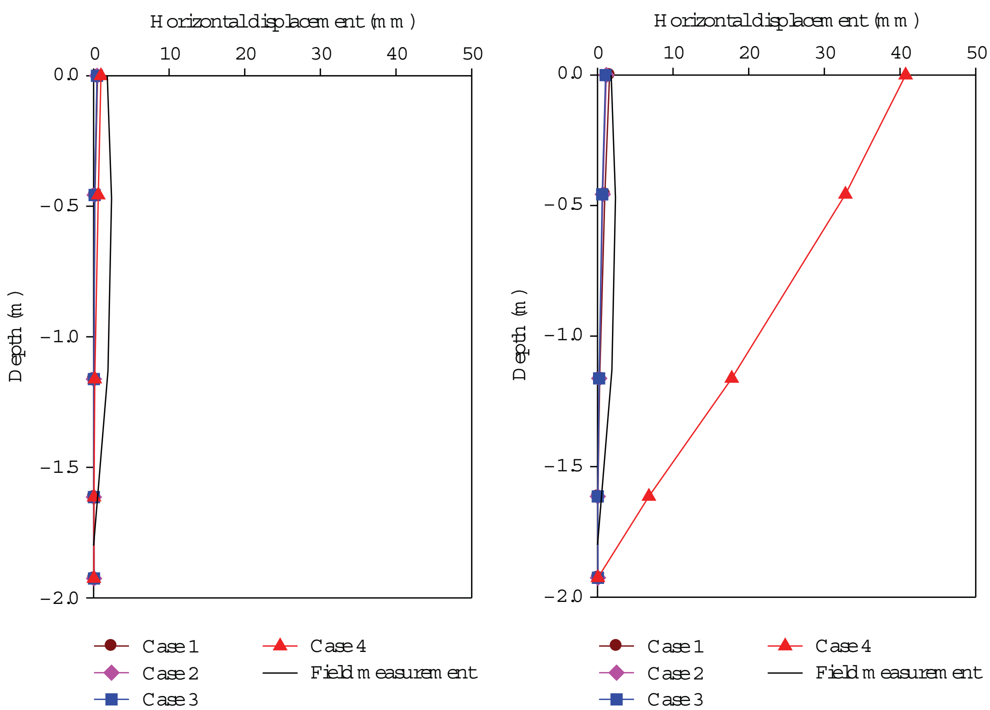

(a) At the end of stage 3 (q_s = 49 kPa)

(b) At the end of stage 4 (q_s = 72 kPa)

FIGURE 6: Distribution of horizontal down-slope displacement at I2 at different surcharge stages.

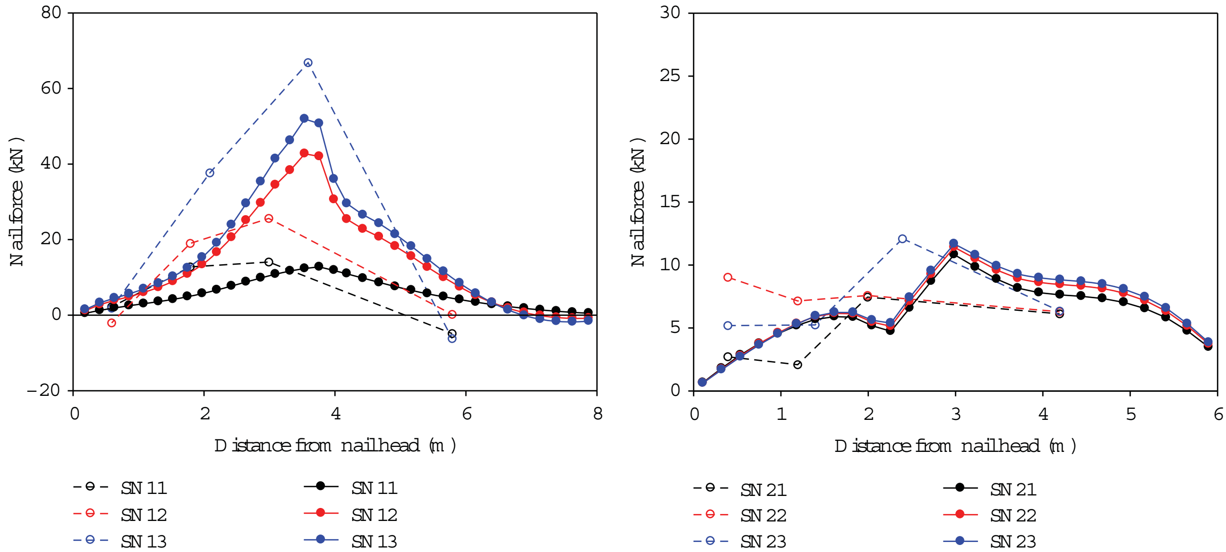

(a) At the upper row of soil nails

(b) At the lower row of soil nails

Figure 7: Distribution of nail force caused by the surcharge loads (case 1: hollow symbol lines denote field measurements, and solid symbol lines are numerical results).

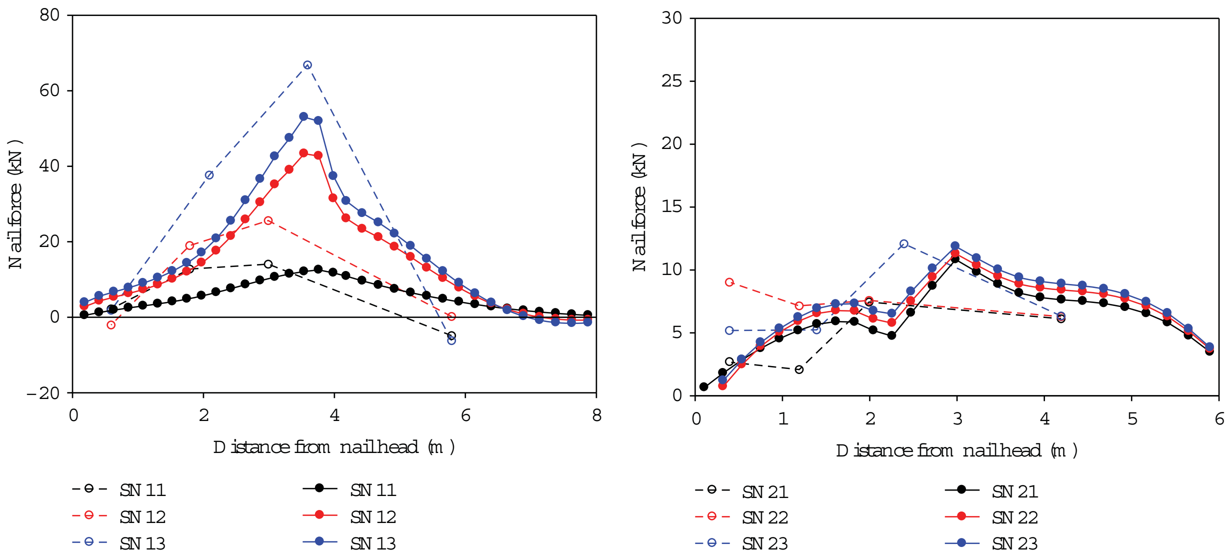

(a) At the upper row of soil nails

(b) At the lower row of soil nails

Figure 8: Distribution of nail force caused by the surcharge loads (case 2: hollow symbol lines denote field measurements, and solid symbol lines are numerical results).

considerations of nail heads. The field measured nail forces were interpreted from the readings of the strain gauges installed on nails SN11~SN15 (upper row) and SN21~SN25 (lower row). The measurements at SN13 and SN23, which were located along the central section (see Figure 1), are directly adopted for comparison. For the other four columns of nails, the measurements of the symmetrically located pair are averaged for comparison considering the symmetry of the test slope. All the three models, despite considering different treatments at the nail heads, predict similar nail force patterns as those observed in the field test. Particularly for the upper rows of soil nail, the numerical results are in good agreement with the field data that relatively larger axial loads would be mobilized in the nail that is located closer to the central section, and a peak value would be mobilized at a nailing depth of about 3.5 m. In contrast, the predictions for the lower rows of soil nails are less dependent on the horizontal distance with the central section for the three cases, which are also shown by the field monitoring data. The distribution patterns of predicted nail force with the nailing depth are also quite similar to the test results. Among the three models, case 3, which models complete constraints of all nail heads, gives

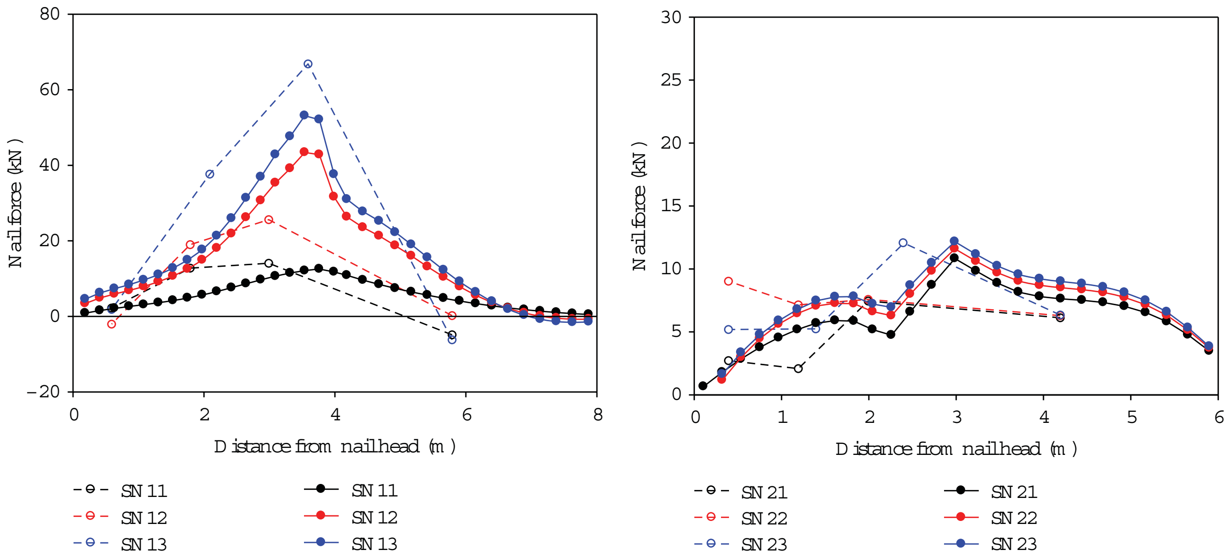

(a) At the upper row of soil nails

(b) At the lower row of soil nails

Figure 9: Distribution of nail force caused by the surcharge loads (case 3; hollow symbol lines denote field measurements, and solid symbol lines are numerical results).

the most notable difference in the axial force response among the lower row of nails and the axial force is larger in the upper portion within the fill slope. This observation can be attributed to the pin-type constraint on all the nail heads and its induced strengthening effect on the interaction between the nails, and the soils in the vicinity of the nail heads. The above comparisons conclude that the developed 3D numerical approach is quite appropriate to model the spatial reinforcement effect of soil nails in the test slope under surcharge loading, and strong dependence of the axial load mobilization is shown by the soil nails in the study slope on the arrangement manner.

Both the numerical results and the field monitoring data illustrate that larger nail forces are mobilized within the upper row of soil nails under the surcharge loading. This is consistent with the relatively larger soil movements (Figures 5 and 6), which also implies greater relative movement along the soil-nail interface. From the 3D representation of the soil-nail interaction, the numerical results show that, for each soil nail, commonly relatively larger normal stress would be mobilized in the interface elements connected to the down face of the nail, which mainly originate from the overburden pressure. Take the results in case 1 as an instance, the maximum normal stress acting on the upper row of three nails are all located at the down face of the middle section, that is, at a buried depth of about 3.5 m, and the complete surcharge pressure induced maximum increase in the normal stress is 226 kPa, 191 kPa, and 10 kPa, respectively, for the three nails located from the central section to the side. The difference in the confining stress exerted on the nails would obviously influence the mobilization of nail force and in turn the pull-out resistance of these soil nails.

Although a surface grid structure was present in the field test, which is also modeled in the numerical analyses using a pin-type multiple point constraint, both the test and numerical results demonstrate that only limited tensile force (<10% of the maximum nail force) is mobilized at the heads of the upper row of soil nails. The observation can be explained by the small relative movement along the soil-nail interface near the slope surface and the low confining stress near the slope surface. Differently, a relatively larger ratio of the maximum nail force is mobilized at the head of each nail arranged at a lower position, particularly as shown by the field measurements at the two soil nails near the central section. This can be attributed to the constraint from the surface grillage beams and the induced structural behavior near the heads. The numerical results from the three models considering various conditions at the nail heads also demonstrate that larger nail force can be triggered at the lower rows of nails by the introduction of stronger constraints at the nail heads.

4.3. Moisture Content Redistribution. Although no water entered into the slope during the surcharge process, the moisture probe readings in the field test showed that the water content within the unsaturated fill slope still underwent slight redistributions during the surcharge process [12]. It is found that the numerical results by the above 3D model are consistent with the previous plane strain study results [13], and a good agreement is also achieved between the field and numerical results, both showing a gradually decreasing trend. The capability of the present model in predicting moisture redistribution is verified. For the surcharge stage considered in this paper, the influence of water content redistribution is believed to be negligible on the slope movement as well as the nail force mobilization.

4.4. Spatial Reinforcement of Soil Nails in the Test Slope. To investigate the 3D reinforcement effect of soil nails on

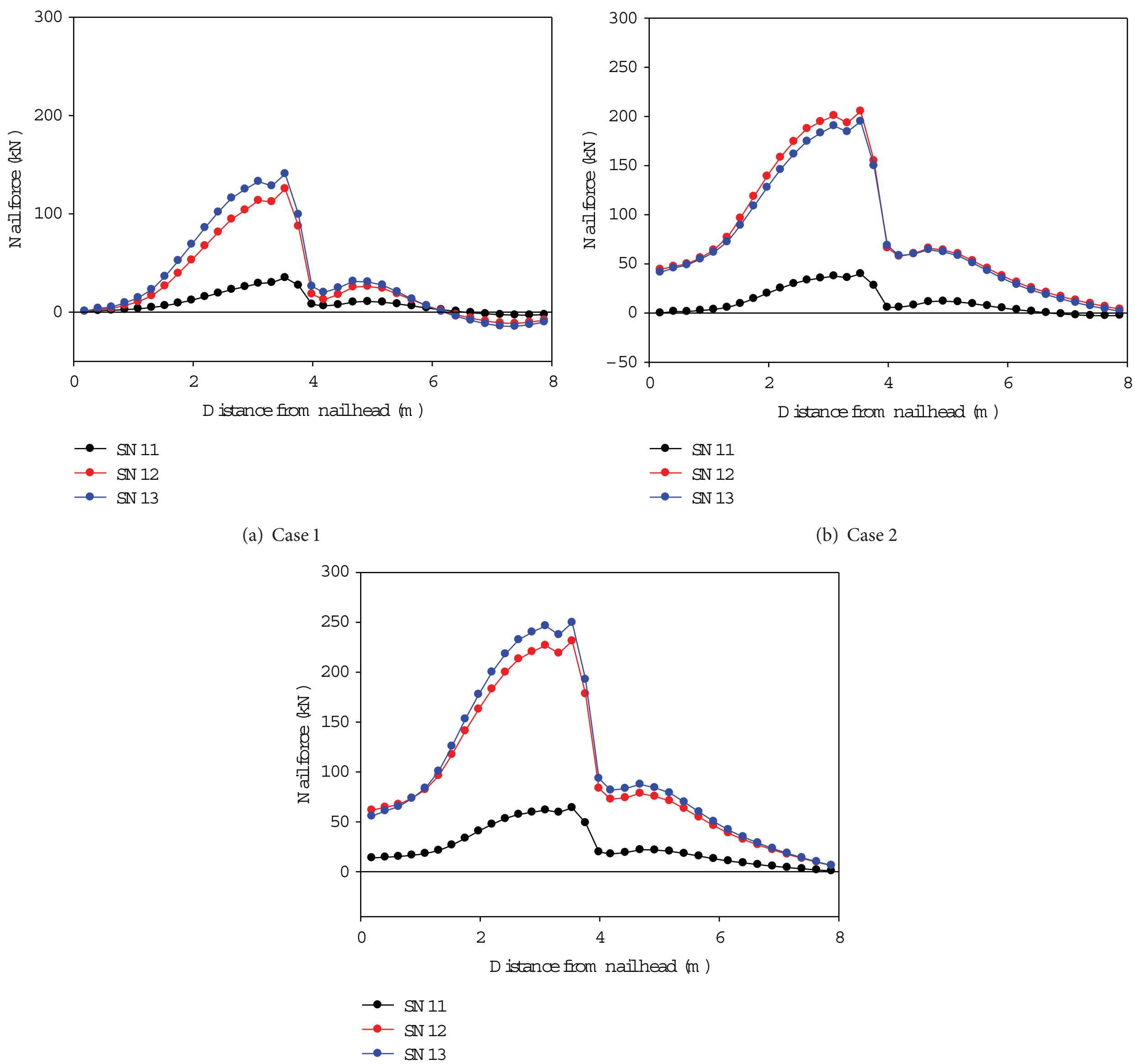

(a) Case 1

(b) Case 2

(c) Case 3

Figure 10: Comparison of axial force distribution in upper row of soil nails mobilized by an extreme surcharge of 129 kPa.

the failure mechanism and bearing capacity of the test slope, a continuous increase of surcharge pressure is simulated for the four slope models in Table 2 until global failure is triggered. It is predicted by the 3D numerical model that for the unreinforced case, the failure mechanism involves a global sliding plane initiating from the crest of the slope near the surcharge area to the slope toe, which is also quite similar to the previous plane strain study results [13]. The predicted failure occurs at a surcharge of about 82 kPa, which is a bit smaller than the results (138 kPa) given by a plane strain analysis. The difference can be caused by the actual 3D loading conditions in the test that the surcharge area only covered two-thirds of the total width of the slope crest. For the other three cases with nail reinforcement considered, the presence of the soil nails significantly increases the rigidity of the soil located below the upper row of nails. Although different constraints at nail heads have been adopted in the models, commonly the failure mechanism consists of a shallow-seated localized plastic zone that originates from the centre of the surcharge area and outcrops near the heads of upper row of nails. A deep-seated zone of large plastic shear strain is also formed near the bottom of the slope, which is where the global failure mechanism of the unreinforced slope is initiated. The development of this shear zone is prohibited by the existence of the two rows of soil nails. The modeling results also show that the surcharge capacity for the three nailed slope models can be increased significantly by the incorporation of the surface structure, which are 129 kPa (case 1), 163 kPa (case 2), and 174 kPa (case 3), respectively.

Figure 10 presents a comparison of the mobilized axial force distributions at a constant surcharge pressure of 129 kPa, that is, at the instant of the failure for the nailed slope model without consideration of the surface grid structure. The results at the upper row of soil nails are chosen for their vicinity to the surcharge area. It can be seen that, for each nail, a larger peak magnitude of nail force would be mobilized when stronger surface connectivity is considered in the numerical model. Take the nail SN11 near to the lateral side as an instance, the peak force predictions show an obvious increase from 35 kN (case 1) to 64 kN (case 3). It can also be observed from the results that, in case 3, a notable tensile axial load is triggered at the head of SN11 owing to the simulated constraint by extended grillage beams.

To further examine the spatial reinforcement effect of soil nails in the test slope, a comparison is also made between the modeling results of current 3D model and those from previous plane strain study [13]. It has been demonstrated by the previous results that the incorporation of bond-slip behavior along the soil-nail interface can significantly influence the mobilization of nail force. Particularly, very significant compressive nail forces are calculated for the portion of upper soil nail buried in in situ soils by the plane strain model, even when the possible tangential slippage has been considered, which deviate from the field measurements and are therefore considered to be unrealistic. The current 3D model takes into account the bond-slip along the soil-nail interface. It has been shown above that the predictions of axial force basically remain tensile for all soil nails and are in better agreement with the test results. Furthermore, for a plane strain assumption based model, the soil nails are modeled as two-dimensional flat plates of equivalent cross-sectional area and stiffness, which cannot represent the spatial arrangement of discrete soil nails and in turn the arching effect by two adjacent nails on the upper portion of soils. The above comparison concludes that only the 3D model presented in this study can reproduce the spatial effect of nail reinforcement in the axial force response as observed in the field test.

5. Conclusions

A 3D numerical model has been developed to back-analyze a field slope test. Using the field test data as a reference, a series of numerical analyses have been conducted to examine the spatial reinforcement effect of two rows of ten cement grouted soil nails in the test fill slope. The study focuses on the behavior of the nailed slope under surcharge loading when different treatments of surface grillage structure connecting nail heads are adopted. Similar to previous plane strain analyses, the 3D modeling results in this study again demonstrate that the presence of the soil nails increases the overall stability of a loose fill slope under surcharge loading. The stabilizing forces mainly come from the upper row of soil nails along which the effective confining pressure is significantly increased due to the surcharge loading. A comparison of nail force distributions between the numerical predictions and the field measurements suggests that the maximum nail force is always mobilized at the middle portion of the nails, corresponding to the depth of the potential global sliding plane.

Both the numerical results and field measurements approve that the axial force response within the two rows of soil nail presents an obvious feature of nonuniform distribution with respect to the spatial arrangements. Relatively larger axial forces are mobilized in the upper row of nails that are closer to the central section and connected by grillage beams at the heads. Different to the previous results by plane strain analyses that the role of a facing structure at the slope surface is of less significance, the numerical results from this study illustrate that the overall response of the nailed slope can be significantly influenced by the various arrangements of surface structure, particularly when an extreme surcharge loading is applied. This is due to the fact that larger slope deformation can be expected when an overburden surcharge is increased near to its capacity, and the multiple point constraint simulating the surface grid structure would impose additional restraint effects on the potential relative displacements at the connected nail heads.

Acknowledgment

The authors acknowledge the support by the State Key Laboratory of Hydroscience and Engineering (no. 2012-KY-04).

References

[1] F. Schlosser, "Behaviour and design of soil nailing," in *Proceedings of the Recent Developments in Ground Improvement Techniques*, pp. 399–413, Bangkok, Thailand, 1982.

[2] N. Gurung and Y. Iwao, "Analytical pull-out model for extensible soil reinforcement," *Journal of Geotechnical Engineering*, vol. 624, pp. 11–20, 1999.

[3] A. Misra and C.-H. Chen, "Analytical solution for micropile design under tension and compression," *Geotechnical and Geological Engineering*, vol. 22, no. 2, pp. 199–225, 2004.

[4] W.-H. Zhou and J.-H. Yin, "A simple mathematical model for soil nail and soil interaction analysis," *Computers and Geotechnics*, vol. 35, no. 3, pp. 479–488, 2008.

[5] L. L. Zhang, L. M. Zhang, and W. H. Tang, "Uncertainties of field pullout resistance of soil nails," *Journal of Geotechnical and Geoenvironmental Engineering*, vol. 135, no. 7, pp. 966–972, 2009.

[6] T. Matsui, K. C. San, and K. Hayashi, "Design and field test on a reinforced cut slope," in *Performance of Reinforced Soil Structures: Proceedings of the International Reinforced Soil Conference*, pp. 235–239, Thomas Telford, London, UK, 1990.

[7] C. Y. Cheuk, C. W. W. Ng, and H. W. Sun, "Numerical experiments of soil nails in loose fill slopes subjected to rainfall infiltration effects," *Computers and Geotechnics*, vol. 32, no. 4, pp. 290–303, 2005.

[8] C.-C. Fan and J.-H. Luo, "Numerical study on the optimum layout of soil-nailed slopes," *Computers and Geotechnics*, vol. 35, no. 4, pp. 585–599, 2008.

[9] M. Zhang, E. Song, and Z. Chen, "Ground movement analysis of soil nailing construction by three-dimensional (3-D) finite element modeling (FEM)," *Computers and Geotechnics*, vol. 25, no. 4, pp. 191–204, 1999.

[10] M. Z. Yang and E. C. Drumm, "Numerical analysis of the load transfer and deformation in a soil nailed slope," *Geotechnical Special Publication*, vol. 96, pp. 102–116, 2000.

[11] W. Zhou, *Experimental and theoretical study on pullout resistance of grouted soil nails [Ph.D. thesis]*, The Hong Kong Polytechnic University, Hong Kong, China, 2008.

[12] J. Li, *Field study of a soil nailed loose fill slope [Ph.D. thesis]*, The University of Hong Kong, Hong Kong, China, 2003.

[13] Y. D. Zhou, C. Y. Cheuk, and L. G. Tham, "Numerical modelling of soil nails in loose fill slope under surcharge loading," *Computers and Geotechnics*, vol. 36, no. 5, pp. 837–850, 2009.

[14] ABAQUS Inc, Analysis user's manual, Version 6.10, 2010.

[15] P. Menétrey and K. J. Willam, "Triaxial failure criterion for concrete and its generalization," *ACI Structural Journal*, vol. 92, no. 3, pp. 311–318, 1995.

[16] E. C. Leong and M. F. Randolph, "Finite element modelling of rock-socketed piles," *International Journal for Numerical & Analytical Methods in Geomechanics*, vol. 18, no. 1, pp. 25–47, 1994.

Hindawi Publishing Corporation
Journal of Applied Mathematics
Volume 2013, Article ID 306849, 10 pages
http://dx.doi.org/10.1155/2013/306849

Research Article

Analytical Solutions of Spherical Cavity Expansion Near a Slope due to Pile Installation

Jingpei Li,[1,2] Yaguo Zhang,[1,2] Haibing Chen,[1,2] and Fayun Liang[1,2]

[1] *Key Laboratory of Geotechnical and Underground Engineering of Ministry of Education, Tongji University, Shanghai 200092, China*
[2] *Department of Geotechnical Engineering, Tongji University, Shanghai 200092, China*

Correspondence should be addressed to Jingpei Li; lijp2773@tongji.edu.cn

Received 5 June 2013; Accepted 18 August 2013

Academic Editor: Ga Zhang

Based on the hypothesis that the penetration of a single pile can be simulated by a series of spherical cavity expansions, this paper presents an analytical solution of cavity expansion near the sloping ground. Compared with the cavity expansion in the half-space, the sloping free boundary has been taken into account as well as the horizontal free boundary. The sloping and horizontal free surfaces are considered by the introduction of a virtual image technique, the harmonic function, and the Boussinesq solution. The results show that the sloping free boundary and the variation of the inclination angle have pronounced influences on the distribution of the stress and displacement induced by the spherical cavity expansion. The present solution provides a simplified and realistic theoretical method to predict the soil behaviors around the spherical cavity near the sloping ground. The approach can also be used for the determination of the inclination angle of the slope according to the maximum permissible displacement.

1. Introduction

There are many situations where foundations need to be located on the top of a slope, such as the piled bridge abutment adjacent to a slope crest. Hence, pile installation in sloping ground has attracted wide concerns [1–3]. In contrast to the horizontal ground surface case, the boundary effects of a slope should be considered for situations of piles embedded adjacent to the slope. The existing boundary not only affects the bearing capacity of piles, but also adds the risk of slope failure [4]. For instance, a riverbank dike, located along the Bailianjing River in Shanghai, was damaged by pile driving in soft clay during the construction of a newly elevated dike [5].

Following the early suggestion [6, 7], solutions of the limit pressures of spherical and cylindrical cavities are used to predict the end bearing and shaft capacities of piles [8, 9], as well as the stress fields and lateral displacements of the surrounding subsoil induced by installation of a pile [10–13]. However, the solutions of a cavity expansion in an infinite medium do not satisfy the stress conditions at the free surface during the pile installation. Sagaseta et al. [14] and Sagaseta [15] considered the problem as strain controlled and obtained strains by using only the incompressibility condition. The presence of the top free surface was considered by means of a virtual image technique and some results for the elastic half-space. Besides, Keer et al. [16] derived a solution for the expansion of spherical cavity in a half-space by using the image source method [17] and the concept of cavity expansion source [18]. These methods can be well used to analyze the boundary effects of the free surface of the half-space, but they are not directly applicable to cavity expansion near a slope. Compared with cavity expansion in a semi-infinite half-space, the slope surface should be taken into account.

In this paper, the expansion caused by pile tip is simulated as a spherical cavity expansion. Theoretical solutions for the expansion of a single spherical cavity near slope are derived by using the virtual image approach. Meanwhile, the correction stress functions and the Boussinesq solutions are introduced to consider the effects of both horizontal ground surface and slope surface in this analysis.

2. Basic Theories and Geometry of the Problem

The concept of the cavity expansion source was first used by Hopkins [18]. The model shown in Figure 1 is a cavity under

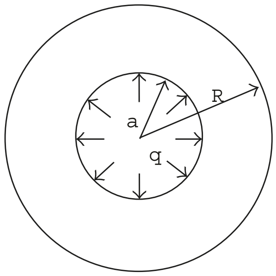

FIGURE 1: Cavity expansion source induced by the uniform pressure on the internal spherical surface.

a uniform pressure q on the internal spherical surface with radius a.

The fields of stress and displacement induced by the pressure are as follows:

$$\sigma_R = \frac{a^3 q}{R^3}, \tag{1}$$

$$\sigma_\varphi = \sigma_\theta = -\frac{a^3 q}{2R^3}, \tag{2}$$

$$u_R = \frac{a^3 q}{4GR^2}, \tag{3}$$

where the R is the distance between the center and the calculation point, the G is the shear modulus of the soil, and the σ_R, σ_φ, and σ_θ refer to radial, hoop, and tangential stresses, respectively. Due to the spherical symmetry, the shear stresses are equal to zero, that is, $\tau_{R\varphi} = \tau_{R\theta} = \tau_{\varphi\theta}$.

The expansion caused by the pile tip is usually simulated as a spherical cavity expansion [19, 20]. Hence, attention will be paid to the solutions of a single cavity expansion adjacent to a slope. As shown in Figure 2, the depth of the cavity below the horizontal ground surface is denoted by h, and the angle between the slope and vertical direction is denoted by β. Unlike cavity expansion in an infinite medium, the analytical solutions of cavity problem near a slope are currently only possible in elastic materials. Accordingly, the soil is assumed to be an isotropic, homogeneous, and linear elastic material, and only small strains occur during the process of the cavity expansion. For simplicity, the gravitational stresses are ignored.

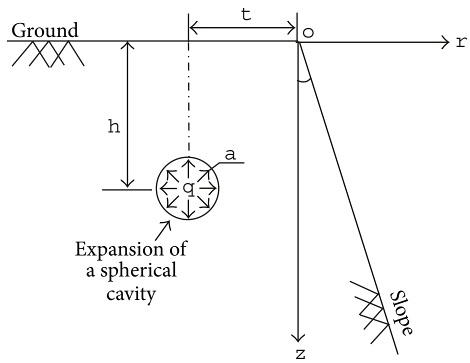

FIGURE 2: Expansion of a spherical cavity near the sloping ground.

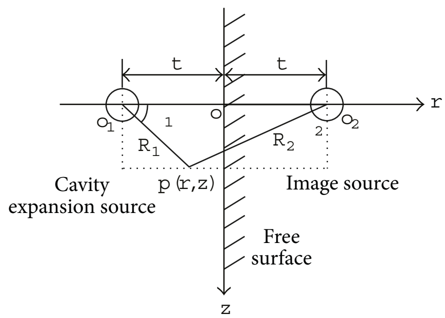

FIGURE 3: A cavity expansion source and its image.

3. The Solution Method

3.1. The Expansion of a Spherical Cavity and Its Image in the Half-Space. The theoretical solution for the expansion of a single spherical cavity in a half-space has been presented by Keer et al. [16], where the free surface of the half-space is horizontal ($z = 0$). Similarly, the solutions can also be derived when the free surface is vertical ($r = 0$). Taking the vertical surface as the plane of symmetry, another virtual spherical cavity is put at the image point which is shown in Figure 3. The coordinate of the calculation point p is (r, z), and t is the horizontal distance between the center of spherical cavity and the vertical free surface. R_1 is the distance from the spherical cavity to point p, and R_2 is the distance from the image to point p. φ_1 and φ_2 are the angles from r direction to R_1 and R_2, respectively.

The stress and displacement components of the cavity expansion in a cylindrical coordinate system can be written as

$$\sigma_r = \sigma_R \cos^2\phi + \sigma_\phi \sin^2\phi - \tau_{R\phi}\sin 2\phi, \tag{4}$$

$$\sigma_z = \sigma_R \sin^2\phi + \sigma_\phi \cos^2\phi + \tau_{R\phi}\sin 2\phi, \tag{5}$$

$$\tau_{rz} = \left(\sigma_R - \sigma_\phi\right)\sin\phi\cos\phi + \tau_{R\phi}\cos 2\phi, \tag{6}$$

$$u_r = u_R\cos\phi, \qquad u_z = u_R \sin\phi. \tag{7}$$

By substituting (1) to (3) into (4) to (7) and using the principle of superposition, the stress and displacement of the spherical cavity and its image in the cylindrical coordinate are as follows:

$$\sigma_r = \frac{a^3 q}{2}\left[\frac{3(t+r)^2}{R_1^5} - \frac{1}{R_1^3} + \frac{3(r-t)^2}{R_2^5} - \frac{1}{R_2^3}\right], \tag{8}$$

$$\sigma_z = \frac{a^3 q}{2}\left[\frac{2}{R_1^3} - \frac{3(t+r)^2}{R_1^5} + \frac{2}{R_2^3} - \frac{3(r-t)^2}{R_2^5}\right], \tag{9}$$

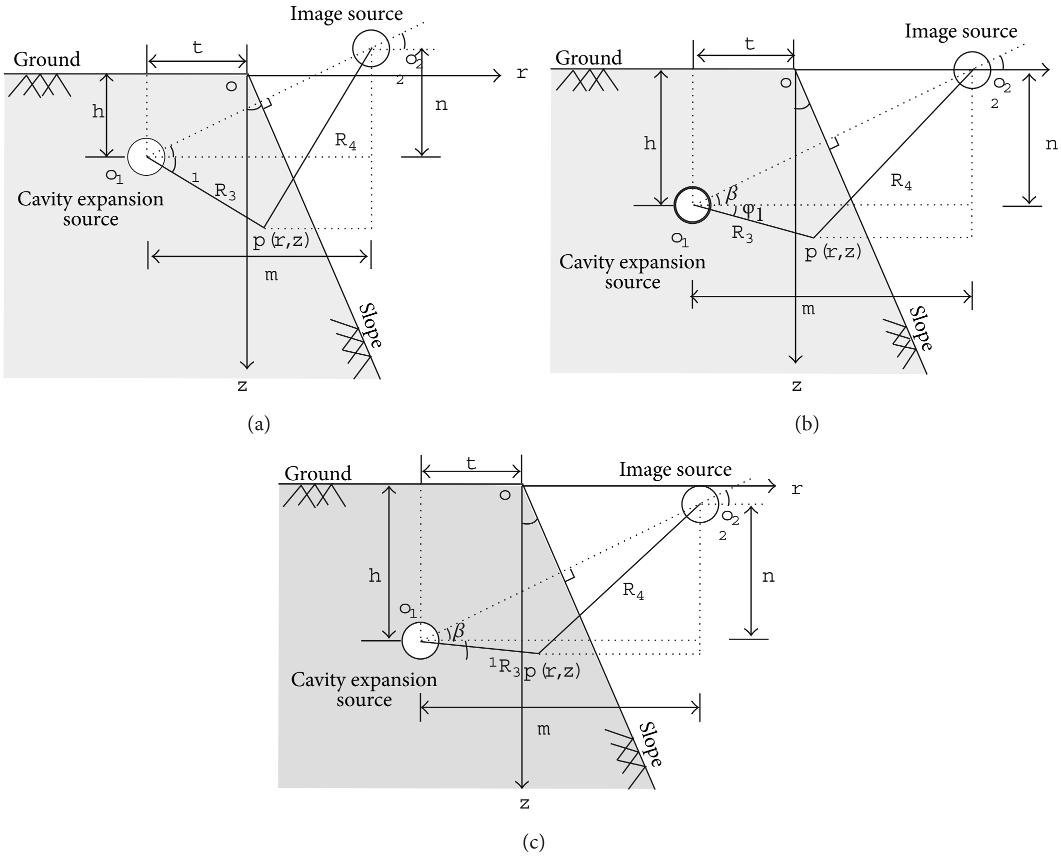

FIGURE 4: The expansion of the single spherical cavity near a slope. (a) The image source is located above the ground surface. (b) The image source is located on the ground surface. (c) The image source is located below the ground surface.

$$\tau_{rz} = \frac{3a^3qz\,(t+r)}{2R_1^5} + \frac{3a^3qz\,(r-t)}{2R_2^5}, \tag{10}$$

$$\sigma_\theta = -\frac{a^3q}{2R_1^3} - \frac{a^3q}{2R_2^3}, \tag{11}$$

$$u_r = \frac{a^3q}{4G}\left(\frac{t+r}{R_1^3} + \frac{r-t}{R_2^3}\right), \tag{12}$$

$$u_z = \frac{a^3q}{4G}\left(\frac{z}{R_1^3} + \frac{z}{R_2^3}\right), \tag{13}$$

where $R_1 = \sqrt{(t+r)^2 + z^2}$ and $R_2 = \sqrt{(t-r)^2 + z^2}$.

The horizontal ground and the slope are both free surfaces, on which the normal and shear stresses are zero. Because of the symmetry, the source and its image produce zero shear stress ($\tau_{rz} = 0$) and a nonzero normal stress ($\sigma_r \neq 0$) on the free surface $r = 0$. Thus, the presence of the normal stress violates the free surface boundary condition

$$\sigma_r\big|_{r=0} = a^3q\left(\frac{3t^2}{R_0^5} - \frac{1}{R_0^3}\right), \tag{14}$$

where $R_0 = \sqrt{t^2 + z^2}$.

3.2. The Expansion of a Spherical Cavity and Its Image Near a Slope. The boundary effects of both ground surface and slope should be investigated during the analysis of the cavity expansion near the sloping ground. The problem turns to be more difficult due to the increase of the slope boundary. Similarly, the virtual image technique is employed to consider the boundary effects of the slope. Taking the slope as the plane of symmetry, the image source is set at the image point as shown in Figure 4.

The solutions of the two cavities expansion (the actual spherical cavity and its virtual image) can be obtained by the principle of superposition. As a result, the stress and displacement components in the cylindrical coordinate system are shown to be

$$\sigma_r^{(0)} = \frac{a^3q}{2}\left[\frac{3(t+r)^2}{R_3^5} - \frac{1}{R_3^3} + \frac{3(t+r-m)^2}{R_4^5} - \frac{1}{R_4^3}\right], \tag{15}$$

$$\sigma_z^{(0)} = \frac{a^3q}{2}\left[\frac{2}{R_3^3} - \frac{3(t+r)^2}{R_3^5} + \frac{2}{R_4^3} - \frac{3(t+r-m)^2}{R_4^5}\right], \tag{16}$$

$$\tau_{rz}^{(0)} = \frac{3a^3q\,(z-h)\,(t+r)}{2R_3^5} + \frac{3a^3q\,(z-h+n)\,(t+r-m)}{2R_4^5}, \tag{17}$$

$$\sigma_\theta^{(0)} = -\frac{a^3 q}{2R_3^3} - \frac{a^3 q}{2R_4^3}, \tag{18}$$

$$u_r^{(0)} = \frac{a^3 q}{4G}\left(\frac{t+r}{R_3^3} + \frac{t+r-m}{R_4^3}\right), \tag{19}$$

$$u_z^{(0)} = \frac{a^3 q}{4G}\left(\frac{z-h}{R_3^3} + \frac{z-h+n}{R_4^3}\right), \tag{20}$$

where the cavity depth below the ground surface is denoted by h, the distance from the source o_1 to the calculation point p is R_3, and the image o_2 to the point p is R_4. According to the relationship of geometry shown in Figure 4, the expressions for R_3 and R_4 are

$$R_3 = \sqrt{(t+r)^2 + (z-h)^2}, \quad R_4 = \sqrt{(m-t-r)^2 + (n+z-h)^2}. \tag{21}$$

With the increasing of depth of the spherical cavity, the image cavity gradually moves from above ground (Figure 4(a)) to the ground below (Figure 4(c)). Accordingly, the expressions of R_3 and R_4 will be changed with the depth of cavities. Specifically, when the virtual image cavity is just on the ground surface as shown in Figure 4(b), the R_4 can be simplified to be

$$R_4 = \sqrt{(m-t-r)^2 + z^2}, \tag{22}$$

$$m = 2\left(h\tan\beta + t\right)\cos^2\beta, \tag{23}$$

$$n = \left(h\tan\beta + t\right)\sin 2\beta, \tag{24}$$

where m and n are defined as the horizontal (r direction) and vertical (z direction) distances between the source and its image, respectively.

3.3. The Correction of the Stresses on the Horizontal Ground. According to the models shown in Figure 4, the actual expansion cavity and its image do produce not only nonzero normal stress but also shear stress on the horizontal ground surface $z = 0$, which can be shown to be as follows:

$$\sigma_z^{(0)}\Big|_{z=0} = \frac{a^3 q}{2}\left[\frac{3h^2}{R_3'^5} - \frac{1}{R_3'^3} + \frac{3(n-h)^2}{R_4'^5} - \frac{1}{R_4'^3}\right], \tag{25}$$

$$\tau_{rz}^{(0)}\Big|_{z=0} = \frac{-3a^3 qh\left(t+r\right)}{2R_3'^5} - \frac{3a^3 q\left(h-n\right)\left(t+r-m\right)}{2R_4'^5}, \tag{26}$$

where $R_3' = \sqrt{(t+r)^2 + h^2}$ and $R_4' = \sqrt{(m-t-r)^2 + (n-h)^2}$.

In order to satisfy the condition of the free horizontal boundary ($z = 0$), the different correction functions are introduced to deal with the normal stress (see (25)) and shear stress (see (26)) on the boundary. Based on the theory of superposition, the stresses on the ground surface can be divided into two parts:

(i) only normal stress on the horizontal ground surface: $\sigma_z^{(1)}|_{z=0} = -\sigma_z^{(0)}|_{z=0}$, $\tau_{rz}^{(1)}|_{z=0} = 0$;

(ii) only shear stress on the horizontal ground surface: $\sigma_z^{(2)}|_{z=0} = 0$, $\tau_{rz}^{(2)}|_{z=0} = -\tau_{rz}^{(0)}|_{z=0}$.

Using the axially symmetric stress function $f(r,z)$ of Kassir and Sih [21] in the first part (i), the corresponding stress and displacement solutions are written as follows:

$$\sigma_r^{(1)} = 2G\left[(1-2\nu)\frac{\partial^2 f}{\partial r^2} - 2\nu\frac{\partial^2 f}{\partial z^2} + z\frac{\partial^3 f}{\partial r^2 \partial z}\right], \tag{27}$$

$$\sigma_\theta^{(1)} = 2G\left[\frac{1}{r}\frac{\partial f}{\partial r} + 2\nu\frac{\partial^2 f}{\partial r^2} + \frac{z}{r}\frac{\partial^2 f}{\partial r \partial z}\right], \tag{28}$$

$$\sigma_z^{(1)} = 2G\left[-\frac{\partial^2 f}{\partial z^2} + z\frac{\partial^3 f}{\partial z^3}\right], \tag{29}$$

$$\tau_{rz}^{(1)} = 2Gz\frac{\partial^3 f}{\partial r \partial z^2}, \tag{30}$$

$$u_r^{(1)} = (1-2\nu)\frac{\partial f}{\partial r} + z\frac{\partial^2 f}{\partial r \partial z}, \tag{31}$$

$$u_z^{(1)} = -2\left(1-\nu\right)\frac{\partial f}{\partial r} + z\frac{\partial^2 f}{\partial z^2}, \tag{32}$$

in which

$$f = A\left(\frac{1}{R_{3t}} + \frac{1}{R_{4t}}\right), \tag{33}$$

where A is a constant. The horizontal ground surface is treated as the plane of symmetry. R_{3t} denotes the distance between the point p and the symmetrical position of the actual cavity O_1. Likewise, R_{4t} is the distance from the point p to the symmetrical position of the image cavity O_2. As a result, their expressions can be written as follows:

$$R_{3t} = \sqrt{(t+r)^2 + (z+h)^2}, \quad R_{4t} = \sqrt{[m-(t+r)]^2 + [z-(n-h)]^2}; \tag{34}$$

f is a harmonic function, that is, $\nabla^2 f = 0$. The corresponding stresses on the free surface are:

$$\sigma_z^{(1)}\Big|_{z=0} = 2GA\left[\frac{1}{R_{3t}'^3} - \frac{3h^2}{R_{3t}'^5} + \frac{1}{R_{4t}'^3} - \frac{3(n-h)^2}{R_{4t}'^5}\right], \tag{35}$$

$$\tau_{rz}^{(1)}\Big|_{z=0} = 0, \tag{36}$$

where $R_{3t}' = R_3'$, and $R_{4t}' = R_4'$.

Thus, the normal stress on the horizontal ground surface $z = 0$ could be eliminated by the stress function f with accurate value of A. According to the following equation:

$$2GA\left[\frac{1}{R_{3t}'^3} - \frac{3h^2}{R_{3t}'^5} + \frac{1}{R_{4t}'^3} - \frac{3(n-h)^2}{R_{4t}'^5}\right] = \frac{a^3 q}{2}\left[\frac{3h^2}{R_3'^5} - \frac{1}{R_3'^3} + \frac{3(n-h)^2}{R_4'^5} - \frac{1}{R_4'^3}\right], \tag{37}$$

it can be obtained that

$$A = -\frac{a^3 q}{4G}. \tag{38}$$

Substituting the above expression of A back into (33), one has

$$f = -\frac{a^3 q}{4G}\left(\frac{1}{R_{3t}} + \frac{1}{R_{4t}}\right), \tag{39}$$

and then the stress and displacement components can be obtained by substituting (39) into (27) to (32).

For the second part (ii), there is only shear stress on the horizontal ground surface. In the same way, the stress harmonic function $g(r, z)$ is given to eliminate the shear on the boundary, and the solutions of the stress and displacement are as follows:

$$\sigma_r^{(2)} = 2G\left(2\frac{\partial^2 g}{\partial r^2} - \frac{2\nu}{r}\frac{\partial g}{\partial r} + z\frac{\partial^3 g}{\partial r^2 \partial z}\right), \tag{40}$$

$$\sigma_\theta^{(2)} = 2G\left(\frac{1}{r}\frac{\partial g}{\partial r} + 2\nu\frac{\partial^2 g}{\partial r^2} + \frac{z}{r}\frac{\partial^2 g}{\partial r \partial z}\right), \tag{41}$$

$$\sigma_z^{(2)} = 2Gz\frac{\partial^3 g}{\partial z^3}, \tag{42}$$

$$\tau_{rz}^{(2)} = 2G\left(\frac{\partial^2 g}{\partial r \partial z} + z\frac{\partial^3 g}{\partial r \partial z^2}\right), \tag{43}$$

$$u_r^{(2)} = 2(1-\nu)\frac{\partial g}{\partial r} + z\frac{\partial^2 g}{\partial r \partial z}, \tag{44}$$

$$u_z^{(2)} = -(1-2\nu)\frac{\partial g}{\partial r} + z\frac{\partial^2 g}{\partial z^2}. \tag{45}$$

Similarly, the expression of stress function can be written as follows:

$$g = B\left(\frac{1}{R_{3t}} + \frac{1}{R_{4t}}\right), \tag{46}$$

where B is a constant. The stress function g satisfies the equilibrium $\nabla^2 g = 0$, and the corresponding stress components on the ground surface $z = 0$ are

$$\begin{gathered}\sigma_z^{(2)}\Big|_{z=0} = 0,\\ \tau_{rz}^{(2)}\Big|_{z=0} = 2GB\left[\frac{3h(t+r)}{R'_{3t}} + \frac{3(h-n)(t+r-m)}{R'_{4t}}\right].\end{gathered} \tag{47}$$

Accordingly, it can be obtained that $B = -a^3 q/4G$.

The final expression for the stress function is then as follows:

$$g = -\frac{a^3 q}{4G}\left(\frac{1}{R_{3t}} + \frac{1}{R_{4t}}\right). \tag{48}$$

Substituting (48) into (40) to (45), the stress and displacement components can be obtained.

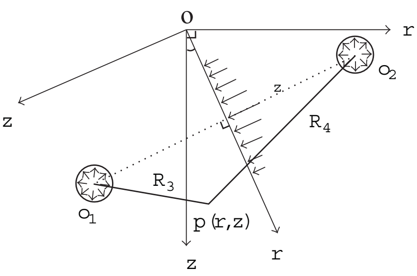

Figure 5: The stress distribution of the slope surface.

3.4. The Correction of the Stresses on the Slope Surface. Considering a virtual source, positive mirror image of the actual cavity with respect to a slope surface will produce the same normal stresses and opposite shear stresses as the actual cavity, the shear stress is eliminated, and the normal stress increases doubly, as shown in Figure 5.

Using the method of coordinate transformation, the normal and shear stresses can be obtained as follows:

$$\begin{aligned}\sigma_{z'}\Big|_{z'=0} &= 3a^3 q\left[\frac{(t + r'\sin\beta)^2 + c^2}{R_0^5} - \frac{1}{R_0^3}\right]\\ &\quad\times \cos^2\beta - 3a^3 q \cdot \left[\frac{(r'\cos\beta - h)(t + r'\sin\beta) + cd}{2R_0^5}\right]\\ &\quad\times \sin 2\beta + \frac{a^3 q}{2}\left[\frac{4}{R_0^3} - \frac{3(t + r'\sin\beta)^2 + 3c^2}{R_0^5}\right]\\ \tau_{r'z'}\Big|_{z'=0} &= 0,\end{aligned} \tag{49}$$

where $c = t + r'\sin\beta - m$, $d = r'\cos\beta - h + n$, and $R_0 = \sqrt{(t + r'\sin\beta)^2 + (r'\cos\beta - h)^2}$.

In order to satisfy the free surface boundary condition as much as possible, the Boussinesq solution has been introduced to correct the normal stress. Stress q' is applied on the surface of the slope, which is equal to the normal stress $\sigma_{z'}|_{z'=0}$ in value but opposite in direction.

As shown in Figure 6, ol is the intersection line of the slope and the horizontal plane. A small element with an area of $\rho d\theta d\rho$ is taken out of the slope lor' (i.e., or' in Figure 5) for analysis. Further, the force exerted on the small element is equal to $q'\rho d\theta d\rho$. Using the Boussinesq solutions, the stress and displacement components of soil under the action of the force ($q'\rho d\theta d\rho$) can be derived as follows:

$$d\sigma_{z'} = \frac{3q' z'^3}{2\pi R'^5}\rho d\theta d\rho,$$

$$d\sigma_{\theta''} = \frac{(1-2\nu) q'}{2\pi R'^2}\left(\frac{R'}{R' + z'} - \frac{z'}{R'}\right)\rho d\theta d\rho,$$

$$d\sigma_{r''} = \frac{q'}{2\pi R'^2}\left[\frac{3r''^2 z'}{R'^3} - \frac{(1-2\nu) R'}{R' + z'}\right]\rho d\theta d\rho,$$

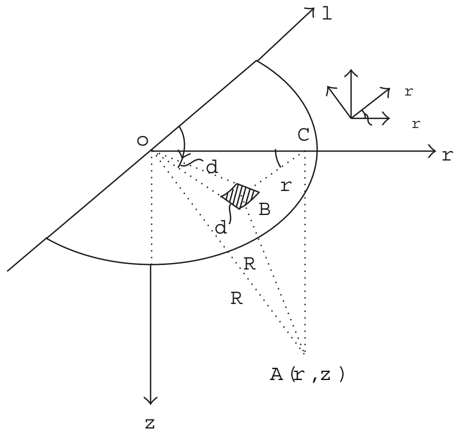

Figure 6: The stress analysis of calculation point by the force on the small element.

$$
\begin{aligned}
d\tau_{r''z'} &= \frac{3q'r''z'^2}{2\pi R'^5}\rho d\theta d\rho, \\
du_{z'} &= \frac{(1+\nu)q'}{2\pi ER'}\left[2(1-\nu)+\frac{z'^2}{R'^2}\right]\rho d\theta d\rho, \\
du_{r''} &= \frac{(1+\nu)q'}{2\pi ER'}\left[\frac{r''z'}{R'^2}-\frac{(1-2\nu)r''}{R'+z'}\right]\rho d\theta d\rho,
\end{aligned}
\tag{50}
$$

in which

$$
\begin{aligned}
r''^2 &= \rho^2 + r'^2 - 2\rho r'\cos\left(\theta-\frac{\pi}{2}\right), \\
R'^2 &= r''^2 + z'^2 = \rho^2 + r'^2 - 2\rho r'\cos\left(\theta-\frac{\pi}{2}\right) + z'^2.
\end{aligned}
\tag{51}
$$

The directions of stress and displacement induced by the force on the small element are not always in accordance with coordinate axes (Figure 6). By means of coordinate transformation, the solutions of stresses and displacements in the coordinate system $r'oz'$ (Figure 5) can be obtained. After that, integrating results with respect to the whole sloping ground surface can lead to the following:

$$
\begin{aligned}
\sigma_{z'} &= \int_0^{\pi}\int_0^{\infty} d\sigma_{z'}, \\
\sigma_{\theta'} &= \int_0^{\pi}\int_0^{\infty}\left(d\sigma_{r''}\sin^2\theta' + d\sigma_{\theta''}\cos^2\theta'\right), \\
\sigma_{r'} &= \int_0^{\pi}\int_0^{\infty}\left(d\sigma_{r''}\cos^2\theta' + d\sigma_{\theta''}\sin^2\theta'\right), \\
\tau_{r'z'} &= \int_0^{\pi}\int_0^{\infty} d\tau_{r''z'}\cos\theta', \\
u_{z'} &= \int_0^{\pi}\int_0^{\infty} du_{z'}, \\
u_{r'} &= \int_0^{\pi}\int_0^{\infty} du_{r''}\cos\theta'.
\end{aligned}
\tag{52}
$$

Hence, the stress and displacement components in the coordinate system *roz* can be derived as follows:

$$
\begin{aligned}
\sigma_r^{(3)} &= \sigma_{r'}\sin^2\beta + \sigma_{z'}\cos^2\beta - \tau_{r'z'}\sin 2\beta, \\
\sigma_z^{(3)} &= \sigma_{r'}\cos^2\beta + \sigma_{z'}\sin^2\beta + \tau_{r'z'}\sin 2\beta, \\
\tau_{rz}^{(3)} &= \frac{1}{2}\left(\sigma_{r'} - \sigma_{z'}\right)\sin 2\beta - \tau_{r'z'}\cos 2\beta, \\
\sigma_\theta^{(3)} &= \sigma_{\theta'}, \\
u_r^{(3)} &= u_{r'}\sin\beta - u_{z'}\cos\beta, \\
u_z^{(3)} &= u_{r'}\cos\beta + u_{z'}\sin\beta,
\end{aligned}
\tag{53}
$$

where $\theta' = \arctan(\rho\sin(\theta-(\pi/2))/(r'-\rho\cos(\theta-(\pi/2))))$, $r' = r\sin\beta + z\cos\beta$, and $z' = -r\cos\beta + z\sin\beta$.

With (53), the stress and displacement fields induced by the stresses q' on the slope can be derived. Using a virtual source of the actual cavity at the image point, the lateral deformations of soil around spherical cavity were predicted by Rao et al. [22]. Meanwhile, the Cerruti solutions are used to eliminate the shear stresses produced by the expansion of both the real and the imaginary spherical cavities in an infinite space. However, their results are inappropriate because of the incorrect using of the Cerruti solutions. It is known that a distributed stress is clearly not a point force in the elementary sense. Hence, the stress should be integrated with respect to the slope surface when it is substituted into the Cerruti solutions.

Accordingly, when considering the effects of both horizontal and sloping free boundaries, the final results of the expansion of a single spherical cavity near a slope (Figure 2) can be obtained by superposition of all the parts stresses and displacements:

$$
\begin{aligned}
\sigma_r &= \sigma_r^{(0)} + \sigma_r^{(1)} + \sigma_r^{(2)} + \sigma_r^{(3)}, \\
\sigma_z &= \sigma_z^{(0)} + \sigma_z^{(1)} + \sigma_z^{(2)} + \sigma_z^{(3)}, \\
\sigma_\theta &= \sigma_\theta^{(0)} + \sigma_\theta^{(1)} + \sigma_\theta^{(2)} + \sigma_\theta^{(3)}, \\
\tau_{rz} &= \tau_{rz}^{(0)} + \tau_{rz}^{(1)} + \tau_{rz}^{(2)} + \tau_{rz}^{(3)}, \\
u_r &= u_r^{(0)} + u_r^{(1)} + u_r^{(2)} + u_r^{(3)}, \\
u_z &= u_z^{(0)} + u_z^{(1)} + u_z^{(2)} + u_z^{(3)}.
\end{aligned}
\tag{54}
$$

4. Discussion of the Solutions

The presence of the horizontal and sloping free surfaces is considered in this paper. Consequently, the present solutions have more extensive applications compared with solutions of Keer et al. [16]. According to Section 3, the solutions for this problem can be derived in four steps (cavity expansion in an infinite medium, cavity and its image expansion in an infinite medium, and the corrections of stresses on horizontal surface and sloping surface). The range of the angle β between the slope and the vertical plane is $0 \leqslant \beta \leqslant \pi/2$.

When $\beta = 0$, the slope turns to be vertical plane, as shown in Figure 3. Meanwhile, it can be derived from (23) and (24) that the horizontal distance between the actual cavity and its image is $m = 2t$, while the vertical distance is $n = 0$. As a result, (15) to (20) convert into (8) to (13) in sequence.

When $\beta = \pi/2$, there is only a free surface in the horizontal direction. In this case, substituting β into (23) and (24), $m = 0$ and $n = 2h$ can be obtained. Accordingly, (15) converts into equations that were proposed by Keer et al. [16].

When $0 < \beta < \pi/2$, there are horizontal and sloping free boundaries as described in this paper. Therefore, the solutions of expansion of spherical cavity in half-space with horizontal and vertical free boundaries or only a horizontal free boundary are the particular cases of present solutions.

As stated above, (15) to (20) can degenerate to the existing solutions for the extreme cases of horizontal ground and vertical slope, which demonstrates the correctness of solutions derived by the first two steps. Steps 3 and 4 involve the correction of stresses on free surface, which is based on an understanding that existing stresses can be offset by the stresses with the same magnitude and opposite direction. In fact, effects of Steps 3 and 4 are further demonstrated by the analysis cases below.

5. Results and Parameters Analysis

In order to consider all the stress components together, the variation of the Mises stress during the expansion of the cavity is analyzed. The parameters in the example analyses are $q = 200$ kPa, $E = 5000$ kPa, $a = 0.25$ m, and $\nu = 0.5$ (incompressible undrained clay). As the distance $(t + r)/a$ increases or the sloping free boundary is approached, the Mises stress decreases very rapidly in the range $2 \leqslant (t + r)/a \leqslant 3$, but then it decreases it decreases more slowly with further increase of the distance $(t+r)/a$, as shown in Figure 7. In order to give a further discussion of the influence from the inclination angle of the slope, the analysis covers with different angles: $\beta = 15^\circ$, $\beta = 30^\circ$, $\beta = 45^\circ$, $\beta = 60^\circ$, and $\beta = 75^\circ$. The corresponding Mises stresses are shown in Figure 7, respectively. Evidently, the angle β has a pronounced influence on the distributions of the Mises stress. At the same point near the spherical cavity, the Mises stress increases with the increase of the angle β. For example, the Mises stress rises from 5.6×10^{-4} kPa to 1.3×10^{-3} kPa, again at the instant of $(t + r)/a = 4$, while the β increases from 15° to 75°. This is consistent with the results for spherical cavity expansion in half-space reported by Keer et al. [16]. The function f_M in Figure 7 represented the Mises stress: $f_M = k_2/(E/h^3)$. Here, $k_2 = \sqrt{I_2}$ (I_2 is the second principle invariance).

If the free surfaces are not taken into account, normal and shear stresses will appear at the place where there ought to be the free surface, so violating the imposed boundary condition of a free surface [13, 15, 16, 23]. As described in Section 3.4, the shear stress on the sloping ground can be eliminated by using the virtual image technique. In order to cancel the normal stress on sloping surface as much as possible, the Boussinesq solutions are introduced. Another group of normal and shear

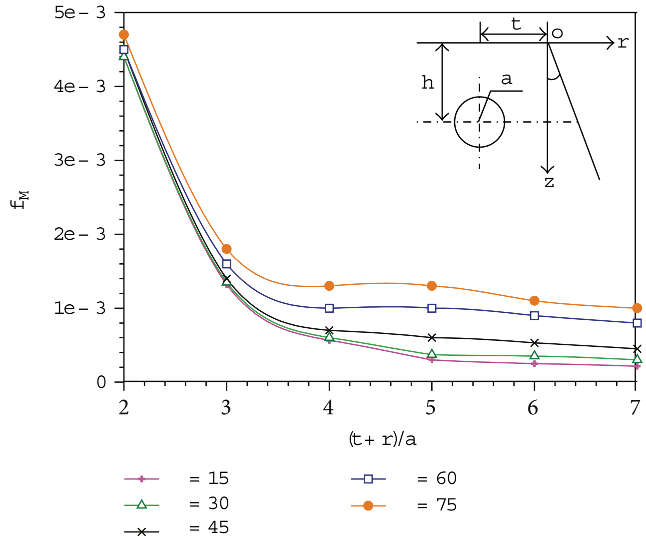

FIGURE 7: The Mises stress varies with the distance $(t + r)/a$.

stresses is produced again when the Boussinesq solutions are applied to correct stresses on the sloping surface, although the original stresses on horizontal free surface have been removed by introduction of harmonic functions (see (39) and (48)). That is because the Boussinesq solutions are aimed at half-space problems.

Figures 8(a) and 8(b) show the normal and shear stresses that vary along the horizontal free surface, respectively, where D is the distance from origin of the coordinate on the horizontal free surface to the opposite direction of the r-axis. The stresses induced by the cavity expansion in an infinite space show large variations, which are determined by the distance from the center to the calculation point. Compared with solutions in an infinite space, both normal and shear stresses on the horizontal free surface corrected by the introduction of the harmonic functions are in close proximity to zero (Figure 8), which demonstrates the validity of the present method. For example, the maximum of the normal stress calculated by present method falls from −0.95 kPa to −0.029 kPa, and the shear stress falls from 0.14 kPa to 0.047 kPa in case that $h = 7a$. With the increase of the distance D/a, the normal and shear stresses on the horizontal free surface decrease gradually. This is because the influence from the stresses on sloping surface weakens when the distance D/a increases.

For the sloping free surface, although stresses have been offset by means of virtual image technique, both normal and shear stresses on the sloping surface are produced again when the harmonic functions (see (39) and (48)) are used to correct the stresses on horizontal free surface. Figures 9(a) and 9(b) show, respectively, the variations of the normal and shear stresses vary along the sloping free surface in cases $l = 4a$ and $5a$, where D is the distance from origin of the coordinate to an arbitrary point on the sloping free surface and l is the distance between the slope and the center of the spherical cavity. Compared to solutions in an infinite space, the stresses on the sloping free surface have been partly corrected by

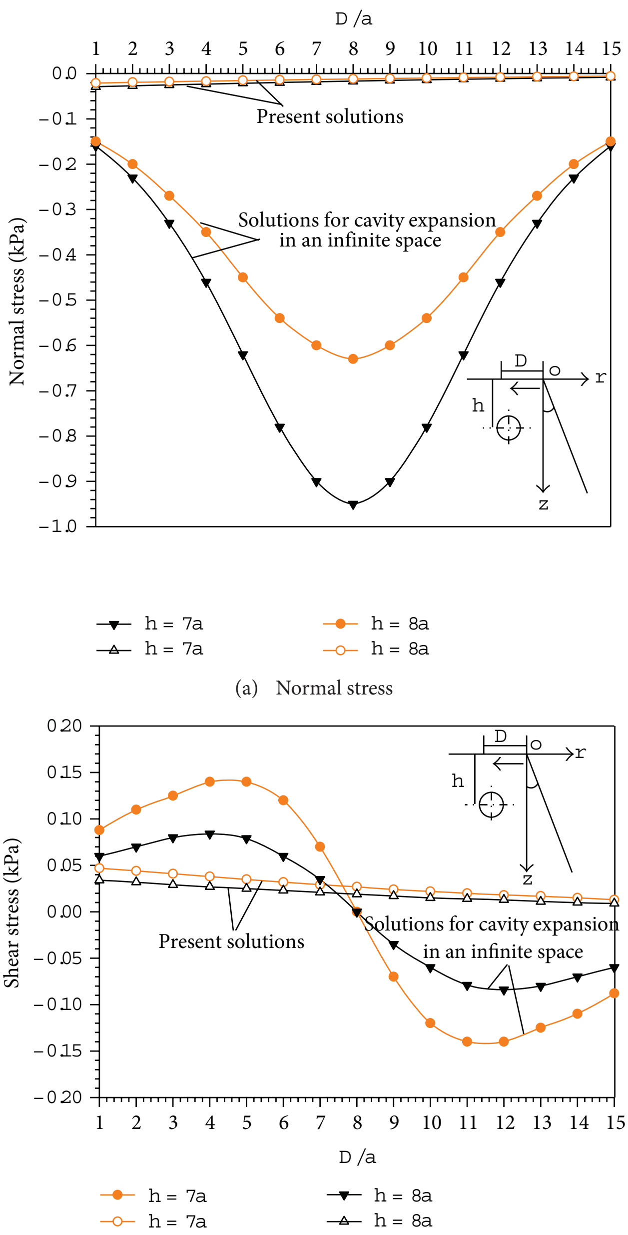

(a) Normal stress

(b) Shear stress

Figure 8: Stress along the horizontal free surface.

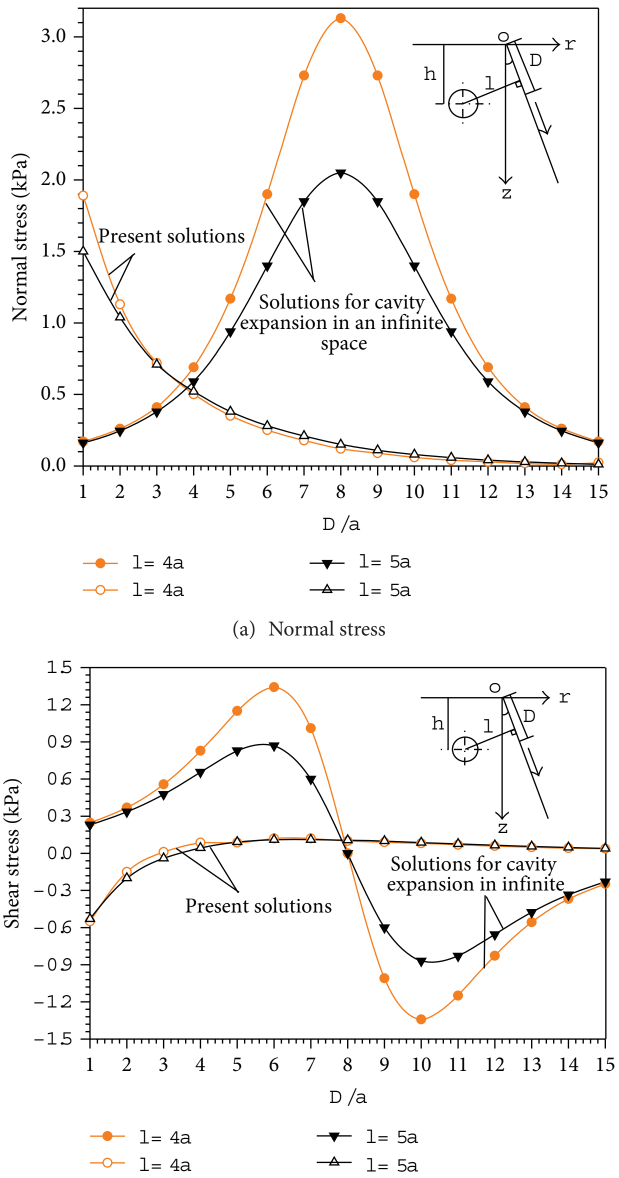

(a) Normal stress

(b) Shear stress

Figure 9: Stress along the sloping free surface.

the introduction of the correction functions. Figures 9(a) and 9(b) show that, after being corrected, both the normal and shear stresses still have larger values in the range $1 \leqslant D/a \leqslant 4$ and then decrease with further increase of D/a. The larger distance of D/a, the smaller the stresses on the slope surface will be produced. The condition of zero stress at the horizontal and sloping free surface is not strictly satisfied. However, this approximate approach is purposeful in reality.

From Figures 8 and 9, the stresses, particularly the shear stresses, on the two free surfaces are close to zero after correction. Thus, the stresses will decrease until zero if the correction processes are iterated continually. It is obvious that the stresses on the free surface decline slowly with the iteration increase, so further trivial corrections are not carried out here.

The displacement of soil induced by the cavity expansion is discussed in this section. Figure 10 illustrates that the slope and its inclination angles have pronounced influence on the distributions of the displacements induced by a cavity expansion source. The displacement decreases with the increase of the distance $(t + r)/a$. Similarly, the displacement decreases rapidly in the range $1 \leqslant (t + r)/a \leqslant 3$, but then more slowly with further increase of $(t + r)/a$. Meanwhile, the displacement induced by a cavity expansion source approaching a free surface, in general, is larger than that in infinite medium (no boundary effect). The findings are in accordance with the results proposed by Keer et al. [16]

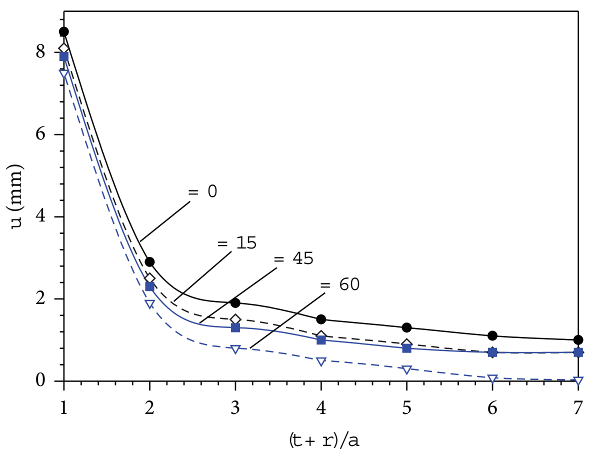

Figure 10: The displacement varies with distance.

and Chai et al. [20]. Here, $u = \sqrt{u_r^2 + u_z^2}$ (u_r and u_z are the displacements in the r and z directions, resp.).

Using the theory of the spherical cavity expansion in an infinite space implies that there is an infinitely thick "soil wall" existing on the side of the slope, which will restrain the lateral displacement induced by the spherical expansion. According to the Figure 2, the slope tends to be flat with the increase of the angle β. As a result, the displacement at the same point in the soil decreases due to the increase of the thickness of "restriction." For instance, when $\beta = 0^\circ$, the displacement is 2.4 times of the displacement induced by cavity with no boundary effect at the instant of $(t + r)/a = 3$. Thus, the presence and inclination angle of the sloping free boundary have a great influence on the displacement due to cavity expansion.

6. Conclusions

Analytical solutions of the cavity expansion near the sloping ground were proposed based on the understanding that expansion caused by pile tip can be simulated as a spherical cavity expansion. Both the horizontal and sloping free surfaces are taken into account by using of a virtual image technique, harmonic functions, and the Boussinesq solutions, and the solutions will convert into the solutions reported by Keer et al. [16] when the sloping ground turn to the horizontal direction.

The results show that the presence and inclination angle of sloping free boundary have a considerable influence on the distributions of the stress and displacement fields induced by the spherical cavity expansion. As the distance from the cavity increases or when the boundary is approached, the Mises stress decreases. With the increase of the angle β between the slope and the vertical plane, the slope tends to flat and the displacement at the same point in the soil decreases with the increase of the "lateral restriction." Likewise, the displacement increases with the decrease of the angle β. Therefore, the existence of the slope increases the risk of the slope failure due to the pile installation.

Acknowledgment

The work reported herein was supported by the National Natural Science Foundation of China (Grant no. 41272288). The above financial support is gratefully acknowledged.

References

[1] K. Georgiadis and M. Georgiadis, "Undrained lateral pile response in sloping ground," *Journal of Geotechnical and Geoenvironmental Engineering*, vol. 136, no. 11, pp. 1489–1500, 2010.

[2] C. W. W. Ng, L. M. Zhang, and K. K. S. Ho, "Influence of laterally loaded sleeved piles and pile groups on slope stability," *Canadian Geotechnical Journal*, vol. 38, no. 3, pp. 553–566, 2001.

[3] L. M. Zhang, C. W. W. Ng, and C. J. Lee, "Effects of slope and sleeving on the behavior of laterally loaded piles," *Soils and Foundations*, vol. 44, no. 4, pp. 99–108, 2004.

[4] C. Sagaseta and A. J. Whittle, "Prediction of ground movements due to pile driving in clay," *Journal of Geotechnical and Geoenvironmental Engineering*, vol. 127, no. 1, pp. 55–66, 2001.

[5] S. L. Shen, J. Han, H. H. Zhu, and Z. S. Hong, "Evaluation of a dike damaged by pile driving in soft clay," *Journal of Performance of Constructed Facilities*, vol. 19, no. 4, pp. 300–307, 2005.

[6] R. F. Bishop, R. Hill, and N. F. Mott, "The theory of indentation and hardness tests," *Proceedings of the Physical Society*, vol. 57, no. 3, pp. 147–159, 1945.

[7] R. Hill, *The Mathematical Theory of Plasticity*, Oxford University Press, Oxford, UK, 1950.

[8] H. S. Yu and G. T. Houlsby, "Finite cavity expansion in dilatant soils: loading analysis," *Geotechnique*, vol. 41, no. 2, pp. 173–183, 1991.

[9] M. F. Randolph, J. Dolwin, and R. Beck, "Design of driven piles in sand," *Geotechnique*, vol. 44, no. 3, pp. 427–448, 1994.

[10] M. F. Randolph, J. P. Carter, and C. P. Wroth, "Driven piles in clay—the effects of installation and subsequent consolidation," *Geotechnique*, vol. 29, no. 4, pp. 361–393, 1979.

[11] J. M. Pestana, C. E. Hunt, and J. D. Bray, "Soil deformation and excess pore pressure field around a closed-ended pile," *Journal of Geotechnical and Geoenvironmental Engineering*, vol. 128, no. 1, pp. 1–12, 2002.

[12] S. L. Chen and N. Y. Abousleiman, "Exact undrained elasto-plastic solution for cylindrical cavity expansion in modified Cam Clay soil," *Geotechnique*, vol. 62, no. 5, pp. 447–456, 2012.

[13] J. C. Chai, N. Miura, and H. Koga, "Lateral displacement of ground caused by soil-cement column installation," *Journal of Geotechnical and Geoenvironmental Engineering*, vol. 131, no. 5, pp. 623–632, 2005.

[14] C. Sagaseta, G. T. Houlsby, J. Norbury, and A. A. Wheeler, "Quasi-static undrained expansion of a cylindrical cavity in clay in the Presence of shaft friction and anisotropic initial stresses," Report, Department of Engineering Science, University of Oxford, 1984.

[15] C. Sagaseta, "Analysis of undrained soil deformation due to ground loss," *Geotechnique*, vol. 37, no. 3, pp. 301–320, 1987.

[16] L. M. Keer, Y. Xu, and V. K. Luk, "Boundary effects in penetration or perforation," *Journal of Applied Mechanics*, vol. 65, no. 2, pp. 489–496, 1998.

[17] R. D. Mindlin and D. H. Cheng, "Nuclei of strain in the semi-infinite solid," *Journal of Applied Physics*, vol. 21, pp. 926–930, 1950.

[18] H. G. Hopkins, "Dynamic expansion of spherical cavities in metals," in *Progress in Solid Mechanics*, I. N. Sneddon and R. Hill, Eds., vol. 1, chapter 3, pp. 83–164, North-Holland, Amsterdam, The Netherlands, 1960.

[19] A. S. Vesic, "Expansion of cavities in infinite soil mass," *Journal of the soil Mechanics and Foundations Division*, vol. 98, no. 3, pp. 265–290, 1972.

[20] J. C. Chai, J. P. Carter, N. Miura, and H. H. Zhu, "Improved prediction of lateral deformations due to installation of soil-cement columns," *Journal of Geotechnical and Geoenvironmental Engineering*, vol. 135, no. 12, pp. 1836–1845, 2009.

[21] M. K. Kassir and G. C. Sih, *Three-Dimensional Crack Problems*, Noordhoff International Publishing, Dordrecht, The Netherlands, 1975.

[22] P. P. Rao, J. P. Li, and Y. Liu, "Analysis of soil squeezing effect for spherical cavity expansion with inclined nonaxisymmetric displacement boundary," *Rock and Soil Mechanics*, vol. 32, no. 9, pp. 2681–2687, 2011 (Chinese).

[23] H. S. Yu, *Cavity Expansion Method in Geomechanics*, Kluwer Academic Publishers, Dordrecht, The Netherlands, 2000.

Hindawi Publishing Corporation
Journal of Applied Mathematics
Volume 2013, Article ID 848324, 10 pages
http://dx.doi.org/10.1155/2013/848324

Research Article

Application of D-CRDM Method in Columnar Jointed Basalts Failure Analysis

Changyu Jin,[1] Xiating Feng,[1] Chengxiang Yang,[1] Dan Fang,[2] Jiangpo Liu,[1] and Shuai Xu[1]

[1] *Key Laboratory of Ministry of Education on Safe Mining of Deep Metal Mines, Northeastern University, Shenyang 110819, China*
[2] *East China Hydropower Investigation and Design Institute, CHECC, Hangzhou 310014, China*

Correspondence should be addressed to Changyu Jin; jcy_snow@163.com

Received 6 June 2013; Revised 3 August 2013; Accepted 20 August 2013

Academic Editor: Ga Zhang

Columnar jointed basalt is a type of joint rock mass formed by the combined cutting effect of original joints and aphanitic microcracks. After excavation unloading, such rock mass manifested distinct mechanical properties including discontinuity, anisotropy, and proneness of cracking. On the basis of former research findings, this paper establishes a D-CRDM method applicable to the analysis of columnar jointed basalt, which not only integrates discrete element and equivalent finite-element methods, but also takes into account the coupling effect of original joints and aphanitic microcracks. From the comparative study of field monitoring data and strain softening constitutive model calculated results, it can be found that this method may well be used for the simulation of mechanical properties of columnar jointed basalts and the determination of rock failure mechanism and failure modes, thus providing references for the selection of supporting measures for this type of rock mass.

1. Introduction

Due to the abundance of internal joints, columnar jointed basalt possesses distinct mechanical properties such as discontinuity, anisotropy and is easy to crack compared with other types of rock mass. For this type of rock mass, its surface rocks instantaneously generate tensile failure right with the beginning of excavation; then aphanitic microcracks start to develop throughout the columns along with the reduction of surface rock confining pressure and induce a secondary failure of original joints, which finally leads to a progressive failure pattern similar to "domino effect." Currently, studies on the unloading mechanical properties of columnar jointed rock mass appear to be quite limited. Based on existing research findings on joint rock mass [1–6], this paper proposes a D-CRDM (discrete element method-crack rock mass deterioration model) analysis method by integrating equivalent continuum and discrete element and uses this method to simulate the unloading mechanical impacts of rock mass after excavation of experimental cavity. The correctness of this analytical method is verified by comparing with the monitoring results; at the same time, the unloading failure mechanism and failure modes of columnar jointed basalts are revealed as well.

2. Failure Modes of Columnar Jointing

Columnar jointed basalt is a type of joint rock mass formed by the combined cutting effect of original joints and aphanitic microcracks, of which the original joint is a type of geological structure generated during the magmatic condensation process. It possesses a clear column surface and a distinct column outline; its cross-section is quadrilateral or pentagonal in shape and has a mosaic structure. Due to the weak strength of original joints, original joints on the surface are prone to spall after excavation. From photos taken on the damaged sites (see Figures 1(a) and 1(b)), it can be observed that such failure and stripping are mainly caused by the opening and sliding of joints, which may be described by block theories and can be analyzed by discontinuous methods such as the discrete element method.

The aphanitic microcracks inside the columns are small joint planes between the two crystal grains. Such small joint planes reduce the rock integrity. Through on-site observations it can be found that large scale spall appeared in the cavern roof or arch corners and created a not very deep pit. According to the sizes of the stripping blocks, it can be initially estimated that this type of failure was induced by the

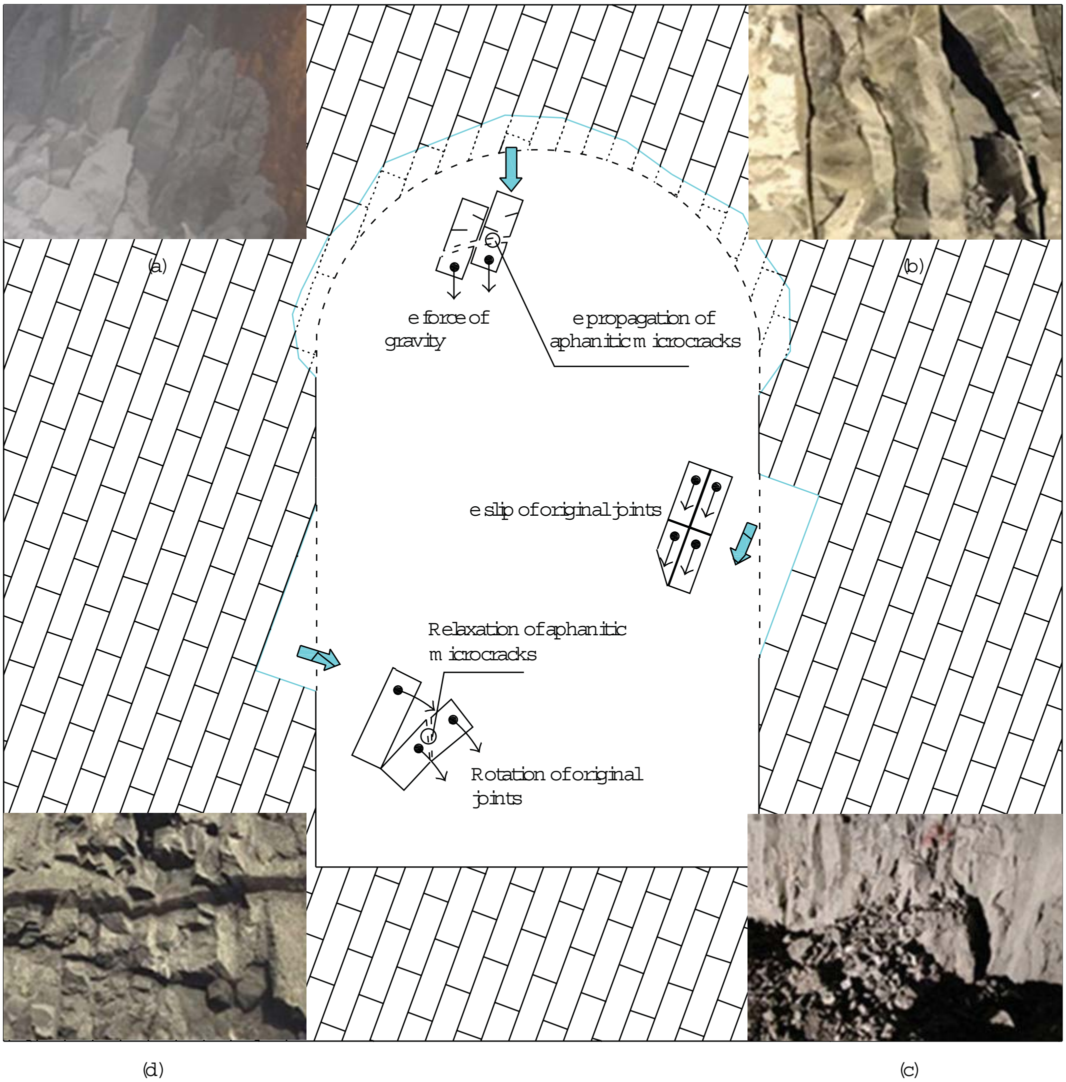

Figure 1: Failure modes of surrounding rock in the cavity.

extending and splitting of aphanitic microcracks. In addition, the surrounding rock on the cavern side wall generated a large amount of broken rocks, especially in the region where the cracking failures of original joints are concentrated, which is seen in the failure model shown in Figures 1(c) and 1(d). Since the aphanitic microcracks are randomly developed inside the columns and it is impossible to count their number, it is more appropriate to adopt equivalent method for analysis and research in light of the research results of the literature [7–11].

3. D-CRDM (Discrete Element Method-Crack Rock Mass Deterioration Model)

D-CRDM analysis method simulates original joints by 3DEC block theory and develops constitutive deterioration model of jointed rock by using its secondary development function in order to implement coupling analysis of these two kinds of joints.

After excavation, the aphanitic microcracks on the surface of surrounding rocks gradually extend and crack under the effect of unloading, resulting in the deterioration of overall mechanical properties of columnar jointed basalt. From a macro perspective, this type of deterioration can be considered as a changing process of Young's modulus E, Poisson's ratio μ, cohesion C, friction angle ϕ, tensile strength T, and other mechanical parameters of the rock mass. Therefore, when adopting numerical simulation method to study the mechanical behaviour of columnar jointed basalt, its constitutive model should accurately reflect two fundamental features of the rock mass; that is, the mechanics parameters change along with the damage of surrounding rock both during and after the yielding course of rock mass. In rock deterioration process, each parameter change should be determined by the mechanical state of rock mass, while the mechanical index of equivalent plastic strain $\bar{\varepsilon}^p$ is usually used to describe different stress state of rock mass, which is defined

$$\bar{\varepsilon}^p = \int \sqrt{\frac{2}{3}} \left(\varepsilon_1^p \varepsilon_1^p + \varepsilon_2^p \varepsilon_2^p + \varepsilon_3^p \varepsilon_3^p \right). \quad (1)$$

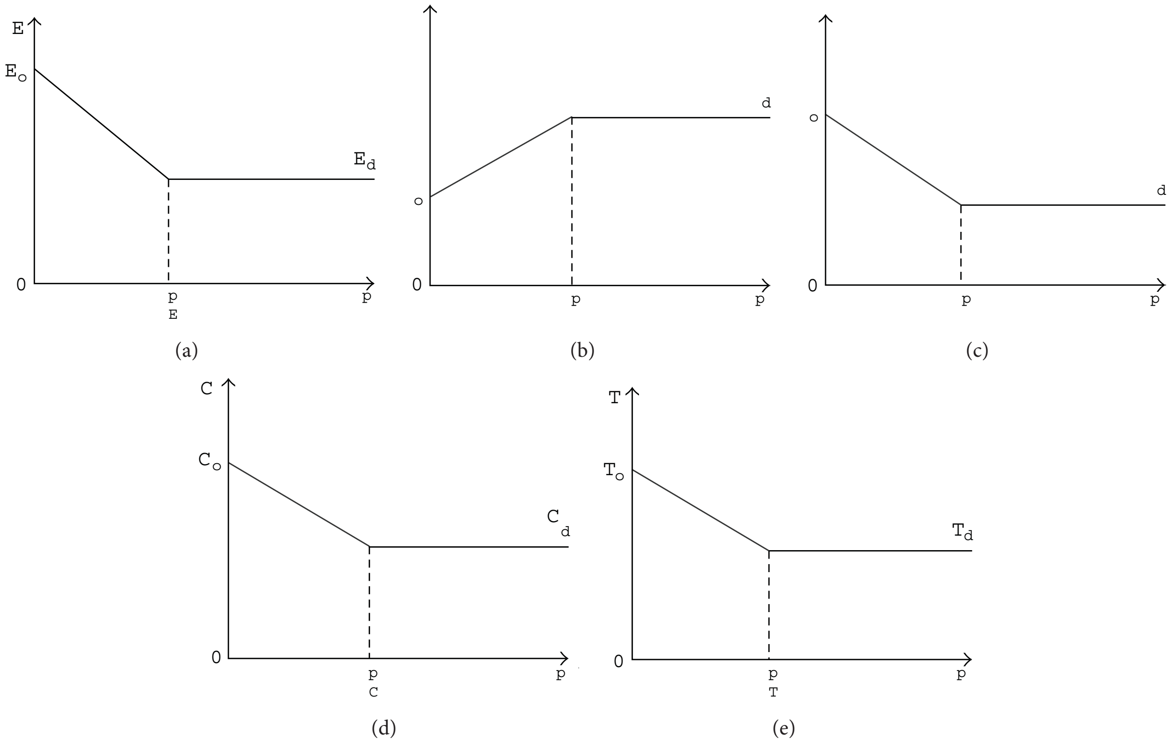

Figure 2: Rock mass mechanical parameters changing curve diagram along with the variation of equivalent plastic strain.

In order to define the change of deformation and strength parameters, it is supposed that each parameter satisfies the function of $\bar{\varepsilon}^p$ the following:

$$
\begin{aligned}
E\left(\bar{\varepsilon}^p\right) &= E_0 \cdot f_E\left(\bar{\varepsilon}^p\right), \\
\mu\left(\bar{\varepsilon}^p\right) &= \mu_0 \cdot f_\mu\left(\bar{\varepsilon}^p\right), \\
C\left(\bar{\varepsilon}^p\right) &= C_0 \cdot f_C\left(\bar{\varepsilon}^p\right), \\
\phi\left(\bar{\varepsilon}^p\right) &= \phi_0 \cdot f_\phi\left(\bar{\varepsilon}^p\right), \\
T\left(\bar{\varepsilon}^p\right) &= T_0 \cdot f_T\left(\bar{\varepsilon}^p\right),
\end{aligned}
\tag{2}
$$

where E_0, μ_0, C_0, φ_0, and T_0 are Young's modulus, Poisson's ratio, cohesion, friction angle, and tensile strength of the columns of columnar jointed basalt in initial state; $E(\bar{\varepsilon}^p)$, $\mu(\bar{\varepsilon}^p)$, $C(\bar{\varepsilon}^p)$, $\varphi(\bar{\varepsilon}^p)$, and $T(\bar{\varepsilon}^p)$ are Young's modulus, Poisson's ratio, cohesion, friction angle and tensile strength for a given plastic strain state, respectively; whereas $f_E(\bar{\varepsilon}^p)$, $f_\mu(\bar{\varepsilon}^p)$, $f_c(\bar{\varepsilon}^p)$, $f_\varphi(\bar{\varepsilon}^p)$, and $f_T(\bar{\varepsilon}^p)$ are the evolution functions which may be linear, piecewise, or nonlinear and can be determined in the aid of the experiences or the correlated experimental test curves.

After excavation of underground cavity, the surrounding rock mass suffered different degrees of damage due to the cracking of aphanitic microcracks in surface columns and new fractures generated hence with. Theoretical analysis and engineering practice both show that the cracks and expansion of joints reduce the rock integrity, resulting in reduced resistance to deformation of rock mass, and its elastic modulus E also decreases with it. When the rock mass is within the scope of elastic range, the Poisson's ratio is generally constant; however, Poisson's ratio will change along the rock mass stress state alteration when the rock mass is beyond the scope of elastic range. Generally, after dilatation of rock mass, the Poisson's ratio of rock mass often increases until it reaches 0.5. Therefore, in rock degradation process, the computation of deformation parameters is a progressively variant procedure along with the change of the mechanical state of rock mass. Since the breaking of original joints continuously reduces columns confining pressure, the tiny cracks inside the columns are progressively cut through, leading to a macroscopic manifestation of large deformation as well as the stripping and falling of aphanitic microcracks. These local deterioration phenomena of rock mass reduce its strength and integrity, which corresponds to the reduction of mechanical parameters including friction angle, cohesion, and tensile strength. Therefore, the process of aphanitic microcracks breakage and new fracture development may be considered as a continuous disintegrating course of the microstructures of the columns, that is, the process of reductions of friction angle φ, cohesion C, and tensile strength T along with the reduction of equivalent plastic strains. In this paper, an example with linear evolution functions is presented in Figure 2.

To achieve the dynamical evolution of above mechanical parameters along with the variation of plastic strain, combined with Mohr-Coulomb elastoplastic constitutive model, the mechanical parameters of the materials are step-by-step updated according to (2) in iterations calculated in

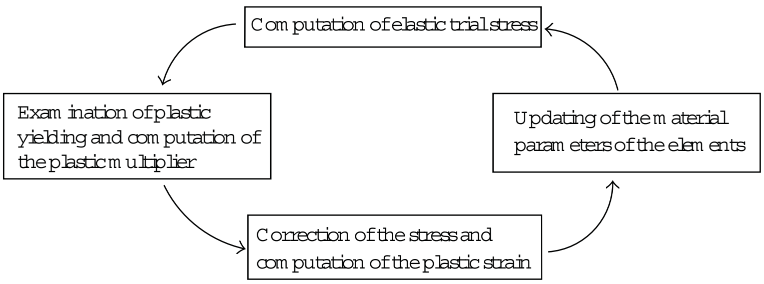

Figure 3: Procedure of the numerical computation used in CRDM.

the 3DEC difference dynamical iterative solution procedure (see Figure 3).

In the process of circulative calculation, the shear yield function uses Mohr-Coulomb yield criterion, which is expressed as a function of equivalent plastic strain; namely,

$$f^s = \sigma_1 - \sigma_3 N_\varphi + 2C\left(\bar{\varepsilon}^p\right)\sqrt{N_\varphi},$$
$$N_{\varphi(\bar{\varepsilon}^p)} = \frac{1+\sin\left[\varphi\left(\bar{\varepsilon}^p\right)\right]}{1-\sin\left[\varphi\left(\bar{\varepsilon}^p\right)\right]}. \tag{3}$$

Taking into account the weakness of tensile strength of columnar jointed basalt, Rankine's strength criteria of maximum tensile stress is also considered when judging whether the rock mass enters into shaping state:

$$f^t = \sigma_t - \sigma_3. \tag{4}$$

After the cracking of aphanitic microcracks, the rock mass goes into yield condition, and since each parameter constantly changes along with the equivalent plastic strain, the yielding surface of this model varies dynamically not as that given in the common elastoplastic constitutive relations. According to the research results of Yingren et al. [12], the straight line equation of side AB in the π plane and the equation of distance between the centre of the π plane and the origin of the principle stress space coordinates system are given as

$$x = \sqrt{2}c\cos\varphi + \frac{\sin\varphi}{\sqrt{3}}y - \sigma_m\sin\varphi,$$
$$d = \frac{1}{\sqrt{3}}\left(\sigma_1+\sigma_2+\sigma_3\right) = \sqrt{3}\sigma_m, \tag{5}$$

where σ_m is the hydrostatic pressure.

The above equations indicate that (1) the slope of line AB is only related to the friction angle φ; the slope of line AB decreases when φ is increasing and deviates to line AB', which means some changes have taken place in the shape of the yielding surface (see Figure 4(a)); (2) when the cohesion changes, the intercept of line AB on x-axis changes correspondently, and line $A'B'$ may become a parallel translation of the straight line AB, which means that the area of the yielding surface in the π plane will expand in a similarity form as shown in Figure 4(b). As the distance between the π plane and the origin of the principle stress space coordinates system depends only on the hydrostatic pressure σ_m, when the internal stress of rock mass changes, that is, when σ_m changes, the yielding surface will be scaled in the meridian plane along the isoclinic line direction (see Figure 4(c)). In addition to the dynamic changes of tensile strength along with the evolution of equivalent plastic strain, this constitutive model presents sufficiently well the dynamic changes of the mechanical properties of columnar jointed basalts after their yielding.

4. Experimental Cavity of Columnar Joints

To verify the correctness of this analysis method and to analyze the unloading mechanism of columnar joints, simulation and analysis were carried out in the experimental cavity of columnar joints located in the Baihetan hydropower station, which is situated in Ningnan county of Sichuan province and Qiaojia county of Yunnan province, the downstream of the Jinsha River. Its dam foundation and the main part of cavity groups are located in the basalts of Upper Permian Emeishan formation ($P_2\beta_3$), where the Emeishan basalts are divided into eleven rock-flowage layers, of which the $P_2\beta_3$ is a basaltic formation mainly consisted of microcrystalline aphanitic joints and oblique lamination. It is the major stratum outcropped in the project area, and columnar joints are developed in partial areas of the middle part of this stratum ($P_2\beta_3^2$ and $P_2\beta_3^3$). In order to explore the unloading properties of columnar jointed basalts and to ensure the stability of dam foundation and underground cavities on the long run, an experimental cavity was excavated in the $P_2\beta_3^2$ stratum for long-term monitoring. This experimental cavity is located in the downstream side of cave PD34 at right bank prospecting line II, with an axial direction of N45°E that is almost consistent with the strike direction of stratum. The cavity has a floor elevation of Δ727.4 m, a vertical embedded depth of about 300 m, and is approximately 160 m away from the bank slope. The in situ stress values in this region are relatively small: the first and the third principal stresses are 4.38 MPa, and 3.23 MPa respectively, with little difference between the two. With reference to the data obtained from laboratory experiments and field triaxial load/unload tests, the calculation parameters of rock mass and structure surfaces were determined as in Tables 1 and 2.

The experimental cavity of columnar jointed basalts, with a total length of 70 m, is divided into two experimental segments, that is, the supported and unsupported experimental

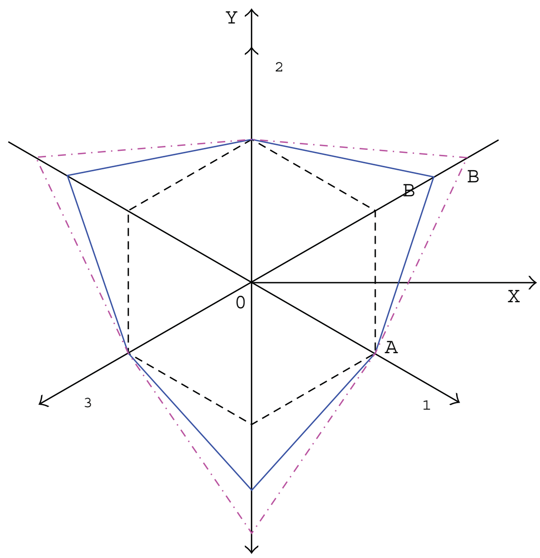

(a) Evolution of the yielding surface in the π surface

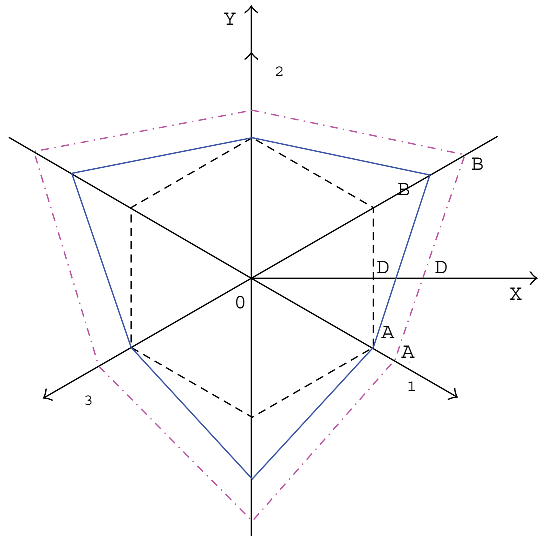

(b) Isoclinic scaling of the yielding surface in the π surface

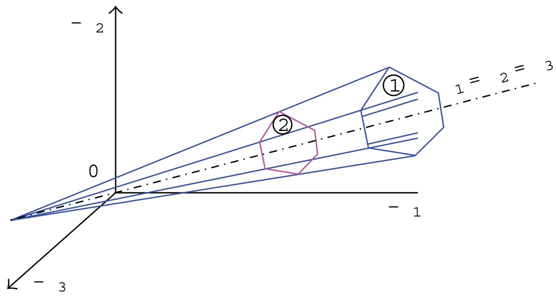

(c) Isoclinic scaling of the yielding surface

FIGURE 4: Evolution characteristics of the successive yielding in CRDM.

TABLE 1: Mechanical parameters of joints.

Normal stiffness /GPa	Shear stiffness /GPa	Frictional angle /°	Cohesion /MPa	Tensile strength /MPa
52.97	12.88	24.3	0.0	0.0

TABLE 2: Equivalent mechanical parameters of the rock.

Young's modulus /GPa		Poisson's ratio		Friction angle /°		Cohesion /MPa		Tensile strength /MPa	
Initial	Residual	Initial	Residual	Initial	Residual	Initial	Residual	Initial	Residual
32.30	15.20	0.21	0.50	35.0	25.0	1.30	0.50	1.25	0.0

segments of 30 m and 40 m, respectively. The cross-section of this experimental cavity is city-gate shaped with dimensions of 13 m × 6.5 m (height × width). According to the geological survey for monitoring section in the unsupported segment, a two-dimensional computational model for the experimental cavity is constructed in which three rock flow age strata $P_2\beta_3^2$, $P_2\beta_3^3$ and $P_2\beta_3^4$ from the bottom to the top are considered. What is more, there is an intraformational disturbed belt of RS3311 in stratum $P_2\beta_3^2$. In order to eliminate the influence of boundary constraints on calculation and to accelerate computing speed, the rock masses within the range of three times the span of cavity and twice the height of cavity were cut into columnar joints, while the rock masses outside this scope were modeled as continuum media. The columnar jointed basalts in rock flowage stratum $P_2\beta_3^3$, where the experimental cavity is located, are ash black ones whose columns are 1~5 m long, 15~25 cm in diameter, and 70° ~ 85° in dip angle; see Figure 5 for specific model. This model adopts tetrahedral elements, with an internal column elements size of 0.15 m, an integrity rock unit of 0.5 m, and total concrete units of 15,000.

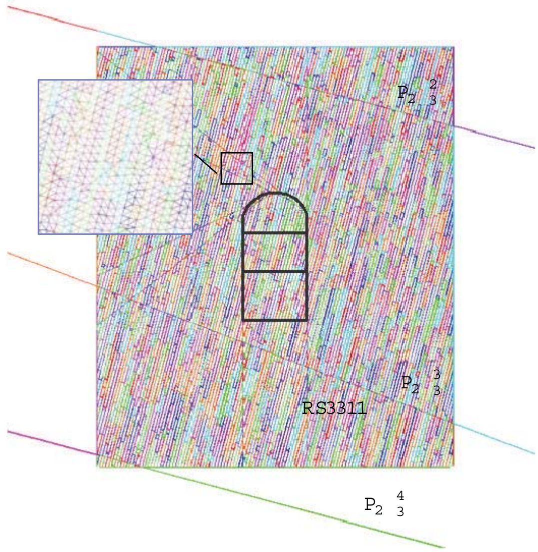

FIGURE 5: Calculated model of computation.

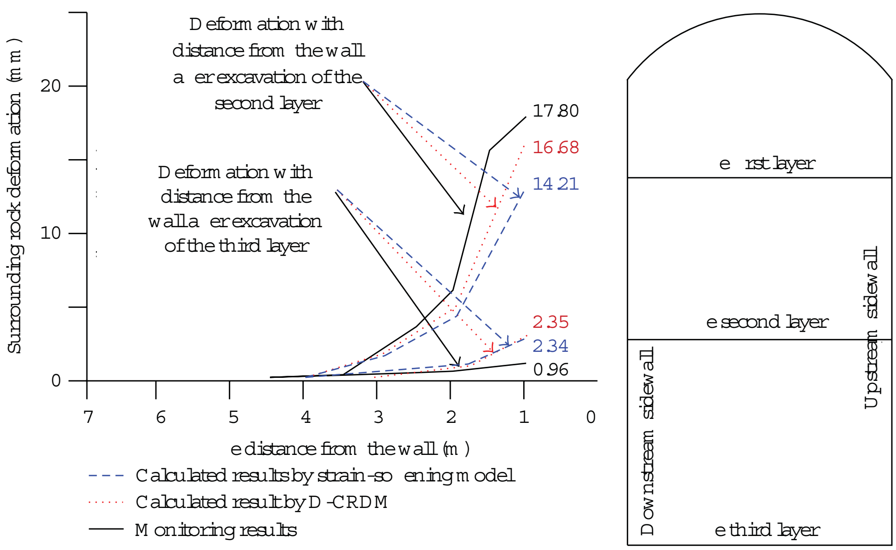

FIGURE 6: Surrounding rock deformation and rock mass failure.

4.1. Analysis of the Displacement Field of Surrounding Rock. The excavation process of the experimental cavity is analyzed by utilizing the simulation method established in this paper. The results reveal that during the excavation of the first layer, deformation of surrounding rock at surface was relatively small; its numerical simulation result is 2.35 mm. During the excavation of the second layer, deformation at each monitoring point increased rapidly (as shown in Figure 6); the numerical simulation value and monitoring datum reached 16.68 mm and 17.80 mm, respectively. These numerical simulation results reveal that the principle cause for the large deformation of surrounding rock is the existence of normal and shear deformations of original joints in rock mass, which are mainly concentrated within 0~4 m of the surrounding rock surface. In addition, the deformation of surrounding rock is also influenced by the dip angles of columnar joints and manifests distinct anisotropic properties; that is, the deformation value of the cavity roof is larger than that of the cavity floor, and the deformation value at the downstream side of cavity is larger than the displacement value of cavity sidewall at the upstream side (as shown in Figure 7). From the comparative study of in situ monitoring results and calculated results of strain-softening constitutive model, it can be found that D-CRDM may accurately simulate the displacement field alteration of surrounding rock during excavation.

4.2. Relaxation of Joints. The failure of jointed rock mass is often due to the expansion and cracking of joints, while the development of these fissures will lead to the reduction of wave velocity. According to the reduction degree of

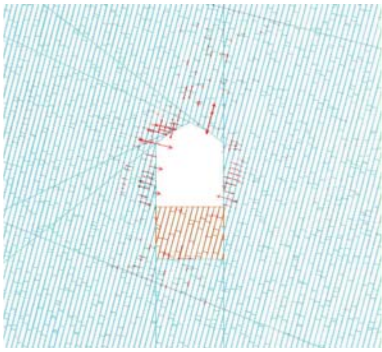

(a) Normal deformation of original joints

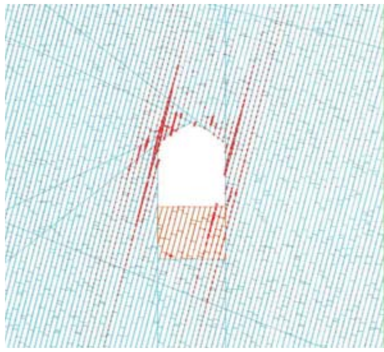

(b) Tangential deformation of joints

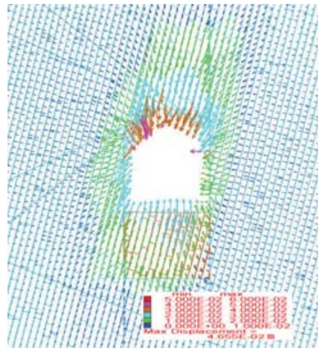

(c) Deformation of surrounding rocks

FIGURE 7: Numerical simulation results of the surrounding rock deformations.

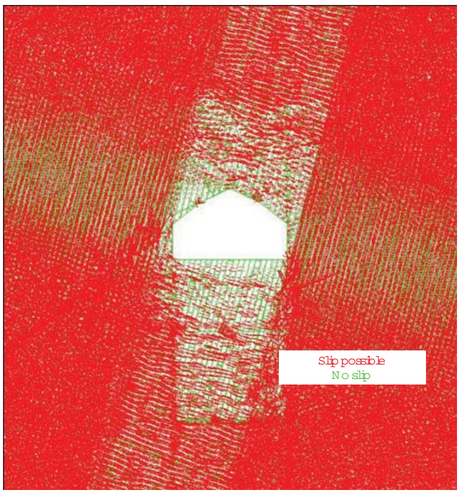

(a) Original joints

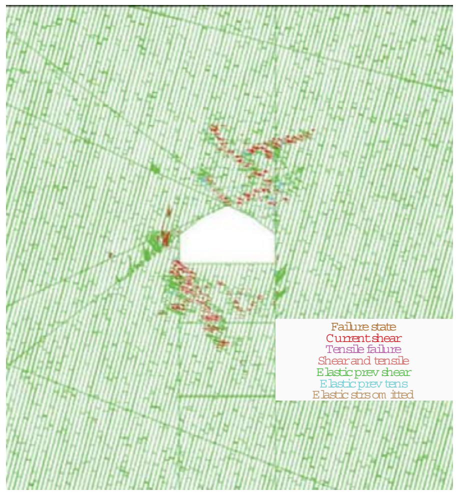

(b) Aphanitic joints

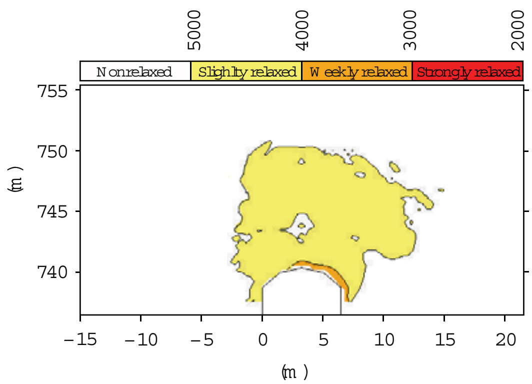

(c) Relaxation zone of columnar joints

FIGURE 8: Relaxation zones of joints after excavation of the first layer.

wave velocity and by modeling on the rock mass integrity evaluation system, a relaxation coefficient of rock mass k is established:

$$k = \frac{v_p^0 - v_p}{v_p^0}, \tag{6}$$

where k is the coefficient of relaxation, v_p is the velocity of longitudinal wave of rock mass at the testing position, and v_p^0 is the eigen wave velocity of nonrelaxed rock mass.

In order to distinguish the relaxation degree of rock mass in a more detailed manner, the relaxation degree of columnar

Table 3: Classification criteria of relaxation degrees.

k	$k \leq 0$	$0 < k \leq 20\%$	$20\% < k \leq 40\%$	$k > 40\%$
v_p/(m/s)	$v_p \geq 5000$	$5000 > v_p \geq 4000$	$4000 > v_p \geq 3000$	$v_p < 3000$
Relaxation evaluations	Nonrelaxed	Slightly relaxed	Weakly relaxed	Strongly relaxed

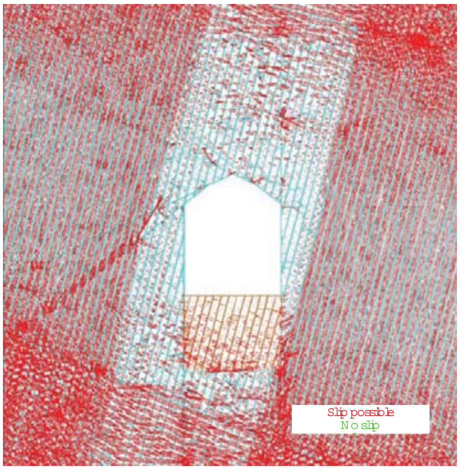

(a) Original joints

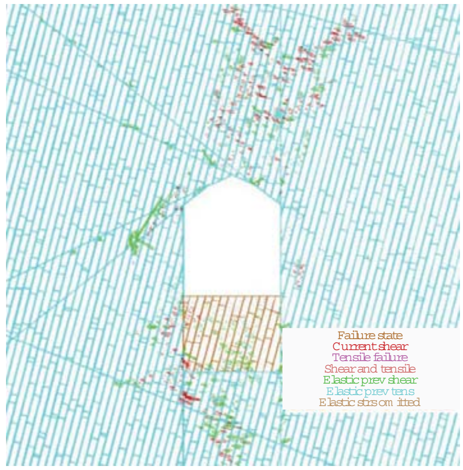

(b) Aphanitic joints

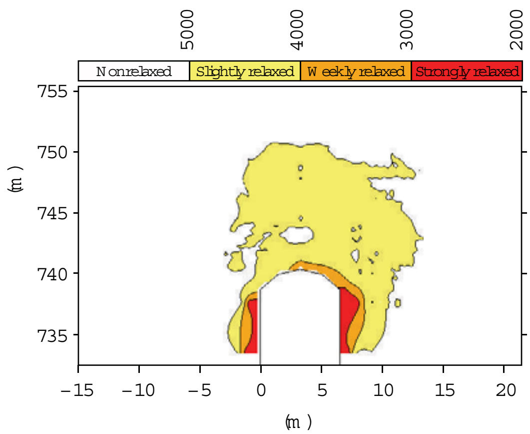

(c) Relaxation zone of columnar joints

Figure 9: Relaxation zones of joints after excavation of the second layer.

joint is subdivided into highly, weakly, and slightly relaxed ones (see Table 3 for further details).

The calculated results obtained by D-CRDM method indicate that after excavation of the first layer of the experimental cavity, the open original joints of upstream and downstream cavity sidewalls were concentrated within 0.5 m of the cavity surface layer. Due to the effect of dip angles of original joints, the joints development area at arch roof basically diffuses along the direction of joint dip angle, with an opening depth almost twice the height of cavity excavation, that is, around 10 m. This is generally consistent with the distribution regularity of relaxation zones of rock mass obtained by in situ acoustic wave tests (Figure 8).

When the experimental cavity was cut into to the second layer, from the contour diagram of joint slipping (as shown in Figure 9) it can be found clearly that the opening zones of original joints on the cavity roof and floor were significantly enlarged, and their heights were also almost equivalent to the cavity height, that is, about 10 m. In addition, a cracking zone of certain depth also appeared on the cavity sidewall. By combining the normal and tangential displacement contour diagrams of original joints, it reveals that the failure and relaxation degree of original joints on cavity sidewall is more intense than those on the roof and floor, with a failure depth of 2~3 m. Due to the same effect of original joints, the joint relaxation zones still develop along the joint dip angle direction, which fully complies with actual observations.

In order to verify the analysis results obtained from wave velocity tests and numerical simulations, a three-dimensional scanning was carried out by using a borehole camera technique on the surrounding rocks inside the borehole that was drilled along the downstream sidewall of experimental cavity.

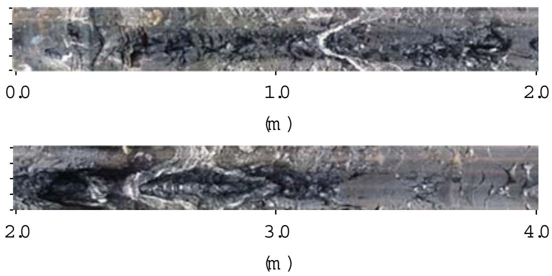

Figure 10: Borehole camera information of columnar joints.

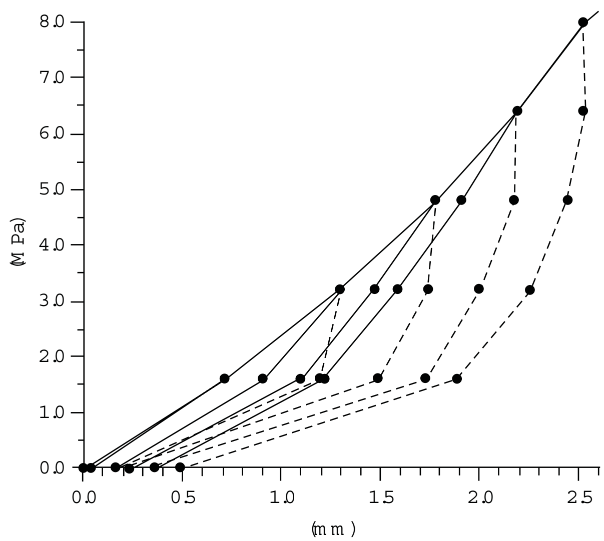

(a) Typical testing curves of field bearing plate

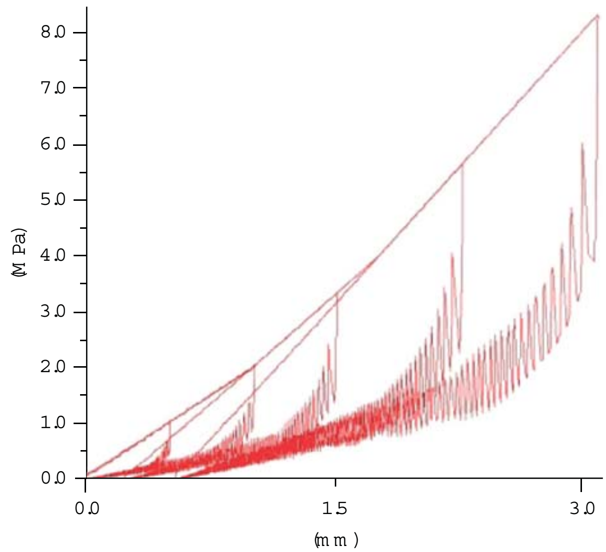

(b) Simulated results of field bearing plate

Figure 11: Contrast between field test and calculated results.

The results showed that the rock mass within 0.0~4.0 m of the surrounding rock on sidewall was obviously relaxed, which further prove the accuracy of above theoretical analysis and field testing (see Figure 10).

4.3. Field Bearing Plate Test. In order to further explore the compression features of columnar joints, a bearing plate test was carried out in the areas where the columnar joints are densely distributed and where the aphanitic microcracks are developed. After the circulative loading and unloading tests of multiple experimental points, it is discovered that most stress-displacement curves are of concave type; that is, under the effect of circulative loading and unloading step-by-step, the Young's modulus of rock mass gradually increases; refer to Figure 11(a) for specific stress routes. Using the formerly proposed method of D-CRDM, a simulation analysis was made to the experiment. As the original joints gradually close during the step-by-step pressuring process of bearing plate, together with the decline of equivalent plastic strain of columns and the gradual increase of Young's modulus, the numerical simulation results basically match with the experimental results, thus further verify that this model complies with the reloading mechanical properties of columnar joints after unloading.

5. Conclusions

By utilizing the D-CRDM analysis method established in this paper, mechanical simulations of both the loading and the reloading after unloading mechanical properties of columnar joints maybe carried out, and multiple field test results have proved the correctness of this method. Meanwhile, the research results of a variety of means also indicate that the failure and instability of columnar jointed basalts are mainly caused by the open failure of original joints; therefore, reinforcing the support of original joints is fundamental to the stability insurance of columnar jointed basalts.

Acknowledgment

Projects 2013BAB02B01, 2013BAB02B03 were supported by the Key Projects in the National Science & Technology Pillar Program During the Twelfth Five-Year Plan Period; projects 51109035, 51274055, 51204030, 51204031, and 11232014 were supported by the National Natural Science Foundation of

China; Projects N110301006, N110501001, and N110401003 were supported by the Fundamental Research Funds for the Central University, China.

References

[1] D. X. Yan, W. Y. Xu, W. T. Zheng, W. Wang, A. C. Shi, and G. Y. Wu, "Mechanical characteristics of columnar jointed rock at dam base of Baihetan hydropower station," *Journal of Central South University of Technology*, vol. 18, no. 6, pp. 2157–2162, 2011.

[2] Y. Wei, M. Xu, W. Wang et al., "Feasibility of columnar jointed basalt used for high-arch dam foundation," *Journal of Rock Mechanics and Geotechnical Engineering*, vol. 3, pp. 461–468, 2011.

[3] S.-J. Di, W.-Y. Xu, Y. Ning, W. Wang, and G.-Y. Wu, "Macro-mechanical properties of columnar jointed basaltic rock masses," *Journal of Central South University of Technology*, vol. 18, no. 6, pp. 2143–2149, 2011.

[4] W. Zhang, J.-P. Chen, C. Liu, R. Huang, M. Li, and Y. Zhang, "Determination of geometrical and structural representative volume elements at the Baihetan dam site," *Rock Mechanics and Rock Engineering*, vol. 45, no. 3, pp. 409–419, 2012.

[5] Z. Yuting, D. Xiuli, and H. Shuling, "Stability evaluation of rock blocks in jointed rock masses considering Earthquake impacts," *Disaster Advances*, vol. 5, no. 4, pp. 127–132, 2012.

[6] Q. Jiang, J. Zhang, and X. Feng, "Health diagnosis and functional rehabilitation for seismic-damaged tunnel suffered from the Wenchuan earthquake: a case study," *Disaster Advances*, vol. 5, no. 4, pp. 738–743, 2012.

[7] M. Sagong, D. Park, J. Yoo, and J. S. Lee, "Experimental and numerical analyses of an opening in a jointed rock mass under biaxial compression," *International Journal of Rock Mechanics and Mining Sciences*, vol. 48, no. 7, pp. 1055–1067, 2011.

[8] M. Singh and B. Singh, "Modified Mohr-Coulomb criterion for non-linear triaxial and polyaxial strength of jointed rocks," *International Journal of Rock Mechanics and Mining Sciences*, vol. 51, pp. 43–52, 2012.

[9] Y. Ren and H. Yang, "Equivalent analysis of ortho gonalvisco elastic joint edrockvia an adaptive algorithm in time domain," *Finite Elements in Analysis and Design*, vol. 46, no. 10, pp. 875–888, 2010.

[10] S. Maghous, D. Bernaud, J. Fréard, and D. Garnier, "Elastoplastic behavior of jointed rock masses as homogenized media and finite element analysis," *International Journal of Rock Mechanics and Mining Sciences*, vol. 45, no. 8, pp. 1273–1286, 2008.

[11] W. G. Pariseau, "An equivalent plasticity theory for jointed rock masses," *International Journal of Rock Mechanics and Mining Sciences*, vol. 36, no. 7, pp. 907–918, 1999.

[12] Z. Yingren, S. Zhujiang, and G. Xiaonan, *The Principles of Geotechnical Plastic Mechanics*, China Architecture and Building Press, Beijing, China, 2002.

Hindawi Publishing Corporation
Journal of Applied Mathematics
Volume 2013, Article ID 385278, 7 pages
http://dx.doi.org/10.1155/2013/385278

Research Article

Micromechanical Formulation of the Yield Surface in the Plasticity of Granular Materials

Homayoun Shaverdi,[1] Mohd. Raihan Taha,[1] and Farzin Kalantary[2]

[1] *Universiti Kebangsaan Malaysia (UKM), 43600 Bandar Baru Bangi, Selangor, Malaysia*
[2] *Department of Geotechnical Engineering, Faculty of Civil Engineering, K. N. Toosi University of Technology, 1346 Vali Asr Street, Vanak, Tehran 19697, Iran*

Correspondence should be addressed to Homayoun Shaverdi; homayoun_shaverdi@yahoo.com

Received 7 June 2013; Revised 31 July 2013; Accepted 15 August 2013

Academic Editor: Pengcheng Fu

An equation is proposed to unify the yield surface of granular materials by incorporating the fabric and its evolution. In microlevel analysis by employing a Fourier series that was developed to model fabric, it is directly included in the strength of granular materials. Inherent anisotropy is defined as a noncoaxiality between deposition angle and principal compressive stress. Stress-induced anisotropy is defined by the degree of anisotropy α and the major direction of the contact normals. The difference between samples which have the same density (or void ratio) but different bedding angles is attributed to this equation. The validity of the formulation is verified by comparison with experimental data.

1. Introduction

There are numerous experimental observations showing that the shape of the failure surface for soils is influenced by the microstructural arrangement (or fabric) (e.g., [1–3]). It has long been known that the failure condition is influenced by the microstructural arrangement of the constituent particles. Several expressions for failure criteria have been proposed to include the effect of fabric and its evolution. Baker and Desai [4] proposed the so-called joint isotropic invariants of stress and appropriate anisotropic tensorial entities. Pastor [5], by using this method, proposed a constitutive model to account for fabric anisotropy.

Pietruszczak and Mroz [6] related inherent anisotropy to the microstructural arrangement within the representative volume of material. They used a second-order tensor whose eigenvectors specify the orientation of the axes of the material symmetry. The failure criteria proposed by Pietruszczak and Mroz [6] were formulated in terms of the stress state and a microstructure tensor. Lade [3], by using the method proposed by Pietruszczak and Mroz [6], related the loading directions to the principal directions of the cross-anisotropic microstructure arrangement of the particles.

In order to connect the microscopic character of the granular materials with overall macroscopic anisotropy, various quantities have been proposed; for example, Oda [1], Oda et al. [2], and Oda [7] defined the fabric of anisotropy by using the distribution of the unit contact normals. Mehrabadi et al. [8] defined another microstructural arrangement and connected these parameters to the overall stress and other mechanical characteristics of granular materials. Gao et al. [9] and Gao and Zhao [10] proposed a generalized anisotropic failure criterion through developing an isotropic failure criterion by introducing two variables to account for fabric anisotropy. The first one is the fabric anisotropy that was proposed by Oda and Nakayama [11] and the second one is the joint invariants of the deviatoric stress tensor and the deviatoric fabric tensor to characterize the relative orientation between stress direction and fabric anisotropy. They related the frictional coefficient η^p to the anisotropic variable A. Fu and Dafalias [12] showed that there is a difference between friction angle in the isotropic and anisotropic cases. In the isotropic case, friction angle would be a direction-independent constant, while in the anisotropic case, it is a function of the bedding angle with respect to the shear plane (in the Mohr-Coulomb failure criterion). Fu and Dafalias [13] by using discrete element method (DEM) investigated the effect of fabric on the shear strength of granular materials. They proposed an anisotropic shear failure criterion on the basis of noncoaxiality between the bedding plane orientation and the shear plane. The inherent fabric anisotropy was taken into account by considering the orientation of the bedding plane with respect to the principal stress axes.

The specification of the condition at failure for anisotropic granular soils constitutes an important problem and numerous criteria have been proposed in the past. In this paper, we endeavor to incorporate the effect of inherent and induced anisotropy in the yield surface. The inherent and induced anisotropies are expressed as explicit functions of the bedding angle β and the magnitude of anisotropy α (in the distribution of contact normals). These two elements (inherent and induced anisotropy) are combined, and the Mohr-Coulomb yield surface which is modified to account for the kinematic yield surface [14–16] is developed by including the fabric and its evolution. The equation of the yield surface that is proposed for granular soils is compared with the experimental results from Oda et al. [17]. It shows that the equation is able to capture the shearing behavior of soils with different bedding angles.

2. Definition of Inherent Anisotropy

Inherent anisotropy is attributed to the deposition and orientation of the long axes of particles [1, 2, 7]. Oda et al. [17] and Yoshimine et al. [18] showed that the drained and undrained response of sand and approaching the critical state failure are actually affected by the direction of the principal stress relative to the orientation of the soil sample. Pietruszczak and Mroz [6] included the effect of fabric by the following equation:

$$F = \tau - \eta g(\theta) p_o, \tag{1}$$

where $\tau = J_2^{1/2}$ is the second invariant of the stress tensor, $p_o = \operatorname{tr}\sigma/3$ is first invariant of the stress tensor, $g(\theta)$ is Lode's angle, and η is a constant for isotropic materials and defined by the following equation for anisotropic materials:

$$\eta = \eta_o \left(1 + \Omega_{ij} l_i l_j\right), \tag{2}$$

where η_o is the constant material parameter, Ω_{ij} describes the bias in material microstructure spatial distribution, and l_i and l_j are the loading directions. Lade [3] by using these formulations proposed a failure criterion for anisotropic materials. Wan and Guo [19] accounted for the effect of inherent anisotropy in microlevel analysis by the ratio of projection of major-to-minor principal values of the fabric tensor along the direction of the principal stresses. Li and Dafalias [20, 21] incorporated this effect by the fabric tensor which was proposed by Oda and Nakayama [11]. These two methods used the same basic approach; they used the principal values of the fabric tensor in their formulations. However, micromechanical studies [2, 11] have shown that in the shearing process, the preferred orientation of the particles in a granular mass may undergo only small changes. Its value may well endure after the onset of the critical state; hence, the fabric anisotropy renders the locus of the critical state line. In this paper, $\cos 2(\beta_i - \beta_\circ)$ is used to model the effect of inherent anisotropy. β_i indicates the variation of the long axes of particles with respect to the major principal stress; $\beta_\circ$ is the angle of deposition with respect to the major principal stress. Hence,

$$\left(\frac{\sigma_1}{\sigma_2}\right)_f \propto \cos 2\left(\beta_i - \beta_\circ\right). \tag{3}$$

3. Definition of Stress-Induced Anisotropy

With increasing shear loads, the contact normals tend to concentrate in the direction of the major compressive stress. Contacts are generated in the compressive direction and disrupted in the tensile direction. These disruption and generation of the contact normals are the main causes of the induced anisotropy in the granular materials [2]. In order to include the fabric evolution (or induced anisotropy), a function in which changes of the contact normals are included must be defined. Wan and Guo [19] used the following equation:

$$\dot{F}_{ij} = x\dot{\eta}_{ij}, \tag{4}$$

where $\dot{F}_{ij}$ shows the evolution of fabric anisotropy, x is a constant, and $\dot{\eta}_{ij}$ is the ratio of the shear stress to the confining pressure, or $\eta = (q/p)$. Dafalias and Manzari [22] related the evolution of fabric to the volumetric strain in the dilatancy equation. The evolution of fabric comes to play only after dilation. Based on DEM simulation presented by Fu and Dafalias [12], Li and Dafalias [23] developed an earlier model (yield surface) to account for fabric and its evolution in a new manner by considering the evolution of fabric tensor towards its critical value.

By using Fourier series, Rothenburg and Bathurst [24] showed that the contact normals distribution, $E(n)$, can be presented as follows:

$$E(n) = \left(\frac{1}{2\pi}\right)\left(1 + \alpha\cos 2\left(\theta - \theta_f\right)\right), \tag{5}$$

where α is the magnitude of anisotropy and θ_f is the major principal direction of the fabric tensor. The variations of the parameters α and θ_f represent the evolution of anisotropy in the granular mass. Experimental data shows that the shear strength of the granular material is a function of the magnitude of α and θ_f [1, 17, 25]. The following equation is used to consider the effect of the induced anisotropy:

$$\left(\frac{\sigma_1}{\sigma_2}\right)_f \propto \left(1 + \left(\frac{1}{2}\right)\alpha\cos 2\left(\theta_\sigma - \theta_f\right)\right). \tag{6}$$

As previously mentioned, the shear strength in the granular medium is a function of inherent and induced anisotropy. The equation can predict the difference between samples due to the fabric which is a combination of the inherent and induced anisotropy as follows [26]:

$$\left(\frac{\sigma_1}{\sigma_2}\right)_f \propto \left[\left(1 + \left(\frac{1}{2}\right)\alpha\cos 2\left(\theta - \theta_f\right)\right)\cos 2\left(\beta_i - \beta_\circ\right)\right]. \tag{7}$$

Another parameter that must be added to the above relation is the rolling strength of the granular material. Oda et al. [25] and Bardet [27] showed the importance of the rolling strength of the particles, especially in a 2D case. This effect is incorporated in the following form [26]:

$$\left(\frac{\sigma_1}{\sigma_2}\right)_f \propto \left[\left(1+\left(\frac{1}{2}\right)\alpha\cos 2\left(\theta-\theta_f\right)\right)\right.$$
$$\left.\times\cos 2\left(\beta_i-\beta_\circ\right) m\exp\left(\cos 2\left(\beta_i-\beta_\circ\right)\right)\right], \tag{8}$$

where m is a constant that depends on the interparticle friction angle ϕ_μ and the shape of the particles. When the samples with equal densities are subjected to the shear loads, the difference in the shear strength due to the fabric can be attributed to (8).

4. Verification of (8) with the Experimental Data

In order to show the ability of (8) to represent the effect of the fabric on the shear strength, the predictions are compared with the experimental tests presented by Konishi et al. [25]. They conducted an experimental study on biaxial deformation of two-dimensional assemblies of rod-shaped photoelastic particle with oval cross section. The samples were confined laterally by a constant force of 0.45 kgf and then compressed vertically by incremental displacement. Two types of particle shapes were used; one was $r_1/r_2 = 1.1$ and the other was $r_1/r_2 = 1.4$, in which r_1 and r_2 are the major and minor axes of cross section respectively. To consider the influence of friction, two sets of experiments were performed on these two particle shapes, one with nonlubricated particles of average friction angle of 52° and the other with particles which had been lubricated with an average friction angle of 26°. The magnitude of the degree of anisotropy α and the major direction of the fabric θ_f are calculated by the following equations:

$$A=\int_0^{2\pi} E(\theta)\sin 2\theta\, d\theta, \tag{9}$$

$$B=\int_0^{2\pi} E(\theta)\cos 2\theta\, d\theta, \tag{10}$$

$$\theta_f=\left(\frac{1}{2}\right)\arctan\left(\frac{A}{B}\right). \tag{11}$$

To show the ability of (8), the proportion of fabric with the shear strength variations is shown in Figure 1. The differences in the shear strength ratio at failure for different bedding angles are attributed to the differences in the developed anisotropic parameters. In other words, the combination of anisotropic parameters (for inherent and induced anisotropy) is proportional to the shear strength. The variation of right-hand side of (8) is proportional to the variation of shear strength ratio for different bedding angles. The right-hand side of (8) is shown by fabric anisotropy in Figure 1. The effect of bedding angle on stress ratio at failure for the different interparticle friction angle ϕ_μ is also shown in Figure 1.

5. Incorporation of the Fabric and Its Evolution in the Yield Surface

Muir Wood et al. [14] proposed the kinematic version of the Mohr-Coulomb yield surface as follows:

$$f=q-\eta_y^f p_o, \tag{12}$$

where q is the deviatoric stress and η_y^f is the size of the yield surface. Muir Wood et al. [14] and Muir Wood [16] assumed that the soil is a distortional hardening material; hence, the current yield surface η_y^f is a function of the plastic distortional strain ε_q^p, and, hence,

$$\eta_y^f=\frac{\varepsilon_q^p}{c+\varepsilon_q^p}\eta^p, \tag{13}$$

where η^p is a limit value of stress ratio which is equal to M at the critical state, $\eta^p=M=q/p$; c is a soil constant.

Wood et al. [14] and Gajo and Muir Wood [15] developed the above equation to include the effect of state parameter $\psi = e-e_{\mathrm{cr}}$, in which e is the void ratio and e_{cr} is the magnitude of the void ratio on the critical-state line, as follows:

$$\eta_y^f=\frac{\varepsilon_q^p}{c+\varepsilon_q^p}\left(M-k\psi\right), \tag{14}$$

where k is a constant.

Li and Dafalias [20] modified the effect of state parameter ψ to account for a wide range of stress and void ratio as follows:

$$\eta^p=M\exp\left(-n_b\psi\right), \tag{15}$$

where n_b is a material constant. Equation (7) can be modified as follows:

$$\eta_y^f=\frac{\varepsilon_q^p}{c+\varepsilon_q^p}M\exp\left(-n_b\psi\right). \tag{16}$$

In the previous section, the shear strength was shown to be a function of inherent and induced anisotropy (see (8)). Thus, the effect of inherent and induced fabric anisotropy for triaxial case can be expressed as follows:

$$\eta_y^f=\frac{\varepsilon_q^p}{c+\varepsilon_q^p}\left(1+\left(\frac{1}{2}\right)\alpha\cos 2\left(\theta_f-\theta_\sigma\right)\right)$$
$$\times\cos 2\left(\beta_i-\beta_\circ\right) M\exp\left(-n_b\psi\right). \tag{17}$$

The magnitudes of α and θ_f approach a constant value in large shear strain [26, 28, 29]. The parameter $\cos 2(\beta_i-\beta_\circ)$ is easily obtained by back calculation but as a rough estimation, its value is close to the magnitude of the bedding angle $\cos\delta$ (for bedding angle δ between 15° and 45°).

Equation (10) can be shown in the following form for multiaxial direction (or in the general form):

$$f=\tau-\eta_y^f g(\theta)\, p_o. \tag{18}$$

It is similar to the equation proposed by Pietruszczak and Mroz [6] and Lade [3] but in this formulation, another function is used for fabric and its evolution.

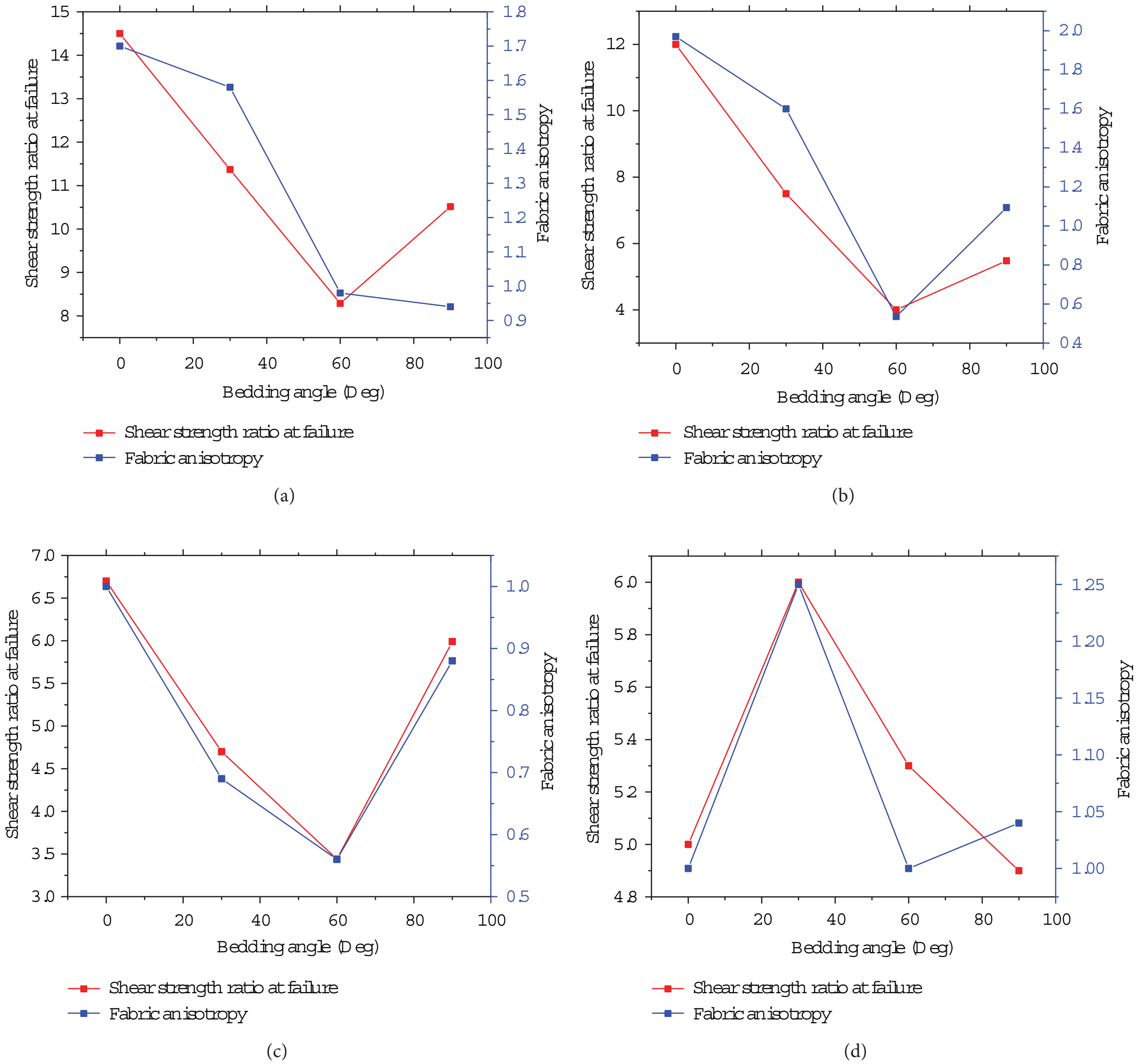

FIGURE 1: Samples with $\phi_\mu = 52^\circ$ and $r_1/r_2 = 1.1$ (a), $\phi_\mu = 26^\circ$ and $r_1/r_2 = 1.1$ (b), $\phi_\mu = 52^\circ$ and $r_1/r_2 = 1.4$ (c), and $\phi_\mu = 26^\circ$ and $r_1/r_2 = 1.4$ (d).

6. Fabric Evolution

The parameters α and θ_f show the status of the fabric and its evolution. These parameters have a great influence on the behavior of the dilatancy equation. Shaverdi et al. [29] proposed an equation which can predict the magnitude of α and θ_f in the presence of the noncoaxiality between stress and fabric. This equation is obtained from the microlevel analysis. To calculate the α parameter, the magnitude of the shear to normal stress ratio on the spatially mobilized plane (SMP) must be determined. In the triaxial case, for example, τ/p may be obtained from the following equation [30]:

$$\frac{\tau}{p} = \sqrt{\frac{\sigma_1}{\sigma_3}} - \sqrt{\frac{\sigma_3}{\sigma_1}}. \tag{19}$$

The parameters α and θ_f may be obtained from the following equations in the presence of noncoaxiality [29]:

$$\alpha = \frac{(\tau/p)\cos\phi_{\mu\text{mob}} - \sin\phi_{\mu\text{mob}}}{\sin\left(2\theta_f + \phi_{\mu\text{mob}}\right) - \left((\tau/p)\cos\left(2\theta_f + \phi_{\mu\text{mob}}\right)\right)}, \tag{20}$$

$$\dot{\theta}_f = \dot{\theta}_\sigma + \left(\frac{1}{2}\right) \cdot d\eta \cdot \left(\theta_\sigma - \theta_f\right), \tag{21}$$

where the dot over θ shows the variation. The most important parameter in the above equation is the interparticle mobilized

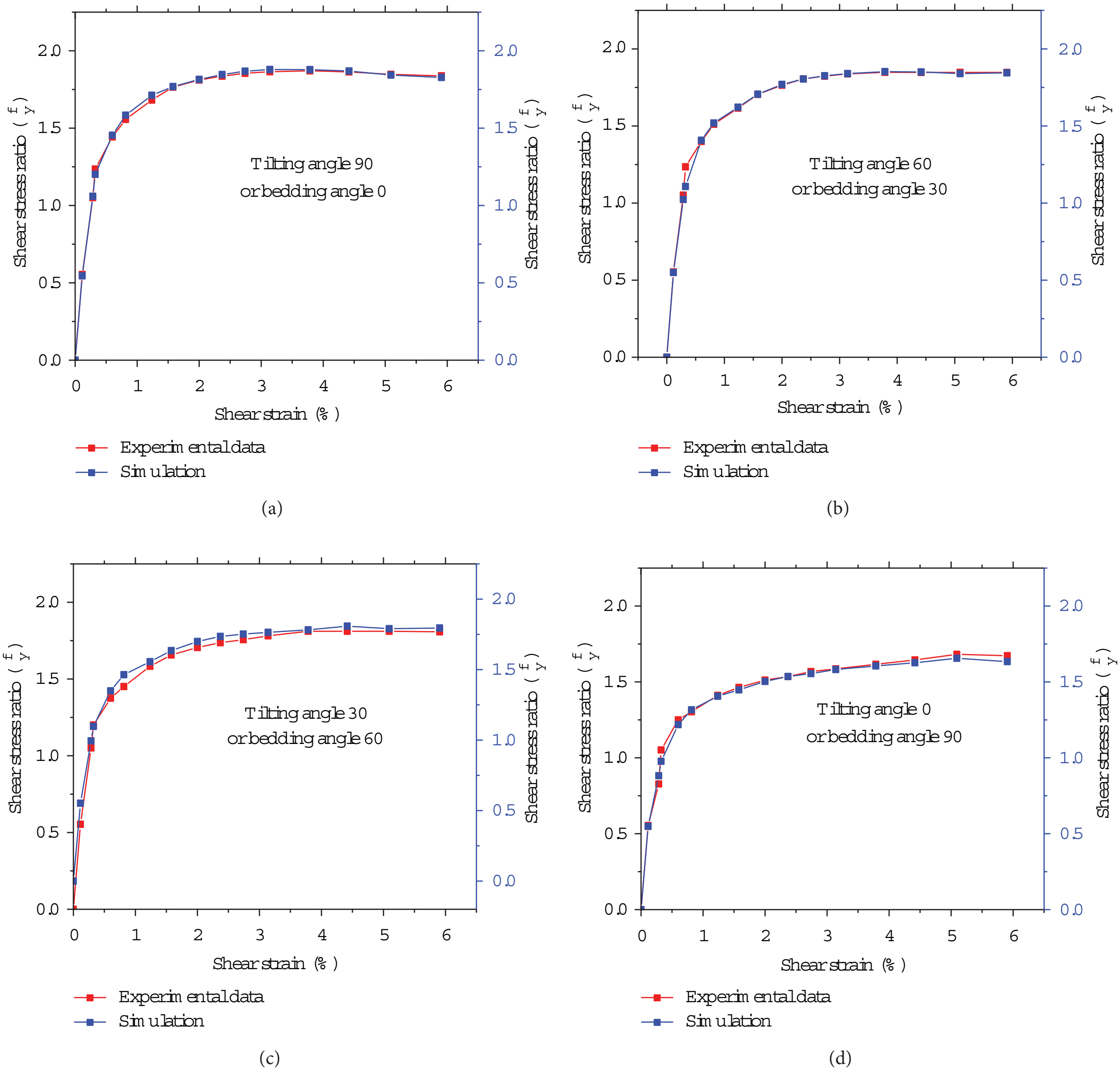

Figure 2: Comparison between experimental data and simulation by using (16) for the confining pressure 0.5 kg/cm^2.

friction angle, $\phi_{\mu\text{mob}}$. This parameter is obtained from the following equation:

$$\tan^{-1}\left(\frac{\tau}{p}\right) = \frac{\theta_\sigma - \theta_f}{z} + \lambda\left(\frac{\dot{\varepsilon}_v}{\dot{\varepsilon}_q}\right) + \phi_{\mu\text{mob}}, \tag{22}$$

where z and λ are material constants. Kuhn [28] and Shaverdi et al. [29] showed that the variation of α with the shear strain is similar to the variation of shear to normal stress ratio with shear strain.

7. Verification of (16) with Experimental Data

Oda et al. [17] conducted some experimental tests on Toyoura sand with an initial void ratio 0.67-0.68 and the confining pressures 0.5 kg/cm^2 and 2 kg/cm^2 to study the effect of bedding angle with tilting angles $\delta = 0^\circ, 30^\circ, 60^\circ$, and 90°. For better modeling, the constant c for the plastic shear strain less than 1% must be modified as follows:

$$c = 0.001 + 0.001\left\langle 1 - m'\varepsilon_q^p\right\rangle, \tag{23}$$

where m' is a constant which depends on confining pressure and $\langle\cdots\rangle$ stands for the positive values only. In this simulation, $m' = 1$ is taken into account for the confining pressure 0.5 kg/cm^2, and $m' = 6.5$ for the confining pressure 2.0 kg/cm^2.

Equation (17) can model the different behavior of the granular soils with the same confining pressure and initial void ratio (density) in which the only difference is due to the fabric and its evolution, as shown in Figures 2 and 3.

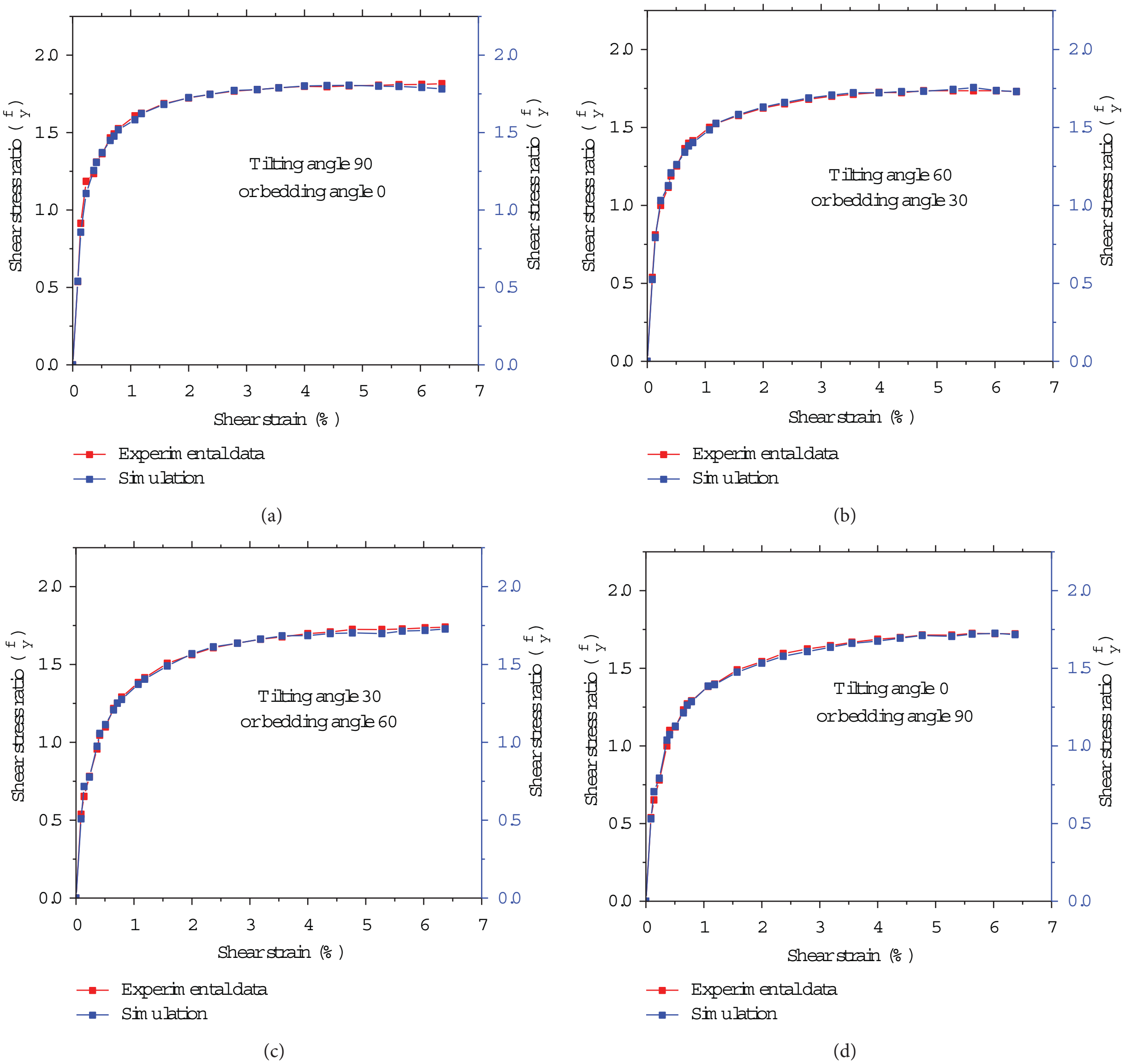

FIGURE 3: Comparison between experimental data and simulation by using (16) for the confining pressure 2.0 kg/cm^2.

8. Conclusion

An equation was proposed to include the effect of inherent and induced anisotropy. This relation was obtained by combining the effect of inherent and induced anisotropy. Rolling resistance is also included in this equation. The differences between the samples due to inherent and induced anisotropy were well captured by applying (8). Verifying the experimental data shows that this equation can predict the ratio of the shear strength at failure of granular materials in the presence of inherent anisotropy as good as possible. The effect of inherent anisotropy was incorporated by a single term $\cos 2(\beta_i - \beta_\circ)$. Induced anisotropy was also included by a simple term $(1 + (1/2)\alpha \cos 2(\theta_f - \theta_\sigma))$ in which α and θ_f can be easily calculated and obtained. The extended Mohr-Coulomb was developed to incorporate the effect of fabric and its evolution. Verification with the experimental tests demonstrated the validity of this formulation.

References

[1] M. Oda, "Initial fabrics and their relations to mechanical properties of granular materials," *Soils and Foundations*, vol. 12, no. 1, pp. 17–36, 1972.

[2] M. Oda, S. Nemat-Nasser, and J. Konishi, "Stress-induced anisotropy in granular mass," *Soils and Foundations*, vol. 25, no. 3, pp. 85–97, 1985.

[3] P. V. Lade, "Failure criterion for cross-anisotropic soils," *Journal of Geotechnical and Geoenvironmental Engineering*, vol. 134, no. 1, pp. 117–124, 2008.

[4] R. Baker and C. S. Desai, "Induced anisotropy during plastic straining," *International Journal for Numerical and Analytical Methods in Geomechanics*, vol. 8, no. 2, pp. 167–185, 1984.

[5] M. Pastor, "Modelling of anisotropic sand behaviour," *Computers and Geotechnics*, vol. 11, no. 3, pp. 173–208, 1991.

[6] S. Pietruszczak and Z. Mroz, "Formulation of anisotropic failure criteria incorporating a microstructure tensor," *Computers and Geotechnics*, vol. 26, no. 2, pp. 105–112, 2000.

[7] M. Oda, "Fabric tensor and its geometrical meaning," in *Mechanics of Granular Materials: An Introduction*, M. Oda and K. Iwashita, Eds., pp. 19–33, Balkema, Rotterdam, The Netherlands, 1999.

[8] M. Mehrabadi, S. Nemat-Nasser, and M. Oda, "On statistical description of stress and fabric in granular materials," *International Journal For Numerical and Analytical Methods in Geomechanics*, vol. 6, no. 1, pp. 95–108, 1982.

[9] Z. Gao, J. Zhao, and Y. Yao, "A generalized anisotropic failure criterion for geomaterials," *International Journal of Solids and Structures*, vol. 47, no. 22-23, pp. 3166–3185, 2010.

[10] Z. W. Gao and J. D. Zhao, "Efficient approach to characterize strength anisotropy in soils," *Journal of Engineering Mechanics*, vol. 138, no. 12, pp. 1447–1456, 2012.

[11] M. Oda and H. Nakayama, "Yield function for soil with anisotropic fabric," *Journal of Engineering Mechanics*, vol. 115, no. 1, pp. 89–104, 1989.

[12] P. Fu and Y. F. Dafalias, "Fabric evolution within shear bands of granular materials and its relation to critical state theory," *International Journal for Numerical and Analytical Methods in Geomechanics*, vol. 35, no. 18, pp. 1918–1948, 2011.

[13] P. Fu and Y. F. Dafalias, "Study of anisotropic shear strength of granular materials using DEM simulation," *International Journal for Numerical and Analytical Methods in Geomechanics*, vol. 35, no. 10, pp. 1098–1126, 2011.

[14] D. M. Wood, K. Belkheir, and D. F. Liu, "Strain softening and state parameter for sand modelling," *Geotechnique*, vol. 44, no. 2, pp. 335–339, 1994.

[15] A. Gajo and D. Muir Wood, "Severn-Trent sand: a kinematic-hardening constitutive model: the $q - p$ formulation," *Geotechnique*, vol. 49, no. 5, pp. 595–614, 1999.

[16] D. Muir Wood, *Geotechnical Modelling*, Taylor and Francis, 2004.

[17] M. Oda, I. Koishikawa, and T. Higuchi, "Experimental study of anisotropic shear strength of sand by plane strain test," *Soils and Foundations*, vol. 18, no. 1, pp. 25–38, 1978.

[18] M. Yoshimine, K. Ishihara, and W. Vargas, "Effects of principal stress direction and intermediate principal stress on undrained shear behavior of sand," *Soils and Foundations*, vol. 38, no. 3, pp. 179–188, 1998.

[19] R. G. Wan and P. J. Guo, "Drained cyclic behavior of sand with fabric dependence," *Journal of Engineering Mechanics*, vol. 127, no. 11, pp. 1106–1116, 2001.

[20] X. S. Li and Y. F. Dafalias, "Constitutive modeling of inherently anisotropic sand behavior," *Journal of Geotechnical and Geoenvironmental Engineering*, vol. 128, no. 10, pp. 868–880, 2002.

[21] X. S. Li and Y. F. Dafalias, "A constitutive, framework for anisotropic sand including non-proportional loading," *Geotechnique*, vol. 54, no. 1, pp. 41–55, 2004.

[22] Y. F. Dafalias and M. T. Manzari, "Simple plasticity sand model accounting for fabric change effects," *Journal of Engineering Mechanics*, vol. 130, no. 6, pp. 622–634, 2004.

[23] X. S. Li and Y. F. Dafalias, "Anisotropic critical state theory: role of fabric," *Journal of Engineering Mechanics*, vol. 138, no. 3, pp. 263–275, 2012.

[24] L. Rothenburg and R. J. Bathurst, "Analytical study of induced anisotropy in idealized granular materials," *Geotechnique*, vol. 39, no. 4, pp. 601–614, 1989.

[25] J. Konishi, M. Oda, and S. Nemat-Nasser, "Inherent anisotropy and shear strength of assembly of oval cross-section rods," in *Proceedings of the IUTAM Symposium on deformation and failure of granular materials*, Delft, The Netherland, 1982.

[26] H. Shaverdi, M. R. Taha, and F. Kalantary, "Effect of fabric on the shear strength of granular materials in biaxial compression," in *Proceedings of the 7th International Conference on Micromechanics of Granular Media*, pp. 615–618, Sydney, Australia, July 2013.

[27] J. P. Bardet, "Observations on the effects of particle rotations on the failure of idealized granular materials," *Mechanics of Materials*, vol. 18, no. 2, pp. 159–182, 1994.

[28] M. R. Kuhn, "Micro-mechanics of fabric and failure in granular materials," *Mechanics of Materials*, vol. 42, no. 9, pp. 827–840, 2010.

[29] H. Shaverdi, M. R. Taha, and F. Kalantary, "Evolution of fabric in the shearing process based on micromechanics," in *Constitutive Modeling of Geomaterials*, Q. Yang, J. Zhang, H. Zheng, and Y. Yao, Eds., pp. 469–475, Springer, Berlin, Germany, 2013.

[30] H. Matsuoka and H. Geka, "A stress-strain model for granular materials considering mechanism of fabric change," *Soils and Foundations*, vol. 23, no. 2, pp. 83–97, 1983.

Hindawi Publishing Corporation
Journal of Applied Mathematics
Volume 2013, Article ID 537185, 15 pages
http://dx.doi.org/10.1155/2013/537185

Research Article

A Unified Elastoplastic Model of Unsaturated Soils Considering Capillary Hysteresis

Tiantian Ma,[1] Changfu Wei,[1,2] Pan Chen,[1] Huihui Tian,[1] and De'an Sun[3]

[1] *State Key Laboratory of Geomechanics and Geotechnical Engineering, Institute of Rock and Soil Mechanics, Chinese Academy of Sciences, Xiaohongshan, Wuchang, Wuhan, Hubei 430071, China*
[2] *College of Civil and Architectural Engineering, Guilin University of Technology, Guilin, Guangxi 541004, China*
[3] *Department of Civil Engineering, Shanghai University, Shanghai 200072, China*

Correspondence should be addressed to Changfu Wei; cfwei@whrsm.ac.cn

Received 14 May 2013; Accepted 26 July 2013

Academic Editor: Pengcheng Fu

Unlike its saturated counterparts, the mechanical behavior of an unsaturated soil depends not only upon its stress history but also upon its hydraulic history. In this paper, a soil-water characteristic relationship which is capable of describing the effect of capillary hysteresis is introduced to characterize the influence of hydraulic history on the skeletal deformation. The capillary hysteresis is viewed as a phenomenon associated with the internal structural rearrangements in unsaturated soils, which can be characterized by using a set of internal state variables. It is shown that both capillary hysteresis and plastic deformation can be consistently addressed in a unified theoretical framework. Within this context, a constitutive model of unsaturated soils is developed by generalizing the modified Cam-Clay model. A hardening function is introduced, in which both the matric suction and the degree of saturation are explicitly included as hardening variables, so that the effect of hydraulic history on the mechanical response can be properly addressed. The proposed model is capable of capturing the main features of the unsaturated soil behavior. The new model has a hierarchical structure, and, depending upon application, it can describe the stress-strain relation and the soil-water characteristics in a coupled or uncoupled manner.

1. Introduction

Occurrence of geohazards is usually related to the failure of unsaturated soils induced by intensive precipitation or variation of the underground water table. Traditionally, in the analysis of such problems, the mechanical and hydraulic properties of unsaturated soils are considered in an uncoupled or partially coupled manner. However, sufficient experimental evidence [1, 2] shows that there exists complicated coupling effect between deformation and seepage processes in unsaturated soils. The seepage process can influence the mechanical properties of soils; for instance, repeated drying-wetting cycles can change the soil strength [3]; skeletal deformation can change the water-retention characteristics of unsaturated soils, which in turn influences the seepage process [3]. Hence, in analyzing unsaturated soil problems, it is crucial to properly characterize the coupling effect of seepage, deformation, and failure in unsaturated soils with arbitrary variation of water content. To address such an issue, a constitutive model must be developed which can effectively describe both the stress-strain relation and soil-water characteristics in a unified and coupled manner.

The first milestone for comprehensive unsaturated soil modeling should be attributed to Alonso et al. [4], who have developed the Barcelona Basic Model (BBM) by extending the modified Cam-Clay model of saturated soils. In the BBM model, two independent stress variables are adopted, and the so-called loading-collapse (LC) yield curve is introduced to express the hardening effect of matric suction on the preconsolidation pressure. In addition, another yield surface, namely, SI, is employed to describe the plastic yielding of the degree of saturation. The BBM model was experimentally validated by Wheeler and Sivakumar [5], based on a series of isotropic compression and triaxial tests on unsaturated soils under suction-controlled conditions. Although the BBM model can capture the main features of unsaturated soils, the mechanical and hydraulic behaviors are addressed in an uncoupled way. Wheeler and Sivakumar [5] have pointed that uncoupled models cannot effectively simulate the variation of the degree of saturation during shearing under constant matric suction, so that they are incapable of describing the mechanical behavior and water retention characteristics of unsaturated soils under undrained conditions.

To resolve these issues, Nuth et al. [6], Sun and Li [7], and Sheng et al. [8] introduced a Bishop's type effective stress instead of net stress as an independent stress variable. These models adopt LC yield curve to describe the wetting-induced collapse phenomenon under various stress states of unsaturated soils. D'Onza et al. [9] presented research work undertaken by seven universities to benchmark different approaches to modeling the behavior of unsaturated soils. Such models consider the effect of matric suction on the yield pressure only and ignore the effect of the degree of saturation.

Based on experimental results, Wheeler et al. [10] have concluded that the degree of saturation has a significant influence on the stress-strain relation. They have suggested that cyclic soil-water characteristic function should be introduced into the elastoplastic constitutive model of unsaturated soils, to describe the influence of the nonmonotonic variation in water content on the skeletal deformation.

An LC curve is one of the key components in the BBM-style models [1, 4, 5, 11, 12], reflecting the hardening effect of matric suction on unsaturated soils. It has been recognized [10] that the models with an LC yield surface have the following limitations. (1) They are insufficient in describing the soil response when the water content varies in a non-monotonic way. In the vicinity of the transition region, when the matric suction is lower than the air entry value, the soil is fully saturated during a drying process, whereas the soil shows apparent unsaturated behavior during wetting. This phenomenon cannot be described by using an LC curve; (2) LC curve predicts the increase of the yield stress with matric suction, without considering the influence of the degree of saturation; (3) at the same matric suction, the mechanical properties of an unsaturated soil can be different due to the different hydraulic histories which the soil has experienced.

The preconsolidation pressure is a key variable, by which the hardening effect of capillarity can be taken into account in an unsaturated soil constitutive model [13]. Two approaches have been proposed to considering the hardening effect of capillarity. Khalili et al. [14] and Tamagnini [15] proposed a hardening function in which the preconsolidation pressure is multiplied by a function of matric suction. On the other hand, Jommi [16] and Li [17] believed that the matric suction should have an additive effect on the strain hardening, and thus the hardening effects of the matric suction and the volumetric deformation should be considered in an additive way. Noticeably, neither of these two approaches considers the contribution of the matric suction and the degree of saturation simultaneously, and thus neither one can effectively address the effect of hydraulic histories.

One of major differences between a saturated soil and its unsaturated counterpart resides in the fact that the mechanical behavior of the unsaturated soil depends not only upon its stress history but also upon its hydraulic history. The hydraulic history can be very well addressed by using a soil-water characteristic relationship, which is capable of describing the capillary hysteresis of the unsaturated soil under an arbitrary wetting/drying path [18, 19]. There are several kinds of hysteretic models for the soil-water characteristics, including empirical models, the domain model [20], the rational extrapolated model [21], and the bounding surface model [19], respectively. Recently, Wei and Dewoolkar [18] identified a link between the capillary hysteresis and an intrinsic dissipation process in unsaturated soil, and developed an internal-variable model of capillary hysteresis, allowing the capillary hysteresis and skeletal deformation to be simulated in a unified framework of elastoplastic theory. Although several constitutive models of unsaturated soils have addressed the effect of capillary hysteresis to a certain degree, they seldom consider the influence of deformation on the water retention characteristic. Miao et al. [22] studied the influence of soil density on the soil-water characteristic curve, suggesting that skeletal compression has significant effect on the soil-water characteristics. Gallipoli et al. [23] have performed experiments and developed the relationship between volumetric strain and the parameters of van Genuchten model [24].

Li [25] has discussed the work-energy-dissipation relations for unsaturated soils, based on the principles of thermodynamics. In his paper, Li [25] has clearly displayed the coupling effect among three phases and developed an elastoplastic framework for coupling the mechanical and hydraulic behavior of unsaturated soils, under which a constitutive model was developed under the triaxial stress state [17]. This framework provides a solid base for developing the constitutive model of unsaturated soils.

In this paper, a new hardening function is proposed, in which the matric suction and the degree of saturation as well as plastic volumetric strain are simultaneously introduced to represent the hardening effect. Based on Li's framework [25], a constitutive model is developed, which can simulate plastic deformation and capillary hysteresis in a coupled and hierarchical manner. If the coupled effect of skeletal deformation and capillary hysteresis is ignored, the new model degenerates into two independent models of unsaturated soils, namely, the stress-strain relationship and the soil-water characteristic curve. When the deformation of soil is excluded, the model ends up with a model for the soil-water characteristics. When the soil becomes fully saturated, the new model can transit smoothly to the modified Cam-Clay (MCC) model.

2. Theoretical Formulation

2.1. Stress State Variables. The displacement work of unsaturated soil can be expressed as [26]

$$W = \left\{\sigma_{ij} - \left[S_r u_w + \left(1 - S_r\right) u_a\right] \delta_{ij}\right\} \dot{\varepsilon}_{ij} - n s_c \dot{S}_r + n\left(1 - S_r\right) u_a \frac{\dot{\rho}_a}{\rho_a}, \tag{1}$$

where σ_{ij} is the total stress tensor; S_r is the degree of saturation; u_a and u_w are the pore air pressure and pore water

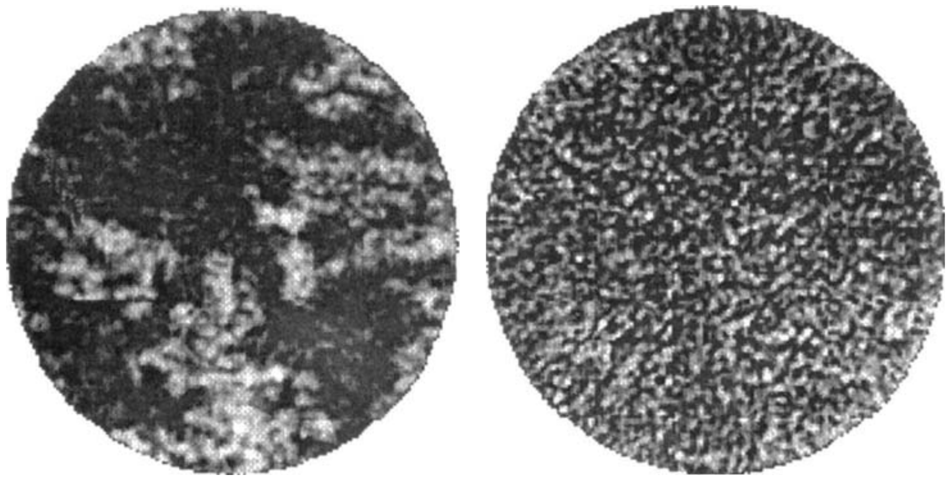

(a)

(b)

Figure 1: CT images of moisture distribution in the unsaturated Estaillades limestone at saturation of 92%: (a) prepared by drying; (b) prepared by wetting (after Cadoret et al. (1998) [31]).

pressure, respectively; δ_{ij} is the unit tensor; s_c is the matric suction, that is, $s_c = u_a - u_w$; ε_{ij} is the infinitesimal strain tensor; n is the porosity; ρ_a is the density of pore air. If the work of air compression is neglected, the third item in the right-hand side disappears, and

$$W = \sigma'_{ij}\dot{\varepsilon}_{ij} - ns_c\dot{S}_r, \tag{2}$$

where σ'_{ij} is the *average skeleton stress* tensor [16], defined by

$$\sigma'_{ij} = \left(\sigma_{ij} - u_a\delta_{ij}\right) + S_r\left(u_a - u_w\right)\delta_{ij}. \tag{3}$$

At the triaxial stress state,

$$p' = \frac{\sigma'_{ii}}{3} = \left(p - u_a\right) + S_r\left(u_a - u_w\right), \qquad q = \sigma'_1 - \sigma'_3, \tag{4}$$

where p' and q are the mean and deviatoric skeleton stresses, respectively; p is the mean total stress. σ'_{ij} is defined by (3) and simply the Bishop's equation for the "effective" stress of unsaturated soils [27], with parameter χ being equal to the degree of saturation S_r.

According to (2), Houlsby [26] proposed that the constitutive behavior of unsaturated soils should be described using stress state variables (σ'_{ij}, ns_c), which are work conjugated to strain variables (ε_{ij}, S_r). Although this proposition is widely introduced in modeling unsaturated soil behavior, it has been recently criticized for choosing parameter χ as the degree of saturation S_r, for example, [14, 28–30]. Based on the equivalency of shear strength (Mohr-Coulomb's type), Khalili and Zargarbashi [28] performed direct experiments to measure parameter χ, confirming that χ is not equal to S_r and depends upon the hydraulic history of the soil.

To reconcile the above-mentioned inconsistency and considering the difficulty and uncertainty in measuring parameter χ, we propose herein that (1), in a general framework for modeling the constitutive behavior of unsaturated soils, the stress variables must be properly conjugated to the strain variables; that is, a robust constitutive model must be thermodynamically consistent, and (2) the dependence of "effective" stress parameter on hydraulic history is constitutive in nature, and the hydraulic hysteretic effect can be simulated in a general constitutive framework. Hence, we suggest that stress variables (σ'_{ij}, ns_c) should be adopted in the constitutive modeling of unsaturated soils. Because porosity n is practically independent of the hydraulic path which the soil experienced, for convenience, s_c instead of ns_c will be used in describing the hydraulic history and the effect of unsaturation. In the following, we will prove that the effect of hydraulic history can indeed be effectively addressed in a constitutive model, which uses (σ'_{ij}, s_c) as stress state variables.

2.2. Hydraulic-History Dependence of Unsaturated Soils. One of salient features of unsaturated soil behavior is its dependence on the hydraulic history. At the same degree of saturation, the moisture distribution in the pore space of a soil can be different, depending upon the wetting/drying history that the soil experienced. Figure 1 illustrates the CT images of the moisture distributions in two limestone samples with the same matrix and the same saturation [31]. It can be seen that the moisture distributions in the two samples are significantly different, and the moisture distribution is more uniform in the sample with a wetting path than that in the sample with a drying path. Remarkably, the nonuniformity of moisture distribution can be induced by the hydraulic history even in a soil with apparently homogeneous solid matrix [32]. Therefore, local heterogeneity (or local structures) can be created in an unsaturated soil merely by its wetting/drying history.

As a consequence, at the same saturation or matric suction, the mechanical response of an unsaturated soil can be different, depending upon the wetting/drying history of the soil. Indeed, it has been very well recognized in the community of geophysics [36–38] that the phase velocity of the first compression wave in a partially saturated geomaterial depends strongly upon its hydraulic history, implying that the stiffness of the material depends upon its wetting/drying history. Generally, at the same saturation, a geomaterial with a drying history is stiffer than that with a wetting history.

We suggest that the phenomenon of capillary hysteresis in unsaturated soils can be tightly related to the local heterogeneity of moisture distribution (i.e., local structures). At the same saturation, the matric suction could be different if the moisture distribution pattern in the pore space is different. Hence, capillary hysteresis can be viewed as a process of local structural rearrangements related to the change of moisture distribution in unsaturated soils.

As such, the role of a soil-water characteristic curve (SWCC) in modeling an unsaturated soil is two-folded: on the one hand, the SWCC describes the capillary hysteresis of the soil during wetting/drying cycles, and, on the other hand, it represents the effect of hydraulic history on the skeletal deformation, if the SWCC can be properly implemented in the stress-strain relationship of the soil.

2.3. Coupling of Dissipative Processes. In modeling the constitutive behavior of unsaturated soils, two coupled irreversible processes (or phenomena) have to be properly addressed, namely, plastic skeletal deformation and capillary hysteresis. Based on the internal-variable theory of plasticity, such irreversible processes are associated with the rearrangements of internal structures in unsaturated soils, which can be characterized by a series of internal state variables (e.g., [18, 39]). Li [25] proposed that the energy dissipation associated with plastic deformation and capillary hysteresis in an unsaturated soil can be expressed as

$$\zeta_i \delta\xi_i = \zeta_i^s \delta\xi_i^s + \zeta_i^f \delta\xi_i^f, \tag{5}$$

where ξ_i ($i = 1, 2, \ldots, N$) is a set of internal state variables, used to characterize the pattern of the internal structures in the soils; ζ_i is the thermodynamic forces conjugated with ξ_i; $\delta\xi_i$ is the evolution of an internal variable. It is clear from (5) that the total dissipation is additively decomposed into two parts, $\zeta_i^s \delta\xi_i^s$ and $\zeta_i^f \delta\xi_i^f$, which represent the incremental dissipations in the soil skeleton and the pore fluids, respectively. $\delta\xi_i^\alpha$ ($\alpha = s, f$) represents the variation of the internal variables of α-phase; ζ_i^α is the thermodynamic force conjugated with ξ_i^α and is a function of state variables and structural variation history. Both ζ_i^α and $\delta\xi_i^\alpha$ are related to the pattern of internal structural rearrangements.

The structural rearrangements of unsaturated soils can be symbolically expressed as [25]

$$H = H\left(H_s, H_f\right), \tag{6}$$

where H_s and H_f represent the patterns of the structural rearrangements associated with plastic deformation in the solid skeleton and capillary hysteresis in the pore fluid, respectively. To account for the interaction between these two dissipation processes, H_s and H_f are further expressed as

$$H_s = H_s\left[H_s', H_s''\left(H_s', s_c, S_r\right)\right], \tag{7a}$$

$$H_f = H_f\left[H_f', H_f''\left(H_f', \boldsymbol{\sigma}', \boldsymbol{\varepsilon}\right)\right], \tag{7b}$$

where H_α' and H_α'' ($\alpha = s, f$) denote the intrinsic structural rearrangement and its interactive counterpart of phase α, respectively. Clearly, H_α'' accounts for the coupling effect. Particularly, H_s'' (H_s', s_c, S_r) represents the effect of hydraulic path on the pattern of the structural rearrangements in the solid skeleton, which implies that the extent that the hydraulic path influences the skeletal plastic deformation depends upon the intrinsic structural rearrangements of the skeleton. Similarly, H_f'' ($H_f', \boldsymbol{\sigma}', \boldsymbol{\varepsilon}$) denotes the influence of skeletal deformation on the dissipation related to capillary hysteresis in fluid phase, and the extent of the influence depends upon the intrinsic structural rearrangements, that is, the distribution pattern of the moisture in pores, of the pore water.

Clearly, the mechanical and water retention behaviors can be described in a unified theoretical framework. In this paper, an elastoplastic constitutive model of unsaturated soils coupling skeletal deformation and capillary hysteresis is developed based on such a framework.

2.4. Yielding and Hardening. The stress-strain relationship is developed by generalizing the modified Cam-Clay model [40], in which the yield function is given by

$$f = q^2 + M^2 p'\left(p' - p_c\right), \tag{8}$$

where M is the slope of critical state line; p_c is the preconsolidation pressure. At full saturation, p_c is a function of plastic volumetric strain only; that is, $p_c = p_{c_0}(\varepsilon_v^p)$. According to the discussions in Section 2.3, under partially saturated conditions, p_c depends upon matric suction and the degree of saturation as well as the plastic volumetric strain. It is suggested herein that, in general, one can assume

$$p_c = p_{c_0}\left(\varepsilon_v^p\right) h\left(\varepsilon_v^p, S_r, s_c\right), \tag{9}$$

where h is a correction function, which accounts for the hardening effect of unsaturation. As discussed in the previous section, h is assumed as a function of s_c and S_r as well as ε_v^p.

To derive an explicit expression for h, one first notes that (1), when the soil is fully saturated, the effect of capillarity on the hardening is vanishing; that is, $h = 1.0$ when $S_r = 100\%$; (2) when the degree of saturation approaches its residual value S_r^{irr}, the water phase becomes discontinuous and occurs only as meniscus water rings at interparticle contacts or as thin film (contractile skin) surrounding the soil particles [41, 42]. In this case, the effect of the degree of saturation on the hardening becomes trivial, and the effect of matric suction approaches to a stable value. In addition, with the increase of plastic volumetric strain, the soil tends to be stiffer, and effect of unsaturation on hardening wanes.

As discussed in Section 2.2, the hardening effect of unsaturation depends upon the hydraulic history that

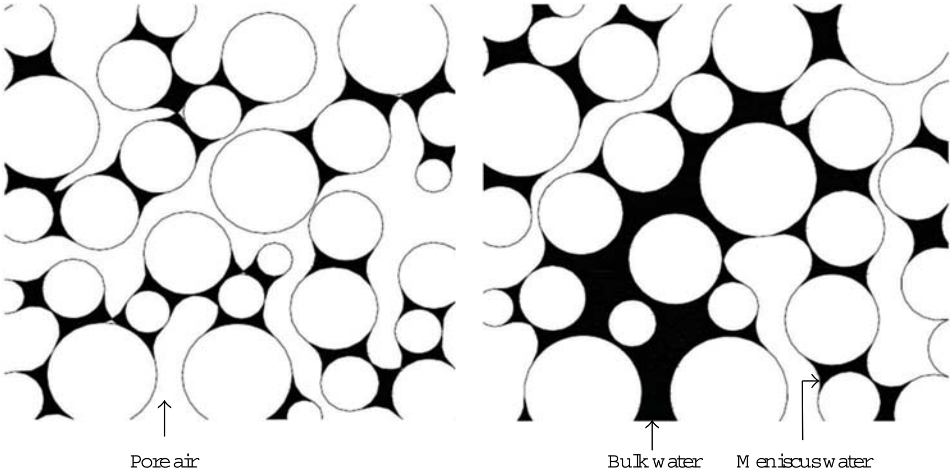

FIGURE 2: Effect of hydraulic history on the moisture distribution: (a) idealized moisture distribution pattern; (b) after several wetting-drying cycles (after Wheeler et al. (2003) [10]).

the soil experienced. To take into account such an effect, we first take a close inspection of the microscopic pattern of the moisture distribution in the pore space. As shown in Figure 2 [10], at the same matric suction, the distribution of moisture in an unsaturated soil sample can be different due to different hydraulic histories that the soil experienced. Figure 2(a) depicts an idealized moisture distribution pattern with specified matric suction, while Figure 2(b) represents the soil after certain wetting/drying cycles, at the same matric suction. Compared to the soil depicted in Figure 2(a), the soil shown in Figure 2(b) has higher saturation and a more heterogeneous structure. In the latter case, some regions in the soil are fully saturated, whereas the other regions remain relatively dry. The pore waters in the wet regions and dry regions influence the mechanical behavior of the soil in different ways. Namely, the negative pore water pressure in the wet regions contributes mainly to modification of the skeleton stress in a way as described by (3), whereas the pore water in the meniscus rings in the dry areas may have a stabilizing effect at the inter-particle contacts, due to the existence of surface tension (e.g., [16, 43]).

The stabilizing effect of meniscus water rings has two contributions [44]: one is related to the contractile films at interfaces between the wetting phase and nonwetting phase, which can pull the particles together, producing a hardening effect on the mechanical behavior; the other is due to the additional normal force at inter-particle contacts induced by the negative pore water pressure in the meniscus water rings, which can decrease the possibility of slippage (plastic strain) at the inter-particle contacts. Clearly, the stabilizing effect of meniscus water rings has a direct influence on the yielding and hardening of unsaturated soils. At specified matric suction, the stabilizing effect of meniscus water rings may become stronger when the quantity of meniscus water rings increases. Because the quantity of meniscus water rings can be represented by the amount of pore air, we suggest that the hardening effect of unsaturation can be collectively characterized by using variable $(1 - S_r)s_c$. Remarkably, at the specified matric suction, the value of $(1 - S_r)s_c$ depends uniquely upon the pattern of moisture distribution in the pores, that is, upon the hydraulic history that the soil experienced.

Based on the above discussions, it is proposed herein that

$$h\left(\varepsilon_v^p, S_r, s_c\right) = r - (r-1)\exp\left\{-m\left\langle 1 - \frac{\varepsilon_v^p}{\varepsilon_{v,\max}^p}\right\rangle \frac{\left(1 - S_r\right)s_c}{\left(1 - S_r^{\mathrm{irr}}\right)}\right\}, \quad (10)$$

where r is a parameter which truncates the effect of high matric suction on the preconsolidation pressures, namely, $r = h|_{s_c \to \infty}$; m is a factor characterizing the changing rate of preconsolidation pressure with the variation of $(1 - S_r)s_c$; $\varepsilon_{v,\max}^p$ is the threshold value of plastic volumetric strain at which the effect of unsaturation becomes trivial; S_r^{irr} is the residual degree of saturation; $\langle\rangle$ is Macauley bracket, defined as $\langle x\rangle = xH(x)$, where $H(x)$ is Heaviside function.

A typical relation among variables h, S_r, and s_c is schematically shown in Figure 3(a) in the three-dimensional space. Equation (10) describes the hardening surface as a function of S_r and s_c, bounded by the dashed and solid lines representing the drying and wetting boundaries, respectively. The projections of the hardening surface on the two-dimensional plots are also shown in Figure 3(a), where on the $S_r : s_c$ plane the projection yields the SWCC curve with capillary hysteresis, on the $s_c : h$ plane it describes the effect of matric suction on the hardening, and on the $S_r : h$ plane it describes the effect of saturation on the hardening. Remarkably, h increases with the decrease in saturation or increase in suction and approaches to a certain value when $S_r \to 0$ or $s_c \to +\infty$.

From the proposed hardening function, the effect of S_r and s_c on the preconsolidation pressure diminishes gradually with the increasing of ε_v^p. When ε_v^p reaches the maximum $\varepsilon_{v,\max}^p$, the influence of S_r and s_c on the preconsolidation

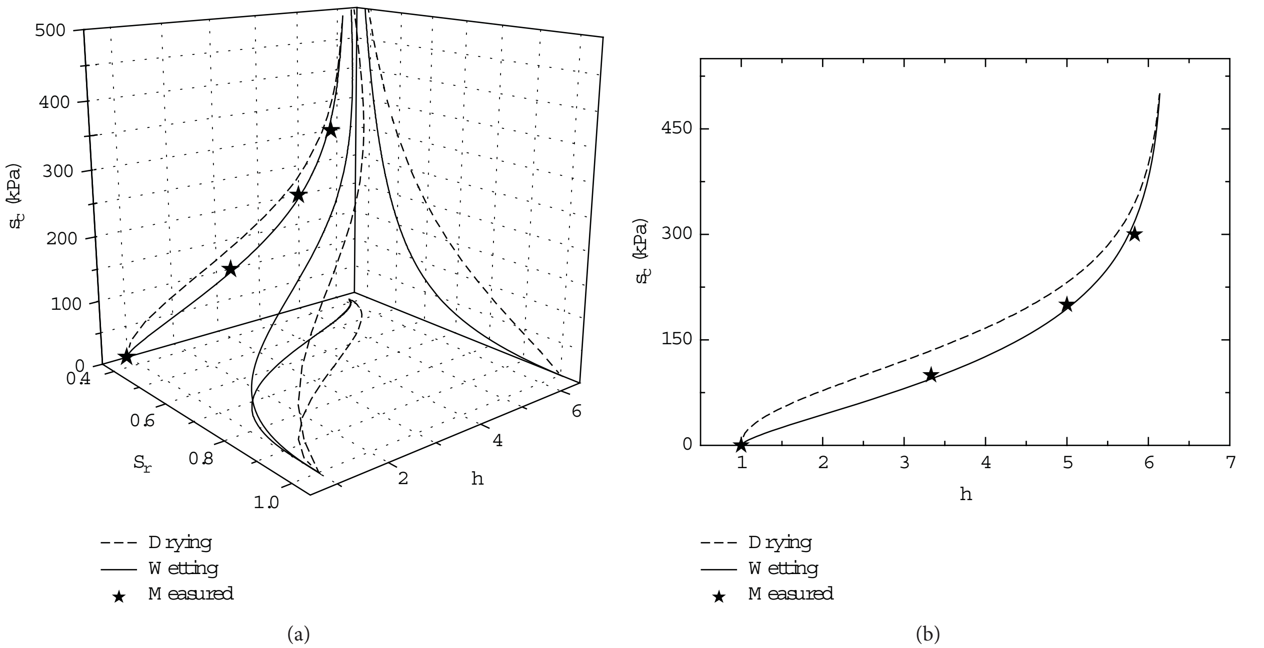

FIGURE 3: Relations among h, s_c, and S_r: (a) three-dimensional view of the hardening surface; (b) projection of the hardening surface on the $s_c : h$ plane (data after Wheeler and Sivakumar (1995) [5]).

pressure disappears, implying that the soil is very dense and the capillary effect can be negligible. The above characteristics are consistent with the actual situation. The proposed function can transit from saturated state to unsaturated state smoothly, where both states can be described in a single framework. In addition, it can be numerically implemented in a straightforward way.

Figure 3(b) shows the projection of the hardening surface on the $s_c : h$ plane, revealing that at the same matric suction the value of p_c for drying is consistently smaller than that for wetting, since at a specified matric suction the degree of saturation for drying is larger than that for wetting. The discrepancy diminishes when the matric suction increases. This typical feature of unsaturated soil behavior cannot be addressed by the existing elastoplastic constitutive frameworks formulated in terms of LC yield surface. The mathematical feature can be physically interpreted by considering that a lower degree of saturation implies a larger number of contact zones between the pore fluid menisci. It can be seen that the simulated hardening parameter h agrees very well with the experimental data for the wetting path that are available in the literature [5].

2.5. Elastoplastic Stress-Strain Relation. Sufficient experimental results [45, 46] show that the influence of meniscus water rings on the shear strength parameters (i.e., c' and ϕ) is negligible, provided that the strength line is plotted on the $p' : q$ plane. Hence it is suggested herein that the critical state line of unsaturated soil is the same as that of its saturated counterpart, and the failure line is simply given by $q = Mp'$, where M is independent of the matric suction or the degree of saturation.

As in the original modified Cam-Clay model, the increments of elastic volumetric strain and deviatoric strain are defined as

$$d\varepsilon_v^e = \frac{\kappa dp'}{vp'}, \qquad d\varepsilon_q^e = \frac{dq}{3G}, \tag{11}$$

where κ is the slope of the unloading-reloading line on the $v - \ln p'$ plane of the soil under the fully saturated condition, v is the specific volume $v = 1 + e$, e the void ratio, and G the shear modulus.

An associated flow rule is adopted herein: thus the plastic potential coincides with the yield function. The incremental plastic volumetric and deviatoric strains are given by

$$d\varepsilon_v^p = d\lambda \frac{\partial f}{\partial p'}, \qquad d\varepsilon_q^p = d\lambda \frac{\partial f}{\partial q}, \tag{12}$$

where $d\lambda$ is the plastic multiplier that can be determined based on the consistency condition; that is,

$$df = \frac{\partial f}{\partial p'} dp' + \frac{\partial f}{\partial q} dq + \frac{\partial f}{\partial p_c} \frac{\partial p_c}{\partial \varepsilon_v^p} d\varepsilon_v^p. \tag{13}$$

Substituting (12) into (13) and solving for $d\lambda$, one obtains

$$d\lambda = -\frac{\left(\partial f/\partial p'\right) dp' + \left(\partial f/\partial q\right) dq}{\left(\partial f/\partial p_c\right)\left(\partial p_c/\partial \varepsilon_v^p\right)\left(\partial f/\partial p'\right)}. \tag{14}$$

The yield surface is moving with the evolution of the internal hardening variable p_c, which is characterized in terms of the double-hardening mechanism [15] in (8).

The capillary-induced hardening is described by (10), while the plastic volumetric strain hardening is given by

$$p_{c_0}\left(\varepsilon_v^p\right) = p_{c_0}^* \exp\left(\frac{\upsilon\varepsilon_v^p}{\lambda-\kappa}\right), \tag{15}$$

where $p_{c_0}^*$ is the initial preconsolidation pressure; λ is the slope of the normal consolidation line on the $\upsilon - \ln p'$ plane of the soil under the fully saturated condition.

2.6. Effect of Deformation on the Soil-Water Characteristic Curve. Whether or not the hydromechanical behavior of an unsaturated soil can be effectively described at the constitutive level depends largely on the characterization of capillary hysteresis. To characterize the capillary hysteresis, an advanced SWCC model, which can properly address the soil-water characteristics of the soil experiencing arbitrarily wetting/drying cycles, should be properly implemented into a generalized mechanical constitutive framework [13].

Wei and Dewoolkar [18] proposed a thermodynamically consistent model for capillary hysteresis in partially saturated porous media. In this model, the capillary hysteresis phenomenon is linked to intrinsic energy dissipation processes, which can be characterized by the series of internal state variables, ξ_i^f, and the dissipative energy is given by $\zeta_i^f\delta\xi_i^f$, as in (5). By virtue of the notion of the bounding surface plasticity, a simplified model of capillary hysteresis is developed. Provided that the main drying-wetting boundary curves have been experimentally determined, the model introduces only one additional parameter to describe all types of scanning curves (primary, secondary, and higher order) under arbitrary hydraulic paths. This model is introduced here to describe the soil-water characteristics.

Experimental results [33] show that in a deformable soil, the sizes and the connectivity of pores may vary with skeletal deformation, which in turn induces change in the soil-water characteristics. For example, the air entry value increases with the decrease of void ratio, and the soil-water characteristic curve may shift upward on the $S_r : s_c$ plane. To address the effect of deformation on the soil-water characteristic curve, one first notes that, in general, the change in the degree of saturation has two contributions: one is the change in the amount of pore water due to seepage or dissipation, and the other is due to the change in the pore volume, namely,

$$dS_r = d\left(\frac{V_w}{V_v}\right) = \frac{dV_w}{V_v} - \left(\frac{V}{V_v}\right)\left(\frac{V_w}{V_v}\right)\left(\frac{dV_v}{V}\right). \tag{16}$$

As the very meaning of a partial differential, the first item of the right-hand side (r.h.s.) represents the change in the degree of saturation under the constant-V_v condition, that is, only due to the change in the amount of pore water, while the second item describes the contribution of the change in volumetric strain. Neglecting the effect of elastic deformation, (16) can be cast into

$$dS_r = dS_r\big|_{d\varepsilon_v=0} + \frac{S_r}{n}d\varepsilon_v^p. \tag{17}$$

According to Wei and Dewoolkar [18], the first term of the r.h.s. can be described by

$$dS_r\big|_{d\varepsilon_v=0} = \frac{-ds_c}{K_p\left(s_c, S_r, \widehat{n}\right)}, \tag{18}$$

where $\widehat{n}$ denotes the hydraulic loading direction, and its value assumes 1 (or −1) for drying (or wetting); K_p is the negative slope of the current soil-water characteristic curve (either scanning or boundary), which is a function of s_c, S_r, and $\widehat{n}$, given by

$$K_p\left(s_c, S_r, \widehat{n}\right) = \overline{K}_p\left(S_r, \widehat{n}\right) + \frac{c\left|s_c - \overline{s}_c\left(S_r, \widehat{n}\right)\right|}{r\left(S_r\right) - \left|s_c - \overline{s}_c\left(S_r, \widehat{n}\right)\right|}, \tag{19}$$

where $\overline{K}_p(S_r, \widehat{n})$ is the negative slope of the corresponding main boundary, which is the main drying boundary if $\widehat{n} = 1$ or the main wetting boundary if $\widehat{n} = -1$; c is a positive material parameter which is used to describe the scanning behavior; $\overline{s}_c(S_r, \widehat{n})$ is the matric suction value on the corresponding main boundary curve; that is, $\overline{s}_c(S_r, 1) = \kappa_{\mathrm{DR}}(S_r)$ for drying and $\overline{s}_c(S_r, -1) = \kappa_{\mathrm{WT}}(S_r)$ for wetting, where $\kappa_{\mathrm{DR}}(S_r)$ and $\kappa_{\mathrm{WT}}(S_r)$ describe the main drying and wetting boundaries, respectively; $r(S_r)$ is the current size of the bounding zone; that is, $r(S_r) = \kappa_{\mathrm{DR}}(S_r) - \kappa_{\mathrm{WT}}(S_r)$.

Although the effect of change in volumetric strain is excluded in calculating $dS_r|_{d\varepsilon_v=0}$ (*via* (18)), the volumetric deformation (or change of void ratio) may induce change in the SWCC curve, as mentioned above. That is, function K_p should depend explicitly upon the void ratio or equivalently, the total plastic volumetric strain ε_v^p (the effect of elastic strain is neglected).

To address this issue, we adopt the following SWCC model by Feng and Fredlund [47] to describe the main boundaries:

$$\kappa_k\left(S_r\right) = b_k\left(\frac{1-S_r}{S_r - S_r^{\mathrm{irr}}}\right)^{1/d_k}, \quad k = \mathrm{DR}, \mathrm{WT}, \tag{20}$$

where b_k and d_k are the positive material parameters and assume different values for wetting and drying. The d_k parameter determines the curvature of the scanning curves, while b_k related to the air-entry value. Ignoring the influence of the elastic volumetric strain and shear strain, b_k and d_k depend on the plastic volumetric strain, ε_v^p. Experimental results [33] suggest that the skeletal deformation changes the position of the SWCC only and leaves the shape of the curve almost unchanged. Thus, for simplicity, we propose that

$$b_k = b_k^0 + \alpha_k\varepsilon_v^p, \qquad d_k = d_k^0, \tag{21}$$

where b_k^0, d_k^0, and α_k are curving-fitting parameters, k = DR, WT.

Due to a lack of experimental data, it is assumed for simplicity that parameter c is constant, independent of the skeletal deformation. Now, for deforming soils, (19) can be replaced by

$$\begin{aligned} &K_p\left(\varepsilon_v^p, s_c, S_r, \widehat{n}\right) \\ &\quad = \overline{K}_p\left(\varepsilon_v^p, S_r, \widehat{n}\right) + \frac{c\left|s_c - \overline{s}_c\left(\varepsilon_v^p, S_r, \widehat{n}\right)\right|}{r\left(\varepsilon_v^p, S_r\right) - \left|s_c - \overline{s}_c\left(\varepsilon_v^p, S_r, \widehat{n}\right)\right|}. \end{aligned} \tag{22}$$

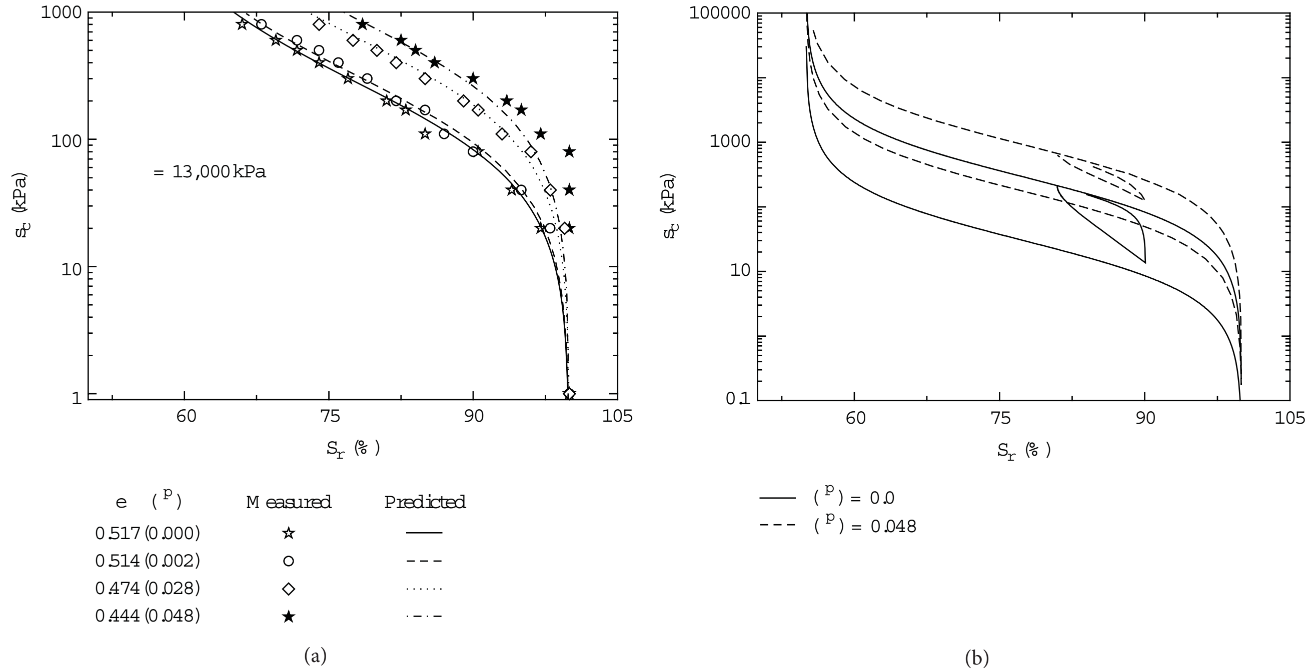

FIGURE 4: Effect of plastic volumetric strain on soil-water characteristic curve (data after Vanapalli et al. (1999) [33]).

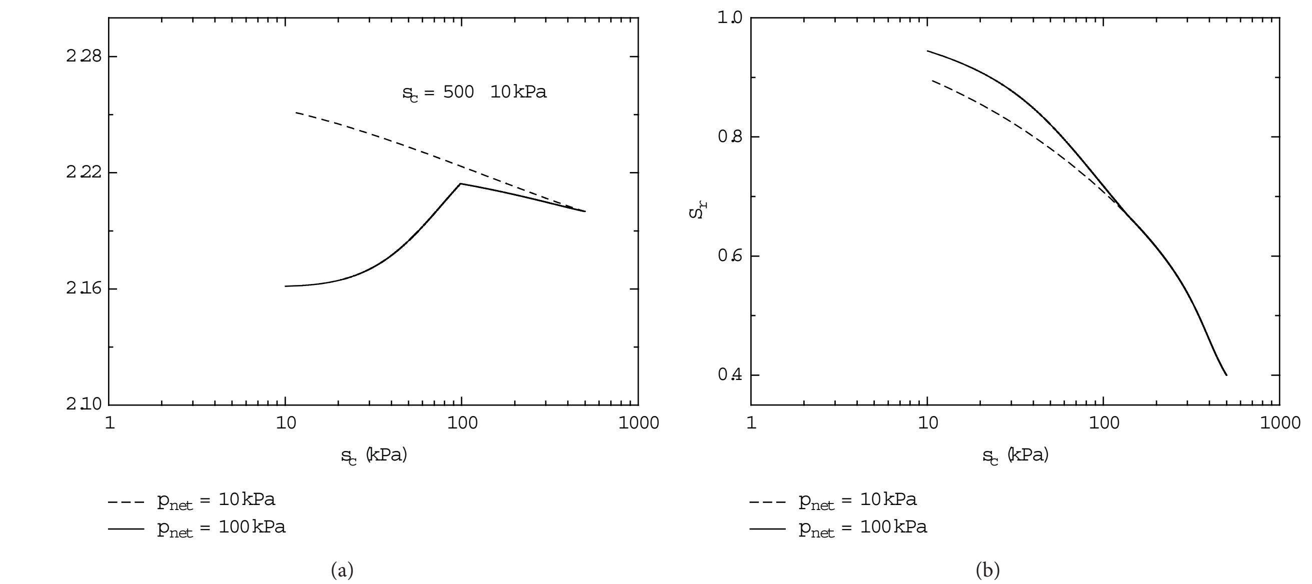

FIGURE 5: Model prediction for wetting tests at different net stresses: (a) relation between mean net stress and specific volume; (b) soil-water characteristic curve. It is assumed here that $b_{\mathrm{DR}}^0 = 290$ kPa, $b_{\mathrm{WT}}^0 = 30$ kPa, $S_r^{\mathrm{irr}} = 0.3$, $d_{\mathrm{DR}}^0 = d_{\mathrm{WT}}^0 = 1.0$, $\alpha_{\mathrm{DR}} = 3500$ kPa, $\alpha_{\mathrm{WT}} = 1500$ kPa, $r = 6.5$, $m = 0.012$, and $\varepsilon_{v,\max}^p = 0.25$.

As an example, Figure 4(a) illustrates the effect of the plastic volumetric strain on the soil-water characteristic curve. The datum points are inferred from the experimental results in [33]. It can be seen that, while the theoretical simulations agree reasonably well with the experimental results, the model is capable of capturing the main features of the SWCC of deformable soils. The effect of plastic volumetric deformation on capillary hysteresis is schematically shown in Figure 4(b).

2.7. Evaluation of Constitutive Parameters. The proposed model avoids using the LC yield curve as in the traditional framework and introduces the matric suction and degree of saturation into the hardening function as independent variables. The constitutive parameters can be divided into the following three groups.

(1) Group 1: conventional constitutive parameters—λ, κ, M, and G.

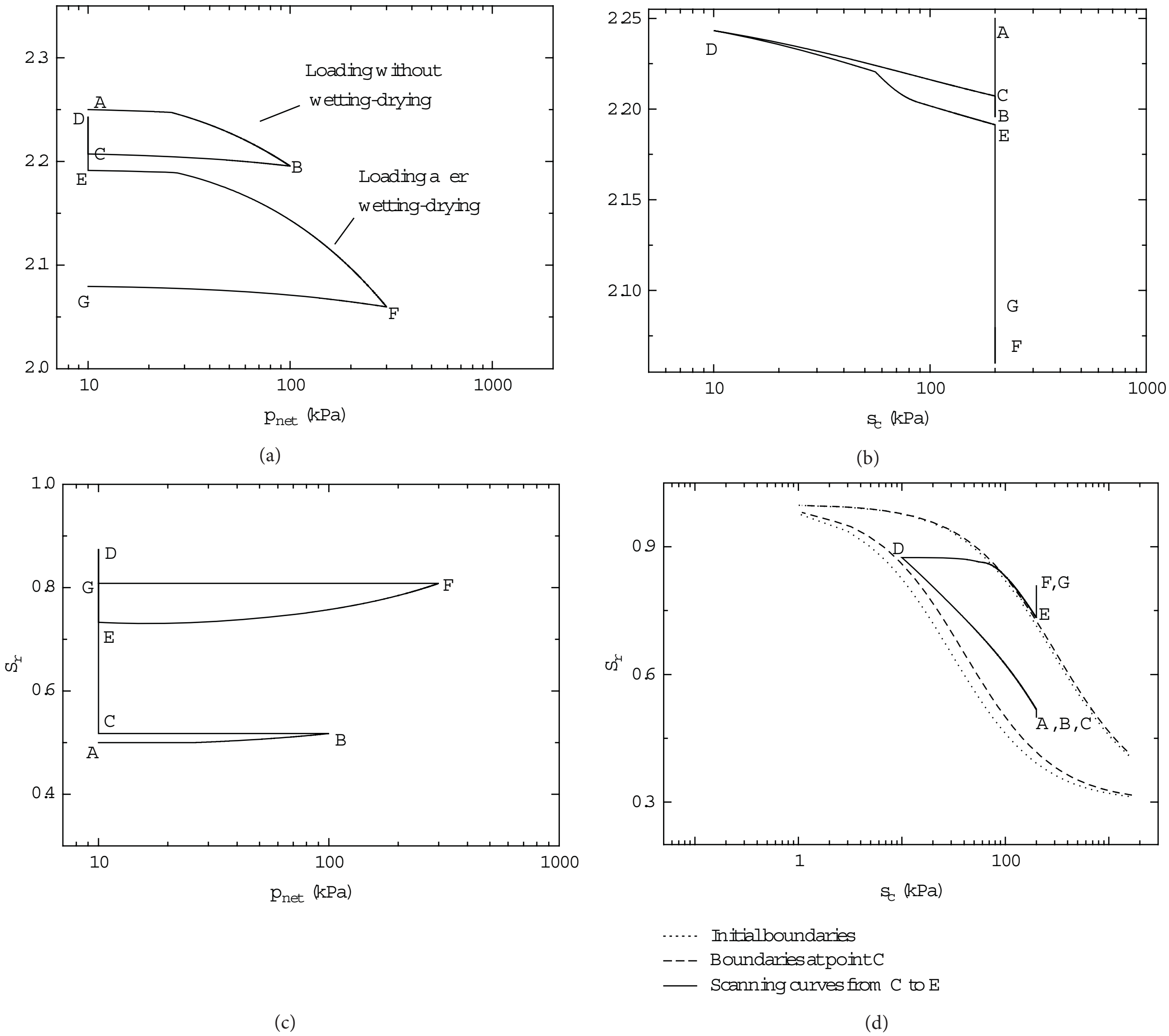

FIGURE 6: Influence of wetting-drying cycle on isotropic compression. It is assumed here that $b^0_{DR} = 290$ kPa, $b^0_{WT} = 30$ kPa, $d^0_{DR} = d^0_{WT} = 1.0$, $S^{irr}_r = 0.3$, $\alpha_{DR} = 1500$ kPa, $\alpha_{WT} = 750$ kPa, $r = 7.5$, $m = 0.0115$, and $\varepsilon^p_{v,max} = 0.25$.

(2) Group 2: soil-water characteristic parameters—b^0_{DR}, b^0_{WT}, d^0_{DR}, d^0_{WT}, S^{irr}_r, and c.

(3) Group 3: coupling parameters—α_{DR}, α_{WT}, r, m, and $\varepsilon^p_{v,max}$.

The parameters in Group 1 can be determined in the same way as those for the modified Cam-Clay model (e.g., [40]). Particularly, λ and κ are determined from the results of isotropic compression tests, while M and G (or Poisson's ratio ν) are obtained by performing the triaxial compression tests on saturated soil.

The parameters in Group 2 can be determined, via a curve-fitting procedure, by measuring the soil-water characteristic curve for the soil experiencing wetting/drying cycles. Parameters b^0_{DR}, b^0_{WT}, d^0_{DR}, d^0_{WT}, and S^{irr}_r are determined based on the measurement of the two boundary curves [47]. With knowledge of the two boundary curves, c is determined by fitting the theoretical simulation of a primary scanning curve with the measured one [18].

Among the parameters in Group 3, r, m, and $\varepsilon^p_{v,max}$ can be determined by measuring the variation of preconsolidation pressure with the matric suction or degree of saturation during a drying process; parameters α_{DR} and α_{WT}, which represent the influence of plastic deformation on the soil-water characteristic curve, can be obtained by comparing the soil-water characteristic curves under deformed and undeformed conditions.

3. Model Performance

3.1. Wetting under Different Net Pressures. Figure 5 shows the simulated results of the wetting tests on an unsaturated clayey soil under constant net pressures of 10 kPa and 100 kPa ($q = 0$ kPa), respectively. The soil sample was wetted from $s_c = 500$ kPa to $s_c = 10$ kPa, while the net pressure remained

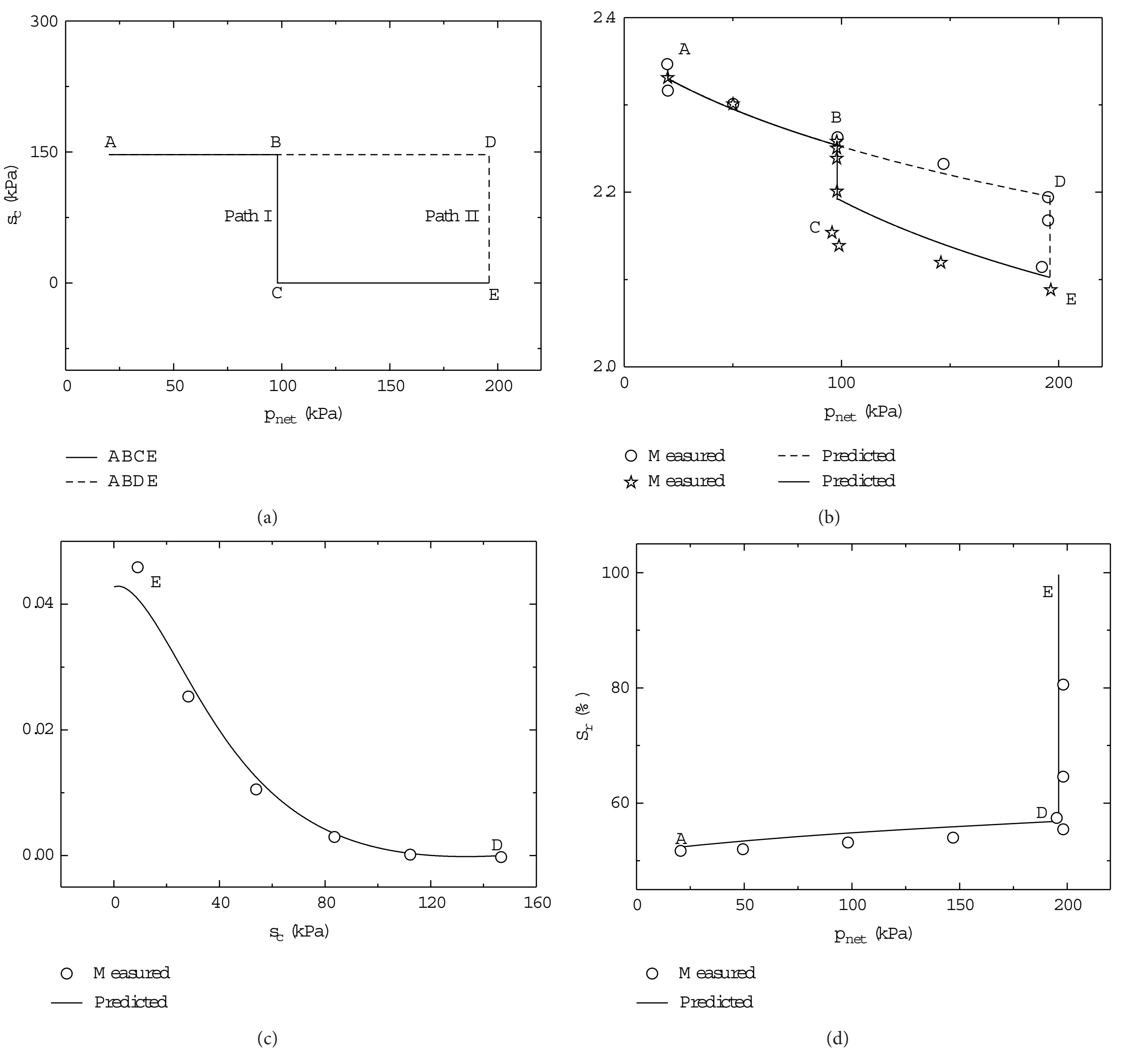

Figure 7: Simulated and measured results of wetting-collapse experiments on Pearl clay: (a) stress paths adopted; (b) relation between p_{net} and v; (c) variation of total volumetric strain with matric suction during the wetting process D-E; (d) variation of the degree of saturation with net pressure for Path A-B-D-E. (data after Sun et al. (2007) [34]).

constant. It can be seen from Figure 5(a) that, under small net pressure (10 kPa), the soil exhibits only elastic swelling during the wetting process, whereas, at high net pressure (100 kPa), after slightly swelling in the early beginning, significant plastic compression can occur. Figure 5(b) shows that plastic volumetric deformation can significantly influence the soil-water characteristics. These simulated results are consistent with experimental observations [34].

During a wetting process, both mean skeleton stress p' and preconsolidation pressure p_c will decrease, triggering two competitive mechanisms. While the soil swells elastically with p' decreasing due to wetting, the yield pressure also becomes smaller and smaller. Under a small net pressure (say 10 kPa in the present case), p' is always smaller than p_c during the whole wetting process, so that only elastic swelling deformation can occur. At high net pressure (say 100 kPa in the present case), however, p' may reach p_c during the wetting process, resulting in plastic deformation.

3.2. Effect of Hydraulic History on Compression. The simulated results of an isotropic loading-unloading compression test on a silty clay are presented in Figure 6. At a constant matric suction of 200 kPa, the soil was first loaded from A ($p_{\text{net}} = 10$ kPa) to B ($p_{\text{net}} = 100$ kPa) and then unloaded to C ($p_{\text{net}} = 10$ kPa); after a wetting-drying cycle C-D-E ($s_c = 200 \rightarrow 10 \rightarrow 200$ kPa) at $p_{\text{net}} = 10$ kPa, the soil was reloaded to F ($p_{\text{net}} = 300$ kPa) and finally unloaded to G ($p_{\text{net}} = 10$ kPa), at a constant matric suction of 200 kPa.

Figure 6(a) reveals that the yielding pressure during isotropic compression at a given value of suction is reduced

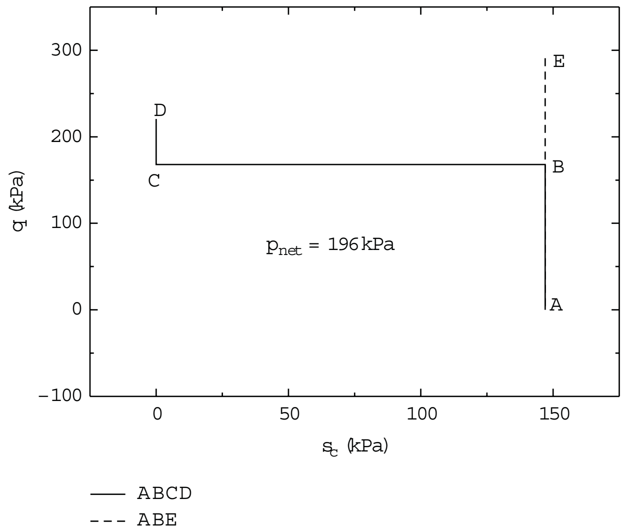

FIGURE 8: Stress paths used in the triaxial tests.

by a preceding wetting-drying cycle, which is consistent with the experimental observation [48]. This phenomenon can be largely attributed to the capillary hysteresis. As shown in Figure 6(c), there has been a significant increase in the degree of saturation during the wetting-drying cycle C-D-E, resulting in a decrease in the preconsolidation pressure. Clearly, the proposed model can correctly predict the dependence of the soil response on its hydraulic history during isotropic compression under constant suction.

Figure 6(b) shows that significant irreversible compression has occurred during the wetting-drying cycle. In the wetting phase from C to D, the stress state resides in the elastic domain (i.e., $p' < p_c$), though both mean skeleton stress p' and preconsolidation pressure p_c decrease simultaneously. In the drying phase from D to E, although both p' and p_c increase simultaneously, p' increases faster than p_c, so that the stress state of the soil touches the yield locus when the matric suction increases up to a certain value, resulting in plastic deformation. Remarkably, if the effect of capillary hysteresis is neglected, the model would have predicted that the soil is elastically compressed to Point C again; that is, C coincides with E.

Figure 6(d) illustrates the effect of deformation on the soil-water characteristics. After the first loading-unloading cycle A-B-C, the SWCC boundaries (both wetting and drying) shift rightward on the $S_r : s_c$ plane, due to the plastic compression of the soil matrix. In the wetting process from C to D, only elastic deformation occurs, and the SWCC boundaries remain unchanged. During the drying process from D to E, plastic deformation occurs, and the SWCC boundaries move rightward with the deformation until the drying boundary crosses Point E. In the reloading process from E to F, plastic deformation further drives the SWCC boundaries rightward, and the SWCC boundaries remain fixed during the unloading process from F to G. Although

TABLE 1: Index properties of Pearl clay [34].

Property	Definition
Grain-size distribution	Silt = 50%, clay = 50%
Atterberg limits	LL = 49%, PI = 27%
Specific gravity	G_s = 2.71

further experimental justification is needed, limited experimental data suggest that the above model prediction is reasonable [34, 35].

3.3. Wetting-Induced Compression (Wetting-Collapse Test). Sun et al. [34] have conducted isotropic compression and wetting-collapse experiments on Pearl clay (a silty clay), the physical properties of which are given in Table 1. In these experiments, two stress paths (i.e., A-B-C-E and A-B-D-E) were adopted (Figure 7(a)). Some of typical experimental results are illustrated in Figures 7(b)–7(d). The initial water content and void ratio of the tested soil samples are about 26% and 1.34, respectively. Due to lacking of experimental data, the hydraulic and mechanical constitutive parameters are determined based on the curve-fitting process and given in Tables 2 and 3, respectively.

Along with Path A-B-C-E, the soil was first compressed under the isotropic condition from Point A (p_{net} = 20 kPa) to Point B (p_{net} = 98 kPa) at a constant matric suction of 147 kPa, then wetted from Point B to the fully saturated condition (Point C) under a constant net pressure of 98 kPa, and finally compressed to Point E (p_{net} = 196 kPa) under fully saturated conditions. With Path A-B-D-E, the soil was compressed under the isotropic condition from Point A (p_{net} = 20 kPa) to Point D (p_{net} = 196 kPa) at a constant matric suction of 147 kPa and then wetted to the fully saturated condition under a constant net pressure of 196 kPa.

The simulations for the variation of specific volume with net pressure are given in Figure 7(b), showing that overall the simulations agree well with the experimental data. It is remarkable, however, that during the loading process C-E, the model overestimates the specific volume. Such a discrepancy can be attributed to the following two reasons: (1) the plastic deformation is underestimated by the model during the wetting process B-C, and (2), when the soil approached to full saturation at Point C (from Point B), small amount of air was trapped in the pores, rendering the soil to be more compressible than expected in the early beginning of the subsequent compression process.

Figure 7(c) illustrates the variation of volumetric strain during the wetting process from D to E. Although slight swelling deformation is predicted in the early beginning of the wetting process, the model simulation agrees generally well with the measurements. Figure 7(d) depicts the variation of saturation with net stress for Path A-B-D-E. The simulated result deviates from the measurement at the final stage of the wetting process D-E; that is, the calculated degree of saturation at Point E is 100%, which is larger than the measured value. Apparently, this discrepancy can be attributed to the air entrapment, which has not been considered in the proposed

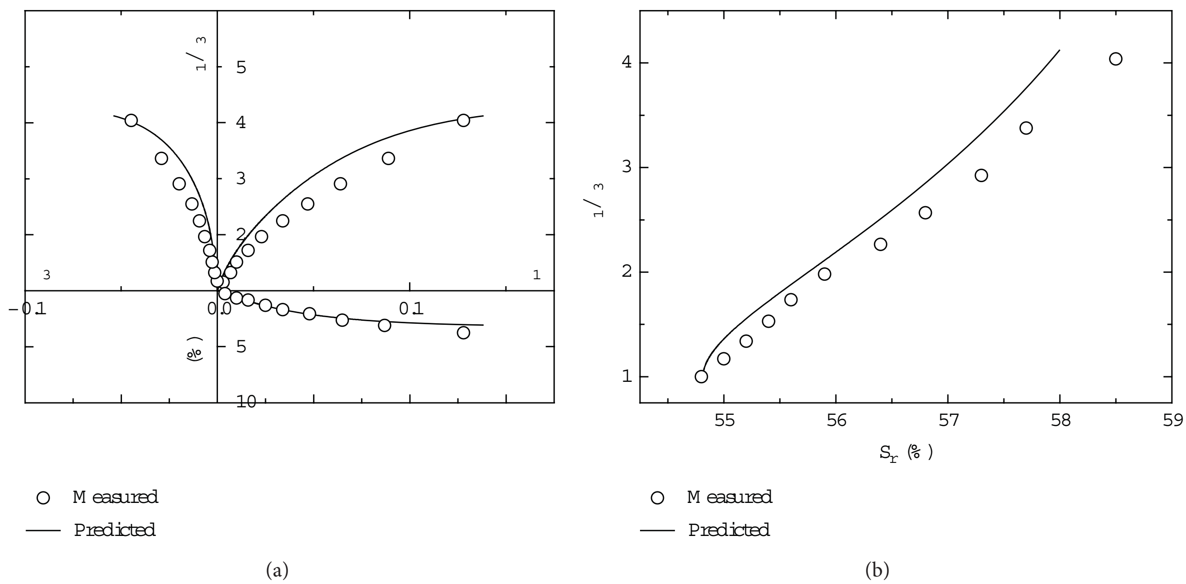

FIGURE 9: Simulated and measured results of triaxial tests with stress Path A-B-E (data after Sun et al. (2007) [2]).

TABLE 2: Mechanical parameters of Pearl clay.

λ	κ	G (kPa)	r	m	$p^*_{c_0}$	$\varepsilon^p_{v,\max}$
0.12	0.03	5000	4.5	0.035	20.15	0.25

model. In spite of this shortcoming, the model can very well predict the trend of variation for the degree of saturation.

3.4. Suction-Controlled Triaxial Tests. Sun et al. [2] have performed a series of suction-controlled triaxial compression tests on Pearl clay. The stress paths adopted in these experiments are illustrated in Figure 8. The experimental results are given in Figures 9 and 10 for Path A-B-E and Path A-B-C-D, respectively. Along with stress path A-B-E, the soil sample was sheared from an initial isotropic state to failure by increasing q under $p_{\text{net}} = 196\,\text{kPa}$ and $s_c = 147\,\text{kPa}$. With stress Path A-B-C-D, the sample was first sheared, under $p_{\text{net}} = 196\,\text{kPa}$ and $s_c = 147\,\text{kPa}$, from Point A to Point B until principal stress ratio σ_1/σ_3 reached about 2.2; then the sample was wetted from Point B to the fully saturated condition (Point C) under constant-p_{net} and constant-q conditions; finally, the sample was sheared to failure from Point C by increasing q.

The material properties adopted in the simulations are the same as those given in Tables 1–3. Figures 9(a) and 9(b) depict the relations among σ_1/σ_3, ε_1, ε_3, and ε_v and the relation between σ_1/σ_3 and the degree of saturation, respectively. For stress Path A-B-E, in the early of shearing, the model predicts that the specimen remains in the elastic domain, as illustrated by the initial vertical line segment in Figure 9(b) (note that the effect of elastic volumetric strain on the degree of saturation has been neglected). From Figure 9(a), it is clear that although the model slightly underestimates the axial strain and the lateral strain, overall it yields good results.

Figure 10(a) shows that the lateral strain is overestimated in the later stage of the shearing process. In spite of this discrepancy, the model simulations agree well with the experimental data. From Figure 10(b), it can be seen that, during the wetting process (from B to C), the model predicts the full saturation at Point C, which is inconsistent with the measurement. This discrepancy is due to the effect of air entrapment in the experiment, which is also responsible for the discrepancy between the predicted and measured strains (see Figure 10(a)). To take into account the air entrapment effect, slight improvement of the proposed model is required, which goes beyond the scope of this paper. Remarkably, the degree of saturation increases during the shearing process, and this feature has been well captured by the proposed model, as illustrated in Figures 9(b) and 10(b).

3.5. Wetting-Drying Cycle under Constant Net Pressure. Figure 11 gives the simulated and experimental results of a wetting-drying experiment on the Pearl clay under constant net pressure. The experimental data are obtained from [35]. The tested sample has an initial void ratio e_0 of 1.08, and it is much denser than those samples mentioned in Sections 3.3 and 3.4 (for latter cases, $e_0 \approx 1.34$). During the wetting-drying cycles, the matric suction first decreased from 196 kPa to 2 kPa (from A$'$ to B$'$), then increased from about 2 to 490 kPa (from B$'$ to C$'$), and finally decreased from 490 to about 2 kPa (from C$'$ to D$'$), while the net pressure remained 20 kPa.

The material properties used in the simulation are given in Tables 1–3. It is noted, however, that several parameters (namely, b_{DR}, b_{WT}, $\varepsilon^p_{v,\max}$, and $p^*_{c_0}$) need to be slightly modified in order to account for the effect of the initial density of the sample. The new values of these parameters are $b_{\text{DR}} = 220\,\text{kPa}$, $b_{\text{WT}} = 60\,\text{kPa}$, $\varepsilon^p_{v,\max} = 0.15$, and $p^*_{c_0} = 37.05\,\text{kPa}$.

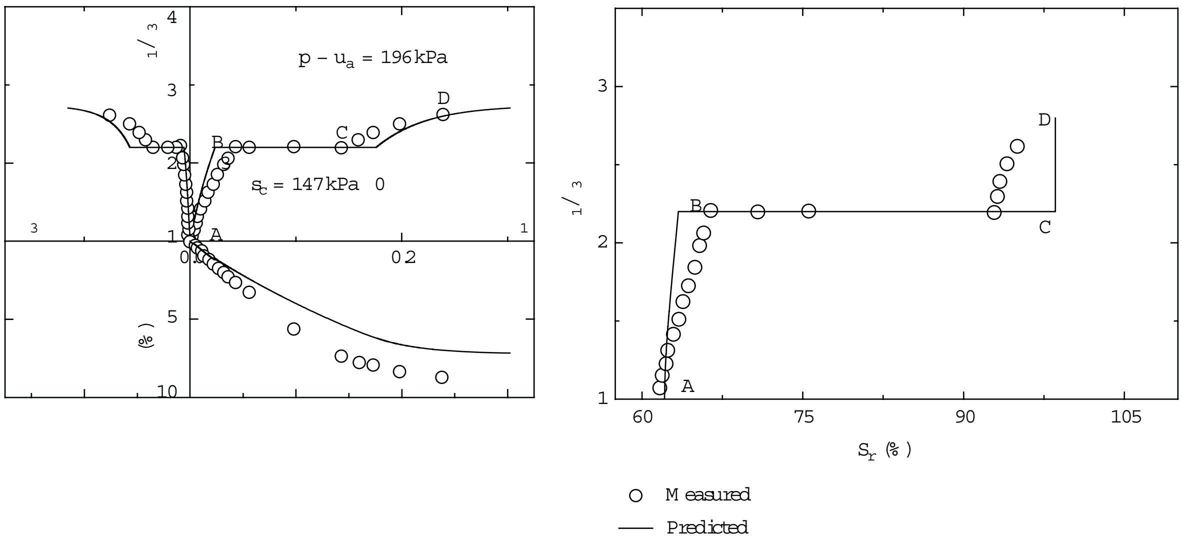

(a) (b)

Figure 10: Simulated and measured results of triaxial tests with stress Path A-B-C-D (data after Sun et al. (2007) [2]).

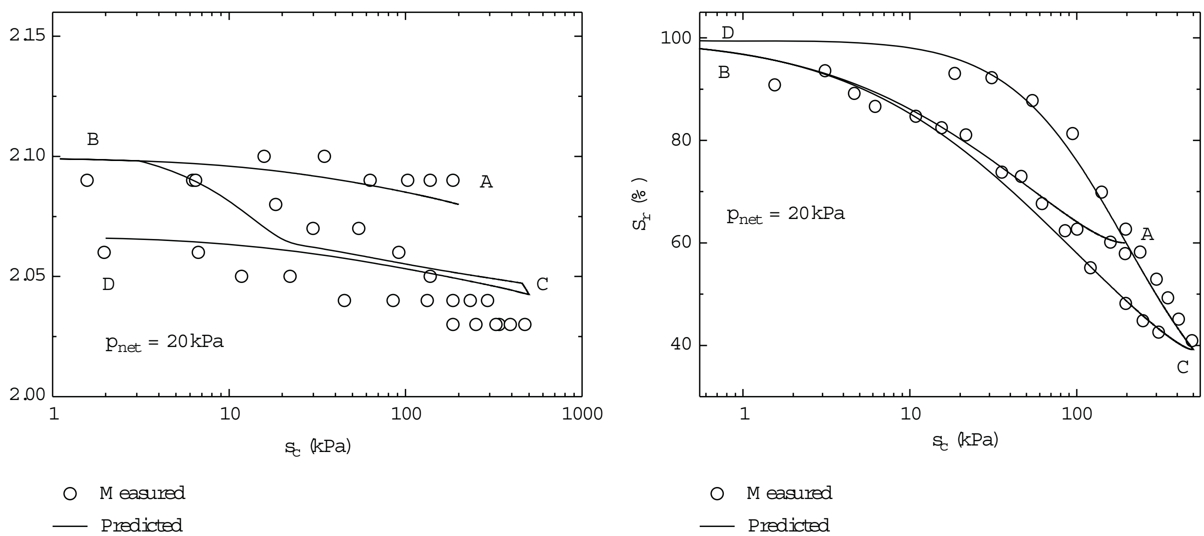

(a) (b)

Figure 11: Response of Pearl clay under wetting-drying cycles: (a) relation between matric suction and specific volume; (b) soil-water characteristic curve (data after Sun et al. (2006) [35]).

Figure 11(a) depicts the variation of the specific volume with matric suction. It can be seen that the model simulation agrees reasonably well with the experimental data. Particularly, the model correctly predicts that plastic deformation occurs during the drying process from B′ to C′. Figure 11(b) illustrates that the model can very well describe the soil-water characteristics of the unsaturated soil under deforming conditions.

4. Conclusions

The two major dissipative mechanisms in unsaturated soils, that is, capillary hysteresis and plastic deformation, are discussed in this paper. The capillary hysteresis is viewed as a phenomenon associated with the internal structural rearrangements in unsaturated soils, which can be characterized by using a set of internal state variables. As such, both capillary hysteresis and plastic deformation are systematically and consistently addressed in a unified theoretical framework. Within this context and based on the modified Cam-Clay model, a constitutive model of unsaturated soils is developed, which can effectively describe the coupling of capillary hysteresis and skeletal deformation.

In the new model, a hardening function is introduced in which both the matric suction and the degree of saturation are explicitly included as hardening variables, so that

Table 3: Hydraulic parameters of Pearl clay.

b^0_{DR} (kPa)	b^0_{WT} (kPa)	d^0_{DR}	d^0_{WT}	S_r^{irr}	c (kPa)	α_{DR} (kPa)	α_{WT} (kPa)
181.15	43.35	1.2	0.8	0.2	1000	350	150

the effect of hydraulic history on the mechanical response can be properly addressed. The soil-water characteristic curve is introduced not only to describe the capillary hysteresis in the unsaturated soils experiencing arbitrary wetting/drying cycles, but also to characterize the effect of hydraulic history on the skeletal deformation. The new model is used to simulate the mechanical response of unsaturated soil under various loading conditions, showing that it is capable of capturing the main features of the unsaturated soil behavior.

The new model has a hierarchical structure, and it can describe the stress-strain relation and the soil-water characteristics in a coupled or uncoupled manner. When the coupling effect of skeletal deformation and capillary hysteresis is neglected, the new model ends up with two major constitutive relationships for unsaturated soils, namely, the stress-strain relationship and the soil-water characteristic curve. Without skeletal deformation, the model describes the soil-water characteristics only. When the soil becomes fully saturated, the model transits smoothly into the modified Cam-Clay model of saturated soils.

Acknowledgments

The research was supported by the Natural Science Foundation of China (Grant no. 11072255) and the Natural Science Foundation of Guangxi (Grant no. 2011GXNSFE018004).

References

[1] S. J. Wheeler, "Inclusion of specific water volume within an elasto-plastic model for unsaturated soil," *Canadian Geotechnical Journal*, vol. 33, no. 1, pp. 42–57, 1996.

[2] D. Sun, D. Sheng, and S. W. Sloan, "Elastoplastic modelling of hydraulic and stress-strain behaviour of unsaturated soils," *Mechanics of Materials*, vol. 39, no. 3, pp. 212–221, 2007.

[3] C. W. W. Ng and Y. W. Pang, "Influence of stress state on soil-water characteristics and slope stability," *Journal of Geotechnical and Geoenvironmental Engineering*, vol. 126, no. 2, pp. 157–166, 2000.

[4] E. E. Alonso, A. Gens, and A. Josa, "A constitutive model for partially saturated soils," *Géotechnique*, vol. 40, no. 3, pp. 405–430, 1990.

[5] S. J. Wheeler and V. Sivakumar, "An elasto-plastic critical state framework for unsaturated soil," *Géotechnique*, vol. 45, no. 1, pp. 35–53, 1995.

[6] M. Nuth, L. Laloui, and B. A. Schrefler, "Analysis of compaction phenomena due to water injection in reservoirs with a three-phase geomechanical model," *Journal of Petroleum Science and Engineering*, vol. 73, no. 1-2, pp. 33–40, 2010.

[7] D. A. Sun and X. Li, "An elastoplastic hydro-mechanical model for unsaturated soils," in *Proceedings of the 7th International Conference on Computational Science (ICCS '07)*, pp. 1138–1145, Springer, Beijing, China, 2007.

[8] D. Sheng, A. Gens, D. G. Fredlund, and S. W. Sloan, "Unsaturated soils: from constitutive modelling to numerical algorithms," *Computers and Geotechnics*, vol. 35, no. 6, pp. 810–824, 2008.

[9] F. D'Onza, D. Gallipoli, S. Wheeler et al., "Benchmark of constitutive models for unsaturated soils," *Géotechnique*, vol. 61, no. 4, pp. 283–302, 2011.

[10] S. J. Wheeler, R. S. Sharma, and M. S. R. Buisson, "Coupling of hydraulic hysteresis and stress-strain behaviour in unsaturated soils," *Géotechnique*, vol. 53, no. 1, pp. 41–54, 2003.

[11] G. Bolzon, B. A. Schrefler, and O. C. Zienkiewicz, "Elastoplastic soil constitutive laws generalized to partially saturated states," *Géotechnique*, vol. 46, no. 2, pp. 279–289, 1996.

[12] Y. J. Cui and P. Delage, "Yielding and plastic behaviour of an unsaturated compacted silt," *Géotechnique*, vol. 46, no. 2, pp. 291–311, 1996.

[13] M. Nuth, *Constitutive modelling of unsaturated soils with hydro-geomechanical couplings [Ph.D. thesis]*, Ecole Polytechnique Fédérale de Lausanne (EPFL), Lausanne, Switzerland, 2009.

[14] N. Khalili, F. Geiser, and G. E. Blight, "Effective stress in unsaturated soils: review with new evidence," *International Journal of Geomechanics*, vol. 4, no. 2, pp. 115–126, 2004.

[15] R. Tamagnini, "An extended Cam-clay model for unsaturated soils with hydraulic hysteresis," *Géotechnique*, vol. 54, no. 3, pp. 223–228, 2004.

[16] C. Jommi, "Remarks on the constitutive modelling of unsaturated soils," in *Experimental Evidence and Theoretical Approaches in Unsaturated Soils. Proceedings of the International Workshop on Unsaturated Soils*, A. Tarantino and C. Mancuso, Eds., pp. 139–153, Balkema, Rotterdam, The Netherlands, 2000.

[17] X. S. Li, "Thermodynamics-based constitutive framework for unsaturated soils. 2: a basic triaxial model," *Géotechnique*, vol. 57, no. 5, pp. 423–435, 2007.

[18] C. Wei and M. M. Dewoolkar, "Formulation of capillary hysteresis with internal state variables," *Water Resources Research*, vol. 42, no. 7, Article ID W07405, 2006.

[19] X. S. Li, "Modelling of hysteresis response for arbitrary wetting/drying paths," *Computers and Geotechnics*, vol. 32, no. 2, pp. 133–137, 2005.

[20] Y. Mualem, "A conceptual model of hysteresis," *Water Resources Research*, vol. 10, no. 3, pp. 514–520, 1974.

[21] J. Y. Parlange, "Capillary hysteresis and the relationship between drying and wetting curves," *Water Resources Research*, vol. 12, no. 2, pp. 224–228, 1976.

[22] L. Miao, F. Jing, and S. L. Houston, "Soil-water characteristic curve of remolded expansive soils," in *Proceedings of the 4th International Conference on Unsaturated Soils*, pp. 997–1004, April 2006.

[23] D. Gallipoli, S. J. Wheeler, and M. Karstunen, "Modelling the variation of degree of saturation in a deformable unsaturated soil," *Géotechnique*, vol. 53, no. 1, pp. 105–112, 2003.

[24] M. T. van Genuchten, "A closed-form equation for predicting the hydraulic conductivity of unsaturated soils," *Soil Science Society of America Journal*, vol. 44, no. 5, pp. 892–898, 1980.

[25] X. S. Li, "Thermodynamics-based constitutive framework for unsaturated soils. 1: theory," *Géotechnique*, vol. 57, no. 5, pp. 411–422, 2007.

[26] G. T. Houlsby, "The work input to an unsaturated granular material," *Géotechnique*, vol. 47, no. 1, pp. 193–196, 1997.

[27] A. W. Bishop, "The principle of effective stress bishop," *Teknisk Ukeblad*, vol. 106, no. 39, pp. 113–143, 1959.

[28] N. Khalili and S. Zargarbashi, "Influence of hydraulic hysteresis on effective stress in unsaturated soils," *Géotechnique*, vol. 60, no. 9, pp. 729–734, 2010.

[29] E. E. Alonso, J.-M. Pereira, J. Vaunat, and S. Olivella, "A microstructurally based effective stress for unsaturated soils," *Géotechnique*, vol. 60, no. 12, pp. 913–925, 2010.

[30] J.-M. Pereira, O. Coussy, E. E. Alonso, J. Vaunat, and S. Olivella, "Is the degree of saturation a good candidate for Bishop's parameter?" in *Proceedings of the 5th International Conference on Unsaturated Soils*, E. E. Alonso and A. Gens, Eds., pp. 913–919, CRC Press, Barcelona, Spain, September 2010.

[31] T. Cadoret, G. Mavko, and B. Zinszner, "Fluid distribution effect on sonic attenuation in partially saturated limestones," *Geophysics*, vol. 63, no. 1, pp. 154–160, 1998.

[32] C. Wei and K. K. Muraleetharan, "Linear viscoelastic behavior of porous media with non-uniform saturation," *International Journal of Engineering Science*, vol. 45, no. 2–8, pp. 698–715, 2007.

[33] S. K. Vanapalli, D. G. Fredlund, and D. E. Pufahl, "The influence of soil structure and stress history on the soil-water characteristics of a compacted till," *Géotechnique*, vol. 49, no. 2, pp. 143–159, 1999.

[34] D. Sun, D. Sheng, and Y. Xu, "Collapse behaviour of unsaturated compacted soil with different initial densities," *Canadian Geotechnical Journal*, vol. 44, no. 6, pp. 673–686, 2007.

[35] D. A. Sun, D. C. Sheng, H. B. Cui, and S. W. Sloan, "A density-dependent elastoplastic hydro-mechanical model for unsaturated compacted soils," *International Journal for Numerical and Analytical Methods in Geomechanics*, vol. 31, no. 11, pp. 1257–1279, 2007.

[36] T. Cadoret, D. Marion, and B. Zinszner, "Influence of frequency and fluid distribution on elastic wave velocities in partially saturated limestones," *Journal of Geophysical Research*, vol. 100, no. 6, pp. 9789–9803, 1995.

[37] R. Knight and R. Nolen-Hoeksema, "A laboratory study of the dependence of elastic wave velocities on pore scale fluid distribution," *Geophysical Research Letters*, vol. 17, no. 10, pp. 1529–1532, 1990.

[38] M. Le Ravalec, Y. Guéguen, and T. Chelidze, "Elastic wave velocities in partially saturated rocks: saturation hysteresis," *Journal of Geophysical Research B*, vol. 101, no. 1, pp. 837–844, 1996.

[39] J. R. Rice, "Inelastic constitutive relations for solids: an internal-variable theory and its application to metal plasticity," *Journal of the Mechanics and Physics of Solids*, vol. 19, no. 6, pp. 433–455, 1971.

[40] K. H. Roscoe and J. B. Burland, "On the generalized stress-strain behavior of 'wet' clay," in *Engineering Plasticity*, pp. 535–609, Cambridge University Press, Cambridge, UK, 1968.

[41] L. Luckner, M. T. van Genuchten, and D. R. Nielsen, "A consistent set of parametric models for the two-phase flow of immiscible fluids in the subsurface," *Water Resources Research*, vol. 25, no. 10, pp. 2187–2193, 1989.

[42] W. S. Sillers, *The mathematical representation of the soil-water characteristic curve [Ph.D. thesis]*, University of Saskatchewan, Saskatchewan, Canada, 1997.

[43] D. Gallipoli, A. Gens, R. Sharma, and J. Vaunat, "An elasto-plastic model for unsaturated soil incorporating the effects of suction and degree of saturation on mechanical behaviour," *Géotechnique*, vol. 53, no. 1, pp. 123–135, 2003.

[44] R. A. Fisher, "On the capillary forces in an ideal soil; correction of formulae given by W. B. Haines," *Journal of Agricultural Science*, vol. 16, no. 3, pp. 492–505, 1926.

[45] N. Lu and W. J. Likos, "Suction stress characteristic curve for unsaturated soil," *Journal of Geotechnical and Geoenvironmental Engineering*, vol. 132, no. 2, pp. 131–142, 2006.

[46] A. Raveendiraraj, *Coupling of mechanical behaviour and water retention behaviour in unsaturated soils [Ph.D. thesis]*, University of Glasgow, Glasgow, UK, 2009.

[47] M. Feng and D. G. Frelund, "Hysteresis influence associated with thermal conductivity sensor measurements," in *Proceedings of the 52nd Canadian Geotechnical Conference and Unsaturated Soil Group, Proceeding from Theory to the Practice of Unsaturated Soil Mechanics*, pp. 651–657, Regina, Canada, 1999.

[48] R. S. Sharma, *Mechanical behavior of an unsaturated highly expansive clays [Ph.D. thesis]*, University of Oxford, Oxford, UK, 1998.

Hindawi Publishing Corporation
Journal of Applied Mathematics
Volume 2013, Article ID 134124, 15 pages
http://dx.doi.org/10.1155/2013/134124

Research Article

Pile-Reinforcement Behavior of Cohesive Soil Slopes: Numerical Modeling and Centrifuge Testing

Liping Wang and Ga Zhang

State Key Laboratory of Hydroscience and Engineering, Tsinghua University, Beijing 100084, China

Correspondence should be addressed to Ga Zhang; zhangga@tsinghua.edu.cn

Received 6 June 2013; Accepted 29 July 2013

Academic Editor: Fayun Liang

Centrifuge model tests were conducted on pile-reinforced and unreinforced cohesive soil slopes to investigate the fundamental behavior and reinforcement mechanism. A finite element analysis model was established and confirmed to be effective in capturing the primary behavior of pile-reinforced slopes by comparing its predictions with experimental results. Thus, a comprehensive understanding of the stress-deformation response was obtained by combining the numerical and physical simulations. The response of pile-reinforced slope was indicated to be significantly affected by pile spacing, pile location, restriction style of pile end, and inclination of slope. The piles have a significant effect on the behavior of reinforced slope, and the influencing area was described using a continuous surface, denoted as *W-surface*. The reinforcement mechanism was described using two basic concepts, *compression effect* and *shear effect*, respectively, referring to the piles increasing the compression strain and decreasing the shear strain of the slope in comparison with the unreinforced slope. The pile-soil interaction induces significant *compression effect* in the inner zone near the piles; this effect is transferred to the upper part of the slope, with the *shear effect* becoming prominent to prevent possible sliding of unreinforced slope.

1. Introduction

Landslides are one of the severest geologic hazards around the world, the prevention of which is of great interest to engineers and researchers. The stabilizing pile, an important reinforcement structure, has been widely used to support unstable slopes in the last few decades [1–3]. Many methods have been proposed to form a good basis for proper design of pile-reinforced slopes [4, 5]; however, there are a few important issues to be clarified for the application of such piles in slope engineering. Therefore, systematical investigations are required on the behavior and reinforcement mechanism of pile-reinforced slopes.

The behavior of pile-reinforced slope can be investigated by using a diverse range of research approaches, which can be generally divided into three categories: field observations, model tests, and numerical analyses. Field observation is an essential approach to obtain first-hand data of reinforced slopes. For example, long-term monitoring was used to analyze the bending moments and displacements of the piles that were employed for a railway embankment [2]. Nevertheless, boundary conditions or loading conditions cannot be easily changed in a field test, which restricts such an approach to the study of the reinforcement mechanism.

Model tests offer a powerful approach to investigate the behavior and failure mechanism of a reinforced slope by efficiently considering various factors. A series of 1 g model tests were used to investigate the behavior of a pile-stabilized sandy slope [6, 7]. The centrifuge model tests play an important role in such a category because they provide an accurate simulation of the gravity stress field and the gravity-related deformation process. Therefore, centrifuge modeling has been widely used to study reinforced slopes with different reinforcement structures, including piles, geomembranes, geotextiles, and soil nails [8–13]. The measurement was finite in the model tests due to the small size of the model and the limitation of measurement technology; for example, the stress state of the slope cannot be measured with sufficient accuracy.

Numerical analysis can yield comprehensive information about the response of the slope; thus, a few different types of numerical methods were developed or used to study the reinforced slopes, such as the limit equilibrium method [14, 15], limit analysis [16], the finite-element method [17], and other rigorous or simplified methods [18]. For example, Won et al. compared the predictions by limit equilibrium analysis and three-dimensional numerical analysis involving a shear strength reduction technique for a slope-pile system [19]. A three-dimensional numerical analysis was used to investigate the influence of sleeving on the pile performance in a sloping ground [20, 21]. The FLAC3D program was used to analyze the response of piles in an embankment slope with a translational failure mode, and the results showed that the pile-soil relative stiffness has a significant influence upon the piles' failure mode [22]. Except for the algorithm, the effectiveness of numerical analysis of reinforced slope is also significantly affected by several aspects, such as the soil model, the soil-structure interface model, and their parameters, which should be acknowledged not to be sufficiently reliable due to the complexity of this problem.

Most previous investigations of the pile-reinforced slope focused on the response of the slope and piles as well as on the influence factors; from those, a few useful conclusions have been achieved. However, the response of the pile-reinforced slope under various types of load applications has not been illustrated in a fully comprehensive view. Moreover, the stabilizing mechanism—for example, why the avoidance of failure is induced by the piles—has not yet been adequately discovered. In other words, further study is needed to clarify how the local pile-soil interaction affects the deformation field of the entire slope and, therefore, increases the stability level. In addition, the deformation trends and main influence factors of the behavior of pile-reinforced slopes have not been fully discovered.

Based on the understanding of the main features of the numerical methods and model tests, an effective approach may be to combine both of the above methods to acquire a comprehensive description of the pile-reinforced slopes. Therefore, the observations from the model tests can be supplemented by a numerical method that has been verified by the model tests. The objective of this paper is to conduct such an attempt for the purpose of reinforcement mechanism analysis of pile-reinforced slope, including (1) to conduct centrifuge model tests of a cohesive soil slope using stabilizing piles, in comparison with the unreinforced slope; (2) to present a numerical scheme of the pile-reinforced slope and to confirm its effectiveness by simulating the centrifuge tests; (3) to analyze the behavior of the reinforced slope by using the test observations and numerical analysis; (4) to describe the reinforcement mechanism; and (5) to discuss the main factors that influence the behavior of reinforced slopes.

2. Centrifuge Model Tests

The centrifuge model tests were conducted using the 50 g ton geotechnical centrifuge at Tsinghua University.

2.1. Model. The soil of the slope model was retrieved directly from the soil mountain of the Beijing Olympic Forest Park. The average grain size of the soil is 0.03 mm, and the plastic limit and liquid limit are 5% and 18%, respectively.

Figure 1 shows the photographic and schematic views of the model slope, reinforced using stabilizing piles. The unreinforced slope is identical except for removal of the piles. The model container for the tests, made of aluminum alloy, is 50 cm long, 20 cm wide, and 35 cm high. A transparent Lucite window was installed in one container side to observe the deformation process of the soil.

The soil was compacted into the container by a 6-cm-thickness layer, with a dry density and water content of 1.4 g/cm^3 and 16%, respectively. The slope was obtained by removing the redundant soil, with an inclination of 1.5 : 1 and height of 25 cm. A 6 cm high horizontal soil layer under the slope was set to diminish the influence of the bottom container. In addition, silicone oil was painted on both sides of the container to decrease the friction on the slope.

A hollow square pipe, made of steel with an elastic modulus of 210 GPa, was used to simulate the stabilizing pile of the reinforced slope. The pipe was 1.4 cm along the side length of the section, with a wall thickness of 1.5 mm. This is equivalent to a prototype pile with a side length of 0.7 m at 50 g-level. These piles were inserted in the slope, without special fixation, at a single row 10 cm apart and 6 cm far away from the slope toe. Half-section piles were used near both container sides to approximate the plane-strain condition (Figure 1(c)).

2.2. Measurements. An image-record and displacement measurement system was used to record the images of soil during the centrifuge tests [23], which are used to determine the displacement history of an arbitrary point of soil, without disturbing the soil itself, by an image-correlation-analysis algorithm [24]. The effectiveness of this measurement system was realized by embedding white particles laterally in the soil (Figure 1(a)). The measurement accuracy can reach 0.02 mm based on the model dimension for the centrifuge tests in this paper. In addition, a few patterns with significant grey difference were affixed onto the pile to obtain displacement history of the pile on the basis of image analysis. The area within the dotted line was used for displacement measurements owing to the requirement of the measurement system (Figure 1(b)); the main deformation zone can be covered. Cartesian coordinates were established with the origin as the intersection between the slope bottom and inner sidewall of the pile; positive directions were specified (Figures 1(b) and 1(c)).

Four pairs of strain gauges were attached to the inner walls of the middle pile to measure the strain distribution along the shaft (Figure 1(b)). They can be used to derive the bending moment and axial load of the pile.

2.3. Test Procedure. The model slope was installed on the centrifuge machine, and increasing centrifugal acceleration was applied at steps of 5 g. Each acceleration step was maintained for several minutes until the deformation of the slope became stable. This process was terminated at 50 g-level when the unreinforced slope exhibited significant failure.

2.4. Observations. It should be noted that all of the results are based on the model dimension in this paper. Figure 2

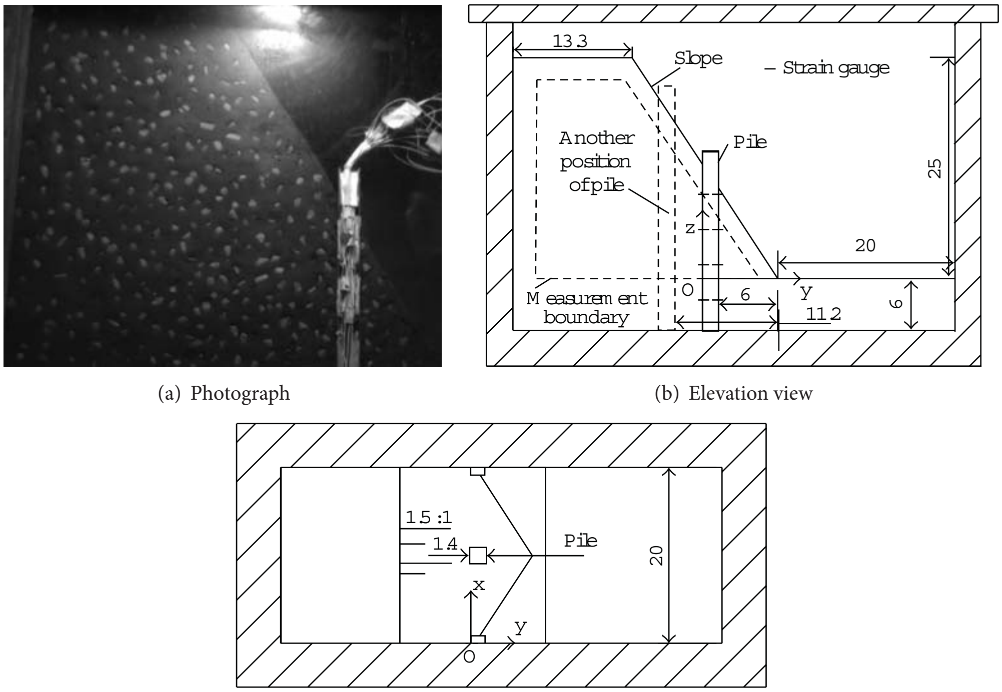

(a) Photograph

(b) Elevation view

(c) Vertical view

Figure 1: Schematic view of the model of reinforced slope (unit: cm).

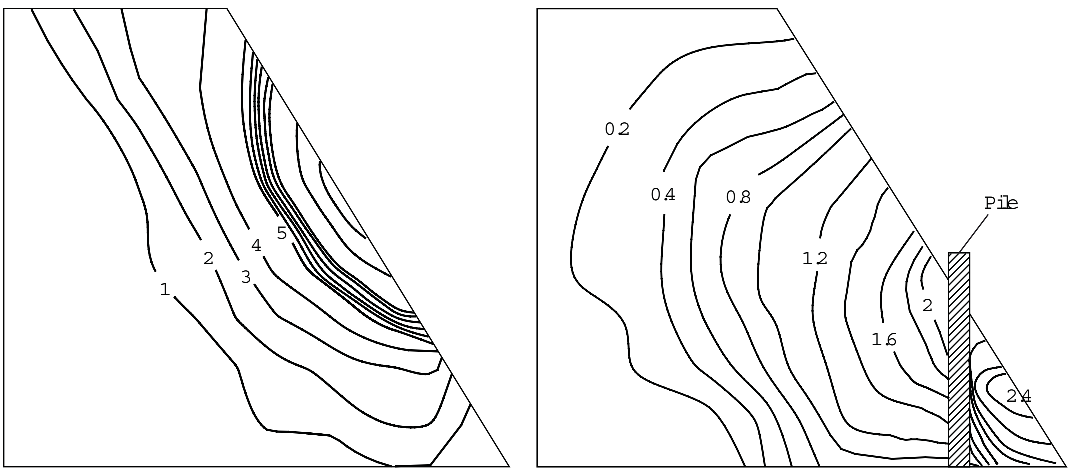

(a) Unreinforced slope at failure state

(b) Pile-reinforced slope

Figure 2: Horizontal displacement contours of slopes at 50 g-level (unit: mm).

shows the horizontal displacement distribution of the pile-reinforced and unreinforced slopes at 50 g-level; the borders in the figures were designated as the dotted area in Figure 1(b), but these do not correspond to the actual slope borders. It can be seen that a significant landslide occurred in the unreinforced slope when the centrifuge acceleration reached 50 g (Figure 2(a)): there was significant concentration of deformation so that the slide body can be easily distinguished from the base body via the contour lines. On the other hand, the reinforced slope only exhibited significant deformation due to the increase of centrifugal acceleration; a landslide was avoided at 50 g-level (Figure 2(b)). This indicated that the piles significantly increased the stability level of the slope. Moreover, the deformation of the reinforced slope was significantly smaller than that of the unreinforced slope, demonstrating that the piles had a significant effect on the deformation of the slope.

3. Numerical Analysis

3.1. Analysis Model. A three-dimensional finite element method was used to simulate the pile-reinforced slope under the condition of the centrifuge model test based on geotechnical stress-strain FEM software, termed TOSS3D, that has been widely used for embankments in China [25]. A new iterative routine was developed to simulate the successive increase of centrifugal acceleration in the software. The explicit increment scheme was used in the nonlinear static FE analysis. A substep was divided into several subincrements to simulate the nonlinear loading. An iterative algorithm was employed to obtain the stress-strain states of the slope within a subincrement, with a trial algorithm used to judge loading states of the geomaterials and contact states of the interface.

A three-dimensional FE mesh was established with accurate simulation of the slope model for centrifuge tests (Figure 3). The soil was described using hexahedron elements with eight nodes. The soil was described using an elastoplasticity model that can reasonably capture the dilatancy behavior of the soil [25]. The model parameters were determined from triaxial compression tests and adjusted slightly in the numerical analysis for a better fit to the test observations. The parameters and their values are listed in Table 1 and their definitions could be referred to [25]. It should be noted that the cohesion strength parameter, c, was a bit greater than the empirical. This may be partially because the boundary effect on the model slope in the centrifuge model tests was considered by the strength parameters of the soil. The interface elements were set between the pile and neighboring soil and between the container sides and neighboring soil. The interface was described using an elastoplasticity damage model, which provides a unified description of monotonic and cyclic behavior, including volumetric behavior [26]. This model was used for many soil-structure systems, such as high concrete-faced rockfill dams [27]. The model parameters were determined by a series of shear tests under constant normal stress conditions. The parameters and their values are listed in Table 2 and their definitions could be referred to [26]. The pile was described using a linear elastic model, with elastic modulus of 210 GPa and Poisson's ratio of 0.3. A soft element set on the pile end to realize the movement of pile. Moreover, another case, with the pile located in the upper slope, as shown in Figure 1(b), was also considered in the mesh. The boundaries of the model slope were all fixed (Figure 3). The mesh was finally obtained according to the symmetry of this problem, involving 8448 nodes and 7140 elements in total.

Table 1: Model parameters of the elastoplasticity model for soil.

c (kPa)	ϕ_0 (°)	R_f	K	n	G	F	D
50	35	0.7	92	0.15	0.05	0.15	1.5

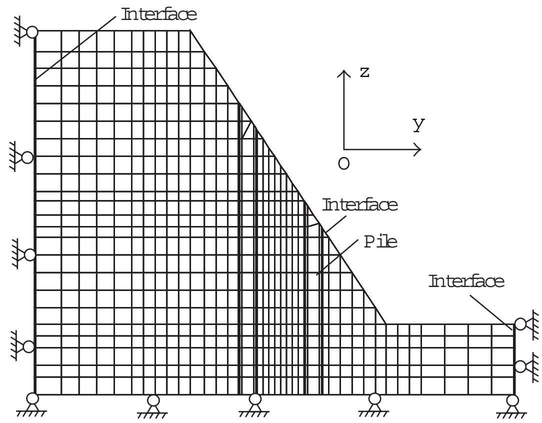

(a) Elevation view

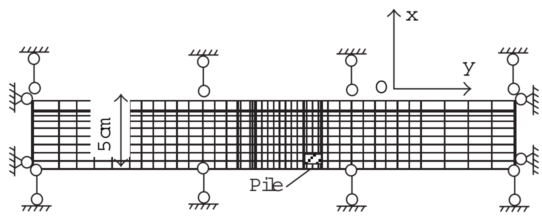

(b) Vertical view

Figure 3: Mesh and boundary of the slope for numerical analysis.

3.2. Verification. The numerical predictions of displacement response of the reinforced slope were compared with the measurements of the centrifuge model test to verify the effectiveness of the numerical analysis.

Figure 4 shows a comparison of test results and numerical predictions of the contours of displacement of the reinforced slope at 50 g-level. It can be seen that the predicted curve showed a good fit to the test result; this demonstrates that the numerical method provides a reasonable description of the overall performance of the slope. Close comparisons of displacement distribution between the test results and numerical predictions were made on several vertical sections (Figure 5). The horizontal and vertical displacements exhibited the maximum at the middle and top of the slope, respectively. These comparisons showed that the numerical prediction curves were in satisfactory agreement with the test results at different locations. In addition, the vertical displacement histories of a typical point of the slope indicated that the vertical displacement increased with increasing centrifugal acceleration (Figure 6), and the numerical prediction showed a good fit to the test observation.

The response of the pile was also used for the comparison of numerical analysis and test results (Figure 7); a satisfactory fit can be found. It should be noted that we used the difference between the vertical strains obtained from the strain gauges on the left and right sides of the pile to consider the bending behavior (Figure 7(b)); this difference exhibited the maximum at the middle part.

According to the comparison results, it can be concluded that the numerical analysis is effective in capturing the primary behavior of a pile-reinforced slope. The numerical results can be further used to analyze the stress response of the reinforced slope, which is important for understanding the reinforcement behavior but difficult to be measured in the centrifuge model tests. Thus, a comprehensive stress-deformation response can be obtained by combining the numerical and physical simulations.

4. Stress-Deformation Behavior

The numerical results have shown that the stress-displacement response of the reinforced slope is approximated for

Table 2: EPDI model parameters of the interface.

$\varepsilon_{vd,ir,ult}$	α	β	φ_0 (°)	G_0	n_0	μ_0	m_0	k_0	m_{k0}	C_e	C_0
0.15	500	1.0	33	30	0.5	300	0.3	0	0.1	0.005	0.005

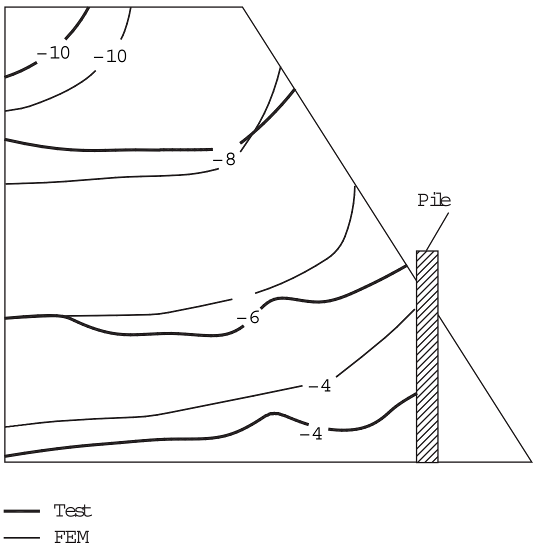

(a) Vertical displacement

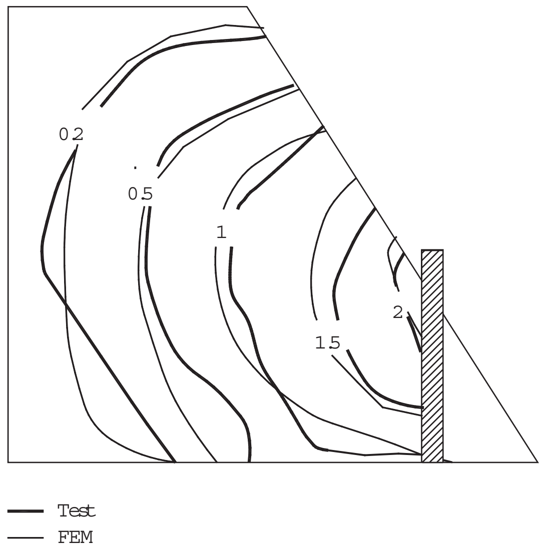

(b) Horizontal displacement

Figure 4: Displacement distribution comparison of numerical analysis and test results (unit: mm).

different sections, whether the piles pass through or not if the pile space is not large, as for most practical cases. Therefore, the behavior of the pile-reinforced slope was analyzed based mainly on the stress-displacement distribution of the lateral side of the slope that the pile passed through, so that the measurement results of the centrifuge model test can be combined with the predictions of numerical analysis.

The stress distribution of the slope was illustrated using numerical analysis at 50 g-level (Figure 8); there was significant stress concentration near the piles. This demonstrated that the piles had a significant effect on the stress state of the neighboring slope, as did the displacement measured by the tests (Figure 2). Figure 9 shows the stress histories of a typical point on the slope. The magnitude of stress increased with increasing centrifugal acceleration; similar rules can be found in the displacement histories (Figure 6). It can be concluded that the stress-deformation response at 50 g-level can be used as a representative time for further analysis.

4.1. Significant Influence Surface. The piles have a more significant influence on the horizontal displacement of the slope than on the vertical displacement, according to the comparison of reinforced and unreinforced slopes. Thus, the distributions of horizontal displacement at horizontal lines of five altitudes were carefully analyzed by comparing the reinforced and unreinforced slopes, covering the overall slope from top to bottom (Figure 10).

A close examination of displacement distribution at a horizontal line, $z = 7.1\,\text{cm}$, showed a significant difference between the reinforced and unreinforced slopes (Figure 10(d)). For the pile-reinforced slope, an evident inflection occurred near the pile. On the left side of the inflection, the horizontal displacement increased significantly from the inner slope area to the piles, whereas this rate of increase became relatively small on the right side. On the other hand, for the unreinforced slope, the horizontal displacement increased from the inner slope at an approximately constant rate near the piles. It can be concluded that the piles significantly changed the displacement distribution of the slope at a certain area near the piles, and this inflection can be regarded as a boundary point to indicate that the piles significantly affected the deformation.

The inflections can be found in the displacement distribution curves of the reinforced slope at all altitudes (Figure 10), including the area above the piles (Figures 10(a)–10(c)). Therefore, a continuous surface was obtained by connecting these inflections using a curve, as shown in Figure 10 by the dotted line, denoted as the *W-surface* in this paper. The horizontal displacement of the pile-reinforced slope exhibited different distribution rules on different sides of the *W-surface*.

Similar to the horizontal displacement, the horizontal stress can also be used to reflect the effect of the piles on the slope. Figure 11 shows the horizontal stress distributions on horizontal lines at two typical altitudes, located near and above the piles, with the position of the *W-surface* being determined from the displacement distribution. It can be seen that the stress distribution curve exhibited a significant change near the *W-surface*. This demonstrated that the *W-surface* outlines the area where the piles have a significant effect on the slope, including the displacement and stress

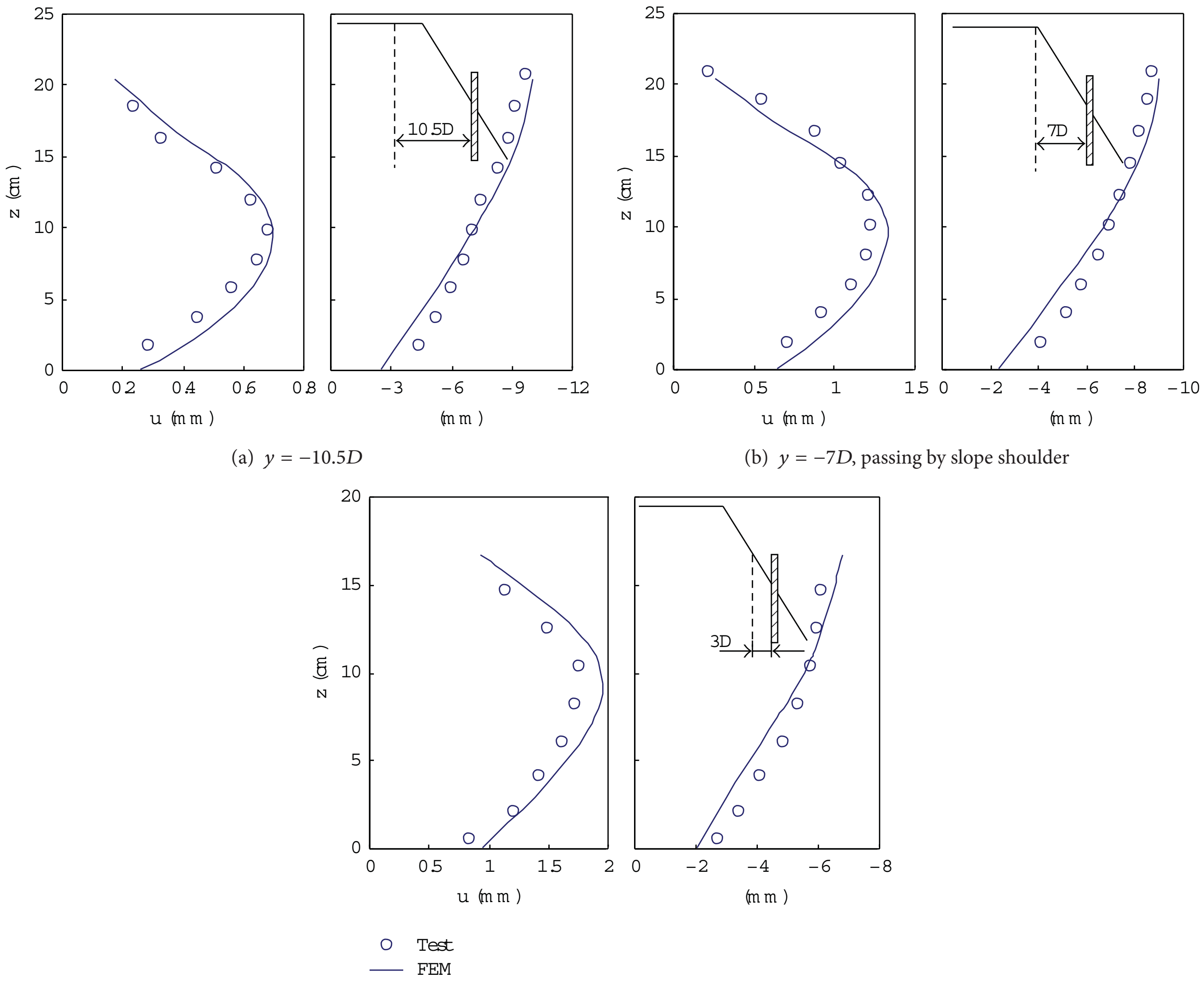

(a) $y = -10.5D$

(b) $y = -7D$, passing by slope shoulder

(c) $y = -3D$

Figure 5: Displacement distribution comparison of numerical analysis and test results on different vertical sections. u: horizontal displacement; v: vertical displacement; D: pile diameter.

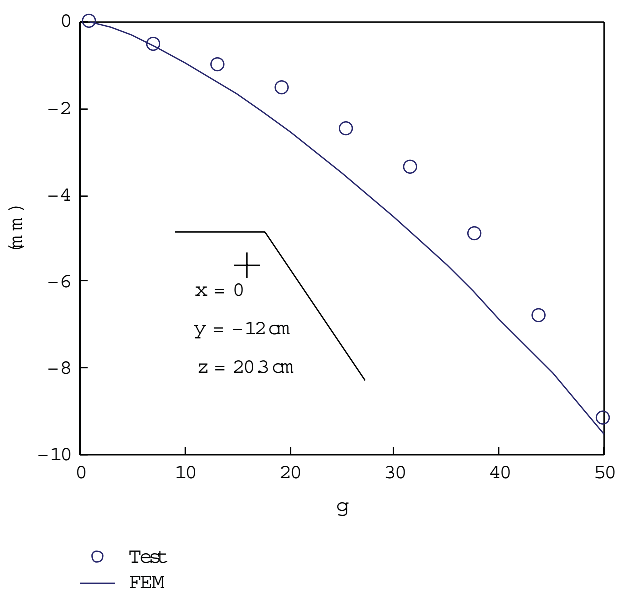

Figure 6: Vertical displacement history of a typical point by numerical analysis and test results. v: vertical displacement; g: g-level.

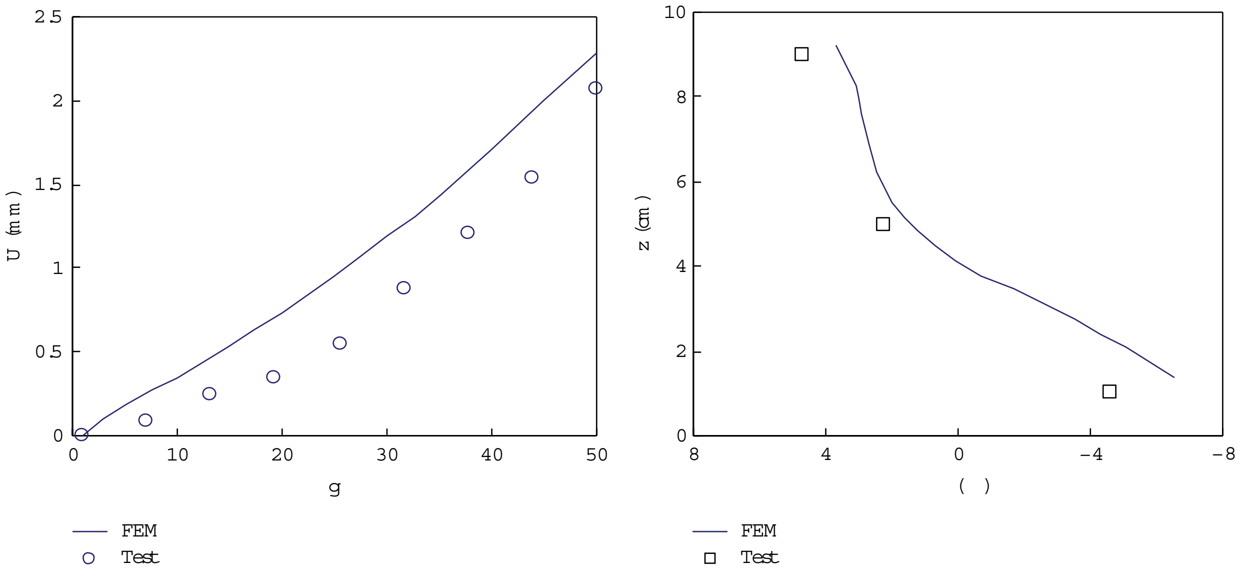

(a) Horizontal displacement of pile top

(b) Vertical strain distribution

Figure 7: Response of the pile by numerical analysis and test results. u: horizontal displacement of pile top; $\Delta\varepsilon$: vertical strain difference between right and left sides of pile.

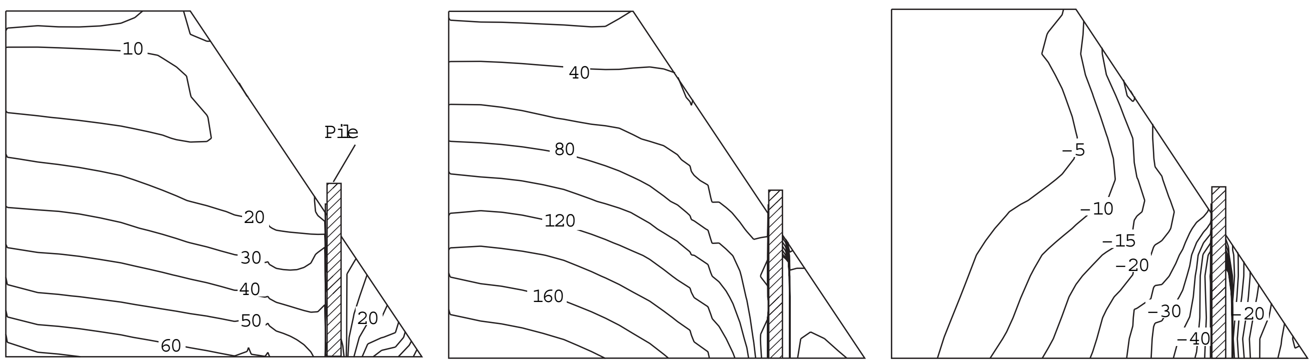

(a) Horizontal stress

(b) Vertical stress

(c) Shear stress

Figure 8: Stress distribution of the slope at 50 g-level by numerical analysis (unit: kPa).

response. Thus, the *W-surface* can be used as an important index to describe the influence of piles on stress-deformation behavior of the reinforced slope.

4.2. Division of Zones. According to the *W-surface*, the reinforced slope behind the piles can be divided into two zones: one is where the slope is significantly affected by the piles, while the other is where the slope is insignificantly affected. The former was further examined by using the horizontal stress distribution of the slope at different vertical sections (Figure 12). The horizontal stress decreased with increasing altitude from the slope bottom; however, there was a significant inflection in the upper part of the slope. From this inflection, the change trend of the stress noticeably altered. It can be concluded that the stress states of the slope were significantly different on the different sides of the inflection, and the reason can be attributed to the effect of the piles.

Thus, another continuous surface was yielded by connecting these inflections using a curve, as the dotted line showed in Figure 12. This surface, denoted as the *L-surface* in this paper, indicates the boundary where the effect of the piles exhibited different features on different sides. Accordingly, the slope can be divided into three zones behind the piles according to these two surfaces (Figure 13).

The stress-deformation behavior exhibited different features in different zones. Zone A is the area at the left side of the *W-surface*, far from the piles. Thus, the piles had a small effect on this zone. For example, the horizontal displacement of the reinforced slope showed a similar distribution to the unreinforced slope in zone A. Zone B is above the *L-surface* and has a free surface. The change of deformation of the slope

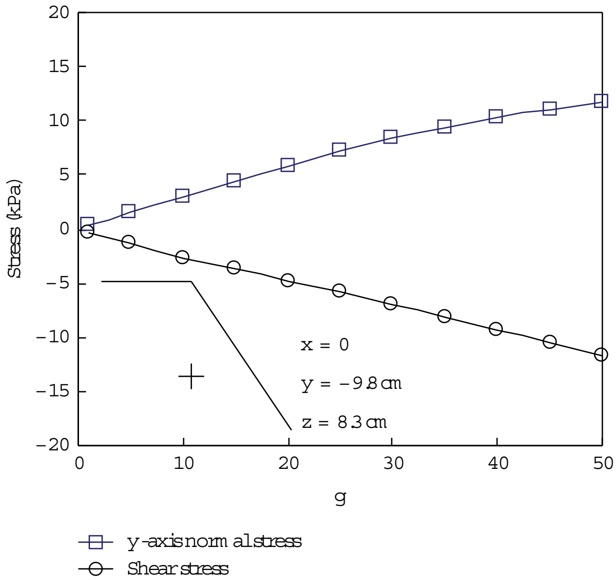

Figure 9: Stress history of a typical point by numerical analysis. *g*: g-level.

became flat in this zone; this demonstrated that the piles significantly restricted the deformation. Zone C is at the right side of the *W-surface* and directly contacts the piles. The piles significantly reduced the horizontal displacement of the soil in this zone; thus, the displacement distribution showed a flat curve. Moreover, the horizontal stress exhibited a significant change with increasing distance from the piles. This demonstrated that the piles induced significant compression effect in this zone.

5. Reinforcement Mechanism

The strain of a soil element within the slope was introduced to analyze the pile-reinforcement mechanism of the slope by comparing the reinforced and unreinforced slopes. This strain can be determined using the measured displacement of the centrifuge model tests because the measurement may be more reliable than the numerical result, especially at the failure state of the unreinforced slope. A two-dimensional, four-node square isoparametric element, 1 cm long, was used for strain analysis. The strain at the center was thought to be the one of this element that was assumed to be uniform within the element.

The deformation of soil can be divided into two independent components owing to shear and compression applications. This implies that shear and compression play different roles in the deformation and failure of a slope. For example, the formation of a slip surface may significantly depend on the increase in shear strain, whereas a tensional crack, which commonly occurs at the top of a slope, is induced mainly by a decrease in compression strain. It can be concluded that the piles significantly changed the strain state of the slope and thus increased the stability level of the slope. Therefore, the pile-reinforcement mechanism can be analyzed using the effects of the piles on the shear and compression strains.

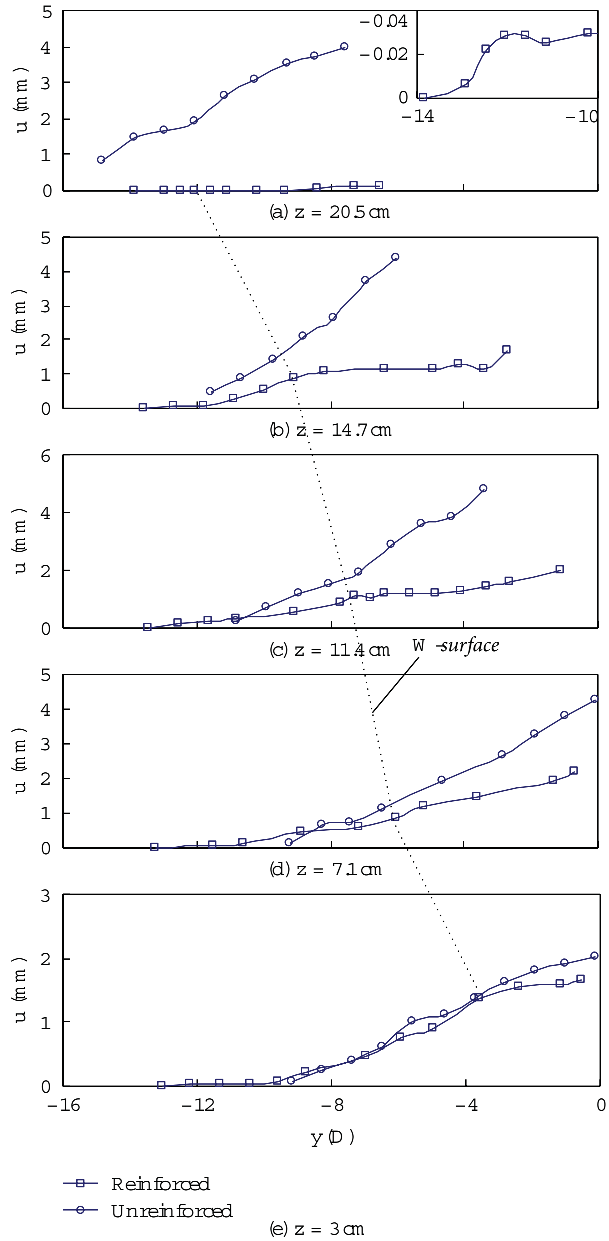

Figure 10: Horizontal displacement distributions on horizontal sections at 50 g-level by test observation. *u*: horizontal displacement; *D*: pile diameter.

The deformation due to shear was indicated by the slope-direction shear strain. The horizontal compression strain was used to indicate the deformation due to compression. Figure 14 shows the strain histories of typical elements in the three zones (positions are shown in Figure 13); the elements of the unreinforced slope, corresponding to those in the reinforced slope, are also presented for comparison. It should be noted that the horizontal compression strains of these elements were all negative, indicating dilation in the horizontal direction.

In zone B, the shear strain of a typical element in the unreinforced slope increased rapidly with increasing centrifugal

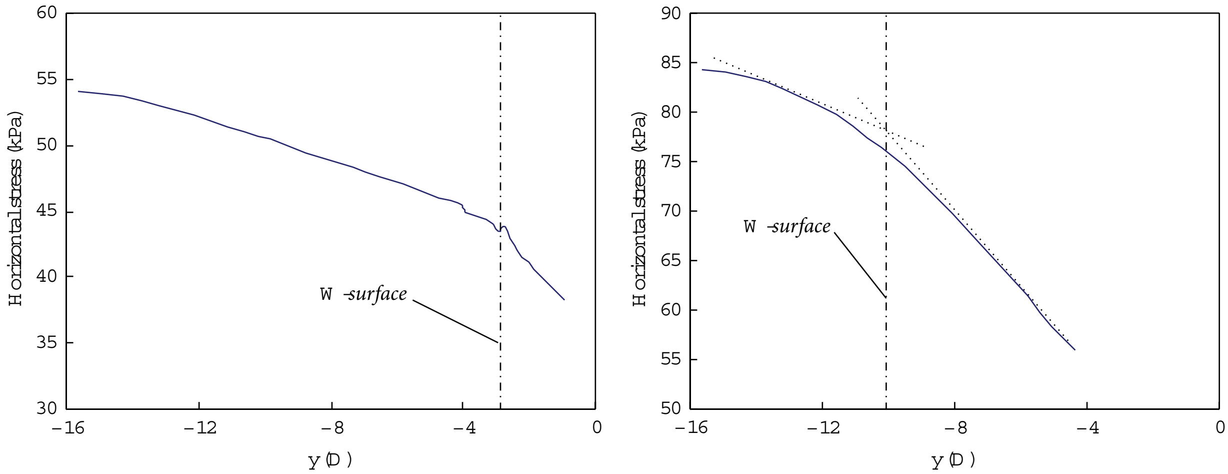

(a) $z = 3.5$ cm

(b) $z = 16.5$ cm

Figure 11: Stress distribution on a horizontal line by numerical analysis.

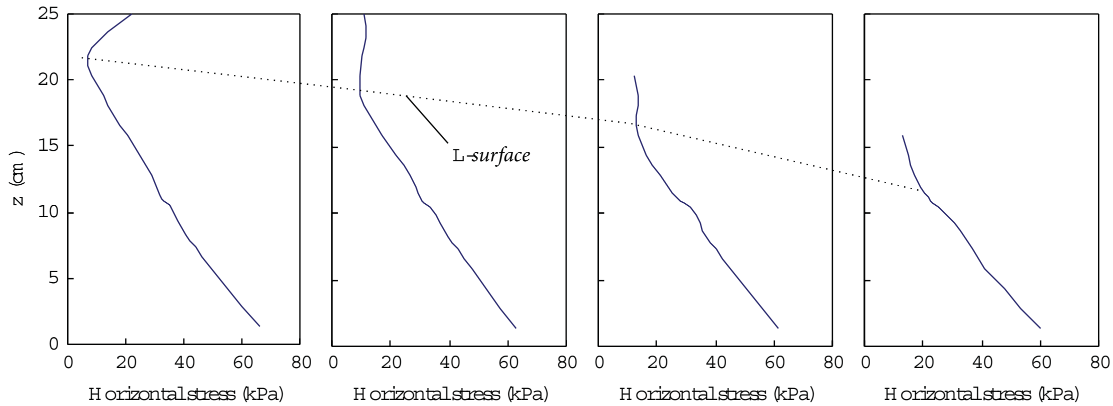

(a) $y = -10.5D$

(b) $y = -7.5D$

(c) $y = -4.5D$

(d) $y = -2.5D$

Figure 12: Stress distributions on different vertical sections at 50 g-level by numerical analysis.

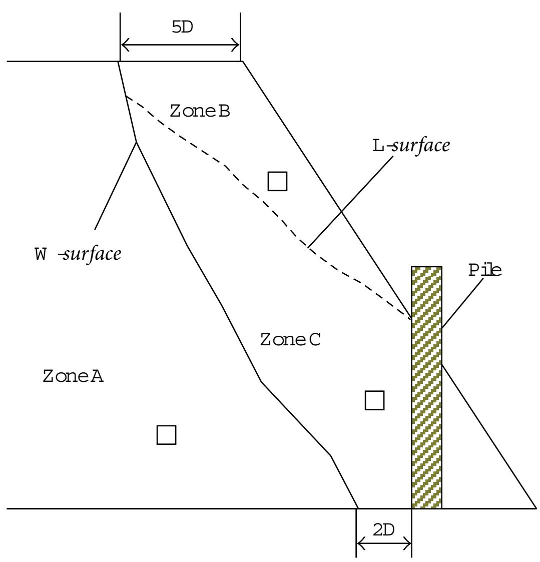

Figure 13: Division of zones with different features. D: pile diameter.

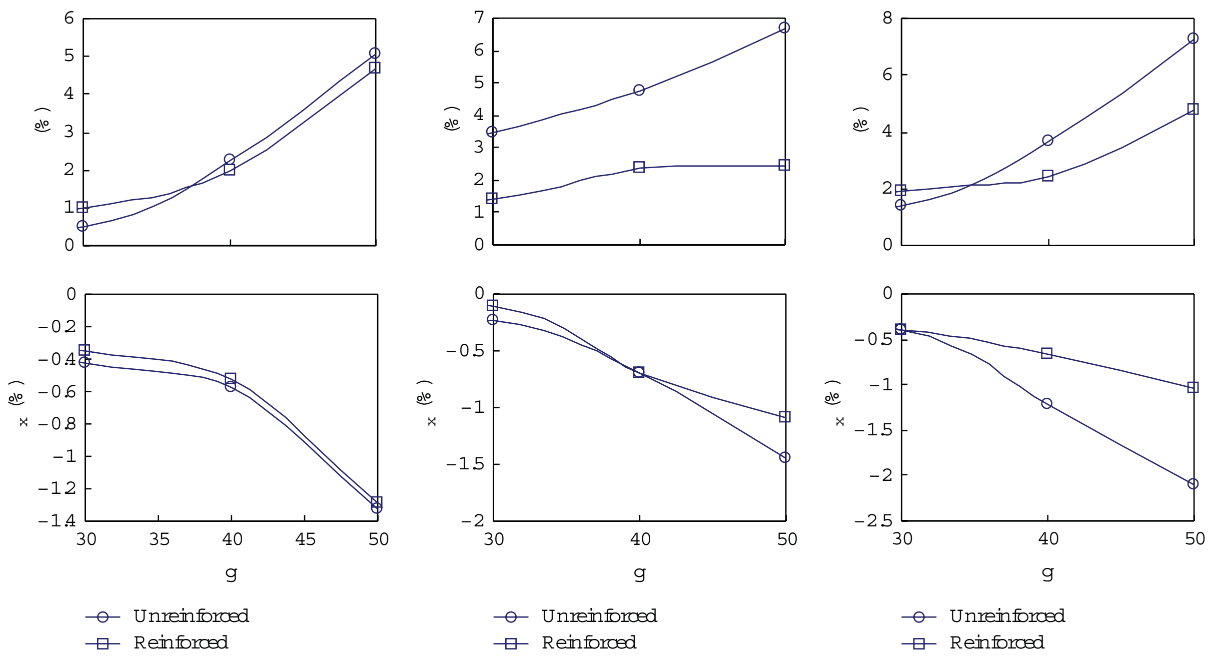

(a) Zone A (b) Zone B (c) Zone C

Figure 14: Strain history of typical elements of different zones by test observation. γ: slope-direction shear strain; ε_x: horizontal compression strain; g: g-level.

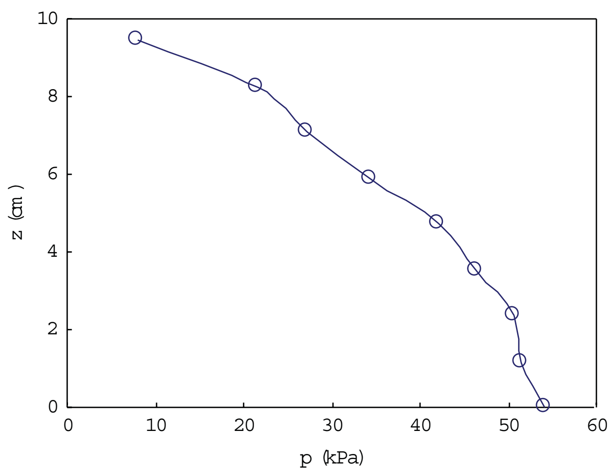

Figure 15: Earth pressure on the pile by numerical analysis. p: earth pressure.

acceleration (Figure 14(b)). This strain reached a significant magnitude at 50 g-level when the landslide, just across this element, occurred. However, the shear strain increased at a smaller rate and reached a lower level far from failure if the piles were used. Thus, a basic concept, *shear effect*, was introduced to describe that shear strain was decreased due to the effect of the piles. In other words, a significant *shear effect* of piles in zone B arrested the formation of a slip surface. Accordingly, the horizontal compression strain increased due to the piles, which was described using another basic concept, *compression effect*. There was also significant *compression effect* of piles in zone B; however, it can be concluded that the *shear effect* was primary.

The history of the compression strain showed that this strain in the reinforced slope was significantly larger than that of the unreinforced one; this demonstrated that there was significant *compression effect* of piles in zone C (Figure 14(c)). Closer examination showed that the *compression effect* was more significant than the *shear effect*, though the *shear effect* of the piles was also distinct.

The compression and shear strains both exhibited minor differences in zone A for the reinforced and unreinforced

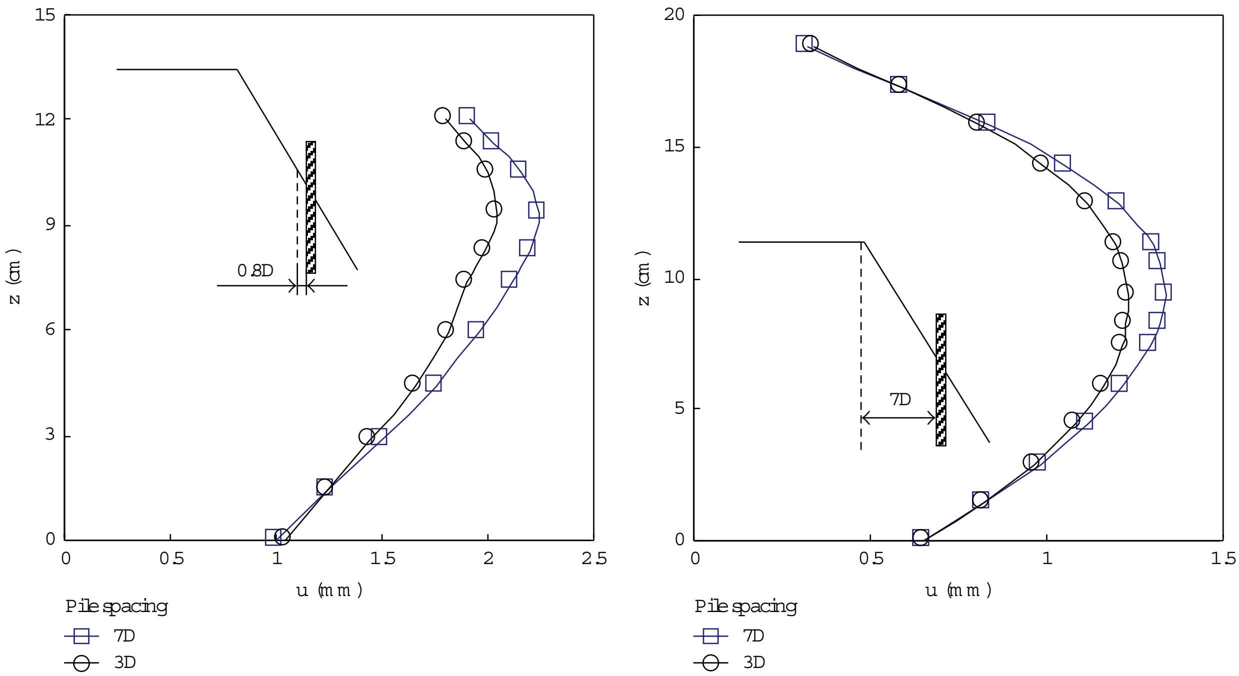

(a) $y = -0.8D$

(b) $y = -7D$, passing by slope shoulder

Figure 16: Influence of pile spacing by numerical analysis. D: pile diameter; u: horizontal displacement.

slopes (Figure 14(a)); this indicated that both the *shear effect* and *compression effect* were negligible in this zone.

Figure 15 shows the earth pressure on the inner side of the pile, obtained by numerical analysis. The earth pressure decreased with increasing altitude, similar to a distribution of earth pressure for a retaining wall. Combined with the strain analysis results at the overall slope level, the reinforcement mechanism can be demonstrated using the *shear effect* and *compression effect* of piles, which were of different levels in different zones, as follows: the pile and neighboring soil exhibited a significant interaction due to loading. This interaction was transferred to the adjacent zone and induced a significant *compression effect* (zone C). This *compression effect* transferred upwards and caused a prominent *shear effect* (zone B), arresting the possible sliding and increasing the stability level of the slope.

6. Influence Factors

The numerical analysis was used to compute different cases to discuss the influence factors of the behavior of pile-reinforced slopes by altering several factors based on the centrifuge test condition, including pile spacing, pile location, restriction style of pile end, and inclination of slope. According to previous analysis, the horizontal displacement of the lateral side of the slope that the piles pass across is used as the characteristic index to illustrate the effect of these factors.

6.1. Pile Spacing. The pile spacing was reduced to $3D$ (pile diameter) from approximately $7D$ of the test condition. Figure 16 compares the horizontal displacements according to the different pile spacings, both obtained from numerical analysis, to discuss the influence rules. The horizontal displacement of the slope exhibited a small decrease when the pile spacing was reduced; such a difference decreased with increasing distance from the piles. The fundamental rules of horizontal displacement were consistent for different pile spacings.

6.2. Location of Pile. The piles were moved upwards several centimeters in the comparison case, as described using the dashed line in Figure 1(b). The horizontal displacements according to new and original locations of piles were obtained from numerical analysis (Figure 17). The horizontal displacement of the slope exhibited a significant decrease near the piles if the pile was located at an upper position, which may be partly attributed to the new location of piles being farther from the free surface of the slope. The difference decreased with increasing distance from the slope surface and can be ignored at the section passing by the slope shoulder (Figure 17(c)). It can be derived that the distributions of horizontal displacement of the pile-reinforced slope were consistent for different pile locations.

6.3. Restriction Style of Pile End. The pile ends were all fixed on the container to prevent the relative movement between the piles and the container bottom, different from the test condition that the piles may move along the container bottom. Figure 18 compares the horizontal displacements according to the different restriction styles, both obtained from numerical analysis. The horizontal displacement of

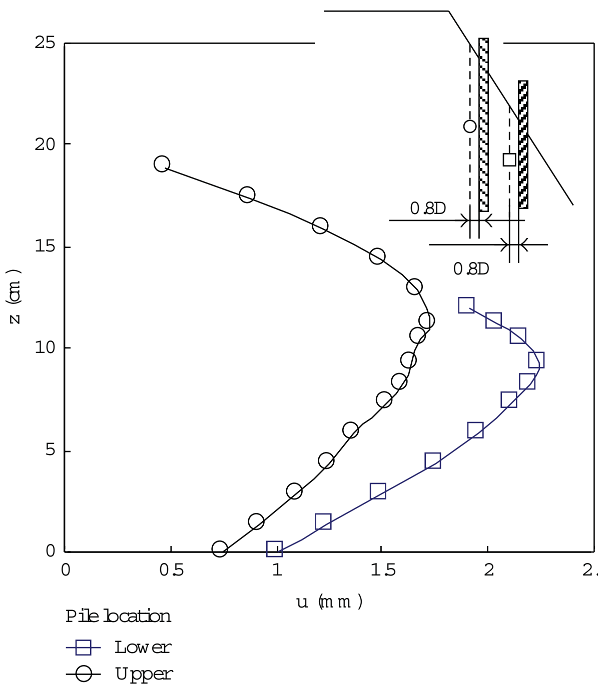

(a) 0.8D from pile

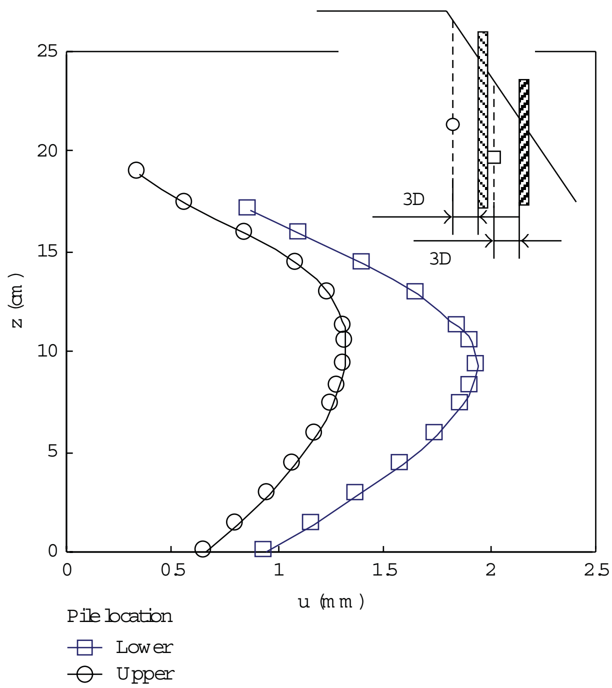

(b) 3D from pile

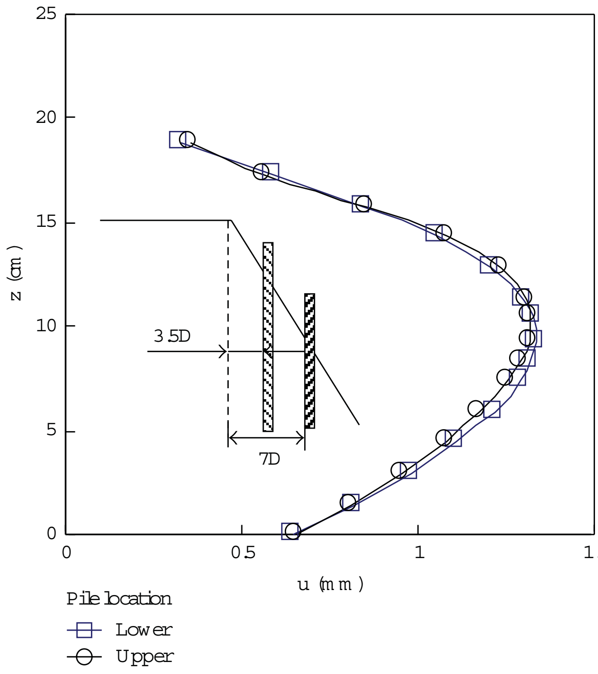

(c) $y = -7D$, passing by slope shoulder

FIGURE 17: Influence of positions of the pile by numerical analysis. D: pile diameter; u: horizontal displacement.

the slope significantly decreased, especially near the piles, when the pile ends were fixed. Overall, the fundamental rules of horizontal displacement of pile-reinforced slope can be found to be consistent regardless whether the restriction style of pile end was altered.

6.4. Inclination of Slope. The inclination of the slope was changed to 1 : 1 from the original 1.5 : 1 in the test condition, and the relative location of piles was maintained as in the original scheme. The horizontal displacements according to the different inclinations of slopes were yielded from numerical analysis (Figure 19). The horizontal displacement of the slope exhibited an evident decrease due to the decrease of inclination of slope. However, the distribution rules of horizontal displacement were consistent for the different inclinations of slope.

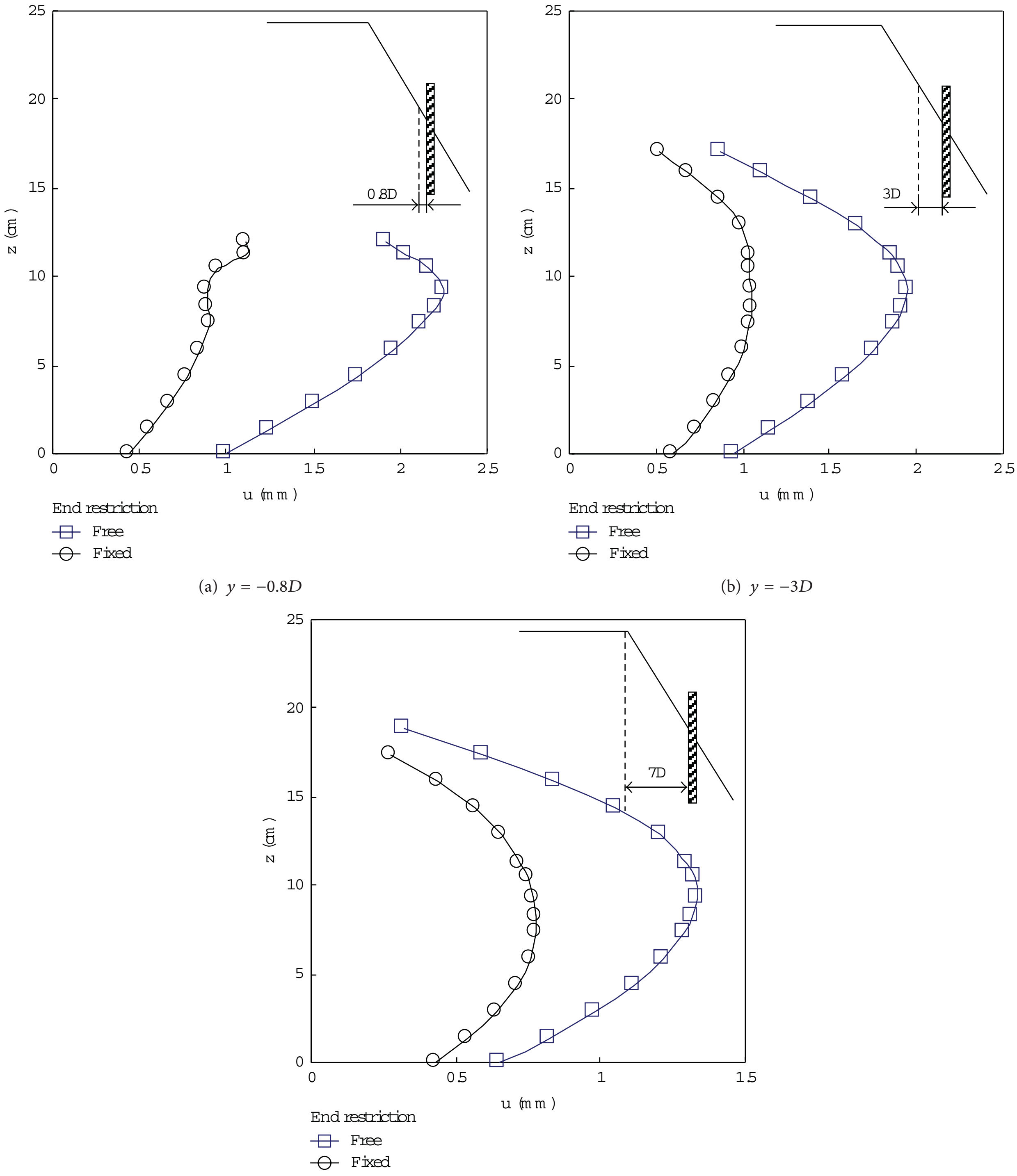

(a) $y = -0.8D$

(b) $y = -3D$

(c) $y = -7D$, passing by slope shoulder

Figure 18: Influence of fixing styles of the pile end by numerical analysis. D: pile diameter; u: horizontal displacement.

6.5. Summary. Based on the numerical analysis, it can be concluded that the behavior of the pile-reinforced slopes was similar for the different factors considered in this paper. As discussed in above texts, the two boundary surfaces, *W-surface* and *L-surface*, can be used as important indicators of the behavior of reinforced slope. Therefore, these surfaces were summarized corresponding to different factors according to the results from numerical analysis (Figure 20). It can be seen that both of the surfaces can be described using a definite format, though their positions and curvatures were affected by different factors. Thus, it is believed that the fundamental rules and reinforcement mechanism, derived in

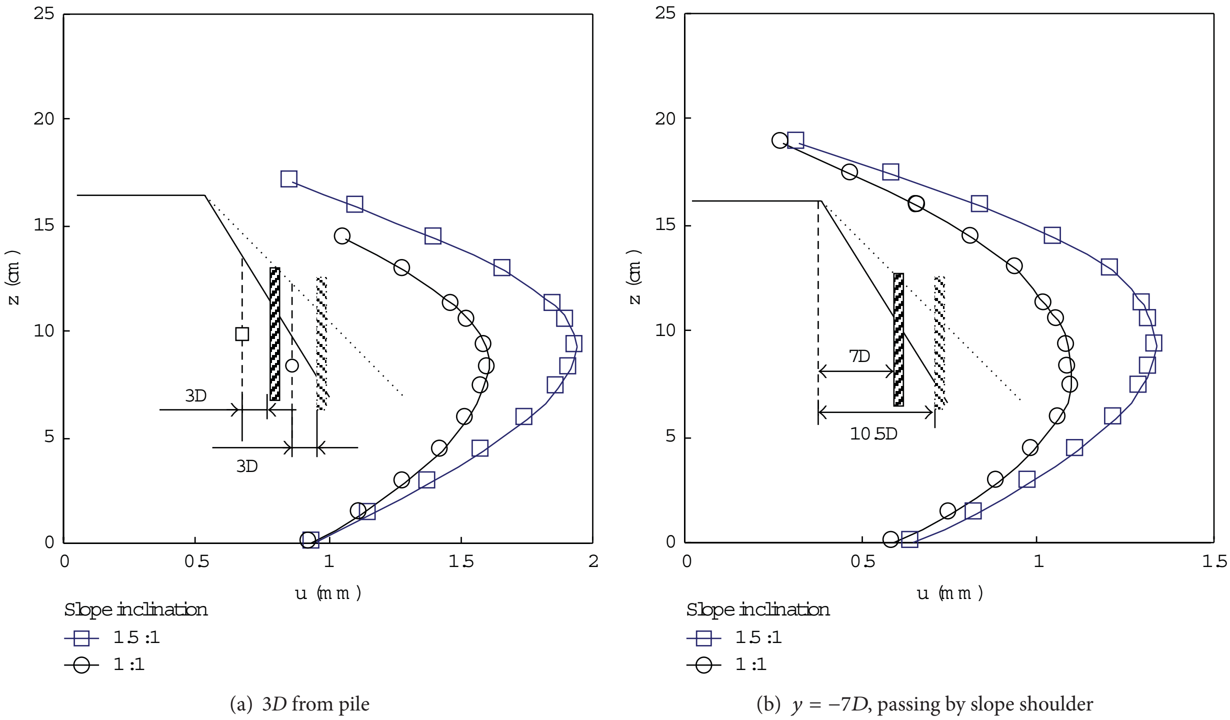

Figure 19: Influence of inclination of the slope by numerical analysis. D: pile diameter; u: horizontal displacement.

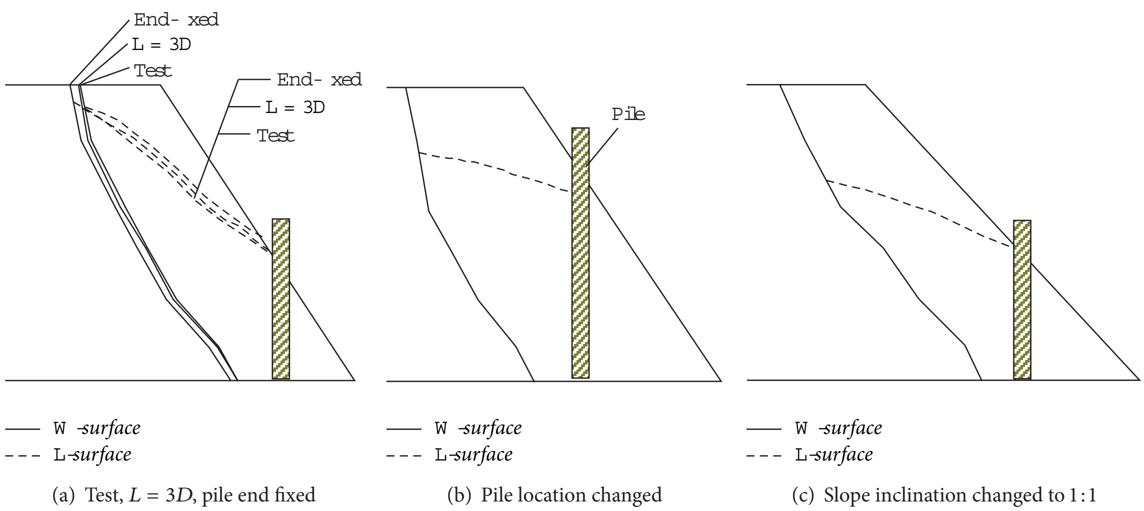

Figure 20: *W-surfaces* and *L-surfaces* considering different factors. L: pile spacing; D: pile diameter.

this paper, may be suitable for most practical pile-reinforced slopes.

7. Conclusions

The pile-reinforcement behavior of cohesive soil slope was investigated using numerical analysis and centrifuge model tests. The behavior and reinforcement mechanism of the pile-reinforced slope were obtained by considering different influence factors. The main conclusions are as follows.

(1) The piles arrested a landslide that occurred in an unreinforced slope, thus, significantly increasing the stability level of the slope.

(2) A numerical model was established and confirmed to be effective in capturing primary behavior of the pile-reinforced slope. Thus, a comprehensive understanding of stress-deformation response can be achieved by combining the numerical and physical simulations.

(3) The piles have a significant effect on the behavior of reinforced slope; the boundary of the influenced area can be described using a continuous surface.

(4) The pile-reinforcement mechanism can be described using two basic concepts: *compression effect* and *shear effect*, which, respectively, refer to the piles increasing the compression strain and decreasing the shear strain in comparison with unreinforced slope. The pile-soil interaction induces significant *compression effect* in the inner zone near the piles; this effect is transferred to the upper part of the slope, with the *shear effect* becoming prominent. As a result, possible sliding is prevented; the stability level of the slope is accordingly increased.

(5) The response of pile-reinforced slope was significantly affected by several factors such as pile spacing, pile location, restriction style of pile end, and inclination of slope; however, the behavior and reinforcement mechanism are consistent for the different factors considered in this paper.

Acknowledgments

The study is supported by National Natural Science Foundation of China (nos. 51129902, 50979045) and the State Key Laboratory of Hydroscience and Engineering (no. 2013-KY-5).

References

[1] C. D. F. Rogers and S. Glendinning, "Improvement of clay soils in situ using lime piles in the UK," *Engineering Geology*, vol. 47, no. 3, pp. 243–257, 1997.

[2] J. A. Smethurst and W. Powrie, "Monitoring and analysis of the bending behaviour of discrete piles used to stabilise a railway embankment," *Geotechnique*, vol. 57, no. 8, pp. 663–677, 2007.

[3] M. Kimura, S. Inazumi, J. K. A. Too, K. Isobe, Y. Mitsuda, and Y. Nishiyama, "Development and application of H-joint steel pipe sheet piles in construction of foundations for structures," *Soils and Foundations*, vol. 47, no. 2, pp. 237–251, 2007.

[4] T. Ito and T. Matsui, "Methods to estimate lateral force acting on stabilizing piles," *Soils and Foundations*, vol. 15, no. 4, pp. 43–59, 1975.

[5] H. G. Poulos, "Design of reinforcing piles to increase slope stability," *Canadian Geotechnical Journal*, vol. 32, no. 5, pp. 808–818, 1995.

[6] M. A. El Sawwaf, "Strip footing behavior on pile and sheet pile-stabilized sand slope," *Journal of Geotechnical and Geoenvironmental Engineering*, vol. 131, no. 6, pp. 705–715, 2005.

[7] M. J. Thompson and D. J. White, "Design of slope reinforcement with small-diameter piles," in *Advances in Earth Structures: Research to Practice*, GSP 151, pp. 67–73, ASCE, 2006.

[8] A. Bouafia and A. Bouguerra, "Centrifuge testing of the behaviour of a horizontally loaded flexible pile near to a slope," *Canadian Geotechnical Journal*, vol. 32, no. 2, pp. 324–335, 1995.

[9] A. Porbaha and D. J. Goodings, "Centrifuge modeling of geotextile-reinforced steep clay slopes," *Canadian Geotechnical Journal*, vol. 33, no. 5, pp. 696–704, 1996.

[10] J. G. Zornberg, N. Sitar, and J. K. Mitchell, "Performance of geosynthetic reinforced slopes at failure," *Journal of Geotechnical and Geoenvironmental Engineering*, vol. 124, no. 8, pp. 670–683, 1998.

[11] N. I. Thusyanthan, S. P. G. Madabhushi, and S. Singh, "Tension in geomembranes on landfill slopes under static and earthquake loading-Centrifuge study," *Geotextiles and Geomembranes*, vol. 25, no. 2, pp. 78–95, 2007.

[12] L. Wang, G. Zhang, and J.-M. Zhang, "Nail reinforcement mechanism of cohesive soil slopes under earthquake conditions," *Soils and Foundations*, vol. 50, no. 4, pp. 459–469, 2010.

[13] L. P. Wang and G. Zhang, "Centrifuge model test study on pile reinforcement behavior of cohesive soil slopes under earthquake conditions," *Landslides*, 2013.

[14] T. Yamagami, J. Jiang -C, and K. Ueno, "A limit equilibrium stability analysis of slopes with stabilizing piles," in *Advances in Earth Structures: Research to Practice*, GSP 101, pp. 343–354, ASCE, 2000.

[15] G. Zhang and L. Wang, "Stability analysis of strain-softening slope reinforced with stabilizing piles," *Journal of Geotechnical and Geoenvironmental Engineering*, vol. 136, no. 11, pp. 1578–1582, 2010.

[16] E. Ausilio, E. Conte, and G. Dente, "Stability analysis of slopes reinforced with piles," *Computers and Geotechnics*, vol. 28, no. 8, pp. 591–611, 2001.

[17] F. Cai and K. Ugai, "Numerical analysis of the stability of a slope reinforced with piles," *Soils and Foundations*, vol. 40, no. 1, pp. 73–84, 2000.

[18] S. Jeong, B. Kim, J. Won, and J. Lee, "Uncoupled analysis of stabilizing piles in weathered slopes," *Computers and Geotechnics*, vol. 30, no. 8, pp. 671–682, 2003.

[19] J. Won, K. You, S. Jeong, and S. Kim, "Coupled effects in stability analysis of pile-slope systems," *Computers and Geotechnics*, vol. 32, no. 4, pp. 304–315, 2005.

[20] C. W. W. Ng and L. M. Zhang, "Three-dimensional analysis of performance of laterally loaded sleeved piles in sloping ground," *Journal of Geotechnical and Geoenvironmental Engineering*, vol. 127, no. 6, pp. 499–509, 2001.

[21] C. W. W. Ng, L. M. Zhang, and K. K. S. Ho, "Influence of laterally loaded sleeved piles and pile groups on slope stability," *Canadian Geotechnical Journal*, vol. 38, no. 3, pp. 553–566, 2001.

[22] G. R. Martin and C.-Y. Chen, "Response of piles due to lateral slope movement," *Computers and Structures*, vol. 83, no. 8-9, pp. 588–598, 2005.

[23] G. Zhang, Y. Hu, and J.-M. Zhang, "New image analysis-based displacement-measurement system for geotechnical centrifuge modeling tests," *Measurement*, vol. 42, no. 1, pp. 87–96, 2009.

[24] G. Zhang, D. Liang, and J.-M. Zhang, "Image analysis measurement of soil particle movement during a soil-structure interface test," *Computers and Geotechnics*, vol. 33, no. 4-5, pp. 248–259, 2006.

[25] G. Zhang, J.-M. Zhang, and Y. Yu, "Modeling of gravelly soil with multiple lithologic components and its application," *Soils and Foundations*, vol. 47, no. 4, pp. 799–810, 2007.

[26] G. Zhang and J.-M. Zhang, "Unified modeling of monotonic and cyclic behavior of interface between structure and gravelly soil," *Soils and Foundations*, vol. 48, no. 2, pp. 231–245, 2008.

[27] G. Zhang and J.-M. Zhang, "Numerical modeling of soil-structure interface of a concrete-faced rockfill dam," *Computers and Geotechnics*, vol. 36, no. 5, pp. 762–772, 2009.

Hindawi Publishing Corporation
Journal of Applied Mathematics
Volume 2013, Article ID 485632, 10 pages
http://dx.doi.org/10.1155/2013/485632

Research Article

Boundary Value Problem for Analysis of Portal Double-Row Stabilizing Piles

Cheng Huang

State Key Laboratory of Geomechanics and Geotechnical Engineering, Institute of Rock and Soil Mechanics, Chinese Academy of Sciences, Wuhan 430071, China

Correspondence should be addressed to Cheng Huang; tjhuangcheng@163.com

Received 10 May 2013; Revised 26 July 2013; Accepted 29 July 2013

Academic Editor: Fayun Liang

This paper presents a new numerical approach for computing the internal force and displacement of portal double-row piles used to stabilize potential landslide. First, the new differential equations governing the mechanical behaviour of the stabilizing pile are formulated and the boundary conditions are mathematically specified. Then, the problem is numerically solved by the high-accuracy Runge-Kutta finite difference method. A program package has been developed in MATLAB depending on the proposed algorithm. Illustrative examples are presented to demonstrate the validity of the developed program. In short, the proposed approach is a practical new idea for analyzing the portal double-row stabilizing pile as a useful supplement to traditional methods such as FEM.

1. Introduction

Double-row stabilizing piles have been widely used in slope reinforcement engineering and treatment of landslide geological disasters, which have some advantages such as larger rigidity, less displacement in the top of the piles, and large resisting force. Existing methods for the analysis of double-row stabilizing piles can be generally classified into the following two categories [1–6]: (1) coupled method (continuum analysis) that simultaneously solves pile response and slope stability [7]; (3) uncoupled method which deals with pile and slope separately. In the uncoupled method, pile-soil interaction is commonly represented by equivalent Winkler or *p*-*y* springs [8–13].

As for coupled method, the finite element method is certainly the most comprehensive approach to study pile-slope stability. However, its use generally requires high numerical costs and accurate measurements of material properties. This makes the use of this method rather unattractive for practical applications [6].

To date, in practical engineering applications, the uncoupled method is the most widely used approach to design the double-row reinforcing piles to increase slope stability due to its simplicity of use. First, the lateral force acting on the pile segment above the slip surface due to soil movement is evaluated usually by the limit equilibrium method. Second, the response of the double-row pile subjected to lateral loading is analysed by FEM modeling it as a beam resting on linear or nonlinear soil/rock spring supports. The FEM modeling is reasonably accurate but complicated and time consuming.

In this paper, a new uncoupled method to compute the response of portal double-row piles subjected to lateral earth pressure loading based on new boundary value problem approach is introduced. First, the new governing differential equations including six variables (three internal forces and three displacements) are formulated and the boundary condition is specified. Second, the high-accuracy Runge-Kutta differential method is used to solve the corresponding system of differential equations to obtain the pile's internal forces and displacements. A program for pile response analysis and graphics edit is developed. At last, the program was verified against the FEM analysis results in terms of pile deflection, bending moment, and shear force along the length of the pile.

The objective of this study is to provide an alternative method for the design of portal double-row pile used for slope stabilization or earth retaining.

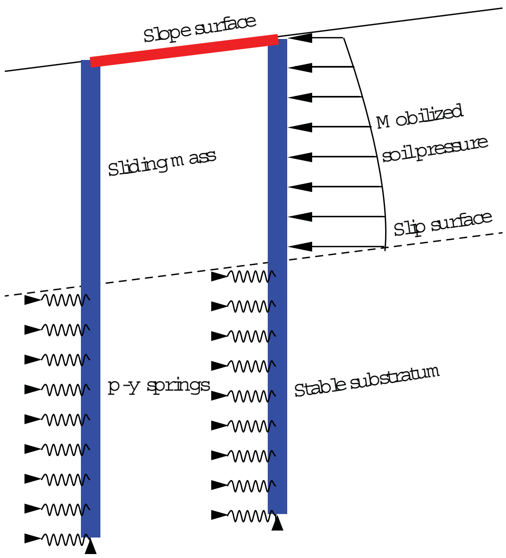

Figure 1: The uncoupled analysis model for the double-row portal stabilizing piles.

2. Derivation of Governing Differential Equations

In order to solve the complicated engineering problem of the response of double-row stabilizing pile under laterally loading by using accurately mathematical model, we often need to define its boundary value problem which involves the governing differential equations and corresponding boundary conditions. Then, closed-form or numerical solutions for the engineering problem can be obtained by many appropriate mathematical methods.

Under the scheme of uncoupled analysis of the pile (as shown in Figure 1), the new governing differential equations for stabilizing piles embedded in slope will be developed in the following according to the general principles of solid and structural mechanics including static force equilibrium, deformation compatibility, and constitutive relationship.

2.1. The Loading Condition. Below the slip surface, the sliding bed is assumed to be stable and cannot move. Before the active force induced by the sliding mass act upon the pile segment above the slip surface, the earth pressure acting at the front and back sides of the pile segment below the slip surface is in equilibrium. So it can be neglected. Only the active force induced by the movement of the sliding mass is considered in the calculation model, which are loaded on the pile segment above the slip surface. Their distribution along the pile shaft can be assumed as uniform, triangular, trapezoidal, and rectangular profiles. Then, the reaction force acting at the pile segment below the slip surface is calculated. These active forces and reaction forces considered are in equilibrium [14].

2.2. The Soil-Pile Interaction Model. Due to its simplicity and reasonable accuracy, the Winkler foundation model is adopted in current analysis to describe the pile-soil interaction behavior. The Winkler method assumed that the substratum is composed of independent horizontal springs. Under the Winkler hypothesis, the soil reaction pressures (p) acting on the pile can be modeled by discrete independent linear or nonlinear springs in the form of the following equation:

$$p = k \cdot w, \tag{1}$$

where k is the spring constant, also called the modulus of horizontal subgrade reaction (it has a unit of force/length^3). The main difference between the different Winkler foundation models available is in the selection of the foundation stiffness coefficients. p is the horizontal soil reaction pressure (it has a unit of force/length^2). w is the horizontal displacement (it has a unit of length).

2.3. The New Equilibrium Differential Equations. Let us consider an isolated free portion of pile, as shown in Figure 2, having a infinitesimal length of ds and acted upon by external distributed normal load q_n and tangential load q_τ. The free segment can be imagined to be cut out of the pile, and the internal forces (M, N, Q) in the original pile may become external forces on the isolated free portion.

Figure 2 also shows the coordinate system used in this paper for introducing the governing equations.

We adopt sign conventions so that the six variables as shown in Figure 2 are positive. The sign convention adopted for forces is that positive sign indicates tensile axial force N, the positive shearing force Q should be directed so that they will tend to rotate the element counterclockwise, and the positive bending moment M will tend to make the element concave leftward. The sign convention adopted for displacements is that the positive normal displacement v points outward normal, the positive tangential displacement u points right when facing outward normal, and the positive φ is counterclockwise. The lateral pressure q_n is considered positive when applied from left to right. The lateral pressure q_τ is considered positive when applied from up to down.

Thus, considering the equilibrium of the above infinitesimal pile segment, as it bends under the action of the applied loads (shown in Figure 2), we arrive at two force equilibrium equations in the directions of u and v and one moment equilibrium equation:

$$\begin{gathered}\left(N + \frac{dN}{ds}ds\right) - N - q_\tau ds - k_s HuDds = 0, \\ \left(Q + \frac{dQ}{ds}ds\right) - Q - q_n ds - k_n Hvbds = 0, \\ \left(M + \frac{dM}{ds}ds\right) - M + \left(Q + \frac{dQ}{ds}ds\right)\frac{ds}{2} + Q\frac{ds}{2} = 0.\end{gathered} \tag{2}$$

Simplifying the above equations and neglecting the higher-order term and the term with the square of the

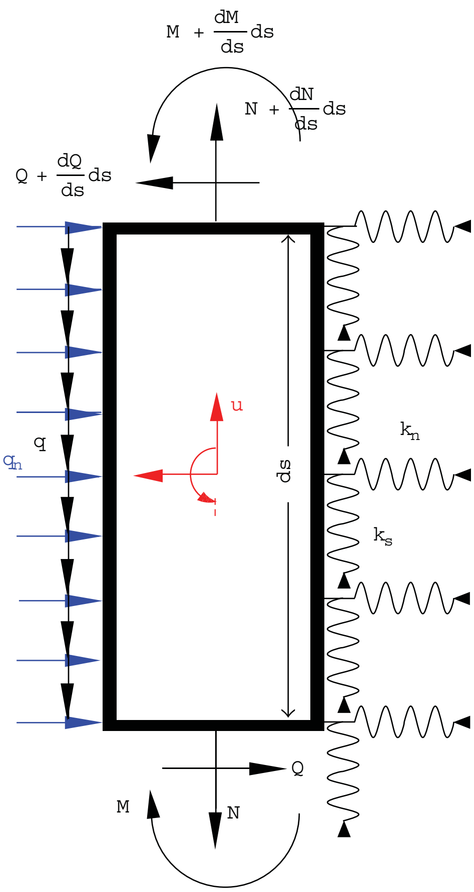

Figure 2: The free-body diagram of infinitesimal isolated segment of pile.

differential, the equilibrium equations now take the following forms:

$$\frac{dN}{ds} = k_s HDu + q_\tau,$$
$$\frac{dQ}{ds} = k_n Hbv + q_n, \quad (3)$$
$$\frac{dM}{ds} = -Q,$$

where $H = \left\{\begin{smallmatrix} 1, & \text{contact,} \\ 0, & \text{noncontact,} \end{smallmatrix}\right.$ the "one" indicates that Winkler reaction force exists and the "zero" indicates that Winkler reaction force does not exist. S is the position coordinate; D is perimeter of the cross-section. b is the width of the cross-section, k_s is the Winkler modulus of vertical subgrade reaction, and k_n is the Winkler modulus of horizontal subgrade reaction.

For the sake of convenience of formula deducing, let

$$X = \begin{bmatrix} N \\ Q \\ M \end{bmatrix}; \quad Z = \begin{bmatrix} u \\ v \\ \varphi \end{bmatrix}; \quad P = \begin{bmatrix} q_\tau \\ q_n \\ 0 \end{bmatrix}. \quad (4)$$

The set of equations of equilibrium (3) can be rewritten in the following matrix form:

$$\frac{dX}{ds} = B \cdot X + L \cdot Z + P, \quad (5)$$

where $B = \left[\begin{smallmatrix} 0 & 0 & 0 \\ 0 & 0 & 0 \\ 0 & -1 & 0 \end{smallmatrix}\right]$; $L = \left[\begin{smallmatrix} k_s HD & 0 & 0 \\ 0 & k_n Hb & 0 \\ 0 & 0 & 0 \end{smallmatrix}\right]$.

2.4. Geometric and Constitutive Equations. When the deformation ($d\overline{u}$, $d\overline{v}$, $d\overline{\varphi}$) of the differential element (shown in Figure 2) induced by the internal forces (N, Q, M) is considered given, the corresponding strains can be expressed as

$$\frac{d\overline{U}}{ds} = \left(\frac{d\overline{u}}{ds}, \frac{d\overline{v}}{ds}, \frac{d\overline{\varphi}}{ds}\right). \quad (6)$$

According to the related theory of elastic beam, the internal forces (N, Q, M) can be related to strains as in the following linear constitutive equation:

$$\frac{d\overline{U}}{ds} = \begin{bmatrix} \frac{d\overline{u}}{ds} \\ \frac{d\overline{v}}{ds} \\ \frac{d\overline{\varphi}}{ds} \end{bmatrix} = \begin{bmatrix} \frac{1}{EA} & 0 & 0 \\ 0 & \frac{\alpha}{GA} & 0 \\ 0 & 0 & \frac{1}{EI} \end{bmatrix} \cdot \begin{bmatrix} N \\ Q \\ M \end{bmatrix}, \quad (7)$$

where α is the constant related to the shape of pile cross-section ($\alpha = 6/5$ for rectangular cross-section; $\alpha = 10/9$ for circular cross-section); A is the cross-sectional area; EI is the flexural rigidity of the pile's cross-section.

Considering the deformation, $d\overline{U}$ can be decomposed into two parts. One part is the dZ induced by the displacement on its direction and another part is the projection of other displacement onto this direction which takes the form $\overline{B}Zds$, where $\overline{B}$ is the a undetermined third-order square matrix. Then, the deformation $d\overline{U}$ can be expressed as

$$d\overline{U} = dZ + \overline{B}Zds. \quad (8)$$

Applying the principle of virtual work to the isolated differential element of pile (shown in Figure 2), $\overline{B}$ can be determined. We suppose that each point of the body is given an infinitesimal virtual displacement δZ satisfying displacement boundary conditions where prescribed. The virtual deformation associated with the infinitesimal virtual displacement is $\delta\overline{U}$. The virtual work of the external surface forces is $-\int \overline{P}^T(\delta Z)ds$, where $\overline{P} = P + LZ$. The virtual work of the internal forces is $\int X^T d(\delta\overline{U})$. By equating the external work to the internal work, we have $-\int \overline{P}^T(\delta Z)ds = \int X^T d(\delta\overline{U})$. Substituting (5) and (8) into the above equation and simplifying yields $\int X^T(B^T - \overline{B})\delta Z ds = 0$. Since this equation is satisfied for arbitrary δZ, the terms in the brackets in the integral must vanish at every point which means that

$\overline{B} = B^T$. At last, we develop the following geometric and constitutive equations:

$$\frac{du}{ds} = \frac{N}{EA}, \quad \frac{dv}{ds} = \frac{\alpha Q}{GA} + \varphi, \quad \frac{d\varphi}{ds} = \frac{M}{EI}. \tag{9}$$

2.5. Matrix Form of the Governing Equations. For the sake of convenience of problem solving, combining the three equilibrium differential equations (3) and the three geometric and constitutive equations (9) leads to a system of six equations:

$$\begin{aligned} \frac{dN}{ds} &= k_s HDu + q_\tau, \\ \frac{dQ}{ds} &= k_n Hbv + q_n, \\ \frac{dM}{ds} &= -Q, \\ \frac{du}{ds} &= \frac{N}{EA}, \\ \frac{dv}{ds} &= \frac{\alpha Q}{GA} + \varphi, \\ \frac{d\varphi}{ds} &= \frac{M}{EJ}. \end{aligned} \tag{10}$$

$$\text{Let } K = \begin{bmatrix} 0 & 0 & 0 & Hk_sD & 0 & 0 \\ 0 & 0 & 0 & 0 & Hk_nb & 0 \\ 0 & -1 & 0 & 0 & 0 & 0 \\ \frac{1}{EA} & 0 & 0 & 0 & 0 & 0 \\ 0 & \frac{\alpha}{GA} & 0 & 0 & 0 & 1 \\ 0 & 0 & \frac{1}{EI} & 0 & 0 & 0 \end{bmatrix}, \quad X = \{N \; Q \; M \; u \; v \; \varphi\}^T, \quad p = \{q_\tau \; q_n \; 0 \; 0 \; 0 \; 0\}^T. \tag{11}$$

Then, we can use matrix notation to present the above equations (10) in the form:

$$\frac{dX}{ds} = KX + p = F(X, s), \tag{12}$$

where K is the coefficients square matrix of six order and X and p represent two column matrices.

This system of six independent differential equations can be solved for six unknown functions (three independent forces and three independent displacements).

3. Boundary Conditions

As mentioned above, there are total six unknowns to be determined (N, Q, M, u, v, φ). Therefore, six boundary conditions are needed for the problem solving.

The boundary conditions for (12) are determined according to the way in which the pile's head and base are supported or restrained. There are three conditions at the base point and three conditions at the head point. We use matrix notation to present these boundary conditions in the following form:

$$C\overline{X}\Big|_{S=0} = o, \quad D\overline{X}\Big|_{S=L} = o, \tag{13}$$

where $S = 0$ indicates the beginning point of calculation (the pile's base point), $S = L$ indicates the end point of calculation (the pile's head point), C is the matrix of boundary condition on the beginning point, and D is the matrix of boundary condition on the end point. They are 3×6 matrices. In this study, the following possible pile end conditions were considered.

(1) Free head (allows both displacement and rotation): $N = Q = 0$, $M = 0$. The corresponding matrix of boundary condition is

$$\begin{bmatrix} 1 & 0 & 0 & 0 & 0 & 0 \\ 0 & 1 & 0 & 0 & 0 & 0 \\ 0 & 0 & 1 & 0 & 0 & 0 \end{bmatrix} \times \begin{Bmatrix} N \\ Q \\ M \\ u \\ v \\ \varphi \end{Bmatrix} = o. \tag{14}$$

(2) In case of bottom end hinged (allows rotation without displacement): $u = v = 0$, $M = 0$. The corresponding matrix of boundary condition is

$$\begin{bmatrix} 0 & 0 & 1 & 0 & 0 & 0 \\ 0 & 0 & 0 & 1 & 0 & 0 \\ 0 & 0 & 0 & 0 & 1 & 0 \end{bmatrix} \times \begin{Bmatrix} N \\ Q \\ M \\ u \\ v \\ \varphi \end{Bmatrix} = o. \tag{15}$$

(3) In case of bottom end fixed (allows neither displacement nor rotation): $u = v = 0$, $\varphi = 0$. The corresponding matrix of boundary condition is

$$\begin{bmatrix} 0 & 0 & 0 & 1 & 0 & 0 \\ 0 & 0 & 0 & 0 & 1 & 0 \\ 0 & 0 & 0 & 0 & 0 & 1 \end{bmatrix} \times \begin{Bmatrix} N \\ Q \\ M \\ u \\ v \\ \varphi \end{Bmatrix} = o. \tag{16}$$

(4) In case of bottom end partially hinged (allows rotation without vertical displacement): $u = 0$, $Q = 0$,

and $M = 0$. The corresponding matrix of boundary condition is

$$\begin{bmatrix} 0 & 1 & 0 & 0 & 0 & 0 \\ 0 & 0 & 1 & 0 & 0 & 0 \\ 0 & 0 & 0 & 1 & 0 & 0 \end{bmatrix} \times \begin{Bmatrix} N \\ Q \\ M \\ u \\ v \\ \varphi \end{Bmatrix} = o. \quad (17)$$

(5) Elastic vertical support at the bottom end: $N = K_v \cdot u \cdot$ Area, $Q = 0$, and $M = 0$. The corresponding matrix of boundary condition is

$$\begin{bmatrix} 1 & 0 & 0 & -K_v \cdot \text{Area} & 0 & 0 \\ 0 & 1 & 0 & 0 & 0 & 0 \\ 0 & 0 & 1 & 0 & 0 & 0 \end{bmatrix} \times \begin{Bmatrix} N \\ Q \\ M \\ u \\ v \\ \varphi \end{Bmatrix} = o, \quad (18)$$

where K_v is the modulus of vertical compressibility. *Area* is the cross-sectional area of the pile.

4. Definition of Boundary Value Problem

Next, we impose the boundary conditions (13) at the pile head and base upon the derived new governing differential equations (12) to define a boundary value problem of the following equations:

$$\begin{aligned} \frac{dX}{ds} &= KX + p, \\ CX|_{S=0} &= o, \\ DX|_{S=L} &= o. \end{aligned} \quad (19)$$

To this end, the response of double-row portal stabilizing pile is mathematically idealised as the boundary value problem of (19).

Thus, many numerical methods to solve the ordinary differential equations can be adopted to solve the boundary value problem of (19).

It should be noted that the existence and uniqueness of solution for the boundary value problem of (19) should be mathematically proved. This matter is however outside the scope of the writer's major. According to the physical character of the problem, we can imagine that the solution exists and is unique. The solution can be validated through comparative studies.

5. Method of Solution

5.1. Uniformity Preprocessing. The orders of magnitude of the section internal forces (N, Q, M) are so much higher than those of the displacements (u, v, φ) that numerical solving of the equations may meet singularity difficulty. So for reasons of numerical stability, it is necessary to perform uniformity preprocessing for the order of magnitude of the element in the coefficient matrix K. We multiply the displacements (u, v, φ) by E and substitute the original displacement variables by the expressions $(Eu, Ev, E\varphi)$. So, we redefine two variables as follows:

$$\widetilde{X} = \begin{Bmatrix} N \\ Q \\ M \\ \overline{u} \\ \overline{v} \\ \overline{\varphi} \end{Bmatrix} = \begin{Bmatrix} N \\ Q \\ M \\ Eu \\ Ev \\ E\varphi \end{Bmatrix},$$

$$\widetilde{K} = \begin{bmatrix} 0 & 0 & 0 & \dfrac{Hk_sD}{E} & 0 & 0 \\ 0 & 0 & 0 & 0 & \dfrac{Hk_nb}{E} & 0 \\ 0 & -1 & 0 & 0 & 0 & 0 \\ \dfrac{1}{A} & 0 & 0 & 0 & 0 & 0 \\ 0 & \dfrac{E\alpha}{GA} & 0 & 0 & 0 & 1 \\ 0 & 0 & \dfrac{1}{I} & 0 & 0 & 0 \end{bmatrix}. \quad (20)$$

Finally, we obtain the following system of ordinary differential equations:

$$\begin{aligned} \frac{d\widetilde{X}}{ds} &= \widetilde{K}\widetilde{X} + p, \\ C \cdot \widetilde{X}\Big|_{S=0} &= o, \\ D \cdot \widetilde{X}\Big|_{S=L} &= o. \end{aligned} \quad (21)$$

This system of six independent differential equations subjected to boundary conditions can be numerically solved for six unknown functions (three forces and three displacements).

5.2. The Runge-Kutta Finite Difference Algorithm. The Runge-Kutta algorithm is commonly used for the solution of the ordinary differential equation of the form $dX/ds = F(X, s)$. So, it is chosen to solve (21).

5.2.1. Derivation of the Recursion Formula. The following finite difference formula (22) is one format of the Runge-Kutta methods:

$$\begin{aligned} X_{n+1} &= X_n + \frac{1}{6}\left(K_1 + 2K_2 + 2K_3 + K_4\right), \\ K_1 &= \delta \cdot F\left(X_n, s_n\right), \\ K_2 &= \delta \cdot F\left(X_n + \frac{1}{2}K_1, s_n + \frac{1}{2}\delta\right), \\ K_3 &= \delta \cdot F\left(X_n + \frac{1}{2}K_2, s_n + \frac{1}{2}\delta\right), \\ K_4 &= \delta \cdot F\left(X_n + K_3, s_n + \delta\right). \end{aligned} \quad (22)$$

The Runge-Kutta algorithm of this type (22) is a numerical method of fifth order, where δ is the stepsize of difference and $F(X,s)=\overline{K}X+p$. For convenience of computation, this formulation may be rewritten in the following form:

$$X_{n+1}=G_nX_n+H_n\delta. \tag{23}$$

As we can see, the value of function at point $(n+1)$ can be determined from the value of function at point (n), where $n=0$ represents the beginning point of calculation and $n=m$ represents the end point of calculation.

In the above equation, G_n and H_n can be obtained from the following recursion formula:

$$\begin{gathered}K_n^{(j)}=\widetilde{K}\left(s_n+\delta_j\right),\qquad P_n^{(j)}=p\left(s_n+\delta_j\right),\\ \alpha_1=\alpha_2=\alpha_3=\frac{1}{2},\qquad \alpha_4=1,\\ \beta_1=\beta_4=\frac{1}{6},\qquad \beta_2=\beta_3=\frac{1}{3},\\ \delta_j=\left(\sum_{k=1}^{j}\gamma_k\right)\delta,\qquad \gamma_1=\gamma_3=0,\qquad \gamma_2=\gamma_4=\frac{1}{2},\\ \Longrightarrow \delta_1=0,\qquad \delta_2=\delta_3=\frac{1}{2}\delta,\qquad \delta_4=\delta,\end{gathered} \tag{24}$$

$$\begin{gathered}G_n=I+\sum_{j=1}^{4}\beta_jG^{(j)},\qquad H_n=\sum_{j=1}^{4}\beta_jH^{(j)},\\ G^{(j)}=\left(\delta K^{(j)}\right)\left(I+\alpha_jG^{(j-1)}\right),\quad G^{(0)}=0,\\ H^{(j)}=\left(\delta K^{(j)}\right)\alpha_jH^{(j-1)}+P^{(j)},\quad H^{(0)}=0,\end{gathered} \tag{25}$$

where I is the identity matrix.

5.2.2. Determination of the Initial Vector X_0. The initial value is the start point of the recursion formula. Now, we discuss in the following how to obtain the initial vector X_0 by using the recursion formula of (23) and imposing the boundary conditions at pile head and base.

Considering the recursion formula of (23), X_n can be expressed in terms of X_0 as follows:

$$X_n=D^{(n)}X_0+F^{(n)}. \tag{26}$$

In the case of $n=0$, we have $D^{(0)}=I$, $F^{(0)}=0$ and substitute it into the recursion formula of (23). We get

$$X_{n+1}=G_n\left(D^{(n)}X_0+F^{(n)}\right)+H_n\delta. \tag{27}$$

It can be rewritten as follows:

$$\begin{gathered}X_{n+1}=\left(G_nD^{(n)}\right)X_0+\left(G_nF^{(n)}+H_n\delta\right),\\ X_n=D^{(n)}X_0+F^{(n)}\Longrightarrow X_{n+1}=D^{(n+1)}X_0+F^{(n+1)},\\ X_{n+1}=\left(G_nD^{(n)}\right)X_0+\left(G_nF^{(n)}+H_n\delta\right),\\ X_{n+1}=D^{(n+1)}X_0+F^{(n+1)}.\end{gathered} \tag{28}$$

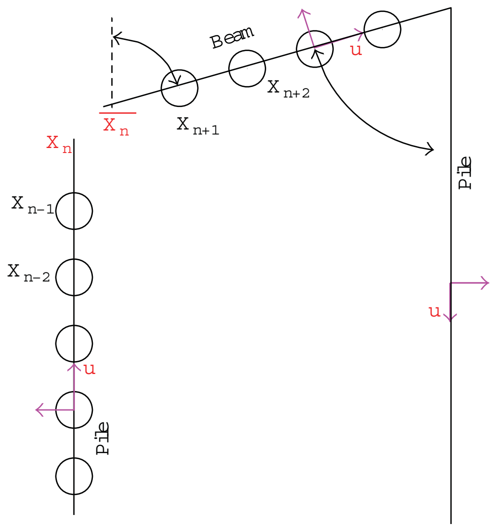

Figure 3: Scheme of local coordinate system transformation between pile and connection beam.

Comparing the above two equations, the recursion formula for $D^{(n)}$ and $F^{(n)}$ is obtained as follows:

$$\begin{gathered}D^{(0)}=I,\quad D^{(n+1)}=G_nD^{(n)},\\ F^{(0)}=0,\quad F^{(n+1)}=G_nF^{(n)}+H_n\delta.\end{gathered} \tag{29}$$

Now considering the case of boundary point: $X_m=D^{(m)}X_0+F^{(m)}$, we substitute the boundary conditions at end point $CX_0=o$, $DX_m=o$ into the above equation. This leads to the equation to solve for X_0:

$$\begin{bmatrix}C\\ DD^{(m)}\end{bmatrix}X_0=\begin{bmatrix}o\\ -DF^{(m)}\end{bmatrix}. \tag{30}$$

The above set of linear algebraic equations can be solved for X_0 by using the method of Gaussian elimination with pivot selection. Once X_0 is known, X_n can be obtained in sequence using the recursion formula of (23).

5.2.3. Coordinate Transformation between Pile and Beam. When solving the problem of double-row portal piles using the recursion formula of (23), due to the direction change of the axes of the pile and the beam at the connection point (shown in Figure 3), first we need to distinguish $\overline{K}$ and p in the recursion formula for the two connected segments. And then in order to satisfy the equilibrium of internal forces and maintain the continuity of displacements at the connection point, we need to introduce the so-called connection matrix to the corresponding formula when dealing with D_m, F_m, and X_n, recursively.

The centroidal axes' rotation from pile to beam at connection point means mathematically that the local coordinate system rotates clockwise by β degree at the connection point (shown in Figure 3).

According to the principle of equilibrium of internal forces, we get

$$\begin{bmatrix} \overline{N} \\ \overline{Q} \end{bmatrix} = \begin{bmatrix} \cos\theta & -\sin\theta \\ \sin\theta & \cos\theta \end{bmatrix} \begin{bmatrix} N \\ Q \end{bmatrix}. \quad (31)$$

And the bending moment remains unchanged.

According to the principle of vector analysis, we get

$$\begin{bmatrix} \overline{u} \\ \overline{v} \end{bmatrix} = \begin{bmatrix} \cos\theta & -\sin\theta \\ \sin\theta & \cos\theta \end{bmatrix} \begin{bmatrix} u \\ v \end{bmatrix}. \quad (32)$$

And the rotation displacement remains unchanged.

Combining the above equations, the corresponding transformation matrix for the local coordinate system rotating clockwise by β degree can be expressed as follows:

$$\begin{bmatrix} \overline{N}_n \\ \overline{Q}_n \\ \overline{M}_n \\ \overline{u}_n \\ \overline{v}_n \\ \overline{\varphi}_n \end{bmatrix} = \begin{bmatrix} \cos\beta & -\sin\beta & 0 & 0 & 0 & 0 \\ \sin\beta & \cos\beta & 0 & 0 & 0 & 0 \\ 0 & 0 & 1 & 0 & 0 & 0 \\ 0 & 0 & 0 & \cos\beta & -\sin\beta & 0 \\ 0 & 0 & 0 & \sin\beta & \cos\beta & 0 \\ 0 & 0 & 0 & 0 & 0 & 1 \end{bmatrix} \times \begin{bmatrix} N_n \\ Q_n \\ M_n \\ u_n \\ v_n \\ \varphi_n \end{bmatrix},$$

$$\overline{X}_n = C_n \cdot X_n. \quad (33)$$

As we can see, the above connection matrix is the so-called orthogonal matrix whose inverse is its transposed matrix.

As shown in Figure 3, the node of difference (no. n) is the connection node. First we need to distinguish $\overline{K}$ and p in the recursion formula for the two connected segments and then insert the connection matrix for transformation from X_n to $\overline{X}_n$ when dealing with the D_m, F_m, and X_n, recursively. The detailed procedure is as follows.

(1) For the calculation of X_n,

$$X_{i+1} = G_i X_i + H_i \delta, \quad (i = 1, 2, \ldots, n-1) \quad (34)$$

$\overline{X}_n = C_n X_n = C_n(G_{n-1}X_{n-1} + H_{n-1}\delta)$, where C_n is the transformation matrix for point n. Thus, $X_{n+1} = G_n\overline{X}_n + H_n\delta$. Next,

$$X_{i+1} = G_i X_i + H_i \delta, \quad (i = n+1, n+2, \ldots m), \quad (35)$$

where m indicates the end point of calculation.

(2) For the calculation of D_m: because $X_n = D^{(n)}X_0 + F^{(n)}$, and

$$\begin{aligned} X_{n+1} &= G_n\overline{X}_n + H_n\delta \\ &= G_n\left(C_nX_n\right) + H_n\delta \\ &= G_n\left(C_n\left(D^{(n)}X_0 + F^{(n)}\right)\right) + H_n\delta \\ &= G_nC_nD^{(n)}X_0 + G_nC_nF^{(n)} + H_n\delta \\ &= D^{(n+1)}X_0 + F^{(n+1)} \\ &\Longrightarrow \begin{cases} D^{(n+1)} = G_nC_nD^{(n)} \\ F^{(n+1)} = G_nC_nF^{(n)} + H_n\delta, \end{cases} \end{aligned} \quad (36)$$

So, the above procedure also applies to calculation of $D^{(m)}$ as follows:

$$\begin{aligned} D^{(i+1)} &= G_iD^{(i)}, \quad (i = 1, 2, \ldots, n-1), \\ D^{(n+1)} &= G_nC_nD^{(n)}, \\ D^{(i+1)} &= G_iD^{(i)}, \quad (i = n+1, n+2, \ldots m). \end{aligned} \quad (37)$$

(3) For the calculation of F_m,

$$\begin{aligned} F^{(i+1)} &= G_iF^{(i)} + H_i\delta, \quad (i = 1, 2, \ldots, n-1), \\ F^{(n+1)} &= G_nC_nF^{(n)} + H_n\delta, \\ F^{(i+1)} &= G_iF^{(i)} + H_i\delta, \quad (i = n+1, n+2, \ldots m), \end{aligned} \quad (38)$$

where m denotes the end point of calculation.

5.2.4. The Solution Flow Process. In short, the proposed solution procedure involves four main steps:

(1) calculating the value of G_n and H_n using the given Equation (25);

(2) calculating $D^{(m)}$ and $F^{(m)}$ using the given recursion formula of (29);

(3) calculating the vector X_0 by solving linear algebraic Equations (30);

(4) calculating X_n using the given recursion formula of (23).

Because the equations and solution formula are all given in form of matrices, a simple computer program has been written on the platform of MATLAB to run this procedure. At last, we can get the shear, bending-moment, and deflection diagram along the pile.

6. Verification

The practical examples of portal double-row piles used to stabilize an potential landslide (shown in Figure 4) are considered herein to verify the developed numerical calculation techniques. Soil strength parameters used in the stability analysis are from laboratory shear testing on the undisturbed soil samples. The resisting (shear) force required to achieve the desired safety factor and transferred by the pile is estimated to be 2147 kN/m. Before the pile is installed, the slope is approaching limit state and the safety factor can be assumed to be one. The values of c and φ can be determined based on experiment data and satisfying this limit state condition. Then, the required resisting force 2147 kN/m can be obtained using back analysis. When this additional force is applied to the specified place of the landslide, the safety factor calculated using the limit equilibrium method can achieve the desired value 1.3. The manual digging discrete reinforced concrete piles were designed to be installed at a spacing of 4 m to increase the factor of safety of the whole slope to the required value of 1.3.

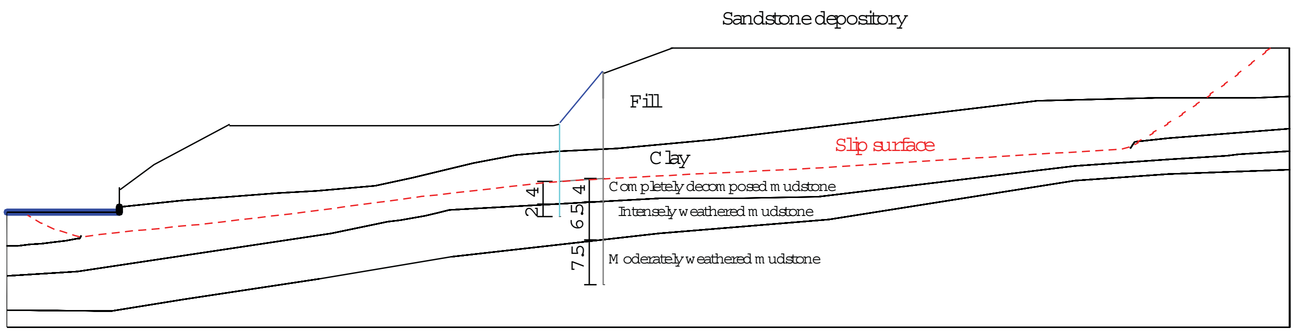

Figure 4: Scheme of portal double-row piles used to stabilize a landslide (units: m).

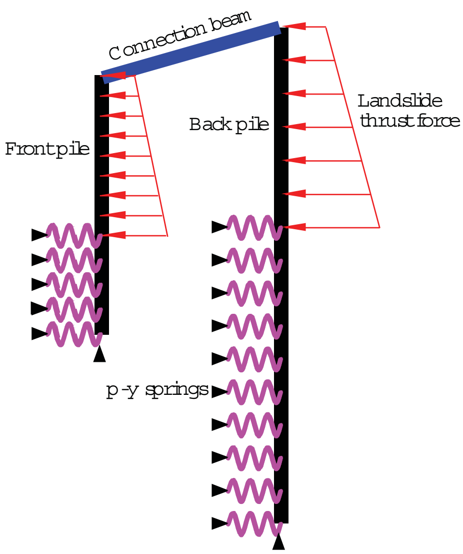

Figure 5: The conceptual calculation model for portal double-row stabilizing pile.

Table 1: Parameters of material properties.

	Young's modulus (GPa)	Shear modulus (GPa)	Modulus of subgrade reaction (MPa/m)
C30 concrete	30	12	/
Completely decomposed mudstone	/	/	80
Intensely weathered mudstone	/	/	110
Moderately weathered mudstone	/	/	150

The front row pile has a length $L = 16.0$ m and sectional dimension 1.5×2.0 m. The length of the portion embedded into the sliding surface is 6.0 m. The back row pile has a length $L = 37.0$ m and sectional dimension 1.5×2.8 m. The length of the portion embedded into the sliding surface is 18.0 m. The sectional dimension of the connection beam is 0.8×0.8 m. The pile is constructed using C30 concrete (assuming that concrete does not crack during working). A lateral force $F = 2147 \times 4$ kN is assumed to act upon the pile segment above the sliding surface. The pressure distribution is considered to have a rectangular shape, as proposed by the Chinese design code (Code for design on retaining structures of railway subgrade no. TB10025-2006).

The conceptual calculation model used to simulate the lateral response of the pile is shown in Figure 5. The boundary condition at the pile base is considered as free head which allows both lateral displacement and rotation.

For simplicity of program editing, the friction force along the pile-soil interface can be neglected. The modulus of horizontal subgrade reaction for the mudstone below the slip surface is listed in Table 1 for the three different mudstone layers. The coefficient of subgrade reaction was determined according to the suggestions for the mudstone in the related Chinese design code and in situ tests. The related Chinese design code provides detailed experiment procedure to determine the modulus of horizontal subgrade reaction.

Then, the developed method is applied to analyze the lateral response of the double-row pile which is also computed by the FEM program we developed. We employ an elastic beam column element to model the pile and horizontal spring element to represent the reactions of the surrounding soil in the FEM model. Comparisons of shear force, bending moment, and deflection of the pile between boundary value method (BVM) and FEM are presented in Figures 6 and 7. Complete agreement between them can be observed.

Through the above comparative studies, it has been found that the program we developed works very well and can replace the existing numerical methods that have been used to design the portal double-row stabilizing pile.

7. Summary and Conclusions

In this paper, a new numerical uncoupled method for calculating the response of portal double-row stabilizing piles is proposed. The theoretical background and a detailed derivation of the proposed numerical solution scheme are described. The feasibility of the method developed was verified using the comparative case study. The proposed method has more higher modeling and computing efficiency than the FEM and can be an alternative method for analyzing

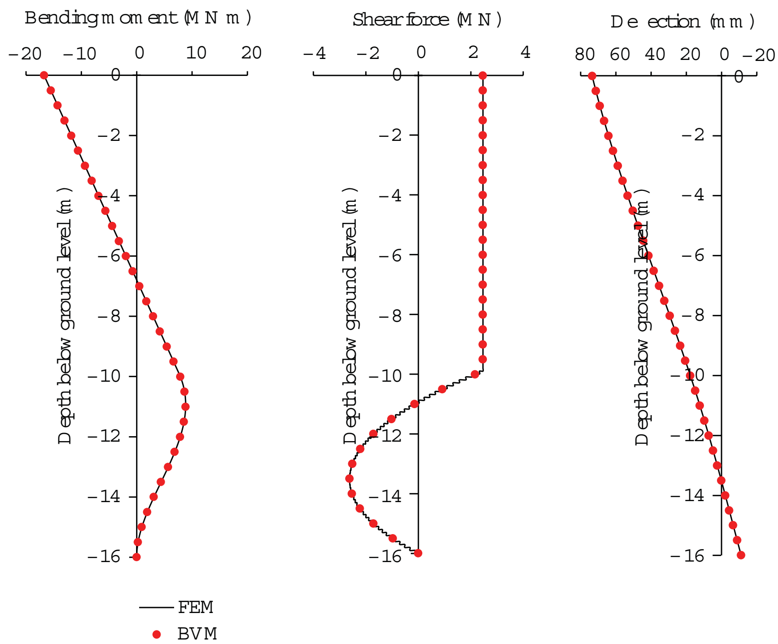

Figure 6: Comparison of internal force and deflection of front row pile between the boundary value method and FEM.

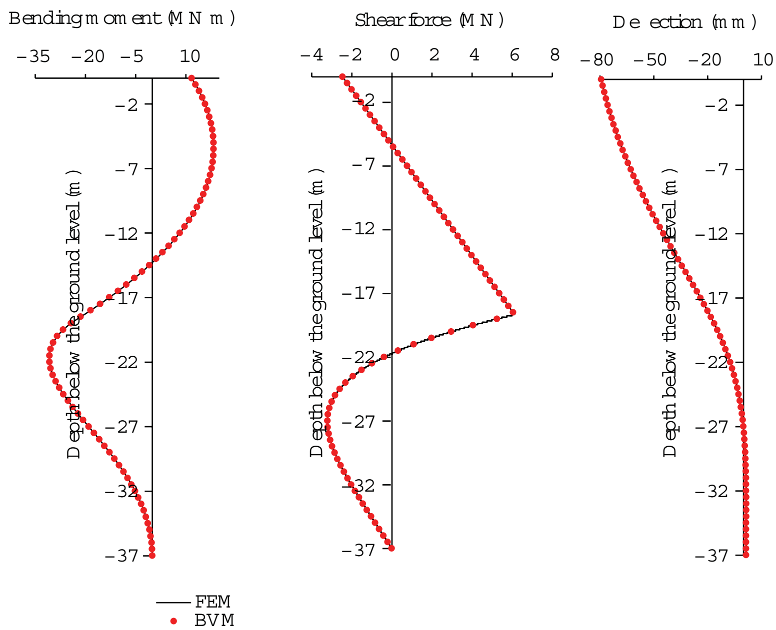

Figure 7: Comparison of internal force and deflection of back row pile between the boundary value method and FEM.

the behavior of portal double-row piles used for slope stabilization.

Acknowledgments

This study was jointly financially supported by grants from the National Natural Science Foundation of China (Grant no. 51008298) and Key Research Program of Chinese Academy of Sciences (no. KZZD-EW-05). The support is gratefully acknowledged. The author also thanks the anonymous referees whose comments helped to improve the work and the presentation of this paper.

References

[1] Y. K. Chow, "Analysis of piles used for slope stabilization," *International Journal for Numerical and Analytical Methods in Geomechanics*, vol. 20, no. 9, pp. 635–646, 1996.

[2] J. A. Smethurst and W. Powrie, "Monitoring and analysis of the bending behaviour of discrete piles used to stabilise a railway embankment," *Geotechnique*, vol. 57, no. 8, pp. 663–677, 2007.

[3] S. Hassiotis, J. L. Chameau, and M. Gunaratne, "Design method for stabilization of slopes with piles," *Journal of Geotechnical and Geoenvironmental Engineering*, vol. 123, no. 4, pp. 314–323, 1997.

[4] H. G. Poulos, "Design of reinforcing piles to increase slope stability," *Canadian Geotechnical Journal*, vol. 32, no. 5, pp. 808–818, 1995.

[5] T. Ito, T. Matsui, and W. P. Hong, "Design method for stabilizing piles against landslide—one row of piles," *Soils and Foundations*, vol. 21, no. 1, pp. 21–37, 1981.

[6] C.-C. Fan and J. H. Long, "Assessment of existing methods for predicting soil response of laterally loaded piles in sand," *Computers and Geotechnics*, vol. 32, no. 4, pp. 274–289, 2005.

[7] J.-R. Peng, M. Rouainia, and B. G. Clarke, "Finite element analysis of laterally loaded fin piles," *Computers and Structures*, vol. 88, no. 21-22, pp. 1239–1247, 2010.

[8] S. Jeong, B. Kim, J. Won, and J. Lee, "Uncoupled analysis of stabilizing piles in weathered slopes," *Computers and Geotechnics*, vol. 30, no. 8, pp. 671–682, 2003.

[9] H. Cheng and R. Wei-Zhong, "Boundary value method of ordinary differential equation system for analysing interaction between landslide and stabilizing pile," *Chinese Journal of Computational Mechanics*, vol. 29, no. 3, pp. 421–426, 2012.

[10] H.-W. Ying, Z.-H. Chu, B.-H. Li, and X.-W. Liu, "Study on calculation method of retaining structure with double-row piles and its application," *Rock and Soil Mechanics*, vol. 28, no. 6, pp. 1145–1150, 2007.

[11] C.-Y. Zhou, Z.-Q. Liu, W. Shang, H. Chen, and S.-R. Wen, "New mode for calculation of portal double row anti-sliding piles," *Rock and Soil Mechanics*, vol. 26, no. 3, pp. 441–449, 2005.

[12] M. Yamin and R. Y. Liang, "Limiting equilibrium method for slope/drilled shaft system," *International Journal for Numerical and Analytical Methods in Geomechanics*, vol. 34, no. 10, pp. 1063–1075, 2010.

[13] W. D. Guo and F. H. Lee, "Load transfer approach for laterally loaded piles," *International Journal for Numerical and Analytical Methods in Geomechanics*, vol. 25, no. 11, pp. 1101–1129, 2001.

[14] T. Ito and T. Matsui, "Methods to estimate lateral force acting on stabilizing piles," *Soils and Foundations*, vol. 15, no. 4, pp. 43–59, 1975.

Hindawi Publishing Corporation
Journal of Applied Mathematics
Volume 2013, Article ID 241482, 12 pages
http://dx.doi.org/10.1155/2013/241482

Research Article

Simplified Boundary Element Method for Kinematic Response of Single Piles in Two-Layer Soil

Fayun Liang,[1,2] Haibing Chen,[1,2] and Wei Dong Guo[3]

[1] *Key Laboratory of Geotechnical and Underground Engineering of Ministry of Education, Tongji University, Shanghai 200092, China*
[2] *Department of Geotechnical Engineering, Tongji University, Shanghai 200092, China*
[3] *School of Civil Mining and Environmental Engineering, University of Wollongong, Wollongong, NSW 2522, Australia*

Correspondence should be addressed to Fayun Liang; fyliang@tongji.edu.cn

Received 15 May 2013; Accepted 23 July 2013

Academic Editor: Ga Zhang

A simple approach is formulated to predict the elastic, kinematic pile bending during harmonic or transient excitation for a circular pile (rather than a simplified thin strip). The kinematic response of a pile embedded in two-layer soil is resolved in the frequency domain caused by the upward propagation of shear waves from the underlying bedrock. The simplified approach is generally valid to nonhomogeneous soil profiles, in light of the good comparison with the dynamic FE method and BDWF solution. It employs the soil-displacement-influence coefficients I_s to consider the pile-soil interaction (resembling the spring constant k_x in the BDWF) and provides conservative estimations of maximum kinematic bending moments at the soil-layer interface (with a sharper stiffness contrast). The accuracy of the approach may be improved by incorporating the interaction of soil into the soil-displacement-influence coefficients I_s for such cases with $V_b/V_a < 3$.

1. Introduction

Kinematic response is one of the key issues in seismic design of pile foundations [1–4], as the dynamic response of the pile structure largely differs from the response at the free field soil caused by seismic wave. In practice, the influence of inertial loading at the pile-head level has conventionally received sufficient attention by design engineers, but not the kinematic seismic response [5]. The existing earthquake investigations [6, 7] and experimental studies [8] demonstrate that at the interface of two-layer soils with a sharp stiffness contrast [2, 3, 9, 10], or at a pile-head with fixed constraints [11, 12], large kinematic bending moments may be induced to inflict damage to the pile. This problem has attracted the attention researchers [13–15] and is highlighted in some advanced seismic codes [16].

The kinematic response in the pile-soil system has been analyzed by considering the effect of the passive pile using rigorous mechanical solutions [17, 18], numerical methods [19–25], and some simplified models [2, 3, 26–30]. Rigorous solutions and numerical methods for the kinematic pile bending are, however, not convenient to design purposes. Empirical formulas are developed for evaluating the bending moment at the pile-head or at the interface of two-layer soils [2, 3, 11]. Among them, a Beam-on-Dynamic-Winkler-Foundation (BDWF) formulation was used successfully in practice, although it was confined to the harmonic excitation at the pile head. The BDWF (or the Winkler model) is underpinned by a frequency-dependent impedance ($= k_x + i\omega C_x$), in which the continuously distributed springs k_x ($\cong \delta E_s$) is empirically related to a dimensionless coefficient δ (used for a given pile-soil system, regardless of layers). Accurate selection of the value δ is not critical to calculating the pile-head deflection but is important to predicting the kinematic bending moment and shear force [19, 31]. An optimized δ is thus required to obtain correct kinematic pile bending at the interface of soil layers. On the other hand, a simplified boundary element formulation proposed by Poulos and Davis [32] offers good estimates of bending moment and shear force for static loading. It would be good to see its accuracy in predicting the kinematic seismic response of pile, especially at the sharp stiffness contrasts between adjacent soil layers.

In this paper, the simplified approach [32] is employed to evaluate the kinematic pile bending during harmonic or transient excitation, concerning piles in two-layer soil. The pile is modeled as a circular shape rather than a thin strip adopted previously [32], and the soil displacement is given by the Mindlin equation with corresponding elastic modulus. A nodal relative displacement is obtained by one-dimensional site response and is then imposed on the pile. The solution was compiled into a program operating in Matlab platform. For some typical cases, a comprehensive study on the kinematic seismic response during harmonic or transient excitation has been carried out, and the results are compared with available dynamic FE method and the BDWF solutions. The study sheds new light on the kinematic bending moment at the interface of two-layer soil and at the pile head and may facilitate the use of the simplified boundary element method to predict the kinematic seismic response of a single pile.

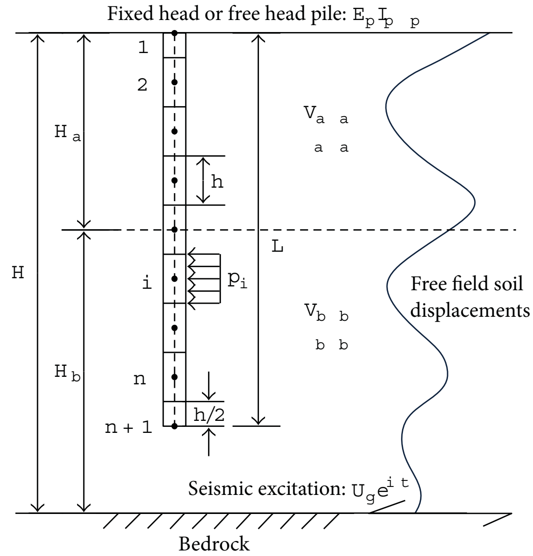

Figure 1: Analysis model of a pile in a two layer soil profile subjected to vertically-propagating seismic SH waves.

2. Simplified Analysis Procedure

2.1. Basic Assumptions for Pile and Soil Model. The one-dimensional model for a floating or end-bearing single pile embedded in a two-layer soil is shown in Figure 1. The circle pile is assumed as linearly hysteretic beam having a length L, a diameter d, a mass density ρ_p, and a bending stiffness E_pI_p. The pile is discretized into $n + 1$ segments of equal lengths h, but for a length of $h/2$ for the top and the tip segments, respectively. Each segment is subjected to a uniformly distributed load p_i over the semicircular area. The pile is head restrained (fixed head) or free to rotate (free head), and sits above a bedrock. The linearly hysteretic soil profile is characterized by an upper-layer of thickness H_a and a shear wave velocity V_a, which is underlain by a lower layer of thickness H_b and shear wave velocity V_b. The two layers have damping ratios β_b and β_a, mass densities ρ_b and ρ_a and Poisson's ratios μ_a and μ_b. A shear wave propagates vertically through the free field soil, which induces the horizontal harmonic motion and horizontal displacements. The motion at the bedrock surface is expressed by the amplitude of either bedrock displacement U_g or the bedrock acceleration $\omega^2 U_g$.

2.2. Calculation of the Horizontal Displacement of the Pile. Kinematic response of a single pile is induced by the free-field soil displacement shown in Figure 1. The Mindlin hypothesis does not meet the needs of dynamic analysis. However, the Mindlin equation is still valid for calculating elastic displacement and stress fields caused by a dynamic loading, provided that the characteristic wavelength in the soil is sufficiently long in comparison with the horizontal distance across the zone of major influence [28, 33], as is noted for nonhomogeneous soil by Poulos and Davis [32]. In the current, simplified BEM formulation, the soil displacement $\mathbf{u}_s$ (due to the pile-soil interface pressure) is gained using the Mindlin solution [34], which is then added together with free-field soil displacement

$$\mathbf{u}_s = \mathbf{I}_s \mathbf{p}_i + \mathbf{u}_e, \tag{1}$$

where $\mathbf{I}_s$ is the soil-displacement-influence coefficient; $\mathbf{p}_i$ is the vector of soil-pile interface pressure over the semi-circular area; and $\mathbf{u}_e$ is the free-field soil displacement estimated using one-dimensional site response for vertically propagating shear waves through an unbounded medium [35].

The dynamic equilibrium under steady-state conditions for the pile may be written in the following form using the finite-difference method [28]:

$$\frac{E_pI_p}{h^4}\mathbf{D}\mathbf{u}_p + \mathbf{M}\ddot{\mathbf{u}}_p + \mathbf{C}_x\left(\dot{\mathbf{u}}_p - \dot{\mathbf{u}}_e\right) = -d\mathbf{p}_p, \tag{2}$$

where $\mathbf{u}_p$ is the horizontal displacement of the pile, with the cap "·" indicating differentiation with time; $\mathbf{p}_p$ is the vector of soil-pile interface pressure; $\mathbf{D}$ is the matrix of finite difference coefficients; $\mathbf{M}$ is the pile mass; and $\mathbf{C}_x$ is the soil radiation damping. Here, the soil damping is the same as that of the simplified boundary element model [28], and

$$C_x = 5d\rho_s V_s, \tag{3}$$

where V_s is the shear wave velocity of soil and ρ_s is the density of soil.

The displacement compatibility between the pile and the adjacent soil offers $\mathbf{u}_s = \mathbf{u}_p$. Taking the displacement as $\mathbf{u}_p$ and substituting (1) into (2) result in the following:

$$\frac{\mathbf{I}_s}{d}\left[\mathbf{M}\ddot{\mathbf{u}}_p + \mathbf{C}_x\dot{\mathbf{u}}_p + \frac{E_pI_p}{h^4}\mathbf{D}\mathbf{u}_p\right] + \mathbf{u}_p = \mathbf{u}_e + \frac{\mathbf{I}_s}{d}\mathbf{C}_x\dot{\mathbf{u}}_e. \tag{4}$$

Equation (4), together with the pile-top and -bottom boundary conditions, leads to $n+5$ unknown displacements, which involve the pile nodes from 1 to $n+1$ (see Figure 1) and 4 additional nodes at the pile top and tip. Equation (4) is resolved in either frequency or time domain and may attain the required accuracy using 21 segments of the pile [32].

2.3. Soil-Displacement-Influence Coefficients. Poulos and Davis [32] obtained soil-displacement-influence coefficients $\mathbf{I}_s$ by integrating the Mindlin equation over a rectangular plane and taking the pile as a thin rectangular vertical strip. Ideally, a circular pile (rather than a thin strip) should be used. In elastic, semi-infinite space, the force P in the horizontal direction at a depth c induces a displacement component u_x, which at any other point (x, y, z) is given by

$$u_x = \frac{P}{G} f(\mu_s, x, y, z, c), \quad (5)$$

where G is shear modulus of soil and μ_s is the Poisson ratio.

The coefficients of the proposed method are obtained in two steps: firstly, (5) is integrated over a rectangular area from a depth c of c_1 to c_2 and across the pile width from $-d/2$ to $d/2$ in Figure 2 which offers

$$u_x(\mu_s, x, y, z, c, s) = \frac{P}{G}\int_{-d/2}^{d/2}\int_{c_2}^{c_1} f(\mu_s, x, y-s, z, c)\, ds. \quad (6)$$

Secondly, (6) is reexpressed in a cylindrical coordinate, which is then integrated over the semi-circular pile surface with respect to the angle θ (see Figure 2) to gain the horizontal component of the displacement. The soil-displacement-influence coefficients, taking as weighted average of the integrated horizontal displacements, are deduced as

$$I_s = \frac{P}{G}\int_0^{\pi/2}\int_{-d/2}^{d/2}\int_{c_2}^{c_1} f\left(\mu_s, \frac{d}{2}\cos\theta, \frac{d}{2}\sin\theta - s, z, c\right)\cos\theta\, dc\, ds\, d\theta. \quad (7)$$

Equation (7) is solved by numerical integration using an adaptive Lobatto rule [36].

2.4. Harmonic Response in the Frequency Domain. Wave produces horizontal harmonic motion in the free field, as shown in Figure 1. This is described by $u(t) = U_g e^{i\omega t}$, and the associated free-field horizontal displacement is given by $u(t) = U_e e^{i\omega t}$. One-dimensional site response analysis can be formulated as

$$\rho\frac{\partial^2 u}{\partial t^2} = G\frac{\partial^2 u}{\partial z^2} + \eta\frac{\partial^3 u}{\partial z^2 \partial t}, \quad (8)$$

where ρ is the mass density, η is viscosity, and $u(z,t)$ is displacement. Equation (8) is resolved in frequency domain analysis [37, 38], allowing the nodal relative displacement to be obtained.

The current dynamic analysis employs time domain analysis and frequency domain analysis [21, 35, 39]. Frequency domain methods are widely used to estimate the dynamic impendences of the pile head. In the strong seismic motions, time domain method (involving the Newton-Raphson iteration and the Newmark method [40]) is used to obtain the nonlinear results. Equation (4) was resolved in time domain [28]. In contrast, to facilitate comparison with the rigorous FE method and BDWF model, (4) is resolved herein in the frequency domain by the following form:

$$\left[\mathbf{E} + \frac{\mathbf{I}_s}{d}\left(\frac{E_p I_p}{h^4}\mathbf{D} - \omega^2\mathbf{M} + i\omega\mathbf{C}_x\right)\right]\mathbf{U}_p = \left(\mathbf{E} + i\omega\frac{\mathbf{I}_s\mathbf{C}_x}{d}\right)\mathbf{U}_e, \quad (9)$$

where $i = \sqrt{-1}$; ω is the excitation frequency; $\mathbf{U}_p$ is the amplitude of pile displacement; $\mathbf{U}_e$ is the amplitude of addition displacement in the free-field soil; and $\mathbf{E}$ is the identity matrix.

A cut-off method [28, 33] is generally used to accommodate soil yield around the pile. If the pressure at the pile-soil interface exceeds the ultimate lateral pressure of soil, the excess pressure is redistributed to other segments through iteration until pressure at all pile nodes within the ultimate values. This study, however, will not consider this yield and will be confined to elastic analysis using the simplified approach for piles in two-layer soil.

3. Validation of Simplified Method

3.1. Comparison with Dynamic Finite-Element Solution. The proposed simple approach is compared with dynamic FE results concerning a free head pile embedded in a two-layer soil deposit [19]. The pile-soil model is the same as that shown in Figure 1, except that the pile tip is extended into the underlying bedrock. The pile-soil system is featured by a ratio of soil layer thickness H_a/H_b of 1, a soil density $\rho_a = \rho_b$, a soil Poisson's ratio $\mu_a = \mu_b = 0.4$, and a soil damping coefficient $\beta_a = \beta_b = 10\%$. The pile has a slenderness ratio L/d of 20, a pile-to-soil stiffness ratio E_p/E_a of 5000, and a pile density ρ_p of 1.60 ρ_a ($\rho_a = 1900\ \mathrm{kg/m^3}$).

A comparison between the simplified approach and FE solution [19] is presented in Figures 3(a) and 3(b), respectively, for the profiles of the pile deflection and bending moment amplitude at the natural frequency of soil deposit ($\omega = \omega_1$). A good agreement is evident. The current, simplified approach can reveal the kinematic bending moments at the interface of the two layers, despite the ~20% overestimation of the maximum bending moment (against FE result) of the pile in Case D.

Figure 4 shows the amplitude spectrum of maximum kinematic bending moment as a function of the frequency ratio ω/ω_1. A good agreement is again observed between the simplified approach and the dynamic FE solution [19]. Both indicate that the peak kinematic bending moment occurs at the inherent frequency of the soil.

3.2. Comparison with BDWF Formulation. The proposed approach for kinematic loading along the pile depth during the lateral ground movements is compared with the BDWF solution [19]. The pile-soil system is the same as the case just discussed in the last section. To examine the sensitivity of the parameters, four groups of 12 cases (Table 1) were studied, by maintaining soil density $\rho_a = \rho_b$, soil Poisson's

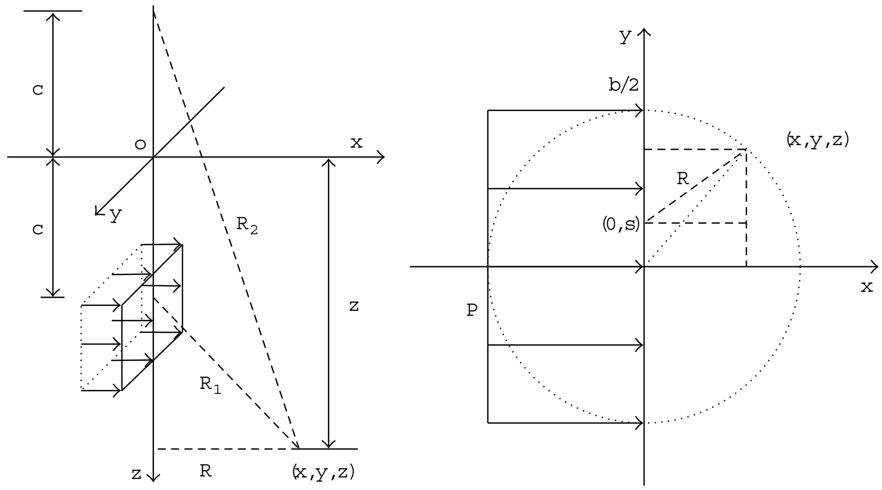

(a) Integrated area

(b) Weighted average area

FIGURE 2: Integrated along the semi-circular pile surface.

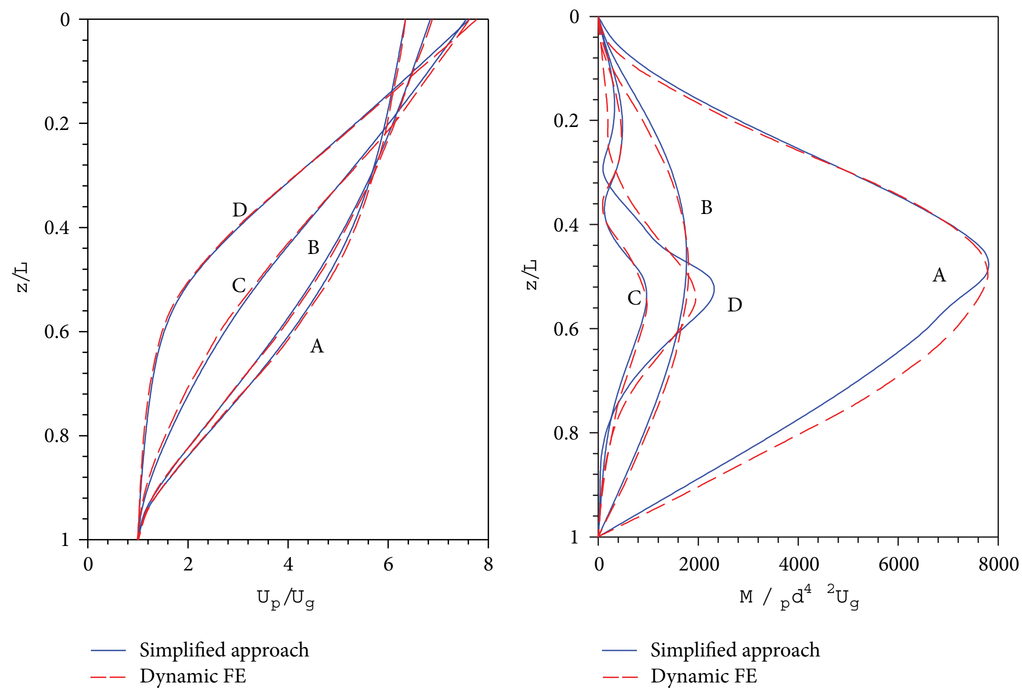

(a) Deflections

(b) Kinematic bending moment

FIGURE 3: Comparison of amplitude of pile deflections and bending moment between FE solution and simplified method in a two-layer soil (A: $V_b/V_a = 0.58$, B: $V_b/V_a = 1$, C: $V_b/V_a = 1.73$, and D: $V_b/V_a = 3$).

ratio $\mu_a = \mu_b = 0.4$, soil damping coefficient $\beta_a = \beta_b = 10\%$, and pile density $\rho_p = 1.60\rho_a$.

As shown in Table 1, the BDWF method adopts an optimized δ to obtain kinematic pile bending at the interface of two-layer soil. In contrast, the current method uses the displacement-influence coefficients $\mathbf{I}_s$ to consider the pile-soil interaction (resembling the spring constant k_x in the Winkler model) and may incorporate the interaction of soil along the pile to improve the accuracy. Nevertheless, when the ratio of the shear wave velocities V_b/V_a of two soil layers exceeds 3, a larger than 15% error (compared with the FE method) in maximum kinematic bending moment may be seen using the simplified method. This is discussed next concerning Case 12 for kinematic bending at the two-layer interface and at the pile head (at the natural frequency of soil deposit).

3.2.1. Kinematic Pile Bending. Figure 5 shows the amplitude distributions of kinematic pile bending and shear force from the simplified method and the BDWF solutions. The

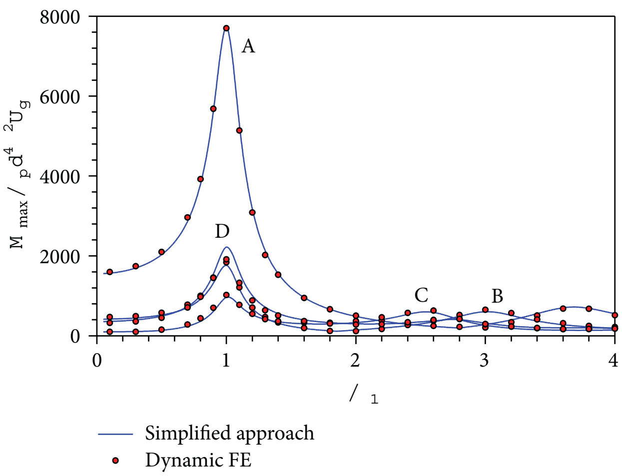

FIGURE 4: Comparison of maximum bending moment amplitude between FE solution and simplified method in a two-layer soil (A: V_b/V_a = 0.58, B: V_b/V_a = 1, C: V_b/V_a = 1.73, and D: V_b/V_a = 3).

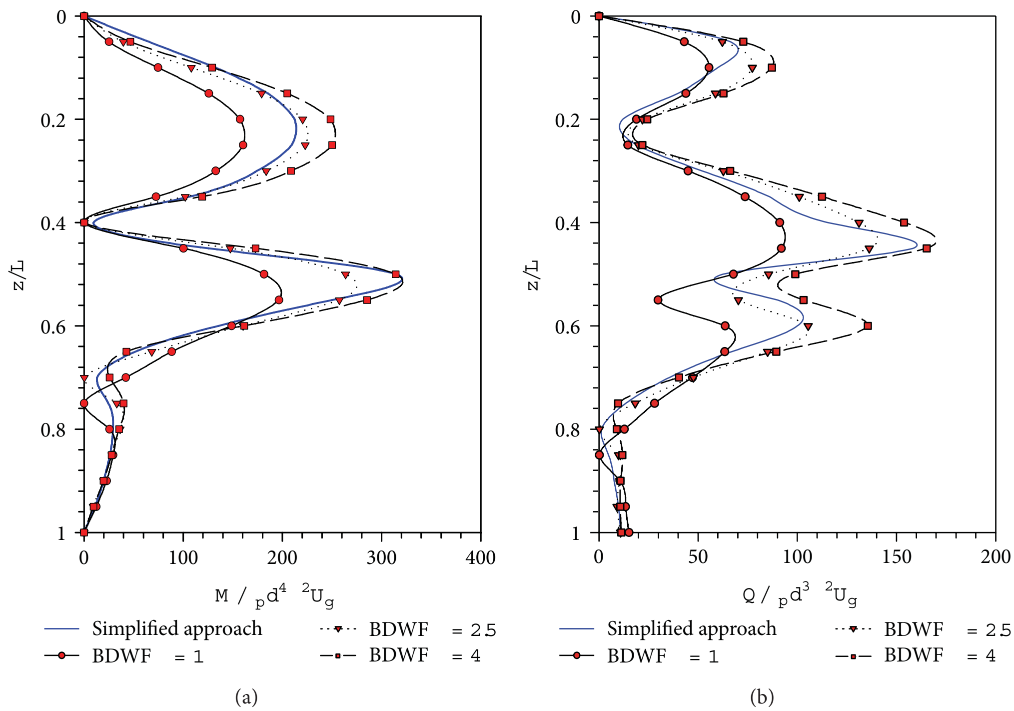

FIGURE 5: Comparison of amplitude of (a) bending moment profile and (b) shear force profile for two-layer soil (Case 12: V_b/V_a = 1.73, E_p/E_a = 500, H_a/H_b = 1, and L/d = 20).

kinematic pile bending and shear force profiles are slightly sensitive to the value δ. At $\delta = 2.5$, the distribution profiles of pile moment and shear force agree with each other between the simplified results and the BDWF solution, although the maximum moment of the simplified method is 17.2% larger than the BDWF solution.

Figure 6 provides the corresponding amplitude spectrum of maximum kinematic pile bending moment in the two-layer soil, owing to variation in the frequency ratio ω/ω_1, among the FE, the BDWF, and the simplified approaches. It shows a consistent trend of variation in bending moment among various approaches.

3.2.2. Kinematic Response of Pile Head. Kinematic responses are obtained in form of the ratio of the amplitudes of pile-head displacement $\mathbf{u}_p(0)$ over the excitation motion $\mathbf{u}_g$ or the ratio of the head displacement $\mathbf{u}_p(0)$ over the free field surface displacement $\mathbf{u}_e(0)$ [17, 26, 39]. The responses for the free-head pile are plotted in Figure 7 for a spectrum of the frequency ratio ω/ω_1. The good agreement of the factors $\mathbf{u}_p(0)/\mathbf{u}_g$ and $\mathbf{u}_p(0)/\mathbf{u}_e(0)$ among the simplified approach, the FE method, and the BDWF solution has been attributed to the predominant effect of the free field soil displacement.

As for fixed-head piles, equally successful prediction is seen in Figure 8, concerning the kinematic response of pile to

Table 1: Comparison of FE, BDWF, and the present simplified approach for dimensionless maximum kinematic pile bending $M_{\max}(\omega_1)/\rho_d d^4 \ddot{U}_g$ during the harmonic excitation.

Case	L/d	E_p/E_a	H_a/H_b	V_a/V_b	Previous $\omega_1 d/V_a$	Computed $\omega_1 d/V_a$	FE method	δ_{comp}	BDWF method	Error1: %	Simplified results	Error2: %
1	10	500	1	0.58	0.0964	0.0968	709	2.21	760	7.2	752	6.0
2	20				0.0482	0.0484	1253	2.41	1282	2.3	1326	5.8
3	40				0.0241	0.0242	2088	2.63	2196	5.2	2313	10.8
4	10	5000	1		0.0964	0.0968	1854	1.66	1623	−12.5	1921	3.6
5	20				0.0482	0.0484	7718	1.81	8019	3.9	7735	0.2
6	40				0.0241	0.0242	13120	1.97	13320	1.5	13406	2.2
7	20	1000	3	1.5	0.0916	0.0910	508	2.27	515	1.4	555	9.2
8	20	10000	1/3		0.1164	0.1159	1113	1.42	1097	−1.4	1119	0.6
9	20		1		0.1058	0.1056	931	1.55	1070	14.9	663	−28.8
10	20		3		0.0913	0.0910	1482	1.70	1433	−3.3	1547	4.4
11	10	500	1	1.73	0.2310	0.2293	86	2.05	79	−8.1	96	11.6
12	20				0.1155	0.1147	269	2.24	253	−5.9	315	17.2
13	40				0.0578	0.0573	656	2.44	577	−12.0	778	18.7
14	10	5000	1		0.2310	0.2293	273	1.54	266	−2.6	265	−2.9
15	20				0.1155	0.1147	998	1.68	860	−13.8	963	−3.5
16	40				0.0578	0.0573	3054	1.83	2825	−7.5	3144	3.0
17	20	1000	3	3	0.1017	0.1009	1046	2.17	1075	2.8	1331	27.3
18	20	10000	1/3		0.2117	0.2094	875	1.35	896	2.4	1217	39.1
19	20		3		0.1415	0.1403	2949	1.48	3042	3.2	3470	17.7
20	20		3		0.1019	0.1009	4867	1.63	4911	0.9	5608	15.2
21	20	1000	3	6	0.1042	0.1037	1486	2.07	1480	−0.4	2077	39.7
22	20	10000	1/3		0.2897	0.2849	1128	1.29	1274	12.9	1827	62.0
23	20		1		0.1535	0.1526	3809	1.42	4193	10.1	5073	33.2
24	20		3		0.1045	0.1037	6730	1.55	6831	1.5	8675	28.9

(1) Values of previous $\omega_1 d/V_a$, FE, δ_{comp}, and BDWF computed form a proposed simple analytical expression [19].
(2) Error1: percentage error in the BDWF moment compared with the FE moment. Error2: percentage error in the elastic moment compared with the FE moment.
(3) The values of computed $\omega_1 d/V_a$ are associated with the computed time interval.

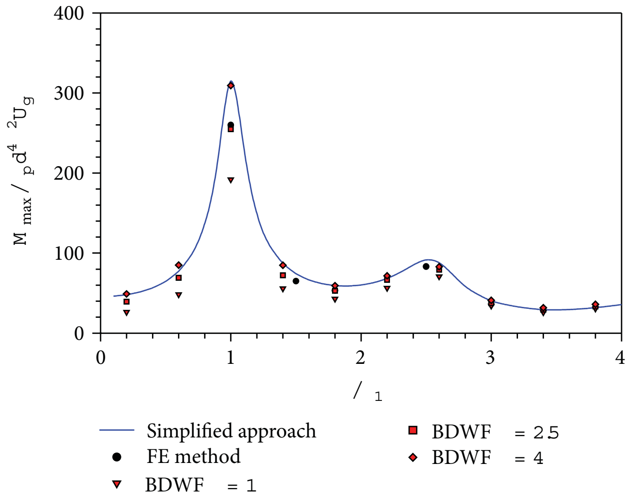

Figure 6: Comparison of maximum kinematic pile bending amplitude between FE, BDWF, and simplified approaches in a two-layer soil (Case 12: $V_b/V_a = 1.73$, $E_p/E_a = 500$, $H_a/H_b = 1$, and $L/d = 20$).

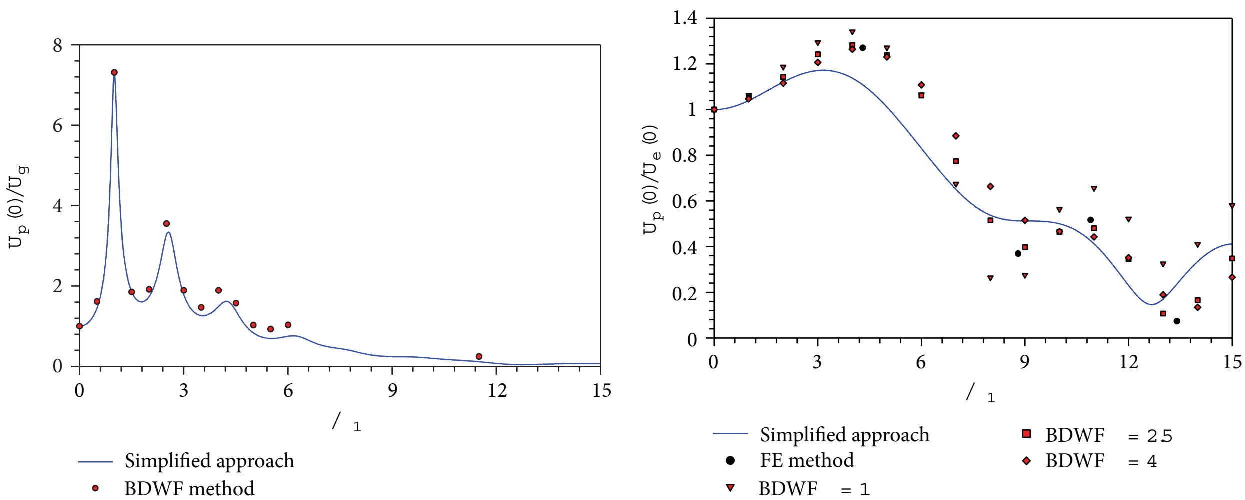

(a) Amplitude of pile-top deflection

(b) Pile-head to ground-surface displacements

Figure 7: Normalized kinematic response of pile head to excitation among FE, BDWF, and simplified methods in a two-layer soil (Case 12: $V_b/V_a = 1.73$, $E_p/E_a = 500$, $H_a/H_b = 1$, and $L/d = 20$).

soil displacement $\mathbf{u}_p(0)/\mathbf{u}_e(0)$ among the simplified method, the rigorous boundary integral method (Fan et al. [18]), and the BDWF (Makris and Gazetas [26]). Nevertheless, the current approach offers slightly larger ratio for $E_p/E_s = 1000$ than the other two solutions at high frequencies.

4. Application under Seismic Excitation

4.1. Seismic Motion and Case Model. The harmonic steady state is rarely seen in a practical engineering design. Kinematic seismic response of a pile should be tailored to cater for the transient excitation [19] owing to earthquake shaking, as is noted in dynamic analysis involving nonlinear pile-soil interaction. A large soil resistance in certain depth may render the nonlinear kinematic pile bending (e.g., caused by SH wave) insignificant compared to pile-head inertial excitation. In addition, previous study [13] does not allow either a detrimental or a beneficial effect on kinematic pile bending to be concluded due to non-linear site response. Consequently, the validity of the simplified method is examined herein for elastic pile and soil.

The performance of the simplified approach for the transient response is examined for six typical seismic accelerograms (see Table 2), which include 4 actual records selected from ground motion database of the Pacific Earthquake Engineering Research Center (PEER) [41] and 2 artificial motions used in seismic design of a typical site in Shanghai (China). The acceleration time histories for seismic events are plotted in Figure 9 and the associated acceleration response spectra are provided in Figure 10.

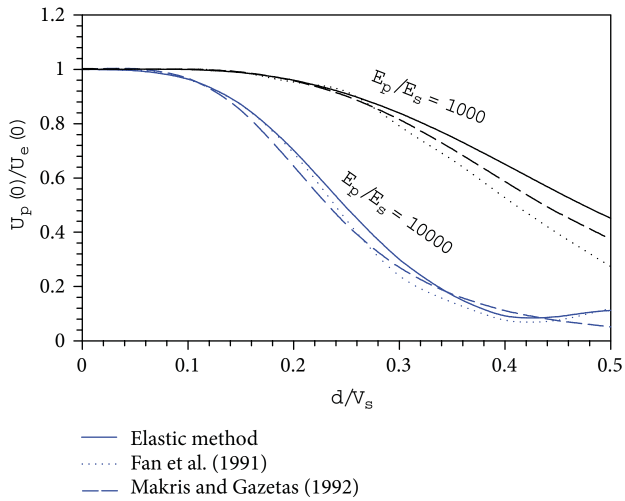

FIGURE 8: Normalized response of a fixed-head pile among simplified approach, BDWF [26], and rigorous results [18] ($L/d = 20$, $\rho_s/\rho_p = 0.7$, $\beta_s = 0.05$, and $\mu_s = 0.4$).

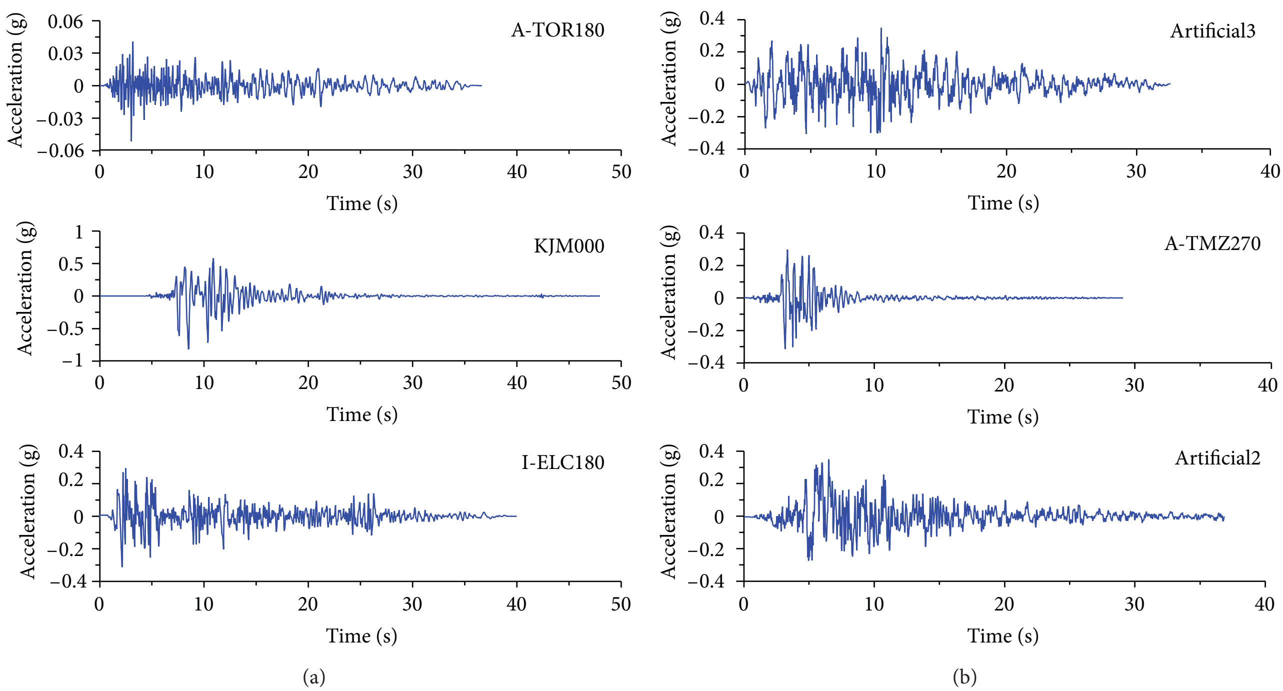

FIGURE 9: Acceleration time history of the input motions at the bedrock roof.

TABLE 2: Ground motions employed in the parametric analysis.

Earthquake	Record label	M_w	PGA (g)	T_p (sec)	T_m (sec)
Whittier Narrows 1987/10/01	A-TOR180	6.0	0.05	0.24	0.42
Kobe 1995/01/16	KJM000	6.9	0.82	0.34	0.64
Imperial Valley 1940/05/19	I-ELC180	7.0	0.31	0.46	0.53
ShangHai3-Elcentrol (IV Site)	Artificial3		0.35	0.58	0.82
Friuli 1976/05/06	A-TMZ270	6.5	0.32	0.64	0.50
ShangHai2 (IV Site)	Artificial2		0.35	0.72	0.75

T_p: predominant period and T_m: mean period.

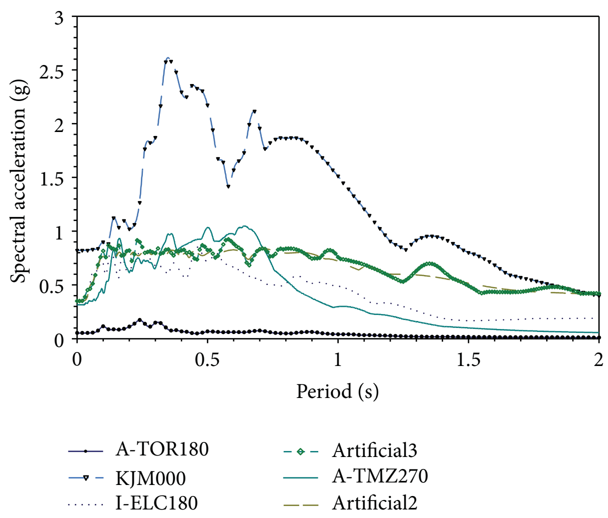

FIGURE 10: Acceleration response spectra (5% damping) of the input motions.

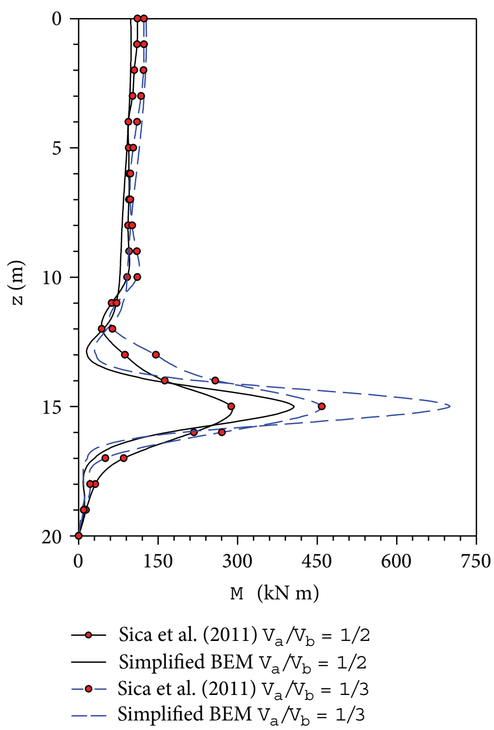

FIGURE 11: Validation of the proposed procedure under the input motion A-TMZ270 ($L/d = 33.3$, $H_a/H_b = 1$, $E_p/E_a = 470$, $\rho_s/\rho_p = 0.76$, and $\mu_a = \mu_b = 0.4$).

4.2. Parametric Investigation. The parametric analysis is again conducted for the pile-soil system shown in Figure 1, with the following profile parameters: bedrock located at $H = 30$ m, density of either soil layer = 1900 kg/m^3, Poisson's ratio = 0.4, soil damping = 5%, pile density = 2500 kg/m^3, and pile-to-soil stiffness ratio $E_p/E_a = 1000$. The shear wave velocity is 100 m/s for the upper soil layer, 150 m/s for the lower layer, and 1000 m/s for the bedrock, respectively. The input signals by Sica et al. [31] were scaled in amplitude to a peak acceleration of 0.35 g [31]. Figure 11 shows the comparison of kinematic pile bending between the simplified proposed approach and the BDWF formulation [31]. A good agreement in the predicted bending moment is evident between the simplified method and the BDWF solution, but for the large difference in the peak bending moment around the layer interface and at a shear wave velocity ratio V_a/V_b of 1/3.

Figure 12 shows the pile-diameter contrast on kinematic bending moment under the six input motions. The ratio of soil layer thickness H_a/H_b is 1, the pile is 20 m in length and 0.6, 0.9, or 1.2 m in diameter, and the head is

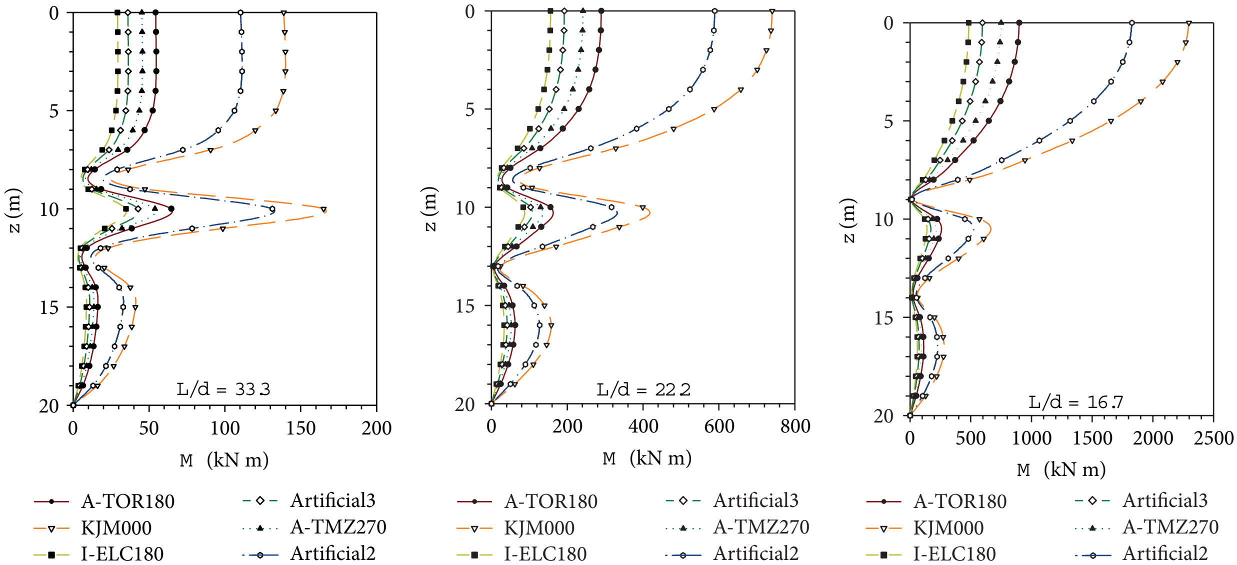

(a) (b) (c)

Figure 12: Pile diameters contrast on kinematic pile bending moment under different input motions.

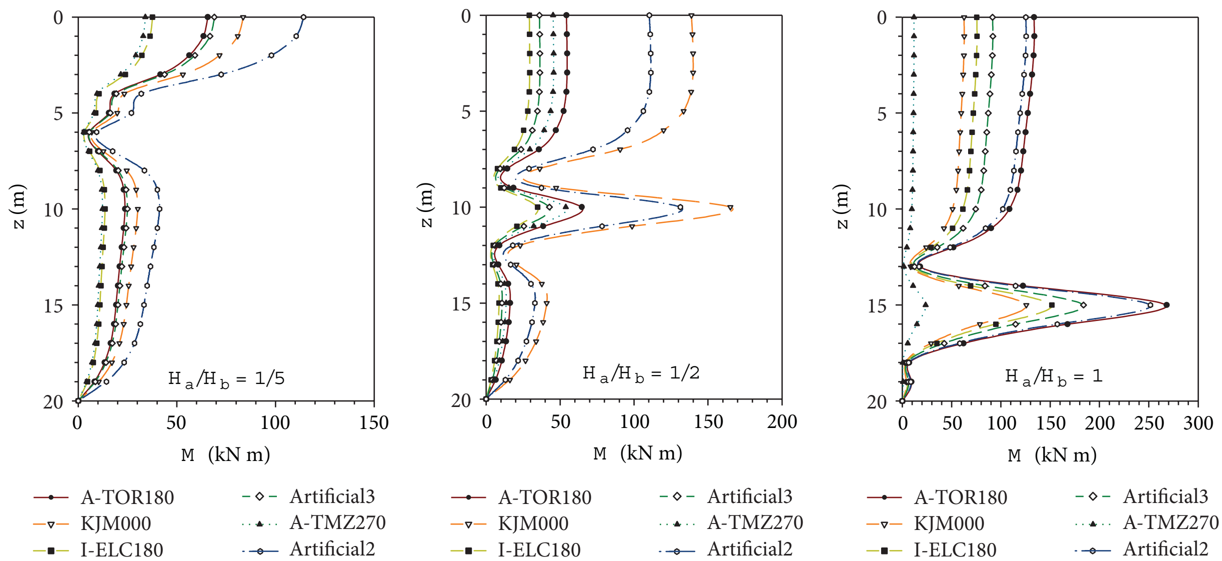

(a) (b) (c)

Figure 13: Depths of the interface between the two layers contrast on kinematic pile bending moment under different input motions.

constrained against rotation (fixed head). The figure indicates that small-diameter piles accommodate more easily to seismically induced soil deformations than lager-diameter piles. Kinematic bending moments at the pile head and the interface of soil layers are nearly proportional to the diameters. This will reduce the safety of pile head, although it does not necessarily increase or reduce the seismic safety of the pile body (depending on the circumstances), as is discussed previously [10, 14].

Figure 13 presents the bending moment profiles owing to variation in the depths of the interface of the two layers under the six input motions. They were obtained for a fixed head pile (20 m in length, 0.6 m in diameter) embedded in a soil with a layer interface located at a depth of 5, 10, or 15 m, respectively. An increase in depth of the interface renders increase in the peak value of kinematic pile bending but has a negligible impact on the kinematic bending moment at the pile head. This preliminary analysis suggests the simplified approach has the potential in modeling kinematic seismic response of piles during the earthquake.

5. Conclusion and Discussions

A simple approach is formulated to predict the elastic, kinematic pile bending during harmonic or transient excitation. The approach employs a circular pile (rather than a simplified thin strip). The kinematic response of a pile embedded in two-layer soil is resolved in the frequency domain owing to specified soil displacement field. The simplified approach is generally valid to nonhomogeneous soil problems, in light of the good comparison with the dynamic FE method and BDWF solution. The main conclusions from the study are as follows.

The simplified method employs the soil-displacement-influence coefficients $\mathbf{I}_s$ to consider the pile-soil interaction (resembling the spring constant k_x in the BDWF). It provides conservative estimation of maximum kinematic bending moments at soil-layer interface (with a sharper stiffness contrast) despite an adequate accuracy in general. The accuracy may be improved by incorporating the interaction of soil into the soil-displacement-influence coefficients $\mathbf{I}_s$ for such cases with $V_b/V_a < 3$.

The parametric studies during the seismic excitation show the impact of pile diameters and depths of the interface of two layers and demonstrate the simplified approach comparing well with published results in gaining kinematic pile bending during the earthquake.

The formulated simple method is intended for elastic soil, elastic pressure on pile-soil interface, and elastic seismic response of the free field soil, for which a judicious choice of elastic modulus of the soil is required. The method may be extended to elastoplastic case though introducing a similar technology as cut-off method [28, 33] in the current procedure.

Acknowledgments

The work reported herein was supported by the National Natural Science Foundation of China (Grants nos. 41172246, 90915011), the National Key Basic Research Program of China (Grant no. 2013CB036304), and the Fundamental Research Funds for the Central Universities, Tongji University. The above financial support is gratefully acknowledged.

References

[1] W. D. L. Finn, "A study of piles during earthquakes: issues of design and analysis," *Bulletin of Earthquake Engineering*, vol. 3, no. 2, pp. 141–234, 2005.

[2] S. Nikolaou, G. Mylonakis, G. Gazetas, and T. Tazoh, "Kinematic pile bending during earthquakes: analysis and field measurements," *Geotechnique*, vol. 51, no. 5, pp. 425–440, 2001.

[3] G. Mylonakis, "Simplified model for seismic pile bending at soil layer interfaces," *Soils and Foundations*, vol. 41, no. 4, pp. 47–58, 2001.

[4] B. A. Bradley, M. Cubrinovski, and J. J. M. Haskell, "Probabilistic pseudo-static analysis of pile foundations in liquefiable soils," *Soil Dynamics and Earthquake Engineering*, vol. 31, no. 10, pp. 1414–1425, 2011.

[5] J. P. Stewart, R. B. Seed, and G. L. Fenves, "Seismic soil-structure interaction in buildings. II: empirical findings," *Journal of Geotechnical and Geoenvironmental Engineering*, vol. 125, no. 1, pp. 38–48, 1999.

[6] T. Tazoh, K. Shimizu, and T. Wakahara, "Seismic observations and analysis of grouped piles," in *Dynamic Response of Pile Foundations-Experiment, Analysis and Observation (GSP 11)*, pp. 1–20, 1987.

[7] K. Tokimatsu, "Behaviour and design of pile foundations subjected to earthquakes," in *Proceedings of the 12th Asian Regional Conference on Soil Mechanics and Geotechnical Engineering*, , vol. 1 and 2, Singapore, 2003.

[8] K. Tokimatsu, H. Suzuki, and M. Sato, "Effects of inertial and kinematic interaction on seismic behavior of pile with embedded foundation," *Soil Dynamics and Earthquake Engineering*, vol. 25, no. 7-10, pp. 753–762, 2005.

[9] R. M. S. Maiorano, L. De Sanctis, S. Aversa, and A. Mandolini, "Kinematic response analysis of piled foundations under seismic excitation," *Canadian Geotechnical Journal*, vol. 46, no. 5, pp. 571–584, 2009.

[10] F. Dezi, S. Carbonari, and G. Leoni, "Kinematic bending moments in pile foundations," *Soil Dynamics and Earthquake Engineering*, vol. 30, no. 3, pp. 119–132, 2010.

[11] L. de Sanctis, R. M. S. Maiorano, and S. Aversa, "A method for assessing kinematic bending moments at the pile head," *Earthquake Engineering & Structural Dynamics*, vol. 39, no. 10, pp. 1133–1154, 2010.

[12] R. Di Laora, G. Mylonakis, and A. Mandolini, "Pile-head kinematic bending in layered soil," *Earthquake Engineering & Structural Dynamics*, vol. 42, pp. 319–337, 2013.

[13] S. Sica, G. Mylonakis, and A. L. Simonelli, "Strain effects on kinematic pile bending in layered soil," *Soil Dynamics and Earthquake Engineering*, vol. 49, pp. 231–242, 2013.

[14] R. Di Laora, A. Mandolini, and G. Mylonakis, "Insight on kinematic bending of flexible piles in layered soil," *Soil Dynamics and Earthquake Engineering*, vol. 43, pp. 309–322, 2012.

[15] M. Saitoh, "Fixed-head pile bending by kinematic interaction and criteria for its minimization at optimal pile radius," *Journal of Geotechnical and Geoenvironmental Engineering*, vol. 131, no. 10, pp. 1243–1251, 2005.

[16] R. Di Laora and A. Mandolini, "Some remarks about Eurocode and Italian code about piled foundations in seismic area," in *Presented at the ERTC-12 Workshop on Evaluation of EC8*, Athens, Greece, 2011.

[17] A. M. Kaynia and E. Kausel, "Dynamic stiffness and seismic response of pile groups," Research Report R82-03, Massachusetts Institute of Technology, Cambridge, Mass, USA, 1982.

[18] K. Fan, G. Gazetas, A. Kaynia, E. Kausel, and S. Ahmad, "Kinematic seismic response of single piles and pile groups," *Journal of Geotechnical Engineering*, vol. 117, no. 12, pp. 1860–1879, 1991.

[19] M. Kavvadas and G. Gazetas, "Kinematic seismic response and bending of free-head piles in layered soil," *Geotechnique*, vol. 43, no. 2, pp. 207–222, 1993.

[20] M. H. El Naggar and M. Novak, "Nonlinear analysis for dynamic lateral pile response," *Soil Dynamics and Earthquake Engineering*, vol. 15, no. 4, pp. 233–244, 1996.

[21] G. Wu and W. D. L. Finn, "Dynamic nonlinear analysis of pile foundations using finite element method in the time domain," *Canadian Geotechnical Journal*, vol. 34, no. 1, pp. 44–52, 1997.

[22] B. K. Maheshwari, K. Z. Truman, M. H. El Naggar, and P. L. Gould, "Three-dimensional nonlinear analysis for seismic soil-pile-structure interaction," *Soil Dynamics and Earthquake Engineering*, vol. 24, no. 4, pp. 343–356, 2004.

[23] F. Dezi, S. Carbonari, and G. Leoni, "A model for the 3D kinematic interaction analysis of pile groups in layered soils,"

Earthquake Engineering & Structural Dynamics, vol. 38, no. 11, pp. 1281–1305, 2009.

[24] M. A. Millán and J. Domínguez, "Simplified BEM/FEM model for dynamic analysis of structures on piles and pile groups in viscoelastic and poroelastic soils," *Engineering Analysis with Boundary Elements*, vol. 33, no. 1, pp. 25–34, 2009.

[25] F. Dezi, S. Carbonari, and G. Leoni, "Static equivalent method for the kinematic interaction analysis of single piles," *Soil Dynamics and Earthquake Engineering*, vol. 30, no. 8, pp. 679–690, 2010.

[26] N. Makris and G. Gazetas, "Dynamic pile-soil-pile interaction. Part II: lateral and seismic response," *Earthquake Engineering & Structural Dynamics*, vol. 21, no. 2, pp. 145–162, 1992.

[27] G. Mylonakis, A. Nikolaou, and G. Gazetas, "Soil-pile-bridge seismic interaction: kinematic and inertial effects. Part I: soft soil," *Earthquake Engineering & Structural Dynamics*, vol. 26, no. 3, pp. 337–359, 1997.

[28] A. Tabesh and H. G. Poulos, "Pseudostatic approach for seismic analysis of single piles," *Journal of Geotechnical and Geoenvironmental Engineering*, vol. 127, no. 9, pp. 757–765, 2001.

[29] T. Juirnarongrit and S. A. Ashford, "Soil-pile response to blast-induced lateral spreading. II: analysis and assessment of the p-y method," *Journal of Geotechnical and Geoenvironmental Engineering*, vol. 132, no. 2, pp. 163–172, 2006.

[30] F. Castelli and M. Maugeri, "Simplified approach for the seismic response of a pile foundation," *Journal of Geotechnical and Geoenvironmental Engineering*, vol. 135, no. 10, pp. 1440–1451, 2009.

[31] S. Sica, G. Mylonakis, and A. L. Simonelli, "Transient kinematic pile bending in two-layer soil," *Soil Dynamics and Earthquake Engineering*, vol. 31, no. 7, pp. 891–905, 2011.

[32] H. G. Poulos and E. H. Davis, "Pile foundation analysis and design," 1980.

[33] H. Elahi, M. Moradi, H. G. Poulos, and A. Ghalandarzadeh, "Pseudostatic approach for seismic analysis of pile group," *Computers and Geotechnics*, vol. 37, no. 1-2, pp. 25–39, 2010.

[34] R. D. Mindlin, "Force at a point in the interior of a semi-infinite solid," *Journal of Applied Physics*, vol. 7, no. 5, pp. 195–202, 1936.

[35] Y. M. A. Hashash, C. Phillips, and D. R. Groholski, "Recent advances in non-linear site response analysis," in *Proceedings of the 5th International Conference in Recent Advances in Geotechnical Eartqhuake Engineering and Soil Dynamics*, 2010.

[36] L. F. Shampine, "Vectorized adaptive quadrature in MATLAB," *Journal of Computational and Applied Mathematics*, vol. 211, no. 2, pp. 131–140, 2008.

[37] D. Park and Y. M. A. Hashash, "Soil damping formulation in nonlinear time domain site response analysis," *Journal of Earthquake Engineering*, vol. 8, no. 2, pp. 249–274, 2004.

[38] G. A. Ordonez, "SHAKE2000: a computer program for the 1-D analysis of geotechnical earthquake engineering problems," 2004.

[39] G. Wu and W. D. L. Finn, "Dynamic elastic analysis of pile foundations using finite element method in the frequency domain," *Canadian Geotechnical Journal*, vol. 34, no. 1, pp. 34–43, 1997.

[40] R. W. Boulanger, C. J. Curras, B. L. Kutter, D. W. Wilson, and A. Abghari, "Seismic soil-pile-structure interaction experiments and analyses," *Journal of Geotechnical and Geoenvironmental Engineering*, vol. 125, no. 9, pp. 750–759, 1999.

[41] P. G. Motion, "Pacific earthquake engineering research center," Tech. Rep., University of California, Berkeley, Berkeley, Calif, USA, 2008.

Hindawi Publishing Corporation
Journal of Applied Mathematics
Volume 2013, Article ID 703251, 8 pages
http://dx.doi.org/10.1155/2013/703251

Research Article

Theoretical Analysis and Experimental Study of Subgrade Moisture Variation and Underground Antidrainage Technique under Groundwater Fluctuations

Liu Jie, Hailin Yao, Pan Chen, Zheng Lu, and Xingwen Luo

State key Laboratory of Geomechanics and Geotechnical Engineering, Institute of Rock and Soil Mechanics, Chinese Academy of Science, Wuhan 430071, China

Correspondence should be addressed to Liu Jie; liujie_whrsm@163.com

Received 22 May 2013; Revised 9 July 2013; Accepted 30 July 2013

Academic Editor: Ga Zhang

Groundwater is a main natural factor impacting the subgrade structure, and it plays a significant role in the stability of the subgrade. In this paper, the analytical solution of the subgrade moisture variations considering groundwater fluctuations is derived based on Richards' equation. Laboratory subgrade model is built, and three working cases are performed in the model to study the capillary action of groundwater at different water tables. Two types of antidrainage materials are employed in the subgrade model, and their anti-drainage effects are discussed. Moreover, numerical calculation is conducted on the basis of subgrade model, and the calculate results are compared with the experimental measurements. The study results are shown. The agreement between the numerical and the experimental results is good. Capillary action is obvious when the groundwater table is rising. As the groundwater table is falling, the moisture decreases in the position of the subgrade near the water table and has no variations in the subgrade where far above the table. The anti-drainage effect of the sand cushion is associated with its thickness and material properties. New waterproofing and drainage material can prevent groundwater entering the subgrade effectively, and its anti-drainage effect is good.

1. Introduction

It is widely accepted that groundwater is an important factor impacting the highway structure in plateau area [1–3]. Climate environment and groundwater significantly impact the engineering properties of subgrade soil, as a result of repeated fluctuations of groundwater with the variation of atmospheric environment. In that situation, groundwater that migrates into the subgrade under capillary action not only causes long-term strength attenuation of subgrade soil but also produces large plastic deformation in early stage of subgrade. Capillary action, as a main external environmental factor, can influence the subgrade stability. Ground waterproof and drainage technology can reduce and control the capillary water effectively, and it becomes the key to design highway subgrade structure.

Recently, considerable studies have been conducted to investigate the groundwater fluctuations [4–10]. Great results have been achieved based on the numerical analysis. In this paper, dynamic analysis on the law of subgrade moisture varying with groundwater fluctuations is conducted by numerical calculation, simplified analytical method, and laboratory model experiment. Two types of underground waterproofing and drainage materials are employed in the subgrade model, and their drainage effect are analyzed. Finally, the calculation and experiment results are contrasted.

2. Analysis of Subgrade Moisture Variation under Groundwater Fluctuations

Many studies [11–13] of groundwater fluctuations in the subgrade are based on numerical method; in this paper, the analytical method is introduced.

2.1. Basic Assumptions

(1) The initial moisture of the subgrade is stationary; the subgrade soil is homogeneous and isotropic.

(2) The rising and falling courses of the groundwater table are consistent, respectively.

2.2. Continuous Rising of Groundwater Table. The rising and falling of groundwater in the subgrade are simplified to be a course of one-dimensional vertical seepage, and the water movement equation can be performed:

$$\frac{\partial\theta}{\partial t} = \frac{\partial}{\partial z}\left[D(\theta)\frac{\partial\theta}{\partial z}\right] - \frac{\partial k(\theta)}{\partial z}, \tag{1}$$

where $D(\theta)$ is diffusion coefficient, $k(\theta)$ is permeability coefficient, t is time, and z is the height of the soil.

Boundary and initial conditions are as follows:

$$\begin{gathered}\theta = \theta_0 \quad t = 0,\ 0 \le z \le \infty,\\ \theta = \theta_s \quad t > 0,\ z = h = vt,\\ \theta = \theta_0 \quad t > 0,\ z = \infty,\end{gathered} \tag{2}$$

where v is rising speed of the groundwater, h is rising height of groundwater in time t. θ_s is saturated water content, θ_0 is initial water content. Applying the Laplace transformation, (1) is solved; $\theta(z,t)$ can be transformed:

$$\tilde{\theta}(z,p) = L(\theta(z,t)) = \int_0^\infty e^{-pt}\theta(z,t)\,dt, \tag{3}$$

and $\partial\theta(z,t)/\partial t$ and $\partial^2\theta(z,t)/\partial z^2$ can be transformed:

$$\begin{gathered}L\left(\frac{\partial\theta(z,t)}{\partial t}\right) = p\tilde{\theta}(z,p) - \theta(z,0),\\ L\left(\frac{\partial^2\theta(z,t)}{\partial z^2}\right) = \frac{d^2\tilde{\theta}(z,p)}{dx^2}.\end{gathered} \tag{4}$$

Equation (1) is converted to be image function ordinary differential equation:

$$D\frac{d^2\tilde{\theta}(h,p)}{dh^2} - p\hat{\theta}(h,p) + \theta_0 = 0. \tag{5}$$

By solving (5), $\tilde{\theta}(z,p)$ is obtained:

$$\tilde{\theta}(z,p) = ae^{z\sqrt{p/D}} + be^{-z\sqrt{p/D}} + \frac{\theta_0}{p}, \tag{6}$$

where a, b is undetermined coefficient and p is Laplace transformation parameters.

Substituting (2) into (6),

$$\begin{gathered}a = 0, \qquad b = \frac{\theta_s - \theta_0}{p}e^{h\sqrt{p/D}},\\ \tilde{\theta}(z,p) = \frac{\theta_s - \theta_0}{p}e^{(h-z)\sqrt{p/D}} + \frac{\theta_0}{p}.\end{gathered} \tag{7}$$

By checking the inverse Laplace transform table, the general expressions of subgrade moisture in arbitrary time and height under the condition of groundwater continuous rising are obtained:

$$\begin{gathered}\theta(z,t) = (\theta_s - \theta_0)\operatorname{erfc}\frac{z - vt}{2\sqrt{Dt}} + \theta_0, \quad vt \le z,\\ \theta(z,t) = \theta_s, \quad vt > z.\end{gathered} \tag{8}$$

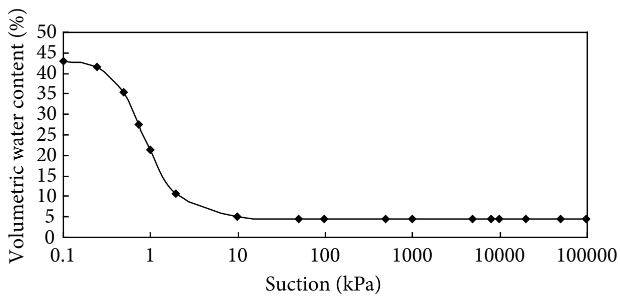

Figure 1: SWCC of sand subgrade.

2.3. Continuous Falling of Groundwater Table. The falling of groundwater meets the water movement equation (1); the boundary and initial conditions (2) are varied:

$$\begin{gathered}\theta = \theta_0 \quad t = 0,\ 0 \le z \le \infty,\\ \theta = \theta_s \quad t > 0,\ z = h_0 - vt,\\ \theta = \theta_0 \quad t > 0,\ z = \infty.\end{gathered} \tag{9}$$

The height of the initial groundwater table is h_0; the other symbols are the same to (2). Substituting (9) into (6), the general expression of subgrade moisture in arbitrary time and height under the condition of groundwater continuous falling is obtained:

$$\theta(z,t) = (\theta_s - \theta_0)\operatorname{erfc}\left(\frac{vt + z - h_0}{2\sqrt{Dt}}\right) + \theta_0. \tag{10}$$

2.4. Numerical Example. There is a sand subgrade; the height of the subgrade is 2 m, and the depth of the groundwater table is 1 m. The rising and falling speed of groundwater table is 0.0002 m/s, and its duration is 60 min. Soil and water parameters are shown in Figure 1.

Design and monitor programs of the experiment are shown in Figure 9. There are three working cases in three model boxes.

Variation of subgrade moisture in the rising and falling course of groundwater table can be seen in Figures 2 and 3. The numerical and analytical calculation results of subgrade moisture variations under groundwater fluctuations are compared in Figure 4. As the groundwater is rising, the capillary action of groundwater is obvious. In the tenth minutes, capillary water rises to 0.45 m, and in the sixth ten minutes, the capillary water rises to 1.7 m. As the groundwater is falling, subgrade moisture in the position near the groundwater table decreases rapidly, but it has no variations in the position far above the groundwater table; that is, because part of the capillary water cannot be discharged timely in a short time and still strands in the pores. The agreement between numerical and analytical methods solving subgrade moisture variations under groundwater fluctuations is good. It is reasonable and practicable using analytical method to obtain the subgrade moisture considering groundwater fluctuations.

Table 1: Basic soil properties of Hongshan clay.

Natural density/(g/cm^3)	Nature water content/%	Specific gravity/(g/cm^3)	Plastic limit/%	Liquid limit/%	Maximum dry density/(g/cm^3)	Optimum water content/%
1.386	21.8	2.76	21.11	43.42	1.88	15.7

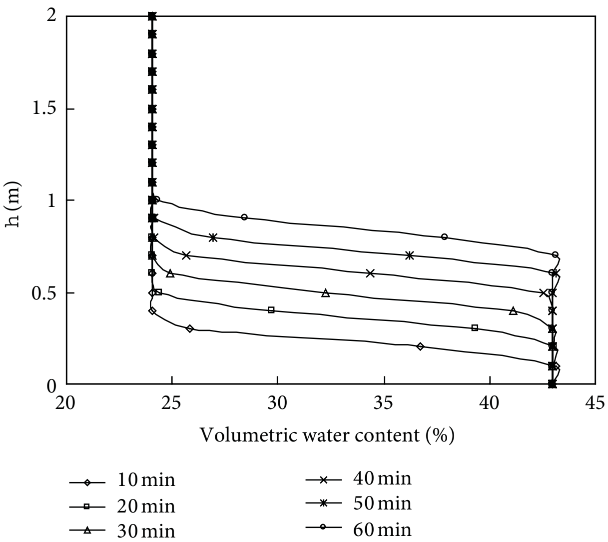

Figure 2: Variation of subgrade moisture in the rising course of groundwater table.

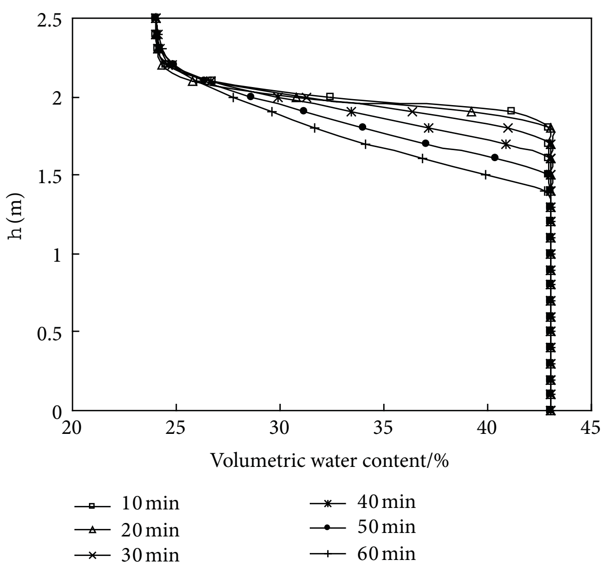

Figure 3: Variation of subgrade moisture in the falling course of groundwater table.

3. Laboratory Model Experiment

3.1. Laboratory Experimental Analysis for Basis Properties and Soil-Water Features of Hongshan Clay. The experimental soil is Hongshan clay; it is typical viscous soil. Table 1 lists its basis physic properties. The natural water content of Hongshan clay is close to its plastic limit and larger than its optimum water content.

3.2. Introduction of SWCC Experiment. The SWCC experiment of Hongshan clay is preparing for the laboratory subgrade model experiment; the experimental instruments are composed of air supply system, penetration instrument, control panel, a constant flow rate maintain system, weighing system, and data acquisition system. The main instruments are shown in Figures 5 and 6.

The diameter of the sample is 5.12 cm; its height is 2.83 cm. The initial water content of the sample is 15.7%, the compactness of the sample is 85 percent of maximum dry density obtaining from Table 1, and the sample is saturated. Different values (5 kPa, 10 kPa, 25 kPa, 50 kPa, 75 kPa, 100 kPa, 150 kPa, 200 kPa, 300 kPa, and 400 kPa) of air pressure are applied progressively on the sample; the weight of discharged water is recorded every day. The water content of the sample is obtained by calculating the discharged water under different air pressures. The step of pressurization, drainage, and weighing is repeated in the process of the experiment, and the SWCC of Hongshan clay is obtained.

The water content obtained from the experiment is mass water content θ_w, the conversion relation between volumetric water content θ_v and mass water content θ_w is $\theta_v = \theta_w \cdot \rho$, and the SWCC represented by volumetric moisture can be got.

Normally, SWCC meets an empirical formula like V-G model, Fredlund-Xing model, and so on. The V-G model is used in this paper, it is

$$\frac{\theta - \theta_r}{\theta_s - \theta_r} = \left(\frac{1}{1 + (\alpha h)^n}\right)^m, \quad \left(m = 1 - \frac{1}{n}, \ 0 < m < 1\right), \tag{11}$$

r, θ, r: empirical coefficients, θ_r: residual water content (cm^3/cm^3); θ_s: saturated water content (cm^3/cm^3); θ: soil water content (cm^3/cm^3).

The permeability function is also based on V-G model:

$$k_w = k_s \frac{\left[1 - \left(a\psi^{(n-1)}\right)\left(1 + (a\psi^n)^{-m}\right)\right]^2}{\left((1 + a\psi)^n\right)^{m/2}}. \tag{12}$$

The empirical coefficients in V-G model are got: $a = 0.021\,\text{kPa}^{-1}$; $n = 1.27$; $m = 0.2126$; the saturated permeability coefficient is $k_s = 4.74 \times 10^{-9}$ m/s. The comparison of SWCC got by experiment and VG model is shown in Figure 7.

3.3. Laboratory Subgrade Model Experiment. The Laboratory subgrade model is built in a plexiglass box with a length of

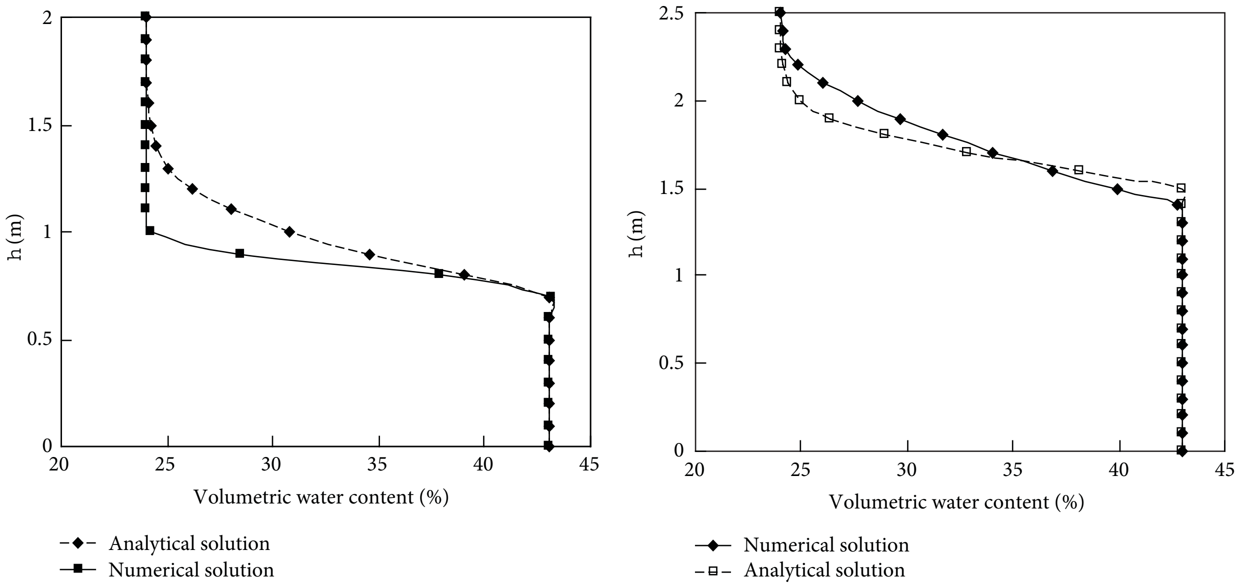

(a) Rising

(b) Falling

Figure 4: Comparison of numerical and analytical methods for solving subgrade moisture variations under groundwater fluctuations.

Figure 5: Outlet and evaporation correction bottle.

Figure 6: Servo flow permeameter.

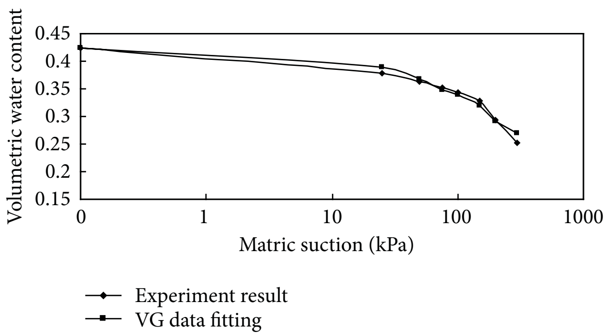

Figure 7: SWCC of Hongshan clay.

2.4 m, a width of 0.8 m, and a height of 1.6 m. It is divided into 3 same boxes along the lengthwise direction, and the filling height of soil is 0.8 m in each box. A layer of gravel is laid at the bottom of the model to speed up the seepage of the groundwater, which thickness is about 10 cm; permeable geotextiles are laid at the top and bottom surface of the gravel, and they cannot only prevent the fine-grained soils falling into the gravel pores influencing the seepage of groundwater, but also prevent the gravel piercing the model box during soil compaction process.

The experiment device is composed of plexiglass box, water tank, and measurement acquisition apparatus. Hongshan clay is used as subgrade/foundation filling material, and groundwater table is controlled by adjusting the water level in the water tank. The design process of water fluctuations is set as 0.1 m → 0.3 m → 0.5 m. Experiment temperature is kept at (25 ± 2°C). The duration of groundwater table in each height is 60 d, 100 d, and 100 d. The initial mass moisture content of subgrade model filling is 21.5%, and its compaction degree is 85%.

Table 2: Conversion relationship of mass and volumetric water content got from the moisture probes.

Mass water content/%	Volumetric water content got from the moisture probes/%								
	1-1#	1-2#	1-3#	2-1#	2-2#	2-3#	3-1#	3-2#	3-3#
18.4	31.9	30	30	30.44	29.4	30.21	26.8	27.7	27.9
19.5	33.5	33	33	30.35	29.83	31.89	33.2	29.3	29.8
21.6	35	36	34.58	35.28	33.63	34.82	34.7	32.7	33.9
23.55	38.6	38.2	36.91	37.76	36.28	39.21	36.1	35.1	36.3
24.92	39.2	40.01	39.88	39.52	39.15	40.64	38.8	38.8	39.2

Figure 8: Subgrade model.

Water content is monitored once per hour in each model box using water content probes (accuracy = ±2%, monitor range = 0~100% (m^3/m^3)). The probes are set at 0.3 m, 0.5 m, and 0.7 m in height. Since the data got from the water content probes is mass water content, it is needed to be converted to volumetric water content. The conversion relationship is presented in Table 2.

Fitting formulas of mass and volumetric water content for each probe are

1-1#: $y = 1.155x + 0.1069$, 1-2#: $y = 1.4618x + 0.0388$, 1-3#: $y = 1.3612x + 0.054793$,

2-1#: $y = 1.5178x + 0.018915$, 2-2#: $y = 1.5271x + 0.006819$, 2-3#: $y = 1.651x - 0.0031$,

3-1#: $y = 1.5182x + 0.0114$, 3-2#: $y = 1.631x + 0.024993$, 3-3#: $y = 1.6998x - 0.032638$,

where x is mass water content and y is volumetric water content.

The subgrade model is shown in Figure 8.

Case 1 (box 1). The height of the foundation is 0.6 m; the height of the subgrade is 0.3 m, there has no drainage facilities.

Case 2 (box 2). The height of the foundation is 0.6 m; the height of the subgrade is 0.3 m; and waterproof sand cushion (about 10 cm thick) is set between the foundation and subgrade.

Case 3 (box 3). The height of the foundation is 0.6 m; the height of the subgrade is 0.3 m; a layer of new antidrainage material, that is, plastic film and plastic drainage plate, is set between foundation and subgrade.

Plastic film is used to prevent the groundwater rising into the subgrade, and plastic drainage plate is employed as a drainage path of water in the subgrade. Plastic film is placed on the plastic drainage plate, which is laid on the foundation, and they are compacted. Some drain holes are drilled in the position of plastic drainage plate in the box, in order to promote the discharge of groundwater. Figure 10 shows the details of the new antidrainage material.

4. Analysis of Experiment Results

4.1. The Tendency of Moisture Variations of Subgrade Model. Variations of subgrade moisture in model boxes 1, 2, and 3 are shown in Figure 11. In Stage 1, the groundwater table is at the height of 0.1 m, and the variation tendency of subgrade moisture is consistent at the height of 0.3 m in three boxes; there are some increases in moisture at the beginning of the experiment, but the variation rate gradually slows as the experiment going on. At the height of 0.5 m, which is far above the groundwater table, the moisture in the subgrade has no variations. After a period of time, the capillary water rises and enters into the interior of subgrade. Subgrade moisture above the water table begins to increase continuously in three boxes. But at the height of 0.7 m, the subgrade moisture in boxes 2 and 3 has no variations. That is, because the thick waterproof sand cushion and antidrainage material are set respectively in boxes 2 and 3, capillary water is prevented from entering the subgrade. From

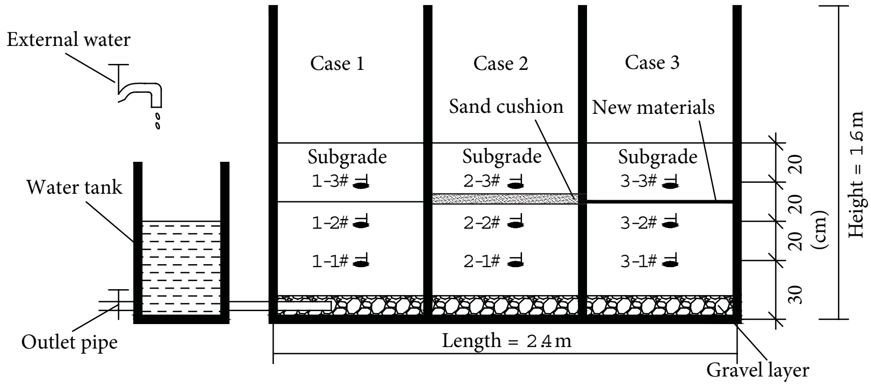

FIGURE 9: Schematic cross-section of subgrade model.

(a) (b)

FIGURE 10: New antidrainage material.

the experiment result, it can be concluded that when the groundwater table is low, thick waterproof sand cushion and antidrainage material can play a good role in waterproof and drainage.

In Stage 2, the groundwater table rises to the height of 0.3 m. The moisture of the subgrade below the water table reaches saturated moisture in three model boxes. In 1# model box, the path of capillary water rising to the higher subgrade is shorter than that in Stage 1. Consequently, the subgrade moisture rises from 35.02% to 40.85% at the height of 0.7 m. In 2# model box, waterproof sand cushion inside the model keeps some water out of the upper subgrade. Due to the maximum rising height of the capillary water that is higher than the thickness of the sand cushion, the sand cushion cannot keep all of the capillary water out of the internal subgrade, and subgrade moisture varies from 32.85% to 34.72% at the height of 0.7 m. In 3# model box, antidrainage material unleashes a good antidrain effect; the subgrade moisture in the position above the material has no variations.

In Stage 3, the groundwater table rises to 0.5 m. In 1# model box, the subgrade moisture above the water table has no variations, since the subgrade moisture has varied completely in the prophase, and it would not vary at this stage. In 2# model box, the sand cushion has no antidrainage effect completely in this stage. Subgrade moisture varies significantly at the height of 0.7 m. In 3# model box, the subgrade moisture in the position above the water table still has no variations, and it can be proved that the new antidrainage material has good antidrainage effect.

4.2. Comparison of Numerical Calculated Subgrade Moisture with Experimental Results. In this paper, we focus on the subgrade moisture variations under the capillary action of the groundwater, so we did not do any physical properties experiments for the waterproof sand cushion in Case 2. Meanwhile, it is difficult to obtain the properties and permeability of the plastic drainage plate by conventional laboratory experiment, so, the analysis is conducted only in Case 1.

Stage 1. Groundwater table stays at the height of 0.1 m, and its duration is 60 d.

Stage 2. Groundwater table rises from the height of 0.1 m to 0.3 m, and its duration is 100 d.

Stage 3. Groundwater rises from the height of 0.3 m to 0.5 m, and its duration is 100 d.

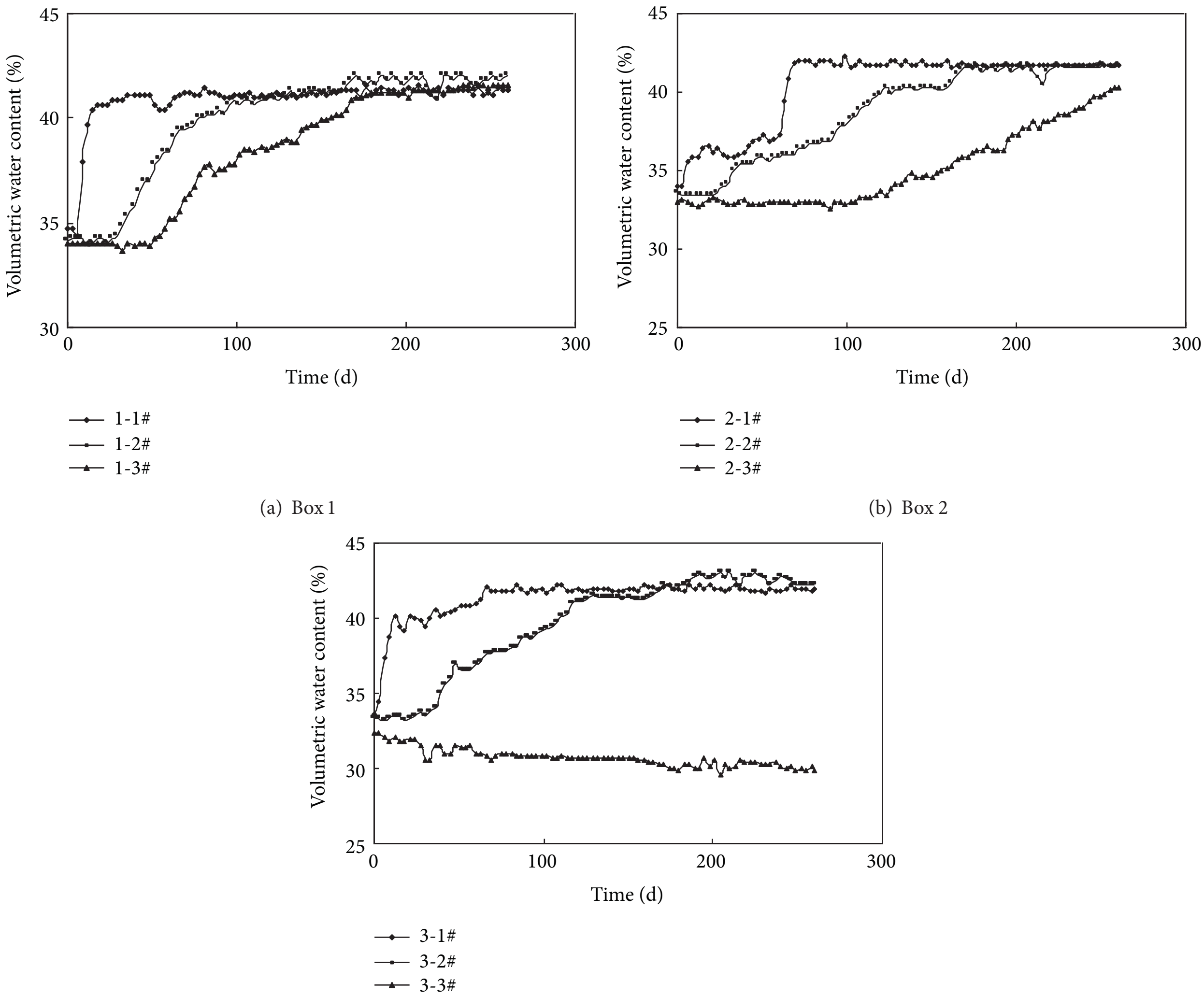

(a) Box 1

(b) Box 2

(c) Box 3

Figure 11: Variations of subgrade moisture in model boxes 1, 2, and 3.

Comparisons of calculated subgrade moisture with experimental results in different stages are shown in Figures 12, 13, and 14. During the process of numerical calculation analysis, the soil water parameters are obtained by SWCC experiment, and its results are precise and not affected by some factors like (environment, initial water content, compaction effects, etc.), the saturation level of the soil got from the model experiment is less than that got from SWCC experiment, but it does not affect the reliability to study the vary trends of the subgrade moisture using laboratory model experiment. The vary trends of subgrade moisture considering groundwater fluctuations which obtained by laboratory model experiment and numerical calculation are consistent.

5. Conclusions

Subgrade moisture increases constantly under the capillary action in the process of groundwater continuous rising, and the variation of the subgrade moisture with the time is significant. In the process of the groundwater continuously falling, the subgrade moisture decreases near the groundwater table and has no variations far above the groundwater table.

The results obtained from the laboratory subgrade model experiment show that sand waterproof cushion can prevent water from entering the upper subgrade when the groundwater is low, but its blocking effect is associated with its material properties, thickness, and the height of the groundwater table. New antidrainage material can completely prevent capillary water from entering the entire range of subgrade, and it has effective antidrainage function.

Although there are many factors affecting the results in the experimental process, a good consistence is obtained between laboratory model experiment and numerical calculation of the moisture variations in subgrade considering groundwater fluctuations. It can be concluded that the subgrade moisture migration law can be well reflected by laboratory subgrade model experiment.

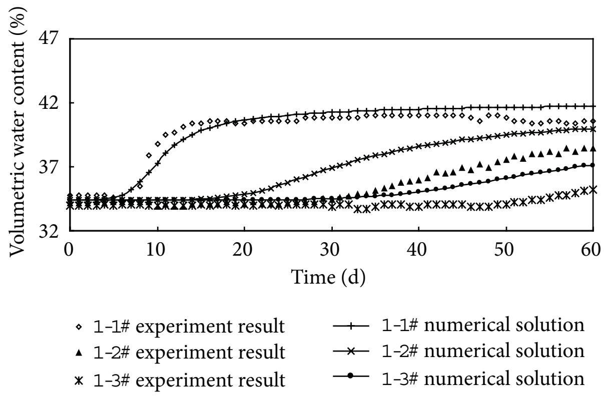

Figure 12: Comparison of calculated subgrade moisture with experimental results in Stage 1.

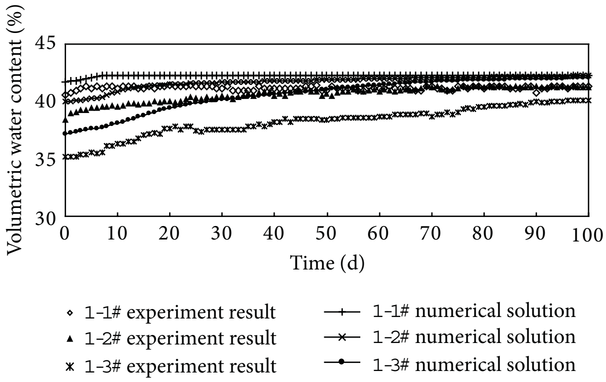

Figure 13: Comparison of calculated subgrade moisture with experimental results in Stage 2.

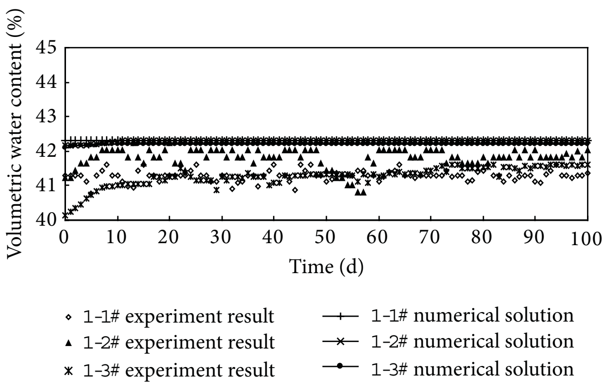

Figure 14: Comparison of calculated subgrade moisture with experimental results in Stage 3.

Acknowledgments

The authors gratefully acknowledge the financial support of the National 973 Project of China (no. 2013CB036405) and the Natural Science Foundation of China (nos. 51209201 and 51279198).

References

[1] A. R. Kacimov, Y. V. Obnosov, and J. Perret, "Phreatic surface flow from a near-reservoir saturated tongue," *Journal of Hydrology*, vol. 296, no. 1–4, pp. 271–281, 2004.

[2] A. W. Warrick, P. J. Wierenga, and L. Pan, "Downward water flow through sloping layers in the vadose zone: analytical solutions for diversions," *Journal of Hydrology*, vol. 192, no. 1–4, pp. 321–337, 1997.

[3] G.-C. Zhang, H.-M. Tang, and B. Hu, "Study of influence of unsaturated seepage on stability of landslide," *Rock and Soil Mechanics*, vol. 28, no. 5, pp. 965–970, 2007.

[4] D.-M. Sun, Y.-M. Zhu, and M.-J. Zhang, "Research on unsteady seepage problem of bank slope due to drawdown of reservoir water level," *Rock and Soil Mechanics*, vol. 29, no. 7, pp. 1807–1812, 2008.

[5] W.-K. Feng, Y.-C. Shi, H.-J. Chai, H.-C. Liu, and F. Ji, "The simplified solution of phreatic saturation line under the actions of rainfall and reservoir water level fluctuation," *Journal of Chengdu University of Technology*, vol. 33, no. 1, pp. 90–94, 2006.

[6] Q. Liu, Z. Zhu, X. He, G. Lu et al., "Unsaturated seepage analysis of the influence of water level fluctuation on pore water pressure of landslide in reservoir area," *Rock and Soil Mechanics*, vol. 29, pp. 85–89, 2008.

[7] J. M. Gasmo, H. Rahardjo, and E. C. Leong, "Infiltration effects on stability of a residual soil slope," *Computers and Geotechnics*, vol. 26, no. 2, pp. 145–165, 2000.

[8] D. G. Fredlund and A. Xing, "Equations for the soil-water characteristic curve," *Canadian Geotechnical Journal*, vol. 31, no. 4, pp. 521–532, 1994.

[9] D. G. Fredlund, A. Xing, M. D. Fredlund, and S. L. Barbour, "The relationship of the unsaturated soil shear strength to the soil-water characteristic curve," *Canadian Geotechnical Journal*, vol. 32, pp. 521–532, 1995.

[10] T. L. Zhan and N. W. Charles, "Analytical analysis of rainfall infiltration mechanism in unsaturated soils," *International Journal of Geomechanics*, vol. 4, no. 4, pp. 273–284, 2004.

[11] Y. Zhang and X. Hu, "Calculation of saturation line of groundwater under reservoir water table uniform rising," *Hydrogeology and Engineering Geology*, no. 5, pp. 46–49, 2007.

[12] Q. Wu and Z. Lin, "Analytic solutions for shallow water table in inclined and layered slope under drawdown condition," *Geological Science and Technology Information*, vol. 26, no. 2, pp. 91–92, 2007.

[13] Q. Wu, H.-M. Tang, L.-Q. Wang, and Z.-H. Lin, "Analytic solutions for phreatic line in reservoir slope with inclined impervious bed under rainfall and reservoir water level fluctuation," *Rock and Soil Mechanics*, vol. 30, no. 10, pp. 3025–3031, 2009.

Hindawi Publishing Corporation
Journal of Applied Mathematics
Volume 2013, Article ID 859803, 12 pages
http://dx.doi.org/10.1155/2013/859803

Research Article

Longwall Mining Stability in Take-Off Phase

María-Belén Prendes-Gero,[1] José Alcalde-Gonzalo,[2] Pedro Ramírez-Oyanguren,[3] Francisco-José Suárez-Domínguez,[1] and Martina-Inmaculada Álvarez-Fernández[4]

[1] *Department of Construction and Manufacture Engineering, Polytechnic School of Mieres, University of Oviedo, Mieres, 33600 Asturias, Spain*
[2] *Department of Exploitation and Prospecting Mines, Mining Engineering School, University of Oviedo, Oviedo, 33004 Asturias, Spain*
[3] *Department of Exploitation Mines, Polytechnic University of Madrid, 28040 Madrid, Spain*
[4] *Department of Exploitation and Prospecting Mines, Mining Engineering School, University of Oviedo, Oviedo, 33004 Asturias, Spain*

Correspondence should be addressed to María-Belén Prendes-Gero; belen@git.uniovi.es

Received 6 June 2013; Accepted 23 July 2013

Academic Editor: Ga Zhang

Mechanised longwall mining is one of the more commonly employed exploitation methods in underground mines in the north of Spain as well as in the rest of the world. It is continuously changing and evolving, with new techniques, technology, equipment, and face management practices and systems appearing for the purposes of improving aspects such as operational and financial performances and, above all, the safety of the miners. Despite its importance, there are no regulations for the mining of longwall coal seams. This work aims to contribute to an advance in the design and optimisation of the roof support in longwall mining, analysing the stability of the roof using a method based on the resistance of materials, which considers the characteristics of the properties of the roof materials. The influence of not only the individual elements of support but also the coalface, which is considered one more supporting element, is investigated. The longitudinal and transverse spacings of the support and the number of walkways constituting the exploitation panel are analysed. The proposed formulation is validated by information gathered in a mine located in the region of Castilla-Leon.

1. Introduction

Important reserves of coal exist in Spain, which can contribute to reducing the energetic dependence on other countries [1]. Though their importance has diminished gradually, the National Plan of Strategic Reservation of Coal 2006–2012 and the New Model of Integral and Sustainable Development of the Mining Regions [2] established a minimal level of production to keep open the possibility of relying on the coal in case of crisis or a considerable increase in the price of crude oil. For Spain, this level of production was established as 9.12 million tons in 2012, and though at present the new National Plan of Coal (2013–2018) is being developed, the principal aim is to allow the continuity of the Spanish developments.

Obtaining the existing reserves requires using levels of mechanisation of labour that allow economic competitiveness as well as safety within the context of the regulation RGNBSM (General Regulation of Basic Procedure of Mining safety, 1985) [3]. In this regard, methods of excavation in longwall mining using individual hydraulic support elements (mechanical props) have special importance (Figure 1). This mining method is commonly used in the coal-bearing deposits of Castilla-Leon in the north of Spain [4].

But longwall mining is not a new approach to coal mining. In fact, the basic principles of longwall mining have been traced back to the latter part of the 17th century, to Shropshire and other counties in England [5]. In the United States, longwall mining is actually 50 percent of the underground coal production [6–8], with 49 operating longwalls producing over 175 million tonnes per year [7]. Besides USA, among the most productive longwalls are those in Australia and the Shenhua coalfield in China. Shenhua was developed from a green-field site in 1992 and now has more than seven major underground mines producing over 200 million tonnes per year. Australia has 29 operating faces with a total longwall production of 47.5 million tonnes.

Figure 1: Mining labour supported by individual hydraulic props.

2. Engineering Background

Longwall mining [9, 10], for panels of coal, is an exploitation method where an extended wall of coal is mined in a sole slice. The wall or longwall is around 150–300 m long and 1-2 m thick, and the slab of coal that is being mined is around 1000–3500 m long and 150–300 m broad. The coal is removed from the wall by shearing machinery, which travels back and forth across the coalface, and load the coal onto a conveyor belt that carries it out of the mine. The area immediately in front of the coalface is supported by a series of hydraulic roof supports, which temporarily hold up the roof strata and provide a working space for the shearing machinery, the face conveyor and of course the mines. After each slice of coal is removed, the hydraulic roof supports, the face conveyor, and the shearing machinery are moved forward.

From that moment, the roof immediately above the seam is allowed to collapse into the void that is left as the face retreats. Miners working along the coalface, operating the machinery, are shielded from the collapsing strata by the canopy of the hydraulic roof supports. As the roof collapses into the goaf behind the roof supports, the fracturing and settlement of the rocks progresses through the overlying strata and results in sagging and bending of the near surface rocks and in some cases subsidence of the ground above [11].

Mechanised longwall mining is ever changing and evolving with new techniques, technology, equipment, face management practices, and systems appearing as a direct means to continually improve all aspects of operational and financial performances [12].

Nevertheless, and in spite of the importance of this method of exploitation, no legal regulation exists regarding the types of support and thickness and characteristics of the rock mass surrounding the excavation, which would guarantee the safe functioning of these developments.

Calculation of the pressure that the working roof wall is to exert on hydraulic props is essential for support design, both to ensure working global stability and to avoid prop punching on gables [13]. These two concepts are analysed in multiple papers, as are the behaviour of the overlying rock strata and the performance of the support. R. Singh and T. N. Singh [14] verified the influence that the additional load on the chock shield was exercising by the broken rock mass in thick seams, with values of limiting span given by the clamped and cantilever beam equations. Ju and Xu [15] analysed the strata behaviour during the operation of great mining height, studying the structural characteristics of key strata (cantilever beam and/or voussoir beam) as well as the movement law. Bilim and Özkan [16] analysed the effect of excavation schedules on the overlying rock strata and the supports. González-Nicieza et al. [17] and Juárez-Ferreras et al. [18, 19] analysed the maximum pressure that the coal hanging wall and footwall are capable of supporting, as well as the density of the props and the conditions of the supports they are resting on so that penetration of the props does not occur.

This work tries to contribute to an advance in the design and optimisation of the roof support in longwall mining, analysing the stability of the roof with a method based on the resistance of materials [20] from the characteristics of the roof materials.

In addition, two very important aspects of the safety and the productivity of the exploitation have been considered: the dimensions and the number of walkways of the panel. The width of the rear walkway at waist level needs to be considered from an ergonomic aspect to allow for lamps and self-rescuers worn by underground personnel. The horizontal dimension across an average person's waist is between 620 and 700 mm, so a rear walkway width of ≥750 mm at waist height is required to permit ergonomically effective passage of people along the face so their productivity is not unnecessarily impeded [12]. The number of walkways impacts the safety of the panels and their productivity due to the fact that it produces variations in the bending moment and deflection laws.

3. Exposition of the Problem

It is considered as a longwall exploitation (Figure 2) if the two dimensions according to the X and Z axes are very large in comparison with the height or dimension along the Y axis. For simplicity, in this paper we consider a length of the workshop b to be equal to 1 m in the Z direction. The supporting hydraulic elements divide the panel into sections or spans; in each span, the following characteristics are considered constants:

(i) length: L_i (m);

(ii) Young's modulus: E_i (Pa);

(iii) thickness: e_i (m);

(iv) load: q_i (N/m).

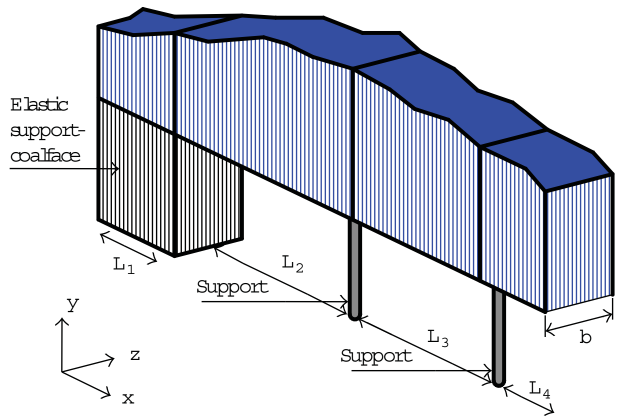

FIGURE 2: Scheme of longwall mining.

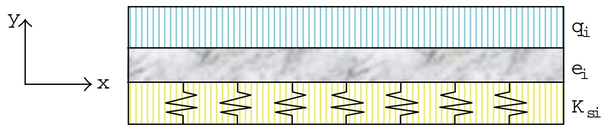

FIGURE 3: Single section.

In addition, it is considered that the stiffness k_e of the supporting elements can be different and it is possible that there exist other supporting elements with stiffness K_s, for example, keys of wood, the coalface, or the protection rock mass between two panels. So, each span, besides the properties previously indicated, presents the following:

(i) stiffness of the uniform support: K_{si} (Pa);

(ii) stiffness of the props: K_{ei} (Pa).

Along with these assumptions is imposed the restriction that within each span the roof rock is perfectly elastic, homogeneous, and isotropic and the neutral axis coincides with the centre line of the thickness.

Considering each roof of a span as a beam subjected to a uniformly distributed load, q_i, acting in the principal plane of the symmetric cross-section (Figure 3), the deflection of this roof is described through a differential equation of fourth degree [20]:

$$K_{ti} \cdot y_i^{IV} + K_{si} \cdot y_i = q_i, \tag{1}$$

where y_i is the deflection in each point and K_{ti} is a constant given by the expression $K_{ti} = E_i \cdot I_i$. with I_i the moment of inertia.

The solution of the differential equation (1) is given by

$$\begin{aligned} y_i(x) = {} & e^{K_i \cdot x} \cdot (A_i \cdot \cos K_i \cdot x + B_i \cdot \sin K_i \cdot x) \\ & + e^{-K_i \cdot x} \cdot (C_i \cdot \cos K_i \cdot x + D_i \cdot \sin K_i \cdot x) + y_{pi}, \end{aligned} \tag{2}$$

where K_i and y_{pi} are given by the expressions $K_i = (K_{si}/K_{ti})^{0.25}$, and $y_{pi} = q_i/K_{si}$, respectively, and A_i, B_i, C_i, and D_i, are constants that must be determined using the boundary conditions, which constitute the unknown quantities of the problem.

Once the deflection is obtained, the angle of rotation at any point of the panel is given by the first derivative of the deflection ($\theta_i(x) = y_i'(x)$):

$$\begin{aligned} \theta_i(x) = {} & K_i \cdot e^{K_i \cdot x} \\ & \cdot \left[(A_i + B_i) \cdot \cos K_i \cdot x + (-A_i + B_i) \cdot \sin K_i \cdot x \right] \\ & + K_i \cdot e^{-K_i \cdot x} \\ & \cdot \left[(-C_i + D_i) \cdot \cos K_i \cdot x - (C_i + D_i) \cdot \sin K_i \cdot x \right]. \end{aligned} \tag{3}$$

The bending moment ($M_i(x) = K_{ti} \cdot y_i''(x)$) and the shear force ($V_i(x) = -K_{ti} \cdot y_i'''(x)$) at every point of the panel are given by (4) and (5), respectively:

$$\begin{aligned} M_i(x) & \\ = K_{ti} \cdot \Big[& 2 \cdot K_i^2 \cdot e^{K_i \cdot x} \cdot (B_i \cdot \cos K_i \cdot x - A_i \cdot \sin K_i \cdot x) \\ & + 2 \cdot K_i^2 \cdot e^{-K_i \cdot x} \\ & \cdot (-D_i \cdot \cos K_i \cdot x + C_i \cdot \sin K_i \cdot x) \Big], \end{aligned} \tag{4}$$

$$\begin{aligned} V_i(x) & \\ = -K_{ti} & \\ \cdot \Big\{ & 2 \cdot K_i^3 \cdot e^{K_i \cdot x} \\ & \cdot \left[(-A_i + B_i) \cdot \cos K_i \cdot x - (A_i + B_i) \cdot \sin K_i \cdot x \right] \\ & + 2 \cdot K_i^3 \cdot e^{-K_i \cdot x} \\ & \cdot \left[(C_i + D_i) \cdot \cos K_i \cdot x + (-C_i + D_i) \cdot \sin K_i \cdot x \right] \Big\}. \end{aligned} \tag{5}$$

As mentioned previously, once the equations that define the problem have been established, it is necessary to determine the boundary conditions (null deflections and null rotations at the ends of the panel) and the conditions of compatibility (equal deflections, rotations, and bending moments in the points between spans) in order to know the constants A_i, B_i, C_i, and D_i.

For this purpose, the panel has been analysed in the phase of take-off by two configurations commonly used in the mines of Castilla-León, with two walkways (panel type 1) and with one walkway (panel type 2).

(i) Panel type 1 has two walkways, three elements of support, and six spans (Figure 4), the first and last spans being supported elastically by the coalface;

(ii) Panel type 2 has one walkway, two elements of support, and five spans (Figure 5), and as in the previous case, the first and last spans are supported elastically by the coalface.

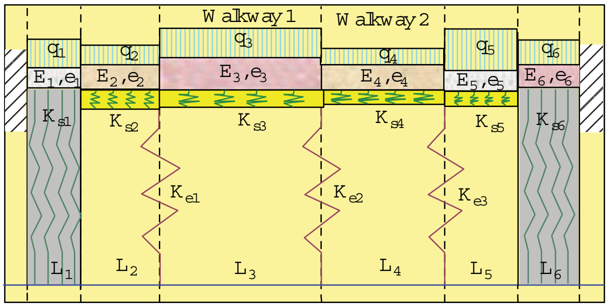

FIGURE 4: Panel type 1.

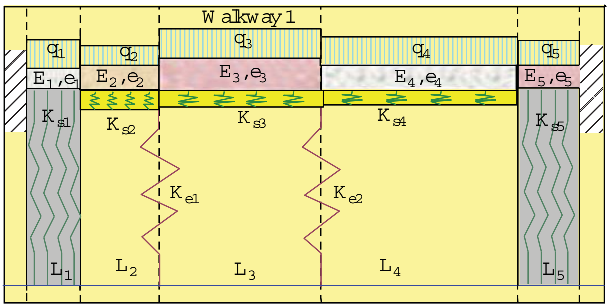

FIGURE 5: Panel type 2.

The application of the boundary and compatibility conditions gives rise to the system of (6); where n will be 6 for panel type 1 and 5 the panel type 2.

$$\begin{gathered} y_1(x_0)=0, \\ y_1'(x_0)=0, \\ y_i(x_i)=y_{i+1}(x_i), \quad i=1,2,\ldots,n-1, \\ y_i'(x_i)=y_{i+1}'(x_i), \quad i=1,2,\ldots,n-1, \\ K_{ti}\cdot y_i''(x_i)=K_{ti+1}\cdot y_{i+1}''(x_i), \quad i=1,2,\ldots,n-1, \\ K_{ti}\cdot y_1'''(x_1)=K_{ti+1}\cdot y_2'''(x_1) \\ K_{ti}\cdot y_i'''(x_i)-K_{ti+1}\cdot y_{1+1}'''(x_i)=K_{ei}\cdot y_i(x_i), \\ i=2,\ldots,n-2, \\ K_{tn-1}\cdot y_{n-1}'''(x_{n-1})=K_{tn}\cdot y_n'''(x_{n-1}), \\ y_n(x_n)=0, \\ y_n'(x_n)=0, \end{gathered} \tag{6}$$

where

$$x_i=\sum_{j=1}^{i}L_i, \quad i=1,2,\ldots,n. \tag{7}$$

Replacing the values of the deflection and its derivatives in (6) and expressing the system in matrix form, the following is obtained:

$$M\cdot U=B, \tag{8}$$

where the transposed matrix of U is given by

$${}^{T}U=\left[{}^{T}U_1 \quad {}^{T}U_2 \quad \cdots \quad {}^{T}U_n\right], \tag{9}$$

where

$${}^{T}U_i=\left[A_i \quad B_i \quad C_i \quad D_i\right], \qquad i=1,2,\ldots,n. \tag{10}$$

Therefore, the not null elements of the matrices $M_{(4n\times4n)}=\{m_{ij}\}$ and $B_{(4n\times1)}=\{b_i\}$ are obtained (the Appendix) for the panel type 1. In panel type 2, the matrixes M and B are equal to the first type in its first 14 rows, with the last ones also being equal with the exception of the following changes of indexes: indexes 5 and 6 of the problem type 1 transform into the indexes 4 and 5, respectively, of the problem type 2.

4. Calculating the Factor of Safety of the Workshop

Once the efforts have been calculated, it is possible to calculate the factor of safety (FS) of the panel dividing the tensile strength of each section ($\sigma_t(x)$) for the normal stress ($\sigma(x)$) (14). If this coefficient is bigger than one, the roof of the panel is capable of supporting the stresses to which it is subjected, and, therefore, the work is realised in safe conditions.

To calculate this FS in each section of the roof, the shear stress (11) and the bending stress (12) are calculated as follows:

$$\tau(x)=\frac{4\cdot V(x)}{3\cdot e\cdot b}, \tag{11}$$

$$\sigma_f(x)=\frac{6\cdot M(x)}{b\cdot e^2}. \tag{12}$$

From (11) and (12), the normal stress is calculated as

$$\sigma(x)=0.5\cdot\left[\sigma_f(x)+\sqrt{\sigma_f^2(x)+4\cdot\tau^2(x)}\right]. \tag{13}$$

Once the stresses are calculated, the FS is given by

$$\mathrm{FS}=\frac{\sigma_t(x)}{\sigma(x)}. \tag{14}$$

5. Practical Case

A panel in the take-off phase is analysed with two configurations commonly used in the mines of Castilla-León and more specifically in the Feixolin mine [17], with two walkways (panel type 1) and with one walkway (panel type 2). Figures 4 and 5 show that in the phase of take-off, the first and last spans rest elastically on the coal, whereas the halfway sections rest on siltstone with an apparent density of 2.75 t/m^3. The hydraulic props are of the type EA 25 manufactured by Salzgitter and reach a maximum extend length of 2.5 m.

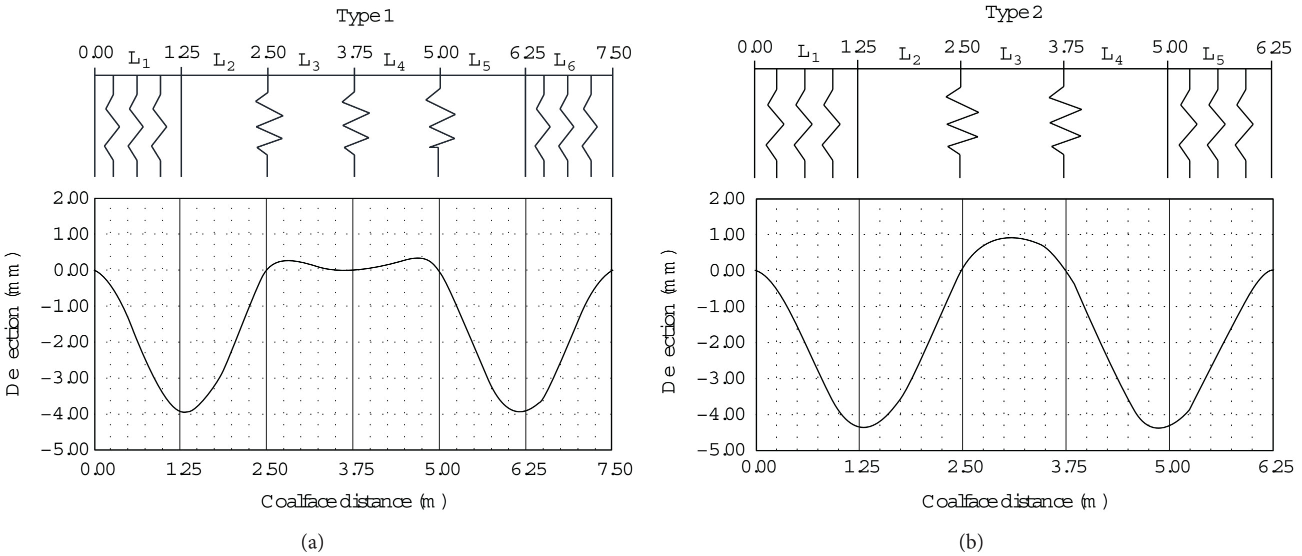

FIGURE 6: Deflection.

To calculate the stiffness of the siltstone, the pressures obtained in the penetration test are considered, and to calculate the stiffness of the props [21], the load-deformation curves from the load plate test are used. All of these calculations were for the Feixolin mine [17]. Table 1 shows the properties used in the analysis.

One of the most important parameters from the safety point of view as well as in terms of accessibility is the deflection of the roof. In this case, it is considered that negative values of the deflection are equivalent to an increase of the deflection and vice versa.

As it is observed in Figure 6 for both configurations analysed, there is a symmetrical deflection from the centre with a shape very similar to that of a bifixed beam, though in this case the curve does not increase progressively to reach a maximum deflection in the centre. On the contrary, several segments are distinguished in the curve. These segments coincide with the changes of spans of the panel. The first and last spans (1 and 6 in panel type 1 and 1 and 5 in panel type 2) present an increase of the deflection reaching the maximum at the edge of the span, that is, at the edge of the elastic support. These maximum values of deflection are −3.98 mm for panel type 1 and −4.39 mm for panel type 2. At this point, the presence of hydraulic props produces a decrease in the value of the deflection, even from negative values that indicate that the roof turns down to positive values at spans 3 and 4 of panel type 1. These positive values are due to the pressure in the opposite direction to the deflection, which is realised by the supports. The deflection descends to 0.31 mm being null in the middle of the workshop. On the contrary, in panel type 2, the decrease of the deformation is constant until the minimum is reached in the middle point of span 3, with 0.96 mm.

In any case, the deflection of the roof can be considered low and barely affects working conditions.

The fall of the roof, that is, the increase of its deflection, depends directly on the stiffness of the hydraulic props. As it is observed in Figure 7, with a stiffness of the props 100 times less, similar curves are obtained. Nevertheless, the values of deflection in the ends of the first spans are major (−5.35 mm). On the other hand, the decrease of this deflection is minor not reaching positive values at any time. This is due to the fact that in these conditions the capacity of support is for the roof and not for the hydraulic props.

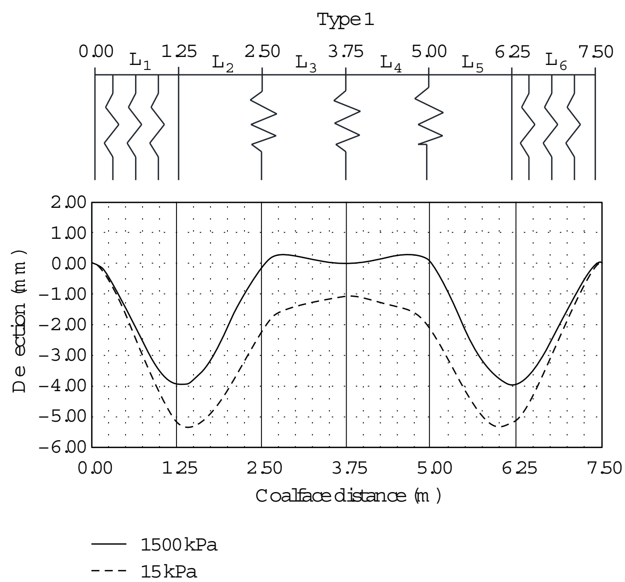

FIGURE 7: Deflection with stiffness of props 100 times minors.

On the contrary, considering an increase in the stiffness of the hydraulic props, it does not suppose a change over the results obtained in the initial conditions (Figure 6). This is because the stiffness of the props initially is so big compared to the stiffness of the rest of the materials that an increase of its value does not produce any effect.

Table 1: Properties of the materials in each section or span.

	Section 1 siltstone	Section 2 siltstone	Section 3 siltstone	Section 4 siltstone	Section 5 siltstone	Section 6 siltstone
Length of span (m)	1.25	1.25	1.25	1.25	1.25	1.25
Thickness (m)	1.5	1.5	1.5	1.5	1.5	1.5
Young's modulus (MPa)	3550	3550	3550	3550	3550	3550
Load (kN/m)	17200	17200	17200	17200	17200	17200
Supporting stiffness (MPa/m)	47.8	47.8	47.8	47.8	47.8	47.8
Tensile strength (MPa)	4.24	4.24	4.24	4.24	4.24	4.24
Prop number	1		2		3	
Prop stiffness (MPa/m)	1500		1500		1500	
Spacing of props (m)	0.55		0.55		0.55	

The bending moment (Figure 8) shows symmetrical curves to the deflection ones. In this case, the maximum values for panels type 1 and type 2 are 5.05 kNm and 5.38 kNm, respectively. The maximum values are at the edges of the elastic supports, whereas the minimum values occur at the points of placement of the hydraulic props.

In this case, a decrease of the stiffness of the props does not produce a change in the shape of the curves and only produces small variations in the maximum values obtained (panel type 1: 5.24 kNm, and panel type 2: 5.50 kNm).

A change in the materials of the roof does not alter the shape of the curve, but it modifies the maximum and minimum values, which does not happen with the deflection. This behaviour is due to how the bending moment is obtained (4), multiplying the second derivative of the deflection by a constant for each section, K_{ti}. For spans of equal thickness, K_{ti} is directly proportional to Young's modulus of the material of the span.

The representation of the rotation angle of the spans produces symmetrical curves from the centre of the panel, as much in the case of type 1 as type 2. In Figure 9, it is observed that the use of props produces fluctuations in the rotation, but always reaching lower values to those presented for zones close to the extremes. The maximum rotation is around 4.79 radians in panel type 1 and 5 radians in panel type 2.

The shear force (Figure 10) presents jumps of values in those spans where the hydraulic props are placed. These maximum values (in absolute value) are in the second and last and the values reached as much in panel type 1 as in panel type 2 are very similar and around 20 kN.

Although most of the parameters shown in Table 1 depend on the type of rock, there are some of them that can vary. The type of support, hence its stiffness (Figure 6), as well as the length of the spans, is a compromise between the safety and the productivity of the panel. While the depth of the panel, that is, the load per unit of length, will increase over time, the exploitation advances.

A decrease in the length of the spans (Figure 11) decreases the value of all the parameters analysed: deflection, rotation angle, bending moment, and shear force. However, decreasing this value means, on the one hand, placing a bigger number of props, thus increasing the cost of production, and on the other reduce the space step for miners. In any case, this length cannot be less than 0.75 m considering all the equipment that the miners wear around their body.

An increase in the length of the spans increases the value of all parameters and specifically the value of the deflection. So it is necessary to find a compromise between length and safety/productivity.

With the advance in the exploitation, the depth of the panels grows and therefore the load on spans increases. This increase results in a greater deflection of the roof (Figure 12) and also an increase of the bending moment and of the shear force.

The analysed parameters, and specifically the shear force and the bending moment, let us know one of the most important points in the design of a panel of longwall: the FS. In the two examples with the properties shown in Table 1, the values of the FS are bigger than 5. That is to say, the studied mine is safe for this design. Nevertheless, it is possible to determine in what spans and in what type of panel a minor FS is produced.

From (14), it is possible to deduce that the FS is directly proportional to the tensile strength and inversely proportional to the sum of the bending moment and the shear force. The variation of the values of the bending moment and shear force (Figures 8 and 10) indicates that the most critical points, in the analysis of the safety, are at the edges of the elastic supports (the borders of the first and last span).

The influence of the distribution of the props, their stiffness, or the number of walkways in the panel over the FS has been analysed. Nevertheless, unless extreme values were used, the FS scarcely varied in its value. On the contrary, changes in the properties of the materials, and especially changes in the Young's modulus, produce great variations in the FS.

6. Conclusions

(i) The calculation of the stability of roofs in longwall mining can be resolved by employing the classic resistance of materials.

(ii) In addition, because the calculation process is very fast, it is possible to design a more appropriate roof support for a specific longwall mining workshop, to

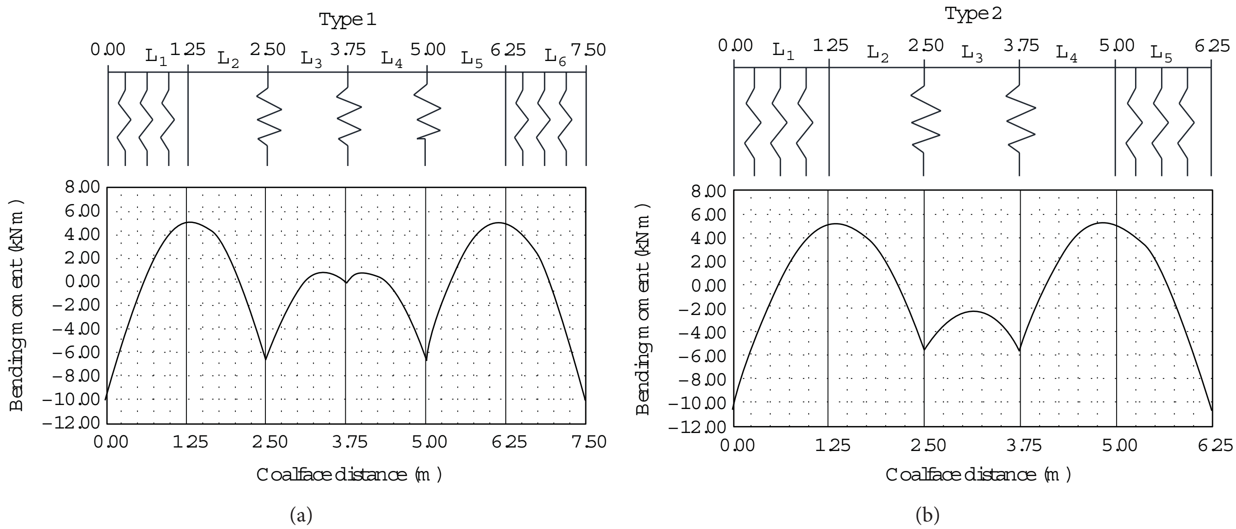

FIGURE 8: Bending moment.

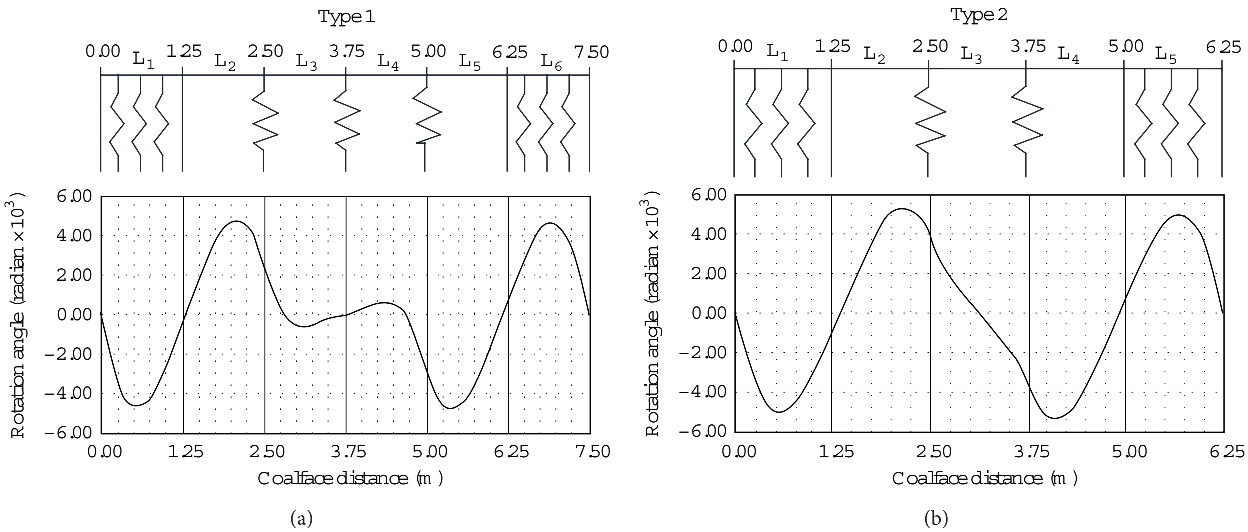

FIGURE 9: Rotation angle.

know the behaviour of the roof as a support element, and to analyse the influence and capacity of the individual support elements and the effect of their longitudinal and transverse spacing.

(iii) While the most influential factor in the deflection of the roof is the stiffness of the props, the bending moment depends directly on the properties of the materials and specifically on their Young's modulus.

(iv) In all cases, the disposition of two walkways in the panel against one walkway reduces the maximum values of the parameters analysed with the exception of the shear force. In any case, these maximum values are placed, for both configurations analysed, in the second and last but one sections. So, these sections are critical in the analysis of the FS.

(v) Finally, the variables that have most influence in the FS, are undoubtedly the depth of the panel and above all the changes in the properties of the rock mass of the roof.

7. Highlights

(i) Analyse the influence that the dimensions and the number of walkways of the panel have on the stability of the roof.

(ii) Study the influence of not only the individual elements of support but also the coalface, which is considered one more supporting element.

(iii) Analyse the configuration of the support (longitudinal and transverse spacing) in longwall mining.

(iv) Know in a simple way the safety factor for a workshop.

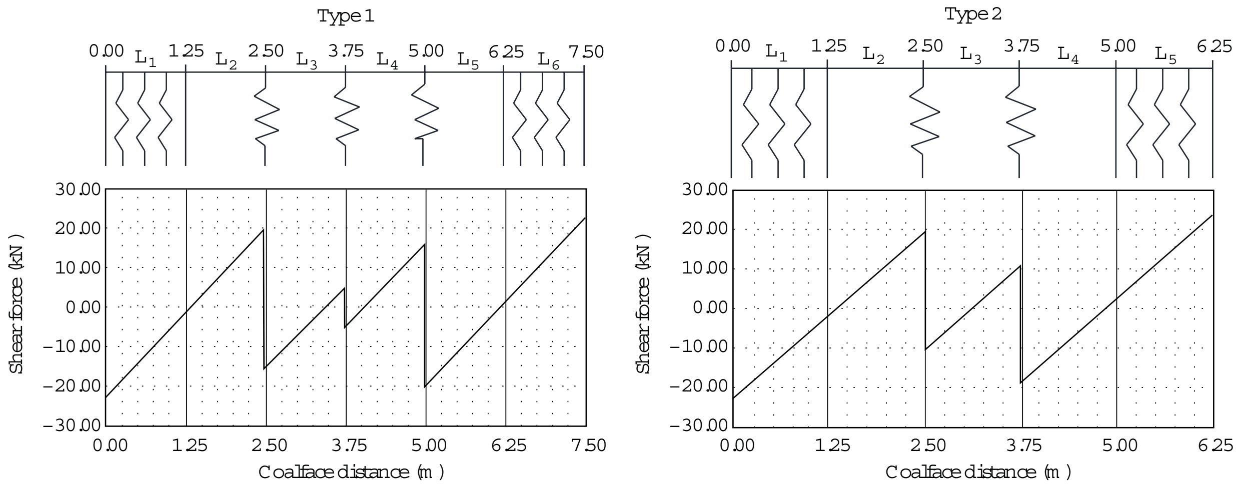

(a) (b)

Figure 10: Shear force.

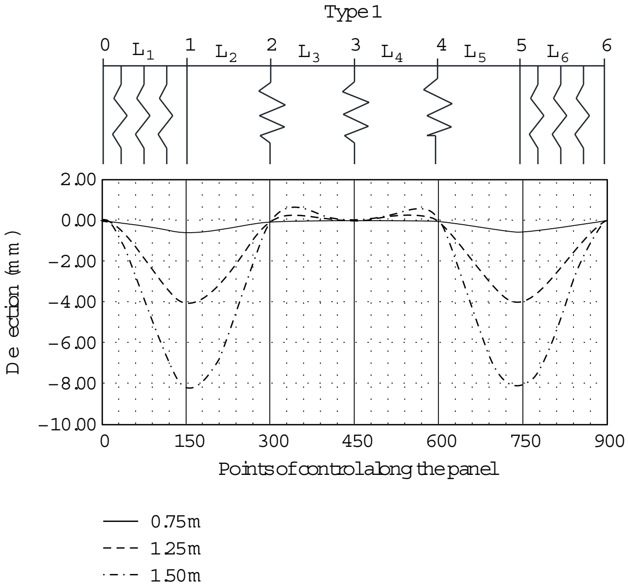

Figure 11: Deflection versus length of spans.

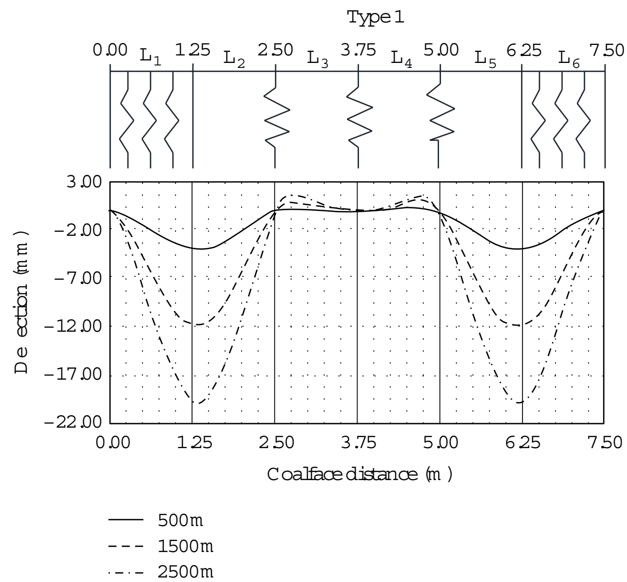

Figure 12: Deflection versus depth of the panel.

Appendix

The not null elements of the matrices $M_{(24\times 24)} = \{m_{ij}\}$ and $B_{(24\times 1)} = \{b_i\}$ of the problem type 1 are as follows.

Row 1.

$$m_{1,1} = m_{1,3} = 1,$$
$$b_1 = -y_{p1}. \tag{A.1}$$

Row 2.

$$m_{2,1} = m_{2,2} = m_{2,4} = 1,$$
$$m_{2,3} = -1. \tag{A.2}$$

Row 3.

$$m_{3,1} = e^{K_1 x_1} \cdot \cos K_1 x_1,$$
$$m_{3,2} = e^{K_1 x_1} \cdot \sin K_1 x_1,$$
$$m_{3,3} = e^{-K_1 x_1} \cdot \cos K_1 x_1,$$
$$m_{3,4} = e^{-K_1 x_1} \cdot \sin K_1 x_1,$$
$$m_{3,5} = -e^{K_2 x_1} \cdot \cos K_2 x_1,$$
$$m_{3,6} = -e^{K_2 x_1} \cdot \sin K_2 x_1,$$
$$m_{3,7} = -e^{-K_2 x_1} \cdot \cos K_2 x_1,$$

$$m_{3,8} = -e^{-K_2 x_1} \cdot \sin K_2 x_1,$$
$$b_3 = y_{p2} - y_{p1}. \tag{A.3}$$

Row 4.

$$\begin{aligned}
m_{4,1} &= K_1 e^{K_1 x_1} \left(\cos K_1 x_1 - \sin K_1 x_1\right), \\
m_{4,2} &= K_1 e^{K_1 x_1} \left(\cos K_1 x_1 + \sin K_1 x_1\right), \\
m_{4,3} &= -K_1 e^{-K_1 x_1} \left(\cos K_1 x_1 + \sin K_1 x_1\right), \\
m_{4,4} &= K_1 e^{-K_1 x_1} \left(\cos K_1 x_1 - \sin K_1 x_1\right), \\
m_{4,5} &= -K_2 e^{K_2 x_1} \left(\cos K_2 x_1 - \sin K_2 x_1\right), \\
m_{4,6} &= -K_2 e^{K_2 x_1} \left(\cos K_2 x_1 + \sin K_2 x_1\right), \\
m_{4,7} &= K_2 e^{-K_2 x_1} \left(\cos K_2 x_1 + \sin K_2 x_1\right), \\
m_{4,8} &= -K_2 e^{-K_2 x_1} \left(\cos K_2 x_1 - \sin K_2 x_1\right).
\end{aligned} \tag{A.4}$$

Row 5.

$$\begin{aligned}
m_{5,1} &= -2K_1^2 e^{K_1 x_1} \sin K_1 x_1, \\
m_{5,2} &= 2K_1^2 e^{K_1 x_1} \cos K_1 x_1, \\
m_{5,3} &= 2K_1^2 e^{-K_1 x_1} \sin K_1 x_1, \\
m_{5,4} &= -2K_1^2 e^{-K_1 x_1} \cos K_1 x_1, \\
m_{5,5} &= 2K_2^2 e^{K_2 x_1} \sin K_2 x_1, \\
m_{5,6} &= -2K_2^2 e^{K_2 x_1} \cos K_2 x_1, \\
m_{5,7} &= -2K_2^2 e^{-K_2 x_1} \sin K_2 x_1, \\
m_{5,8} &= 2K_2^2 e^{-K_2 x_1} \cos K_2 x_1.
\end{aligned} \tag{A.5}$$

Row 6.

$$\begin{aligned}
m_{6,1} &= -2K_1^3 e^{K_1 x_1} \left(\cos K_1 x_1 + \sin K_1 x_1\right), \\
m_{6,2} &= 2K_1^3 e^{K_1 x_1} \left(\cos K_1 x_1 - \sin K_1 x_1\right), \\
m_{6,3} &= 2K_1^3 e^{-K_1 x_1} \left(\cos K_1 x_1 - \sin K_1 x_1\right), \\
m_{6,4} &= 2K_1^3 e^{-K_1 x_1} \left(\cos K_1 x_1 + \sin K_1 x_1\right), \\
m_{6,5} &= 2K_2^3 e^{K_2 x_1} \left(\cos K_2 x_1 + \sin K_2 x_1\right), \\
m_{6,6} &= -2K_2^3 e^{K_2 x_1} \left(\cos K_2 x_1 - \sin K_2 x_1\right), \\
m_{6,7} &= -2K_2^3 e^{-K_2 x_1} \left(\cos K_2 x_1 - \sin K_2 x_1\right), \\
m_{6,8} &= -2K_2^3 e^{-K_2 x_1} \left(\cos K_2 x_1 + \sin K_2 x_1\right).
\end{aligned} \tag{A.6}$$

Row 7.

$$\begin{aligned}
m_{7,5} &= e^{K_2 x_2} \cdot \cos K_2 x_2, \\
m_{7,6} &= e^{K_2 x_2} \cdot \sin K_2 x_2, \\
m_{7,7} &= e^{-K_2 x_2} \cdot \cos K_2 x_2, \\
m_{7,8} &= e^{-K_2 x_2} \cdot \sin K_2 x_2, \\
m_{7,9} &= -e^{K_3 x_2} \cdot \cos K_3 x_2, \\
m_{7,10} &= -e^{K_3 x_2} \cdot \sin K_3 x_2, \\
m_{7,11} &= -e^{-K_3 x_2} \cdot \cos K_3 x_2, \\
m_{7,12} &= -e^{-K_3 x_2} \cdot \sin K_3 x_2, \\
b_7 &= y_{p3} - y_{p2}.
\end{aligned} \tag{A.7}$$

Row 8.

$$\begin{aligned}
m_{8,5} &= K_2 e^{K_2 x_2} \left(\cos K_2 x_2 - \sin K_2 x_2\right), \\
m_{8,6} &= K_2 e^{K_2 x_2} \left(\cos K_2 x_2 + \sin K_2 x_2\right), \\
m_{8,7} &= -K_2 e^{-K_2 x_2} \left(\cos K_2 x_2 + \sin K_2 x_2\right), \\
m_{8,8} &= K_2 e^{-K_2 x_2} \left(\cos K_2 x_2 - \sin K_2 x_2\right), \\
m_{8,9} &= -K_3 e^{K_3 x_2} \left(\cos K_3 x_2 - \sin K_3 x_2\right), \\
m_{8,10} &= -K_3 e^{K_3 x_2} \left(\cos K_3 x_2 + \sin K_3 x_2\right), \\
m_{8,11} &= K_3 e^{-K_3 x_2} \left(\cos K_3 x_2 + \sin K_3 x_2\right), \\
m_{8,12} &= -K_3 e^{-K_3 x_2} \left(\cos K_3 x_2 - \sin K_3 x_2\right).
\end{aligned} \tag{A.8}$$

Row 9.

$$\begin{aligned}
m_{9,5} &= -2K_2^2 e^{K_2 x_2} \sin K_2 x_2, \\
m_{9,6} &= 2K_2^2 e^{K_2 x_2} \cos K_2 x_2, \\
m_{9,7} &= 2K_2^2 e^{-K_2 x_2} \sin K_2 x_2, \\
m_{9,8} &= -2K_2^2 e^{-K_2 x_2} \cos K_2 x_2, \\
m_{9,9} &= 2K_3^2 e^{K_3 x_2} \sin K_3 x_2, \\
m_{9,10} &= -2K_3^2 e^{K_3 x_2} \cos K_3 x_2, \\
m_{9,11} &= -2K_3^2 e^{-K_3 x_2} \sin K_3 x_2, \\
m_{9,12} &= 2K_3^2 e^{-K_3 x_2} \cos K_3 x_2.
\end{aligned} \tag{A.9}$$

Row 10.

$$\begin{aligned} m_{10,5} &= -2K_{t2}K_2^3e^{K_2x_2}\left(\cos K_2x_2 + \sin K_2x_2\right) \\ &\quad - K_{e1}e^{K_2x_2}\cos K_2x_2, \\ m_{10,6} &= 2K_{t2}K_2^3e^{K_2x_2}\left(\cos K_2x_2 - \sin K_2x_2\right) \\ &\quad - K_{e1}e^{K_2x_2}\sin K_2x_2, \\ m_{10,7} &= 2K_{t2}K_2^3e^{-K_2x_2}\left(\cos K_2x_2 - \sin K_2x_2\right) \\ &\quad - K_{e1}e^{-K_2x_2}\cos K_2x_2, \\ m_{10,8} &= 2K_{t2}K_2^3e^{-K_2x_2}\left(\cos K_2x_2 + \sin K_2x_2\right) \\ &\quad - K_{e1}e^{-K_2x_2}\sin K_2x_2, \\ m_{10,9} &= 2K_{t3}K_3^3e^{K_3x_2}\left(\cos K_3x_2 + \sin K_3x_2\right), \\ m_{10,10} &= -2K_{t3}K_3^3e^{K_3x_2}\left(\cos K_3x_2 - \sin K_3x_2\right), \\ m_{10,11} &= -2K_{t3}K_3^3e^{-K_3x_2}\left(\cos K_3x_2 - \sin K_3x_2\right), \\ m_{10,12} &= -2K_{t3}K_3^3e^{-K_3x_2}\left(\cos K_3x_2 + \sin K_3x_2\right), \\ b_{10} &= K_{e1}y_{p3}. \end{aligned} \tag{A.10}$$

Row 11.

$$\begin{aligned} m_{11,9} &= e^{K_3x_3}\cdot\cos K_3x_3, \\ m_{11,10} &= e^{K_3x_3}\cdot\sin K_3x_3, \\ m_{11,11} &= e^{-K_3x_3}\cdot\cos K_3x_3, \\ m_{11,12} &= e^{-K_3x_3}\cdot\sin K_3x_3, \\ m_{11,13} &= -e^{K_4x_3}\cdot\cos K_4x_3, \\ m_{11,14} &= -e^{K_4x_3}\cdot\sin K_4x_3, \\ m_{11,15} &= -e^{-K_4x_3}\cdot\cos K_4x_3, \\ m_{11,16} &= -e^{-K_4x_3}\cdot\sin K_4x_3, \\ b_{11} &= y_{p4} - y_{p3}. \end{aligned} \tag{A.11}$$

Row 12.

$$\begin{aligned} m_{12,9} &= K_3e^{K_3x_3}\left(\cos K_3x_3 - \sin K_3x_3\right), \\ m_{12,10} &= K_3e^{K_3x_3}\left(\cos K_3x_3 + \sin K_3x_3\right), \\ m_{12,11} &= -K_3e^{-K_3x_3}\left(\cos K_3x_3 + \sin K_3x_3\right), \\ m_{12,12} &= K_3e^{-K_3x_3}\left(\cos K_3x_3 - \sin K_3x_3\right), \\ m_{12,13} &= -K_4e^{K_4x_3}\left(\cos K_4x_3 - \sin K_4x_3\right), \\ m_{12,14} &= -K_4e^{K_4x_3}\left(\cos K_4x_3 + \sin K_4x_3\right), \\ m_{12,15} &= K_4e^{-K_4x_3}\left(\cos K_4x_3 + \sin K_4x_3\right), \\ m_{12,16} &= -K_4e^{-K_4x_3}\left(\cos K_4x_3 - \sin K_4x_3\right). \end{aligned} \tag{A.12}$$

Row 13.

$$\begin{aligned} m_{13,9} &= -2K_3^2e^{K_3x_3}\sin K_3x_3, \\ m_{13,10} &= 2K_3^2e^{K_3x_3}\cos K_3x_3, \\ m_{13,11} &= 2K_3^2e^{-K_3x_3}\sin K_3x_3, \\ m_{13,12} &= -2K_3^2e^{-K_3x_3}\cos K_3x_3, \\ m_{13,13} &= 2K_4^2e^{K_4x_3}\sin K_4x_3, \\ m_{13,14} &= -2K_4^2e^{K_4x_3}\cos K_4x_3, \\ m_{13,15} &= -2K_4^2e^{-K_4x_3}\sin K_4x_3, \\ m_{13,16} &= 2K_4^2e^{-K_4x_3}\cos K_4x_3. \end{aligned} \tag{A.13}$$

Row 14.

$$\begin{aligned} m_{14,9} &= -2K_{t3}K_3^3e^{K_3x_3}\left(\cos K_3x_3 + \sin K_3x_3\right) \\ &\quad - K_{e2}e^{K_3x_3}\cos K_3x_3, \\ m_{14,10} &= 2K_{t3}K_3^3e^{K_3x_3}\left(\cos K_3x_3 - \sin K_3x_3\right) \\ &\quad - K_{e2}e^{K_3x_3}\sin K_3x_3, \\ m_{14,11} &= 2K_{t3}K_3^3e^{-K_3x_3}\left(\cos K_3x_3 - \sin K_3x_3\right) \\ &\quad - K_{e2}e^{-K_3x_3}\cos K_3x_3, \\ m_{14,12} &= 2K_{t3}K_3^3e^{-K_3x_3}\left(\cos K_3x_3 + \sin K_3x_3\right) \\ &\quad - K_{e2}e^{-K_3x_3}\sin K_3x_3, \\ m_{14,13} &= 2K_{t4}K_4^3e^{K_4x_3}\left(\cos K_4x_3 + \sin K_4x_3\right), \\ m_{14,14} &= -2K_{t4}K_4^3e^{K_4x_3}\left(\cos K_4x_3 - \sin K_4x_3\right), \\ m_{14,15} &= -2K_{t4}K_4^3e^{-K_4x_3}\left(\cos K_4x_3 - \sin K_4x_3\right), \\ m_{14,16} &= -2K_{t4}K_4^3e^{-K_4x_3}\left(\cos K_4x_3 + \sin K_4x_3\right), \\ b_{14} &= K_{e2}y_{p3}. \end{aligned} \tag{A.14}$$

Row 15.

$$\begin{aligned} m_{15,13} &= e^{K_4x_4}\cdot\cos K_4x_4, \\ m_{15,14} &= e^{K_4x_4}\cdot\sin K_4x_4, \\ m_{15,15} &= e^{-K_4x_4}\cdot\cos K_4x_4, \\ m_{15,16} &= e^{-K_4x_4}\cdot\sin K_4x_4, \end{aligned}$$

$$\begin{aligned} m_{15,17} &= -e^{K_5 x_4} \cdot \cos K_5 x_4, \\ m_{15,18} &= -e^{K_5 x_4} \cdot \sin K_5 x_4, \\ m_{15,19} &= -e^{-K_5 x_4} \cdot \cos K_5 x_4, \\ m_{15,20} &= -e^{-K_5 x_4} \cdot \sin K_5 x_4, \\ b_{15} &= y_{p5} - y_{p4}. \end{aligned} \tag{A.15}$$

Row 16.

$$\begin{aligned} m_{16,13} &= K_4 e^{K_4 x_4} \left(\cos K_4 x_4 - \sin K_4 x_4\right), \\ m_{16,14} &= K_4 e^{K_4 x_4} \left(\cos K_4 x_4 + \sin K_4 x_4\right), \\ m_{16,15} &= -K_4 e^{-K_4 x_4} \left(\cos K_4 x_4 + \sin K_4 x_4\right), \\ m_{16,16} &= K_4 e^{-K_4 x_4} \left(\cos K_4 x_4 - \sin K_4 x_4\right), \\ m_{16,17} &= -K_5 e^{K_5 x_4} \left(\cos K_5 x_4 - \sin K_5 x_4\right), \\ m_{16,18} &= -K_5 e^{K_5 x_4} \left(\cos K_5 x_4 + \sin K_5 x_4\right), \\ m_{16,19} &= K_5 e^{-K_5 x_4} \left(\cos K_5 x_4 + \sin K_5 x_4\right), \\ m_{16,20} &= -K_5 e^{-K_5 x_4} \left(\cos K_5 x_4 - \sin K_5 x_4\right). \end{aligned} \tag{A.16}$$

Row 17.

$$\begin{aligned} m_{17,13} &= -2K_4^2 e^{K_4 x_4} \sin K_4 x_4, \\ m_{17,14} &= 2K_4^2 e^{K_4 x_4} \cos K_4 x_4, \\ m_{17,15} &= 2K_4^2 e^{-K_4 x_4} \sin K_4 x_4, \\ m_{17,16} &= -2K_4^2 e^{-K_4 x_4} \cos K_4 x_4, \\ m_{17,17} &= 2K_5^2 e^{K_5 x_4} \sin K_5 x_4, \\ m_{17,18} &= -2K_5^2 e^{K_5 x_4} \cos K_5 x_4, \\ m_{17,19} &= -2K_5^2 e^{-K_5 x_4} \sin K_5 x_4, \\ m_{17,20} &= 2K_5^2 e^{-K_5 x_4} \cos K_5 x_4. \end{aligned} \tag{A.17}$$

Row 18.

$$\begin{aligned} m_{18,13} &= -2K_{t4} K_4^3 e^{K_4 x_4} \left(\cos K_4 x_4 + \sin K_4 x_4\right) \\ &\quad - K_{e3} e^{K_4 x_4} \cos K_4 x_4, \\ m_{18,14} &= 2K_{t4} K_4^3 e^{K_4 x_4} \left(\cos K_4 x_4 - \sin K_4 x_4\right) \\ &\quad - K_{e3} e^{K_4 x_4} \sin K_4 x_4, \\ m_{18,15} &= 2K_{t4} K_4^3 e^{-K_4 x_4} \left(\cos K_4 x_4 - \sin K_4 x_4\right) \\ &\quad - K_{e3} e^{-K_4 x_4} \cos K_4 x_4, \\ m_{18,16} &= 2K_{t4} K_4^3 e^{-K_4 x_4} \left(\cos K_4 x_4 + \sin K_4 x_4\right) \\ &\quad - K_{e3} e^{-K_4 x_4} \sin K_4 x_4, \\ m_{18,17} &= 2K_{t5} K_5^3 e^{K_5 x_4} \left(\cos K_5 x_4 + \sin K_5 x_4\right), \\ m_{18,18} &= -2K_{t5} K_5^3 e^{K_5 x_4} \left(\cos K_5 x_4 - \sin K_5 x_4\right), \\ m_{18,19} &= -2K_{t5} K_5^3 e^{-K_5 x_4} \left(\cos K_5 x_4 - \sin K_5 x_4\right), \\ m_{18,20} &= -2K_{t5} K_5^3 e^{-K_5 x_4} \left(\cos K_5 x_4 + \sin K_5 x_4\right), \\ b_{18} &= K_{e3} y_{p4}. \end{aligned} \tag{A.18}$$

Row 19.

$$\begin{aligned} m_{19,17} &= e^{K_5 x_5} \cdot \cos K_5 x_5, \\ m_{19,18} &= e^{K_5 x_5} \cdot \sin K_5 x_5, \\ m_{19,19} &= e^{-K_5 x_5} \cdot \cos K_5 x_5, \\ m_{19,20} &= e^{-K_5 x_5} \cdot \sin K_5 x_5, \\ m_{19,21} &= -e^{K_6 x_5} \cdot \cos K_6 x_5, \\ m_{19,22} &= -e^{K_6 x_5} \cdot \sin K_6 x_5, \\ m_{19,23} &= -e^{-K_6 x_5} \cdot \cos K_6 x_5, \\ m_{19,24} &= -e^{-K_6 x_5} \cdot \sin K_6 x_5, \\ b_{19} &= y_{p6} - y_{p5}. \end{aligned} \tag{A.19}$$

Row 20.

$$\begin{aligned} m_{20,17} &= K_5 e^{K_5 x_5} \left(\cos K_5 x_5 - \sin K_5 x_5\right), \\ m_{20,18} &= K_5 e^{K_5 x_5} \left(\cos K_5 x_5 + \sin K_5 x_5\right), \\ m_{20,19} &= -K_5 e^{-K_5 x_5} \left(\cos K_5 x_5 + \sin K_5 x_5\right), \\ m_{20,20} &= K_5 e^{-K_5 x_5} \left(\cos K_5 x_5 - \sin K_5 x_5\right), \\ m_{20,21} &= -K_6 e^{K_6 x_5} \left(\cos K_6 x_5 - \sin K_6 x_5\right), \\ m_{20,22} &= -K_6 e^{K_6 x_5} \left(\cos K_6 x_5 + \sin K_6 x_5\right), \\ m_{20,23} &= K_6 e^{-K_6 x_5} \left(\cos K_6 x_5 + \sin K_6 x_5\right), \\ m_{20,24} &= -K_6 e^{-K_6 x_5} \left(\cos K_6 x_5 - \sin K_6 x_5\right). \end{aligned} \tag{A.20}$$

Row 21.

$$\begin{aligned} m_{21,17} &= -2K_5^2 e^{K_5 x_5} \sin K_5 x_5, \\ m_{21,18} &= 2K_5^2 e^{K_5 x_5} \cos K_5 x_5, \\ m_{21,19} &= 2K_5^2 e^{-K_5 x_5} \sin K_5 x_5, \\ m_{21,20} &= -2K_5^2 e^{-K_5 x_5} \cos K_5 x_5, \\ m_{21,21} &= 2K_6^2 e^{K_6 x_5} \sin K_6 x_5, \end{aligned}$$

$$\begin{aligned} m_{21,22} &= -2K_6^2 e^{K_6 x_5} \cos K_6 x_5, \\ m_{21,23} &= -2K_6^2 e^{-K_6 x_5} \sin K_6 x_5, \\ m_{21,24} &= 2K_6^2 e^{-K_6 x_5} \cos K_6 x_5. \end{aligned} \tag{A.21}$$

Row 22.

$$\begin{aligned} m_{22,17} &= -2K_5^3 e^{K_5 x_5} \left(\cos K_5 x_5 + \sin K_5 x_5\right), \\ m_{22,18} &= 2K_5^3 e^{K_5 x_5} \left(\cos K_5 x_5 - \sin K_5 x_5\right), \\ m_{22,19} &= 2K_5^3 e^{-K_5 x_5} \left(\cos K_5 x_5 - \sin K_5 x_5\right), \\ m_{22,20} &= 2K_5^3 e^{-K_5 x_5} \left(\cos K_5 x_5 + \sin K_5 x_5\right), \\ m_{22,21} &= 2K_6^3 e^{K_6 x_5} \left(\cos K_6 x_5 + \sin K_6 x_5\right), \\ m_{22,22} &= -2K_6^3 e^{K_6 x_5} \left(\cos K_6 x_5 - \sin K_6 x_5\right), \\ m_{22,23} &= -2K_6^3 e^{-K_6 x_5} \left(\cos K_6 x_5 - \sin K_6 x_5\right), \\ m_{22,24} &= -2K_6^3 e^{-K_6 x_5} \left(\cos K_6 x_5 + \sin K_6 x_5\right). \end{aligned} \tag{A.22}$$

Row 23.

$$\begin{aligned} m_{23,21} &= e^{K_6 x_6} \cdot \cos K_6 x_6, \\ m_{23,22} &= e^{K_6 x_6} \cdot \sin K_6 x_6, \\ m_{23,23} &= e^{-K_6 x_6} \cdot \cos K_6 x_6, \\ m_{23,24} &= e^{-K_6 x_6} \cdot \sin K_6 x_6, \\ b_{23} &= -y_{p6}. \end{aligned} \tag{A.23}$$

Row 24.

$$\begin{aligned} m_{24,21} &= e^{K_6 x_6} \left(\cos K_6 x_6 - \sin K_6 x_6\right), \\ m_{24,22} &= e^{K_6 x_6} \left(\cos K_6 x_6 + \sin K_6 x_6\right), \\ m_{24,23} &= -e^{-K_6 x_6} \left(\cos K_6 x_6 + \sin K_6 x_6\right), \\ m_{24,24} &= e^{-K_6 x_6} \left(\cos K_6 x_6 - \sin K_6 x_6\right). \end{aligned} \tag{A.24}$$

References

[1] I. Rosal-Fernandez, "How costly is the maintenance of the coal-mining jobs in Europe? The Spanish case 1989–1995," *Energy Policy*, vol. 28, no. 8, pp. 537–547, 2000.

[2] Ministry of Industry, Energy and Tourism. Institute for Restructuring of Coal Mining and Alternative Development of Mining Regions. Report of the national strategic coal reserve 2006–2012 and new model for comprehensive and sustainable development of mining regions, 2013, http://www.irmc.es/.

[3] RGNBSM, General Regulation of Basic Procedure of Mining Safety. Spain, Ministry of Industry and Energy, 2006, (Spanish).

[4] J. Gómez de las Heras, Provisions and design support in unions panel-gallery on pit-horizontal layers machined. Madrid, Geo-Miner Technologic Institute of Spain, Ministry of Industry, Trade and Tourism, 1988, (Spanish).

[5] R. Lindsay Galloway, *A History of Coal Mining in Great Britain*, Augustus M. Kelley, New York, NY, USA, 1969.

[6] Energy Information Administration, Office of Coal, Nuclear, Electric and Alternate Fuels, *Longwall Mining*, U. S. Department of Energy, Washington, DC, USA, 1995.

[7] Medium-term coal market report 2012, OECD Publishing. IEA, 2012.

[8] Coal mining. World coal. World Coal Institute, 2009.

[9] P. Darling, *SME Mining Engineering Handbook*, Society for Mining, Metallurgy, and Exploration (SME), 3rd edition, 2011.

[10] A. A. Waddington and D. R. Kay, "Recent development in the incremental profile method of predicting subsidence, tilt and strain over a series of longwall Panels," in *Proccedings of the International Conference on Geomechanics/Ground Control in Mining and Underground Construction*, Wollongong, Australia, July 1998.

[11] A. García-Bello, J. Ordieres-Meré, and C. González-Nicieza, "Generalization of the influence function method in mining subsidence," *International Journal of Surface Mining, Reclamation and Environment*, vol. 10, no. 4, pp. 195–202, 1996.

[12] G. W. Mitchell, "Longwall mining," in *Australasian Coal Mining Practice*, R. J. Kininmonth and E. Y. Baafi, Eds., pp. 340–373, The Australasian Institute of Mining and Metallurgy, Melbourne, Australia, 2010.

[13] M. S. Venkata Ramayya and L. Sudhakar, "Selection of powered roof support for weak coal roof," *Journal of Mines, Metals and Fuels*, vol. 50, no. 4, pp. 114–117, 2002.

[14] R. Singh and T. N. Singh, "Investigation into the behaviour of a support system and roof strata during sublevel caving of a thick coal seam," *Geotechnical and Geological Engineering*, vol. 17, no. 1, pp. 21–35, 1999.

[15] J. Ju and J. Xu, "Structural characteristics of key strata and strata behaviour of a fully mechanized longwall face with 7.0 m height chocks," *International Journal of Rock Mechanics and Mining Sciences*, vol. 58, pp. 46–54, 2013.

[16] N. Bilim and I. Özkan, "Determination of the effect of roof pressure on coal hardness and excavation productivity: an example from a Çayırhan lignite mine, Ankara, Central Turkey," *International Journal of Coal Geology*, vol. 75, no. 2, pp. 113–118, 2008.

[17] C. González-Nicieza, A. Menéndez-Díaz, A. E. Álvarez-Vigil, and M. I. Álvarez-Fernández, "Analysis of support by hydraulic props in a longwall working," *International Journal of Coal Geology*, vol. 74, no. 1, pp. 67–92, 2008.

[18] R. Juárez-Ferreras, C. González-Nicieza, A. Menéndez-Díaz, A. E. Álvarez-Vigil, and M. I. Álvarez-Fernández, "Forensic analysis of hydraulic props in longwall workings," *Engineering Failure Analysis*, vol. 16, no. 7, pp. 2357–2370, 2009.

[19] R. Juárez-Ferreras, C. González-Nicieza, A. Menéndez-Díaz, A. E. Álvarez-Vigil, and M. I. Álvarez-Fernández, "Measurement and analysis of the roof pressure on hydraulic props in longwall," *International Journal of Coal Geology*, vol. 75, no. 1, pp. 49–62, 2008.

[20] S. P. Timoshenko and J. N. Goodier, *Theory of Elasticity*, McGraw- Hill, New York, NY, USA, 1970.

[21] V. I. Klishin and T. M. Tarasik, "Stand tests of hydraulic props in dynamic loads," *Journal of Mining Science*, vol. 37, no. 1, pp. 77–84, 2001.

Hindawi Publishing Corporation
Journal of Applied Mathematics
Volume 2013, Article ID 420536, 19 pages
http://dx.doi.org/10.1155/2013/420536

Research Article

A Model of Anisotropic Property of Seepage and Stress for Jointed Rock Mass

Pei-tao Wang,[1,2] Tian-hong Yang,[1,2] Tao Xu,[1,2] Qing-lei Yu,[1,2] and Hong-lei Liu[1,2]

[1] *Key Laboratory of Ministry of Education on Safe Mining of Deep Metal Mines, Northeastern University, Shenyang 110819, China*
[2] *School of Resources & Civil Engineering, Northeastern University, Shenyang 110819, China*

Correspondence should be addressed to Tian-hong Yang; yang_tianhong@126.com

Received 30 March 2013; Revised 18 June 2013; Accepted 19 June 2013

Academic Editor: Pengcheng Fu

Joints often have important effects on seepage and elastic properties of jointed rock mass and therefore on the rock slope stability. In the present paper, a model for discrete jointed network is established using contact-free measurement technique and geometrical statistic method. A coupled mathematical model for characterizing anisotropic permeability tensor and stress tensor was presented and finally introduced to a finite element model. A case study of roadway stability at the Heishan Metal Mine in Hebei Province, China, was performed to investigate the influence of joints orientation on the anisotropic properties of seepage and elasticity of the surrounding rock mass around roadways in underground mining. In this work, the influence of the principal direction of the mechanical properties of the rock mass on associated stress field, seepage field, and damage zone of the surrounding rock mass was numerically studied. The numerical simulations indicate that flow velocity, water pressure, and stress field are greatly dependent on the principal direction of joint planes. It is found that the principal direction of joints is the most important factor controlling the failure mode of the surrounding rock mass around roadways.

1. Introduction

Underground mining has been considered a high-risk activity worldwide. Violent roof failure or rock burst induced by mining has always been a serious threat to the safety and efficiency of mines in China. Accurate and detailed characterization for rock masses can control stable excavation spans, support requirements, cavability, and subsidence characteristics, and thus influence the design of mining layouts and safety of mines. Rock mass is a geologic body composing of the discontinuities which have a critical influence on deformational behavior of blocky rock systems [1]. The mechanical behavior of this material depends principally on the state of intact rock whose mechanical properties could be determined by laboratory tests and existing discontinuities containing bedding planes, faults, joints, and other structural features. The distributions and strength of these discontinuities are both the key influencing factors for characterizing the discontinuous and anisotropic materials. Amadei [2] pointed out the importance of anisotropy of jointed rock mass and discussed the interaction existing between rock anisotropy and rock stress. Because of computational complexity and the difficulty of determining the necessary elastic constants, it is usual for only the simplest form of anisotropy, transverse isotropy, to be used in design analysis [3]. The key work is to study the principal direction of elasticity or permeability and then assume the jointed rock mass as transversely isotropic geomaterial.

Extensive efforts have been made to investigate the mechanical response of transversely anisotropic rock material. Zhang and Sanderson [4] used the fractal dimension to describe the connectivity and compactness of fracture network and found that the deformability and the overall permeability of fractured rock masses increase greatly with increasing fracture density. By using the artificial transversely isotropic rock blocks, the mechanical properties with different dip angles were obtained by Tien and Tsao [5]. Brosch et al. [6] evaluated the fabric-dependent anisotropy of a particular gneiss by studying the strength values and elastic parameters along different directions. Exadaktylos and Kaklis [7] presented the explicit representations of stresses and strains at any point of the anisotropic circular disc compressed diametrically. The stress concentration in uniaxial compression for a plane strain model was investigated, and a formulation of failure criteria for elastic-damage and elastic-plastic anisotropic geomaterials is formed by Exadaktylos [8]. A methodology to determine the equivalent elastic properties of fractured rock masses was established by explicit representations of stochastic fracture systems [9], and the conditions for the application of the equivalent continuum approach for representing mechanical behavior of the fractured rock masses were investigated. Such anisotropy has an effect on the interpretation of stress distributions. Amadei's results indicate that an anisotropy ratio (damaged elastic modulus to intact elastic modulus) of between 1.14 and 1.33 will have a definite effect on the interpreted in situ state of stress [10]. Hakala et al. [11] concluded that the anisotropy ratio of Finland rock specimens is about 1.4 and suggested to be taken into account in the interpretation of stress measurement results.

Moreover, in rock engineering like mining and tunnel engineering, interactions between in situ stress and seepage pressure of groundwater have an important role. Groundwater under pressure in the joints defining rock blocks reduces the normal effective stress between the rock surfaces and therefore reduces the potential shear resistance which can be mobilized by friction. Since rock behavior may be determined by its geohydrological environment, it may be essential in some cases to maintain close control of groundwater conditions in the mine area. Therefore, accurate description of joints is an important topic for estimating and evaluating the deformability and seepage properties of rock masses.

Many researchers have done a lot of studies on the seepage and anisotropic mechanical behaviors of the jointed rock mass. Using homogeneous samples like granite or basalt, Witherspoon et al. [12] investigated and defined the permeability by fracture aperture in a closed fracture. Based on geometrical statistics, Oda [13] has studied and determined the crack tensor of moderately jointed granite by treating statistically the crack orientation data via a stereographic projection. Using Oda's method, Sun and Zhao [14] determined the anisotropy in permeability using the fracture orientation and the in situ stress information from the field survey. For fractured rock system, attempts have been made by Jing et al. [15–18] and Bao et al. [19] to investigate the permeability. Using UDEC code, Jing et al. studied the permeability of discrete fracture network, such as the existence of REV in [15], relations between fracture length and aperture in [16] or stress effect on permeability in [17], or solute transport in [18]. Bao et al. [19] have discussed the mesh effect on effective permeability for a fractured system using the upscaled permeability field. It would help the workers to spend less computational effort and memory requirement to investigate effective permeability. The key for determining deformation modulus and hydraulic parameters is to study representative elementary volume (REV) and scale effects of fractured rock mass [9, 20–22]. However, the difficulty of testing jointed rock specimens, at scales sufficient to represent the equivalent continuum, indicated that it is necessary to postulate and verify methods of synthesizing rock mass properties from those of the constituent elements like intact rock and fractures.

Although great progress has been made, it is difficult to study the anisotropic deformation of large-scale rock mass, ground water permeability change, and interaction between stress and seepage due to the geological complexity of discontinuities. Qiao et al. [23] have pointed out that the rock mass which is not highly fractured and has only few sets of joint system usually behaves anisotropically. However, the mechanical properties directionality of highly jointed rock mass is usually ignored. In particular, since the limitation of mesh generation, the numerical method can hardly deal with the highly jointed specimens. The discontinuity like fault could be treated as specific boundary. An effective solution should be found to characterize the influence of joints on the rock mass.

In this paper, based on equivalent continuum theory and theoretical analysis, a mathematical model for anisotropic property of seepage and elasticity of jointed rock mass is described. A permeability analysis code is developed to evaluate the anisotropic permeability for DFN model based on VC++ 6.0 in this paper. The DFN model could be analyzed to evaluate the REV size and anisotropic property of permeability, which would provide important evidence for the finite element model. The outline is as follows. First, 3D images involving detailed geometrical properties of rock mass, such as trace lengths, outcrop areas, joint orientations, and joint spacing, were captured using ShapMetriX3D system. According to the statistical parameters for each set of discontinuities, fracture network is generated using Monte Carlo method, and jointed rock samples in different sections could be captured. Next, permeability tensors and elasticity tensors of rock mass of the sample are calculated by discrete medium seepage method and geometrical damage theory, respectively. Finally, using the finite element method (FEM), an anisotropic mechanical model for rock mass is built. An engineering practice of roadway stability at the Heishan Metal Mine, in Hebei Iron and Steel Group Mining Company, is described. Then the stress and seepage fields surrounding the roadway were numerically simulated. On the basis of the modeled results, the influences of joint planes on stress, seepage, and damage zone were analyzed. It is expected throughout this study to gain an insight into the influences of discontinuities on the mechanical behavior of rock mass and offer some scientific evidence for the design of mining layouts or support requirements.

2. Generation of a Fracture System Model by ShapeMetriX3D

Traditional methods for rock mass structural parameters in mining engineering applications include scanline surveying [24] and drilling core method [25]. The process generally requires physical contact with rock mass exposure and therefore is hazardous. Additionally, taking manual measurements is time consuming and prone to errors due to sampling difficulties or instrument errors. ShapeMetriX3D is a tool for the geological and geotechnical data collection and assessment

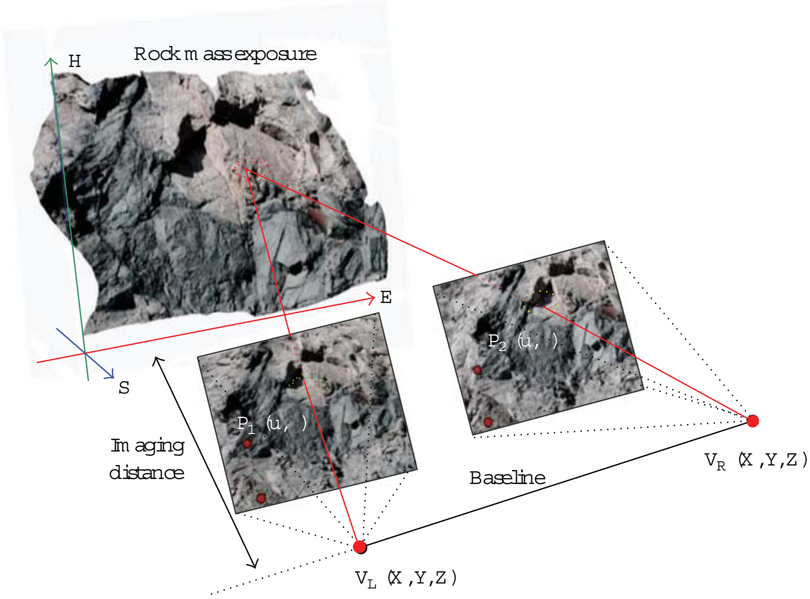

FIGURE 1: Imaging principle of the 3D surface measurement.

for rock masses [26]. The equipment is used for the metric acquisition of rock and terrain surfaces and for the contact-free measurement of geological/geotechnical parameters by metric 3D images. The images are captured using Nikon D80 camera with 22.3 megapixel. As shown in Figure 1, two images are acquired to reproduce the 3D rock mass face. Details information related to the measurements is reported in [27] by Gaich et al. The measurements could be taken at any required number and extent, even in regions that are not accessible. During measuring process, two digital images taken by a calibrated camera serve for a 3D reconstruction of the rock face geometry which is represented on the computer by a photorealistic spatial characterization as shown in Figure 1. From it, measurements are taken by marking visible rock mass features, such as spatial orientations of joint surfaces and traces, as well as areas, lengths, or positions. Finally, the probability statistical models of discontinuities are established. It is generally applied in the typical situations such as long rock faces at small height and rock slopes with complex geometries [28]. Almost any rock face can be reconstructed at its optimum resolution by using this equipment and its matching software. By using this system we can increase working safety, reduce mapping time, and improve data quality.

In order to accurately represent rock discontinuities, ShapeMetriX3D (3GSM) in this paper is used for the metric acquisition of rock mass exposure and for the contact-free measurement of geological parameters by metric 3D images. Stereoscopic photogrammetry deals with the measurement of three-dimensional information from two images showing the same object or surface but taken from two different angles, just as shown in Figure 1.

From the determined orientation between the two images and a pair of corresponding image points $P_1(u,v)$ and $P_2(u,v)$, imaging rays (colored in red) are reconstructed whose intersection leads to a 3D surface point $P(X,Y,Z)$. By automatic identification of corresponding points within the image pair, the result of the acquisition is a metric 3D image that covers the geometry of the rock exposure. Once the image of a rock wall is ready, geometric measurements can be taken as shown in Figure 2. There are a total of three groups of discontinuities in this bench face.

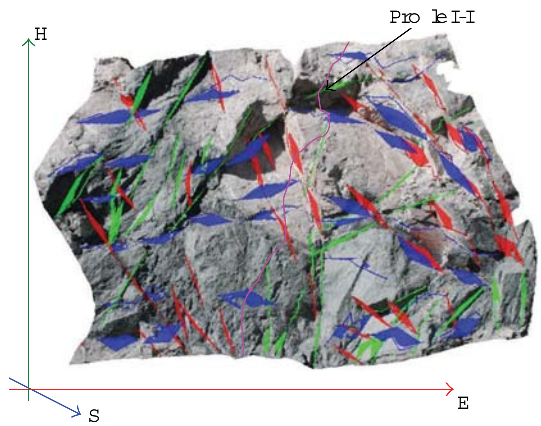

FIGURE 2: Geological mapping and geometric measurements of stereoscopic restructuring model.

Figure 3 is facilitated to show the 3-dimensional distribution of the trace along the section of Profile I-I from the stereoscopic model shown in Figure 2. The height of this rock face is approximately 5.0 m with a distance of 2.0 m perpendicular to the trace. The measured orientation in a hemispherical plot could also be captured as in Figure 4(a). Figure 4(b) shows the results of the distribution of joints.

The generated 3D rock face is about 5 m × 5 m with a high resolution enough to distinguish the fractures. According to

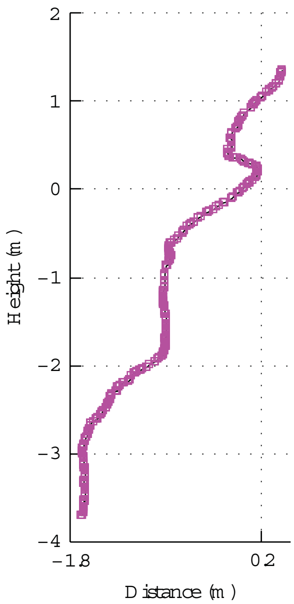

Figure 3: Length and sketch of Profile I-I by stereoscopic model.

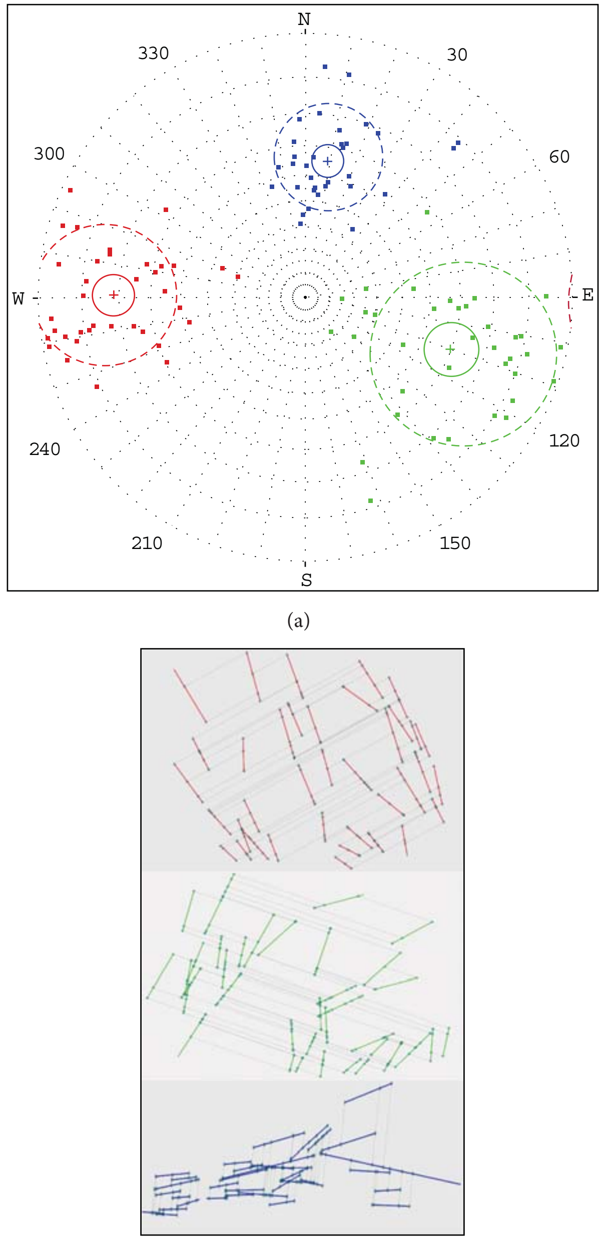

(a)

(b)

Figure 4: Stereographic plot and the distribution of total three sets of joints.

the survey results, the geologic data like joint density, dip angle, trace length, and spacing can be acquired. Baghbanan and Jing [16] generated the DFN models whose orientations of fracture sets followed the Fisher distribution. In this paper, four different probability statistical models are used to generate the DFN models. The dip angle, dip direction, trace length, and spacing all follow one particular probability statistical model. Table 1 shows the basic information about the fracture system parameters. Type I of the probability statistical model in Table 1 stands for negative exponential distribution, Type II for normal distribution, Type III for logarithmic normal distribution, and Type IV for uniform distribution. Based on the probability models, the particular fracture network could be generated using Monte Carlo method [29, 30].

3. Constitutive Relation of Anisotropic Rock Mass

Due to the existence of joints and cracks, the mechanical properties (Young's modulus, Poisson's ratio, strength, etc.) of rock masses are generally heterogeneous and anisotropic. Three preconditions should be confirmed in this section: (i) anisotropy of rock mass is mainly caused by IV or V-class structure or rock masses containing a large number of discontinuities; (ii) rock masses according to (i) could be treated as homogeneous and anisotropic elastic material; (iii) seepage tensor and damage tensor of rock mass with multiset of joints could be captured by the scale of representative elementary volume (REV).

3.1. Stress Analysis. Elasticity represents the most common constitutive behavior of engineering materials, including many rocks, and it forms a useful basis for the description of more complex behavior. The most general statement of linear elastic constitutive behavior is a generalized form of Hooke' Law, in which any strain component is a linear function of all the stress components; that is,

$$\varepsilon_{ij} = [\mathbf{S}]\,\sigma_{ij}, \tag{1}$$

where $[\mathbf{S}]$ is the flexibility matrix, ε_{ij} is the strain, and σ_{ij} is the stress.

Many underground excavation design analyses involving openings where the length to cross-section dimension ratio is high are facilitated considerably by the relative simplicity of the excavation geometry. In this section, the roadway is

TABLE 1: Characteristics of 3 sets of discontinuities for the slope exposure.

Set	Density (m^{-1})	Fracture characteristics											
		Dip direction (°)			Dip angle (°)			Trace length (m)			Spacing (m)		
		Type	Mean value	Standard deviation	Type	Mean value	Standard deviation	Type	Mean value	Standard deviation	Type	Mean value	Standard deviation
1#	1.2	II	90.73	13.88	III	71.24	15.05	II	0.86	0.23	IV	0.83	0.75
2#	1.3	II	289.96	22.89	IV	59.85	8.4	II	0.89	0.28	IV	0.76	0.73
3#	3.3	III	189.05	14.55	III	55.29	13.35	II	0.85	0.25	IV	0.3	0.31

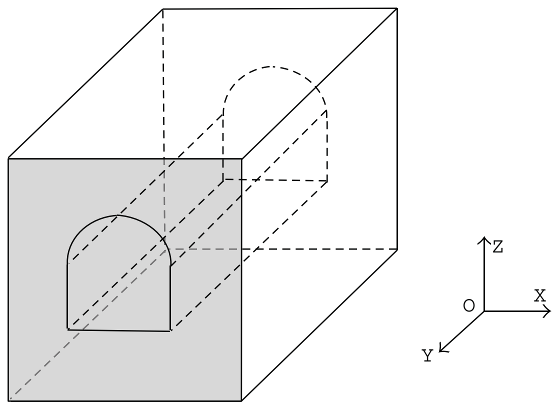

FIGURE 5: A diagrammatic sketch for underground excavation.

uniform cross section along the length and could be properly analyzed by assuming that the stress distribution is the same in all planes perpendicular to the long axis of the excavation (Figure 5). Thus, this problem could be analyzed in terms of plane geometry.

The state of stress at any point can be defined in terms of the plane components of stress (σ_{11}, σ_{22}, and σ_{12}) and the components (σ_{33}, σ_{23}, and σ_{31}). In this research, the Z direction is assumed to be a principal axis and the antiplane shear stress components would vanish. The plane geometric problem could then be analyzed in terms of the plane components of stress since the σ_{33} component is frequently neglected. Equation (1), in this case, may be recast in the form

$$\begin{bmatrix}\varepsilon_{11}\\ \varepsilon_{22}\\ \varepsilon_{12}\end{bmatrix} = [\mathbf{S}]\,[\sigma] = \begin{bmatrix} \dfrac{1}{E_1}-\dfrac{\nu_{31}^2}{E_3} & -\left(\dfrac{\nu_{12}}{E_1}+\dfrac{\nu_{31}^2}{E_3}\right) & 0 \\ -\left(\dfrac{\nu_{12}}{E_1}+\dfrac{\nu_{31}^2}{E_3}\right) & \dfrac{1}{E_1}-\dfrac{\nu_{31}^2}{E_3} & 0 \\ 0 & 0 & \dfrac{2(1+\nu_{12})}{E_1}\end{bmatrix} \times \begin{bmatrix}\sigma_{11}\\ \sigma_{22}\\ \sigma_{12}\end{bmatrix}, \tag{2}$$

where $[\mathbf{S}]$ is the flexibility matrix of the material under plane strain conditions. The inverse matrix $[\mathbf{S}]^{-1}$ (or $[\mathbf{E}]$) could be expressed in the form

$$\begin{bmatrix}\sigma_{11}\\ \sigma_{22}\\ \sigma_{12}\end{bmatrix} = [\mathbf{E}]\,[\varepsilon] = \begin{bmatrix} \dfrac{E_1^2\left(E_3-E_1\nu_{31}^2\right)}{\Delta} & \dfrac{-E_1^2\left(E_3\nu_{21}+E_1\nu_{31}^2\right)}{\Delta} & 0 \\ \dfrac{-E_1^2\left(E_3\nu_{21}+E_1\nu_{31}^2\right)}{\Delta} & \dfrac{E_1^2\left(E_1\nu_{31}^2-E_3\right)}{\Delta} & 0 \\ 0 & 0 & \dfrac{E_1}{2(1+\nu_{12})}\end{bmatrix} \begin{bmatrix}\varepsilon_{11}\\ \varepsilon_{22}\\ \varepsilon_{12}\end{bmatrix}, \tag{3}$$

where Δ is expressed as follows:

$$\Delta = -E_1E_3 + E_1E_3\nu_{21}^2 + E_1^2\nu_{31}^2 + E_1^2\nu_{31}^2 + 2E_1^2\nu_{21}\nu_{31}^2. \tag{4}$$

The moduli E_1 and E_3 and Poisson's ratios ν_{31} and ν_{12} could be provided by uniaxial strength compression or tension in 1 (or 2) and 3 directions.

The mechanical tests including laboratory and in situ tests for rock masses in large scale can hardly capture the elastic properties directly. Hoek-Brown criterion [31–33] could calculate the mechanical properties of weak rocks masses by introducing the Geological Strength Index (GSI). Nevertheless, the anisotropic properties cannot be captured using this criterion, and thus the method for analyzing anisotropy of jointed rock mass needs a further study.

In this paper, the original joint damage in rock mass is considered as macro damage field. In elastic damage mechanics, the elastic modulus of the jointed material may

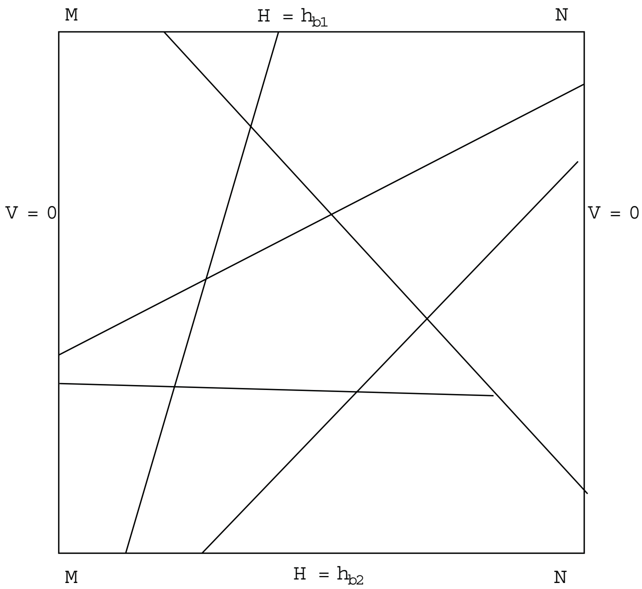

FIGURE 6: Fracture network schematic diagram in seepage area. MN and $M'N'$ are the constant head boundaries with the hydraulic head of h_{b1} and h_{b2} respectively; MM' and NN' are the impervious boundaries with flow V of zero.

degrade and the Young's modulus of the damaged element is defined as follows [34]:

$$E = E_0 (1 - D), \tag{5}$$

where D represents the damage variable and E and E_0 are the elastic moduli of the damaged and intact rock samples, respectively. In this equation, all parameters are scalar.

With the geometric information of the fracture sample, the damage tensor [35] could be defined as

$$D_{ij} = \frac{l}{V} \sum_{k=1}^{N} \alpha^{(k)} \left(n^{(k)} \otimes n^{(k)}\right), \quad (i, j = 1, 2, 3), \tag{6}$$

where N is the number of joints, l is the minimum spacing between joints, V is the volume of rock mass, $n^{(k)}$ is the normal vector of the kth joint, and $a^{(k)}$ is the trace length of the kth joint (for 2 dimensions).

According to the principal of energy equivalence [36], the flexibility matrix for the jointed rock sample can be obtained as

$$S'_{ij} = (1 - D_i)^{-1} S_{ij} (1 - D_j)^{-1}, \tag{7}$$

where S_{ij} is the flexibility matrix for intact rock; D_i and D_j are the principal damage values in i and j directions, respectively. For plane strain geometric problem, the constitutive relation, where the coordinates and principal damage have the same direction, could be expressed as follows:

$$\begin{bmatrix} \sigma_{11} \\ \sigma_{22} \\ \sigma_{12} \end{bmatrix} = \begin{bmatrix} \frac{E_0 (\nu_0 - 1)(D_1 - 1)^2}{2\nu_0^2 + \nu_0 - 1} & \frac{-E_0 \nu_0 (D_1 - 1)(D_2 - 1)}{2\nu_0^2 + \nu_0 - 1} & 0 \\ \frac{-E_0 \nu_0 (D_1 - 1)(D_2 - 1)}{2\nu_0^2 + \nu_0 - 1} & \frac{E_0 (\nu_0 - 1)(D_2 - 1)^2}{2\nu_0^2 + \nu_0 - 1} & 0 \\ 0 & 0 & \frac{E_0 (D_1 - 1)(D_2 - 1)}{2(1 + \nu_0)} \end{bmatrix} \begin{bmatrix} \varepsilon_{11} \\ \varepsilon_{22} \\ \varepsilon_{12} \end{bmatrix}, \tag{8}$$

where E_0 is the Young's modulus of intact rock and ν_0 is Poisson's ratio for intact rock.

The parameters could be easily captured by laboratory tests. Equation (7) gives the principal damage values D_1 and D_2. Based on geometrical damage mechanics, all elements in this matrix could be obtained by the method mentioned previously, and the anisotropic constitutive relation of jointed rock sample could finally be confirmed.

3.2. Seepage Analysis. The seepage parameters of rock mass are quantized form of permeability and also are the basis to solve seepage field of equivalent continuous medium. Based on the attribute of fractured rock mass and by taking engineering design into account, fractured rock mass is often considered to be anisotropic continuous medium. In the fracture network shown in Figure 6, a total number of N cross points or water heads and M line elements are contained. Parameters can be obtained with the model such as water head, the related line elements, equivalent mechanical fissure width, seepage coefficient, and so on. The corresponding coordinates of each point could be acquired. For a fluid flow analysis based on the law of mass conservation, the fluid equations on a certain water head take the form [37]

$$\left(\sum_{j=1}^{N'} q_j \right)_i + Q_i = 0, \quad (i = 1, 2, \ldots, N), \tag{9}$$

where q_j is the quantity of flow from line element j to water head i, N' is the total number of line elements intersect at i, and Q_i is the fluid source term. In the joint network, each line element would be assigned a length l_j and fissure width b_j to investigate the permeability.

According to the hydraulic theory [38], for a single joint seepage, the flow quantity q_j of line element j can be expressed as

$$q_j = \frac{\rho b_j^3}{12\mu} \cdot \frac{\Delta h_j}{l_j}, \tag{10}$$

where Δh_j is the hydraulic gradient, μ is the coefficient of flow viscosity, ρ is the density of water, and b_j is the fissure width of joint. On the basis of (9) and (10), the governing equations can be represented as (11) for seepage in fracture network

$$\left(\sum_{j=1}^{N'} \frac{\rho b_j^3}{12\mu} \cdot \frac{\Delta h_j}{l_j} \right)_i + Q_i = 0. \tag{11}$$

Based on the discrete fracture network method [39], an equivalent continuum model for seepage has been established [28, 40, 41]. The hydraulic conductivity can be acquired based on Darcy's Law on the basis of water quantity in the network (see (12)).

Boundary conditions in the model shown in Figure 6 are as follows:

(a) MN and $M'N'$ as the constant head boundary;

(b) MM' and NN' as the impervious boundary with flow V of 0.

Then the hydraulic conductivity can be defined as

$$K = \frac{\Delta q \cdot M'M}{\Delta H \cdot MN}, \tag{12}$$

where Δq is the total quantity of water in the model region ($m^2 \cdot s^{-1}$), ΔH is the water pressure difference between inflow and outflow boundaries (m), K is the equivalent hydraulic conductivity coefficient in the MM' direction ($m \cdot s^{-1}$), and MN and $M'M$ are the side lengths of the region (m).

Based on Biot equations [42], the steady flow model is given by

$$K_{ij} \nabla^2 p = 0, \tag{13}$$

where K_{ij} is the hydraulic conductivity and p is the hydraulic pressure. For plane problems, the dominating equation of seepage flow is as follows in (14). The direction of joint planes is considered to be the principal direction of hydraulic conductivity

$$K_{ij} = \begin{bmatrix} K_{11} & K_{12} \\ K_{21} & K_{22} \end{bmatrix}. \tag{14}$$

3.3. Coupling Mechanism of Seepage and Stress

3.3.1. Seepage Inducted by Stress. The coupling action between seepage and stress makes the failure mechanism of rock complex. The investigations on this problem have pervasive theoretical meaning and practical value. The principal directions associated with the symmetric crack tensor are coaxial with those of the permeability tensor.

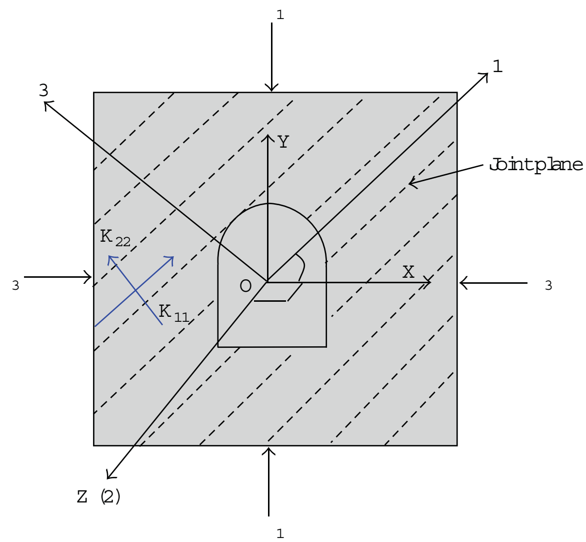

Figure 7: The relationship between planes of joints and the principal stress direction.

The first invariant of the crack tensor is proportional to the mean permeability, while the deviatoric part is related to the anisotropic permeability [13]. Generally, the change of stress which is perpendicular to the joints plane is the main factor leading to the increase or decrease of the ground water permeability. In the numerical model, seepage is coupled to stress describing the permeability change induced by the change of the stress field. The coupling function can be described as follows as given by Louis [43]:

$$K_f = K_0 e^{-\beta\sigma}, \tag{15}$$

where K_f is the current groundwater hydraulic conductivity, K_0 is the initial hydraulic conductivity, σ is the stress perpendicular to the joints plane, and β is the coupling parameter (stress sensitive factor to be measured by experiment) that reflects the influence of stress. The larger β is, the greater the range of stress induced the permeability [44].

3.3.2. Stress Inducted by Seepage. On the basis of generalized Terzaghi's effective stress principle [45], the stress equilibrium equation could be expressed as follows for the water-bearing jointed specimen:

$$\sigma_{ij} = E_{ijkl}\varepsilon_{kl} - \alpha_{ij} P \delta_{ij}, \tag{16}$$

where σ_{ij} is the total stress tensor, E_{ijkl} is the elastic tensor of the solid phase, ε_{kl} is the strain tensor, α_{ij} is a positive constant which is equal to 1 when individual grains are much more incompressible than the grain skeleton, P is the hydraulic pressure, and δ_{ij} is the Kronecker delta function.

3.4. Coordinate Transformation. Generally, planes of joints are inclined at an angle to the major principal stress direction as shown in Figure 7. In establishing these equations, the X, Y, and 1, 3 axes are taken to have the same Z (2) axis, and the angel θ is measured from the x to the 1 axis.

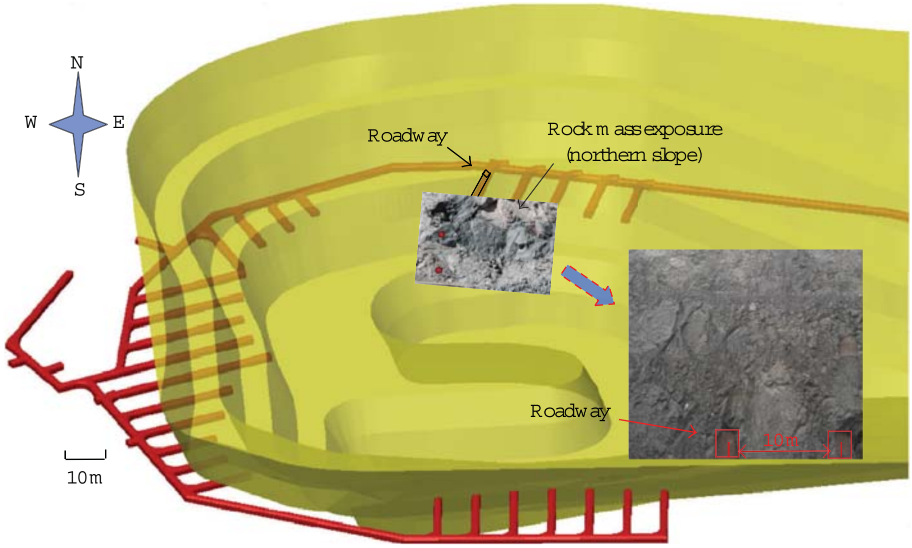

FIGURE 8: The rock mass exposure of northern slope in Heishan open pit mine.

Considering the hydraulic pressure needs no coordinate transformation, and (16) will be expressed as

$$\begin{bmatrix} \sigma_{11} \\ \sigma_{22} \\ \tau_{12} \end{bmatrix} = [\mathbf{T}_\sigma]^{-1} [\mathbf{E}] [\mathbf{T}_\varepsilon] \begin{bmatrix} \varepsilon_{11} \\ \varepsilon_{22} \\ \gamma_{12} \end{bmatrix} - \alpha_{ij} \begin{bmatrix} P \\ P \\ 0 \end{bmatrix} \delta_{ij}, \quad (17)$$

where $[\mathbf{T}_\sigma]^{-1}$ is the reverse matrix for stress coordinates transformation and $[\mathbf{T}_\varepsilon]$ is the strain coordinates transformation matrix, and they can be expressed as follows:

$$[\mathbf{T}_\sigma]^{-1} = \begin{bmatrix} \cos^2\theta & \sin^2\theta & -2\cos\theta\sin\theta \\ \sin^2\theta & \cos^2\theta & 2\sin\theta\cos\theta \\ \sin\theta\cos\theta & -\sin\theta\cos\theta & \cos^2\theta - \sin^2\theta \end{bmatrix},$$

$$[\mathbf{T}_\varepsilon] = \begin{bmatrix} \cos^2\theta & \sin^2\theta & \cos\theta\sin\theta \\ \sin^2\theta & \cos^2\theta & -\sin\theta\cos\theta \\ -2\sin\theta\cos\theta & 2\sin\theta\cos\theta & \cos^2\theta - \sin^2\theta \end{bmatrix}. \quad (18)$$

Similarly, the coordinate transformation form can be expressed as

$$K_{11} = \frac{K'_{11} + K'_{22}}{2} + \frac{K'_{11} - K'_{22}}{2}\cos 2\theta,$$
$$K_{12} = K_{21} = -\frac{K'_{11} - K'_{22}}{2}\sin 2\theta, \quad (19)$$
$$K_{22} = \frac{K'_{11} + K'_{22}}{2} - \frac{K'_{11} - K'_{22}}{2}\cos 2\theta,$$

where K'_{11} is the hydraulic conductivity coefficient along the distribution direction of joint planes, K'_{22} is perpendicular to the distribution direction, and θ is measured from the coordinate system x to the optimal direction of permeability.

4. A Case Study

4.1. Description of the Area under Study. The model described above is applied to evaluate the seepage field and stress field of jointed rock roadway in the Heishan Metal Mine (Figure 8). The mine is located in Chengde city, Hebei province, in northern China. Heishan Metal Mine has transferred from open pit mining to underground mining since 2009. The deformation and stability of the roadways for mining the hanging-wall ore become the key technique issue. The elevation of the crest of the slope is 920 m. The roadway in the research is in 674 m level of the high northern slope. The rock mass is mainly composed of anorthosite and norite in the northern slope area. The anisotropic properties of seepage and stress field will be discussed in detail.

4.2. Capture of Joint Network. Depending on the 3D contact-free measuring system, discontinuities on the exposure could be easily captured. The collection process for the geology information of northern slope in Heishan Metal Mine has been discussed previously. A 3D fracture network of rock mass could be obtained using the Monte Carlo method by analyzing the statistical parameters (Figure 9(a)). Finally, the fracture network is generated and expanded to the roadway, and the fracture network perpendicular to the center line of roadway, could be easily captured (Figure 9(b)).

4.3. Permeability Investigation. According to the symmetry of geometry, the method for solving the hydraulic conductivity coefficient in different directions of fracture network is presented to save computational time [41].

Rotated every 15° clockwise and exerted certain water pressure on the boundary shown in Figure 10, the hydraulic conductivity coefficient of verticaldirection $K_{[90]}$, 75° direction $K_{[75]}$, 60° direction $K_{[60]}$, 45° direction $K_{[45]}$, 30° direction $K_{[30]}$, and 15° direction $K_{[15]}$ could be acquired, respectively. Then the permeability tensors by fracture parameters

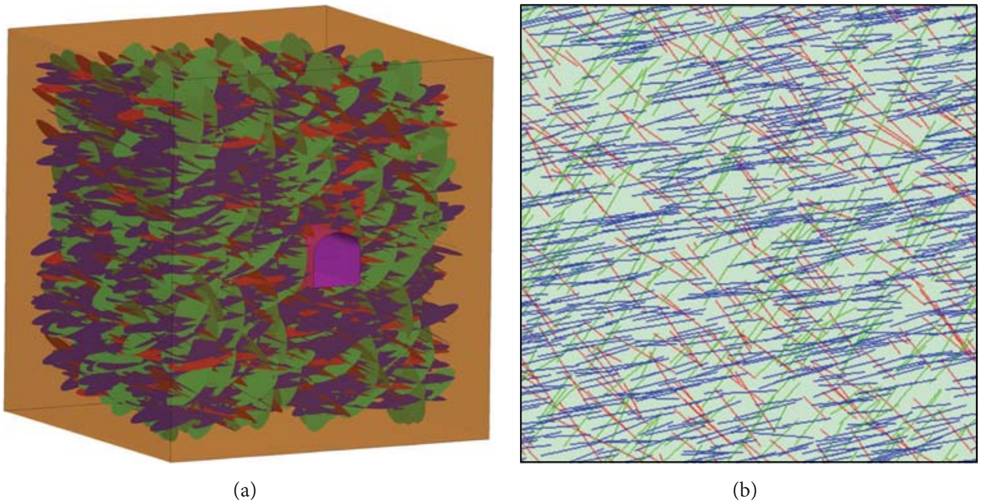

FIGURE 9: Joint network based on the statistical data using Monte Carlo method. (a) 3D joint network in rock mass; (b) profile with 10 m edge length perpendicular to the roadway.

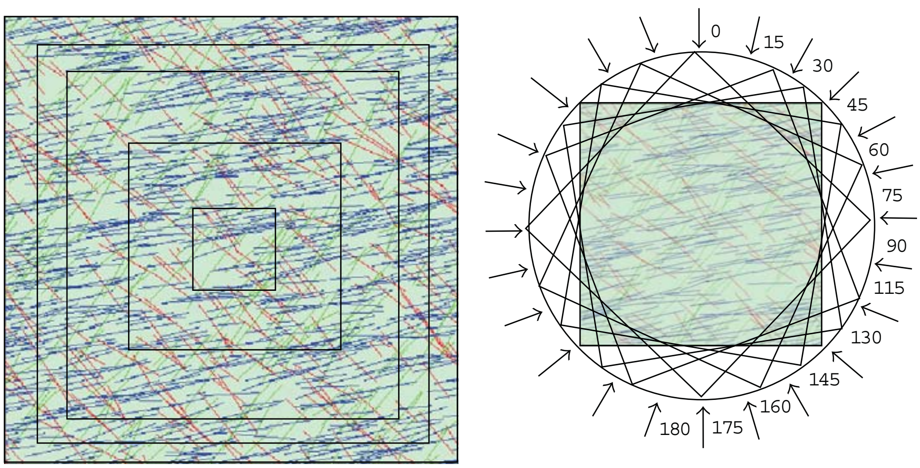

FIGURE 10: Generated fracture network by Monte Carlo method (side length of internal squares is 1 m, 4 m, 7 m, 8 m, and 9 m, resp.).

can be determined. By enlarging the geometric size of the fracture network, the permeability scale effect can be investigated finally.

Based on the algorithm in Section 3.2, the size effect of rock mass in different sizes of statistics window is studied. The region of fracture network is enlarged from 1 m to 9 m with different step lengths until the equivalent parameters in different directions achieve a stable value. With a fixed center of this region, the equivalent permeability is calculated rotating every 15° clockwise as shown in Figure 11.

The variation of hydraulic conductivity coefficients with the increase of direction angles and sample size is depicted in Figure 12. The main direction angle is approximated to 15°. It can be seen that the anisotropy of seepage property is apparent with the distribution of joints. Seven hydraulic conductivity coefficients of different sizes (1 m, 3 m, 4 m, 5 m, 6 m, 8 m, and 9 m) are chosen to be compared with those of the sample whose size is 7 m. The coefficient deviation between one particular size and 7 m would be found and presented in Figure 13. Values of permeability decrease with the increase of sample size and tend to stabilize when the sample size comes to 7 m.

The principal values of permeability in maximum and minimum in a rock sample with joint plane angle being 15° are listed in Table 2. The principal permeability values decrease from 4.23 ($\times 10^{-6}$ m/s) to 2.66 ($\times 10^{-6}$ m/s) as the sample size increases from 1 m to 9 m along the main direction. According to the results discussed previously, the REV is 7 m × 7 m for this fracture sample, and the related hydraulic conductivity is 2.77 ($\times 10^{-6}$ m/s) for maximum and 0.87 ($\times 10^{-6}$ m/s) for minimum. The ratio for the maximum to minimum hydraulic conductivity value is 3.18.

4.4. Damage Tensor. Similar to the algorithm in Section 3.1, the size effect of sample damage in different sizes of statistics window is studied. The region of fracture network is enlarged from 3 m to 12 m with different step lengths until the damage

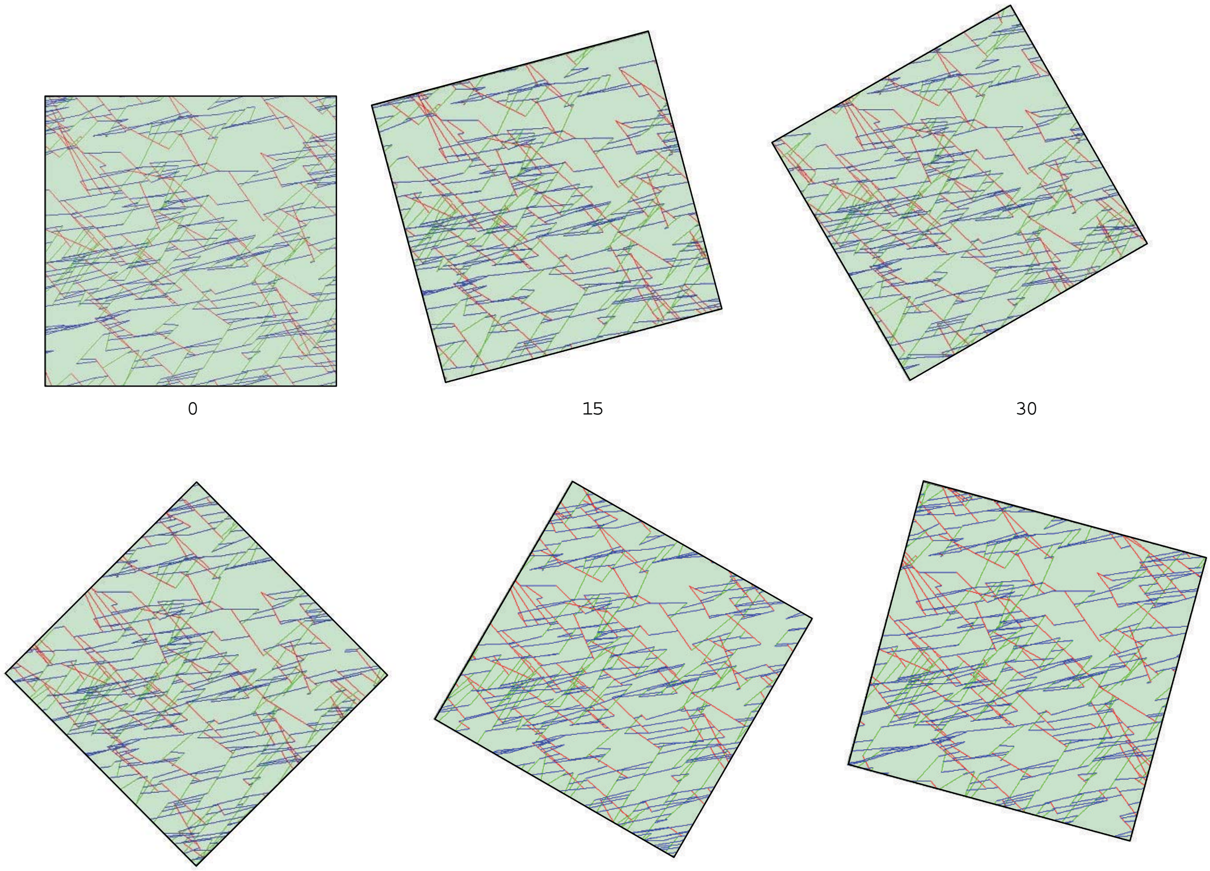

Figure 11: Fracture network in the study area with edge length of 7 m.

values in different directions stabilize. With a fixed center of this region, the principal damage values are calculated rotating every 15° clockwise. Figure 14 shows the sample damage in different sizes and directions. Similar to the deviation analysis of permeability, the damage values also fluctuatingly tend to stability according to the deviation of the damage tensor in different sizes and directions shown in Figure 15. In this study, the size of representative elementary volume is also 7 m in length, and the initial damage tensor of REV of jointed rock mass could also be obtained. The principal damage values D_1 and D_2 for fracture sample are 0.17 for minimum and 0.50 for maximum, and the principal direction angle θ of damage tensor is approximately 105° which is perpendicular to the direction of principal permeability. The related rock parameters, including undamaged Young's modulus E_0, Poisson's ratio ν_0, and uniaxial tensile strength, et al, are listed in Table 3. It should be noted that the elasticity and strength of rock could be determined in the laboratory tests. Finally, the constitutive relation can be found according to (8). Equations (17) and (19) can be introduced into the FEM simulations.

4.5. Geometry and Boundary Conditions. A numerical model of Heishan Metal Mine is established in order to simulate the mechanism of stress and seepage in jointed rock mass, taking into account the anisotropic property, as shown in Figure 16. Table 3 shows the basic mechanical properties. Parameters listed in Table 4 are the hydraulic conductivity coefficients K_{ij}, damage tensor D_{ii} and Young's modulus E_{ij}, and shear modulus G_{ij} of the fracture sample along joint

Table 2: Principal values $K_{[15]}$ of fracture hydraulic conductivity at different sizes.

Sample size (m)		1	4	7	8	9
Principal value of hydraulic conductivity ($\times 10^{-6}$ m/s)	Maximum	4.23	3.28	2.77	2.69	2.66
	Minimum	0.80	0.97	0.87	0.88	0.85
	Ratio	5.29	3.38	3.18	3.06	3.13

Table 3: Parameters used in the model to validate the model in simulating the anisotropic properties of stress and seepage.

Material parameters	Values
Undamaged Young's modulus E_0 (GPa)	65
Undamaged Poisson's ratio ν_0	0.23
Density (kg/m^{-3})	2700
Principal direction angle of joint plane θ (°)	15
Coupling parameter β (Pa^{-1})	0.5

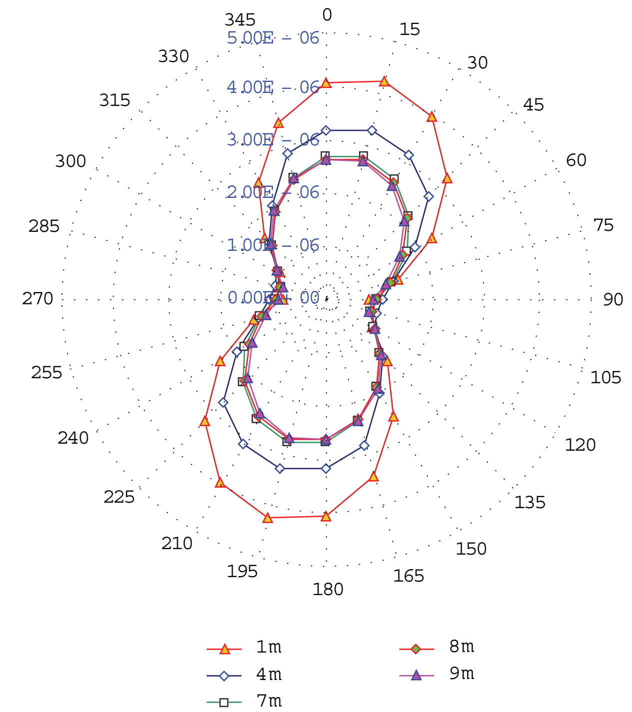

Figure 12: Permeability tensor of the rock mass (unit: m/s).

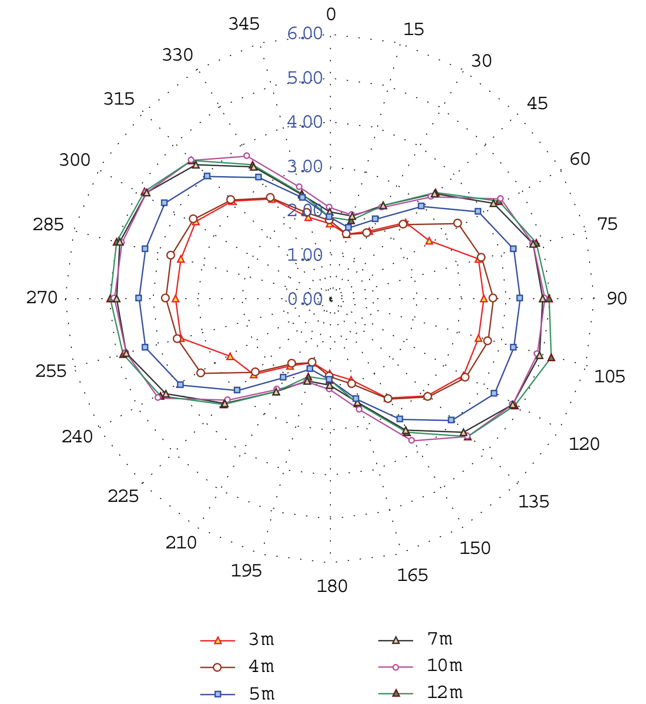

Figure 14: Damage tensor ($\times 10^{-1}$).

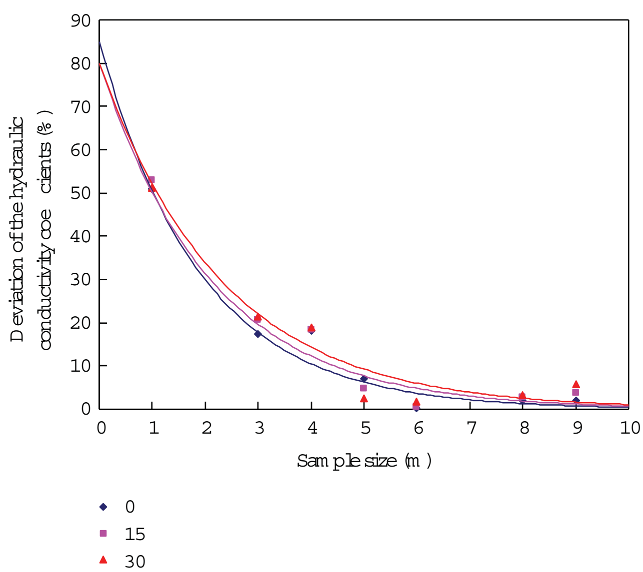

Figure 13: Deviation of the permeability values to that of 7 m sample under different directions of samples in different sizes.

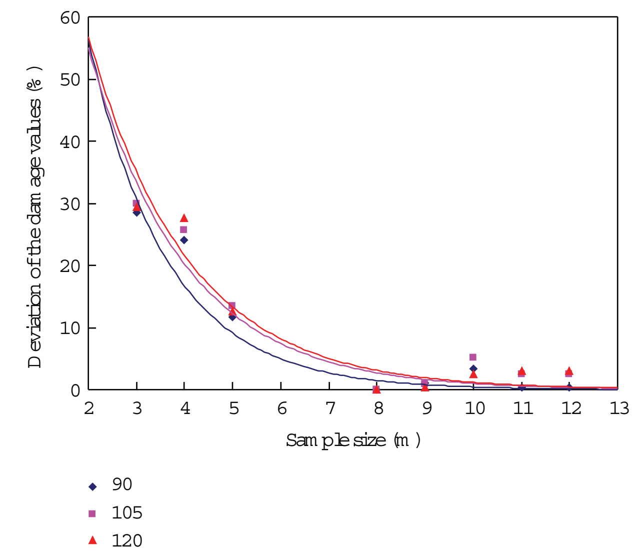

Figure 15: Deviation of the damage tensor to 7 m sample under different directions of samples in different sizes.

Table 4: The hydraulic conductivity coefficients K_{ij}, damage tensor D_{ii} and Young's modulus E_{ij}, and shear modulus G_{ij} of the fracture sample along joint plane direction.

Subscripts ij	K_{ij} ($\times 10^{-6}$ m/s)	D_{ii}	E_{ij} (GPa)	G_{ij} (GPa)
11	2.77	0.50	18.83	—
22	0.87	0.17	51.91	—
12	—	—	9.34	10.97

plane direction used in the finite element code. The model contains two roadways with a 3.5 m × 3 m three-centered arch section within a 50 m × 50 m domain. The bottom boundary of the domain is fixed in all directions, and the left and the right boundaries are fixed in the horizontal direction. In this regard, a pressure (σ_s) of 5.97 MPa is applied on the top boundary of the model to represent the 221 m deep overburden strata. Under the steady-state groundwater flow condition, a hydrostatic pressure, p_w, of 2.21 MPa is applied

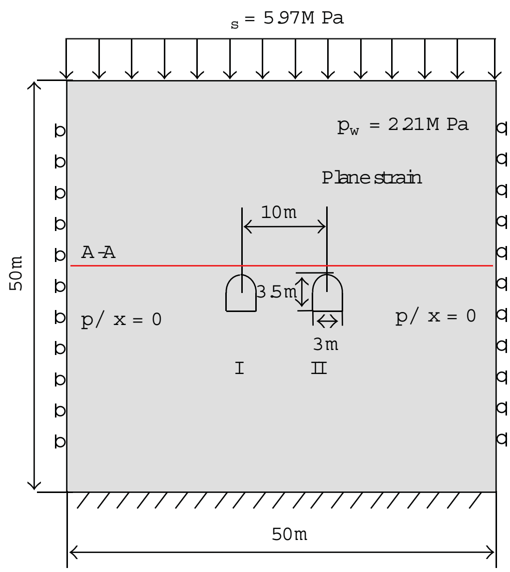

(a)

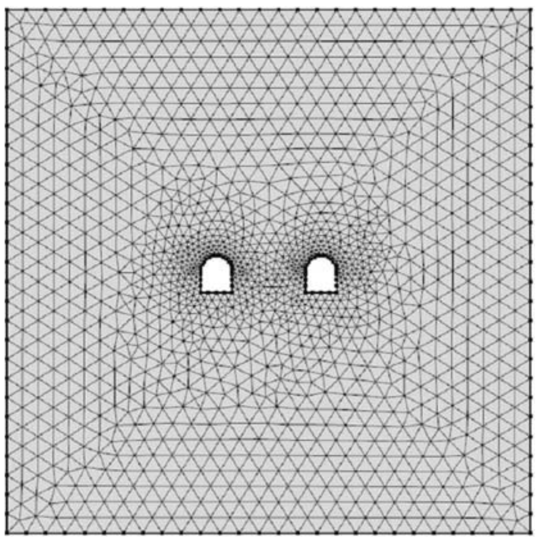

(b)

FIGURE 16: Plane strain roadway model: (a) boundary conditions; (b) the finite element mesh.

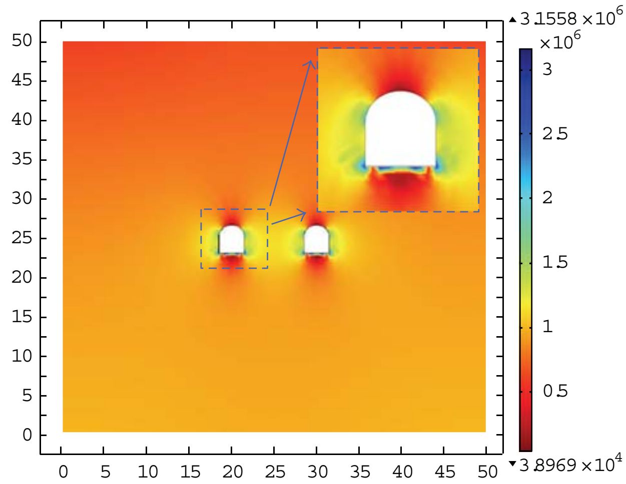

FIGURE 17: Contours of the first principal stress for $\theta = 15^{\circ}$ case.

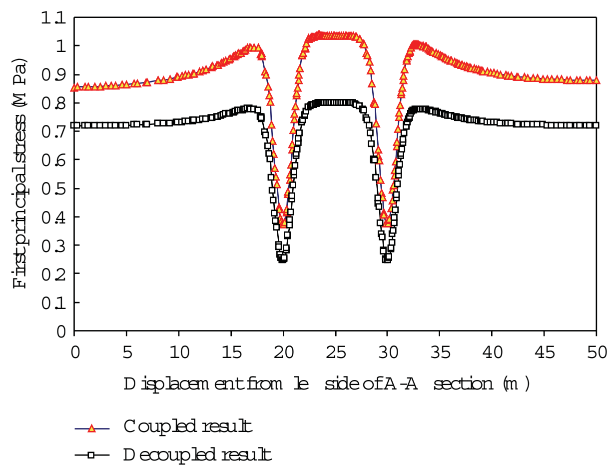

FIGURE 18: Contrast of first principal stress between coupled and decoupled model.

upon top boundary. No-flow conditions are imposed on the three boundaries of the rectangular domain. The initial water pressure on the roadways boundaries is 0 MPa. All the governing equations described previously are implemented into COMSOL Multiphysics, a powerful PDE-based multiphysics modeling environment. The model is assumed to be in a state of plane strain (with no change in elastic strain in the vertical direction) and static mechanical equilibrium.

4.6. Results and Discussion

4.6.1. Stress Distribution. Adverse performance of the rock mass in the postexcavation stress field may be caused by either failure of the anisotropic medium or slip on the weakness planes [3]. The elastic stress distribution around the roadways directly influences the deformation of rock and thus determines the design process.

Figure 17 shows the contour of first principal stress coupled with the seepage process. The orientation and magnitude of maximum principal stress controlled the distribution of the stress concentration in the heterogeneous media. The simulation result shows that the principal stress concentration zones appear mainly in rock surrounding the roadways. There exist maximum stress concentration areas in the arch foot and floor. Measures should be taken to control the deformation and assure the construction safety.

To characterize the response of the stress to the hydraulic mechanics, a comparison of two scenarios is also presented as shown in Figure 18. The first principal stress in the stress-seepage coupled model along the horizontal section A-A$'$ where $y = 27$ is compared with a decoupled models. The result shows that the first principal stress increases when the seepage process is considered. Figure 19 shows

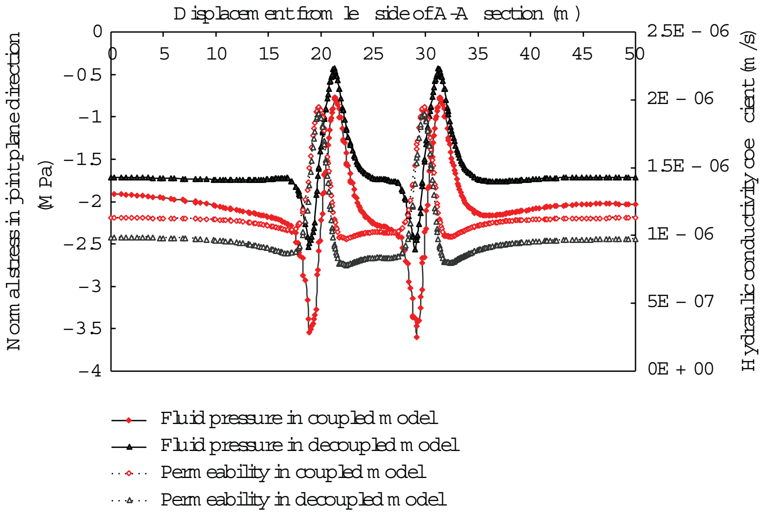

FIGURE 19: Observed changes of normal stress in joint plane direction and hydraulic conductivity between coupled and decoupled models.

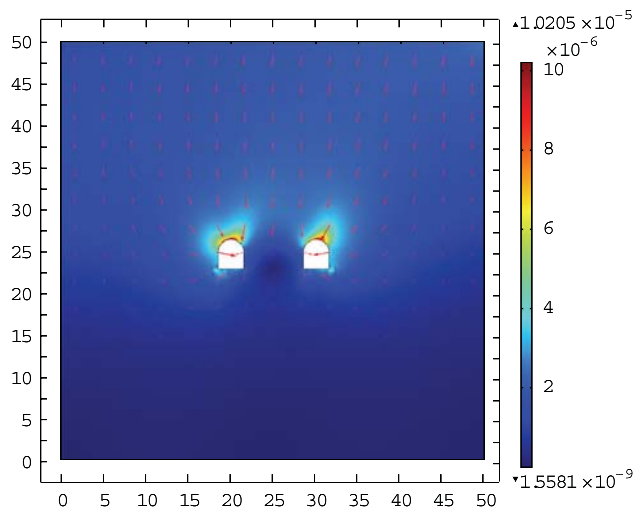

FIGURE 20: Darcy's velocity magnitude (m/s).

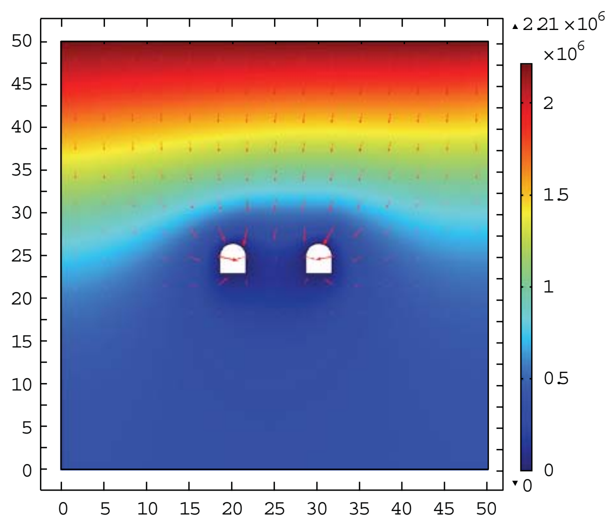

FIGURE 21: The seepage pressure distribution (Pa).

a plot of normal stress in joint plane direction and hydraulic conductivity along the horizontal section A-A$'$ where $y = 27$ as is shown in Figure 16. The coupled and decoupled model could be analyzed using Comsol Multiphysics code. In the coupled case, the governing equations for solid and fluid phase are solved in weakly coupled sense. For the sake of convenient contrast, the normal stress distribution as well as hydraulic conductivity is plotted when no seepage-coupled process is considered. The result shows that the normal stress will be underestimated when no coupling of seepage process is included. Moreover, the compressive stress leads to the decrease of permeability, and the hydraulic conductivity increases when seepage process is included.

4.6.2. Seepage Distribution. Flow velocity with the angle of joint plane being 15° is shown in Figure 20. All the process is not considered time dependent. Therefore, the velocity

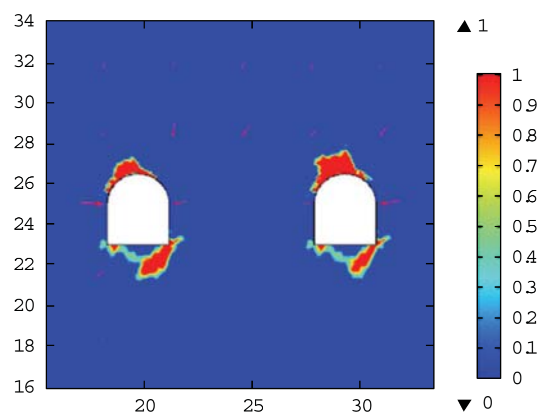

FIGURE 22: Damage zone of the simulating model (the direction of damage zone is approximately perpendicular to that of the joint planes whose angle is 15°).

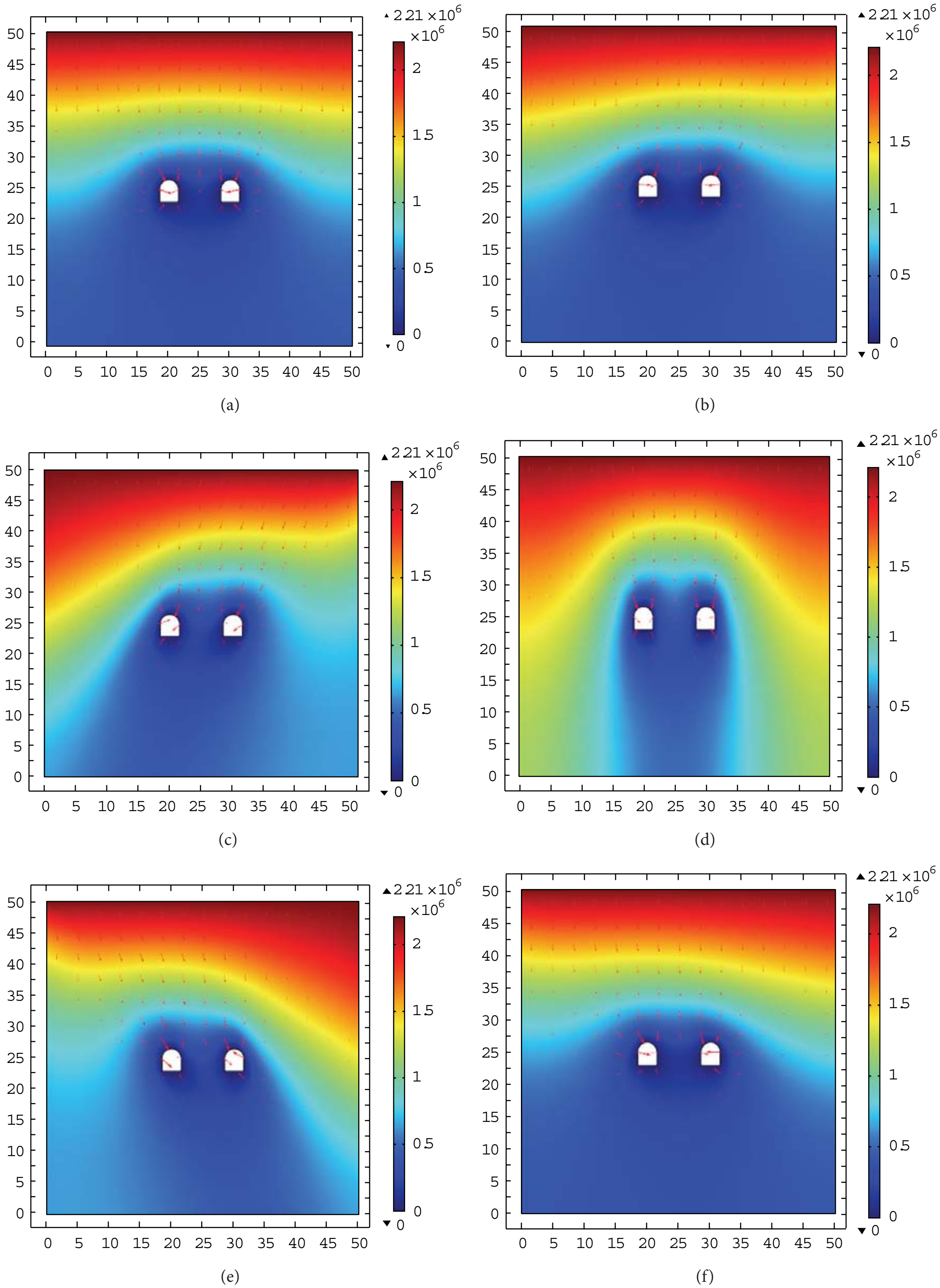

Figure 23: Contour of the fluid pressure and flow velocity vectors in different joint plane directions.

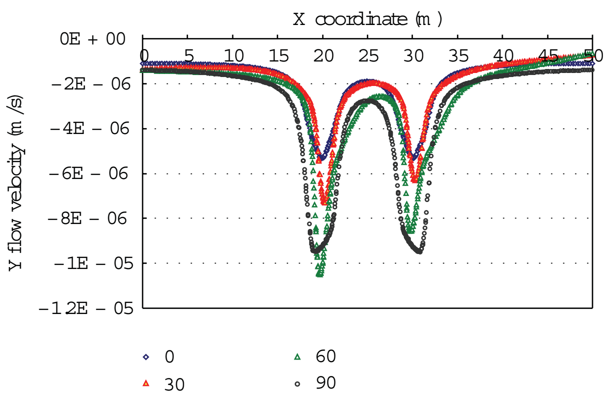

Figure 24: The flow velocity in y direction along the horizontal section A-A′ for different numerical models, at $\theta = 0^{\circ}$, 30°, 60°, and 90°.

change is induced by the permeability variation caused by the compressive stress upon the joint plane. In this case study, water flows along the principal direction of joint plane where the permeability is largest in the model. An asymmetric seepage field is observed, and maximum of flow velocity is distributed on right top of the roadways roof. Moreover, the seepage pressure is also asymmetrically distributed as shown in Figure 21.

4.6.3. Damage Zone. For underground mining, two principal engineering properties of the joint planes should be considered. They are low tensile strength in the direction perpendicular to the joint plane and the relatively low shear strength of the surfaces. The anisotropic strength parameters as tensile and compressive strength parameters for jointed rock mass are discussed by Chen et al. [46], Claesson and Bohloli [47], Nasseri et al. [48], Gonzaga et al. [49], and Cho et al. [50]. As discussed previously, the fluid pressure and velocity are sensitive to the joint plane angles θ. In this section, the Hoffman anisotropic strength criterion is used to assess the damage zone in this numerical model as shown in

$$\frac{\sigma_1^2}{X_t X_c} - \frac{\sigma_1 \sigma_2}{X_t X_c} + \frac{\sigma_2^2}{Y_t Y_c} + \frac{X_c - X_t}{X_t X_c}\sigma_1 + \frac{Y_c - Y_t}{Y_t Y_c}\sigma_2 + \frac{\tau_{12}^2}{S^2} = 1. \quad (20)$$

The properties X_t and Y_t represent the tensile strength along joint plane direction and perpendicular to joint plane direction, respectively. X_c and Y_c represent the compressive strength along joint plane direction and perpendicular to joint plane direction, respectively. S is the shear strength of the material along the joint direction. σ_1 represents the normal stress along the principle direction of elasticity and σ_2 represents the normal stress perpendicular to the principle direction of elasticity. τ_{12} represents the shear stress.

The shear strength of the joints can be described by the simple Coulomb law

$$S = c + \sigma_2 \tan\phi, \quad (21)$$

where c is cohesive strength and ϕ is the effective angle of friction of the joint surfaces.

Table 5: Mechanical properties of rock mass in the direction of joint plane.

Tensile strength (MPa)	X_t	16.0
	Y_t	4.0
Compressive strength (MPa)	X_c	120
	Y_c	96
Shear strength (MPa)	c	1.5
	ϕ	50

It should be noted that the mechanical parameters be acquired from laboratory or in situ tests. However, it is difficult to directly employ the strength parameters for jointed rock mass due to the inaccessibility of the tests for huge rock mass. Based on the in situ and laboratory tests of Heishan Metal Mine, the tensile, compressive, and shear strength parameters are listed in Table 5.

The direction of joint plane is 15°, and thus the tensile strength in the direction perpendicular to joint plane is relatively low, compared with that in other directions. Figure 22 shows the damage zone in this case study and the failure area mainly distributes in the direction perpendicular to the weakness plane, which gives an illustration of the roadway failure mode in tabular orebodies. Moreover, the failure of covered rock mass and the rock pillar in and between the two roadways does not influence each other in this case study, and thus the choice of roadway's interval is proper from the aspect of the mechanics analysis.

4.7. Further Discussion. These simulations were performed to develop an understanding of the mechanics of joints and influence on stress and seepage fields and to gauge the ability of the proposed transversely anisotropic model to capture the response of jointed rock mass. For this purpose, a total of six scenarios with the joint plane angles θ ranging from 0° to 150° with an interval of 30° are simulated in order to examine the effect of joint plane directions; see Figure 7 for the definition of θ. And the anisotropic properties of seepage field and damage zones are examined in these simulations.

4.7.1. Seepage Field. Figure 23 presents the fluid pressure distribution and flow field arrows with different joint plane directions. It can be seen that the maximum pressure, which is located on the top boundary, equals the initial fluid pressure (2.21 MPa). The fluid pressure distribution on top of the roadways differs with the increase of directions.

When the joint plane is parallel or perpendicular to the floors of roadways, the fluid pressure distributions and flow arrows are all axially symmetric, which agrees with expectations. The fluid pressure in the 30° or 60° case is distributed unsymmetrically as shown in Figures 23(b) and 23(c).

The flow velocity in y direction along the horizontal section A-A′ where $y = 27$ m as shown in Figure 16(a) curves are plotted in Figure 24 for $\theta = 0^{\circ}$, 30°, 60°, and 90°, respectively. In all cases the absolute value of velocity increases approximately exponentially above the roadways.

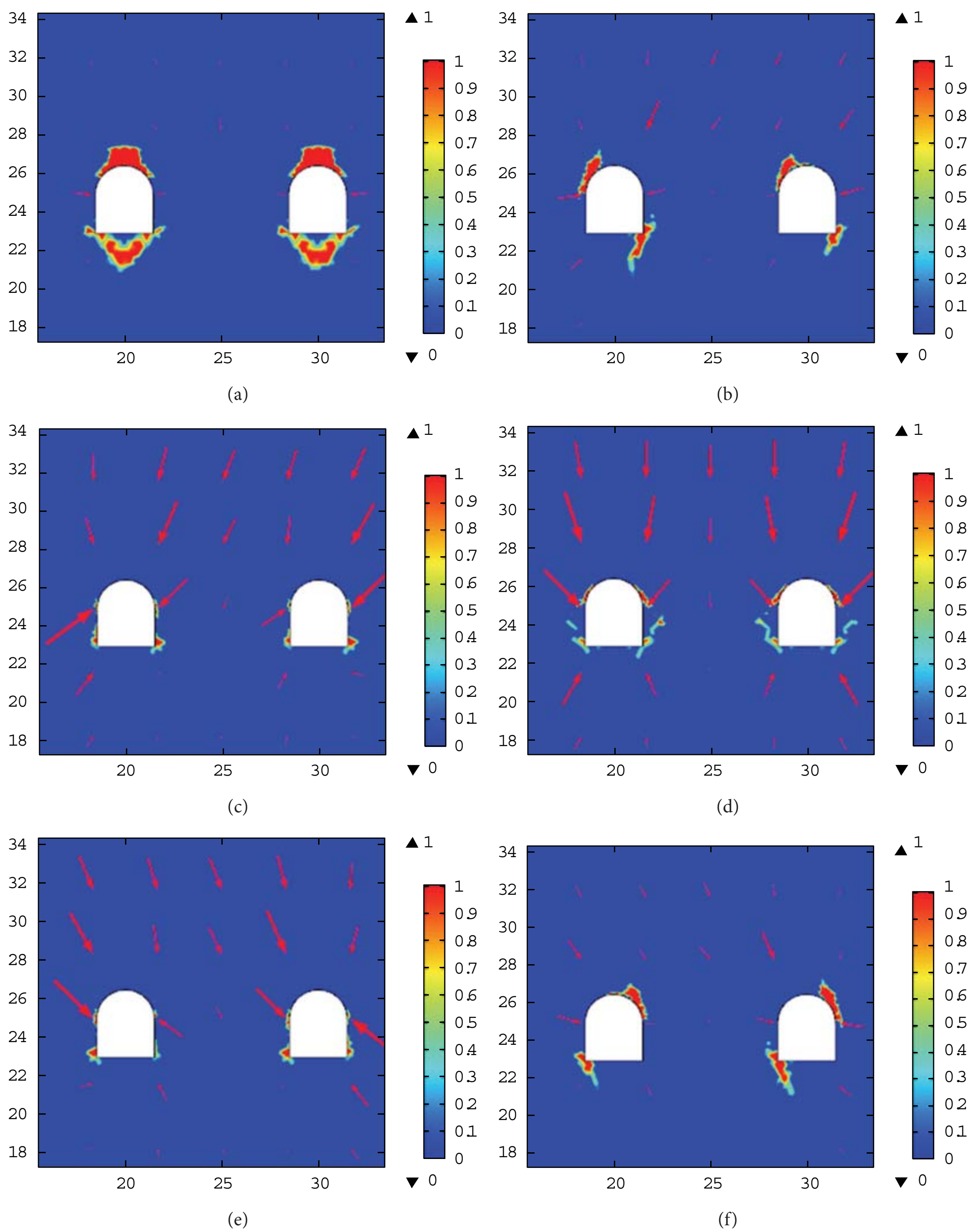

Figure 25: The damaged zone under different principal elastic directions (red arrows represent the flow velocity vector).

As shown in Figure 24, the flow velocity in scenario where $\theta = 0^\circ$ is in the lowest level. The reason is that the joint plane in this scenario is horizontally distributed and the compressive stress leads to the decrease of permeability. When angle of joint plane increases to 30°, flow velocities above both roadways increase and Roadway I has a more higher velocity than Roadway II. The scenario where $\theta = 60^\circ$ has similar performance. However, when the joint plane is vertically distributed, flow velocity above Roadway I is lower than that where $\theta = 60^\circ$. The flow velocity in the case where joints are vertically or horizontally distributed is symmetric.

4.7.2. Damage Zone. The effect of joint plane angle on the damage zone is illustrated by using the Hoffman anisotropic strength criterion as shown in (23). The damage zones in different angles of joint planes are shown in Figure 25 and could be an index to visualize the potential failure mode of the roadway.

It is clear from Figures 25(a) to 25(f) that an increase of the joint plane angle has significantly influenced the shape and size of damage zone. When the joints are horizontally distributed ($\theta = 0^\circ$), the tensile strength in the direction perpendicular to joint planes is much lower and thus the damage zone mainly concentrates within roof and bottom of roadways. This failure mainly manifests as roof falling and floor heave. Similarly, when the angle increases to 30°, the damage zones mainly concentrate in the rock mass of left roof and right floor within the roadways which is also in the direction perpendicular to joint planes. Compared with the result in Figure 25(b), the direction of damage zone with $\theta = 60^\circ$ shown in Figure 25(c) rotated significantly and the area also increases. When the joints are vertically distributed ($\theta = 90^\circ$), the principal direction of damage zone is nearly horizontal. Lateral rock mass surrounding the roadways stabilizes with the increase of joint plane angle in this study, and the pillar between two roadways is also stable. The scenarios where $\theta = 120^\circ$ or $\theta = 150^\circ$ have the similar response to the joint plane direction with that of 60° or 30°. Qualitatively, the simulation results are in good agreement with the results by Jia et al. [51] and Huang et al. [52]. The model in this study could to some extent be effectively used to analyze the anisotropic property for jointed rock mass.

5. Conclusion

The main purpose is to introduce the anisotropic model of seepage and stress and apply the model to the jointed rock mass. The coupled finite element analysis was performed, and the effects of joint planes direction on stress field, flow velocity, and Darcy's velocity were verified. A more reliable model for the stability analysis of rock engineering and risk evaluation of water inrush was provided. Based on the results of a series of numerical simulations under different scenarios, the following conclusions are drawn.

(1) A linkage of digital information of fractures and mechanical analysis is realized. Relations between digital images involving detailed geometrical properties of rock mass and the quantitative determination of hydraulic parameters as well as elastic properties were realized. The results show that the scale for both damage tensor and permeability tensor of the rock mass's REV in northern slope of Heishan Metal Mine is 7 m × 7 m.

(2) We examine the model for seepage-stress coupled analysis on anisotropic properties. The numerical simulations in this study have indicated that the existence of joint planes greatly affects the seepage properties and stress field. In anisotropic rock, water flows mainly along the joint planes, and water pressure is asymmetrically distributed where the angle of joint plane is 15° in the northern slope of Heishan Metal Mine.

(3) The influence of fractures cannot be neglected in stability analysis of rock mass. The numerical results visualized the damage zones in different directions of joint planes. The direction of damage zones was found perpendicular to that of joint planes which agrees well with the field observations and theoretical analysis.

The work reported in this paper is an initial effort on the influence of joint orientation on the anisotropic property of seepage and stress in jointed rock masses. A model for more complex jointed rock mass remains to be quantified.

Nomenclature

D: Damage variable (dimensionless)
E: Damaged Young's modulus (Pa)
E_0: Undamaged Young's modulus (Pa)
G: Shear modulus (Pa)
K_{ij}: Hydraulic conductivity coefficient (m/s)
K_{ii}^{j}: Hydraulic conductivity coefficient along joint plane direction (m/s)
p: Fluid pressure (Pa)
S_{ij}: Flexibility coefficient (Pa^{-1})
N: The number of joints
l: Minimum spacing between joints (m)
V: Volume of rock mass (m^3)
Δh_j: The hydraulic gradient;
$n^{(k)}$: The normal vector of the kth joint (dimensionless)
$a^{(k)}$: The trace length of the kth joint (m)
Q_i: The fluid source term (m^3)
$[\mathbf{T}_\sigma]^{-1}$: The reverse matrix for stress coordinates transformation
$[\mathbf{T}_\varepsilon]$: The strain coordinates transformation matrix
X_t: The tensile strength in joint direction (Pa)
Y_t: The tensile strength perpendicular to direction (Pa)
X_c: The compressive strength in joint direction (Pa)
Y_c: The compressive strength perpendicular to direction (Pa)
S: The shear strength of the material (Pa).

Greek Symbols

α_{ij}: Positive constant
β: Coupling coefficient (Pa^{-1})
σ_{ij}: Stress tensor (Pa)
$\sigma_1, \sigma_2, \sigma_3$: The first, second, and third principal stresses (Pa)
ε_{ij}: Total strain tensor (dimensionless)
θ: Angle of joint plane (°)
ν: Damaged Poisson's ratio (dimensionless)
ν_0: Undamaged Poisson's ratio (dimensionless)
ρ: Density of water ($\mathrm{kg/m}^3$)
μ: Coefficient of flow viscosity (Pa·s)
ϕ: Effective angle of friction of the joint surfaces.

Conflict of Interests

The authors declare that there is no conflict of interests.

Acknowledgments

This study was performed at Center for Rock Instability & Seismicity Research (CRISR), Northeastern University, Shenyang, China. The work presented in this paper was financially supported by the National Basic Research Program of China (No. 2013CB227900). The Natural Science Foundation of China (Grant No. 51174045, 50904013, 51034001, 50934006, 41172265), the basic scientific research funds of Ministry of Education of China (No. N090101001, N120601002) and the project supported by the Specialized Research Fund for the Doctoral Program of Higher Education of China (Grant No. 20120042120053) also give financial support to this research.

References

[1] W. G. Pariseau, S. Puri, and S. C. Schmelter, "A new model for effects of impersistent joint sets on rock slope stability," *International Journal of Rock Mechanics and Mining Sciences*, vol. 45, no. 2, pp. 122–131, 2008.

[2] B. Amadei, "Importance of anisotropy when estimating and measuring in situ stresses in rock," *International Journal of Rock Mechanics and Mining Sciences and Geomechanics*, vol. 33, no. 3, pp. 293–325, 1996.

[3] B. H. G. Brady and E. T. Brown, *Rock Mechanics For Underground Mining*, Springer, Amsterdam, The Netherlands, 2004.

[4] X. Zhang and D. J. Sanderson, "Numerical study of critical behaviour of deformation and permeability of fractured rock masses," *Marine and Petroleum Geology*, vol. 15, no. 6, pp. 535–548, 1998.

[5] Y. M. Tien and P. F. Tsao, "Preparation and mechanical properties of artificial transversely isotropic rock," *International Journal of Rock Mechanics and Mining Sciences*, vol. 37, no. 6, pp. 1001–1012, 2000.

[6] F. J. Brosch, K. Schachner, M. Blümel, A. Fasching, and H. Fritz, "Preliminary investigation results on fabrics and related physical properties of an anisotropic gneiss," *Journal of Structural Geology*, vol. 22, no. 11-12, pp. 1773–1787, 2000.

[7] G. E. Exadaktylos and K. N. Kaklis, "Applications of an explicit solution for the transversely isotropic circular disc compressed diametrically," *International Journal of Rock Mechanics and Mining Sciences*, vol. 38, no. 2, pp. 227–243, 2001.

[8] G. E. Exadaktylos, "On the constraints and relations of elastic constants of transversely isotropic geomaterials," *International Journal of Rock Mechanics and Mining Sciences*, vol. 38, no. 7, pp. 941–956, 2001.

[9] K.-B. Min and L. Jing, "Numerical determination of the equivalent elastic compliance tensor for fractured rock masses using the distinct element method," *International Journal of Rock Mechanics and Mining Sciences*, vol. 40, no. 6, pp. 795–816, 2003.

[10] B. Amadei, *Rock Anisotropy and the Theory of Stress Measurements*, Springer, 1983.

[11] M. Hakala, H. Kuula, and J. A. Hudson, "Estimating the transversely isotropic elastic intact rock properties for in situ stress measurement data reduction: a case study of the Olkiluoto mica gneiss, Finland," *International Journal of Rock Mechanics and Mining Sciences*, vol. 44, no. 1, pp. 14–46, 2007.

[12] P. A. Witherspoon, J. S. Y. Wang, K. Iwai, and J. E. Gale, "Validity of cubic law for fluid flow in a deformable rock fracture," *Water Resources Research*, vol. 16, no. 6, pp. 1016–1024, 1980.

[13] M. Oda, "Permeability tensor for discontinuous rock masses," *Geotechnique*, vol. 35, no. 4, pp. 483–495, 1985.

[14] J. Sun and Z. Zhao, "Effects of anisotropic permeability of fractured rock masses on underground oil storage caverns," *Tunnelling and Underground Space Technology*, vol. 25, no. 5, pp. 629–637, 2010.

[15] K.-B. Min, L. Jing, and O. Stephansson, "Determining the equivalent permeability tensor for fractured rock masses using a stochastic REV approach: method and application to the field data from Sellafield, UK," *Hydrogeology Journal*, vol. 12, no. 5, pp. 497–510, 2004.

[16] A. Baghbanan and L. Jing, "Hydraulic properties of fractured rock masses with correlated fracture length and aperture," *International Journal of Rock Mechanics and Mining Sciences*, vol. 44, no. 5, pp. 704–719, 2007.

[17] A. Baghbanan and L. Jing, "Stress effects on permeability in a fractured rock mass with correlated fracture length and aperture," *International Journal of Rock Mechanics and Mining Sciences*, vol. 45, no. 8, pp. 1320–1334, 2008.

[18] Z. Zhao, L. Jing, I. Neretnieks, and L. Moreno, "Numerical modeling of stress effects on solute transport in fractured rocks," *Computers and Geotechnics*, vol. 38, no. 2, pp. 113–126, 2011.

[19] K. Bao, A. Salama, and S. Sun, "Upscaling of permeability field of fractured rock system: numerical examples," *Journal of Applied Mathematics*, Article ID 546203, 20 pages, 2012.

[20] W. Z. Chen, J. P. Yang, J. L. Yang, X. B. Qiu, and C. C. Cao, "Hydromechanical coupled model of jointed rock mass and its application to pressure tunnels," *Chinese Journal of Rock Mechanics and Engineering*, vol. 27, no. 9, pp. 1569–1571, 2006.

[21] W. Chen, J. Yang, X. Zou, and C. Zhou, "Research on macromechanical parameters of fractured rock masses," *Chinese Journal of Rock Mechanics and Engineering*, vol. 27, no. 8, pp. 1569–1575, 2008.

[22] J. P. Yang, *Study of macro mechanical parameters of fractured rock mass [Ph.D. thesis]*, Wuhan institute of the Chinese academy of sciences geotechnical engineering, Wuhan, China, 2009.

[23] C. Qiao, Z. Zhang, and X. Li, "Anisotropic strength characteristics of jointed rock mass," in *Proceedings of the ISRM-Sponsored International Symposium on Rock Mechanics, Rock Characterisation Modelling and Engineering Design Methods*, p. 140, 2009.

[24] A. Robertson, "The interpretation of geological factors for use in slope theory," in *Proceedings of the Symposium on Theoretical Background to Planning of Open Pit Mines*, pp. 55–71, Johannesburg, South Africa, 1970.

[25] C.-Y. Wang and K. T. Law, "Review of borehole camera technology," *Chinese Journal of Rock Mechanics and Engineering*, vol. 24, no. 19, pp. 3440–3448, 2005.

[26] Austrian Startup Company, *ShapeMetriX3D Model Merger User Manual*, Earth Products China, Shenyang, China, 2008.

[27] A. Gaich, W. Schubert, and M. Poetsch, "Three-dimensional rock mass documentation in conventional tunnelling using Joint-MetriX3D," in *Proceedings of the 31st ITA-AITES World Tunnel Congress*, E. Yücel and T. Solak, Eds., pp. 59–64, A.A. Balkema Publishers, Istanbul, Turkey, 2005, Underground Space Use: Analysis of the Past and Lessons for the Future.

[28] T. Yang, Q. Yu, S. Chen, H. Liu, T. Yu, and L. Yang, "Rock mass structure digital recognition and hydro-mechanical parameters characterization of sandstone in Fangezhuang coal mine," *Chinese Journal of Rock Mechanics and Engineering*, vol. 28, no. 12, pp. 2482–2489, 2009.

[29] P. T. Wang, T. H. Yang, Q. L. Yu, H. L. Liu, and P. H. Zhang, "Characterization on jointed rock masses based on PFC2D," *Frontiers of Structural and Civil Engineering*, vol. 7, no. 1, pp. 32–38, 2013.

[30] Y. Y. Jiao, X. L. Zhang, and T. C. Li, *DDARF Method For Simulating the Whole Process of Rock Failure*, Science Publishing House, Beijing. China, 2010.

[31] E. Hoek and E. T. Brown, "Practical estimates of rock mass strength," *International Journal of Rock Mechanics and Mining Sciences*, vol. 34, no. 8, pp. 1165–1186, 1997.

[32] P. Marinos and E. Hoek, "Estimating the geotechnical properties of heterogeneous rock masses such as flysch," *Bulletin of Engineering Geology and the Environment*, vol. 60, no. 2, pp. 85–92, 2001.

[33] E. Hoek, C. Carranza-Torres, and B. Corkum, "Hoek-Brown failure criterion-2002 edition," in *Proceedings of the 5th North American Rock Mechanics Symposium and 17th Tunneling Association of Canada Conference (NARMS-TAC '02)*, pp. 267–271, 2002.

[34] J. Lemaitre and R. Desmorat, *Engineering Damage Mechanics*, Springer, Berlin, Germany, 2005.

[35] T. Kawamoto, Y. Ichikawa, and T. Kyoya, "Deformation and fracturing behaviour of discontinuous rock mass and damage mechanics theory," *International Journal for Numerical and Analytical Methods in Geomechanics*, vol. 12, no. 1, pp. 1–30, 1988.

[36] F. Sidoroff, "Description of anisotropic damage application to elasticity," in *Proceedings of the IUTAM Colloquium on Physical Nonlinearities in structural analysis*, pp. 237–244, 1981.

[37] Y. Wu and Z. Zhang, *An Introduction to Rock Mass Hydraulics*, Southwest Jiaotong University Press, Chengdu, China, 2005.

[38] D. T. Snow, "Anisotropie Permeability of Fractured Media," *Water Resources Research*, vol. 5, no. 6, pp. 1273–1289, 1969.

[39] K. Hestir and J. C. S. Long, "Analytical expressions for the permeability of random two-dimensional Poisson fracture networks based on regular lattice percolation and equivalent media theories," *Journal of Geophysical Research*, vol. 95, no. 13, pp. 21565–21581, 1990.

[40] T. Yang and Y. Xiao, "Structural plane survey and analysis of permeability characteristics of open pit mine slope rock mass," *Site Investigation Science and Technology*, vol. 16, no. 3, pp. 27–30, 1998.

[41] Y. X. Xiao, C. F. Lee, and S. J. Wang, "Assessment of an equivalent porous medium for coupled stress and fluid flow in fractured rock," *International Journal of Rock Mechanics and Mining Sciences*, vol. 36, no. 7, pp. 871–881, 1999.

[42] M. A. Biot, "General theory of three-dimensional consolidation," *Journal of Applied Physics*, vol. 12, no. 2, pp. 155–164, 1941.

[43] C. Louis, "Rock hydraulics," in *Rock Mechanics*, L. Muller, Ed., pp. 287–299, Springer, New York, NY, USA, 1974.

[44] T. H. Yang, T. Xu, H. Y. Liu, C. A. Tang, B. M. Shi, and Q. X. Yu, "Stress-damage-flow coupling model and its application to pressure relief coal bed methane in deep coal seam," *International Journal of Coal Geology*, vol. 86, no. 4, pp. 357–366, 2011.

[45] K. Terzaghi, R. B. Peck, and G. Mesri, *Soil Mechanics in Engineering Practice*, Wiley-Interscience, New York, NY, USA, 1996.

[46] C.-S. Chen, E. Pan, and B. Amadei, "Determination of deformability and tensile strength of anisotropic rock using Brazilian tests," *International Journal of Rock Mechanics and Mining Sciences*, vol. 35, no. 1, pp. 43–61, 1998.

[47] J. Claesson and B. Bohloli, "Brazilian test: stress field and tensile strength of anisotropic rocks using an analytical solution," *International Journal of Rock Mechanics and Mining Sciences*, vol. 39, no. 8, pp. 991–1004, 2002.

[48] M. H. B. Nasseri, K. S. Rao, and T. Ramamurthy, "Anisotropic strength and deformation behavior of Himalayan schists," *International Journal of Rock Mechanics and Mining Sciences*, vol. 40, no. 1, pp. 3–23, 2003.

[49] G. G. Gonzaga, M. H. Leite, and R. Corthésy, "Determination of anisotropic deformability parameters from a single standard rock specimen," *International Journal of Rock Mechanics and Mining Sciences*, vol. 45, no. 8, pp. 1420–1438, 2008.

[50] J.-W. Cho, H. Kim, S. Jeon, and K.-B. Min, "Deformation and strength anisotropy of Asan gneiss, Boryeong shale, and Yeoncheon schist," *International Journal of Rock Mechanics and Mining Sciences*, vol. 50, pp. 158–169, 2012.

[51] P. Jia, C.-A. Tang, T.-H. Yang, and S.-H. Wang, "Numerical stability analysis of surrounding rock mass layered by structural planes with different obliquities," *Dongbei Daxue Xuebao/Journal of Northeastern University*, vol. 27, no. 11, pp. 1275–1278, 2006.

[52] S. Huang, J. Xu, X. Ding, and A. Wu, "Study of layered rock mass composite model based on characteristics of structural plane and its application," *Chinese Journal of Rock Mechanics and Engineering*, vol. 29, no. 4, pp. 743–756, 2010.

Hindawi Publishing Corporation
Journal of Applied Mathematics
Volume 2013, Article ID 456931, 13 pages
http://dx.doi.org/10.1155/2013/456931

Research Article

Temperature and Pressure Dependence of the Effective Thermal Conductivity of Geomaterials: Numerical Investigation by the Immersed Interface Method

Duc Phi Do and Dashnor Hoxha

Laboratoire PRISME, EA4229, Polytech Orléans, 8 rue Léonard de Vinci, 45072 Orléans Cedex 2, France

Correspondence should be addressed to Duc Phi Do; duc-phi.do@univ-orleans.fr

Received 12 February 2013; Revised 30 May 2013; Accepted 3 June 2013

Academic Editor: Ga Zhang

The present work aims to study the nonlinear effective thermal conductivity of heterogeneous composite-like geomaterials by using a numerical approach based on the immersed interface method (IIM). This method is particularly efficient at solving the diffusion problem in domains containing inner boundaries in the form of perfect or imperfect interfaces between constituents. In this paper, this numerical procedure is extended in the framework of non linear behavior of constituents and interfaces. The performance of the developed tool is then demonstrated through the studies of temperature- and pressure-dependent effective thermal conductivity of geomaterials with imperfect interfaces.

1. Introduction

The estimation of the effective transfer properties of heterogeneous media such as geomaterials is still nowadays a challenging research field despite perpetual advances of research and an increasing number of published works. For this class of materials, the overall properties depend not only on the properties of the matrix, the shape and spatial distribution of inclusions, an the volume fractions and properties of constituents, but also on the transfer field's distribution in the medium and, in many situations, on the interfacial properties between phases.

An example of this type of problems is that of the effective thermal conductivity of geomaterials with thermal conductivity of constituents being a function of temperature which lead to an overall nonlinear thermal conductivity. The study of the temperature dependence of thermal conductivity of porous medium like rocks and soils thas been intensively carried out in the last decade due to the large number of applications such as geothermal reservoirs, underground storage of nuclear waste, and petroleum and natural gas geology. Various researches conducted on different types of rocks, soils, and minerals have shown that the thermal conductivity of geomaterials decreases when the temperature increases [1–11] even if in some exceptional cases the conductivity slightly increases with temperature.

In addition to the nonlinearity of constituent's law, the behavior of the interfaces and their state could also play an important role on the nonlinearity of effective properties. Very often these interfaces are favorite places of cracking by debonding that generally leads to a modification of transport properties of the interface.

From a numerical point of view, the effect of cracking at the boundary of grains to the overall thermal conductivity can be accounted for by considering the fully or partially debonded inclusions embedded in the homogeneous matrix of materials. This last feature is an important problem not only in gesocience materials, but also in general engineering science materials, and various modeling techniques have been developed to deal with it such as perturbation expansion method [12, 13] or adaptive finite element method [14, 15]. In particular, the immersed interface method (IIM), under such conditions performs quite well. This method, considered as an extension of the finite difference method for the case of media with discontinuities in uniform Cartesian grid points stencil, allows in the case of imperfect interfaces to capture the jump of state and/or flux variables across the interface. Uniform Cartesian grids avoid mesh regeneration and allow for fast flow solvers which contribute to the simplicity and efficiency of the IIM method. Otherwise, the IIM can be used in conjunction with the level set method to treat various problems involving moving interface, non linear interface and free boundary problems (such as Stefan problems and crystal growth, the incompressible flows with moving interface modeled by Navier-Stokes equations to mention a few). Interested readers could refer to [16, 17] and references cited therein for an overview of the advantages and applications of this method.

In a previous work of the present authors [18], the IIM was used to take into account the interfacial resistance between linear constituent phases. In this context, the IIM allows calculating the effective transfer properties and enables demonstrating the role of various factors such as shape, size, spatial distribution, and volume fraction of constituents as well as their properties of constituents and those of interface on overall effective properties.

In the present paper, this numerical approach is extended to the evaluation of effective thermal conductivity of geomaterials considering the nonlinearity of constituents and the presence of imperfect interfaces. The paper is organized as follows. Firstly, we describe the principle of IIM used to solve the non linear heat transfer problem with the presence of contact resistance. Then, the application of the numerical procedure to evaluate the effective thermal conductivity of non linear composite-like geomaterials is studied by counting for the interfacial resistance between phases. In the whole paper, a lower underlined symbol indicates a vector while a bold one represents a second-order tensor.

2. Solving Nonlinear Heat Transfer Problem by the Immersed Interface Method

2.1. Mathematical Model. The problem considered here is that of a heterogeneous material constituted by a matrix containing inclusions of smooth shapes whose properties are different from that of the matrix. Moreover, the interfaces between the matrix and any inclusion (Figure 1) are considered to be thin layers (no thickness) having their own properties and sufficiently smooth to assure the existence of all derivatives involved in equations developed later. The interfaces are not necessarily perfect so that a jump in some variables (state or/and flux variables) could be observed across them. For the sake of simplicity, the presentation of the method is limited here on 2D steady state heat transfer problem without source. The extension of the method for more general cases presents no conceptual difficulties. Local behavior of each constituent phase of heterogeneous media is characterized by the conservation and Fourier law written as

$$\operatorname{div}\left(\underline{q}\right) = 0,$$
$$\underline{q} = -\mathbf{K}(u) \cdot \underline{\operatorname{grad}(u)}, \quad (1)$$

where $\underline{q}$ and $\mathbf{K}$ stand for the flux and the second order tensor of thermal conductivity. As the behavior of constituents is

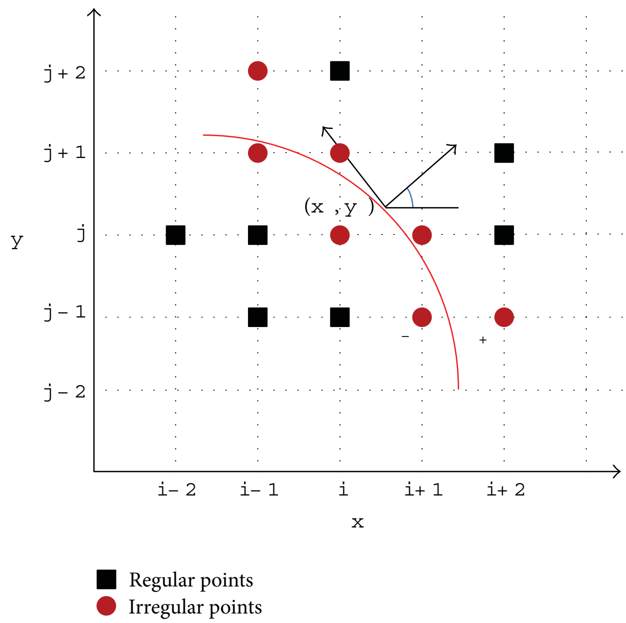

Figure 1: Schematic presentation of the problem of interface in a uniform Cartesian grid for the interface problem.

assumed non linear, $\mathbf{K}$ is supposed to be a known function of the temperature u.

Without losing the generality, in what follows, the isotropic behavior will be considered; that is, $\mathbf{K}(u) = K(u) \cdot \mathbf{1}$ with $\mathbf{1}$ being unity second-order tensor. The combination of these two equations leads to the following non linear partial differential equation with respect to the unknown u:

$$\operatorname{div}\left(\mathbf{K}(u) \cdot \underline{\operatorname{grad}(u)}\right) = 0. \quad (2)$$

The technique of resolution of this type of elliptical equation by IIM method was first used by [19] in the context of magnetorheological fluids problem of perfect interface (i.e., assuming the continuity of flux q and of the solution u across the interface). In the extended mathematical framework adopted here, a jump of solution $[u]$ on the contact between matrix and an inclusion is considered:

$$[u] = u^{+} - u^{-},$$
$$\left[K(u)\frac{\partial u}{\partial n}\right] = K^{+}(u)\, u_n^{+} - K^{-}(u)\, u_n^{-} = 0 \quad (3)$$

with $\underline{n}$ being the outward oriented unitary normal vector to the interface.

From a physical point of view, these conditions describe an imperfect contact between phases (e.g., due to the presence of the roughness or air film at the interface). This imperfection is often stated in thermal or hydraulic transport problems even if it is very difficult to be measured experimentally.

A common hypothesis used by many authors (see, e.g., [12, 13, 18] and references cited therein) is to consider the jump of the solution u across the interface being proportional to the normal component of flux across the interface, with the coefficient of proportionality being a characteristic interface parameter, α, called the resistance of interface:

$$[u] = u^{+} - u^{-} = -\alpha\left(\underline{q}\cdot\underline{n}\right) = \alpha K^{+}(u)\,u_{n}^{+} = \alpha K^{-}(u)\,u_{n}^{-}. \tag{4}$$

It easy to observe that the perfect interface problem is a special case of the problem with resistance of interface equal to zero ($\alpha = 0$).

Hereafter, the superscripts (+) and (−) present values evaluated at two opposed sides of a given interface (Figure 1).

2.2. Iterative Resolution of Nonlinear Elliptical Equation by Immersed Interface Method. Like finite difference method from which it has been derived, the IIM uses a uniform Cartesian grid which does not need to coincide with the interfaces or boundaries of internal domains to obtain discretized form of equation:

$$\frac{\partial}{\partial x}\left(K\frac{\partial u_{i,j}}{\partial x}\right) + \frac{\partial}{\partial y}\left(K\frac{\partial u_{i,j}}{\partial y}\right) = \sum_{m=1}^{ns}\gamma_m u_{i+im,j+jm} + C_{i,j} = 0. \tag{5}$$

This equation is written at each node of the grid with coordinates (x_i, y_j), identified in the 2D case by the couple of indexes (i, j). Since the behavior of constituents is supposed non linear, then $K = K(u_{i,j})$. To resolve the system of (2) obtained by the discretization of differential equation, we use the so-called substitution method, similar to that proposed by [19]. Following this scheme, from an initial guess of solution u^0, the $(k+1)$th iterative step consists to obtain a new estimation of solution u^{k+1} of partial derivative equation employing the known information of the previous step u^k.

Bearing in mind spatial and temporal discretization, the solution u and the thermal conductivity K must be written as $u_{i,j} = u^{k+1}(x_i, y_j)$ and $K = K(u_{i,j}^k)$. However, in order to keep simple formulas, this dependency is omitted from notation but it is implicitly assumed for the rest of the paper. Other parameters ns and γ_m represent, respectively, the number of grid points and the weighting coefficient of mth node involved in the evaluation of the solution at point (x_i, y_j), and indexes im and jm take values in the set $\{0, \pm1, \pm2, \ldots\}$. Since γ_m coefficients, indexes im and jm, and the correction term $C_{i,j}$ depend on point (i, j), it needs to be written γ_{ijm}. Again for the sake of simplicity, this dependency is omitted from notation and is assumed implicitly. Furthermore, a constant number of stencils is kept for all nodes of the same type but different for regular and irregular points.

A *regular point* is a grid node away from the interface (see Figure 1) for which the centered FDM differentiation scheme of differential equation to be solved is used. For such nodes, the stencil contains five points so that $ns = 5$. All nodes where the approximation of solution involves only points on the same side of the interface are regular points and the approximation of solution at these points coincides with classical formula of a standard five points stencil. For these points the approximation of the partially derivative equation to the second-order accuracy demonstrates a vanishing correction term ($C_{i,j} = 0$) and is given as follows:

$$\begin{aligned}\frac{\partial}{\partial x}\left(K\frac{\partial u_{i,j}}{\partial x}\right) + \frac{\partial}{\partial y}\left(K\frac{\partial u_{i,j}}{\partial y}\right) &= \frac{K_{i,j-1/2}}{h^2}u_{i,j-1} + \frac{K_{i-1/2,j}}{h^2}u_{i-1,j} \\ &\quad + \frac{K_{i+1/2,j}}{h^2}u_{i+1,j} + \frac{K_{i,j+1/2}}{h^2}u_{i,j+1} \\ &\quad - \frac{K_{i,j-1/2} + K_{i-1/2,j} + K_{i+1/2,j} + K_{i,j+1/2}}{h^2}u_{i,j} + O\left(h^3\right),\end{aligned} \tag{6}$$

where

$$\begin{aligned} K_{i,j} &= K\left(u^k\left(x_i, y_j\right)\right), \qquad u_{i,j} = u^{k+1}\left(x_i, y_j\right), \\ K_{i\pm1/2,j} &= \frac{1}{2}\left(K_{i,j} + K_{i\pm1,j}\right), \\ K_{i,j\pm1/2} &= \frac{1}{2}\left(K_{i,j} + K_{i,j\pm1}\right). \end{aligned} \tag{7}$$

If the grid point is near the interface, the points involved in the approximation of the solution would be from materials in both sides of interface. These points are called irregulars since the use of the standard five points stencil does not insure any more the second-order accuracy of the solution. As discussed in a [18, 20] and [16, 17, 19] a good choice in order to maintain the second-order accuracy at irregular points is to take a stencil of nine points, that is, for these irregular nodes $ns = 9$.

The procedure of constructing a second order accurate solution at irregular points is detailed in the previously mentioned references and is briefly described here. Let (x^*, y^*) be the projection on the interface of an irregular node (x_i, y_j). A local coordinates system attached to the projected point is assumed with two axis (ξ, η) coinciding with normal and tangential directions of the interface at this point (Figure 1):

$$\begin{aligned} \xi &= \left(x - x^*\right)\cos\theta + \left(y - y^*\right)\sin\theta, \\ \eta &= -\left(x - x^*\right)\sin\theta + \left(y - y^*\right)\cos\theta, \end{aligned} \tag{8}$$

with θ being the angle between x and ξ axes.

The relationship between the global and local coordinates systems gives

$$\begin{aligned} u_\xi &= u_x\cos\theta + u_y\sin\theta; \qquad u_\eta = -u_x\sin\theta + u_y\cos\theta; \\ K_\xi &= K_x\cos\theta + K_y\sin\theta; \qquad K_\eta = -K_x\sin\theta + K_y\cos\theta, \end{aligned} \tag{9}$$

where u_x and K_x indicate, respectively, the derivative of u and K with respect to x.

It is then possible to replace the original discretized equation (5) by one written in the local coordinate of (ξ, η):

$$\frac{\partial}{\partial x}\left(K\frac{\partial u_{i,j}}{\partial x}\right)+\frac{\partial}{\partial y}\left(K\frac{\partial u_{i,j}}{\partial y}\right) = \frac{\partial}{\partial \xi}\left(K\frac{\partial u_{i,j}}{\partial \xi}\right)+\frac{\partial}{\partial \eta}\left(K\frac{\partial u_{i,j}}{\partial \eta}\right) = \sum_{m=1}^{ns}\gamma_m u_{i+im,j+jm}+C_{i,j}. \tag{10}$$

Further, in respect of local coordinates system, the solution $u_{i+im,j+jm}$ at a grid point could be written as a Taylor expansion at (x^*, y^*) so that

$$u\left(x_{i+im}, y_{j+jm}\right) = u\left(\xi_m, \eta_m\right) = u^{\pm}+\xi_m u_{\xi}^{\pm}+\eta_m u_{\eta}^{\pm}+\frac{1}{2}\xi_m^2 u_{\xi\xi}^{\pm} + \frac{1}{2}\eta_m^2 u_{\eta\eta}^{\pm}+\xi_m\eta_m u_{\xi\eta}^{\pm}+\frac{1}{2}\xi_m\eta_m^2 u_{\xi\eta\eta}^{\pm}+O\left(h^3\right). \tag{11}$$

The reasons of keeping third-order derivative of solution $u_{\xi\eta\eta}$ in Taylor's development (11) are related to their presence on the interface conditions relations as it will be clear later (see (15)). Additionally, the values $u^{\pm}, u_{\xi}^{\pm}, u_{\eta}^{\pm}, u_{\xi\xi}^{\pm}, u_{\eta\eta}^{\pm}, u_{\xi\eta}^{\pm}$, and $u_{\xi\eta\eta}^{\pm}$ in (11) represent the solution and its derivatives determined at projection point (x^*, y^*) of the interface. The (+) or (−) sign is chosen depending on whether (ξ_m, η_m) belongs to the (+) or (−) side of the interface.

By replacing in (10) each component $u_{i+im,j+jm}$ as given by (11) and rearranging terms, the following expression of the truncation error at an irregular point is obtained (i, j):

$$\kappa_{i,j} = a_1u^- + a_2u^+ + a_3u_{\xi}^- + a_4u_{\xi}^+ + a_5u_{\eta}^- + a_6u_{\eta}^+ + a_7u_{\xi\xi}^- + a_8u_{\xi\xi}^+ + a_9u_{\eta\eta}^- + a_{10}u_{\eta\eta}^+ + a_{11}u_{\xi\eta}^- + a_{12}u_{\xi\eta}^+ + a_{13}u_{\xi\eta\eta}^- + a_{14}u_{\xi\eta\eta}^+ - C_{i,j} + O\left(\max_m\left|\gamma_m\right|h^3\right). \tag{12}$$

The coefficients $\{a_1, a_2, \ldots, a_{14}\}$ of (12) depend on the position of the stencil point relative to the interface:

$$a_1 = \sum_{(m\in M^-)}\gamma_m; \qquad a_2 = \sum_{(m\in M^+)}\gamma_m;$$
$$a_3 = \sum_{(m\in M^-)}\gamma_m\xi_m; \qquad a_4 = \sum_{(m\in M^+)}\gamma_m\xi_m;$$
$$a_5 = \sum_{(m\in M^-)}\gamma_m\eta_m; \qquad a_6 = \sum_{(m\in M^+)}\gamma_m\eta_m;$$
$$a_7 = \frac{1}{2}\sum_{(m\in M^-)}\gamma_m\xi_m^2; \qquad a_8 = \frac{1}{2}\sum_{(m\in M^+)}\gamma_m\xi_m^2;$$
$$a_9 = \frac{1}{2}\sum_{(m\in M^-)}\gamma_m\eta_m^2; \qquad a_{10} = \frac{1}{2}\sum_{(m\in M^+)}\gamma_m\eta_m^2;$$
$$a_{11} = \sum_{(m\in M^-)}\gamma_m\xi_m\eta_m; \qquad a_{12} = \sum_{(m\in M^+)}\gamma_m\xi_m\eta_m;$$
$$a_{13} = \frac{1}{2}\sum_{(m\in M^-)}\gamma_m\xi_m\eta_m^2; \qquad a_{14} = \frac{1}{2}\sum_{(m\in M^+)}\gamma_m\xi_m\eta_m^2, \tag{13}$$

where the sets $M^{\pm}$ are defined as

$$M^{\pm} = \left\{m : \left(\xi_m, \eta_m\right) \in \Omega^{\pm}\right\}. \tag{14}$$

At this end it is important to specify the relations of the solution and its derivatives at both sides of the interface. After some algebraic manipulation, from the contact conditions (3) the following relations are deduced:

$$\begin{aligned}
&u^+ = u^- + \alpha K^- u_{\xi}^-, \qquad u_{\xi}^+ = \rho u_{\xi}^-,\\
&u_{\eta}^+ = \left(1-\alpha\chi'' K^-\right)u_{\eta}^- + \alpha K_{\eta}^- u_{\xi}^- + \alpha K^- u_{\xi\eta}^-,\\
&u_{\xi\xi}^+ = \rho u_{\xi\xi}^- - \frac{\left[K_{\eta}^+u_{\eta}^+ - K_{\eta}^-u_{\eta}^- + K_{\xi}^+u_{\xi}^+ - K_{\xi}^-u_{\xi}^- + K^+u_{\eta\eta}^+ - K^-u_{\eta\eta}^-\right]}{K^+};\\
&u_{\eta\eta}^+ = u_{\eta\eta}^- - \chi''\left(u_{\xi}^+ - u_{\xi}^-\right) + \alpha\left(\chi'' K_{\xi}^- + K_{\eta\eta}^-\right)u_{\xi}^- + \alpha K_{\eta}^-\left(u_{\xi\eta}^- - \chi'' u_{\eta}^-\right) + \alpha K_{\eta}^-\left(u_{\xi\eta}^- - \chi'' u_{\eta}^-\right)\\
&\qquad + \alpha K^-\left(\chi'' u_{\xi\xi}^- + u_{\xi\eta\eta} - 2\chi'' u_{\eta\eta}^-\right) - \alpha\left(\chi''\right)^2 K^- u_{\xi}^-,\\
&u_{\xi\eta}^+ = \frac{\left(K_{\eta}^-u_{\xi}^- - K_{\eta}^+u_{\xi}^+\right)}{K^+} + \rho\left(u_{\xi\eta}^- - \chi'' u_{\eta}^-\right) + \chi'' u_{\eta}^+,\\
&u_{\xi\eta\eta}^+ = \rho u_{\xi\eta\eta}^- + \chi''\left(\rho u_{\xi\xi}^- - u_{\xi\xi}^+\right) + \frac{\left[u_{\xi}^-\left(\chi'' K_{\xi}^- + K_{\eta\eta}^-\right) - u_{\xi}^+\left(\chi'' K_{\xi}^+ + K_{\eta\eta}^+\right)\right]}{K^+}\\
&\qquad + 2\frac{\left[K_{\eta}^-u_{\xi\eta}^- - K_{\eta}^+u_{\xi\eta}^+ - \chi''\left(K_{\eta}^-u_{\eta}^- - K_{\eta}^+u_{\eta}^+\right)\right]}{K^+} - 2\chi''\left(\rho u_{\eta\eta}^- - u_{\eta\eta}^+\right),
\end{aligned} \tag{15}$$

with $\rho = K^-/K^+$. The curvature χ'' of the interface at (x^*, y^*) is the second order derivative of function $\xi = \chi(\eta)$ with respect to η. We note also that at (x^*, y^*) we have $\chi(0) = 0$ and for a smooth interface (as assumed here) $\chi'(0) = 0$.

The interface relations (15) are used to recast (12) in a compact form using only quantities from one side of the interface (the Ω^- side, e.g.):

$$\kappa_{i,j} = B_1u^- + B_2u_{\xi}^- + B_3u_{\eta}^- + B_4u_{\xi\xi}^- + B_5u_{\eta\eta}^- + B_6u_{\xi\eta}^- + B_7u_{\xi\eta\eta}^- + O\left(\max_m\left|\gamma_m\right|h^3\right), \tag{16}$$

where B_i $(i = 1, 7)$ are expressions of coefficients $\{a_1, a_2, \ldots, a_{14}\}$ and other quantities used in (15). Since we are looking for a second order accuracy, the coefficients B_i of $\kappa_{i,j}$ expression must vanish in the same time with the correction term $C_{i,j}$. These constraints lead to following system of equations with respect to variables a_i:

$$\begin{aligned}
& a_1 + a_2 = 0, \\
& a_2 \alpha K^- + a_3 + a_4 \rho + a_6 \alpha K^-_\eta + a_8 c_8^{(2)} \\
& \qquad + a_{10} c_{10}^{(2)} + a_{12} c_{12}^{(2)} + a_{14} c_{14}^{(2)} = K^-_\xi, \\
& a_5 + a_6 \left(1 - \alpha \chi'' K^-\right) + a_8 c_8^{(3)} - 2\alpha \chi'' K^-_\eta a_{10} \\
& \qquad + a_{14} c_{14}^{(3)} + \chi'' \left(1 - \rho - \alpha \chi'' K^-\right) a_{12} = K^-_\eta, \\
& a_7 + \left(\rho - \alpha \chi'' K^-\right) a_8 + \alpha \chi'' K^- a_{10} + 3\alpha \left(\chi''\right)^2 K^- a_{14} = K^-, \\
& a_9 + \left(1 - 2\alpha \chi'' K^-\right) a_{10} + \left(\rho - 1 + 2\alpha \chi'' K^-\right) a_8 \\
& \qquad + 3\chi'' \left(1 - \rho - 2\alpha \chi'' K^-\right) a_{14} = K^-, \\
& \alpha K^- a_6 - \left(2\alpha K^-_\eta - \alpha \rho K^+_\eta\right) a_8 + 2\alpha K^-_\eta a_{10} + a_{11} \\
& \qquad + \left(\rho + \alpha \chi'' K^-\right) a_{12} + a_{14} c_{14}^{(6)} = 0, \\
& -\alpha K^- a_8 + \alpha K^- a_{10} + a_{13} + \left(\rho + 3\alpha \chi'' K^-\right) a_{14} = 0,
\end{aligned} \tag{17}$$

where

$$\begin{aligned}
c_8^{(2)} &= -\left(\alpha K^-_\eta K^+_\eta + \alpha K^+ K^-_{\eta\eta} - K^-_\xi + \rho K^+_\xi\right) / K^+ \\
&\quad - \left(1 + \alpha K^-_\xi - \rho\right) \chi'' + \alpha K^- \left(\chi''\right)^2, \\
c_{10}^{(2)} &= \chi'' \left(1 - \rho\right) + \alpha K^-_{\eta\eta} + \alpha \chi'' \left(K^-_\xi - \chi'' K^-\right), \\
c_{12}^{(2)} &= \frac{\left(K^-_\eta - \rho K^+_\eta\right)}{K^+} + \alpha \chi'' K^-_\eta, \\
c_{14}^{(2)} &= \frac{\left(-2K^-_\eta K^+_\eta + 2\rho \left(K^+_\eta\right)^2\right)}{\left(K^+\right)^2} \\
&\quad + \frac{\left(\alpha \chi'' K^-_\eta K^+_\eta + K^-_{\eta\eta} - \rho K^+_{\eta\eta}\right)}{K^+} \\
&\quad + 3\chi'' \left(\alpha K^-_{\eta\eta} + \chi'' + \alpha \chi'' K^-_\xi - \rho \chi'' \left(1 + \alpha \chi'' K^+\right)\right), \\
c_8^{(3)} &= \frac{\left(K^-_\eta - K^+_\eta\right)}{K^+} + \alpha \chi'' \left(2K^-_\eta + \rho K^+_\eta\right), \\
c_{14}^{(3)} &= \frac{-\chi'' \left(3K^-_\eta - K^+_\eta - 2\rho K^+_\eta\right)}{K^+} - \left(\chi''\right)^2 \left(6\alpha K^-_\eta + \alpha \rho K^+_\eta\right), \\
c_{14}^{(6)} &= \frac{2\left(K^-_\eta - \rho K^+_\eta\right)}{K^+} + \alpha \chi'' \left(6K^-_\eta + \rho K^+_\eta\right).
\end{aligned} \tag{18}$$

Since all coefficients a_i are defined as functions of γ_m (see (13)), one could write the system (17) in a compact form as

$$[\mathbf{A}] \cdot \underline{\gamma} = \underline{b} \tag{19}$$

with the vector $\underline{\gamma} = [\gamma_1, \gamma_2, \ldots, \gamma_{ns}]^t$ and $\underline{b} = [0, K^-_\xi, K^-_\eta, K^-, K^-, 0, 0]^t$.

Thus, the central point to obtain the solution of the problem (2) by using IIM is to construct and resolve the system (19). Note that, at irregular points, the set of (19) could be obtained using at least six points stencil as proposed in the original IIM method [21]. However, as discussed in some recent works [16, 17, 19], nine-point stencil ($ns = 9$) is preferred because the resulting linear system of equations is in this case a block tridiagonal one.

However, using of a nine points stencil ($ns = 9$) leads to an underdetermined system (19) whose solution could be obtained by using the *maximum principle* [16, 17, 19] and an optimization approach. For that, the following constrained quadratic optimization problem is considered:

$$\min_{\gamma} \left\{ \frac{1}{2} \left\| \gamma - g \right\|_2^2 \right\}, \tag{20}$$

with

$$\begin{aligned}
\gamma_m &\geq 0 \quad \text{if } (im, jm) \neq (0,0), \\
\gamma_m &< 0 \quad \text{if } (im, jm) = (0,0).
\end{aligned} \tag{21}$$

In this equation, the vector $\underline{g} = [g_1, g_2, \ldots, g_{ns}]^t$ has the following components:

$$\begin{aligned}
g_m &= \frac{K_{i+im/2, j+jm/2}}{h^2}, \\
&\quad \text{if } (im, jm) \in \{(-1,0), (1,0), (0,-1), (0,1)\}, \\
g_m &= -\frac{K_{i,j-1/2} + K_{i-1/2,j} + K_{i+1/2,j} + K_{i,j+1/2}}{h^2}, \\
&\quad \text{if } (im, jm) = (0,0), \\
g_m &= 0 \text{ otherwise.}
\end{aligned} \tag{22}$$

This vector $\underline{g}$ represents in effect the coefficients of the standard five points stencil to whom the solution of the optimization problem has to coincide in case of continuous properties of constituent phases (i.e., when $[K] = 0$).

The existence of the solution of the optimization problem (20) as well as the convergence of the substitution method in that case has been demonstrated in [16, 17] and will not be discussed here. We just mention that, as in a previous work of these authors [18], this optimization problem is solved by using the optimization toolbox available in *MATLAB*.

2.3. Computing Solution, Its Derivatives at Interface, and Effective Properties. As previously outlined, the non linear transfer problem is treated here by using an iterative procedure consisting for each iteration to solve a linearized partial differential equation. The resolution of this later by using the IIM method needs to determine the set of weighting coefficients γ_m. At each irregular point, these coefficients have to be evaluated by solving an undetermined system via an optimization approach. The coefficients $K^{\pm}$, $K^{\pm}_{\xi}$, and $K^{\pm}_{\eta}$ of this system of (17) are in reality defined as functions of the solution $u(x^*, y^*)$ at interface. For the substitution scheme followed here, these coefficients are calculated at each step from the solution of the previous iteration u^k at projection point (x^*, y^*).

The solution value at this point $u(x^*, y^*)$ is interpolated from solution at grid points using a least squares scheme. For this interpolation, grid points situated at the same side of the considered point (x_i, y_j) are used. As discussed in chapter 6 of [17] as well as in the contribution of [19], using this approach by involving in least squares approximation at least six points of the same side avoids to use the interface relations and maintains the second order accuracy. For example, if the irregular point (x_i, y_j) belongs to Ω^-, one can interpolate the solution at its projection point (x^*, y^*) from the values of points in the same side Ω^- as follows:

$$u^-(x^*, y^*) = \sum_{(x_m, y_n)\in\Omega^-, |(x_m, y_n)-(x^*, y^*)|\le R_\varepsilon} \gamma_{m,n} u_{m,n}, \tag{23}$$

where R_ε can be chosen between $4.1h$ and $6.1h$.

The same method of least squares scheme is also used to calculate the derivatives of the solution u_x and u_y using u_ξ by applying relation (9). Note that once the value of the solution u^- is known (and so are the values of $K^- = K(u^-)$) as well as its derivative u^-_ξ at Ω^- side of the interface, it is possible to evaluate the respective values at the other side Ω^+ of interface by using the following interface relation:

$$u^+ = u^- + \alpha K^- u^-_\xi; \qquad K^+ = K(u^+). \tag{24}$$

The same approach can be used to determine the coefficients K^-_x and K^-_y at (x^*, y^*) by involving values of $K_{m,n} = K(u_{m,n})$ determined at grid points situated at the same side Ω^- (or Ω^+). We obtain finally $K^{\pm}_{\xi}$ and $K^{\pm}_{\eta}$ from the relation written in (9).

Once all coefficients of the finite difference scheme are known, it is possible to solve the system of (5) and obtain the solution (u^{k+1}) of the $(k+1)$th step at all grid nodes. The iterative calculation is finished when the convergence criterion is reached. For all numerical simulations presented in the next sections, the norm of residue of the iterative scheme is fixed to 10^{-6}. These results numerically confirm the convergence of the iterative procedure which is obtained after only a small number of iteration (~5 iterations).

From the solution of the transfer problem, one could use it to calculate the overall conductivity of the heterogeneous media from the well-known relation of volume average quantities:

$$\langle \underline{q} \rangle = -\mathbf{K}^{\text{eff}} \cdot \left\{ \langle \underline{\text{grad}(u)} \rangle + \frac{1}{|\Omega|} \int_\Gamma \alpha \left[\underline{q}(s) \cdot \underline{n}(s) \right] \underline{n}(s)\, ds \right\}, \tag{25}$$

where $\langle\cdot\rangle$ denotes the average over all elements of the representative volume.

3. Variation of the Effective Thermal Conductivity of Geomaterials with respect to Temperature and Pressure

3.1. Temperature Dependence. Beginning from the pioneer work of [3], the temperature-dependent thermal properties of geomaterials have been studied for a long time in relation with various engineering applications such as geothermal reservoirs, underground storage of nuclear waste or petroleum and natural gas geology. This subject is always in continuous progress with a remarkable number of results conducted on different types of soils and rocks in the last decade [2, 4, 6–9]. A general tendency of decreasing of thermal conductivity as a function of temperature can be stated from these contributions. At the same time, a thermal damage is reported as a consequence of the contrast of constituent properties of geomaterials when the temperature increases. This type of damage known as thermal cracking developed principally in contacts of constituent phases of the heterogeneous media like geomaterials.

In this part, we use the IIM method to solve the problem of effective thermal conductivity estimation of geomaterials whose constituent thermal conductivities depend on temperature. In addition, the effects of cracking interfaces with temperature on the effective thermal conductivity are considered using imperfect interface. In that case, the nonlinearity of effective thermal property reflects not only the nonlinearity of the intrinsic properties of matrix and inclusions but also the properties of interfaces, which when debonding produce an extra thermal resistance. In order to describe the progressive cracking of interfaces when the temperature evolves, the properties of interface are supposed to vary with coordinates following a known function. In the simplest case a piecewise interfacial resistance function that takes some values for debonding parts of interfaces and some other values for intact ones could be used. As an example, the debonding parts of the interface of a circular inclusion could be given in function of an angle ϕ measured from an arbitrary chosen direction (Figure 2). In extreme cases, full interface could be considered as debonded. One could anticipate that, because of the temperature dependent conductivity of local constituents and interface debonding, the overall conductivity would be highly temperature dependent [14, 15, 22–26]. As demonstrated in a previous contribution from the authors [18], the contact resistance leads also to a size-dependent behavior of heterogeneous materials as observed in reality: for the same volumetric fraction of inclusions, a more pronounced effect of the interface is observed for smaller inclusions. If not otherwise stated in following simulations, the size of inclusion is equal to $R = 1\,\mu$m.

For the sake of clarity, the geometry as well as the initial and boundary conditions of the considered problem is depicted in Figure 2. More precisely, a constant initial temperature u is considered in whole sample, and the mixed boundary conditions consist in applying the temperatures u and $u + \Delta u$ at the two opposing faces (to the Oy direction in the examples presented here) of the rectangular domain, whereas the zero heat flux is supposed to be to two other

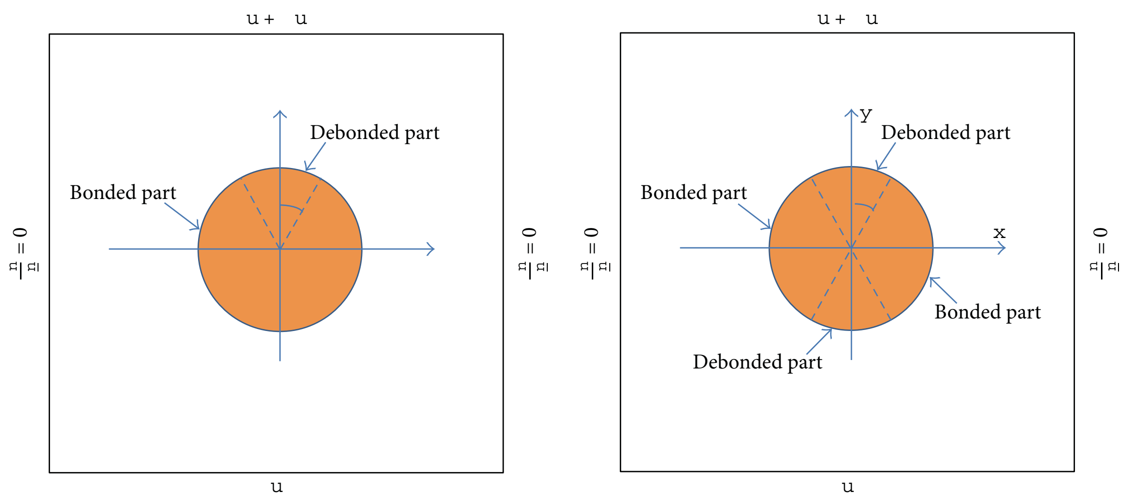

(a) (b)

FIGURE 2: (a) Single partial debonding of circular inclusion. (b) Double partial debonding of circular inclusion.

faces in the orthogonal direction (faces normal to the Ox direction) to the first. In what follows, a constant 320 × 320 grid is used for all calculations. This value obtained from the analysis of the sensitivity of numerical results to the grid density in previous work [18] gives excellent agreement with the analytical solutions in the context of the linear problem.

For illustration purposes, we consider a sample of Callovo-Oxfordian argillite (see, e.g., [18] for a brief description) constituted by a clay matrix with quartz inclusions at the mesoscopic level. The constant thermal conductivity of the matrix is taken as $K_1(u) = 1.8\,(\mathrm{W}\cdot\mathrm{m}^{-1}\cdot\mathrm{K}^{-1})$. Otherwise the thermal conductivity of quartz significantly decreases with temperature and following evolution is reported in published works [1, 3]: $K_2(u) = 7.7/(0.0045\times u - 0.3863)\,(\mathrm{W}\cdot\mathrm{m}^{-1}\cdot\mathrm{K}^{-1})$. It must emphasize however that despite simple expressions of thermal conductivities used for this material, one could use any expression provided by experimental considerations. Concerning the thermal resistance of interface in debonded parts, an arbitrary value is taken equal to $10^{-6}\,(\mathrm{m}^2\cdot\mathrm{K}\cdot\mathrm{W}^{-1})$, while perfect interface conditions ($\alpha = 0$) are supposed for bonded parts.

For simulations, firstly the sample of heterogeneous material with a single circular inclusions and partially (simple or double) debonded interface is considered. As the illustration in Figure 3, the temperature fields are presented on the material containing a single circular inclusion with, respectively, simple and double debonding interface. The debonding, introduced in these simulations as an extra resistance of the interface, is the reason of temperature jumps manifested in the temperature profiles (Figure 4), respectively, in one side and in two sides of inclusion according to debonding interface geometry (single partial debonding in Figure 2(a) or double partial debonding in Figure 2(b)).

The variation of the overall thermal conductivity of the considered heterogeneous material with temperature as well as with the volume fraction of constituents is shown in Figure 5. Firstly, due to the decrease of the thermal conductivity of solid inclusion, the same tendency is obtained for the homogenized thermal property. The reduction between 300°K and 500°K of this property is much more pronounced in case of perfect interface with higher volume fraction of minerals inhomogeneity (Figure 5(a)). For the perfect interface case, the effective thermal conductivity is always higher than that of the clay matrix $K_1 = 1.8\,(\mathrm{W}\cdot\mathrm{m}^{-1}\cdot\mathrm{K}^{-1})$ because of a higher thermal conductivity of inclusion in all considered range of temperature. On the contrary, in the case of fully debonded interface, under the effect of thermal resistance of the interface, the effective thermal conductivity could be smaller than that of the matrix (Figure 5(b)).

During thermal cracking, interfaces debonding is progressive. If this debonding is orientated and happened preferentially at some directions, then the overall properties could become anisotropic. Such situation is simulated by supposing a partially debonding of a circular inclusion. Figure 6 illustrates the evolution of effective thermal conductivities in the vertical and horizontal directions in such situation. In both directions the thermal conductivity decreases when the debonding angle (angle $\phi 2(b)$) increases from $\phi = 0$ (perfect interface) to $\phi = \pi/2$. However, because of the orientation of the debonded part of the interface, the thermal conductivity in the vertical direction decreases quicker than in horizontal direction introducing an anisotropy on macroscopic thermal conductivity of the homogenized material.

While single inclusion structure model assumes a periodic material, in cases when this hypothesis is not satisfied a more realistic description of the microstructure is needed. The IIM could be successfully used in such conditions where complex structures are studied. This feature is illustrated here by considering a clayey rock with 60 quartz inclusions counting for 20% of the volume. While all inclusions have the same diameter, their positions are randomly obtained by using a Monte Carlo procedure. As described in our previous work [18], the number of inclusion used in simulations is sufficient for having convergent results for homogenized thermal conductivity of the random medium.

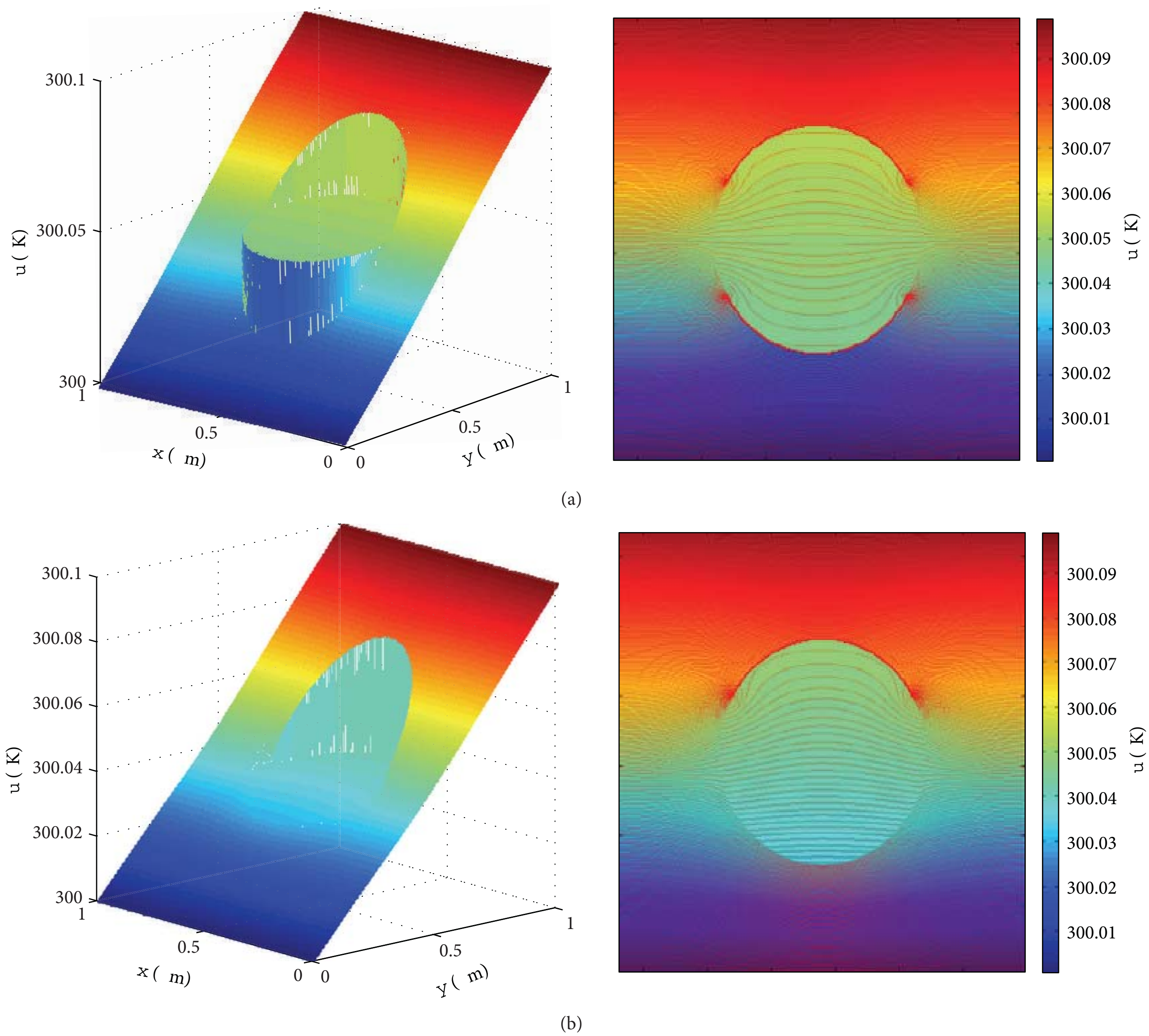

Figure 3: Temperature field in the heterogeneous media with. (a) Double partial debonding of circular inclusion; (b) single partial debonding of circular inclusion.

For illustration purposes, we consider a hypothetic cracking evolution described by a linear evolution of debonding angle with temperature $\phi = a \times u + b$ with $a = \pi/300$ and $b = -273\times\pi/300$, which means that the interfaces are perfect at 273°K and completely debonded at 573°K. Note also that the position of debonded part is randomly generated at the boundary of each inclusion.

The contours of temperature field in elementary representative volume at some temperature levels are presented in Figure 7, in which one could clearly distinguish the progressive debonding of inclusions illustrated by the increase of the debonded arc length of inclusions. Finally, as performed in Figure 8(a), the comparison between two cases of perfectly bonded and partially debonded of random inclusions has elucidated the important increase of the nonlinearity of effective thermal conductivity with temperature in the latter case. Further, due to the random distribution of circular inclusions as well as the debonded part of each inclusion, these numerical results always display the quasi-isotropic of the overall thermal property where $K_{\text{eff}}^{yy}/K_{\text{eff}}^{xx} \approx 1$ as observed in Figure 8(b).

3.2. Pressure Dependence. In addition to the temperature dependence, the variation of the thermal conductivity of geomaterials with respect to applied pressure is also an important issue of research. Based on experimental results realized on different types of rock, many authors showed that the increase of pressure augments the thermal conductivity of materials [2, 27–29]. For example, in their work, Abdulagatova et al. [28] measured the thermal conductivity of sandstone at pressures up to 400 MPa. They found that the thermal conductivity of a rock increases rapidly between 0.1 and 100 MPa,

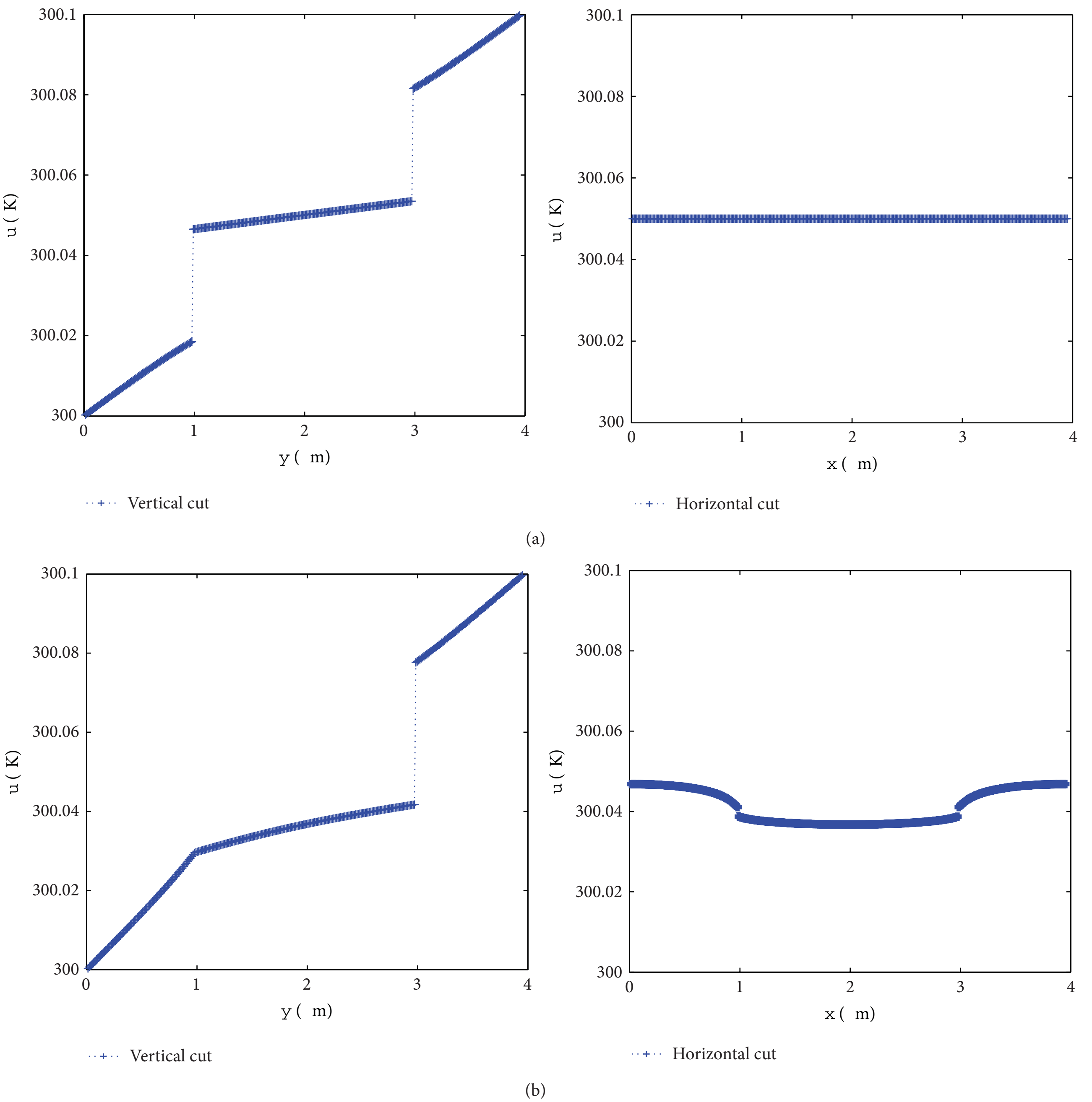

Figure 4: Distribution of temperature following the vertical and horizontal cuts at the center of circular inclusion: (a) double partial debonding; (b) single partial debonding.

and at high pressure (>100 MPa), a weak linear dependence of the thermal conductivity with pressure was observed. The increasing effect of pressure on thermal behavior was explained by the closure of microcrack which caused the approaching of the rock grains to each other at moderate pressure. If pressure is still further increased, the reduction of the rock's intrinsic porosity may take place. These results confirm the observation presented in the previous work of Clauser and Huenges [1].

The influence of pressure on the effective thermal conductivity will be carried out here by supposing that the applied pressure will close continuously the debonded part of inclusions. This simplification aims to illustrate the evolution of the thermal conductivity under pressure but obviously a more sophisticated study needs to be conducted to explicitly account for the mechanism of this closure of debonded inclusions. This case of study can be realized in the context of the thermomechanical coupled behaviour of geomaterials and will be discussed in our near future work. Thus, in the present paper, we will define the variation of debonding angle with respect to pressure as follows: $\phi = \phi_0(1 + (P/P_0)^n)^{(1-n)/n}$. This function presents a rapid decrease of

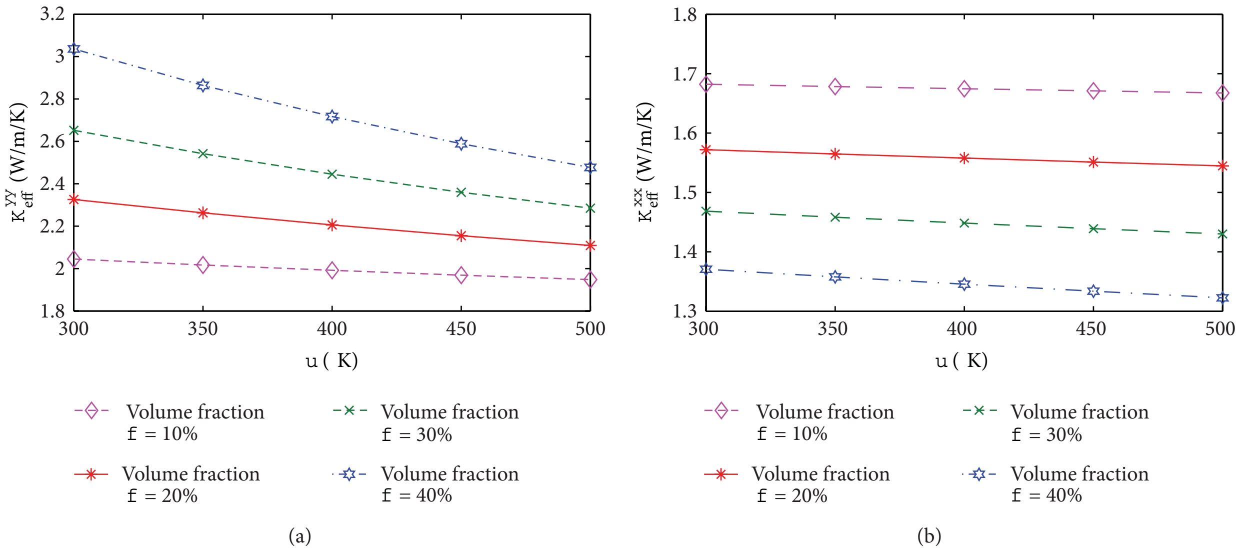

FIGURE 5: Effective thermal conductivity K_{eff}^{yy} as a function of temperature and volume fraction of inclusion: (a) case of perfect interface; (b) case of completely debonded interface.

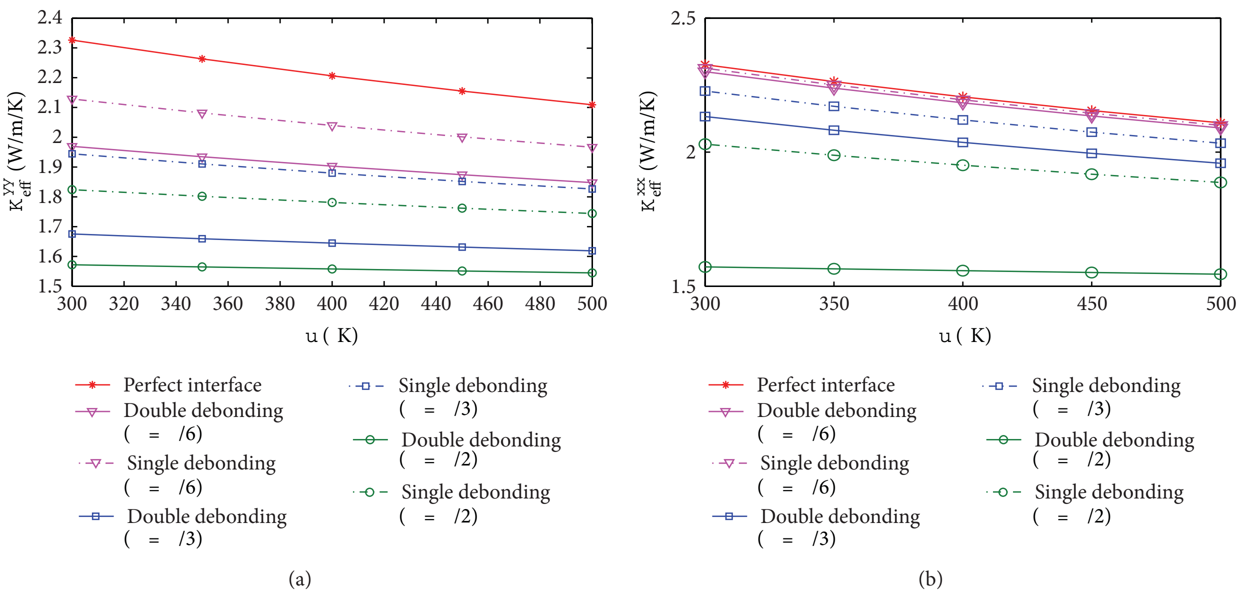

FIGURE 6: Effective thermal conductivity as a function of temperature and debonding angle: (a) vertical direction K_{eff}^{yy}; (b) horizontal directions K_{eff}^{xx}.

debonding angle with moderate pressure P and is inversely proportional with high pressure. Otherwise, to take into account the temperature effect, the initial debonding angle ϕ_0 of random inclusions may vary as a function of temperature as considered in previous section. As an example, in Figure 9, we present the variation of the effective thermal conductivity of the heterogeneous rock with respect to pressure as well as temperature with the value $P_0 = 10\,\text{MPa}$ and $n = 2$. These results show the quick increase of the overall thermal conductivity between the atmospheric pressure and 100 MPa, while a quasi linear evolution can be observed for the range of pressure from 100 MPa to 200 MPa.

3.3. Comparison with Experimental Results. In this subsection, we compare our numerical prediction with some experimental results published in the literature. As an example, in their contribution, Jobmann and Buntebarth [7] investigated the evolution of the thermal conductivity of the bentonite-quartz mixture with respect to temperature within 20°C to 150°C. Their main purpose of using this admixture is to accelerate the heat flow through the geotechnical barrier consisting of bentonite for the deep geological disposal of waste. To increase the thermal conductivity of the barrier, which needs to be similar to ones of the host rock, different quartz contents in the admixture have been tested. The grain

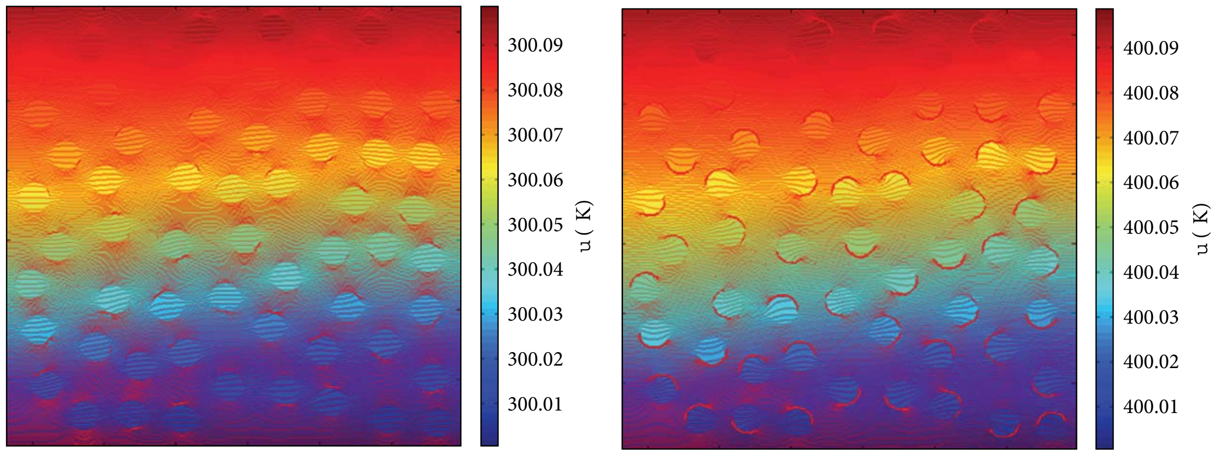

(a) (b)

FIGURE 7: Contour of temperature in the heterogeneous media at different state of applied temperature.

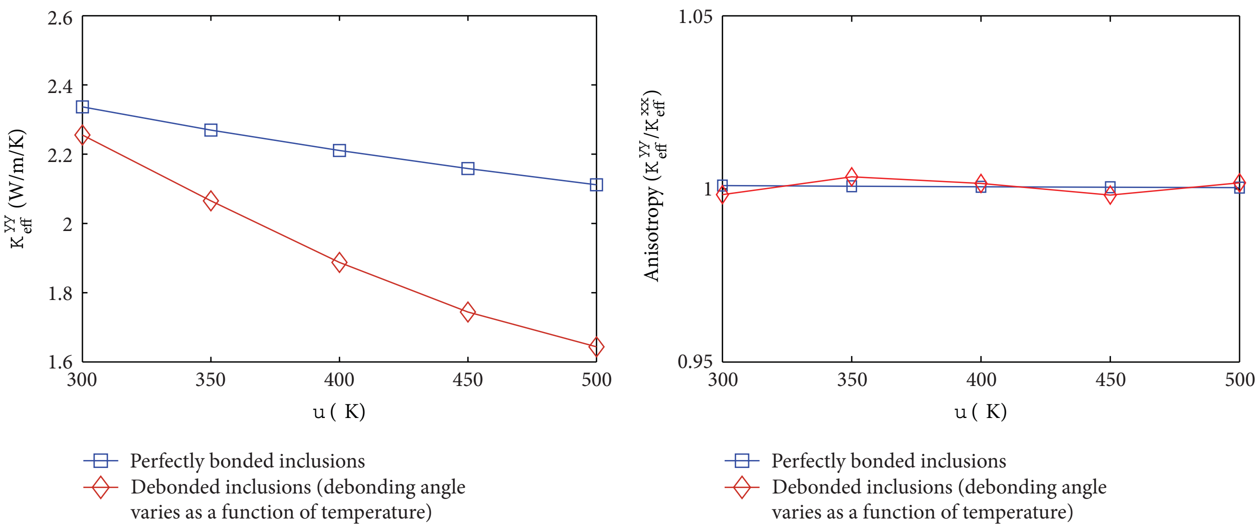

(a) (b)

FIGURE 8: Effective thermal conductivity of the randomly heterogeneous media as a function of temperature: (a) result estimated in the vertical direction K_{eff}^{yy}; (b) anisotropy of the effective thermal conductivity $K_{eff}^{yy}/K_{eff}^{xx}$.

size of quartz was about 0.3 mm. The results of these measures showed that the thermal conductivity of the bentonite-quartz mixtures slightly increase with respect to the quartz content. Moreover, due to the temperature dependence of the thermal conductivity of quartz while the thermal property of bentonite is almost constant about 0.95 ($W \cdot m^{-1} \cdot K^{-1}$), the overall thermal conductivity of the mixture decreases with respect to temperature.

In Figure 10, we present the comparison of the numerical and experimental results with different quartz content of the bentonite-quartz mixture. In these numerical simulations the thermal resistance of interface is equal to 2×10^{-4} ($m^2 \cdot K \cdot W^{-1}$) while the two coefficients of the debonding angle's evolution function with temperature (see Section 3.1) are $a = \pi/720$ and $b = -53 \times \pi/720$, respectively. These values are obtained from an inverse analysis so that both experiment and simulation agree at best. We can state that the tendency observed in the experiment is well captured by the numerical estimations using the IIM method.

4. Conclusions

The immersed interface method (IIM) was adapted in the present work to solve the elliptical transfer equation taking into account the contact resistance of interface in non linear heterogeneous composite-like geomaterials. This numerical tool is then used to derive the temperature- and pressure-dependent effective thermal conductivity of geomaterial with imperfect contact between matrix and inclusion. The imperfection of interface modeled as the partial or full debonding of inclusions is created during a thermophysical phenomenon called thermal cracking under heat load while

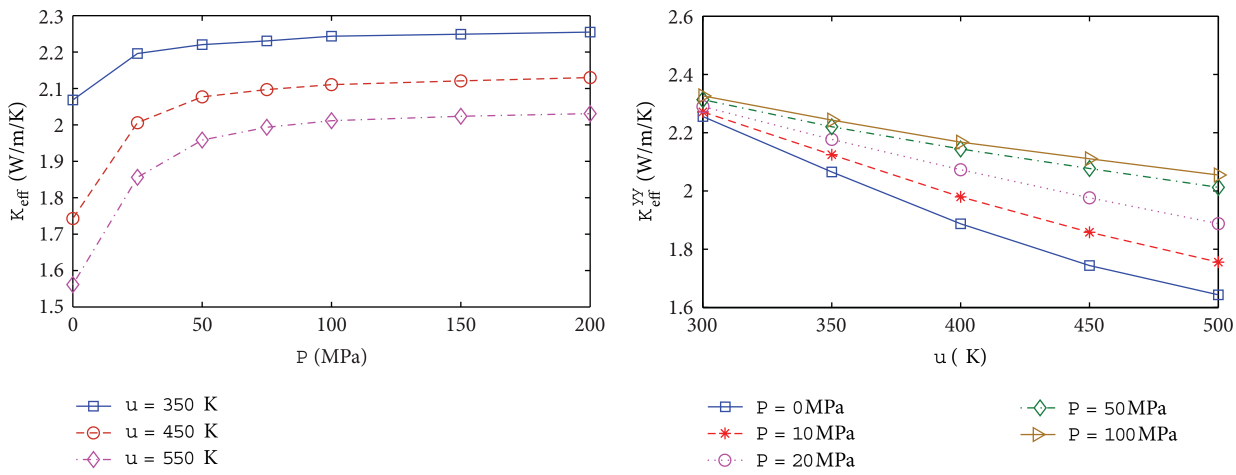

(a) (b)

FIGURE 9: Effective thermal conductivity of the randomly heterogeneous media as a function of pressure and temperature.

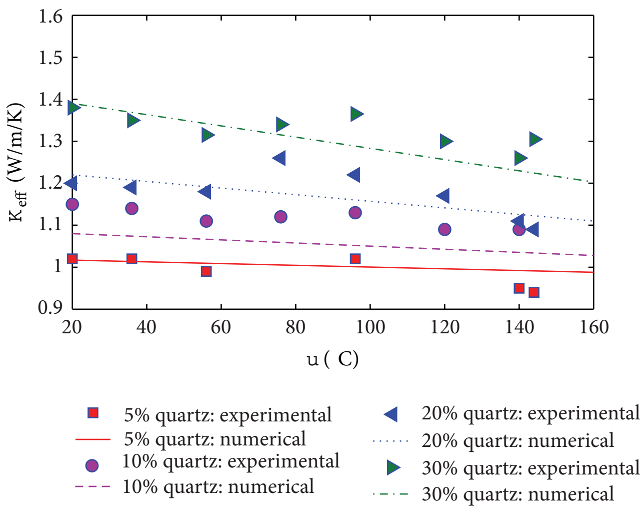

FIGURE 10: Contour of temperature in the heterogeneous media at different state of applied temperature.

a continuous closure of this imperfect interface is considered under pressure. The numerical results highlight that the overall conductivity at the macroscale depend strongly on the applied temperature and pressure through the state of debonding inclusions. The efficiency of numerical tool is demonstrated both in periodic structures and random ones allowing us to study in details temperature fields in a heterogeneous material with interfaces and its effective properties counting for the role of the microstructure complexity on the overall properties.

References

[1] C. Clauser and E. Huenges, "Thermal conductivity of rocks and minerals," in *Rock Physics and Phase Relations: A Handbook of Physical Constants, Rock Physics and Phase Relations*, T. J. Ahrens, Ed., AGU, Washington, DC, USA, 1995.

[2] Z. Z. Abdulagatova, I. M. Abdulagatov, and S. N. Emirov, "Effect of pressure, temperature, and oil-saturation on the thermal conductivity of sandstone up to 250 MPa and 520 K," *Journal of Petroleum Science and Engineering*, vol. 73, no. 1-2, pp. 141–155, 2010.

[3] F. Birch and H. Clark, "The thermal conductivity of rocks and its dependence upon temperature and composition," *American Journal of Science*, vol. 238, pp. 529–558, 1940.

[4] A. Aurangzeb, L. A. Khan, and A. Maqsood, "Prediction of effective thermal conductivity of porous consolidated media as a function of temperature: a test example of limestones," *Journal of Physics D*, vol. 40, no. 16, article 030, pp. 4953–4958, 2007.

[5] K. Midttømme, E. Roaldset, and P. Aagaard, "Thermal conductivity of selected claystones and mudstones from England," *Clay Minerals*, vol. 33, no. 1, pp. 131–145, 1998.

[6] A. Aurangzeb, S. Mehmood, and A. Maqsood, "Modeling of effective thermal conductivity of dunite rocks as a function of temperature," *International Journal of Thermophysics*, vol. 29, no. 4, pp. 1470–1479, 2008.

[7] M. Jobmann and G. Buntebarth, "Influence of graphite and quartz addition on the thermo-physical properties of bentonite for sealing heat-generating radioactive waste," *Applied Clay Science*, vol. 44, no. 3-4, pp. 206–210, 2009.

[8] H.-D. Vosteen and R. Schellschmidt, "Influence of temperature on thermal conductivity, thermal capacity and thermal diffusivity for different types of rock," *Physics and Chemistry of the Earth*, vol. 28, no. 9-11, pp. 499–509, 2003.

[9] H. Kanamori, N. Fujii, and H. Mizutani, "Thermal diffusivity measurement of rock-forming minerals from 300° to 1100°K," *Journal of Geophysical Reasearch*, vol. 73, pp. 595–605, 1968.

[10] A. M. A. El Sayed, "Thermophysical study of sandstone reservoir rocks," *Journal of Petroleum Science and Engineering*, vol. 76, no. 3-4, pp. 138–147, 2011.

[11] D. Wang, X. Lu, Y. Song, R. Shao, and T. Qi, "Influence of the temperature dependence of thermal parameters of heat conduction models on the reconstruction of thermal history of igneous-intrusion-bearing basins," *Computers and Geosciences*, vol. 36, no. 10, pp. 1339–1344, 2010.

[12] F. Ni, G. Q. Gu, and K. M. Chen, “Effective thermal conductivity of nonlinear composite media with contact resistance,” *International Journal of Heat and Mass Transfer*, vol. 40, no. 4, pp. 943–949, 1997.

[13] E.-B. Wei and Y. M. Poon, “Effective thermal conductivity of graded nonlinear composites with heat contact resistance,” *Physics Letters A*, vol. 359, no. 6, pp. 685–692, 2006.

[14] E. Monteiro, J. Yvonnet, and Q. C. He, “Computational homogenization for nonlinear conduction in heterogeneous materials using model reduction,” *Computational Materials Science*, vol. 42, no. 4, pp. 704–712, 2008.

[15] A. H. Muliana and J. S. Kim, “A two-scale homogenization framework for nonlinear effective thermal conductivity of laminated composites,” *Acta Mechanica*, vol. 212, no. 3-4, pp. 319–347, 2010.

[16] Z. Li, “An overview of the immersed interface method and its applications,” *Taiwanese Journal of Mathematics*, vol. 7, no. 1, pp. 1–49, 2003.

[17] Z. Li and K. Ito, *The Immersed Interface Method: Numerical Solutions of PDEs Involving Interfaces and Irregular Domains*, vol. 33 of *Frontiers in Applied Mathematics*, SIAM, Philadelphia, Pa, USA, 2006.

[18] D. P. Do and D. Hoxha, “Effective transfer properties of partially saturated geomaterials with interfaces using immersed interface method,” *International Journal for Numerical and Analytical Methods in Geomechanics*, 2013.

[19] K. Ito and Z. Li, “Solving a nonlinear problem in magneto-rheological fluids using the immersed interface method,” *Journal of Scientific Computing*, vol. 19, no. 1-3, pp. 253–266, 2003.

[20] D. P. Do, D. Hoxha, S. Wu, and N. Belayachi, “Numerical homogenization of transfer properties of heterogeneous media by immersed interface method,” in *Proceedings of the 6th European Congrees on Computational Methods in Applied Sciences and Engineering (ECCOMAS ’12)*, Vienna, Austria, 2012.

[21] R. J. LeVeque and Z. L. Li, “The immersed interface method for elliptic equations with discontinuous coefficients and singular sources,” *SIAM Journal on Numerical Analysis*, vol. 31, no. 4, pp. 1019–1044, 1994.

[22] A. Alzina, E. Toussaint, A. Béakou, and B. Skoczen, “Multiscale modelling of thermal conductivity in composite materials for cryogenic structures,” *Composite Structures*, vol. 74, no. 2, pp. 175–185, 2006.

[23] L. Gao and Z.-Y. Li, “Nonlinear thermal conductivity of granular composite medium,” *Solid State Communications*, vol. 100, no. 1, pp. 53–56, 1996.

[24] A. Ghobeity, A. S. Deakin, and J. R. Dryden, “Thermal field around a partially debonded spherical particle,” *International Journal of Heat and Mass Transfer*, vol. 50, no. 3-4, pp. 680–686, 2007.

[25] S. Kim, M. C. Kim, and K. Y. Kim, “Non-iterative estimation of temperature-dependent thermal conductivity without internal measurements,” *International Journal of Heat and Mass Transfer*, vol. 46, no. 10, pp. 1801–1810, 2003.

[26] J. A. Kołodziej and A. Uściłowska, “Application of MFS for determination of effective thermal conductivity of unidirectional composites with linearly temperature dependent conductivity of constituents,” *Engineering Analysis with Boundary Elements*, vol. 36, no. 3, pp. 293–302, 2012.

[27] K. Gorgtilti, Y. S. Durutürk, A. Demirci, and B. Poyraz, “Influences of uniaxial stress and moisture content on the thermal conductivity of rocks,” *International Journal of Rock Mechanics and Mining Sciences*, vol. 45, no. 8, pp. 1439–1445, 2008.

[28] Z. Abdulagatova, I. M. Abdulagatov, and V. N. Emirov, “Effect of temperature and pressure on the thermal conductivity of sandstone,” *International Journal of Rock Mechanics and Mining Sciences*, vol. 46, no. 6, pp. 1055–1071, 2009.

[29] A. Demirci, K. Görgülü, and Y. S. Durutürk, “Thermal conductivity of rocks and its variation with uniaxial and triaxial stress,” *International Journal of Rock Mechanics and Mining Sciences*, vol. 41, no. 7, pp. 1133–1138, 2004.

Hindawi Publishing Corporation
Journal of Applied Mathematics
Volume 2013, Article ID 739068, 10 pages
http://dx.doi.org/10.1155/2013/739068

Research Article

A Mathematical Approach to Establishing Constitutive Models for Geomaterials

Guang-hua Yang,[1] Yu-xin Jie,[2] and Guang-xin Li[2]

[1] *Guangdong Provincial Research Institute of Water Conservancy and Hydropower, Guangzhou 510610, China*
[2] *State Key Laboratory of Hydroscience and Engineering, Tsinghua University, Beijing 100084, China*

Correspondence should be addressed to Yu-xin Jie; jieyx@tsinghua.edu.cn

Received 1 March 2013; Accepted 25 May 2013

Academic Editor: Pengcheng Fu

The mathematical foundation of the traditional elastoplastic constitutive theory for geomaterials is presented from the mathematical point of view, that is, the expression of stress-strain relationship in principal stress/strain space being transformed to the expression in six-dimensional space. A new framework is then established according to the mathematical theory of vectors and tensors, which is applicable to establishing elastoplastic models both in strain space and in stress space. Traditional constitutive theories can be considered as its special cases. The framework also enables modification of traditional constitutive models.

1. Introduction

The mechanical properties of geomaterials are complex and essential to make a numerical prediction; thus, many researchers have paid attention to constitutive relations of geomaterials. The simplest constitutive model for geomaterials is the elastic model, among which the common nonlinear models are the Cauchy elastic model, the hyperelastic model, and the hypoelastic model. The Cauchy elastic model assumes that the stress (or strain) in the material depends on the current strain (or stress) only, and not on its history. The constitutive equation for the hyperelastic model is established by the strain energy function or complement energy function. The hypoelastic model assumes that the stress state of an elastic material is associated with both the strain state and the stress path. The typical hypoelastic models are the E-μ and E-B models proposed by Duncan et al. [1, 2] and the K-G model [3–5].

According to the experimental results, most deformations of geomaterials are plastic deformations. Therefore, traditional plasticity theory has often been used to establish constitutive models for soil. For example, Drucker et al. [6] described the deformation property of soil by traditional elastoplastic theory and proposed a model with conical yield surface affected by hydrostatic pressure. Roscoe et al. [7] proposed a plastic cap model for normally consolidated clay, which is well known as the Cambridge model. Subsequently, Roscoe and Burland [8] modified the dilatancy equation in the Cambridge model and proposed a modified Cambridge model with elliptical yield surface. Wroth and Bassett [9] and Poorooshasb et al. [10] extended the model to sandy soil, and Yao et al. [11, 12] extended the model to sandy soil and overconsolidated soil. There are plenty of elastoplastic models, such as models with a single yield surface proposed by Desai et al. [13, 14] and Lade et al. [15–18], models with a double yield surface, and three surface models [19]. The concepts of the bounding surface [20–23] and the subloading surface [24, 25], endochronic theory [26], and disturbed states [27] have also been applied to establishing constitutive models for geomaterials.

In this paper, a theoretical framework on establishing constitutive models for geomaterials is proposed, the initial thought of which is provided by the first author in 1988 and in 1990s [28–31], and it has been implemented by some researchers to simulate the behavior of jointed rock masses [32] and soil-structure interface [33].

2. Classical Elastoplastic Theory of Geomaterials

The incremental form of a stress-strain relationship in traditional geomechanics is generally expressed as

$$\mathrm{d}\sigma_{ij} = D_{ijkl}\mathrm{d}\varepsilon_{kl}. \tag{1}$$

Determining D_{ijkl} is the major topic for constitutive models of geomaterials. Obviously, D_{ijkl} can be obtained by fitting experimental data, given that experiments on stress and strain tensors are conducted. However, it is extremely difficult to do so. Therefore, experiments on the stress-strain relationship of geomaterials are usually conducted in principal stress/strain space; that is, only the relationship between the principal stress σ_i ($i = 1, 2, 3$) and the principal strain ε_i ($i = 1, 2, 3$), is obtained. To obtain D_{ijkl}, the constitutive tensor in general coordinate space should be derived from the stress-strain relationship in principal stress/strain space. From a mathematical point of view, these can be treated as the problems of coordinate transformation [34–36].

The relationship between the plastic strain increment and stress increment in principal stress/strain space is defined as

$$\left\{\mathrm{d}\varepsilon_i^p\right\}_{3\times1} = [A]_{3\times3}\{\mathrm{d}\sigma_i\}_{3\times1}, \tag{2a}$$

$$[A]_{3\times3} = \begin{bmatrix} a_{11} & a_{12} & a_{13} \\ a_{21} & a_{22} & a_{23} \\ a_{31} & a_{32} & a_{33} \end{bmatrix}, \tag{2b}$$

where a_{ij} are the functions of total stress σ_i, total strain ε_i ($i = 1, 2, 3$) or stress path.

When the matrix rank of $[A]$ is 1, or $|A| = 0$, there exists a vector $\{\alpha_1 \ \ \alpha_2 \ \ \alpha_3\}^T$ and coefficients β_1, β_2, β_3 to express $[A]$ as

$$[A] = \{\beta_1 \ \ \beta_2 \ \ \beta_3\}^T \{\alpha_1 \ \ \alpha_2 \ \ \alpha_3\}, \tag{3}$$

Therefore, substituting (3) into (2a) and (2b) gives

$$\left\{\mathrm{d}\varepsilon_i^p\right\} = \{\beta_1 \ \ \beta_2 \ \ \beta_3\}^T \{\alpha_1 \ \ \alpha_2 \ \ \alpha_3\} \{\mathrm{d}\sigma_i\}, \tag{4a}$$

that is,

$$\left\{\mathrm{d}\varepsilon_i^p\right\} = \mathrm{d}\lambda\{\beta_1 \ \ \beta_2 \ \ \beta_3\}^T, \tag{4b}$$

where

$$\mathrm{d}\lambda = \sum_{i=1}^{3}\alpha_i \mathrm{d}\sigma_i. \tag{5}$$

According to (4b),

$$\mathrm{d}\varepsilon_1^p : \mathrm{d}\varepsilon_2^p : \mathrm{d}\varepsilon_3^p = \beta_1 : \beta_2 : \beta_3. \tag{6}$$

β_i ($i = 1, 2, 3$) is a function of σ_i or ε_i. When $\boldsymbol{\beta} = \{\beta_1 \ \ \beta_2 \ \ \beta_3\}^T$ is of a field with potential, there is a potential function Q such that

$$\beta_i = \frac{\partial Q}{\partial \sigma_i}. \tag{7}$$

Substituting (7) into (4b), we have

$$\mathrm{d}\varepsilon_i^p = \mathrm{d}\lambda\frac{\partial Q}{\partial \sigma_i}. \tag{8}$$

If we assume that $\mathrm{d}\varepsilon_i^p$ and σ_i have the same principal directions, the coordinate transformation can be expressed as follows:

$$\mathrm{d}\varepsilon_{ij}^p = \mathrm{d}\varepsilon_i^p\frac{\partial \sigma_i}{\partial \sigma_{ij}}. \tag{9}$$

Substituting (9) into (8) gives

$$\mathrm{d}\varepsilon_{ij}^p = \mathrm{d}\lambda\frac{\partial Q}{\partial \sigma_{ij}}. \tag{10}$$

Similarly, from elastic potentials theory, there is a potential function W in principal stress space, and ε_i is defined as

$$\varepsilon_i = \frac{\partial W}{\partial \sigma_i}. \tag{11}$$

If we assume that σ_i and ε_i have the same principal direction, the coordinate transformation can be expressed as follows:

$$\varepsilon_{ij} = \varepsilon_i\frac{\partial \sigma_i}{\partial \sigma_{ij}}. \tag{12}$$

Substituting (11) into (12),

$$\varepsilon_{ij} = \frac{\partial W}{\partial \sigma_{ij}}. \tag{13}$$

In conclusion, traditional plastic potential theory corresponds to the case that the matrix $[A]$ in (2a) and (2b) has rank 1, and $\boldsymbol{\beta}$ can be expressed as the gradient vector of a potential function. Based on mathematical principles, a more general potential function-based constitutive framework can be established according to vector field theory and tensor theory as described below.

3. Derivation of Constitutive Framework from Vector Field Theory

Obviously, when the three principal components of the plastic strain increment, $\mathrm{d}\varepsilon_i^p$ ($i = 1, 2, 3$), are considered to be components of a vector $\mathbf{d}\boldsymbol{\varepsilon}^{\mathbf{p}}$, the principal components can be expressed as three linearly independent 3D vectors by a vector fitting method. The gradient vectors of three linearly independent potential functions are selected as the linearly independent vectors.

When $\mathbf{d}\boldsymbol{\varepsilon}^{\mathbf{p}}$ is expressed in principal stress space, the coordinate orientations of $\mathbf{d}\boldsymbol{\varepsilon}^{\mathbf{p}}$ and σ_i are the same, and Φ_1, Φ_2, Φ_3 are three linearly independent potential functions in principal stress space, and then the following expression is obtained:

$$\mathrm{d}\varepsilon_i^p = \sum_{k=1}^{3}\lambda_k\frac{\partial \Phi_k}{\partial \sigma_i}, \tag{14}$$

where λ_k $(i = 1, 2, 3)$ are the coefficients. Suppose that the principal directions of $\mathbf{d\varepsilon^p}$ and σ_i are the same, and we substitute (14) into (9), giving the tensor expression in general coordinate space as

$$d\varepsilon_{ij}^{p} = \sum_{k=1}^{3} \lambda_k \frac{\partial \Phi_k}{\partial \sigma_{ij}}. \tag{15}$$

Similarly, $\mathbf{d\varepsilon^p}$ can also be expressed in strain space. Let Ψ_1, Ψ_2, Ψ_3 be three linearly independent potential functions in principal strain space, and the following expression is obtained:

$$d\varepsilon_{ij}^{p} = \sum_{k=1}^{3} \mu_k \frac{\partial \Psi_k}{\partial \varepsilon_{ij}}. \tag{16}$$

Define the plastic stress increment as

$$\{d\sigma^{p}\} = [D_e]\{d\varepsilon^{p}\}, \tag{17}$$

where $[D_e]$ is the elastic stiffness matrix, and then the expressions in stress space and strain space are

$$d\sigma_{ij}^{p} = \sum_{k=1}^{3} \beta_k \frac{\partial G_k}{\partial \sigma_{ij}}, \tag{18}$$

$$d\sigma_{ij}^{p} = \sum_{k=1}^{3} \alpha_k \frac{\partial F_k}{\partial \varepsilon_{ij}}. \tag{19}$$

For the total stress and the total strain, consider the three principal stresses and the three principal strains as vectors in three-dimensional space with the same principal directions, and the following expressions are obtained:

$$\begin{aligned} \sigma_{ij} &= \sum_{k=1}^{3} \eta_k \frac{\partial W_k}{\partial \varepsilon_{ij}}, \\ \varepsilon_{ij} &= \sum_{k=1}^{3} \chi_k \frac{\partial \Omega_k}{\partial \sigma_{ij}}, \end{aligned} \tag{20}$$

where W_k, Ω_k $(i = 1, 2, 3)$ are potential functions with linearly independent gradient vectors in strain space and stress space, respectively.

4. Derivation of Constitutive Framework from Tensor Theory

If A_{ij} and E_{ij} are symmetric second-order tensors with the same principal directions, the following equations are obtained according to tensor theory and vector fitting:

$$A_{ij} = \sum_{k=1}^{3} \overline{\lambda}_k \frac{\partial I_{Ek}}{\partial E_{ij}}, \tag{21}$$

$$E_{ij} = \sum_{k=1}^{3} \overline{\beta}_k \frac{\partial I_{Ak}}{\partial A_{ij}}, \tag{22}$$

where I_{Ek} $(k = 1, 2, 3)$ are three independent invariants of E_{ij}, and I_{Ak} $(k = 1, 2, 3)$ are three independent invariants of A_{ij}. For example, for the stress tensor σ_{ij}, the three independent invariants can be $I_{\sigma 1} = \sigma_{ii}$, $I_{\sigma 2} = (1/2)\sigma_{ij}\sigma_{ji}$, $I_{\sigma 3} = (1/3)\sigma_{ik}\sigma_{kn}\sigma_{nm}$; $I_{\sigma 1} = p$, $I_{\sigma 2} = q$, $I_{\sigma 3} = \theta$; or $I_{\sigma 1} = \sigma_1$, $I_{\sigma 2} = \sigma_2$, $I_{\sigma 3} = \sigma_3$, where p is the mean stress, q is the deviatoric stress, θ is the Lode's angle, and σ_1, σ_2, and σ_3 are the three principal stresses.

If $A_{ij} = d\varepsilon_{ij}^{p}$, $E_{ij} = \sigma_{ij}$, $I_{\sigma k}$ $(k = 1, 2, 3)$ are invariants of σ_{ij}, it can be obtained from (21) that

$$d\varepsilon_{ij}^{p} = \sum_{k=1}^{3} \overline{\lambda}_k \frac{\partial I_{\sigma k}}{\partial \sigma_{ij}}, \tag{23}$$

which is equivalent to (15) when $\Phi_k = I_{\sigma k}$.

If $A_{ij} = d\varepsilon_{ij}^{p}$, $E_{ij} = \varepsilon_{ij}$, $I_{\varepsilon k}$ $(k = 1, 2, 3)$ are invariants of ε_{ij}, then

$$d\varepsilon_{ij}^{p} = \sum_{k=1}^{3} \overline{\alpha}_k \frac{\partial I_{\varepsilon k}}{\partial \varepsilon_{ij}}. \tag{24}$$

If $A_{ij} = \varepsilon_{ij}$, $E_{ij} = \sigma_{ij}$, then

$$\begin{aligned} \sigma_{ij} &= \sum_{k=1}^{3} \overline{\beta}_k \frac{\partial I_{\varepsilon k}}{\partial \varepsilon_{ij}}, \\ \varepsilon_{ij} &= \sum_{k=1}^{3} \overline{\lambda}_k \frac{\partial I_{\sigma k}}{\partial \sigma_{ij}}. \end{aligned} \tag{25}$$

Equation (25) corresponds to (20), respectively, when $W_k = I_{\varepsilon k}$, $\Omega_k = I_{\sigma k}$.

Similarly, if $A_{ij} = \Delta\varepsilon_{ij}$, $E_{ij} = \Delta\sigma_{ij}$, then according to (21), we have

$$\Delta\varepsilon_{ij} = \sum_{k=1}^{3} \overline{\lambda}_k \frac{\partial I_{\sigma k}}{\partial (\Delta\sigma_{ij})}. \tag{26}$$

It should be noted that the derivations from vector field theory and from tensor theory are actually coincident. The potential functions in the derivation from vector field theory are functions of invariants, which degenerate to tensor form after composite derivation.

5. Elastoplastic Matrix in Stress Space

Without considering the effect of the Lode's angle θ and rotation of principal stress, the relations for the plastic strain increment and stress increment are expressed as

$$d\varepsilon_{v}^{p} = A\,dp + B\,dq, \tag{27a}$$

$$d\overline{\varepsilon}^{p} = C\,dp + D\,dq, \tag{27b}$$

where A, B, C, D are parameters.

The following equation is obtained from the potential functions $\Phi_1 = p$, $\Phi_2 = q$ in (15) without considering the effect of the Lode's angle:

$$d\varepsilon_{ij}^{p} = \lambda_1 \frac{\partial p}{\partial \sigma_{ij}} + \lambda_2 \frac{\partial q}{\partial \sigma_{ij}}. \tag{28}$$

In matrix form, this is

$$\{\mathrm{d}\varepsilon^{p}\} = \lambda_1 \left\{\frac{\partial p}{\partial \sigma}\right\} + \lambda_2 \left\{\frac{\partial q}{\partial \sigma}\right\}. \tag{29}$$

It is obvious that

$$\lambda_1 = \mathrm{d}\varepsilon_v^{p}, \qquad \lambda_2 = \mathrm{d}\bar{\varepsilon}^{p}. \tag{30}$$

According to (27a), (27b), (29), and (30),

$$\{\mathrm{d}\varepsilon^{p}\} = (A\mathrm{d}p + B\mathrm{d}q)\left\{\frac{\partial p}{\partial \sigma}\right\} + (C\mathrm{d}p + D\mathrm{d}q)\left\{\frac{\partial q}{\partial \sigma}\right\}. \tag{31}$$

Since

$$\mathrm{d}p = \left\{\frac{\partial p}{\partial \sigma}\right\}^{T}\{\mathrm{d}\sigma\}, \qquad \mathrm{d}q = \left\{\frac{\partial q}{\partial \sigma}\right\}^{T}\{\mathrm{d}\sigma\}, \tag{32}$$

it follows that

$$\{\mathrm{d}\varepsilon^{p}\} = \left[C_p^{\sigma}\right]\{\mathrm{d}\sigma\}, \tag{33a}$$

$$\begin{aligned}\left[C_p^{\sigma}\right] = {} & A\left\{\frac{\partial p}{\partial \sigma}\right\}\left\{\frac{\partial p}{\partial \sigma}\right\}^{T} + B\left\{\frac{\partial p}{\partial \sigma}\right\}\left\{\frac{\partial q}{\partial \sigma}\right\}^{T} \\ & + C\left\{\frac{\partial q}{\partial \sigma}\right\}\left\{\frac{\partial p}{\partial \sigma}\right\}^{T} + D\left\{\frac{\partial q}{\partial \sigma}\right\}\left\{\frac{\partial q}{\partial \sigma}\right\}^{T},\end{aligned} \tag{33b}$$

where $[C_p^{\sigma}]$ is the plastic compliance matrix.

Since $\{\mathrm{d}\varepsilon\} = \{\mathrm{d}\varepsilon^{e}\} + \{\mathrm{d}\varepsilon^{p}\}$, then

$$\{\mathrm{d}\varepsilon\} = \left[C_{ep}^{\sigma}\right]\{\mathrm{d}\sigma\}, \tag{34a}$$

where

$$\left[C_{ep}^{\sigma}\right] = \left[C_e\right] + \left[C_p^{\sigma}\right]. \tag{34b}$$

$[C_e]$ is the elastic compliance matrix and $[C_{ep}^{\sigma}]$ is the elastoplastic compliance matrix.

Therefore, the elastoplastic model in stress space can be established once the parameters A, B, C, and D are determined. Note that A, B, C, and D are not constants, which evolve with stress and strain, as presented in the following sections.

6. Elastoplastic Matrix in Strain Space

According to (17), the plastic stress increment is defined as $\{\mathrm{d}\sigma^{p}\} = [D_e]\{\mathrm{d}\varepsilon^{p}\}$, where $[D_e]$ is the elastic matrix and $\{\mathrm{d}\varepsilon^{p}\}$ is the plastic strain increment.

ε_v, $\bar{\varepsilon}$, and ψ are three invariants of the strain tensor, where ψ is the strain Lode's angle. If we ignore the effect of Lode's angle and take ε_v and $\bar{\varepsilon}$ as potential functions, that is, $F_1 = \varepsilon_v$, $F_2 = \bar{\varepsilon}$ in (19), then

$$\mathrm{d}\sigma_{ij}^{p} = \lambda_1 \frac{\partial \varepsilon_v}{\partial \varepsilon_{ij}} + \lambda_2 \frac{\partial \bar{\varepsilon}}{\partial \varepsilon_{ij}}. \tag{35}$$

Written in matrix form,

$$\{\mathrm{d}\sigma^{p}\} = \lambda_1 \left\{\frac{\partial \varepsilon_v}{\partial \varepsilon}\right\} + \lambda_2 \left\{\frac{\partial \bar{\varepsilon}}{\partial \varepsilon}\right\}. \tag{36}$$

Obviously,

$$\lambda_1 = \mathrm{d}p^{p}, \qquad \lambda_2 = \mathrm{d}q^{p}. \tag{37}$$

From the definition of (17),

$$\mathrm{d}p^{p} = K_e \mathrm{d}\varepsilon_v^{p} = K_e\left(\mathrm{d}\varepsilon_v - \mathrm{d}\varepsilon_v^{e}\right) = K_e \mathrm{d}\varepsilon_v - \mathrm{d}p, \tag{38a}$$

$$\mathrm{d}q^{p} = 3G_e \mathrm{d}\bar{\varepsilon}^{p} = 3G_e\left(\mathrm{d}\bar{\varepsilon} - \mathrm{d}\bar{\varepsilon}^{e}\right) = 3G_e \mathrm{d}\bar{\varepsilon} - \mathrm{d}q, \tag{38b}$$

where K_e, G_e are the elastic bulk modulus and shear modulus.

Considering

$$\mathrm{d}\varepsilon_v^{e} = \frac{1}{K_e}\mathrm{d}p, \tag{39a}$$

$$\mathrm{d}\bar{\varepsilon}^{e} = \frac{1}{3G_e}\mathrm{d}q, \tag{39b}$$

substituting (39a) and (39b) into (27a) and (27b) yields

$$\mathrm{d}\varepsilon_v = \left(\frac{1}{K_e} + A\right)\mathrm{d}p + B\mathrm{d}q, \tag{40a}$$

$$\mathrm{d}\bar{\varepsilon} = C\mathrm{d}p + \left(\frac{1}{3G_e} + D\right)\mathrm{d}q. \tag{40b}$$

It can now be calculated that

$$\mathrm{d}p = \bar{A}\mathrm{d}\varepsilon_v + \bar{B}\mathrm{d}\bar{\varepsilon}, \tag{41a}$$

$$\mathrm{d}q = \bar{C}\mathrm{d}\varepsilon_v + \bar{D}\mathrm{d}\bar{\varepsilon}, \tag{41b}$$

where

$$\begin{gathered}\bar{A} = \frac{1}{|A|}\left(D + \frac{1}{3G_e}\right), \qquad \bar{B} = -\frac{B}{|A|}, \qquad \bar{C} = -\frac{C}{|A|}, \\ \bar{D} = \frac{1}{|A|}\left(A + \frac{1}{K_e}\right), \\ |A| = \frac{3DG_e + AK_e + 1}{3K_eG_e} + (AD - BC).\end{gathered} \tag{42}$$

Substituting (41a) and (41b) into (37), (38a), and (38b) gives

$$\lambda_1 = \mathrm{d}p^{p} = \left(K_e - \bar{A}\right)\mathrm{d}\varepsilon_v - \bar{B}\mathrm{d}\bar{\varepsilon}, \tag{43a}$$

$$\lambda_2 = \mathrm{d}q^{p} = -\bar{C}\mathrm{d}\varepsilon_v + \left(3G_e - \bar{D}\right)\mathrm{d}\bar{\varepsilon}. \tag{43b}$$

In addition,

$$\mathrm{d}\varepsilon_v = \left\{\frac{\partial \varepsilon_v}{\partial \varepsilon}\right\}^{T}\{\mathrm{d}\varepsilon\}, \qquad \mathrm{d}\bar{\varepsilon} = \left\{\frac{\partial \bar{\varepsilon}}{\partial \varepsilon}\right\}^{T}\{\mathrm{d}\varepsilon\}. \tag{44}$$

Substituting (44) into (43a), (43b), and (36) yields

$$\{\mathrm{d}\sigma^{p}\} = \left[D_p^{\varepsilon}\right]\{\mathrm{d}\varepsilon\}, \tag{45a}$$

where

$$\left[D_p^\varepsilon\right] = \left(K_e - \overline{A}\right)\left\{\frac{\partial\varepsilon_v}{\partial\varepsilon}\right\}\left\{\frac{\partial\varepsilon_v}{\partial\varepsilon}\right\}^T - \overline{B}\left\{\frac{\partial\varepsilon_v}{\partial\varepsilon}\right\}\left\{\frac{\partial\overline{\varepsilon}}{\partial\varepsilon}\right\}^T - \overline{C}\left\{\frac{\partial\overline{\varepsilon}}{\partial\varepsilon}\right\}\left\{\frac{\partial\varepsilon_v}{\partial\varepsilon}\right\}^T + \left(3G_e - \overline{D}\right)\left\{\frac{\partial\overline{\varepsilon}}{\partial\varepsilon}\right\}\left\{\frac{\partial\overline{\varepsilon}}{\partial\varepsilon}\right\}^T, \tag{45b}$$

that is,

$$\left[D_p^\varepsilon\right] = \frac{1}{|A|}\left\{\alpha A\left\{\frac{\partial\varepsilon_v}{\partial\varepsilon}\right\}\left\{\frac{\partial\varepsilon_v}{\partial\varepsilon}\right\}^T + B\left\{\frac{\partial\varepsilon_v}{\partial\varepsilon}\right\}\left\{\frac{\partial\overline{\varepsilon}}{\partial\varepsilon}\right\}^T + C\left\{\frac{\partial\overline{\varepsilon}}{\partial\varepsilon}\right\}\left\{\frac{\partial\varepsilon_v}{\partial\varepsilon}\right\}^T + \frac{D}{\alpha}\left\{\frac{\partial\overline{\varepsilon}}{\partial\varepsilon}\right\}\left\{\frac{\partial\overline{\varepsilon}}{\partial\varepsilon}\right\}^T\right\}, \tag{45c}$$

where $\alpha = K_e/3G_e = 2(1+\mu_e)/9(1-2\mu_e)$, and μ_e is the elastic Poisson ratio.

Hence, the total stress increment can be expressed as

$$\begin{aligned}\{\mathrm{d}\sigma\} &= \left[D_e\right]\{\mathrm{d}\varepsilon^e\} = \left[D_e\right](\{\mathrm{d}\varepsilon\} - \{\mathrm{d}\varepsilon^p\}) \\ &= \left[D_e\right]\{\mathrm{d}\varepsilon\} - \{\mathrm{d}\sigma^p\} = \left[D_e\right]\{\mathrm{d}\varepsilon\} - \left[D_p^\varepsilon\right]\{\mathrm{d}\varepsilon\} \\ &= \left[D_{ep}^\varepsilon\right]\{\mathrm{d}\varepsilon\},\end{aligned} \tag{46a}$$

where

$$\left[D_{ep}^\varepsilon\right] = \left[D_e\right] - \left[D_p^\varepsilon\right]. \tag{46b}$$

The duality of stress and strain is evident in (45a), (45b), (45c), (33a), and (33b).

It should be noted that it is practically impossible to obtain the total strain in soil, and thus the elastoplastic matrix in stress space is more applicable. However, if we could further extend the framework to the space of strain increment, the practicability becomes promising.

7. Relationship with Traditional Elastoplastic Model

7.1. General Form. The elastoplastic compliance matrix of the traditional elastoplastic model is

$$\left[C_{ep}^\sigma\right] = \left[C_e\right] + \frac{1}{A_H}\left\{\frac{\partial g}{\partial\sigma}\right\}\left\{\frac{\partial f}{\partial\sigma}\right\}^T, \tag{47}$$

where f and g are the yield function and plastic potential function, $A_H = -\partial f/\partial H\{\partial H/\partial\varepsilon^p\}^T\{\partial g/\partial\sigma\}$ is the plastic hardening modulus, and H is the hardening parameter.

f and g are usually expressed in terms of the stress invariants, p, q, θ. If the effect of the Lode's angle θ is not considered, the expression only concerns p and q, that is,

$$\left\{\frac{\partial f}{\partial\sigma}\right\} = \frac{\partial f}{\partial p}\left\{\frac{\partial p}{\partial\sigma}\right\} + \frac{\partial f}{\partial q}\left\{\frac{\partial q}{\partial\sigma}\right\}, \tag{48a}$$

$$\left\{\frac{\partial g}{\partial\sigma}\right\} = \frac{\partial g}{\partial p}\left\{\frac{\partial p}{\partial\sigma}\right\} + \frac{\partial g}{\partial q}\left\{\frac{\partial q}{\partial\sigma}\right\}. \tag{48b}$$

Substituting (48a) and (48b) into (47), we have

$$\begin{aligned}\left[C_{ep}^\sigma\right] &= \left[C_e\right] + \frac{1}{A_H} \\ &\times \left\{\frac{\partial g}{\partial p}\frac{\partial f}{\partial p}\left\{\frac{\partial p}{\partial\sigma}\right\}\left\{\frac{\partial p}{\partial\sigma}\right\}^T + \frac{\partial g}{\partial p}\frac{\partial f}{\partial q}\left\{\frac{\partial p}{\partial\sigma}\right\}\left\{\frac{\partial q}{\partial\sigma}\right\}^T\right. \\ &\left. + \frac{\partial g}{\partial q}\frac{\partial f}{\partial p}\left\{\frac{\partial q}{\partial\sigma}\right\}\left\{\frac{\partial p}{\partial\sigma}\right\}^T + \frac{\partial g}{\partial q}\frac{\partial f}{\partial q}\left\{\frac{\partial q}{\partial\sigma}\right\}\left\{\frac{\partial q}{\partial\sigma}\right\}^T\right\}.\end{aligned} \tag{49}$$

Comparing this with (33a), (33b), (34a), and (34b), it follows that

$$A = \frac{1}{A_H}\frac{\partial g}{\partial p}\frac{\partial f}{\partial p}, \qquad B = \frac{1}{A_H}\frac{\partial g}{\partial p}\frac{\partial f}{\partial q}, \qquad C = \frac{1}{A_H}\frac{\partial g}{\partial q}\frac{\partial f}{\partial p}, \qquad D = \frac{1}{A_H}\frac{\partial g}{\partial q}\frac{\partial f}{\partial q}. \tag{50a}$$

Equation (33a) and (33b) can be seen as a general formula for traditional constitutive models, and (49) is a special form of (33a) and (33b). For associated models, when $f = g$,

$$A = \frac{1}{A_H}\left(\frac{\partial f}{\partial p}\right)^2, \qquad B = C = \frac{1}{A_H}\frac{\partial f}{\partial p}\frac{\partial f}{\partial q}, \qquad D = \frac{1}{A_H}\left(\frac{\partial f}{\partial q}\right)^2. \tag{50b}$$

Most traditional constitutive models are to determine the relationship between f, g and p, q, which can be used to calculate the four model parameters A, B, C, and D indirectly. It can be seen from (50a) and (50b) that the traditional nonassociated models actually assume that

$$AD - BC = 0. \tag{51a}$$

The associated models still need to satisfy (51a) and also require

$$B = C. \tag{51b}$$

Rewrite (27a) and (27b) into matrix form

$$\begin{Bmatrix}\mathrm{d}\varepsilon_v^p \\ \mathrm{d}\overline{\varepsilon}^p\end{Bmatrix} = \begin{bmatrix}A & B \\ C & D\end{bmatrix}\begin{Bmatrix}\mathrm{d}p \\ \mathrm{d}q\end{Bmatrix}. \tag{52}$$

Clearly (51a) requires the determinant rank of the coefficient matrix in (52) to be 1 or requires $\mathrm{d}\varepsilon_v^p$ and $\mathrm{d}\overline{\varepsilon}^p$ to be linearly correlated. Equation (51b) additionally requires the coefficient matrix to be symmetric.

The traditional elastoplastic model in stress space can be translated to strain space by the duality of (45a), (45b), (45c), (33a), and (33b). Substituting (50a) and (50b) into (42), (45a), (45b), and (45c) yields the expression in strain space

$$\left[D_{ep}^{\varepsilon}\right] = \left[D_e\right] - \frac{1}{\beta} \times \left\{ \alpha \frac{\partial g}{\partial p}\frac{\partial f}{\partial p} \left\{\frac{\partial \varepsilon_v}{\partial \varepsilon}\right\} \left\{\frac{\partial \varepsilon_v}{\partial \varepsilon}\right\}^T + \frac{\partial g}{\partial p}\frac{\partial f}{\partial q} \left\{\frac{\partial \varepsilon_v}{\partial \varepsilon}\right\} \left\{\frac{\partial \bar{\varepsilon}}{\partial \varepsilon}\right\}^T + \frac{\partial g}{\partial q}\frac{\partial f}{\partial p} \left\{\frac{\partial \varepsilon_v}{\partial \varepsilon}\right\} \left\{\frac{\partial \bar{\varepsilon}}{\partial \varepsilon}\right\}^T + \frac{1}{\alpha}\frac{\partial g}{\partial q}\frac{\partial f}{\partial q} \left\{\frac{\partial \bar{\varepsilon}}{\partial \varepsilon}\right\} \left\{\frac{\partial \bar{\varepsilon}}{\partial \varepsilon}\right\}^T \right\}, \tag{53a}$$

where

$$\beta = A_H \left|A\right| = \frac{1}{3G_e}\frac{\partial g}{\partial p}\frac{\partial f}{\partial p} + \frac{1}{K_e}\frac{\partial g}{\partial q}\frac{\partial f}{\partial q} + \frac{A_H}{3K_e G_e}. \tag{53b}$$

Hence, the stiffness matrix of (53a) and (53b) is obtained using f and g from the traditional constitutive models, and the transformation from stress space to strain space is thus achieved. Obviously, the transformation only changes the mathematical calculation method of the coefficient and elastoplastic matrices and has no influence on a particular model itself or the loading-unloading criterion of the model. Therefore, the transformation is applicable to all traditional elastoplastic models.

7.2. Modified Cambridge Model. In the modified Cambridge model,

$$f = g = p + \frac{q^2}{M^2 p} - p_0 e^{(1+e_0)/(\lambda-\kappa)H} = 0, \tag{54}$$

and so

$$\frac{\partial f}{\partial p} = 1 - \frac{\eta^2}{M^2}, \qquad \frac{\partial f}{\partial q} = \frac{2\eta}{M^2},$$
$$A_H = \frac{1+e_0}{\lambda-\kappa}\left(1 - \frac{\eta^2}{M^2}\right) p_0 e^{(1+e_0)/(\lambda-\kappa)H}, \tag{55}$$

where $\eta = q/p$, H is the hardening parameter ($= \varepsilon_v^p$, for the modified Cambridge model), M is the stress ratio at critical state, p_0 is the initial mean stress, e_0 is the initial void ratio, λ is the slope of the normal compression line (NCL), and κ is the slope of the unloading line. The elastoplastic compliance matrix in stress space is expressed as

$$\left[C_{ep}^{\sigma}\right] = \left[C_e\right] + \frac{1}{A_H} \times \left\{ \left(1 - \frac{\eta^2}{M^2}\right)^2 \left\{\frac{\partial p}{\partial \sigma}\right\} \left\{\frac{\partial p}{\partial \sigma}\right\}^T + \frac{2\eta}{M^2}\left(1 - \frac{\eta^2}{M^2}\right) \left\{\frac{\partial p}{\partial \sigma}\right\} \left\{\frac{\partial q}{\partial \sigma}\right\}^T + \frac{2\eta}{M^2}\left(1 - \frac{\eta^2}{M^2}\right) \left\{\frac{\partial q}{\partial \sigma}\right\} \left\{\frac{\partial p}{\partial \sigma}\right\}^T + \frac{4\eta^2}{M^4} \left\{\frac{\partial q}{\partial \sigma}\right\} \left\{\frac{\partial q}{\partial \sigma}\right\}^T \right\}. \tag{56}$$

The elastoplastic stiffness matrix in strain space is

$$\left[D_{ep}^{\varepsilon}\right] = \left[D_e\right] - \frac{1}{\beta} \times \left\{ \frac{K_e}{3G_e}\left(1 - \frac{\eta^2}{M^2}\right)^2 \left\{\frac{\partial \varepsilon_v}{\partial \varepsilon}\right\} \left\{\frac{\partial \varepsilon_v}{\partial \varepsilon}\right\}^T + \frac{2\eta}{M^2}\left(1 - \frac{\eta^2}{M^2}\right) \left\{\frac{\partial \varepsilon_v}{\partial \varepsilon}\right\} \left\{\frac{\partial \bar{\varepsilon}}{\partial \varepsilon}\right\}^T + \frac{2\eta}{M^2}\left(1 - \frac{\eta^2}{M^2}\right) \left\{\frac{\partial \varepsilon_v}{\partial \varepsilon}\right\} \left\{\frac{\partial \bar{\varepsilon}}{\partial \varepsilon}\right\}^T + \frac{3G_e}{K_e}\frac{4\eta^2}{M^4} \left\{\frac{\partial \bar{\varepsilon}}{\partial \varepsilon}\right\} \left\{\frac{\partial \bar{\varepsilon}}{\partial \varepsilon}\right\}^T \right\}, \tag{57a}$$

where

$$\beta = \frac{1}{3G_e}\left(1 - \frac{\eta^2}{M^2}\right)^2 + \frac{1}{K_e}\frac{4\eta^2}{M^4} + \frac{A_H}{3G_e K_e}. \tag{57b}$$

A new hardening parameter for the modified Cambridge model was proposed by Yao et al. [12] as

$$H = \int \mathrm{d}H = \int \frac{M_f^4 - \eta^4}{M^4 - \eta^4} \mathrm{d}\varepsilon_v^p = \int \frac{1}{\Omega} \mathrm{d}\varepsilon_v^p. \tag{58a}$$

in which

$$\Omega = \frac{M^4 - \eta^4}{M_f^4 - \eta^4}, \tag{58b}$$

where M_f is the potential failure stress ratio.

Yao improved the modified Cambridge model by replacing $H = \varepsilon_v^p$ with (58a) and (58b), which changes A_H in the modified Cambridge model to $(1/\Omega)A_H$. The improved constitutive model is a unified hardening model and is suitable for sandy soil, which actually replaces $\{\mathrm{d}\varepsilon^p\}$ by $\Omega\{\mathrm{d}\varepsilon^p\}$ with (49), or the following expression with (52):

$$\frac{\mathrm{d}\varepsilon_v^p}{\mathrm{d}\varepsilon_v^p\big|_c} = \frac{\mathrm{d}\bar{\varepsilon}^p}{\mathrm{d}\bar{\varepsilon}^p\big|_c} = \Omega = \frac{M^4 - \eta^4}{M_f^4 - \eta^4}, \tag{59}$$

where $\mathrm{d}\varepsilon_v^p\big|_c$, $\mathrm{d}\bar{\varepsilon}^p\big|_c$ are the volumetric strain and shear strain, respectively, that are calculated by the modified Cambridge model.

This modification can be further improved. For instance, the volumetric strain and shear strain of triaxial testing are first calculated by the modified Cambridge model, and then the ratio of the volumetric strain and shear strain can be fitted according to the test results, that is

$$\frac{\mathrm{d}\varepsilon_v^p}{\mathrm{d}\varepsilon_v^p\big|_c} = \xi\left(p, q\right), \qquad \frac{\mathrm{d}\bar{\varepsilon}^p}{\mathrm{d}\bar{\varepsilon}^p\big|_c} = \zeta\left(p, q\right). \tag{60}$$

Therefore, (52) is modified to

$$\begin{Bmatrix} \mathrm{d}\varepsilon_v^p \\ \mathrm{d}\bar{\varepsilon}^p \end{Bmatrix} = \begin{bmatrix} \xi A & \xi B \\ \zeta C & \zeta D \end{bmatrix} \begin{Bmatrix} \mathrm{d}p \\ \mathrm{d}q \end{Bmatrix}. \tag{61}$$

ξ and ζ can be estimated by polynomial fitting or other fitting methods. Yao's hardening model is obtained when $\xi = \zeta = (M^4 - \eta^4)/(M_f^4 - \eta^4)$.

The above-mentioned modification method can be extended to other elastoplastic models. The correction coefficients ξ and ζ can be fitted based on the triaxial testing results or other testing results. The obtained matrix can improve the calculation accuracy of existing elastoplastic models or be used to establish new modified models. Note that there is no physical mechanism involved in the framework, and thus the loading-unloading criterion and the evolution of internal state variables of the original model should still be employed in the modified one.

8. Application: A Simple Model

Theoretically, the constitutive model of soil would be established if the parameters A, B, C, and D in (27a), (27b), (33a), and (33b) are obtained by experiments such as conventional triaxial test, isotropic compression test, and p = Const. test.

For example, the equations for the tangent modulus E_t and tangential Poisson ratio μ_t are obtained by fitting the curve from triaxial testing, that is

$$E_t = \frac{\partial(\sigma_1 - \sigma_3)}{\partial \varepsilon_1}, \tag{62a}$$

$$\mu_t = -\frac{\partial \varepsilon_3}{\partial \varepsilon_1} = \frac{1}{2}\left(1 - \frac{\partial \varepsilon_v}{\partial \varepsilon_1}\right). \tag{62b}$$

E_t and μ_t can be curve fitted by a polynomial or by the formulae in the Duncan-Chang E-μ model [1]. However, two supplementary equations are needed as there are four unknown parameters in (27a) and (27b). Therefore, an isotropic compression test or p = Const. test should be conducted, or the assumptions $AD - BC = 0$ and $B = C$ are made.

In conventional triaxial test, $\sigma_3 = \text{Const}$, $\mathrm{d}p = (1/3)\mathrm{d}\sigma_1$, $\mathrm{d}q = \mathrm{d}\sigma_1$, $\mathrm{d}\varepsilon_v = \mathrm{d}\varepsilon_1 + \mathrm{d}\varepsilon_2 + \mathrm{d}\varepsilon_3 = (1 - 2\mu_t)\mathrm{d}\varepsilon_1$, and $\mathrm{d}\bar{\varepsilon} = (2/3)(1 + \mu_t)\mathrm{d}\varepsilon_1$. According to (62a), (62b), (27a), and (27b) and the assumption in (51a) and (51b), we have

$$A = \frac{K_{ep}^2}{\omega}, \qquad B = C = \frac{K_{ep}G_{ep}}{\omega}, \qquad D = \frac{G_{ep}^2}{\omega}, \tag{63a}$$

where

$$\begin{aligned} K_{ep} &= \frac{1 - 2\mu_t}{E_t} - \frac{1 - 2\mu_e}{E_e}, \\ G_{ep} &= \frac{2(1 + \mu_t)}{3E_t} - \frac{2(1 + \mu_e)}{3E_e}, \\ \omega &= G_{ep} + \frac{1}{3}K_{ep} = \frac{1}{E_t} - \frac{1}{E_e}. \end{aligned} \tag{63b}$$

E_e is the elastic modulus, and the elastic Poisson ratio μ_e is generally taken as 0.3 for soil. It is obvious that $\omega > 0$ is always fulfilled in (63a) and (63b).

By substituting (63a) and (63b) into (33a), (33b), or (35), the elastoplastic compliance matrix in stress space or the stiffness matrix in strain space is obtained. For convenience, we call this model the multiple potential surface model (MPS model).

It should be noted that, contrary to the Duncan-Chang model (DC model), E_t and μ_t in the MPS model are not limited by the generalized Hooke's law; that is, the MPS model is still available when $\mu_t > 0.5$ and the stiffness matrix of the model is not singular. Actually, E_t and μ_t in the new model are not the traditional modulus and Poisson ratio, but just the slope of the curves.

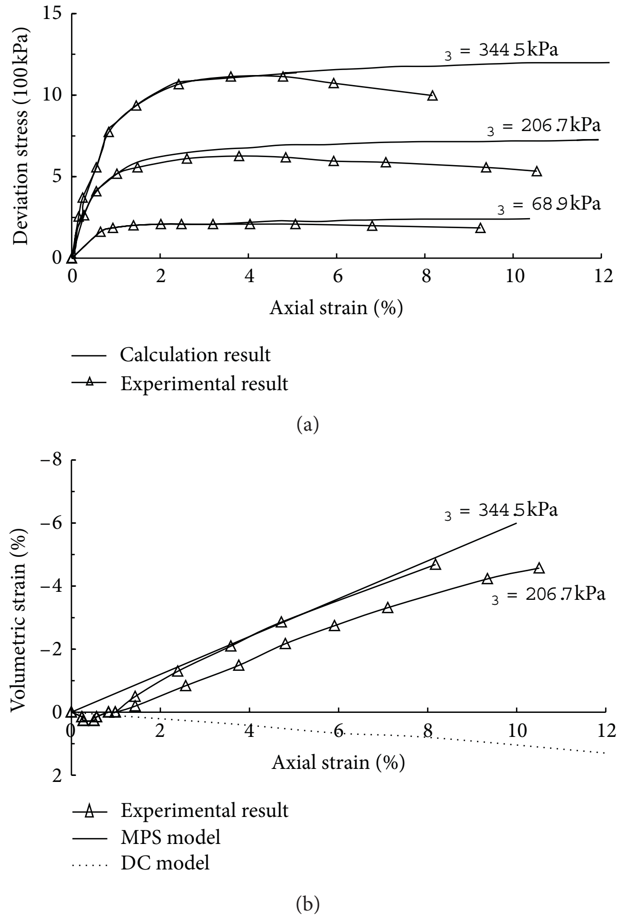

Figure 1: Calculation and test results for triaxial test of Ottawa silica sand.

Figure 1 shows the calculation and test results for triaxial testing of Ottawa silica sand conducted by Wu [37]. The unit weight of the sand is 16.8 kN/m^3 (=107 pcf). The test is a conventional consolidated-drained triaxial compression test (CD test). The confining pressures were 68.9, 206.7, and 344.5 kPa (= 10, 30, and 50 psi, resp.). During the CD test, confining pressure was firstly applied and then the specimen was consolidated. Deviation stress $(\sigma_1 - \sigma_3)$ was applied in the axial direction after consolidation. Variations of deviation stress and volumetric strain *versus* axial strain can be acquired in the test.

The calculations were made using the MPS model as well as the Duncan-Chang model, during which E_t, E_e, and μ_t were calculated by the method proposed by Duncan and Chang [1], that is

$$\begin{aligned} E_t &= \left[1 - \frac{R_f(1 - \sin\phi)(\sigma_1 - \sigma_3)}{2c\cos\phi + 2\sigma_3\sin\phi}\right]^2 K P_a \left(\frac{\sigma_3}{P_a}\right)^n, \\ E_e &= K_{ur} P_a \left(\frac{\sigma_3}{P_a}\right)^n, \end{aligned} \tag{64}$$

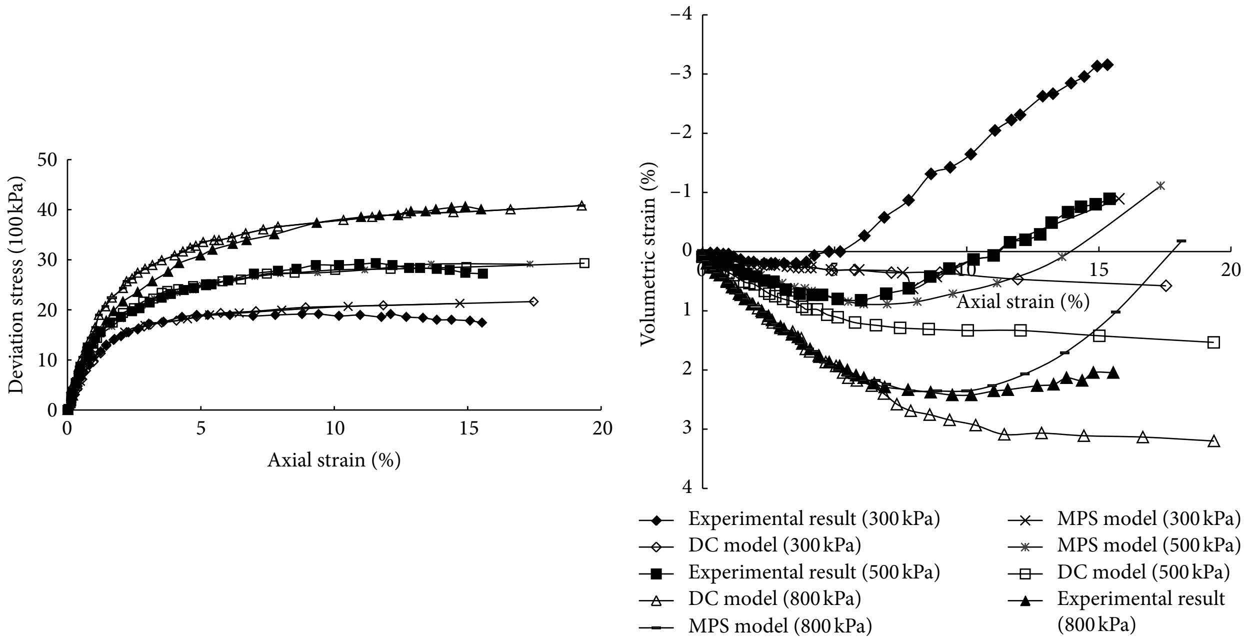

(a) (b)

Figure 2: Calculation and test results for triaxial test of rockfill material.

$$\mu_t = \frac{G - Flg(\sigma_3/P_a)}{(1 - A^*)^2}, \tag{65a}$$

$$A^* = \frac{D(\sigma_1 - \sigma_3)}{KP_a(\sigma_3/P_a)^n\left[1 - R_f(1 - \sin\phi)(\sigma_1 - \sigma_3)/(2c\cos\phi + 2\sigma_3\sin\phi)\right]}, \tag{65b}$$

where c is the cohesion of the soil, ϕ is the friction angle of the soil, P_a is the atmospheric pressure, 100 kPa; K, K_{ur}, n, R_f, G, F, and D are parameters.

The parameters in the calculation are taken as $c = 0$ kPa, $\phi = 38^\circ$, $K = 1116$, $K_{ur} = 1500$, $n = 0.65$, $R_f = 0.88$, $F = 0$, and $D = 0$, which are the same for both the DC and MPS models. The value of G for the DC model is taken as 0.45 while for the MPS model it is 0.8, which is larger than 0.5. Although the calculation results for deviation stress are identical for the two models, the MPS model can reproduce the dilation of soil. Because of the limitation that $\mu_t < 0.5$ in the DC model, the dilatation of soil is not revealed and $\varepsilon_v < 0$ is not achieved.

Figure 2 shows the calculation and test results of consolidated-drained triaxial compression test (CD test) of a rock-fill material from Hengshan Dam in China. The unit weight of the material is 20.7 kN/m^3. The confining pressures were 300, 500, and 800 kPa, respectively.

The parameters for E_t are $c = 178$ kPa, $\phi = 40.4^\circ$, $K = 1915$, $K_{ur} = 2490$, $n = 0.18$, and $R_f = 0.85$, which are also the same for both the DC and MPS models. μ_t in the DC model is still calculated using (65a) and (65b), and $G = 0.6$, $F = 0.37$, and $D = 0.023$ in the calculation, while μ_t in the MPS model is calculated using the method proposed by Shen and Zhang [38],

$$\mu_t = \frac{1}{2} - c_d\left(\frac{\sigma_3}{P_a}\right)^{n_d}\frac{E_i R_f}{(\sigma_1 - \sigma_3)_f}\frac{1 - R_d}{R_d} \times \left(1 - \frac{R_f S_l}{1 - R_f S_l}\frac{1 - R_d}{R_d}\right), \tag{66a}$$

$$E_i = KP_a\left(\frac{\sigma_3}{P_a}\right)^n, \tag{66b}$$

in which $S_l = (\sigma_1 - \sigma_3)/(\sigma_1 - \sigma_3)_f$; $(\sigma_1 - \sigma_3)_f$ is the deviation stress at failure, $(2c\cos\phi + 2\sigma_3\sin\phi)/(1 - \sin\phi)$; c_d, n_d, and R_d are parameters; $c_d = 0.000224$, $n_d = 2.24$, and $R_d = 0.85$ in the calculation.

Again, the calculation results for deviation stress are identical for the two models, while the MPS model reproduces the dilatation of soil giving better results than the DC model. Obviously, more appropriate results of volumetric strain can be acquired using the MPS model if we improve the calculation method of μ_t. However, this is impossible for the DC model due to the limitation that μ_t cannot exceed 0.5 for the nonlinear elastic model.

9. Conclusions

The main tasks in establishing the constitutive equations for geomaterials are the determination of stress-strain relations in principal stress/strain space and the coordinate transformation of the relationship from principal stress/strain space to general coordinate space. The stress (or strain) and stress increment (or strain increment) in principal stress/strain space is expressed as a vector in a potential field in traditional elastic potential theory and plastic potential theory. However, the vector can be expressed more generally as the gradient vector of linearly independent potential functions. Based on this framework, the traditional models can be easily transformed from stress space to strain space and can be modified in a general way. This framework can also be used to establish new models based on curve fitting. Since it investigates constitutive models from a mathematical point of view independent of the material itself and relevant physical mechanism, the framework can be potentially used in a wider range, not limited to geomaterials. However, the lack of physical insights of materials and constitutive models may also hinder its development, for example, the constitutive model based on the framework may be oversimplified. The loading-unloading criteria as well as the evolutions of internal state variables are not considered in the framework. Therefore, the current framework is mainly useful for modifying the existing models. In the next research, Lode's angle and noncoaxiality should also be investigated, and more test results are needed to make the verification.

Acknowledgments

The support of the Natural Science Foundation of China (51279085), National Basic Research Program of China (973 Program 2013CB036402), and the State Key Laboratory of Hydroscience and Engineering (sklhse-2012-D-01) is gratefully acknowledged.

References

[1] J. M. Duncan and C. Y. Chang, "Nonlinear analysis of stress and strain in soils," *ASCE Journal of the Soil Mechanics and Foundations Division*, vol. 96, no. 5, pp. 1629–1653, 1970.

[2] J. M. Duncan, P. Byren, K. Wong, and P. Mabry, "Strength, stress-strain and bulk modulous parametres for finite element analysis of stress and movements in soils masses," Tech. Rep. UCB/GT/80O01, University of California, Berkeley, Calif, USA, 1980.

[3] D. Battelino and B. Majes, "A hypoelastic model of soils accounting for failure," in *Proceedings of the 9th International Conference on Soil Mechanics and Foundation Engineering*, pp. 39–42, Tokyo, Japan, 1977.

[4] L. Domaschuk and P. Valliappan, "Nonlinear settlement analysis by finite element," *ASCE Journal of the Geotechnical Engineering Division*, vol. 101, no. 7, pp. 601–614, 1975.

[5] D. J. Naylor, "Stress-strain laws for soils," in *Developments in Soil Mechanics*, C. R. Scott, Ed., chapter 2, pp. 39–68, Applied Science, London, UK, 1978.

[6] D. C. Drucker, R. E. Gibson, and D. J. Henkek, "Soil mechanics and work hardening theories of plasticity," *ASCE Journal of the Soil Mechanics and Foundations Division*, vol. 81, no. 1, pp. 1–14, 1955.

[7] K. H. Roscoe, A. N. Schofield, and A. Thurairajah, "Yielding of clay in states wetter than critical," *Geotechnique*, vol. 13, no. 3, pp. 211–240, 1963.

[8] K. H. Roscoe and J. B. Burland, "On the generalised stress-strain behaviour of an ideal wet clay," in *Engineering Plasticity* , J. Heyman and F. A. Leckie, Eds., pp. 535–609, Cambridge University Press, Cambridge, UK, 1968.

[9] C. P. Wroth and R. H. Bassett, "A stress-strain relationship for the shearing behavior of sand," *Geotechnique*, vol. 15, no. 1, pp. 32–56, 1965.

[10] H. B. Poorooshasb, I. Holubec, and A. N. Sherbome, "Yielding and flow of sand in triaxial compression," *Canadian Geotechnical Journal*, vol. 3, no. 4, pp. 179–190, 1966.

[11] Y. P. Yao, T. Luo, D. A. Sun, and H. Matsuoka, "A simple 3-D constitutive model for both clay and sand," *Chinese Journal of Geotechnical Engineering*, vol. 24, no. 2, pp. 240–246, 2002.

[12] Y.-P. Yao, W. Hou, and A.-N. Zhou, "UH model: three-dimensional unified hardening model for overconsolidated clays," *Geotechnique*, vol. 59, no. 5, pp. 451–469, 2009.

[13] C. S. Desai and M. O. Faruque, "Constitutive model for geological materials," *Journal of Engineering Mechanics*, vol. 110, no. 9, pp. 1391–1408, 1984.

[14] C. S. Desai, S. Somasundaram, and G. Frantziskonis, "A hierarchical approach for constitutive modelling of geologic materials," *International Journal for Numerical and Analytical Methods in Geomechanics*, vol. 10, no. 3, pp. 225–257, 1986.

[15] P. V. Lade and J. M. Duncan, "Elasto-plastic stress-strain theory for cohesionless soil with curved yield surfaces," *International Journal of Solids and Structures*, vol. 13, no. 11, pp. 1019–1035, 1977.

[16] M. K. Kim and P. V. Lade, "Single hardening constitutive model for frictional materials. I. Plastic potential function," *Computers and Geotechnics*, vol. 5, no. 4, pp. 307–324, 1988.

[17] P. V. Lade and M. K. Kim, "Single hardening constitutive model for frictional materials II. Yield critirion and plastic work contours," *Computers and Geotechnics*, vol. 6, no. 1, pp. 13–29, 1988.

[18] P. V. Lade and M. K. Kim, "Single hardening constitutive model for frictional materials III. Comparisons with experimental data," *Computers and Geotechnics*, vol. 6, no. 1, pp. 31–47, 1988.

[19] Y. R. Zheng and D. J. Yan, "Multi-yield surface model for soils on the basis of test fitting," in *Computer Methods and Advances in Geotechnics*, pp. 97–104, Taylor & Francis, Boca Raton, Fla, USA, 1994.

[20] Y. F. Dafalias and L. R. Herrmann, "Bounding surface soil plasticity model," *Microstructural Science*, vol. 1, pp. 335–345, 1980.

[21] Y. F. Dafalias, "Bounding surface plasticity. I: mathematical foundation and hypoplasticity," *Journal of Engineering Mechanics*, vol. 112, no. 9, pp. 966–987, 1986.

[22] Y. Dafalias and L. R. Hermann, "Bounding surface plasticity. II: application to isotropic cohesive soils," *Journal of Engineering Mechanics*, vol. 112, no. 12, pp. 1263–1291, 1986.

[23] A. Anandarajah and Y. F. Dafalias, "Bounding surface plasticity. III: application to anisotropic cohesive soils," *Journal of Engineering Mechanics*, vol. 112, no. 12, pp. 1292–1318, 1986.

[24] K. Hashiguchi, "Subloading surface model in unconventional plasticity," *International Journal of Solids and Structures*, vol. 25, no. 8, pp. 917–945, 1989.

[25] K. Hashiguchi and Z.-P. Chen, “Elastoplastic constitutive equation of soils with the subloading surface and the rotational hardening,” *International Journal for Numerical and Analytical Methods in Geomechanics*, vol. 22, no. 3, pp. 197–227, 1998.

[26] Z. P. Bazant, “Endochronic inelasticity and incremental plasticity,” *International Journal of Solids and Structures*, vol. 14, no. 9, pp. 691–714, 1978.

[27] C. S. Desai and J. Toth, “Disturbed state constitutive modeling based on stress-strain and nondestructive behavior,” *International Journal of Solids and Structures*, vol. 33, no. 11, pp. 1619–1650, 1996.

[28] G. H. Yang, “Building the generalized plastic potential theory in constitutive relation of soils,” in *Proceedings of the 3rd National Conference on the Numerical Analysis and Analytical Method for Rock and Soil Mechanics*, pp. 140–148, Zhuhai, China, 1988.

[29] G. H. Yang, “A law for the general form of tensor in the constitutive equation of the soil and rock materials,” in *Proceedings of the Theory and Application of Water Power and Structure Engineering*, pp. 315–321, Dalian, China, 1993.

[30] G. H. Yang, “Study on the mathematical constitutive theory of soils,” in *Proceedings of the 3rd National Young Scholar Conference on Rock and Soil Mechanics Engineering*, pp. 100–112, Dalian, China, 1995.

[31] G. H. Yang, “A new strain space elasto-plastic constitutive model for soils,” in *Proceedings of the 2nd international conference on soft soil engineering*, pp. 255–262, Nanjing, China, 1996.

[32] W. Zhou, Y. Liu, and J. Zhao, “Multi-potential based discontinuous bifurcation model for jointed rock masses and its application,” *Computer Methods in Applied Mechanics and Engineering*, vol. 192, no. 33-34, pp. 3569–3584, 2003.

[33] A. Zhou and T. Lu, “Elasto-plastic constitutive model of soil-structure interface in consideration of strain softening and dilation,” *Acta Mechanica Solida Sinica*, vol. 22, no. 2, pp. 171–179, 2009.

[34] A. Anandarajah, K. Sobhan, and N. Kuganenthira, “Incremental stress-strain behavior of granular soil,” *ASCE Journal of the Geotechnical Engineering Division*, vol. 121, no. 1, pp. 57–68, 1995.

[35] H. Matsuoka and T. Nakai, “Stress-strain relationship of soil based on the ‘SMP’,” in *Proceedings of the 9th International Conference on Soil Mechanics and Foundation Engineering*, pp. 153–162, Tokyo, Japan, 1977.

[36] T. Nakai and H. Matsuoka, “Constitutive equation for soils based on the extended concept of “Spatial Mobilized Plane” and its application to finite element analysis,” *Soils and Foundations*, vol. 23, no. 4, pp. 87–105, 1983.

[37] J. T. H. Wu, “Predicting performance of the Denver walls: general report,” in *Proceedings of the International Symposium on Soft Geosynthetic-Reinforced Soil Retaining Walls*, Balkema A. A., Tokyo, Japan, November 1992.

[38] Z. J. Shen and W. M. Zhang, “Analysis of effective stress and movements of Lubuge dam,” in *Numerical Methods in Geomechanics: Innsbruck 1988*, Balkema A.A., Rotterdam, The Netherlands, 1988, Proceeding of the 6th International Conference on Numerical Methods in Geomechanics, Innsbruck, Austria.

Hindawi Publishing Corporation
Journal of Applied Mathematics
Volume 2013, Article ID 784583, 19 pages
http://dx.doi.org/10.1155/2013/784583

Research Article

Bending Moment Calculations for Piles Based on the Finite Element Method

Yu-xin Jie, Hui-na Yuan, Hou-de Zhou, and Yu-zhen Yu

State Key Laboratory of Hydroscience and Engineering, Tsinghua University, Beijing 100084, China

Correspondence should be addressed to Yu-xin Jie; jieyx@tsinghua.edu.cn

Received 17 March 2013; Accepted 1 June 2013

Academic Editor: Fayun Liang

Using the finite element analysis program ABAQUS, a series of calculations on a cantilever beam, pile, and sheet pile wall were made to investigate the bending moment computational methods. The analyses demonstrated that the shear locking is not significant for the passive pile embedded in soil. Therefore, higher-order elements are not always necessary in the computation. The number of grids across the pile section is important for bending moment calculated with stress and less significant for that calculated with displacement. Although computing bending moment with displacement requires fewer grid numbers across the pile section, it sometimes results in variation of the results. For displacement calculation, a pile row can be suitably represented by an equivalent sheet pile wall, whereas the resulting bending moments may be different. Calculated results of bending moment may differ greatly with different grid partitions and computational methods. Therefore, a comparison of results is necessary when performing the analysis.

1. Introduction

As the finite element method (FEM) develops, pile foundations are increasingly being analyzed using FEM [1–8]. Solid elements are used to simulate soil or rock in geotechnical engineering. Other structures embedded in soil such as piles, cut-off walls, and concrete panels are also often simulated with solid elements. However, internal force and bending moment are generally used for engineering design. So it is necessary to calculate the bending moment with stress and displacement obtained using FEM.

Theoretically, the following two methods are both appropriate.

(a) Calculating Bending Moment with Stress. The bending moment is directly calculated by summing the total moments of the elements across the specified pile section. When using this method, sufficient grids are necessary to partition the pile section.

(b) Calculating Bending Moment with Displacement. The bending moment is indirectly calculated using the quadratic differential of deflection (lateral displacement) of the pile. This method uses fewer grids, but the differential process will result in reduced accuracy.

The bending moment can also be obtained by integrating the area of the shear force diagram [9] which is a complex process and is not considered in this paper.

As we know, shear locking occurs in first-order (linear) fully integrated elements that are subjected to bending, while second-order reduced-integration elements can yield more reasonable results in this case and are often used in the analysis of piles subjected to lateral pressure [1–4, 10]. However, calculating second-order elements is time consuming and increases complexity and computational effort, particularly when the problem involves contact conditions. So we consider that the linear element method with appropriate meshing is still useful for the analysis of piles.

A row of piles can be simplified as a plane strain wall (sheet pile wall) and modeled using 2D plane strain elements [11–13]. This simplification can greatly reduce computational effort. However, the influence of bending moment on the computational results merits further research.

In this paper, a series of calculations on cantilever beam, pile, and sheet pile wall examples were conducted to study the abovementioned problems. The main aim of the work was to

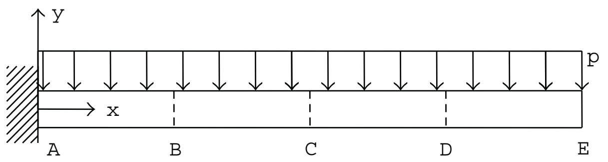

Figure 1: Cantilever beam.

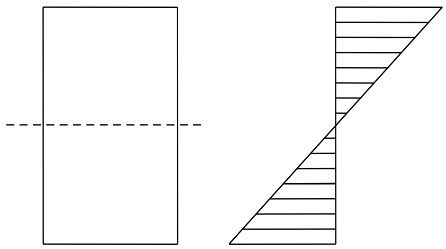

Figure 2: Computing of bending moment with stress.

Table 1: Deflection error with element CPS4.

Mesh	Deflection error (%)			
	B	C	D	E
1 × 32	−28.57	−28.69	−28.74	−28.76
4 × 32	−27.20	−27.31	−27.34	−27.36
8 × 32	−27.12	−27.23	−27.27	−27.29
16 × 32	−27.10	−27.22	−27.25	−27.27
32 × 32	−27.10	−27.21	−27.25	−27.26
1 × 64	−10.67	−10.83	−10.89	−10.92
4 × 64	−8.45	−8.61	−8.66	−8.68
8 × 64	−8.32	−8.48	−8.54	−8.57
16 × 64	−8.29	−8.45	−8.54	−8.54
32 × 64	−8.28	−8.45	−8.50	−8.53
64 × 64	−8.28	−8.44	−8.50	−8.53
1 × 128	−4.70	−4.87	−4.93	−4.97
4 × 128	−2.12	−2.31	−2.37	−2.40
8 × 128	−1.97	−2.17	−2.23	−2.27
16 × 128	−1.94	−2.13	−2.20	−2.23
32 × 128	−1.93	−2.13	−2.19	−2.23
64 × 128	−1.93	−2.13	−2.19	−2.22
128 × 128	−1.92	−2.13	−2.19	−2.22
2 × 4	−95.94	−95.94	−95.93	−95.92
2 × 8	−85.66	−85.68	−85.68	−85.67
2 × 16	−60.03	−60.08	−60.09	−60.09
2 × 32	−27.50	−27.60	−27.63	−27.65
2 × 64	−8.93	−9.08	−9.12	−9.15
2 × 128	−2.69	−2.86	−2.91	−2.94
2 × 256	−0.99	−1.16	−1.22	−1.25

investigate the computational methods for bending moment and the influences of element type and mesh partition. Hence, no interface element was introduced, that is, the pile was assumed to be fully attached to the soil, and the soil and pile were both assumed to have linear elastic behavior.

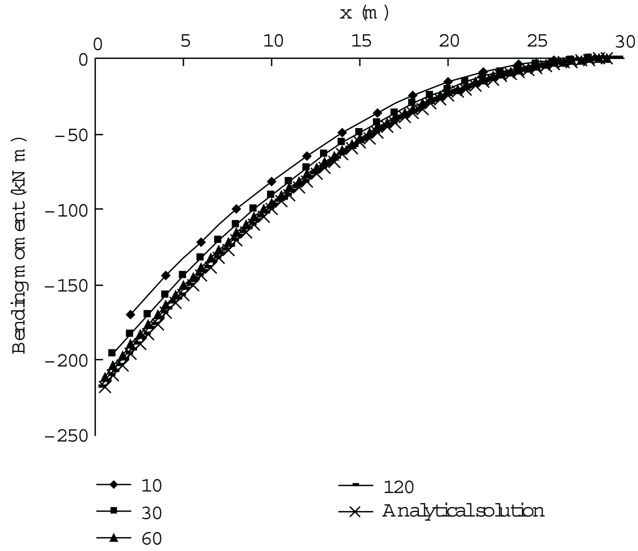

Figure 3: Calculation versus analytical solution of bending moment.

Table 2: Deflection error with element CPS8R.

Mesh	Deflection error (%)			
	B	C	D	E
1 × 32	0.15	0.05	0.01	−0.01
2 × 32	0.33	0.15	0.09	0.05
4 × 32	0.38	0.18	0.11	0.07
8 × 32	0.40	0.19	0.12	0.08
1 × 64	0.27	0.12	0.07	0.04
2 × 64	0.36	0.17	0.10	0.07
4 × 64	0.39	0.18	0.12	0.08
8 × 64	0.40	0.19	0.12	0.08

2. Cantilever Beam Example

2.1. Analytical Solution. The cantilever beam example is shown in Figure 1. The width of the square beam is 1 m. The length L is 30 m. A distributed load $p = 0.5$ kPa is applied to the beam. The analytical solution equations are

$$M = \frac{1}{2}p(L-x)^2, \tag{1a}$$

$$\omega = \frac{pL^4}{2EI}\left(\frac{k^2}{2} - \frac{k^3}{3} + \frac{k^4}{12}\right), \tag{1b}$$

where M = bending moment, x = the position coordinate, $k = x/L$, E = the Young's modulus, I = the moment of inertia, $\omega = -u_y$ is the deflection of the beam, and u_y = displacement in the y direction.

The beam parameters are taken as Young's modulus $E = 2 \times 10^4$ MPa and Poisson's ratio $\nu = 0.17$ in the computation. The element used in the FEM is the 4-node first-order plane stress element (CPS4). The following two methods were used to calculate the bending moment.

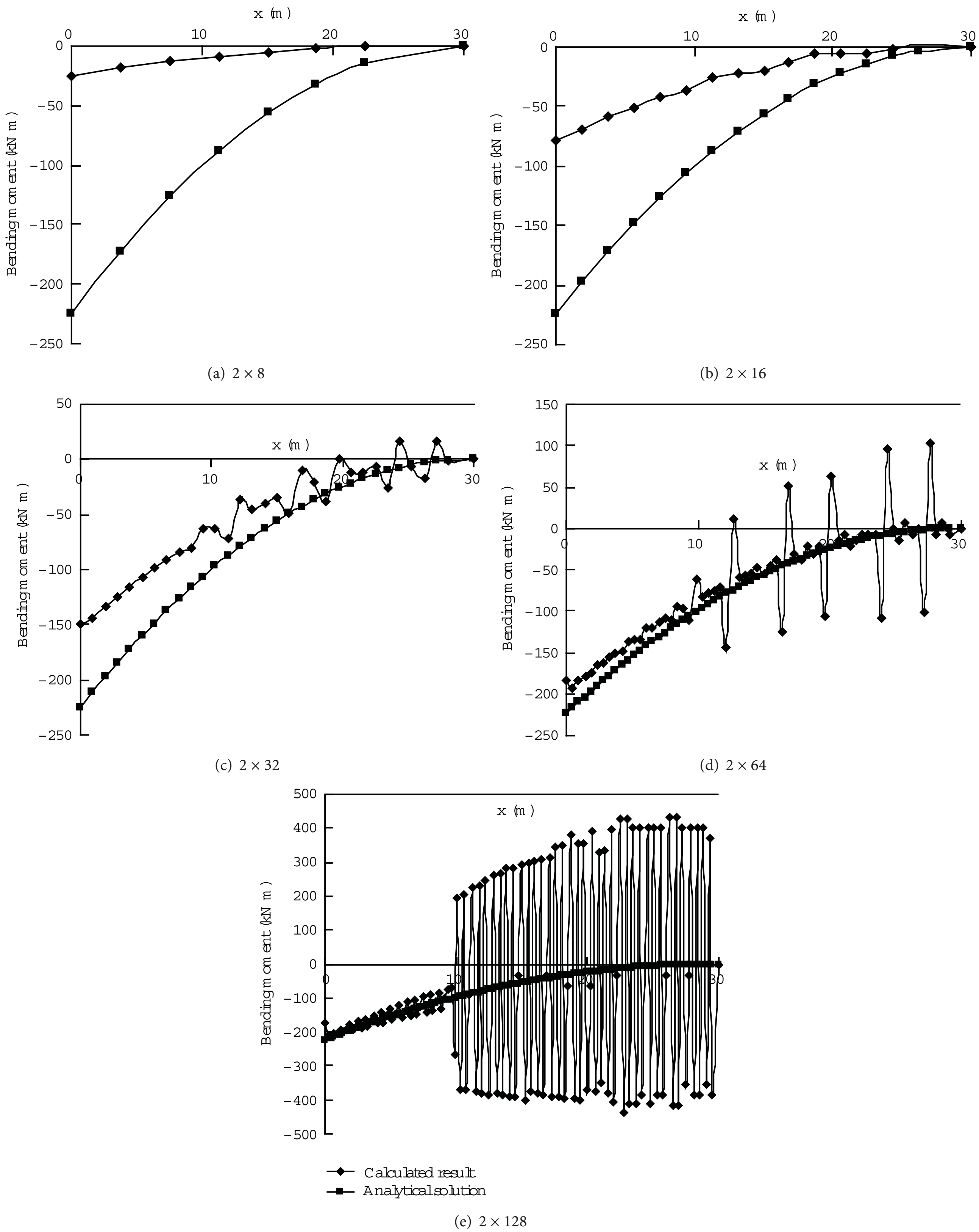

Figure 4: Bending moment calculated with displacement (with CPS4).

Table 3: Bending moment error (%).

Element type	Mesh	Computed with stress			Computed with displacement		
		B	C	D	B	C	D
CPS4	2 × 8	−89.19	−88.99	−88.02	−89.99	−91.72	−95.28
	2 × 16	−70.02	−69.89	−69.22	−66.44	−65.26	−57.81
	2 × 32	−45.73	−45.67	−45.37	−32.89	−36.96	−59.74
	2 × 64	−31.89	−31.87	−31.78	−13.19	−3.40	−620.48
	2 × 128	−27.25	−27.24	−27.22	−24.98	−620.48	−3143.38
	4 × 64	−14.42	−14.40	−14.27			
	8 × 64	−10.03	−10.01	−9.87			
	16 × 64	−8.93	−8.91	−8.77			
	4 × 128	−8.56	−8.55	−8.52			
	8 × 128	−3.86	−3.85	−3.81			
	16 × 128	−2.68	−2.67	−2.64			
CPS8R	2 × 32	−33.25	−33.15	−32.59			
	2 × 64	−33.31	−33.28	−33.11			
	2 × 128	−33.32	−33.31	−33.24			
	4 × 64	−6.65	−6.63	−6.52			
	8 × 64	−1.57	0.02	0.09			

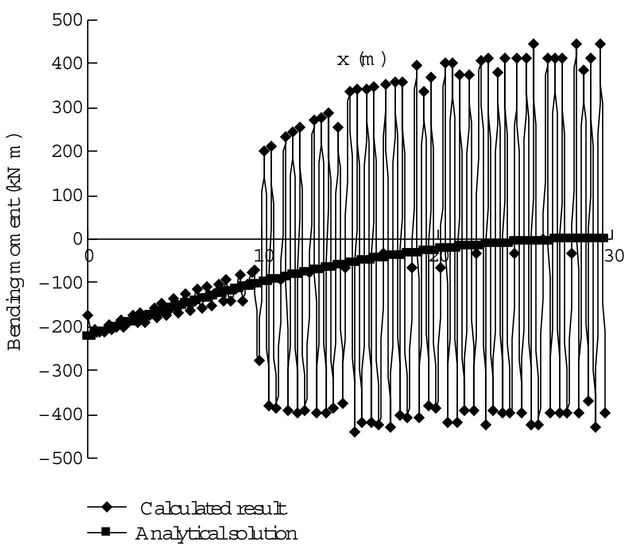

Figure 5: Bending moment calculated with displacement (2 × 64, with CPS8R).

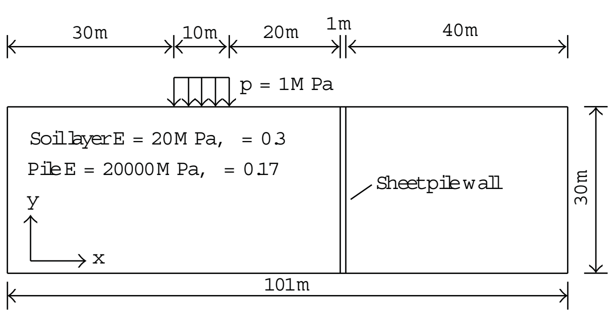

Figure 6: A sheet pile wall subjected to surface load.

Table 4: Horizontal displacement of the wall (with CPE8R).

Item	Horizontal displacement
U_m (m)	0.03647
U_t (m)	−0.00528

Table 5: Calculated bending moment in the wall (with CPE8R).

Item	Computed with displacement	Computed with stress
M_b (kN·m)	2939.947	2650.037
M_m (kN·m)	−906.667	−902.366

(a) Calculating Bending Moment with Stress. The bending moment was directly computed with the normal stress on the cross-section (see Figure 2):

$$M = \sum \sigma_i A_i l_i, \tag{2}$$

where σ_i = normal stress at the centroid of the element, A_i = corresponding area of the element, and l_i = distance between the centroid and the midline of the beam section.

(b) Calculating Bending Moment with Displacement. The bending moment was calculated using the following quadratic differential of deflection [14]:

$$M = EI\frac{d^2\omega}{dx^2}. \tag{3}$$

Equation (3) can be transformed into a difference scheme, and the bending moment was calculated by the difference operation of lateral displacement. Figure 3 is the comparison of the computed bending moment with analytically exact results, where ω is calculated using (1b) with the number of

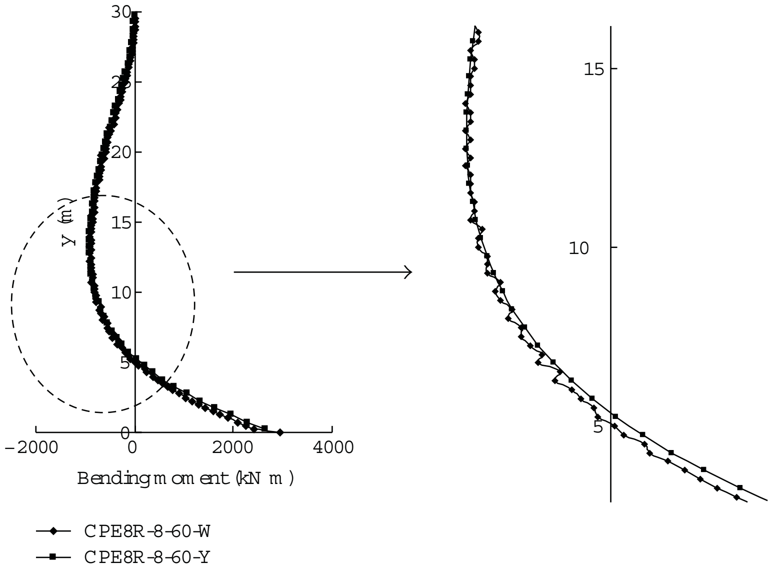

Figure 7: Bending moment calculated with element CPE8R.

Table 6: Calculated horizontal displacement of the wall (with CPE4).

Item	Grid number along the length	Grid number across wall section: 2 Displacement (m)	2 Error (%)	4 Displacement (m)	4 Error (%)	8 Displacement (m)	8 Error (%)
U_m	15	0.02875	−21.16	0.02835	−22.25	0.02825	−22.52
	30	0.03475	−4.71	0.03411	−6.47	0.03395	−6.89
	60	0.03673	0.74	0.03601	−1.24	0.03584	−1.72
U_t	15	−0.00144	−72.71	−0.00122	−76.86	−0.00117	−77.88
	30	−0.00450	−14.71	−0.00420	−20.48	−0.00412	−21.90
	60	−0.00541	2.49	−0.00509	−3.63	−0.00501	−5.14

Table 7: Calculated bending moment in the wall (with CPE4).

Item		Grid number along the length	Grid number across wall section: 2 Bending moment (kN·m)	2 Error (%)	4 Bending moment (kN·m)	4 Error (%)	8 Bending moment (kN·m)	8 Error (%)
M_b	Computed with stress	15	1096.813	−58.61	1335.297	−49.61	1393.136	−47.43
		30	1714.913	−35.29	2052.434	−22.55	2133.281	−19.50
		60	2073.363	−21.76	2454.809	−7.37	2546.233	−3.92
	Computed with displacement	15	1073.083	−63.50	1048.292	−64.34	1042.292	−64.55
		30	1966.567	−33.11	1880.900	−36.02	1860.867	−36.70
		60	2724.200	−7.34	2521.400	−14.24	2478.267	−15.70
M_m	Computed with stress	15	−535.650	−40.64	−658.054	−27.07	−687.977	−23.76
		30	−657.713	−27.11	−805.006	−10.79	−840.821	−6.82
		60	−694.513	−23.03	−850.134	−5.79	−887.903	−1.60
	Computed with displacement	15	−690.833	−23.81	−679.167	−25.09	−676.667	−25.37
		30	−851.667	−6.07	−840.000	−7.35	−836.667	−7.72
		60	−900.000	−0.74	−886.667	−2.21	−886.667	−2.21

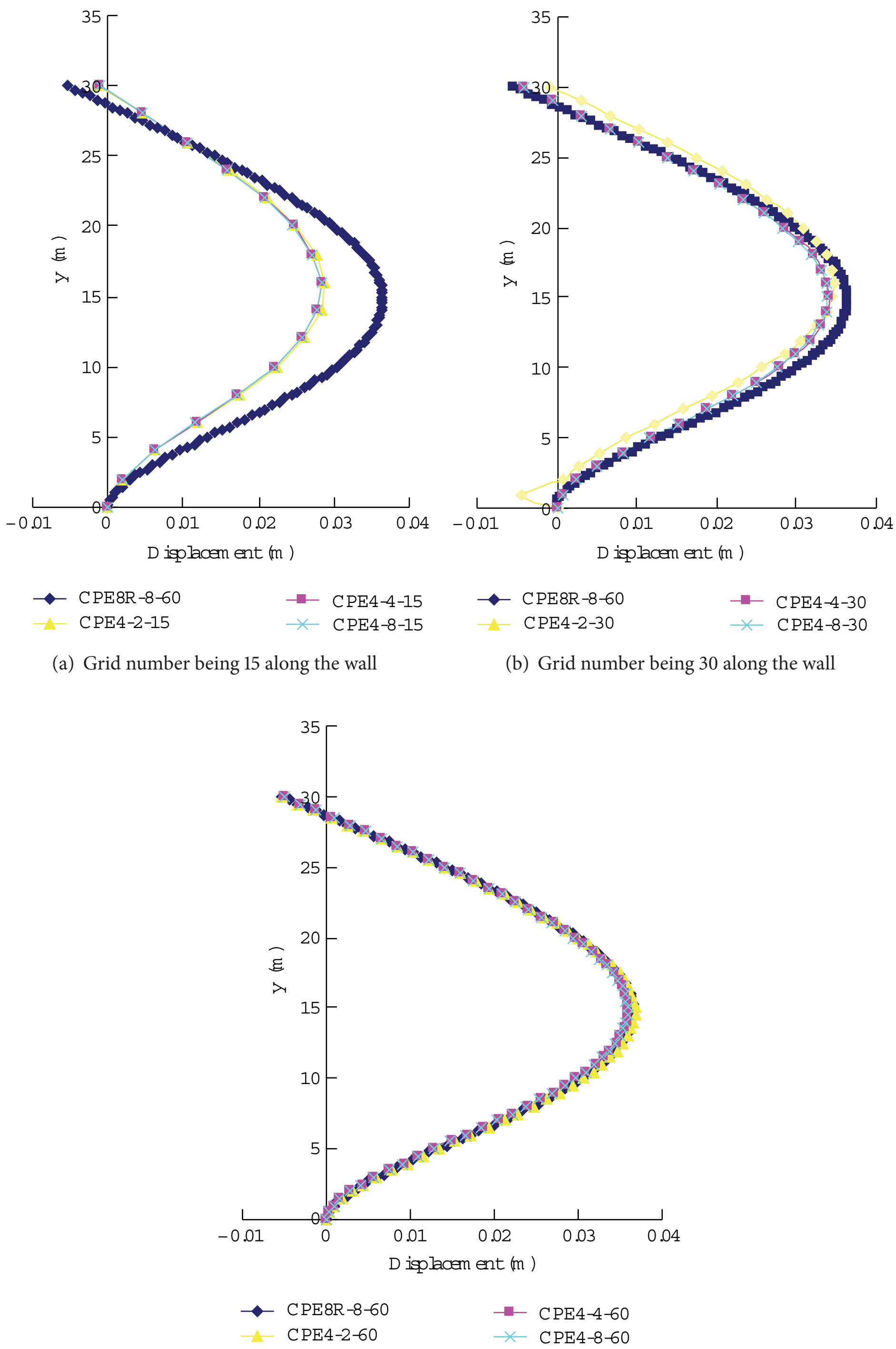

(a) Grid number being 15 along the wall

(b) Grid number being 30 along the wall

(c) Grid number being 60 along the wall

Figure 8: Comparison of horizontal displacements.

interpolation points being 10, 30, 60, and 120. This shows that the method used here achieved a good result for the bending moment.

2.2. Errors in Displacement and Bending Moment. We used several meshes to do the computation. Grids along the length of the beam were 32, 64, and 128 (in the x direction, see Figure 1). Sectional partitions were 1, 2, 4, 8, 16, and 32. Two element types, CPS4 and the 8-node reduced-integration element (CPS8R), were employed in the analysis. The results are shown in Tables 1, 2, and 3 and in Figures 4 and 5, where the term $m \times n$ denotes that there are m grids along the y direction and n grids along the x direction; B, C, D, and E are positions for error calculation (see Figure 1).

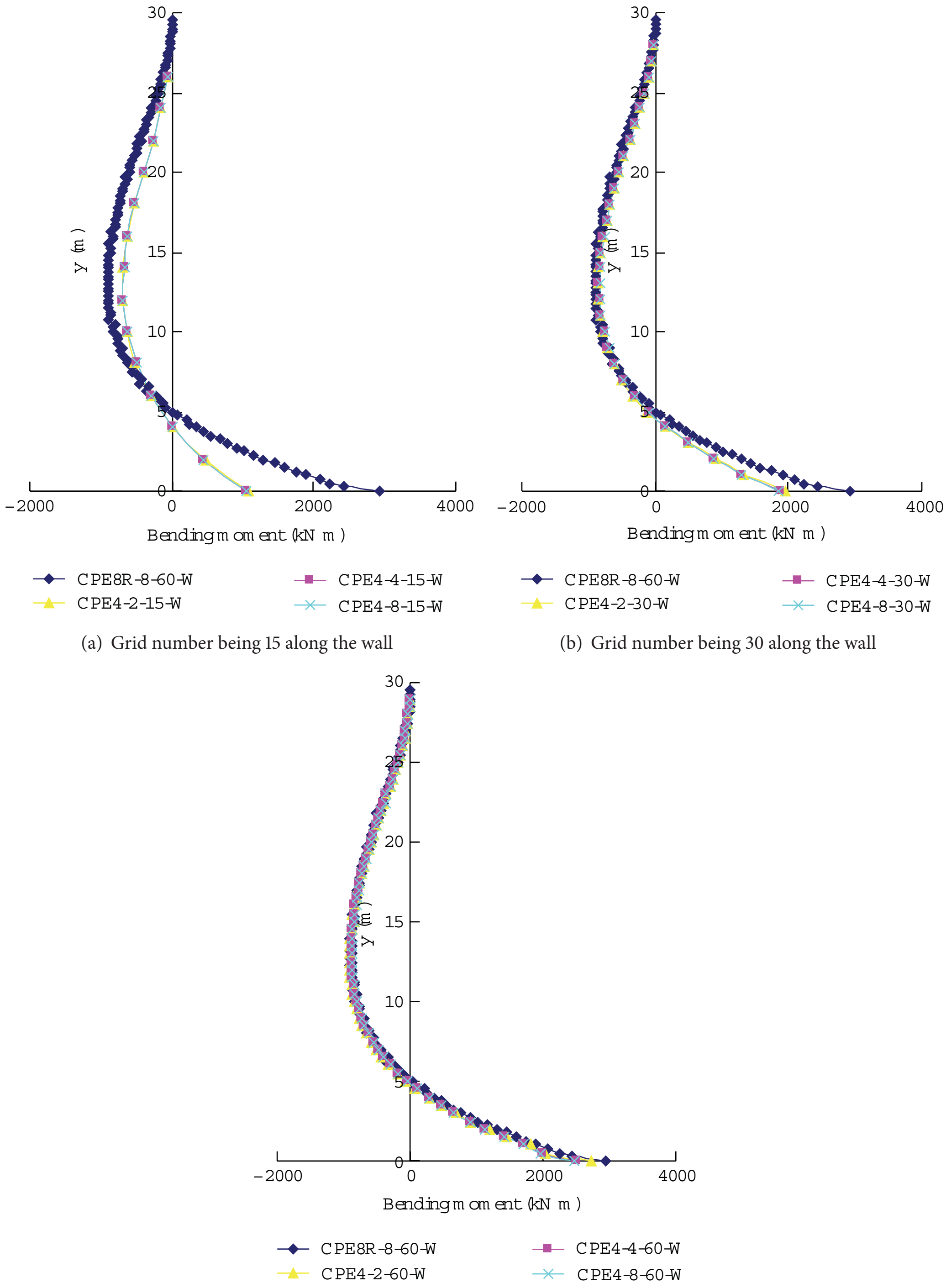

(a) Grid number being 15 along the wall

(b) Grid number being 30 along the wall

(c) Grid number being 60 along the wall

FIGURE 9: Comparison of bending moments calculated with displacement.

The errors in the tables are defined as

$$\varepsilon_\omega = \frac{\omega_c - \omega}{\omega} \times 100\,(\%)\,, \tag{4a}$$

$$\varepsilon_M = \frac{M_c - M}{M} \times 100\,(\%)\,, \tag{4b}$$

where ε_ω = relative error of deflection, ε_M = relative error of bending moment, ω_c = calculated deflection using FEM, ω = analytically exact deflection from (1b), M_c = calculated bending moment using FEM, and M = analytically exact bending moment from (1a).

From Table 1, we can see that the deflection using CPS4 is smaller than the analytical solution, which implies that the

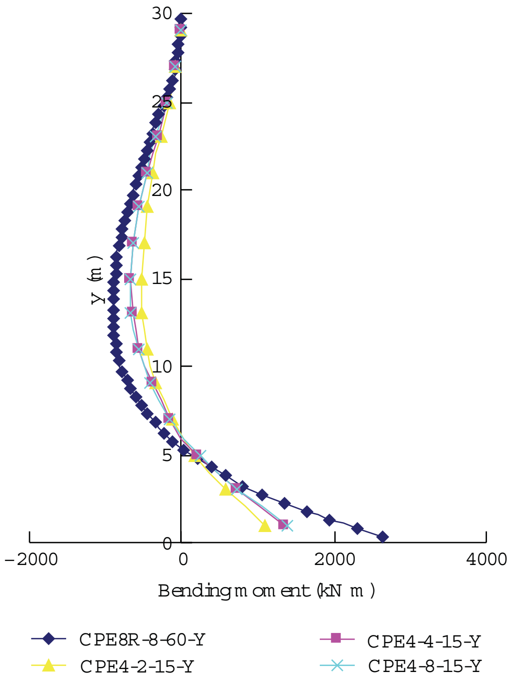

(a) Grid number being 15 along the wall

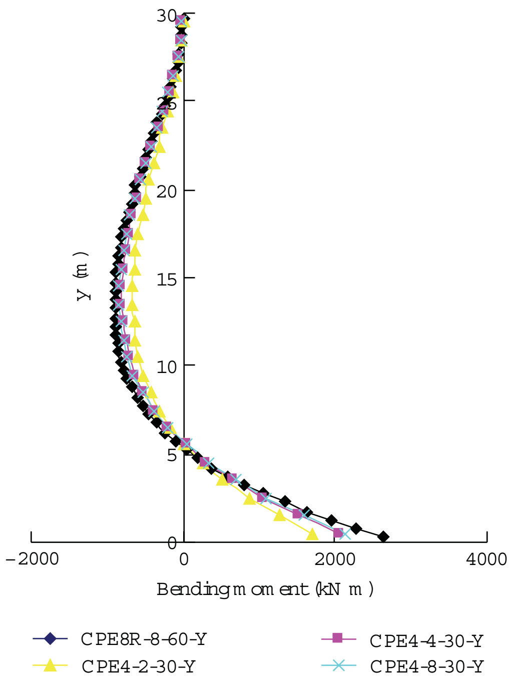

(b) Grid number being 30 along the wall

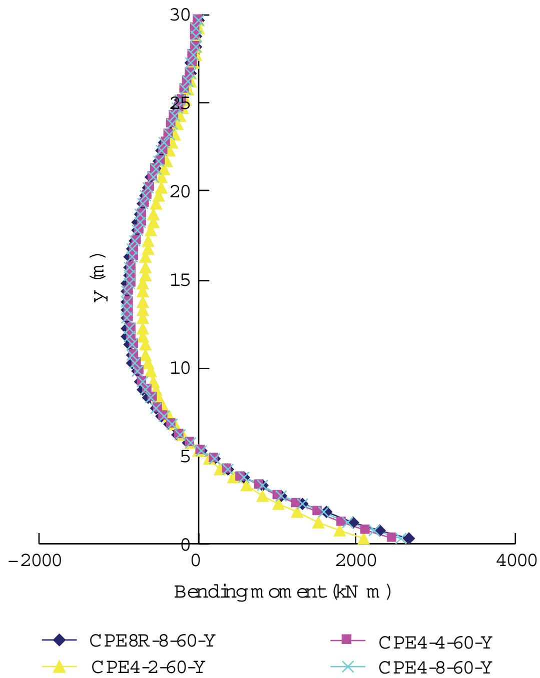

(c) Grid number being 60 along the wall

FIGURE 10: Comparison of bending moments calculated with stress.

shear locking occurs with the first-order element. Shear locking can be easily overcome with second-order reduced-integration elements, that is, using fewer grids can produce approximately the same results (see Table 2).

Although using the rectangular first-order element induces shear locking in the beam, we can still obtain a good result with sufficient partitions along the length of the beam; if we partition the beam lengthways in 128 elements, the relative error can be smaller than 3% (see Table 1).

Table 3 and Figure 4 show the computational results of bending moment for the first-order element. They indicate

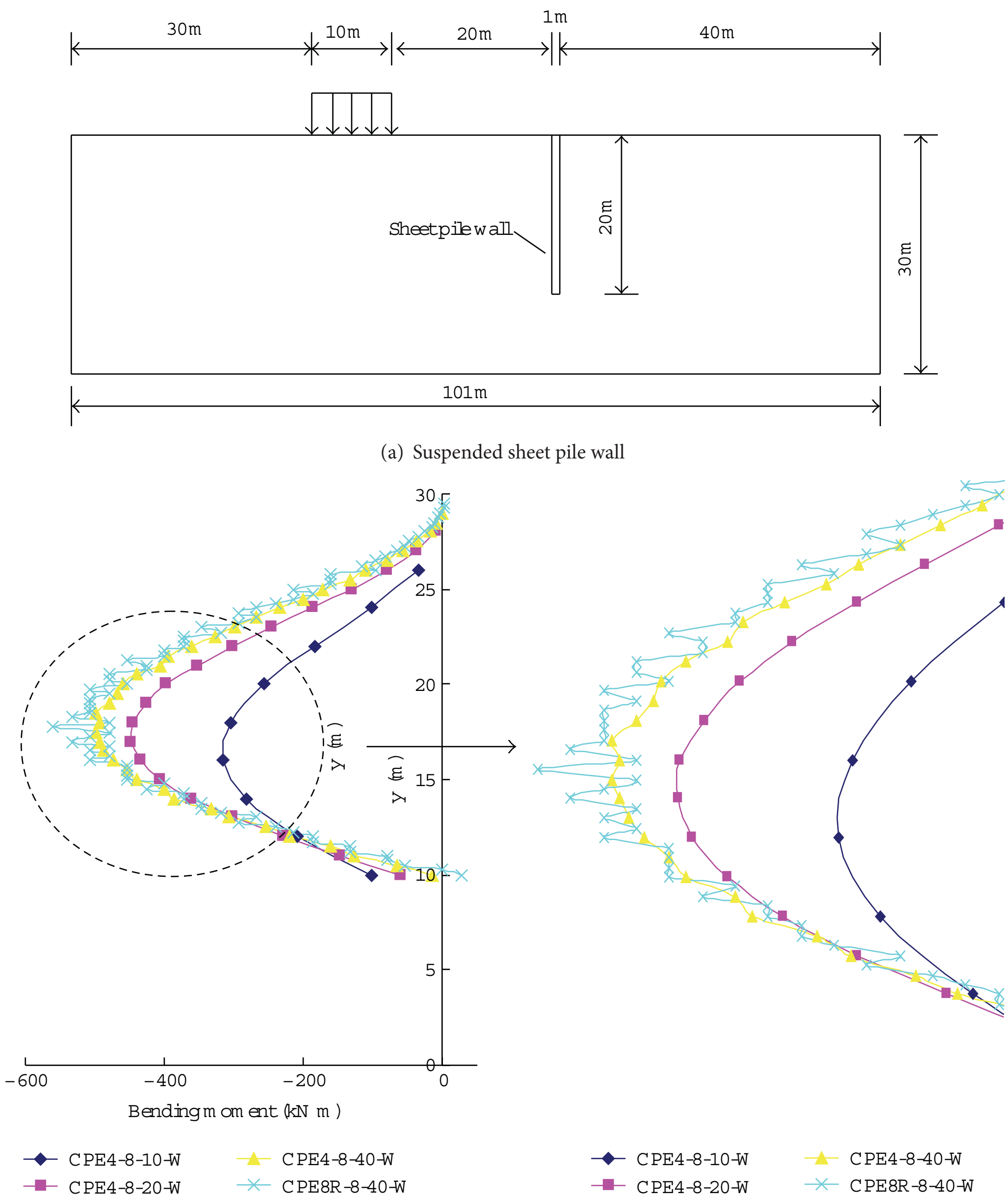

(a) Suspended sheet pile wall

(b) Bending moments along the wall

FIGURE 11: Bending moments calculated with displacement for suspended sheet pile wall.

that if the bending moment is to be calculated with stress, sufficient partitions across the cross-section are necessary. Fluctuation can lead to unreliable results when bending moment is calculated with displacement. The effect of variation is even stronger when increasing the grid density. The reason may be that the loss of accuracy occurs for each difference operation and the initial small error will be greatly magnified after two operations.

A similar calculation of bending moment was done using CPS8R. Figure 5 shows even more notable variation occurring for the bending moments calculated with displacement.

TABLE 8: Horizontal displacement of the pile (with C3D20R).

Item	Horizontal displacement (m)
U_m	0.045113
U_t	−0.007570

TABLE 9: Calculated bending moment in the pile (with C3D20R).

Item	Computed with displacement	Computed with stress
M_b (kN·m)	3967.200	4706.848
M_m (kN·m)	−1146.667	−1101.314

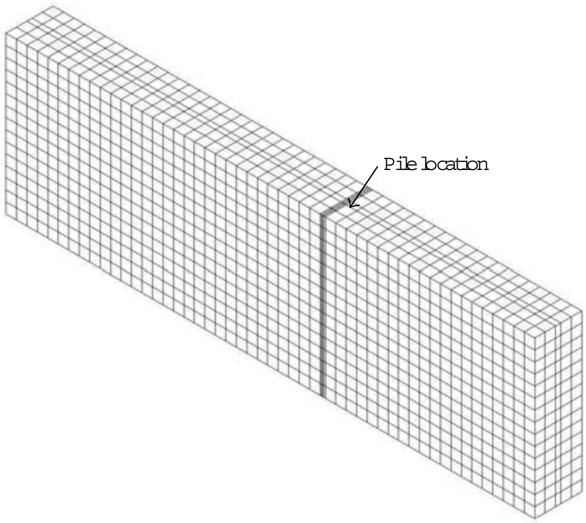

Figure 12: 3-D finite element mesh.

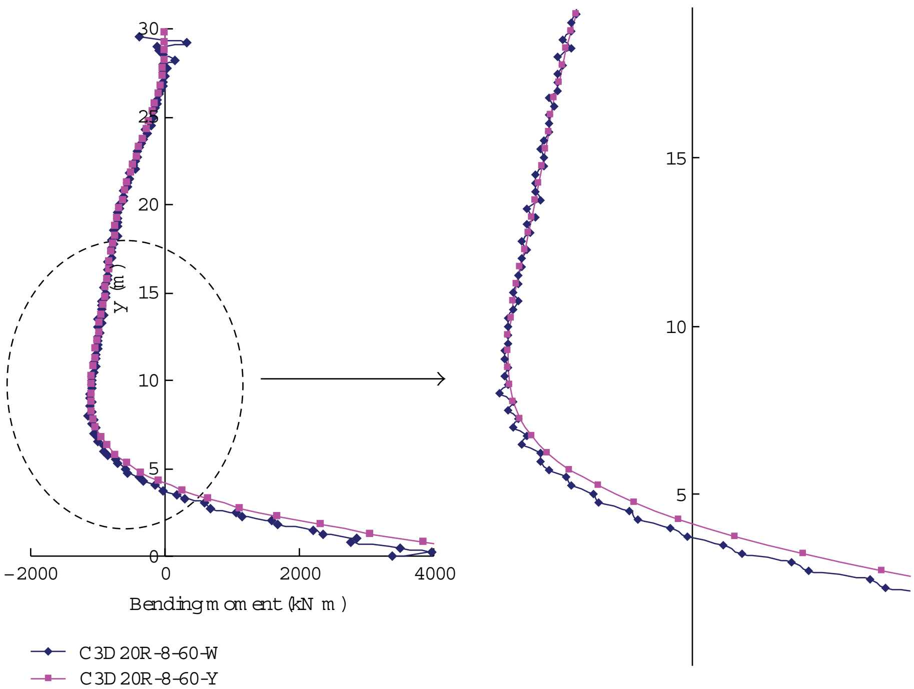

Figure 13: Bending moment calculated with element C3D20R.

Table 10: Calculated horizontal displacement of the pile (with C3D8).

Item	Grid number along the length	Grid number across pile section: 2 Displacement (m)	2 Error (%)	4 Displacement (m)	4 Error (%)	8 Displacement (m)	8 Error (%)
U_m	15	0.042865	−4.98	0.042764	−5.21	0.042740	−5.26
	30	0.044506	−1.35	0.044408	−1.56	0.044384	−1.62
	60	0.044896	−0.48	0.044796	−0.70	0.044774	−0.75
U_t	15	−0.006532	−13.71	−0.006488	−14.29	−0.006478	−14.43
	30	−0.007278	−3.85	−0.007238	−4.38	−0.007229	−4.51
	60	−0.007452	−1.56	−0.007414	−2.06	−0.007405	−2.17

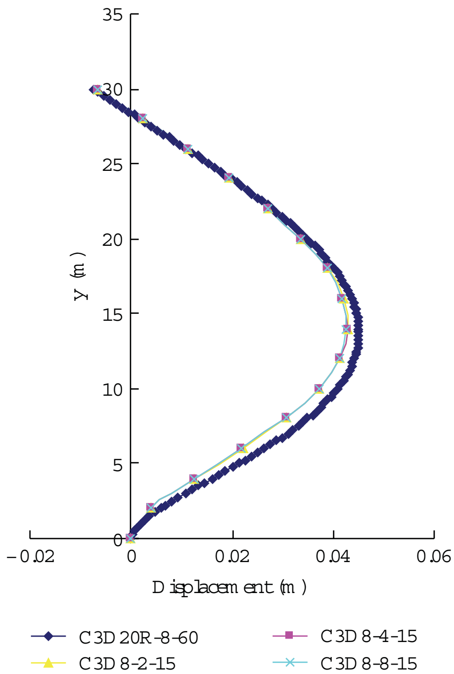

(a) Grid number being 15 along the pile shaft

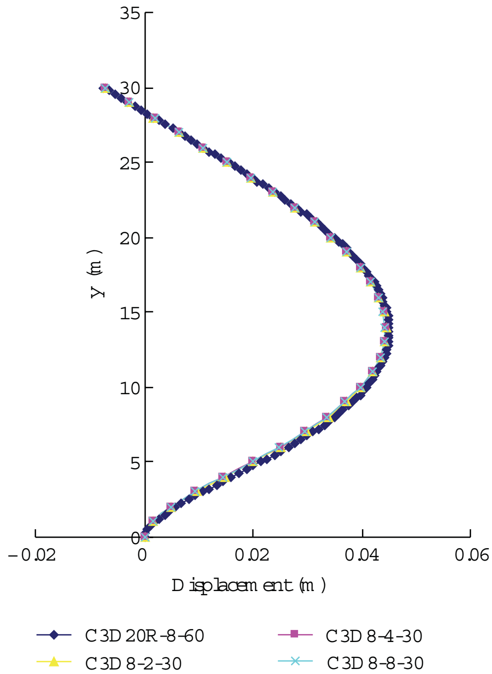

(b) Grid number being 30 along the pile shaft

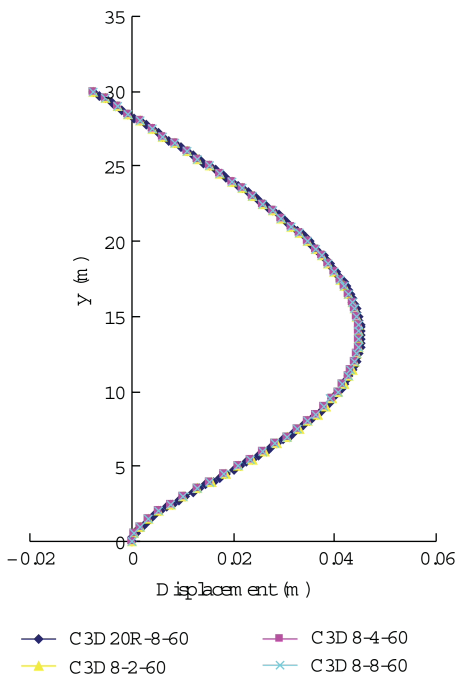

(c) Grid number being 60 along the pile shaft

FIGURE 14: Comparison of horizontal displacements.

3. 2D Analysis of a Sheet Pile Wall

Figure 6 shows a sheet pile wall subjected to a load $p = 1$ MPa. The bottom of the domain and the pile tip are fully restrained from moving in any direction while both sides of the domain are restrained in the x direction, while free in the y direction. The length of the pile is the same as that of the above beam, 30 m, and the width is 1 m. We used different mesh partitions to do the calculation with the rectangular first-order element (CPE4).

Since there is no analytical solution for this problem, referring to the above analysis of the cantilever beam, the results using a grid partition of 8×60, the 8-node plane strain element, reduced integration (CPE8R) were considered as

Table 11: Calculated bending moment in the pile (with C3D8).

Item		Grid number along the length	Grid number across pile section					
			2		4		8	
			Bending moment (kN·m)	Error (%)	Bending moment (kN·m)	Error (%)	Bending moment (kN·m)	Error (%)
M_b	Computed with stress	15	2184.875	−53.58	2668.929	−43.30	2787.809	−40.77
		30	3172.975	−32.59	3831.406	−18.60	3992.286	−15.18
		60	3793.750	−19.40	4545.541	−3.43	4729.851	0.49
	Computed with displacement	15	1881.417	−52.58	1863.667	−53.02	1859.417	−53.13
		30	3248.333	−18.12	3179.000	−19.87	3163.000	−20.27
		60	4082.267	2.90	3933.733	−0.84	3895.867	−1.80
M_m	Computed with stress	15	−816.513	−25.86	−1004.993	−8.75	−1051.735	−4.50
		30	−847.748	−23.02	−1041.848	−5.40	−1089.858	−1.04
		60	−858.825	−22.02	−1053.395	−4.35	−1102.111	0.07
	Computed with displacement	15	−1063.333	−7.27	−1060.000	−7.56	−1059.583	−7.59
		30	−1108.333	−3.34	−1105.000	−3.63	−1103.333	−3.78
		60	−1126.667	−1.74	−1126.667	−1.74	−1120.000	−2.33

Table 12: Soil layers and parameters.

No.	Soil layer	Elevation of layer top (m)	Elevation of layer bottom (m)	Poisson's ratio ν	Young's modulus (MPa)
1	Muck	−5.3	−7.2	0.35	1.0
2	Mucky soil	−7.2	−24.2	0.40	1.0
3	Silty fine sand	−24.2	−36.3	0.25	10
4	Clay	−36.3	−54.1	0.33	10
5	Clay	−54.1	−56.6	0.33	25
6	Medium sand	−56.6	−62.2	0.25	30
7	Clay	−62.2	−71.4	0.3	30
8	Clay	−71.4	−77.2	0.3	30
9	Clay	−77.2	−86.1	0.3	30
10	Clay	−86.1	−120.0	0.3	50

"exact." The displacement at the top of the wall, U_t, and the maximum displacement in the middle, U_m, are shown in Table 4. The bending moment at the tip of the wall, M_b, and the maximum bending moment in the middle, M_m, are shown in Table 5. Figure 7 shows the distribution of bending moment calculated along the wall. Though a small variation occurs in the bending moment distribution calculated with displacement (CPE8R-8-60-W), it is quite close to that calculated with stress (CPE8R-8-60-Y).

The calculated results using CPE4 are presented in Tables 6 and 7 and Figures 8, 9, and 10. The relative errors in the tables are relevant to those calculated with CPE8R. We find that the displacements calculated with first-order elements are smaller than those with 8-node elements, reduced-integration, whereas the values are close if they have the same partition (8×60) along the height of the wall, which implies that the shear locking is not distinct as for the cantilever beam. The bending moments calculated with displacement approximate those with stress and have insignificant variation. However, if the wall is suspended in the soil, obvious variation occurs for the element CPE8R as shown in Figure 11.

4. Pile Examples

4.1. 3D Analysis of a Pile. Figure 12 shows a pile and its surrounding soil in 3D view. The length of the pile is 30 m, and the width of the square pile is 1 m, which is also the same as that of the above-mentioned beam. The width of the computational domain is 9 m. The applied load, material properties, and boundary conditions are the same as those of the above-mentioned sheet pile wall.

3-D analyses were made with different mesh partitions of the pile shaft. The results with a grid partition of 8×60, a 20-node brick element and reduced integration (C3D20R) were considered as "exact". Displacement at the top of the pile, U_t, and maximum displacement in the middle, U_m, are shown in Table 8, while the bending moment at the tip of the pile, M_b, and maximum bending moment in the middle, M_m, are shown in Table 9. Figure 13 is the distribution of moment calculated along the pile. Again, the moment calculated with displacement (C3D20R-8-60-W) is close to that calculated with stress (C3D20R-8-60-Y) and insignificant variation is found.

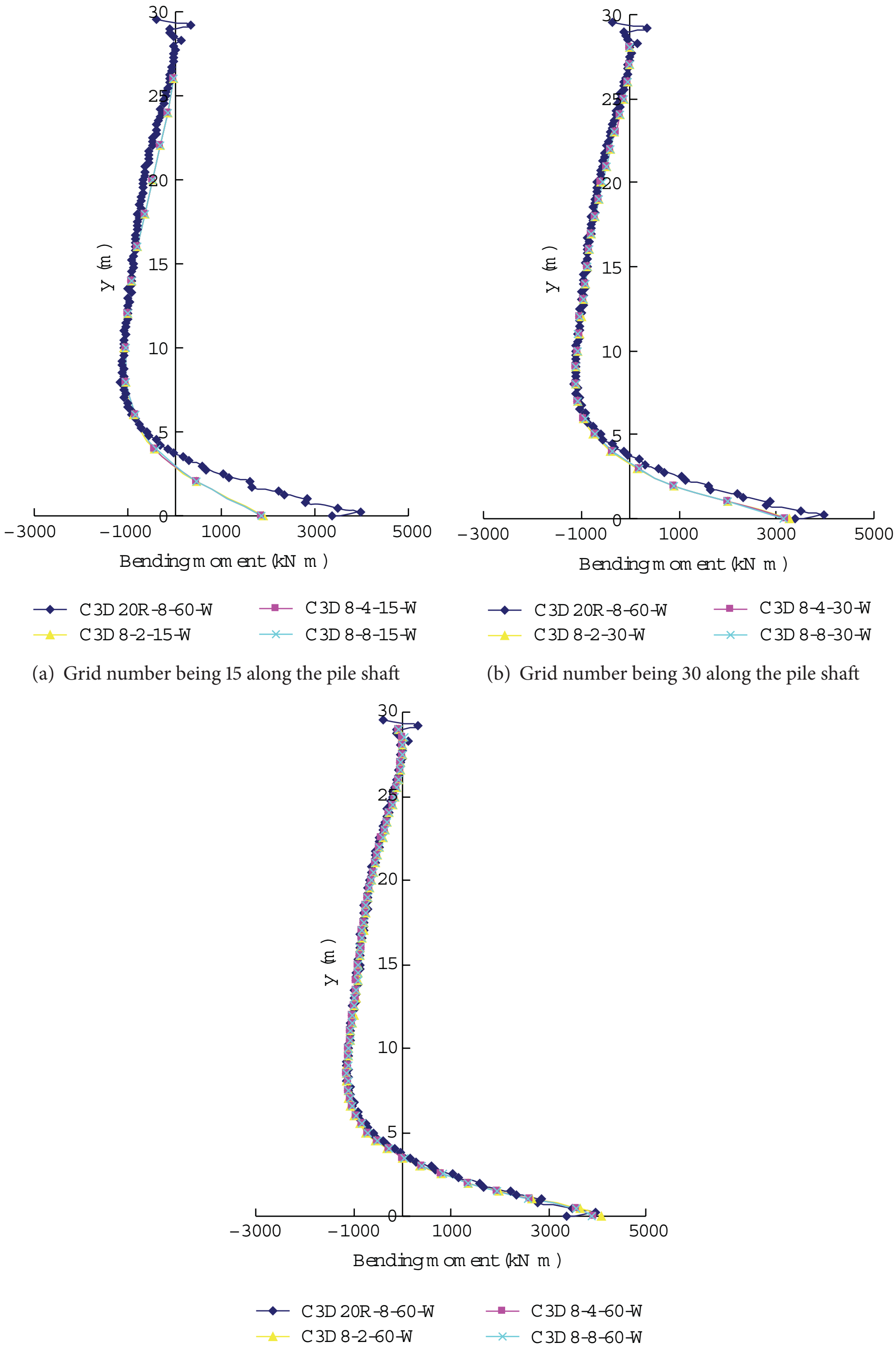

(a) Grid number being 15 along the pile shaft

(b) Grid number being 30 along the pile shaft

(c) Grid number being 60 along the pile shaft

Figure 15: Comparison of bending moments calculated with displacement.

The calculation results with first-order element (C3D8) are presented in Tables 10 and 11 and Figures 14, 15, and 16. The relative errors in the tables are relevant to those calculated with C3D20R. As before, displacements calculated with first-order elements are smaller than those with C3D20R and the values are close if they have the same partition (8×60) along the length of the pile. Bending moments calculated with displacement approximate those with stress and have insignificant variation. This indicates that the response of the pile is similar to that of the above-mentioned wall for displacement and bending moment computations.

4.2. 3-D Analysis of Piles for a Bridge Abutment. Figure 17 shows the cross-section of the piles of a bridge and a polder

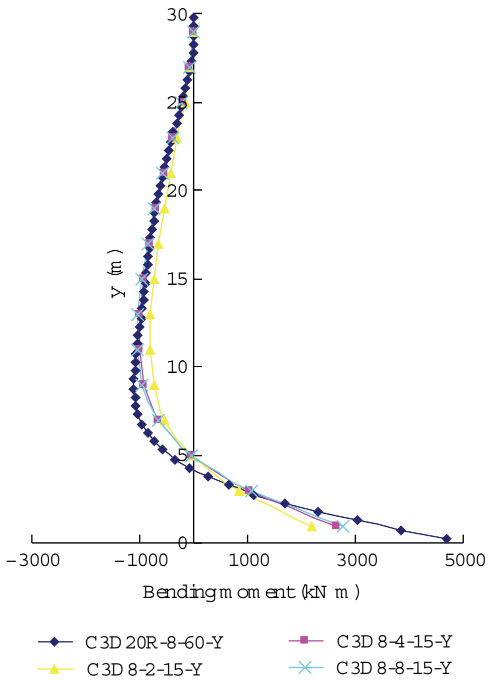

(a) Grid number being 15 along the pile shaft

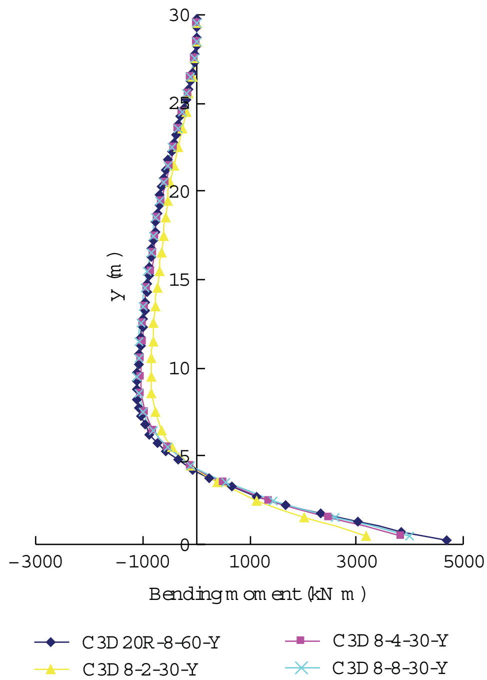

(b) Grid number being 30 along the pile shaft

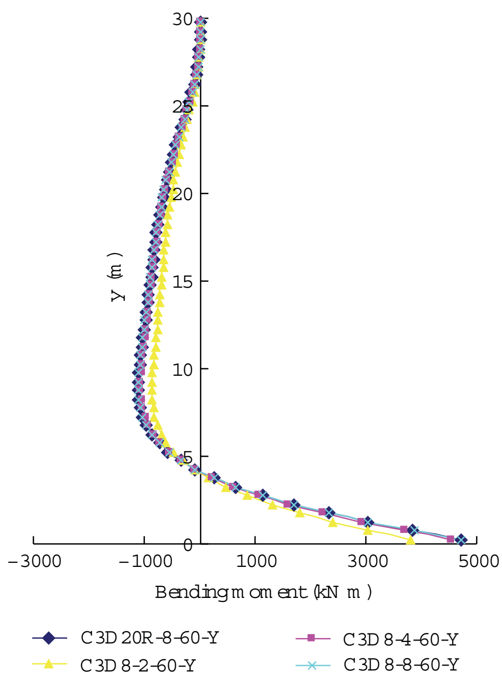

(c) Grid number being 60 along the pile shaft

FIGURE 16: Comparison of bending moments calculated with stress.

dike. Figure 18 shows one of the meshes for the computation. The length of the computational domain is 700 m and the width is 60 m, which equals the abutment span. The elevation of the ground surface is −5.3 m, the elevation of the bottom of the domain is −120 m, and the elevation of the pile tip is −90 m. Each round pile is represented by an equivalent square pile with a width of 1.33 m, and the four piles are connected by a pile cap (see Figure 18(b)). The flyash is filled to 4.63 m (see Figure 17).

The weight of the dike and the flyash was simulated with a distributed load acting on the ground surface, respectively. The effective unit weight of the dike is 18 kN/m^3 above the water level and 11 kN/m^3 below the water level. The effective unit weight of the flyash is 13.5 kN/m^3 and 5.9 kN/m^3, respectively.

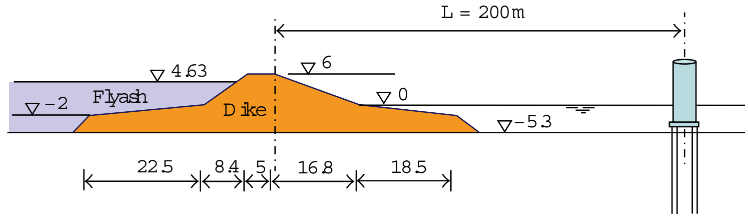

FIGURE 17: Cross-section of the piles of a bridge and a polder dike (in m).

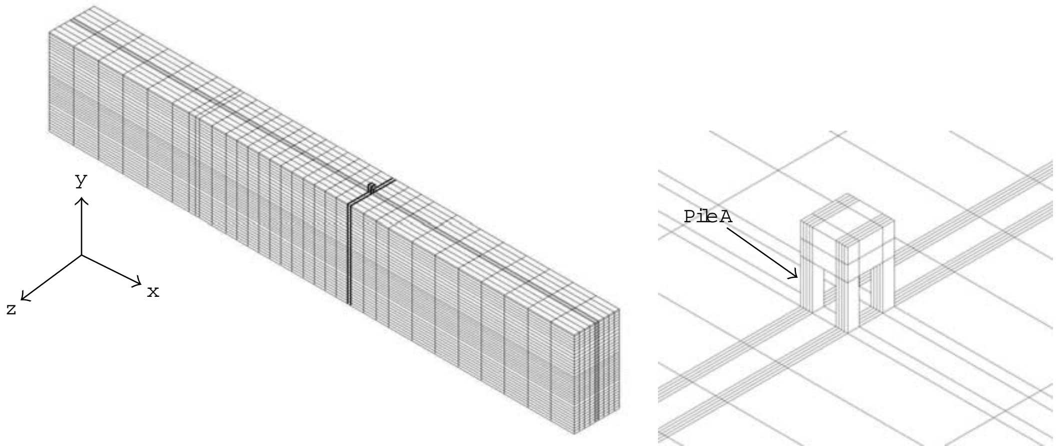

(a) Computation domain

(b) Meshes for piles

FIGURE 18: 3-D finite element mesh for the piles.

Again, linear elastic model was used to simulate the soil and the pile. The parameters of the soil strata are presented in Table 12, while Young's modulus and Poisson's ratio for the pile are the same as those of the above-mentioned sheet pile wall.

Five meshes (M1 to M5) were used to make the computation. The partitions of the piles and the total number of elements and nodes in each mesh are listed in Table 13. Mesh M3 has the most number of elements and nodes and the most grids (4×42) for the pile. Again, the results for M3, a 20-node brick element with reduced integration (C3D20R-M3), were considered as "exact" to calculate the relative errors.

The calculated displacements with different meshes and element types are presented in Table 14 and the distributions are shown in Figure 19. The results agree closely with each other, that is, with fewer linear elements, one can achieve satisfactory displacement results.

Figure 20 shows the distribution of bending moment with C3D20R-M3. As a whole, the moment calculated with displacement (C3D20R-M3-W) is similar to that calculated with stress (C3D20R-M3-Y). However, notable variation occurs for the moment calculated with displacement, particularly at the upper part of the pile.

Figure 21 shows the bending moment calculated with stress obtained from element type C3D8 and meshes M1, M2, M3, and M5. Mesh M4 has no partition across the pile section so we cannot calculate the bending moment. It is obvious that the results for M3 and M2 are closer to that of C3D20R-M3 than for M1 and M5. Mesh M5 has only two grids across the pile section, and the moment calculated for M5 is unreliable and quite different from other results.

Figure 22 shows the bending moment calculated with displacement. It is found that unlike C3D20R, the distribution has insignificant variation for the linear element (C3D8) with different meshes and agrees closely with each other, which implies that calculations with linear elements may produce fewer and smaller fluctuations than high-order elements in this case.

4.3. 2-D Analysis of a Pile Row. Generally, a pile row can be replaced by a sheet pile wall with stiffness chosen as the average of the pile stiffness and that of the soil between the piles [11–13],

$$EI = E_p I_p + E_s I_s, \tag{5}$$

where E = equivalent modulus of the sheet pile wall, I = moment of inertia of the sheet pile wall, E_p, E_s = Young's moduli of the pile and the soil, respectively, and I_p, I_s = moments of inertia of the pile and the soil, respectively.

If the piles are at a spacing of u and each pile is squared with a width of d, the equivalent modulus can be

$$E = \frac{E_p d + E_s (u - d)}{u}. \tag{6}$$

Table 13: Meshes for the analysis.

Item	C3D20R-M3	C3D8-M1	C3D8-M2	C3D8-M3	C3D8-M4	C3D8-M5
Element number	22620	9541	15855	22620	13497	14283
Node number	99996	11208	18264	25824	15600	16488
Grids for pile	4 × 42	4 × 16	4 × 26	4 × 42	1 × 26	2 × 26
CPU-time (s)	1451.8	67.1	132.6	217.5	124.0	121.0

Table 14: Calculated horizontal displacement of pile A.

Item		At elevation of −5.3 m	At elevation of −90 m
C3D20R-M3	Displacement (m)	0.02024	0.00642
C3D8-M1	Displacement (m)	0.020093	0.006339
	Error (%)	−0.71	−1.22
C3D8-M2	Displacement (m)	0.019967	0.006355
	Error (%)	−1.33	−0.96
C3D8-M3	Displacement (m)	0.019897	0.006368
	Error (%)	−1.68	−0.77
C3D8-M4	Displacement (m)	0.019971	0.006355
	Error (%)	−1.31	−0.96
C3D8-M5	Displacement (m)	0.019967	0.006355
	Error (%)	−1.33	−0.97

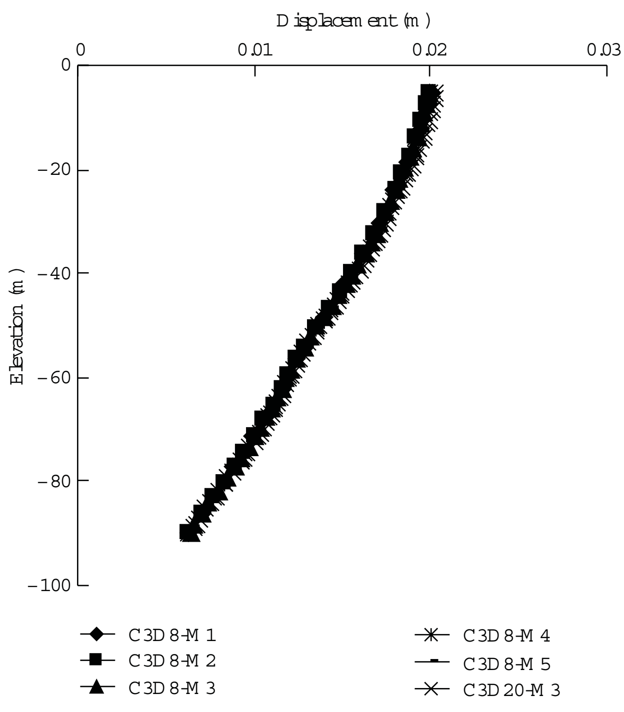

Figure 19: Comparison of horizontal displacements.

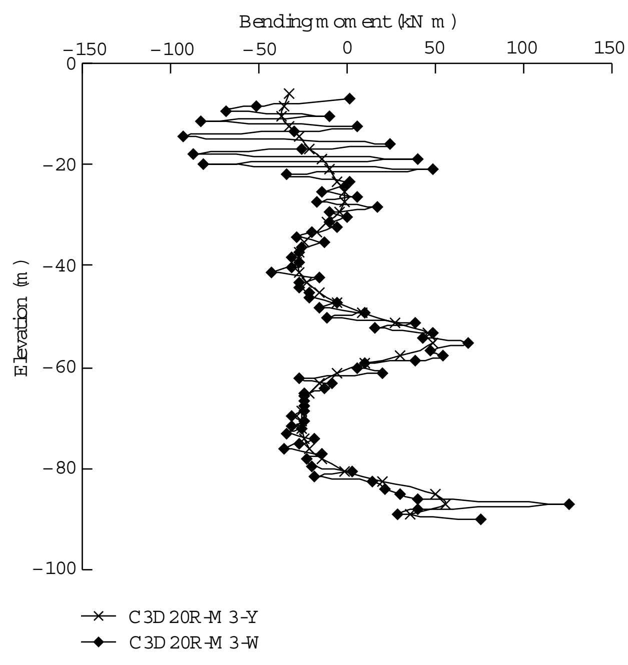

Figure 20: Bending moment calculated with element C3D20R.

In the analysis, the spacing of the pile row was assumed to be $u = 2$ m, 9 m, 100 m, and 1000 m. Other parameters are the same as those of the above analyses. The configurations are shown in Figures 6 and 12. As in the preceding studies, the grid partition for the pile shaft was 8×60. The computational results are shown in Figure 23 and Tables 15 and 16, in which "-D" denotes that the 2-D analysis was conducted with the equivalent modulus of the piles and ($\times E_p/E$) denotes that the bending moment was modified by multiplying by E_p/E. It is found that the calculated displacements of the "equivalent sheet pile wall" are in close agreement with that of the pile row. However, the results for the bending moment show some difference, particularly at the fixed tip of the pile.

Table 15: Comparison of horizontal displacements calculated by 2-D and 3-D analyses.

Pile spacing	2 m		9 m		100 m		1000 m	
Element type	CPE4-D	C3D8	CPE4-D	C3D8	CPE4-D	C3D8	CPE4-D	C3D8
U_m (m)	0.04008	0.04016	0.04391	0.04477	0.04543	0.04575	0.04608	0.04575
U_t (m)	−0.00675	−0.00672	−0.00776	−0.007405	−0.00782	−0.00732	−0.00766	−0.00732

Table 16: Comparison of bending moments by 2-D and 3-D analyses ($u = 9$ m).

Element type	CPE4-D-W (EI)	CPE4-D-W (E_pI_p)	C3D8-W	CPE4-D-Y	CPE4-D-Y ($\times E_p$/E)	C3D8-Y
M_b (kN·m)	4422.84	4387.73	3895.87	636.48	5682.86	4729.85
M_m (kN·m)	−1061.76	−1053.33	−1120.00	−117.02	−1044.83	−1102.11

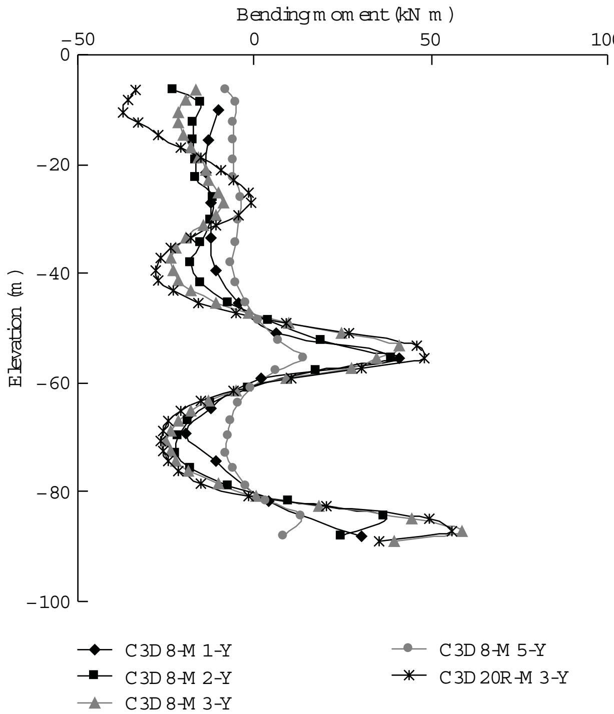

Figure 21: Bending moments calculated with stress.

5. Conclusions

The bending moment computational methods for piles were investigated using a series of calculation examples in this study, and the following conclusions were reached.

(1) Compared to a cantilever beam, shear locking is not significant for the passive pile embedded in soil, so higher-order elements are not always necessary for the computation. Computation with first-order (linear) elements and appropriate grid partition can produce similar good results as for higher-order elements.

(2) The number of the grids along the length of the pile plays an important role in the analysis. With an increase in grid number, the calculated displacement and bending moment are closer to theoretical results. Increasing the grid number across the pile section is helpful for increasing the accuracy of the bending moment calculated with stress, while it has insignificant influence on displacement and the related bending moment calculation.

(3) Calculating bending moment with stress can produce good results, but many grids are needed to partition the pile section. Calculating bending moment with displacement needs fewer grids across the pile section, but it may result in fluctuations of the results, especially for the cantilever beam presented in Section 2. The reason may be that the bending moment calculated with stress corresponds to the "integration" operation of stress, while the bending moment calculated with displacement corresponds to the "difference" operation of displacement. The difference operation may amplify the error, and the initial small error will be greatly magnified after two operations. Consequently, if the fluctuations of bending moment calculated with displacement are evident, it is suggested that the bending moment should be calculated with stress.

(4) When calculating the displacements of the piles, a pile row can be suitably represented by an equivalent sheet pile wall which has the same flexural stiffness per unit width as the piles and the soil it replaces. The displacements of the wall can agree closely with that of the pile row, while bending moments may differ from each other.

(5) A special attention should be given to meshing and the computational method for bending moment. Calculated results may differ greatly with different grid partitions and computational methods. Comparison of results using different meshes is necessary when performing the analysis.

It should be noted that, in order to clearly reveal the influences of element type and mesh partition, only linear elastic model was used in this study to simulate the soil and the pile. Obviously, introduction of constitutive models for the analysis of actual soil and pile will further complicate the problem, and thus, more attention should be paid to the calculation methods of bending moment.

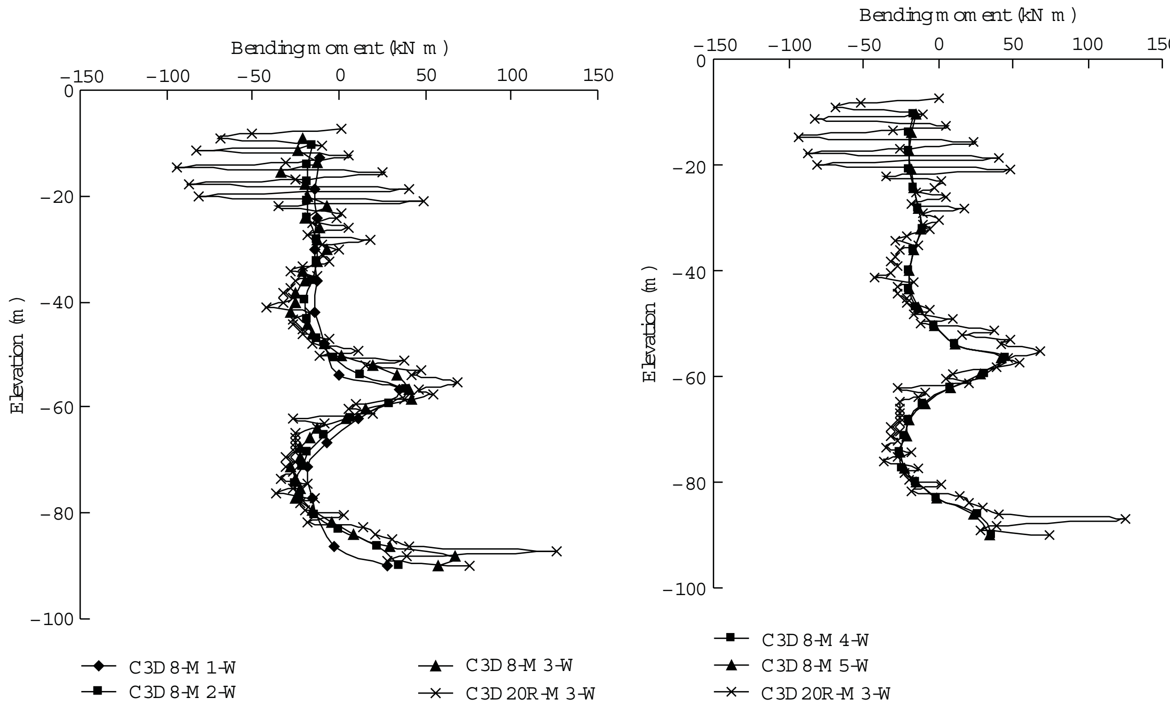

(a) With mesh M1, M2, and M3

(b) With mesh M4 and M5

FIGURE 22: Bending moments calculated with displacement.

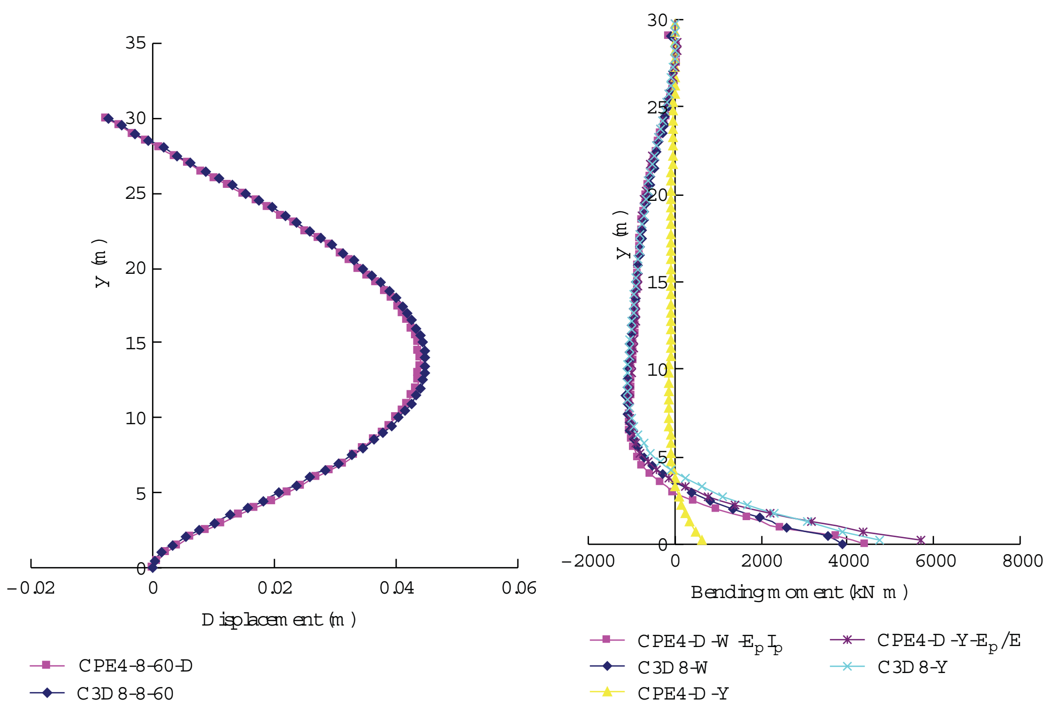

(a) Horizontal displacement

(b) Bending moment

FIGURE 23: Comparison of computational results with 2-D and 3-D analyses.

Notation

CPS4:	4-node plane stress element
CPS8R:	8-node plane stress element, reduced-integration
CPE4:	4-node plane strain element
CPE8R:	8-node plane strain element, reduced-integration
C3D8:	8-node brick element
C3D2R:	20-node brick element, reduced-integration
-m-n or $m \times n$:	Computation made with m grids across the cross-section, and n grids along the length of the pile shaft
-M1:	Computation made with mesh M1
-W:	Bending moment calculated with displacement
-Y:	Bending moment calculated with stress
-D:	Computation of the equivalent sheet pile wall made with equivalent modulus
-W-E_pI_p:	Bending moment calculated with displacement and stiffness of the pile shaft (E_pI_p)
-Y-E_p/E:	Bending moment calculated with stress and modified by multiplying by E_p/E
CPE4-m-n:	Computation made with element CPE4 and the mesh division of the pile shaft being $m \times n$
C3D8-M1:	Computation made with element C3D8 and mesh M1
U_t:	Displacement at the top of the pile
U_m:	Maximum displacement at the middle of the pile
M_b:	Bending moment at the tip of the pile
M_m:	Maximum bending moment at the middle of the pile.

Acknowledgments

The supports from the National Basic Research Program of China (973 Program 2013CB036402), the Natural Science Foundation of China (51279085), the State Key Laboratory of Hydroscience and Engineering (2013-KY-4), and the Special Scientific Research Fund of IWHR (YAN JI 1238) are gratefully acknowledged.

References

[1] M. F. Bransby and S. M. Springman, "3-D finite element modeling of pile groups adjacent to surcharge loads," *Computers and Geotechnics*, vol. 19, no. 4, pp. 301–324, 1996.

[2] L. F. Miao, A. T. C. Goh, K. S. Wong, and C. I. Teh, "Three-dimensional finite element analyses of passive pile behaviour," *International Journal for Numerical and Analytical Methods in Geomechanics*, vol. 30, no. 7, pp. 599–613, 2006.

[3] J. L. Pan, A. T. C. Goh, K. S. Wong, and A. R. Selby, "Three-dimensional analysis of single pile response to lateral soil movements," *International Journal for Numerical and Analytical Methods in Geomechanics*, vol. 26, no. 8, pp. 747–758, 2002.

[4] Z. Yang and B. Jeremić, "Numerical study of group effects for pile groups in sands," *International Journal for Numerical and Analytical Methods in Geomechanics*, vol. 27, no. 15, pp. 1255–1276, 2003.

[5] D. A. Brown and C. F. Shie, "Three dimensional finite element model of laterally loaded piles," *Computers and Geotechnics*, vol. 10, no. 1, pp. 59–79, 1990.

[6] C. S. Desai and J. T. Christian, *Numerical Methods in Geotechnical Engineering*, McGraw-Hill, New York, NY, USA, 1977.

[7] A. Muqtadir and C. S. Desai, "Three dimensional analysis of a pile-group foundation," *International Journal for Numerical and Analytical Methods in Geomechanics*, vol. 10, no. 1, pp. 41–58, 1986.

[8] J. S. Pressley and H. G. Poulos, "Finite element analysis of mechanisms of pile group behavior," *International Journal for Numerical and Analytical Methods in Geomechanics*, vol. 10, no. 2, pp. 213–221, 1986.

[9] G. R. Martin and C. Y. Chen, "Response of piles due to lateral slope movement," *Computers and Structures*, vol. 83, no. 8-9, pp. 588–598, 2005.

[10] O. C. Zienkiewicz and R. L. Taylor, *The Finite Element Method*, Elsevier, Singapore, 2005.

[11] E. A. Ellis and S. M. Springman, "Modelling of soil-structure interaction for a piled bridge abutment in plane strain FEM analyses," *Computers and Geotechnics*, vol. 28, no. 2, pp. 79–98, 2001.

[12] T. Hara, Y. Yu, and K. Ugai, "Behaviour of piled bridge abutments on soft ground: a design method proposal based on 2D elasto-plastic-consolidation coupled FEM," *Computers and Geotechnics*, vol. 31, no. 4, pp. 339–355, 2004.

[13] D. P. Stewart, R. J. Jewell, and M. F. Randolph, "Numerical modelling of piled bridge abutments on soft ground," *Computers and Geotechnics*, vol. 15, no. 1, pp. 21–46, 1993.

[14] Y. Q. Long and S. H. Bao, *Structural Mechanics Course, Advanced*, Education Press, Beijing, China, 2001.